CCI Marseille · Provence

Groupe ESIM

Proceedings of the Twelfth International

WORKSHOP ON WATER WAVES AND FLOATING BODIES

Carry-le-Rouet, 16-19 March, 1997

REPORT DOCUMENTATION PAGE

Form Approved
OMB No. 0704-0188

1. AGENCY USE ONLY *(Leave blank)*	2. REPORT DATE	3. REPORT TYPE AND DATES COVERED
	1997	Conference Proceedings 16 - 19 March 1997

4. TITLE AND SUBTITLE
Proceedings of the
Twelfth International Workshop on Water Waves and Floating Bodies

5. FUNDING NUMBERS
N00014-97-1-0517

6. AUTHOR(S)
B. Molin, Editor

7. PERFORMING ORGANIZATION NAME(S) AND ADDRESS(ES)
Mr. B. Molin
Groupe Ecole Superieure, d'Ingenieurs de Marseille
Department Genie Mer, IMT-Technopole de Chateau-Gombert
13451 Marseille cedex 20
France

8. PERFORMING ORGANIZATION REPORT NUMBER

9. SPONSORING/MONITORING AGENCY NAME(S) AND ADDRESS(ES)
Technical Director
Office of Naval Research International Field Office Europe
PSC 802 Box 39
FPO, AE 09499

10. SPONSORING/MONITORING AGENCY REPORT NUMBER

11. SUPPLEMENTARY NOTES

12a. DISTRIBUTION AVAILABILITY STATEMENT
Approved for public release, distribution is unlimited

12b. DISTRIBUTION CODE

13. ABSTRACT *(Maximum 200 words)*

The Workshop was held at "Vacanciel la Calanque' in Carry-le-Rouet, near Marseille, from 16th to 19th March. It was followed by a Special Meeting dedicated to the memory of Georg Weinblum, in celebration of the 100th anniversary of his birth.

The Workshop was attended by over 100 participants.

This publication contains extended abstracts of the presentations, and summaries of the discussions. Appended are written abstracts of the Georg Weinblum lectures.

14. SUBJECT TERMS
wave drift, time domain calculations, high speed vessels, dispersion, free surface flow, wave-current, motion simulation, standing waves

15. NUMBER OF PAGES

16. PRICE CODE

17. SECURITY CLASSIFICATION OF REPORT	18. SECURITY CLASSIFICATION OF THIS PAGE	19. SECURITY CLASSIFICATION OF ABSTRACT	20. LIMITATION OF ABSTRACT

Proceedings of the

TWELFTH INTERNATIONAL WORKSHOP ON WATER WAVES AND FLOATING BODIES

Carry-le-Rouet, 16-19 March, 1997

Edited by

B. MOLIN

Ecole Supérieure d'Ingénieurs de Marseille

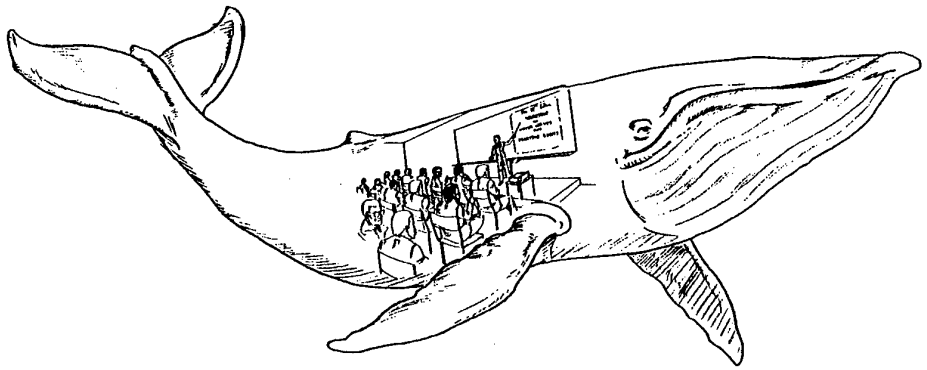

Also including written abstracts to the 'Georg Weinblum Special Meeting' held at Carry-le-Rouet on 19-20 March, 1997

Cover photograph: the Georg Weinblum Special Meeting lecturers (courtesy D.H. Peregrine).
Back, from left to right: *H. Maruo, M. Tulin, T. Wu, J. Breslin, J. Wehausen, F. Ursell*
Front, from left to right: *T. Miloh, L. Larsson, N. Newman, E. Tuck, O. Faltinsen, S. Sharma*

ABSTRACT

The Workshop was held at 'Vacanciel la Calanque' in Carry-le-Rouet, near Marseille, from 16th to 19th March. It was followed by a Special Meeting dedicated to the memory of Georg Weinblum, in celebration of the 100th anniversary of his birth.

The Workshop was attended by over 100 participants.

This publication contains extended abstracts of the presentations, and summaries of the discussions. Appended are written abstracts of the Georg Weinblum lectures.

SPONSORS (in alphabetic order)

Association Universitaire de Mécanique (AUM)
Conseil Général des Bouches du Rhône
Direction de la Recherche et de la Technologie (DRET)
Groupement de Recherches en Génie Océanique et Côtier (GReGOC)
Ministère des Affaires Etrangères
Ministère de l'Education Générale, de l'Enseignement Supérieur et de la Recherche
Office of Naval Research Europe
Single Buoy Moorings Inc. (S.B.M.)

This work relates to Department of the Navy Grant N00014-97-1-0517 issued by the Office of Naval Research European Office. The United States has a royalty-free license throughout the world in all copyrightable material contained herein.

TABLE OF CONTENTS

WORKSHOP INFORMATION

Ordering information for recent Workshop Proceedings

11th (1996)
V. BERTRAM
Institut für Schiffbau
Lämmersieth 90
22305 Hamburg
GERMANY
e-mail: bertram@schiffbau.uni-hamburg.d400.de

12th (1997)
B. MOLIN
Ecole Supérieure d'Ingénieurs de Marseille
Technopôle de Château-Gombert
13451 Marseille Cedex 20
FRANCE
e-mail: molin@esim.imt-mrs.fr

Contacts for future Workshops

13th (1998)
Prof. A.J. HERMANS
Delft University of Technology
Department of Applied Mathematics
Mekelweg 4
2628 CD Delft
THE NETHERLANDS
e-mail: a.j.hermans@math.tudelft.nl

14th (1999)
Prof. R.F. BECK and W.W. SCHULTZ
University of Michigan
Dept. of Naval Architecture & Marine Eng
2600 Draper Rd
48109 Ann Arbor, Michigan
USA
e-mail: rbeck@engin.umich.edu
e-mail: schultz@engin.umich.edu

15th (2000)
Prof. T. MILOH
University of Tel-Aviv
School of Eng.
Ramat-Aviv
69978 Tel-Aviv
ISRAEL
e-mail: miloh@eng.tau.ac.il

LIST OF PRESENTATIONS

SLENDER BODY APPROXIMATION FOR YAW VELOCITY TERMS IN THE WAVE DRIFT DAMPING MATRIX

J.A.P.Aranha & M.R.Martins
Dep. of Naval Eng., USP, CP61548, S.P., Brazil

1. INTRODUCTION

Consider a *slender ship* with length L and beam B (ε = B/L << 1) and suppose a coordinated system with the x-axis being coincident with the longitudinal axis while the z-axis is vertical, pointing upwards, the origin of the system being at the intersection of the free surface with the mid section; the ship cross section is defined by the contour line $\partial C(x)$ and the ship water line by ∂W. Points in $\partial C(x)$ are defined by the radius vector

$$\mathbf{r}_c = y_c\mathbf{j} + z_c\mathbf{k} \in \partial C(x). \tag{1}$$

Let $p_{20}(x,\mathbf{r}_c)$ be the *steady second order* pressure field due to a harmonic wave with amplitude A, frequency ω and incident in the β direction; one assumes here that $p_{20}(x,\mathbf{r}_c)$ includes Dirac δ-functions at the points where $\partial C(x)$ intersects ∂W, these concentrated forces per unit of length being related with the change in the wetted surface of the ship. The sectional steady drift coefficients are then defined by the expressions

$$\begin{Bmatrix} d_x(x;\omega,\beta) \\ d_y(x;\omega,\beta) \\ n_z(x;\omega,\beta) \end{Bmatrix} = \int_{\partial C(x)} p_{20}(x,\mathbf{r}_c) \cdot \begin{Bmatrix} n_x(x,\mathbf{r}_c) \\ n_y(x,\mathbf{r}_c) \\ -y_c n_y(x,\mathbf{r}_c) \end{Bmatrix} d\partial C(x), \tag{2}$$

where $(n_x;n_y)$ are components of the normal $\mathbf{n}$; defining the *moments* of (2) by the expressions

$$\begin{Bmatrix} M_{x,j} \\ M_{y,j} \\ M_{z,j} \end{Bmatrix} = \int_{-L/2}^{L/2} x^j \cdot \begin{Bmatrix} d_x(x;\omega,\beta) \\ d_y(x;\omega,\beta) \\ n_z(x;\omega,\beta) \end{Bmatrix} dx, \; j = 0,1,2, \tag{3}$$

the generalized steady drift force vector in the horizontal plane has obviously the components

$$
\begin{aligned}
D_x(\omega,\beta) &= M_{x,0}(\omega,\beta);\\
D_y(\omega,\beta) &= M_{y,0}(\omega,\beta);\\
N_z(\omega,\beta) &= M_{z,0}(\omega,\beta) + M_{y,1}(\omega,\beta).
\end{aligned}
\tag{4}
$$

The intention now is to express *all* elements of the Wave Drift Damping matrix, including the ones related to the *yaw motion*, in terms of the *moments* $\{M_{x,j};\ M_{y,j};\ M_{z,j}\}$. In the present study the influence of the coupling between the second order steady potential and the slow ship motion will not be considered, although it can be obtained by integration of quadratic functions of the first order (linear) solution.

2. THE YAW TERMS IN WDD MATRIX

The first column of the WDD matrix, the one related with the *surge* velocity U_x, is exactly given by the expression

$$
\begin{Bmatrix} B_{11}(\omega,\beta)\\ B_{21}(\omega,\beta)\\ B_{61}(\omega,\beta)\end{Bmatrix} = \frac{\omega}{g}\left[\omega\cos\beta\frac{\partial}{\partial\omega} - 2\sin\beta\frac{\partial}{\partial\beta} + 4\cos\beta\right]\cdot\begin{Bmatrix} D_x(\omega,\beta)\\ D_y(\omega,\beta)\\ N_z(\omega,\beta)\end{Bmatrix};
\tag{5a}
$$

the second column, related to the *sway* velocity U_y, is given by

$$
\begin{Bmatrix} B_{12}(\omega,\beta)\\ B_{22}(\omega,\beta)\\ B_{62}(\omega,\beta)\end{Bmatrix} = \frac{\omega}{g}\left[\omega\sin\beta\frac{\partial}{\partial\omega} + 2\cos\beta\frac{\partial}{\partial\beta} + 4\sin\beta\right]\cdot\begin{Bmatrix} D_x(\omega,\beta)\\ D_y(\omega,\beta)\\ N_z(\omega,\beta)\end{Bmatrix},
\tag{5b}
$$

both results being proven in Aranha (1996).

Observing the essentially two-dimensional feature of the wave diffraction by a slender body, one can introduce here, by inspection, the *sectional* WDD coefficients influenced by the *sway* velocity, given by (see (5b))

$$
\begin{Bmatrix} b_{12}(x;\omega,\beta)\\ b_{22}(x;\omega,\beta)\\ b_{62}(x;\omega,\beta)\end{Bmatrix} = \frac{\omega}{g}\left[\omega\sin\beta\frac{\partial}{\partial\omega} + 2\cos\beta\frac{\partial}{\partial\beta} + 4\sin\beta\right]\cdot\begin{Bmatrix} d_x(x;\omega,\beta)\\ d_y(x;\omega,\beta)\\ n_z(x;\omega,\beta)\end{Bmatrix}.
\tag{5c}
$$

Expression (5c) can be also proven exactly, as a blend of a two-dimensional result derived in Aranha (1994) and the three dimensional one given in Aranha (1996), and it can be used to obtain a *slender body approximation* for the elements of the WDD matrix related with the *yaw motion*. In

fact, for a *slender body* the *yaw* motion is seen, at the cross section x, as being a *sway* motion with amplitude $x.\Omega$, Ω being the yaw angular velocity; it turns out that the related *seccional* WDD coefficients are then given by

$$\begin{aligned} b_{16}(x;\omega,\beta) &= x\cdot b_{12}(x;\omega,\beta);\\ b_{26}(x;\omega,\beta) &= x\cdot b_{22}(x;\omega,\beta);\\ b_{66}(x;\omega,\beta) &= x\cdot b_{62}(x;\omega,\beta). \end{aligned} \tag{5d}$$

Integrating (5d) along the ship length, observing the contribution of the sway term b_{26} to the yaw moment and ignoring terms of relative order ε^2, one obtains finally, with the help of (3), that:

$$\begin{Bmatrix} B_{16}(\omega,\beta)\\ B_{26}(\omega,\beta)\\ B_{66}(\omega,\beta) \end{Bmatrix} = \frac{\omega}{g}\left[\omega\sin\beta\frac{\partial}{\partial\omega} + 2\cos\beta\frac{\partial}{\partial\beta} + 4\sin\beta\right]\cdot\begin{Bmatrix} M_{x,1}(\omega,\beta)\\ M_{y,1}(\omega,\beta)\\ M_{y,2}(\omega,\beta) \end{Bmatrix}. \tag{6}$$

3. GEOMETRIC OPTICS APPROXIMATION

The slender body approximation (6) can be checked directly against numerical results, as the ones derived by Grue & Palm (1996), for instance. While waiting the slender body code that allows one to determine the *moments* $\{M_{x,j};\ M_{y,j};\ M_{z,j}\}$, one presents here analytical expressions for the high frequency limit, where geometric optics approximation can be used. These limits have an importance in themselves, since they are analytic and hold in a range of frequencies where numerical results are most questionable.

Consider a wave incident on a vertical wall with α being the angle between the wave direction and the normal $\mathbf{n}$. It is trivial to show in this case that the elementary drift force on an element ds of the wall is given by

$$d\mathbf{F} = \frac{1}{2}\rho g A^2\cos^2\alpha\,\mathbf{n}\,ds\,.$$

In high frequency one can consider the body as if it were a vertical cylinder infinitely long with cross section coincident with the water line ∂W. Assuming symmetry with respect to y-axis and that r(x) is the half beam of the body, the transition between the "illuminated" and "shadow" zones in the geometric optics limit is defined by a single variable $x_0(\beta)$, given by the expression

$$\text{Max}\,|r'(x)| \le |\tan\beta| \;\Rightarrow x_0(\beta) = \frac{L}{2};$$
$$\text{Max}\,|r'(x)| > |\tan\beta| \;\Rightarrow |r'(x_0(\beta))| = |\tan\beta|. \tag{7a}$$

Introducing the variables $\{\xi = 2x/L;\ \xi_0(\beta) = 2x_0(\beta)/L\}$ and the integrals

$$I_1 = \int_0^1 \frac{\xi . r'(\xi)}{1+(r'(\xi))^2} d\xi;$$
$$S_0(\beta) = \int_0^{\xi_0(\beta)} \frac{1}{1+(r'(\xi))^2} d\xi\ ;\ C_0(\beta) = \int_{\xi_0(\beta)}^1 \frac{r'(\xi)}{1+(r'(\xi))^2} d\xi; \tag{7b}$$
$$S_2(\beta) = \int_0^{\xi_0(\beta)} \frac{\xi^2}{1+(r'(\xi))^2} d\xi\ ;\ C_2(\beta) = \int_{\xi_0(\beta)}^1 \frac{\xi^2 . r'(\xi)}{1+(r'(\xi))^2} d\xi.$$

The following expressions are then obtained in the high frequency limit:

$$\hat{B}_{16} = \frac{B_{16}}{\rho B^2 \omega A^2} = \left(\frac{L}{B}\right)^2 I_1 \sin\beta;$$
$$\hat{B}_{26} = \frac{B_{26}}{\rho B^2 \omega A^2} = \left(\frac{L}{B}\right)^2 I_1 \cos\beta; \tag{7c}$$
$$\hat{B}_{66} = \frac{B_{66}}{\rho B^3 \omega A^2} = \frac{1}{2}\left(\frac{L}{B}\right)^3 [S_2(\beta)\ \sin\beta + C_2(\beta)\ \cos\beta];$$
$$\hat{B}_{22} = \frac{B_{22}}{\rho B \omega A^2} = 2\left(\frac{L}{B}\right) [S_0(\beta)\ \sin\beta + C_0(\beta)\ \cos\beta].$$

Table (1) compares (7c) with high frequency numerical results obtained by Grue & Palm (1996) for different values of β.

	$\hat{B}_{16}$		$\hat{B}_{26}$		$\hat{B}_{66}$	
β	NUM	(7c)	NUM	(7c)	NUM	(7c)
$\pi/2$	−1.2	−3.4	0.	0.	21.4	24.6
$3\pi/4$	−0.8	−2.4	1.1	2.4	18.7	17.4
π	0.	0.	1.7	3.4	5.0	7.9

TABLE (1):Comparision between numerical results for KL=16 and (7c)

* * *

DISCUSSION

Eatock Taylor R.: I do not think one should try to draw conclusions about the reliability of your drift damping formula for moving bodies by refering to the slow convergence of results for a truncated cylinder. It is well known that the sharp corners in this case lead to slow convergence, particularly in the surge-heave coupling coefficient which is proportional to the slow forward speed (see the 1993 OTC paper by Teng and myself). The problem vanishes when a small corner radius is used, but the hemisphere analysed by John Grue is a much better test case than the truncated cylinder in the context of this controversy.

Aranha J.: I agree, in some aspect at least, with you, since the cylinder problem seems to be plagued with small numerical imprecisions to which the WDD formula is very sensitive. If I recall well, Kinoshita & al. results, shown in the presentation, were obtained by a quasi-analytic method and the convergence does not seem to be very good when the cylinder is free to oscillate.
However, the cylinder problem is one of the most obvious in our field and it seems natural, in this context, to look at it to confirm the validity of the formula.
With respect to your suggestion, that it would be better to look to the sphere, Grue's results, shown in the conference, together with a similar result, shown in my JFM (1996) paper, point both to a perfect agreement between the WDD formula and numerical results.

Grue J.: Your abstract and presentation are based on the work Aranha (1996) JFM, which you claim provides a formula for wave drift damping based on strict proof. First you find an expression for the far-field amplitude of the diffracted-radiated waves (with current), next conservation of momentum is applied to find the force.
Denote the far-field amplitude of the diffracted-radiated waves by H_u, which may be expanded by $H_u = H_o + \tau H_1$, where $\tau = U\, w/g$.
Consider the difference between your and our formulae for H_1. I have tried to show that this difference is zero, however, it is generally not. The following figure illustrates this. The body is a freely floating hemisphere moving with small forward speed. Dashed line: Aranha (1996), solid line: Nossen et al. (1991).
In this example your and our wave drift damping coefficients (B_{11}) are in close agreement, see figure 1a. For other geometries, e.g. ships, there is a general disagreement, of the order 100 %, except possibly for long waves.

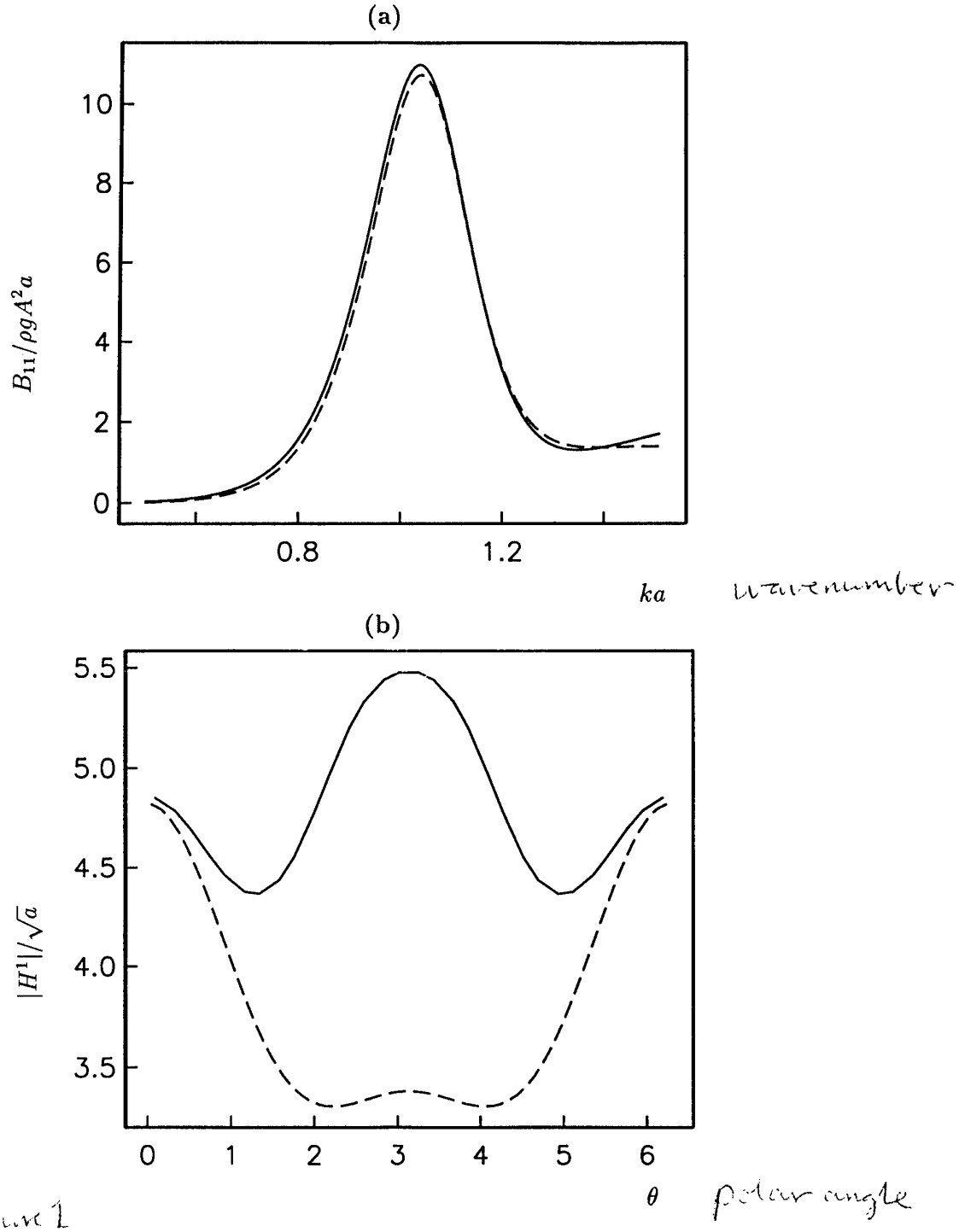

Figure 1

~~Figure 1~~: For a half immersed sphere, 400 panels on S_B and 880 panels on S_F, in head waves, the figures shows: (a): B_{11} computed by complete theory (solid line), and Aranha's formulae (dashed line). (b): The far-field amplitude function H^1 for translatory motion at $ka = 0.9$, computed by complete theory (solid line), and Aranha's theory (dashed line).

Aranha J.: Two things must be said about this:

1) I should thank J. Grue since he provided just another example of a 3D-body, free to oscillate, where the agreement between the numerical results and WDD formula is perfect.

2) With respect to the behavior of the $H_1(\theta)$ function one has obviously a misunderstanding since, otherwise, how could one obtain a complete agreement in the force computation with a complete disagreement in the far-field behavior? The point is that in my work the far-field is well behaved, it does not have the secular term that Grue's approach has (recall Malenica in the 10th IWWWFB, Oxford, 1995).

If Grue intends to make a comparison, it is not enough to differentiate the $A_u(\theta)$ coefficient with respect to U ; it is necessary to differentiate also the wavenumber, that depends also on U. In this way he would obtain secular terms in my expression that should be matched to his secular terms.

The way he has done compares two distinct things and it has no relevance for the discussion.

A time domain method to compute transient non linear hydrodynamic flows

M. BA, A.FARCY (ENSMA) and M. GUILBAUD, (CEAT, Université de Poitiers)
Laboratoire d'Etudes Aérodynamiques-URA CNRS n°191,
43 rue de l'Aérodrome, 86036 Poitiers CEDEX, FRANCE

Introduction

Today, most of the numerical codes for the computations of ship seakeeping or for the diffraction-radiation motions for platforms are solved in the frequency domain using a linear form of the free surface boundary conditions, called the Neumann-Kelvin approach. The water can be considered as incompressible and inviscid and the flow around the body as irrotationnal except on some lines or surfaces, so the Laplace equation is valid in the fluid domain. These problems can be solved by panel methods using either Rankine (aerodynamic) or Kelvin singularities. For more complicated (non harmonic) motions, the time domain has to be chosen instead of the frequency one and in his case, the Green's function is so complicated (Newman, 1995, Mas et Clément, 1995) that no computational codes have been developed up to day. But these linearized approaches are limited to small harmonic motions with mean constant forward speed and the body condition has to be satisfied on the mean position of the exact body surface. For motions with larger amplitudes, this simplification is no more possible and the body condition has to be satisfied of the body exact position, implying also that the free surface conditions cannot more be linearized. So these previous problems are fully non linear and the flow analysis is more easily done in the time domain.

If less developed than the computations in the frequency domain, the calculations using the time domain (cf. Beck ,1994 for review) become more popular with the development of computers. We present here the first results obtained with a non linear method to compute transient free surface flows. To reduce the computational time, the surface source distribution on the free surface and on the body are replaced by source points desingularized, as proposed by Cao et al.(1990). To check the validity of the method, computations are presented on the transient flow around a submerged source with impulsive start. The results are compared with those of linearised computations. Finally some results on a submerged ellipsoid are also presented.

Formulation of the non linear problem

The flow of an ideal and incompressible fluid of infinite depth is considered with the undisturbed free surface located in the plane z=0. The frame of co-ordinates uses the z-axis positive upwards and the x-axis pointing in the direction of the mean velocity of the body. The surface tension is neglected. As the problem starts from rest, the flow is irrotational implying the existence of a velocity potential ϕ, satisfying the Laplace equation in the fluid domain. This potential must also satisfy the body condition on the surface S_B of the body :

$$\frac{\partial \phi}{\partial n} = \vec{V}_E \cdot \vec{n} \quad \text{on } S_B \qquad (1),$$

where $\vec{n}$ is the unit normal vector directed into the fluid and $\vec{V}_E$ is the local velocity of the body. A condition of non perturbation when the depth of immersion goes to infinity must also be satisfied. On the instantaneous free surface, the potential must also satisfy both the kinematic and the dynamic boundary conditions ; if the free surface elevation is given by z=E(x,y,t), those conditions are given by :

$$\frac{\partial E}{\partial t} - \frac{\partial \phi}{\partial z} + \frac{\partial E}{\partial x}\frac{\partial \phi}{\partial x} + \frac{\partial E}{\partial y}\frac{\partial \phi}{\partial y} = 0 \quad \text{on } z = E(x,y,z,t), \qquad (2)$$

$$\frac{\partial \phi}{\partial t}+\frac{1}{2}\left|\overrightarrow{grad}\,\phi\right|^2+gE=0 \text{ on } z=E(x,y,t) \qquad (3).$$

Finally, the fluid disturbance must vanish at infinity, and the following initial conditions have also to be satisfied :

$$\phi=0 \text{ for } t\le 0 \text{ in the whole fluid domain, and } E(x,y,t)=0 \text{ for } t\le 0 \quad (4).$$

The two previous conditions (2) and (3) can be written using the material derivatives, enabling to compute the variation of a physical quantity following a fluid particle and leading to the kinematic condition as :

$$\frac{D\vec{X}_p}{Dt}=\overrightarrow{grad}\,\phi \quad (5),$$

where $\vec{X}_p(x(t),y(t),z(t),t)$ is the location of a fluid particle on the free surface. The dynamic condition can be written as :

$$\frac{D\phi}{Dt}=-gE+\frac{1}{2}\overrightarrow{grad}\,\phi\cdot\overrightarrow{grad}\,\phi \qquad (6).$$

Method of resolution

At each time step, the potential is assumed to be known on the free surface, the real location of which being also known. Conditions (4) is used at the beginning of this time marching procedure. For the next time step, equation (5) is used to compute the new free surface elevation and equation (6) to obtain the new value of the potential on the free surface. So, at each time step, a new mixed problem with a Neumann condition on the body (known normal potential derivative) and a Dirichlet problem on the free surface (known potential) has to be solved. To satisfy the boundary conditions, the body is divided into quadrilateral panels and a part of the free surface, into rectangular panels. To reduce the computational time, point sources are distributed on the free surface instead of using surface source distribution on panels. The potential and the velocity induced by these point sources being singular when the collocation points is located on source positions, a desingularised technique has been followed (Cao et al., 1990 or Beck, 1994). So point sources are located into the body or above the free surface. The source displacement, with distance L_d, is done along the normal to the panel. The choice of L_d is difficult and the values do not be too large or too small in order to obtain correct results. Beck (1994) has proposed as optimum value $L_d=(S_F)^{0.25}$ where S_F is the area of the panel containing the source on the body or the mean value of the areas of the four panels surrounding a source on the free surface.

Applications

Wave field due to an submerged doublet with a constant mean forward speed

The flow generated by the impulsive start of a doublet (source and sink of same intensity located 0.1m apart in the x direction) from rest. The forward speed and doublet intensity are quickly set to their steady values U_∞ and σ_0 using the following relations:

$$V(t)=U_\infty\left(1-e^{-4t}\right) \text{ and } \sigma(t)=\sigma_0\left(1-e^{-4t}\right) \quad (7).$$

This doublet travels along an axis parallel to the x axis, 1mm deep under the free surface. The initial mesh on the free surface is located at $0\le y\le 20$m and $-7.5\le x\le 7.5$m and is subdivided into a mesh of 40x30 panels(figure 1). The nodes are equidistant in the x direction but in the y one, the distance between two nodes increases of 10%, both in the positive and negative y direction. The doublet intensity, σ_0 is assumed to be known, the unknowns for this problem are the intensities of the point sources on the free surface. These values are computed by writing that the potential is given on the free surface. For each time step, a new location of the free surface and the new distribution of the potential for the next time step are obtained from equations (5)

and (6). In these equations, the right hand sides are analytically computed because point sources are used; the time derivatives in the left hand sides are computed by a fourth order Runge-Kutta method.

On figure 2, the free surface elevation above the doublet is plotted for 3 values of σ_0 (0.05-0.75 and 0.9) for a fully converged computations (t=40s), with a time step Δt=0.2s. The results obtained with the use of the steady forward speed Green's function, so corresponding to a linear and steady computation, are also plotted. It can be observed on this plot that, as the doublet intensity increases, the non linear wave amplitudes become greater than that the ones computed by the linear method. The difference is maximum for the first crest above the doublet. The evolution of the free surface is presented on the figure 3 (σ_0=0.05) and for four values of the time t=4-10-16 and 25s, showing the evolution of the unsteady solution towards the steady one.

Wave field due to a submerged ellipsoid starting from rest

Computations have been done on a ellipsoid with horizontal axis a=5m and lateral one, b=1m. The horizontal axis is located at the distance h=1.586m under the undisturbed free surface. In this case, the mesh on the free surface is made of square panels (40 in the x direction and 20 in the lateral one). The singularity intensities on the body are obtained from the body condition (eq. 2). The expression proposed by Beck(1994) for the desingularisation distance has been modified at both longitudinal ends of the ellipsoid. The evolution of the free surface with time is presented on figure 4 for a Froude number based on the depth of immersion h, $F = U_\infty / \sqrt{gh} = 1.26$, for 4 time values. After the impulsive start, t=1.8s, a crest can be observed on front part of the body and the level decreases on the rear part. As the time increases, the wave becomes steepest and a second crest appears immediately upstream of the body. At t=12s, the shape of the first wave become smoother and the second wave propagates with a V-shape; at the same time, a second trough and a third crest appears. A second V-shape wave appears and become important at t=30s, but its amplitude is weaker than the one of the first wave. Finally at t=45s, a quasi-steady state is obtained.

Conclusion

First results obtained in the time domain using a non linear method to compute transient flows close to a free surface are presented. The method uses desingularized source points, on the free surface and on the body, modified at both ends of bodies, to avoid numerical difficulties, keeping relatively low the computational time. The converged results have been first checked for a submerged doublet with known strength by comparing with steady calculations achieved with a panel method using the linear steady Green's function, showing good agreement. The evolution of the free surface with time has been also studied. The second application presented concerns a submerged ellipsoid. Work is on progress to optimise the computational time and to extent the validity of the method to surface-piercing bodies.

References

Beck R.F., "Time-domain computations for floating bodies", Applied Ocean Research, 16, 267-282, 1994.

Cao Y., Schultz, W.W. and Beck R.F., "Three-dimensional desingularised boundary integral methods for potential problems", Int. J. for Num. Methods in Fluids, Vol. 12, 785-803, 1991.

Mas S. and Clément A., "Computation of the finite time-domain Green function in the large time rang", 10th Int. Work. on Water Waves and Floating bodies", Oxford, 1995.

Newman J.N., "The approximation of free-surface Green functions", Fritz Ursell retirement meeting, 1990.

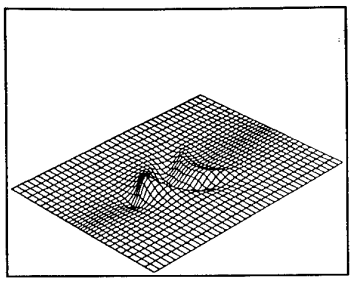

Fig. 1 : Mesh of the free surface

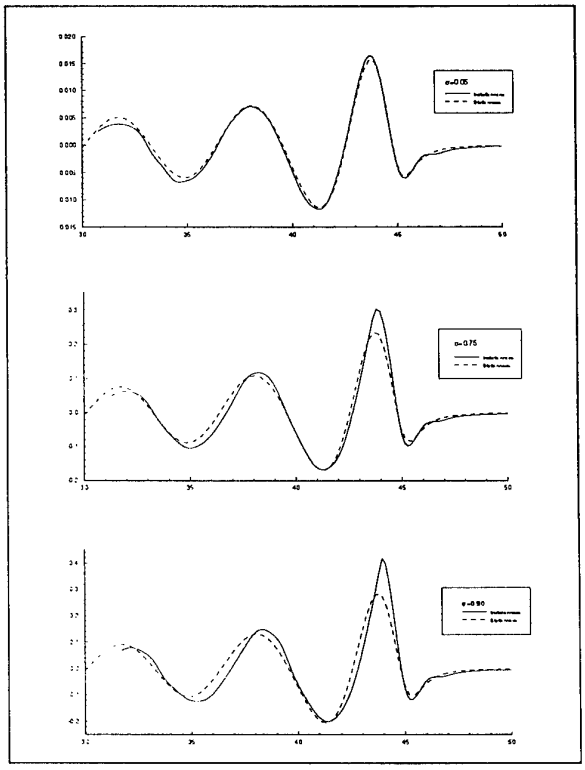

Fig. 2 : Free surface elevation at t=40s

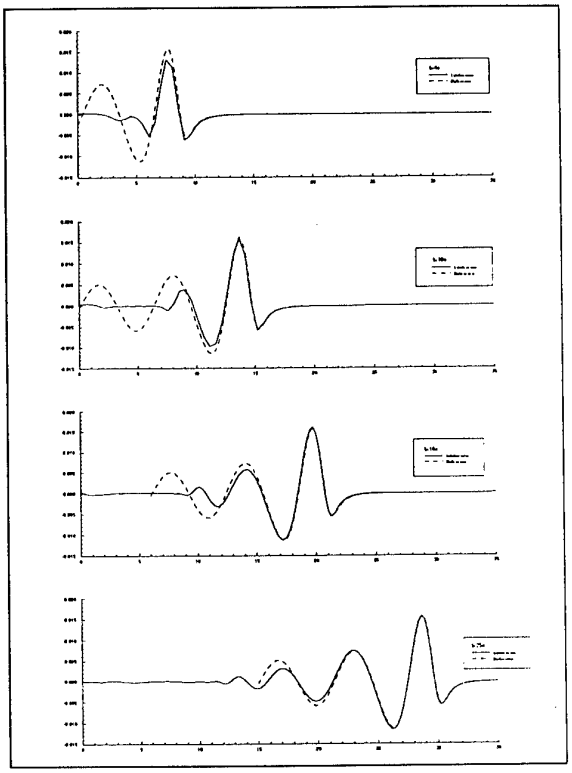

Fig. 3 : Evolution of the free surface

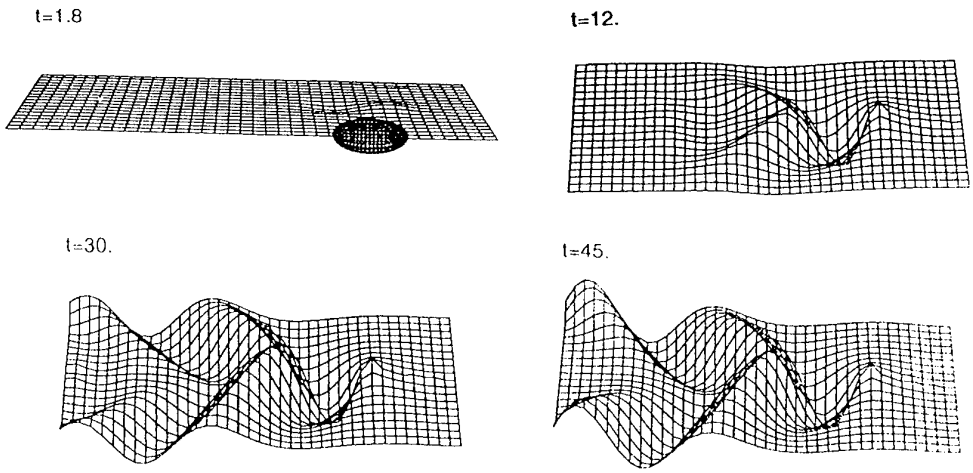

Fig. 4 : Wave fied due to a submerged ellipsoid starting from rest

Time Domain Calculations in Finite Water Depth

A. K. Bratland* F. T. Korsmeyer† J. N. Newman‡

1 Introduction

Hydrodynamic computations in the time domain using a free-surface Green function have been presented in numerous papers [Bingham *et al.* 1994, Lin & Yue 1990, Beck & Magee 1990]. This abstract demonstrates the extension of this type of analysis to finite depth. This transient approach may be used to compute the first-order, frequency-domain hydrodynamic coefficients. We present these here to validate the method by comparison to computations made directly in the frequency domain for zero speed. With the addition of forward speed to the analysis the first-order steady force becomes important. It has been shown that this steady force (with components referred to as resistance, sinkage, and trim) is the limit as time becomes infinite of the force computed when the body is impulsively accelerated in surge. Since the prediction of squat (maximum draught; sinkage plus trim) is particularly important in finite depth, we present these results for various depth-based Froude numbers to demonstrate the forward-speed analysis.

The finite-depth analysis is carried out similarly to our previous infinite-depth approach. The potential problem is cast as a boundary integral equation. The only boundary appearing in this equation is the body boundary itself due to the choice of a Green function which satisfies the (transient) free-surface condition and, in the present work, the bottom (no-flux) boundary condition. One advantage of the time-domain approach is that the same Green function can be used both for moving-ship problems with nonzero forward velocity U and for fixed structures where $U = 0$.

2 The Green function

The appropriate Green function may be written as the sum of a Rankine and a wave part, which we define in the forms

$$G^{(0)} = \frac{1}{r} + \frac{1}{r'} - 2\int_0^\infty \frac{e^{-kh}}{\cosh kh} \cosh k(z+h) \cosh k(c+h) J_0(kR) dk \tag{1}$$

$$G_t^w = 2\int_0^\infty \frac{\sqrt{gk \tanh kh}}{\cosh kh \sinh kh} \sin(t\sqrt{gk \tanh kh}) \cosh k(z+h) \cosh k(c+h) J_0(kR) dk \tag{2}$$

[Newman 1992] describes effective algorithms for the integral in (1), and outlines the fundamental difficulties associated with the efficient evaluation of (2). The approach which we have implemented here is to express (2) as the sum of two terms involving the normalized function $F(X, V, T)$, as defined by [Newman 1992] equation 25, and then to consider the difference function $F - F_\infty$ where F_∞ can be evaluated from the corresponding infinite-depth Green function. Then we expand this difference function in triple Chebyshev expansions, in unit squares of the rectangular domain $0 \le X \le 16$ and $0 \le T \le 33$. (Physically, the variables X and T correspond to the horizontal distance from the source to the field point, and the time t, nondimensionalized in terms of the depth h and gravity g.) The coefficients of these Chebyshev expansions are pre-evaluated, and stored for routine use. At each time step of the convolution, T =constant and the triple expansions are reduced to double expansions in the normalized horizontal and vertical coordinates X and V, which are then evaluated for each combination of source and field points.

*Techpower, Norway
†Research Laboratory of Electronics, Massachusetts Institute of Technology
‡Department of Ocean Engineering, Massachusetts Institute of Technology

One point to note is the large-time asymptotic behavior of the Green function, since this affects the corresponding behavior of computed hydrodynamic forces. In the infinite-depth case (2) is exponentially small, but for $h < \infty$ $G_t^w \rightarrow \mathcal{O}(1/t)$. When $U \neq 0$, and coordinates are used which move with the ship, $G_t^w \rightarrow \mathcal{O}1/t + \mathcal{O}\sin(\omega_c t)/t$, where ω_c denotes the critical frequency. This is given in the infinite-depth limit by $\tau_c = \omega_c U/g = 1/4$, while the variation of τ_c with depth is shown in Figure 5.

3 Results

For zero speed we compare Fourier-transformed time-domain computations to computations made directly in the frequency domain with a similar boundary integral method, for the surge and heave motions of a hemisphere. From the asymptotic behavior of the Green function it is clear that the time record has to be longer for finite water depth than infinite water depth. Alternatively we could approximate the large time behavior based on the asymptotic analysis. For the added-mass and damping coefficients presented in Figure 1 we have calculated to a maximum time of T=25 and assumed the impulse-response function to be zero beyond that. The results from the frequency-domain code ("FD") and time-domain code ("TD") agree within graphical accuracy. At low frequency, the heave added-mass rises steeply, in a manner which appears consistent with the the result of [Yeung 1981] that $A_{33} \rightarrow \infty$ as $\omega \rightarrow 0$. Figure 2 shows the corresponding results for the exciting force, with similar confirmation from the frequency-domain computations.

The large time limit of the radiation potential forced by impulsive surge acceleration, ϕ^r, can be considered as the steady potential. That means the steady forces, with Neumann-Kelvin linearization, can be written as the large time limit of

$$F_j(t) = \rho U \iint_{\overline{S}_b} \frac{\partial}{\partial x} \phi^r \, dS. \tag{3}$$

Figure 3 shows computations of $F_3(t)$ and $F_5(t)$ for the Wigley hull. By applying the equations of hydrostatic equilibrium

$$\begin{aligned} C_{33}x_3 + C_{35}x_5 &= F_3 \\ C_{53}x_3 + C_{55}x_5 &= F_5 \end{aligned}$$

the "steady" sinkage and trim are found. The sinkage is shown in Figure 4. The sinkage increases with decreasing water depth, or with increasing values of the Froude number $F_{nh} = \frac{U}{\sqrt{gh}}$. .

For large values of time, the transient results oscillate at the critical frequency, with slowly-decreasing amplitude, about the steady limiting values. While computations at higher depth-based Froude number are of interest, the finite computational domain for the evaluation of the Green function described in §2, poses a restriction. Work is presently underway to remove this limitation, permitting the estimation of squat closer to the critical Froude number.

References

[Beck & Magee 1990] Beck, R. F. and Magee, A. R., Time domain analysis for predicting ship motions, *Proc. IUTAM Symp. Dynamics of Marine Vehicles & Structures in Waves*, London, 1990.

[Bingham *et al.* 1994] Bingham, H. B., Korsmeyer, F. T. and Newman, J. N., Predicting the seakeeping characteristics of ships, 20^{th} *Symp. Naval Hydro.*, Santa Barbara, 1994.

[Lin & Yue 1990] Lin, W. -M. and Yue, D. K. -P., Numerical solutions for large-amplitude ship motions in the time domain, 18^{th} *Symp. Naval Hydro.*, Ann Arbor, 1990.

[Newman 1992] Newman J. N., The approximation of free-surface Green functions. In P. A. Martin and G. R. Wickham, editors, *Wave asymptotics*, 107-135. Cambridge University Press, 1992.

[Yeung 1981] Yeung R. W., Added Mass and Damping of a vertical Cylinder in Finite-Depth Waters. *Applied Ocean Research*, Vol 3, no 3, 119-133, 1981.

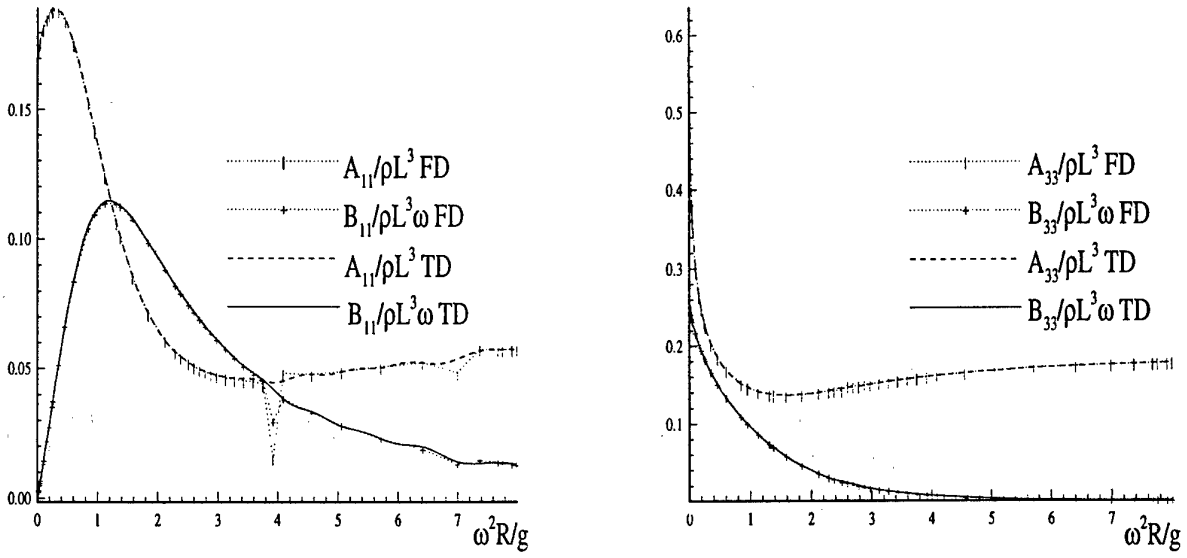

Figure 1: The added-mass and damping coefficients of a hemisphere for surge (left) and heave (right) for water depth $h = 1.2R$. "TD" denotes Fourier transformed time-domain computations, "FD" denotes frequency-domain computations.

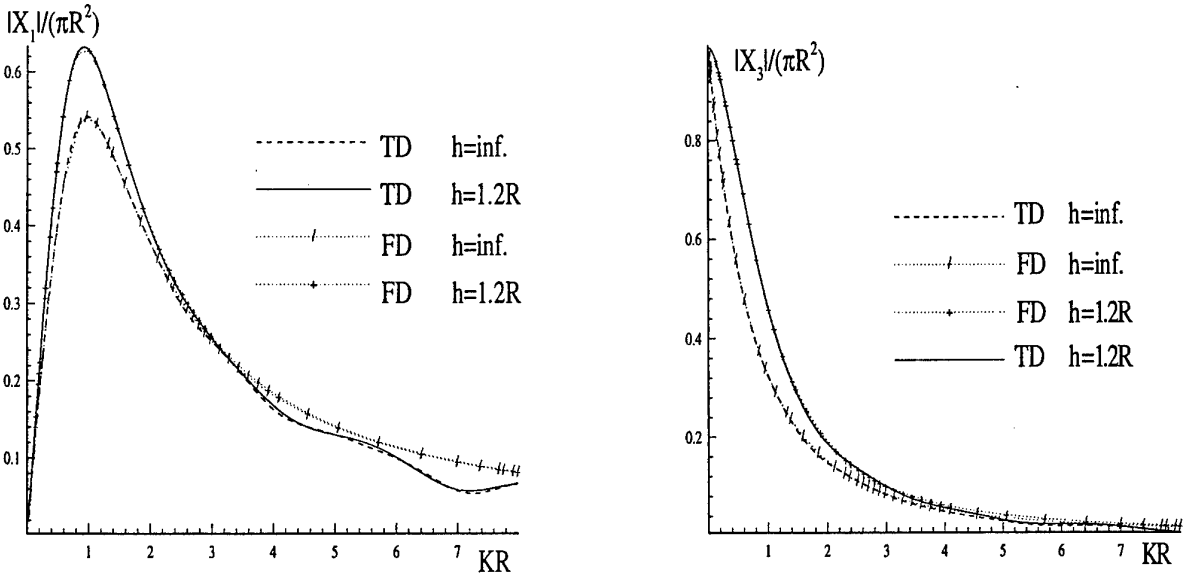

Figure 2: The exciting-force coefficients of a hemisphere for surge (left) and heave (right) for water depths $h = 1.2R$ and $h \to \infty$. "TD" denotes Fourier transformed time-domain computations, "FD" denotes frequency-domain computations.

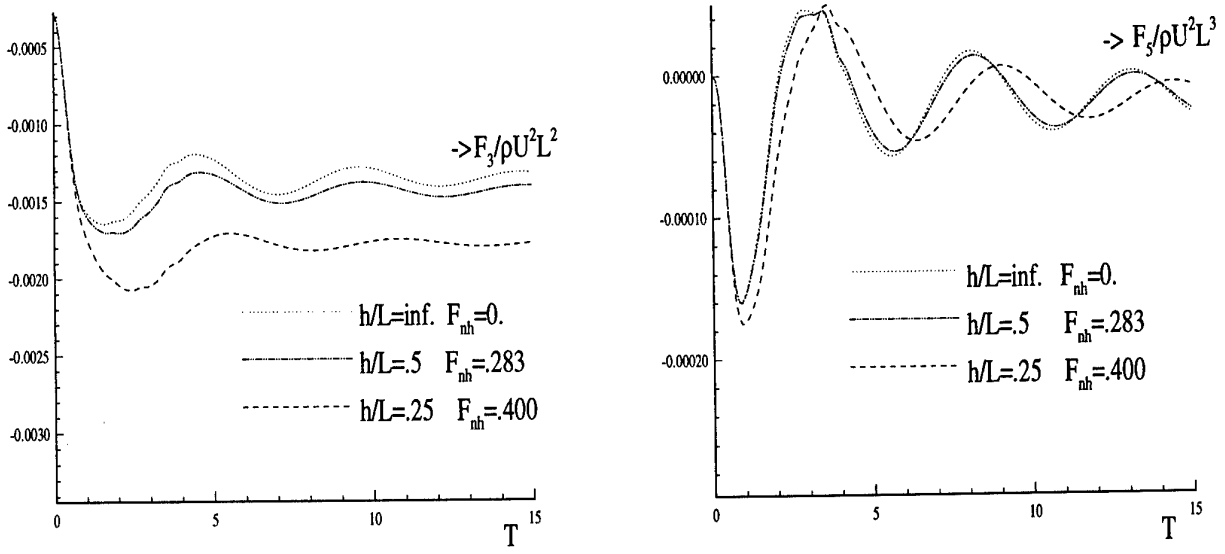

Figure 3: The approach to the steady vertical force and moment on a Wigley hull for $F_n = 0.2$, for the water depths and depth-based Froude numbers indicated.

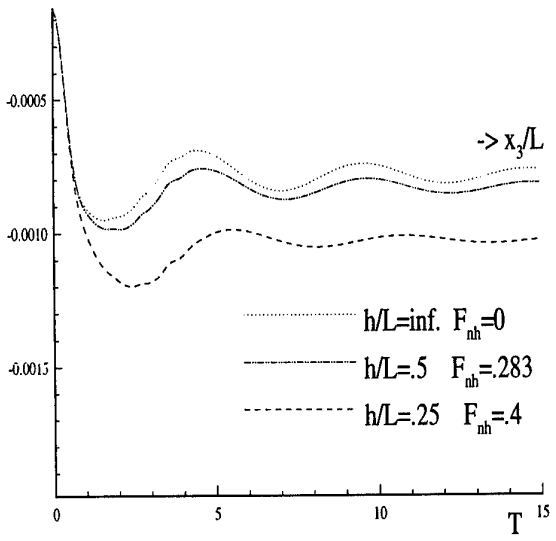

Figure 4. The approach to the "steady" sinkage for a Wigley hull for $F_n = 0.2$, for the water depths and depth-based Froude numbers indicated.

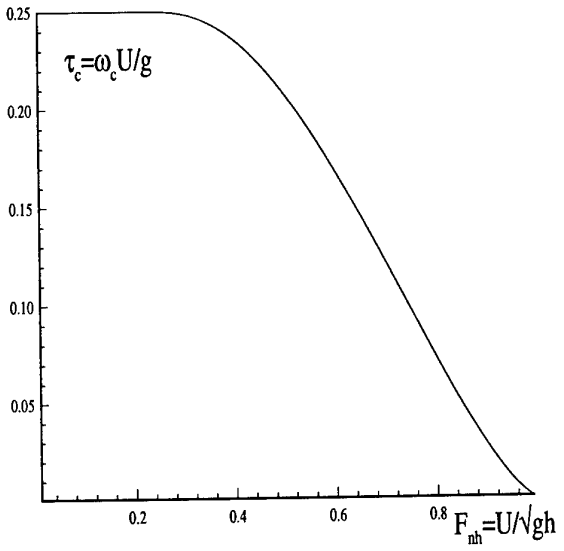

Figure 5. The depth dependence of τ_c.

DISCUSSION

Tuck E.O.: I am encouraged by the fact that the rate of decay of transients seems to be as rapid at the higher $F_{nh} = 0.400$ as it is at the lower $F_{nh} = 0.283$. As $F_{nh} \to 1$, one might expect that, since the flow is ultimately unsteady then, the transients might decay less rapidly, perhaps not at all.

Bratland A.K., Korsmeyer T., Newman J.N.: In our results $F_{nh} << 1$, and the Green function has the asymptotic behaviour as written in abstract. As $F_{nh} \to 1$ another asymptotic must be considered. Newman has shown that, as $F_{nh} \to 1$ and $t \to \infty$

$$G_t \approx T^{-2/3} A_i\left(-\left(\frac{1}{4}T\right)^{3/2}\left(1 - X^2/T^2\right)\right)$$

where $T = t\sqrt{g/h}$ $X = \frac{Ut}{h}$.

This must be examined closer, but we think you are right in suggesting slower decay.

Clément A.: In preceeding Workshops (Kyushu, Oxford), I presented the results of S. Mas' work about numerical computations of the time-domain Green function in finite water depth, and we observed that the gradient of the function was much more difficult to obtain through series and asymptotic expansions. Do you need to compute the gradient of the Green function in your numerical method? If so, did you observe this difference in the divergence of the algorithms?

Bratland A.K., Korsmeyer T., Newman J.N.: The gradient is required in the kernel of the integral equation. The Green function is represented by Chebyshev expansions which can be differentiated term-by-term. This avoids the analytic difficulties which have been discussed at past Workshops, but we are limited to a finite computational domain in (X,T) as noted in Section 2 of our abstract.

The 12th international Workshop on Water Waves and Floating Bodies, Marseilles, 1997

A time-domain algorithm for motions of high speed vessels using a new free surface condition.

Tim H.J. Bunnik and Aad J. Hermans
Department of Applied Mathematics, Delft University of Technology, The Netherlands

1 Introduction

When a ship is designed, it is important to know its behaviour in real sea-keeping at forward speed. This behaviour can be predicted performing model tests in towing tanks, but this is quit expensive. The introduction of fast and large computers has given the possibility to write simulation programs that can partly replace physical tests. A lot of research has therefore been carried out recent years. Prins [2] developed a time-domain algorithm to compute the behaviour of several floating bodies in current and waves based on potential flow. Sierevogel [1] contributed an absorbing boundary condition independent of frequency. Both used the double body potential to approximate the steady potential. This approximation is valid for low speeds, but when we increase speed, non-linear effects in the steady potential become more important. At MARIN a program has been developed (RAPID) by Raven [3] that calculates the steady potential satisfying the exact non-linear free surface condition. We use this potential to linearize the time dependent free surface condition. We solve the potential flow problem with this boundary condition in the time domain using a Rankine source distribution. We put the source panels at some distance above the free surface. This promising 'raised panel approach' was also used by Raven [3]. It has the advantage of resulting in a much smoother potential. Besides it is easier to include non-linear effects in the future. Because we assume the speed to be high, upwind differences must be used to obtain a stable iteration procedure. An absorbing boundary condition seems not to be necessary in the frequency range we're interested in (Strouhal number $\tau \gg \frac{1}{4}$). The calculations are carried out for a fictive analytical hull shape. For this hull hydrodynamic coefficients like added mass and damping are calculated. In our presentation we will compare these coefficients with results from other methods, investigate the influence of some of our most important parameters and look at the influence of reflected waves.

2 Mathematical model

We consider a ship moving at constant speed U. A coordinate system $Oxyz$ is introduced in the frame of reference following the forward speed of the body, with the x- and y-axes in the mean free surface and the z-axis vertical upward. The forward speed is in the direction of the negative x-axis. The fluid is assumed to be incompressible and inviscid, and the flow irrotational. We can therefore introduce a velocity potential Φ whose gradient equals the fluid velocity and that satisfies the Laplace equation. On the free surface $z = \zeta(x, y)$ this potential must satisfy:

$$\frac{\partial^2 \Phi}{\partial t^2} + 2\vec{\nabla}\Phi \cdot \vec{\nabla}\left(\frac{\partial \Phi}{\partial t}\right) + \frac{1}{2}\vec{\nabla}\Phi \cdot \vec{\nabla}\left(\vec{\nabla}\Phi \cdot \vec{\nabla}\Phi\right) + g\frac{\partial \Phi}{\partial z} = 0 \quad \text{at } z = \zeta \tag{1}$$

We linearize this condition by splitting the potential in a steady and unsteady part:

$$\Phi(\vec{x}, t) = \phi(\vec{x}, t) + \Phi_R(\vec{x}) \tag{2}$$

The steady potential satisfies the exact time-independent free surface condition and a zero normal velocity condition on the hull and is calculated by RAPID (RAised Panel Iterative Dawson). If we assume the unsteady potential to be small (small amplitudes of motion and waves), we can neglect higher order terms in ϕ and find:

$$\frac{\partial^2 \phi}{\partial t^2} + 2\vec{\nabla}\Phi_R \cdot \vec{\nabla}\frac{\partial \phi}{\partial t} + \vec{\nabla}\Phi_R \cdot \vec{\nabla}\left(\vec{\nabla}\phi \cdot \vec{\nabla}\Phi_R\right) + \frac{1}{2}\vec{\nabla}\phi \cdot \vec{\nabla}\left(\vec{\nabla}\Phi_R \cdot \vec{\nabla}\Phi_R\right) + g\frac{\partial \phi}{\partial z}$$

$$-\frac{1}{g}\left(\frac{\partial\phi}{\partial t}+\vec{\nabla}\Phi_R\cdot\vec{\nabla}\phi\right)\frac{\partial}{\partial z}\left(\frac{1}{2}\vec{\nabla}\Phi_R\cdot\vec{\nabla}\left(\vec{\nabla}\Phi_R\cdot\vec{\nabla}\Phi_R\right)+g\frac{\partial\Phi_R}{\partial z}\right)=0 \quad \text{at } z=\zeta_R \tag{3}$$

The last term is a transfer term that occurs because we linearize around the steady free surface in stead of the actual free surface. Most of the terms contain derivatives of steady velocities. First order derivatives can be calculated accurate. The transfer term contains second order derivatives. We are still busy finding a numerical scheme to obtain these derivatives. Until then the transfer term is omitted. On the hull of the ship we have the same linearized boundary condition Prins and Sierevogel used:

$$\frac{\partial\phi}{\partial n}=\frac{\partial\vec{\alpha}}{\partial t}\cdot\vec{n}+\left(\left(\vec{\nabla}\Phi_R\cdot\vec{\nabla}\right)\vec{\alpha}-\left(\vec{\alpha}\cdot\vec{\nabla}\right)\vec{\nabla}\Phi_R\right)\cdot\vec{n} \tag{4}$$

with $\vec{\alpha}$ the displacement vector. Again, we need stationary speed derivatives. We solve the Laplace equation with these linear boundary condition using a source distribution on the hull and above the free surface. The boundaries are divided in N panels, and on each panel the source strength σ is assumed to be constant. The potential is now given by:

$$\phi(\vec{x},t)=\sum_{j=1}^{N}\sigma_j(t)\iint_{\partial\Omega_j}G\left(\vec{x},\vec{\zeta}\right)dS_\zeta \qquad G=\frac{-1}{4\pi r} \tag{5}$$

If we choose N collocation points on the hull and free surface and apply the corresponding boundary conditions, we obtain N equations for the N unknown source strengths.

3 Test case

Before developing a numerical algorithm we have to choose some kind of hull. The calculations will be made for a mathematical hull shape given by the formula:

$$\left(\frac{z}{d/L}\right)^2+\left(\frac{y}{b(x)}\right)^2=1$$

$$b(x)=\frac{B}{2L}\left(1-8x^2+16x^4\right)$$

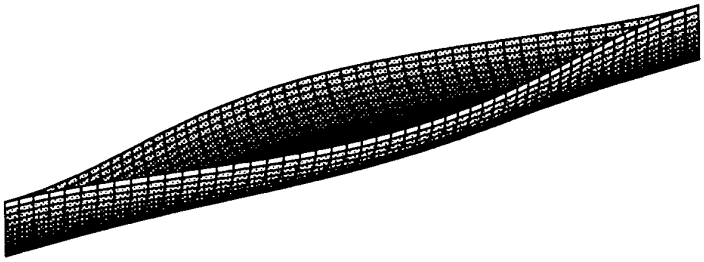

Figure 1: Mathematical hull shape used in calculations

We use $\frac{d}{L}=0.1$ and $\frac{B}{L}=0.2$. The advantage of a mathematical hull is the easy refinement of the grid. In our test study, that's very useful.

4 Numerical method

In our new free surface condition, time and spatial derivatives of the unsteady potential occur. The time derivatives are discretized by second order explicit schemes, therefore using only the current potential and potentials on previous time levels. The spatial derivatives are more complicated. They are decomposed in a derivative in a direction perpendicular and parallel to the free surface (see figure 2). The derivative parallel to the free surface is obtained using upwind differences because of it's well known stabilising properties. We found out that in our case it's absolutely necessary to use upwind differences to avoid wiggles in the solution. The difference becomes this way:

$$\frac{\partial\phi}{\partial l_{||}}(\vec{x}_i)=\sum_{j=1}^{m}\gamma_{ij}\phi(\vec{x}_j) \tag{6}$$

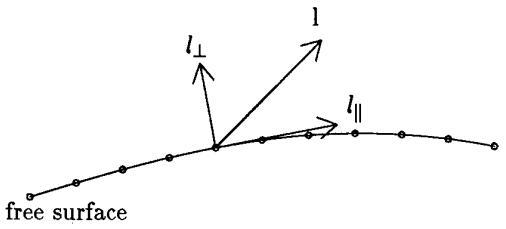

Figure 2: Decomposition of differentiation direction

with m the number of collocation points on the free surface. The coefficients γ_{ij} are non-zero only for some nearby collocation points upstream of the point $\vec{x}_i$. In case of a rectangular grid and uniform flow, this means for example:

$$\vec{\nabla}\Phi_R \cdot \vec{\nabla}\phi(\vec{x}_i) = U\frac{\frac{3}{2}\phi(\vec{x}_i) - 2\phi(\vec{x}_i - \Delta x) + \frac{1}{2}\phi(\vec{x}_i - 2\Delta x)}{\Delta x} + \mathcal{O}\left((\Delta x)^2\right) \tag{7}$$

The derivative in a direction perpendicular to the stationary free surface is obtained by changing the order of integration and differentiation in (5):

$$\frac{\partial\phi}{\partial l_\perp} = \sum_{j=1}^{N}\sigma_j(t)\iint_{\partial\Omega_j}\frac{\partial G}{\partial l_\perp}\left(\vec{x},\vec{\zeta}\right)dS_\zeta \tag{8}$$

Second order derivatives of the unsteady potential are treated the same way. After discretizing the boundary conditions, the boundaries are divided in panels and collocation points are chosen. Applying the discretized boundary conditions in each collocation point gives us a matrix equation for the unknown source strengths:

$$A\vec{\sigma} = \vec{f} \tag{9}$$

Initially all source strengths are put zero. The time iteration starts by giving the ship one of possible 6 sinusoidal motions (translational or rotational). After a few periods a periodical wave pattern arises around the ship. When there is no reflection, the wave pattern is the same after each period of movement. When that state has been reached, the forces on the ship can be calculated and hydrodynamic coefficients like added mass and damping can be calculated.

5 Results

We mentioned we don't need an absorbing boundary condition because we consider high speeds and frequencies. In that case, the waves propagate downstream. The upwind difference scheme causes the waves not to reflect against the edge of the computational domain behind the ship. We only get reflections from the edge beside the ship. If we choose that edge far away enough, the reflected wave will end up behind the ship and not affect the wave pattern around the ship. Because our main goal is to calculate forces on the hull we can accept these reflections. If we want to predict the total wave pattern, or decrease the speed of the ship, we must add an absorbing boundary condition.

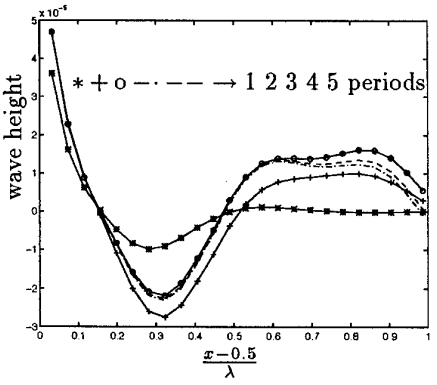

Figure 3: Wave pattern behind ship.
Distances : 0.75λ and λ

In figure (3), (4) and (5) is shown what happens to the wave pattern after 1,2,3,4 and 5 periods behind the ship if we change the size of the computational domain. In the absence of reflections the wave pattern should not change anymore after a few periods. The pictures show a change in wave pattern at some distance behind the ship, an indication of the presence of reflected waves there. Choosing the edge of the free surface behind the ship further away doesn't influence the reflections. If we choose the edge of the free surface beside the ship further away, the reflections end up further downstream. In figure (3) the the free surface edge beside the ship was 0.75 wavelength away from the ship and the edge behind the ship one wavelength away, with the wavelength $\lambda = \frac{8\pi F_n^2}{(1-\sqrt{1+4\tau})^2}$. All calculations were done for $F_n = \frac{U}{\sqrt{gL}} = 0.4$ and $\tau = \frac{\omega U}{g} = 2.55$. In figure (4) we see the same reflections if we choose the edge behind the ship further away and don't change the distance to the free surface edge beside the ship. In figure (5) is shown that the reflections occur closer to the ship if the distance to the free surface edge beside the ship is 0.25λ.
In our presentation we will also look at hydrodynamic coefficients like added mass and damping and compare these with results from other methods.

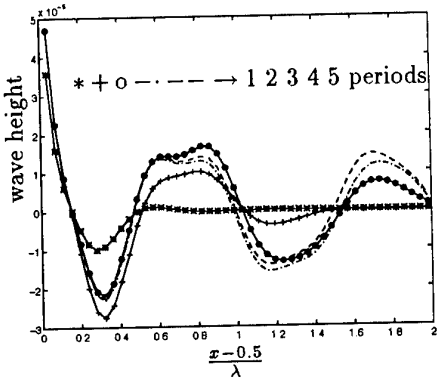

Figure 4: Wave pattern behind ship. Distances : 0.75λ and 2λ

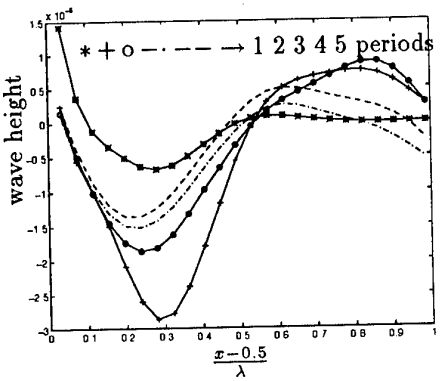

Figure 5: Wave pattern behind ship. Distances : 0.25λ and λ

6 Conclusions and further research

We have developed an algorithm to determine added mass and damping of a ship at high speed using a new boundary condition. Because of the high speed the reflected waves don't spoil the results. Next step is to add an absorbing boundary condition so we can decrease speed. After that we want to determine drift forces by introducing an incoming wave field. Also some attention still has to be paid to the transfer term in our free surface condition.

Acknowledgements

Financial support for this work and steady velocities at hull and free surface are given by the Maritime Research Institute Netherlands.

References

[1] L.M. Sierevogel and A.J. Hermans. Absorbing boundary condition for floating two-dimensional objects in current and waves. *Journal of engineering mathematics, 1996*

[2] H.J. Prins. *Time-Domain Calculations of Drift Forces and Moments.* PhD Thesis, Delft University of Technology, 1995.

[3] H.C. Raven. *A Solution Method for the Nonlinear Ship Wave Resistance Problem.* PhD Thesis, Delft University of Technology, 1996.

DISCUSSION

Ferrant P.: I would like to know how you plan to account for incoming waves in your model. It is not clear to me how you can combine a linearised incident wave with the non-linear steady solution given by RAPID.

Bunnik T.H.J., Hermans A.J.: There are two ways of doing this. The first and easiest way is to split up the time-dependent potential ϕ into an incoming potential and an extra potential: $\phi_{tot} = \phi_{inc} + \tilde{\phi}$.
The separate potentials no longer represent physical waves close to the body, but the sum does.
If this approach doesn't work a wavemaker can be introduced, upstream of the body. The interaction between incoming wave and steady wavefield is then automatically included when the wave travels downstream.

Bertram V.:
1) The 'new' condition has been derived already by Newman (1978), but it is satisfying to see it now implemented in codes.
2) I would recommend modifying RAPID for a frequency approach for $\tau > 0.25$; the problem is then very similar to a shallow-water steady wave resistance problem. So all techniques including radiation and open-boundary conditions work just as well. Since the computations are easily parallelized in the frequency domain, this approach is in my experience very efficient.
Congratulations on a most interesting paper!

Bunnik T.H.J., Hermans A.J.:
1) Thank you for noticing.
2) It is possible in a time-domain approach to obtain information about a range of frequencies by using some kind of impulse response functions.
If we want to extend the method to non-linear, we can't use the frequency-domain approach because of its limitation to linear problems.

Magee A.: Since you have developed a time-domain method, why not calculate the impulse response functions to obtain the added mass and damping at <u>all</u> frequencies? This may help as well with wave reflection difficulties as you can finish the calculations before the wave reflections reach the ship.

Bunnik T.H.J., Hermans A.J.: We are certainly going to try this. The main problem is, that when waves of all frequencies are generated, high frequencies cannot be resolved on the frequency-independent grid (short waves) and low-frequency waves travel very fast and their reflections will reach the ship before stopping the calculation.

NONLINEAR WAVE-BODY INTERACTIONS IN A NUMERICAL WAVE TANK

M. Serdar CELEBI and Moo-Hyun KIM*
Texas A&M University
College Station, TX 77843, USA

1 Introduction

The time-domain nonlinear free-surface waves and wave-body interactions are investigated in a 3-dimensional numerical wave tank using an Indirect Boundary Integral Method (IBIM). Simple Rankine sources are used outside the solution domain to desingularize boundary integrals (Cao et al., 1991). To update the position of the fluid particles on the free surface, fully-nonlinear free-surface boundary conditions are integrated with respect to time using the Eulerian-Lagrangian time marching technique. A regridding algorithm is used to eliminate the possible instabilities in the region of high gradients without using artificial smoothing. The input waves entering from the upstream boundary are generated by either a piston-type wave maker or by prescribing actual wave data or analytic solutions. The energy of outgoing waves are gradually removed in the artificial damping zone by viscous dissipation rather than by being transmitted out of the solution domain. When simulating open-sea conditions instead of a numerical wave tank, the artificial damping zone (absorbing beach) is employed at all side walls to prevent possible contamination due to wall reflection. Unlike Cao *et al.* (1991), side walls and ϕ_n-type damping zone are used in the present numerical wavetank. The developed computer program was verified through mass and energy conservations and comparisons with experiments as well as analytic first- and second-order diffraction solutions.

2 Mixed boundary value problem

The ideal fluid is assumed so that a velocity potential exists and the fluid velocity is given by its gradient. The value of the potential, at each time step, is given on the free surface (Dirichlet boundary condition) and the value of the

normal derivative of the potential (Neumann boundary condition) is known on the body surface and the bottom surface. The free-surface potentials and elevations are determined by integrating the following nonlinear free-surface boundary conditions with respect to time.

$$\frac{\delta\eta}{\delta t} = \frac{\partial\phi}{\partial z} - (\nabla\phi - \mathbf{v}).\nabla\eta - U_o(t)\frac{\partial\eta}{\partial x} \qquad \text{on } S_F \qquad (1)$$

$$\frac{\delta\phi}{\delta t} = -g\eta - 1/2\nabla\phi.\nabla\phi + \mathbf{v}.\nabla\phi - \frac{P_a}{\rho} - U_o(t)\frac{\partial\phi}{\partial x} \qquad \text{on } S_F \quad (2)$$

where

$$\frac{\delta}{\delta t} \equiv \frac{\partial}{\partial t} + \mathbf{v}.\nabla$$

is the time derivative following the moving node, U_o is forward velocity, and $\mathbf{v} = -U_o i + \nabla\phi$ dictates the material node approach. $\nabla\phi$ on the right-hand side can be determined after solving the boundary value problem for ϕ. Using the material node approach, $\nabla\eta$ term drops in eq.(1). A Lagrangian-Eulerian method, in which a mixed BVP is solved at each time step, is used on the free surface to time step the unknown potentials and wave elevations. A Runge-Kutta-Fehlberg method is employed for this purpose. Indirect boundary integral methods utilize the source density $\sigma(\vec{r}_s)$ which is used to determine the unknown velocity potential. Then, a weighted residual method (collocation method) is used to solve the integral equations for the unknown $\sigma(\vec{r}_s)$. In order to determine the unknown source strengths, an efficient iterative method called Generalized Minimal Residual (GMRES) Technique (Saad and Schultz, 1986) is used.

For an accurate free-surface flow computation, mass/volume, momentum, and energy conservations should be satisfied in the computational domain. For instance, the total energy conservation in a wave tank, following Contento and Casole (1995), can be expressed as

$$\varepsilon(t) = \dot{W}_W(t) + \dot{E}_o(t) - \dot{W}_B(t) - \dot{E}_\Omega(t) \qquad (3)$$

where $\dot{W}_W(t)$ is the power delivered by the wavemaker and given by

$$\dot{W}_W(t) = \int_{\partial W} p\frac{\partial\phi}{\partial n} dS$$

$\dot{E}_o(t)$ is the rate of energy flux through the open boundary and given by

$$\dot{E}_o(t) = \int_{\partial W_o} \frac{\partial \phi}{\partial t} \frac{\partial \phi}{\partial n} dS \tag{4}$$

$\dot{W}_B(t)$ is the rate of work done by fluid on the body and given by

$$\dot{W}_B(t) = -\int_{\partial B} p \frac{\partial \phi}{\partial n} dS \tag{5}$$

$\dot{E}_\Omega(t)$ is the rate of energy in the fluid and defined by a potential and kinetic contribution

$$\begin{aligned} \dot{E}_\Omega(t) &= \dot{E}_{\Omega_{POT}}(t) + \dot{E}_{\Omega_{KIN}}(t) \\ &= \frac{d}{dt}[\frac{1}{2}\rho g \int_{\partial W \cup \partial F \cup \partial B} \eta^2 \, \mathrm{d}S - \frac{1}{2}\rho \int_{\partial \Omega} \phi \frac{\partial \phi}{\partial n} \, \mathrm{d}S] \end{aligned} \tag{6}$$

where Ω is the boundary of 3-D solution domain. Then, $\varepsilon(t)$ can be compared with the amplitude of the power delivered by the wavemaker to obtain the absolute error in the solution domain.

3 Numerical results

First, the developed computer program was verified through mass, momentum, and energy conservation. The performance of artificial damping zone was tested for various wave conditions. As can be seen in Figure 1, the ϕ_n-type beach is more effective for shorter waves. Second, we conducted two fully-nonlinear diffraction computations with bottom-mounted and truncated uniform vertical cylinders. The simulation results are compared with Mercier & Niedzwecki's (1994) experiments and Kim & Yue's (1989) second-order diffraction computation. The comparison with Mercier & Niedzwecki (1994) showed that the present fully-nonlinear computation agreed better with experiments than the second-order diffraction computation, as can be seen in Figure 2.

4 References

[1] CAO Y., SCHULTZ W., BECK R.F., 1991, *Three Dimensional Desingularized Boundary Integral Methods for Potential Problems*, Int. Journal of Num. Meth. in Fluids, Vol.12, 785-803

[2] MERCIER R.S., NIEDZWECKI J.M., 1994, *Experimental measurement of Second-order Diffraction by a Truncated Vertical Cylinder in Monochromatic Waves*, Proc. Behavior of Offshore Structures, BOSS'94, Vol.2, 265-287

[3] KIM M.H., YUE D.K.P., 1989, *The Complete Second-Order Diffraction Solution for an Axisymmetric Body, Part 1*, Journal of Fluid Mechanics, vol.200, 235-264.

[4] SAAD Y., SCHULTZ M.H., *GMRES: A Generelized Minimal Residual Algorithm for Solving Nonsymmetric Linear Systems*, SIAM, J. Sci. Statist. Comput., 7, 856-869.

[5] CONTENTO, CASOLE, 1995, *On the Generation and Propagation of waves in 2-D Numerical Wave Tanks*, Int. Offshore and Polar Eng. Conf., Vol 3, 10-18.

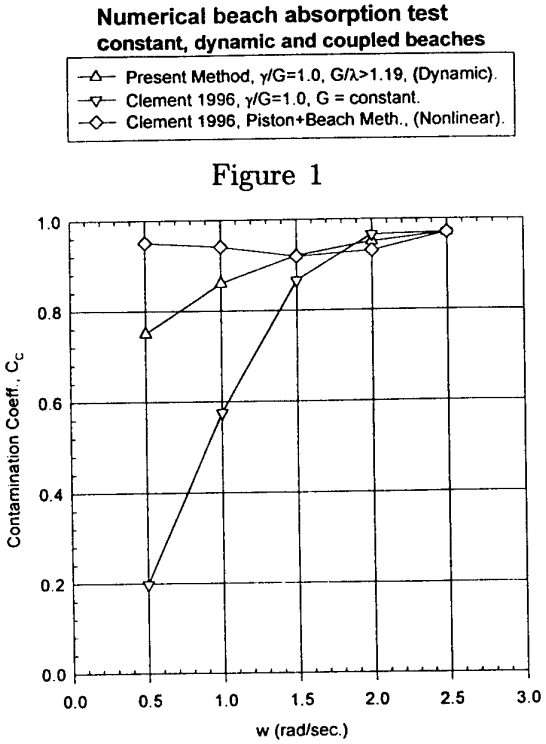

Figure 1

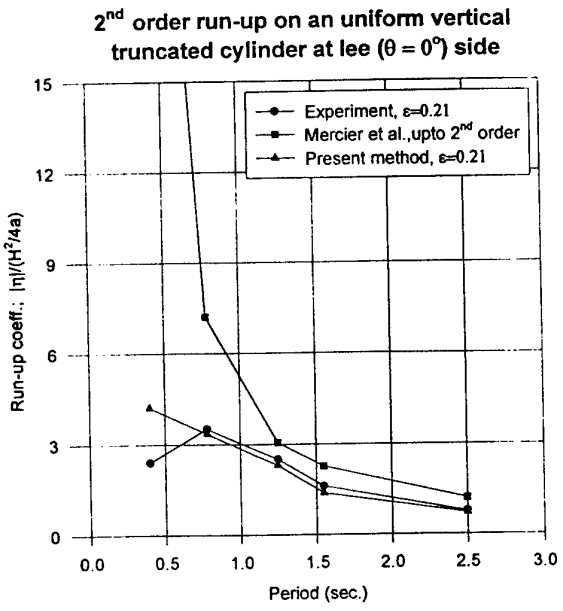

Figure 2

DISCUSSION

Berkvens P.J.F.: In your results on waves diffracting around a cylinder, some very short waves are visible along the waterline. Do you think there is a relation between these short waves and the problems that P. Ferrant encounters when he has waves diffracting around a cylinder in the presence of current?

Celebi S., Kim M-H.: The very small kinks along the waterline is just a graphical noise and short waves around the cylinder are diffracted waves. The desingularized BIEM method is relatively robust at the body-free surface intersection line and we did not experience any numerical problems there.

Grilli S.: Which phase velocity did you use in your Orlanski condition for the bi-chromatic problem?
And what did you do in case of singularity of the celerity?

Celebi S., Kim M-H.: We numerically calculated the phase velocity on the free surface directly from Orlanski condition. In doing this, we selected several points close to the open boundary and the phase velocities are averaged.
In this procedure, the point where singularity occurs is excluded.

Laget O.: Can you tell some precisions on the outside boundary condition you have used?
Do you use both the absorbtion beach and the Orlanski condition? How do you compute the phase velocity and on which variable do you apply the Orlanski condition (free surface deformation, velocity, pressure?)

Celebi S., Kim M-H.: We applied Orlanski condition for the velocity potential and the phase velocity was numerically obtained. For the time derivative of the velocity potential, dynamic free-surface condition was used. We did not combine Orlanski and numerical beach yet.

Paper submitted for the 12th International WWWFB, Marseille, France(16-19 March 1997)

Dispersion relation and far-field waves

Xiao-Bo CHEN, Bureau Veritas, CRD, Rueil-Malmaison, (France)
Francis NOBLESSE, DTMB, NSWC-CD, Bethesda, MD (USA)

A theoretical formulation of wave diffraction-radiation by ships or offshore structures, motivated by the practical and theoretical importance of free-surface potential flows and the formidable complexities of existing calculation method based on free-surface Green function, is recently developed and summarized in *Noblesse, Chen and Yang* (1996). One of important results is the analysis of the classical Fourier representation of free-surface effects, as a two-dimensional linear superposition of elementary plane progressive waves $\exp[-i(\alpha\xi+\beta\eta+ft)]$, given in *Noblesse and Chen* (1995), which defines the wave potential $\phi^W(\xi,\eta)$ in terms of the single Fourier integral

$$4\pi\phi^W = -i\sum\int_{D=0} ds[\text{sign}(D_f)+\text{sign}(\xi D_\alpha+\eta D_\beta)]\exp[-i(\xi\alpha+\eta\beta)]A/\|\nabla D\| \tag{1}$$

along every curve, called dispersion curve, defined in the Fourier plane (α,β) by the dispersion relation $D=0$. Here, ds is the arc length along a dispersion curve, $\|\nabla D\|^2 = D_\alpha^2+D_\beta^2$ and f is the frequency. The Fourier representation (1) is valid for steady and time-harmonic free-surface flows, in infinite or finite water depth, generated by an arbitrary distribution of singularities defined by the generic amplitude function A, which is given by a distribution of the elementary wave function $\exp[kz+i(\alpha x+\beta y)]$ over the surface of the wave generator (e.g. ship or offshore structure). Here, $k=\sqrt{\alpha^2+\beta^2}$ is the wavenumber.

Considerable information about important far-field features of the waves defined by the Fourier representation (1) have been revealed in *Chen* (1996), via a stationary-phase analysis of (1). Specifically, the constant-phase curves (e.g. crest lines) and the related wavelengths, directions of wave propagation, and phase and group velocities can be determined explicitly from the dispersion function D. This stationary-phase analysis of (1), which provides direct relationships between the dispersion curves $D=0$ in the Fourier plane and the corresponding wave systems in the physical plane, is briefly summarized here for the generic case of dispersive waves characterized by an arbitrary dispersion function D, and for the specific case of time-harmonic ship waves in deep water.

Generic dispersive waves

The far-field features of ϕ^W are determined by the stationary points of the phase function $\varphi=\xi\alpha+\eta\beta$ along the dispersion curves. The stationary points are defined by $\varphi'=\xi\alpha'+\eta\beta'=0$ and satisfy the relation :

$$\xi D_\beta - \eta D_\alpha = 0 = h\|\nabla D\|\sin(\gamma-\theta) \tag{2}$$

Here, h and θ are the polar coordinates of the field point $(\xi,\eta)=h(\cos\theta,\sin\theta)$. Furthermore, γ is defined by $(\cos\gamma,\sin\gamma)=(D_\alpha,D_\beta)/\|\nabla D\|$ and thus represents the angle between the unit vector normal to a dispersion curve and the α axis. The wavelength of the waves corresponding to a stationary point (2) is given by $\lambda=2\pi/k$ where k is the wavenumber at the stationary point.

Expression (2) shows that a point of stationary phase on a given dispersion curve is defined by $\gamma=\theta$ or $\gamma=\theta+\pi$. Thus, a point of a dispersion curve generates waves in the physical space in a direction normal to the dispersion curve. The sign function $\text{sign}(\xi D_\alpha+\eta D_\beta)$ in (1) is equal to 1 if $\gamma=\theta$ or -1 if $\gamma=\theta+\pi$. Expression (1) therefore indicates that a point of a dispersion curve generates waves in the direction of the normal vector ∇D to the dispersion curve if $\text{sign}(D_f)=1$, or in the opposite direction if $\text{sign}(D_f)=-1$. Furthermore, at the stationary point $\varphi'=0$, the second derivative of the phase function is expressed as :

$$\varphi'' = c\sqrt{\alpha'^2+\beta'^2}\,d \quad \text{with} \quad d=h(\xi\alpha'-\eta\beta')/(2\xi\eta) \tag{3}$$

where α' and β' are differentiation of α and β with respect to the integral variable along the dispersion curves, and the curvature c is given by :

$$c=(-D_\alpha^2D_{\beta\beta}+2D_\alpha D_\beta D_{\alpha\beta}-D_\beta^2D_{\alpha\alpha})/\|\nabla D\|^3 \tag{4}$$

As $d\neq 0$ in the expression (3), $\varphi''=0$ only at the point of inflection where $c=0$. Two points on both sides of the inflection point may have the same unit normal and then two groups of waves may propagate in the same direction but with different wave number. In fact, an inflection point (α_c,β_c) of a dispersion curve, determined

by $c=0$, defines a cusp line along which two distinct wave systems are found. The corresponding angle γ_c is defined by

$$\gamma_c = \tan^{-1}(D_\beta/D_\alpha)_c \tag{5}$$

where the subscript c indicates evaluation at (α_c, β_c).

The curves along which the phase φ is constant, equal to $C_n^\pm = \pm 2\pi - \text{sign}(\varphi'')\pi/4$, are given by

$$(\xi,\eta) = C_n^\pm (D_\alpha, D_\beta)/(\alpha D_\alpha + \beta D_\beta) \quad \text{with} \quad \text{sign}(C_n^\pm) = \text{sign}(\alpha D_\alpha + \beta D_\beta)\,\text{sign}(D_f) \tag{6}$$

The phase velocity $\vec{v}^f$, determined by the stationary-phase relation (2), is given by

$$\vec{v}^f = -(\alpha,\beta) f/k^2 \tag{7}$$

which is orthogonal to constant-phase curves (6) and different, both in magnitude and in direction, from the group velocity $\vec{v}^g$, at which wave energy is transported, defined by

$$\vec{v}^g = -(\partial f/\partial\alpha, \partial f/\partial\beta) = (D_\alpha, D_\beta)/D_f \tag{8}$$

Expresions (8) and (6) yield $(\xi,\eta)\cdot\vec{v}^g > 0$, which shows that wave energy is propagated away from a wave generator in accordance with the radiation condition.

Far-field features of time-harmonic ship waves

The foregoing results, valid for generic dispersive waves, are now applied to the particular case of time-harmonic ship waves in deep water, for which the dispersion function is given by

$$D = (f - F\alpha)^2 - k \tag{9}$$

For $\tau = fF < 1/4$, three dispersion curves defined by $D=0$ intersect the axis $\beta=0$ at four values of α, denoted $\alpha_o^\pm$ and $\alpha_i^\pm$. The *ring, inner V* and *outer V* waves correspond to the interior curve comprised between α_i^- and α_i^+, the exterior right curve located in $\alpha_o^+ \le \alpha < \infty$, and the exterior left curve located in $-\infty < \alpha \le \alpha_o^-$, respectively. For $\tau > 1/4$, only two distinct dispersion curves intersect the axis $\beta=0$ at α_i^+ and α_o^+. The *ring-fan* and *inner V* waves are respectively associated with the dispersion curves in the left $(-\infty < \alpha \le \alpha_i^+)$ and right $(\alpha_o^+ \le \alpha < \infty)$ regions.

The wavelengths of the *transverse* waves (the waves at the ship track $\eta=0$), in the various component wave systems described above, have already been given in *Noblesse, Chen and Yang* (1996). In th same way, the wavelengths at the edges (cusp lines) of the wedges containing the inner and outer V waves and the ring-fan waves are given by $\lambda_c = 2\pi/k_c$ where k_c is the wavenumber at the inflection points determined by the relation

$$F^4 k_c^2 - (3/2)F^2 k_c + \text{sign}(f - F\alpha) 4\tau F\sqrt{k_c} - 3\tau^2 = 0 \tag{10}$$

The corresponding wedge angle γ_c is

$$\gamma_c = \tan^{-1}(\pm 1/\sqrt{6F^2 k_c - 1}\,) \tag{11}$$

The group velocity (8) is now written as

$$\vec{v}^g = -[F + \text{sign}(f - F\alpha)\alpha/(2k^{3/2}), \text{sign}(f - F\alpha)\beta/(2k^{3/2})] \tag{12}$$

in the system of coordinates moving with the mean forward motion of the ship, and

$$\vec{V}^g = \vec{v}^g + (F,0) = -\,\text{sign}(f - F\alpha)(\alpha,\beta)/(2k^{3/2}) \tag{13}$$

in the absolute system of coordinates. The absolute velocity $\vec{V}^g$ is orthogonal to the constant-phase curves, whereas the relative velocity $\vec{v}^g$ is not.

The foregoing simple analytical relationships between the dispersion curves in the Fourier plane and important features of the corresponding far-field waves in the physical plane are illustrated in the attached figures for the four distinct cases which must be considered for time-harmonic flows with forward speed.

References

F. Noblesse, X.B. Chen and **C. Yang** (1996) *Fourier-Kochin theory of free-surface flows*, 21st Symposium on Naval Hydrodynamics, Trondheim, Norway.

F. Noblesse and **X.B. Chen** (1995) *Decomposition of free-surface effects into wave and near-field components*, Ship Technology Research (42) 167-185.

X.B. Chen (1996) *Evaluation des champs de vagues générés par un navire avançant dans la houle*, Rapport final du Projet DRET/BV no.95 378.

Figure 1: Inner V waves

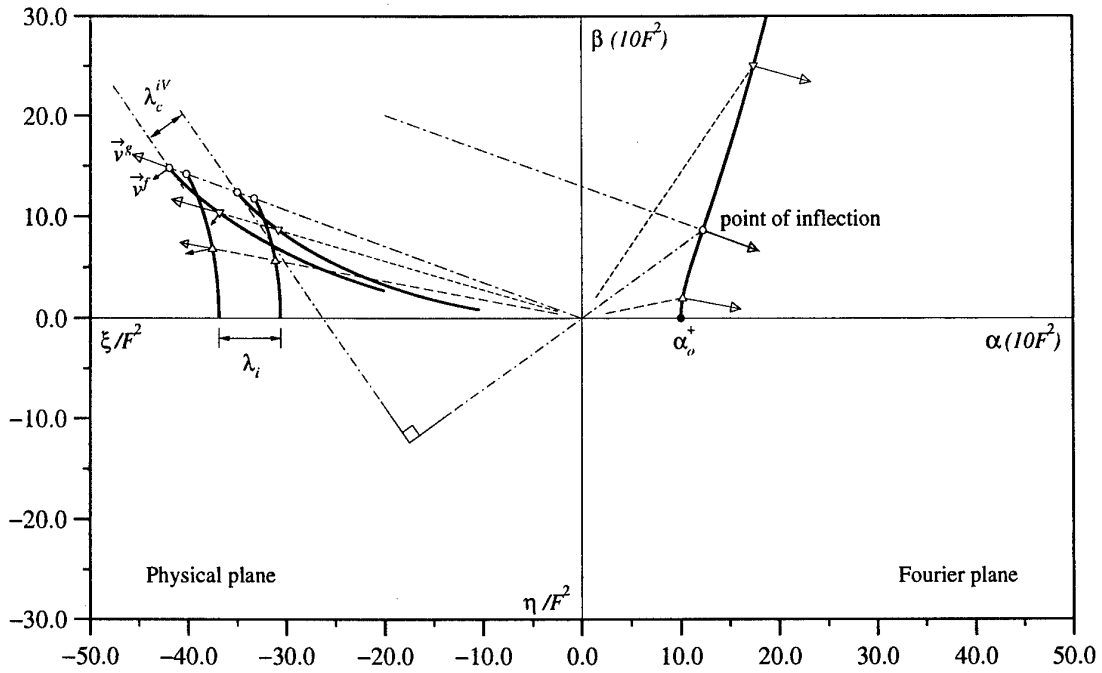

The right exterior dispersion curve ($\alpha_o^+ \leq \alpha < \infty$) is associated with the inner V waves, for $\tau \geq 0$. Two groups of waves systems (the transverse and divergent waves) correspond to two portions of the dispersion curve ($\alpha_o^+ \leq k \leq k_c$) and ($k_c \leq k < \infty$), respectively.

Figure 2: Ring waves

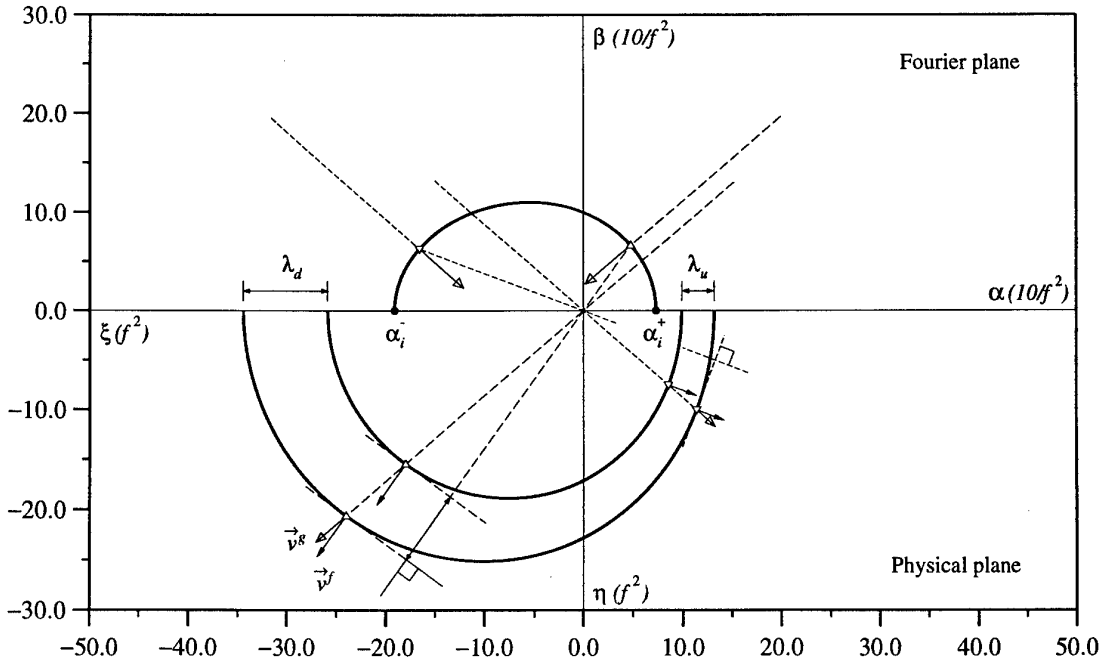

The interior dispersion curve comprised between α_i^- and α_i^+ is associated with the ring waves, for $\tau < 1/4$.

Figure 3: Outer V waves

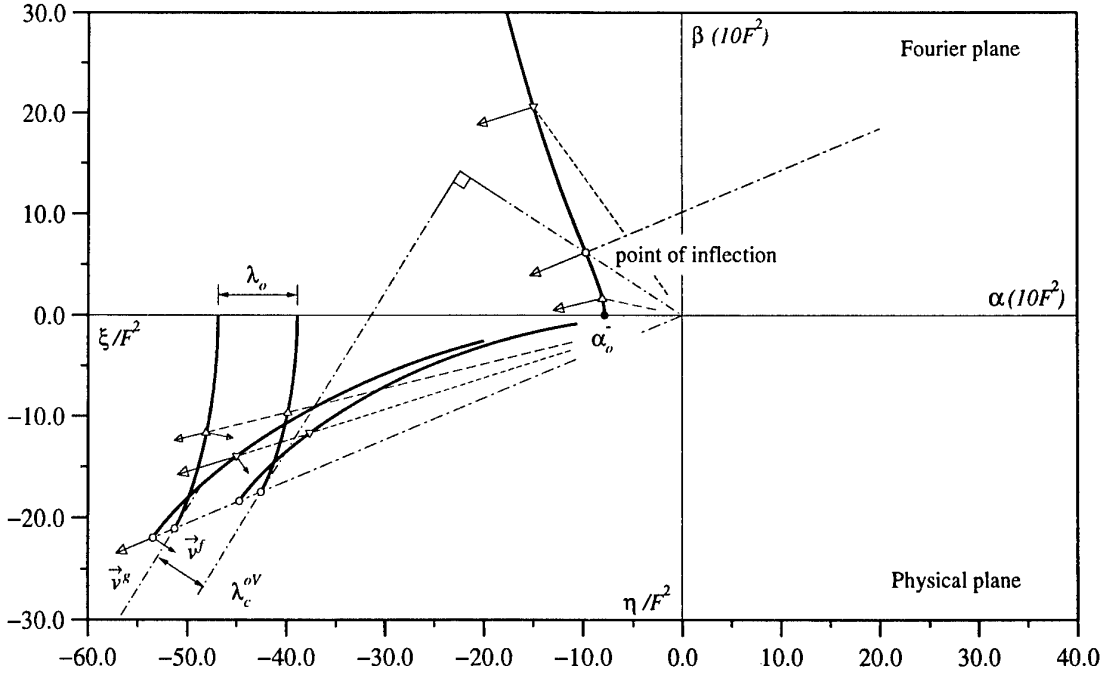

The left exterior dispersion curve ($-\infty < \alpha \leq \alpha_o^-$) is associated with the outer V waves, for $\tau < 1/4$. Two groups of waves systems (the transverse and divergent waves) correspond to two portions of the dispersion curve ($-\alpha_o^- \leq k \leq k_c$) and ($k_c \leq k < \infty$), respectively.

Figure 4: Ring-fan waves

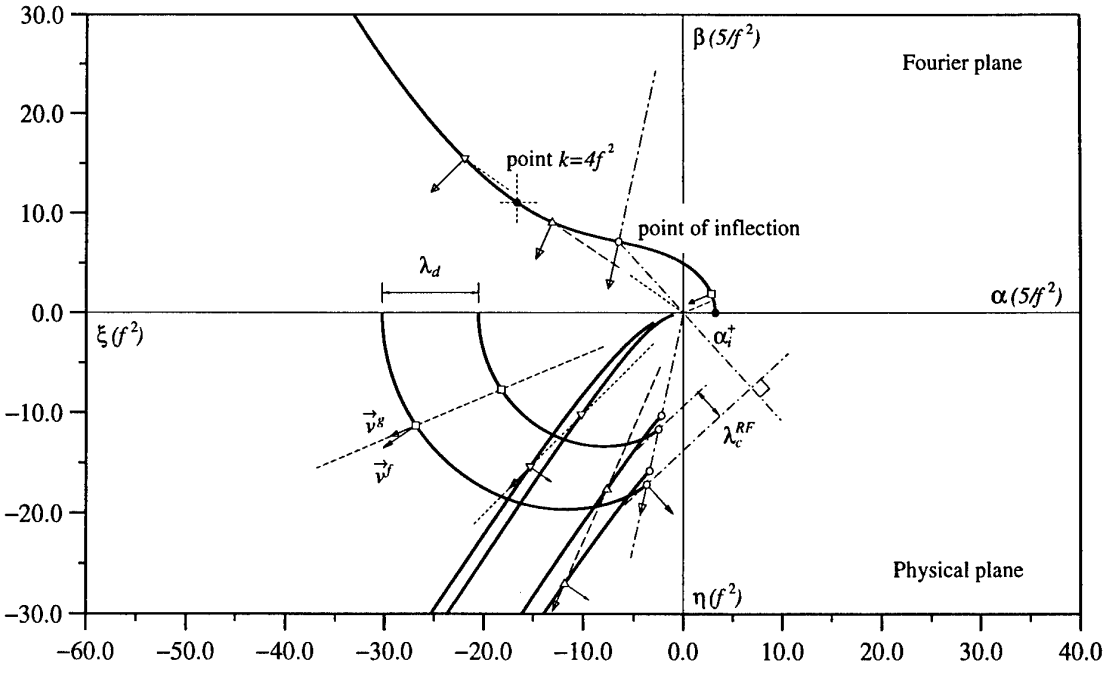

The left dispersion curve ($-\infty < \alpha \leq \alpha_i^+$) is associated with the ring-fan waves, for $\tau > 1/4$. Three groups of waves systems (the partial-ring waves, the outer-fan waves and the inner-fan waves) correspond to three portions of the dispersion curve ($\alpha_i^+ \leq k \leq k_c$), ($k_c \leq k \leq 4f^2$) and ($4f^2 \leq k < \infty$), respectively.

DISCUSSION

Schultz W.W.: What new conclusions (or discrepancies) are obtained in your Fourier analysis over the simple ray theory of Eggers (1957)?

Chen X.B., Noblesse F.: The results and the analysis we have summarized differ from those given in Eggers (1957) and elsewhere, in a number of ways. First of all, our results are valid for generic dispersive waves generated by arbitrary distributions of singularities. Thus, the results can directly be applied to a broad class of dispersive waves, including steady and time-harmonic water waves with or without forward speed in homogeneous or density-stratified water of infinite or finite depth. The results we have given provide simple and elegant explicit relationships between the so-called dispersion curves, defined in the Fourier plane by the dispersion relation and the corresponding far-field waves. These relationships include expressions, both in fixed (attached to the earth) and moving (attached to a translating distribution of singularities) systems of coordinates, for the phase and group velocities of the various wave components associated with each distinct dispersion curve. It is also shown that cusp lines of far-field wave patterns are explicitly related to inflection points of the dispersion curves, which yield closed-form expressions for cusp-angles. In particular, for the case of time-harmonic ship waves in deep water considered for illustrative purposes, two particular *exact* values of τ, namely $\tau = \sqrt{2/27}$ (at which no waves propagate upstream) and $\tau = \sqrt{8/3}$ (where unsteady waves are contained within the wedges of the steady waves), are given (to the authors' knowledge, only numerical approximations to these exact values of τ have previously been given).

Magee A.: Using the relation you developed for group velocity, for a given τ and F, can you calculate the time for a disturbance to reflect off tank walls and return to the ship. In other words, can you find the τ and F values free from tank reflections?

Chen X.B., Noblesse F.: Indeed, the relationship we have given, specifically the expressions for the wave propagation angles and the group velocity, can be directly used to determine the time required for the various components of the waves diffracted-radiated by a ship model advancing at constant speed in a water tank to be reflected at the walls of the tank.

A shortcut for computing time-domain free-surface potentials avoiding Green function evaluations.

A. CLÉMENT

ÉCOLE CENTRALE de NANTES
Laboratoire de Mécanique des Fluides - division Hydrodynamique Navale
CNRS URA 1217, E.C.N , Nantes, FRANCE

The numerical solution of transient hydrodynamic problems in the frame of the linearized potential theory requires the computation of convolution integrals. These integrals may be regarded as the memory of the free-surface fluid. Since they extend from the initial state of rest up to the current time t, the mass storage and *cpu* time required for their computation grow quickly with time, roughly quadratically. Consequently, in time-domain seekeeping computations, the major part of *cpu* is spent in evaluating these convolutions (Magee 1991).

Let us consider, for instance, the generation of surface waves by the prescribed motion (**V**) of a body around its equilibrium position (S) in a perfect fluid.

The resulting velocity potential $\Phi(M,t)$ must satisfy the following boundary integral equation :

$$\frac{\Phi(M,t)}{2} - \iint_S \Phi(M',t)\frac{\partial G_0(M,M')}{\partial n'}ds' = -\iint_S \mathbf{V}.\mathbf{n}(M',t)G_0(M,M')ds'$$
$$+\iint_S ds' \int_0^t \Phi(M',\tau)\frac{\partial F(M,M',t-\tau)}{\partial n'}d\tau - \iint_S ds' \int_0^t \mathbf{V}.\mathbf{n}(M',t)F(M,M',t-\tau)d\tau \qquad (1)$$

where G_0 and F are respectively the impulsive and the memory part of the Green function. In the present study we focus our attention on the convolution integrals in the RHS of (1). They may be written in the general form :

$$S = \int_0^T Q(\tau)F(r,Z+Z',t-\tau)d\tau \qquad (2)$$

where, when the water depth is infinite (Finkelstein 1957, Wehausen & Laitone 1960) :

$$F(r,\zeta,\xi) = \int_0^\infty \sqrt{K}\sin(\sqrt{K}\xi)J_0(Kr)e^{K\zeta}\,dK \qquad (3)$$

with : $$r = \sqrt{(X-X')^2+(Y-Y')^2}$$

Up to now, the efforts made to speed up the numerical computation of integrals like (2) in the numerical implementations of BEM to solve integral equations like (1) were essentially :

- derivation of alternative faster expressions of the Green function F, better suited to numerical calculation (Jami (1982), Newman (1985), Beck & Liapis (1987), ...),
- tabulation of the memory part of the Green function in order to replace the evaluation of F by a bi-linear interpolation in

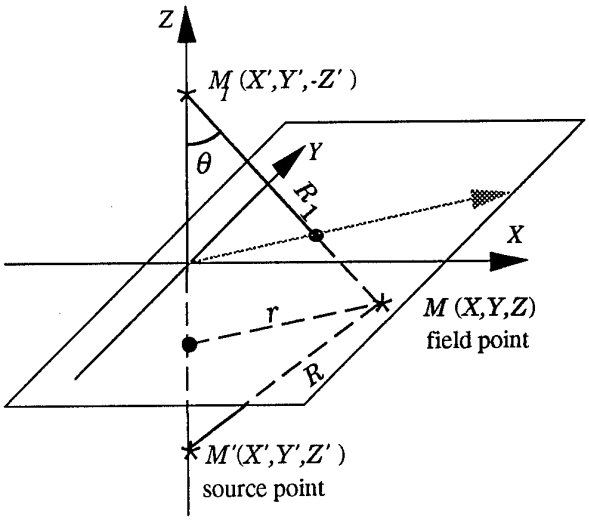

Fig.1 : Definition sketch.

a precomputed table (Ferrant-1988, Magee & Beck-1989).
An alternative method to evaluate the convolution products (2) without computing explicitly the Green function was proposed by Clément (1991). It is based on the identification of the Green function considered as a SISO (Single-Input-Single-Output) linear time-invariant process. The identification parametric *model* of the process is a linear ODE linking the input $Q(M',t)$, the output $S(M,t)$, and their derivatives. Once such a model has been found, S can be recovered from the knowledge of Q by simply integrating the ODE from a time step to the next one, instead of computing convolution integrals like (2). Doing so could save a huge amount of computer time and memory (Clément 1992).

1. A parametric time-varying model

In our first papers related to this topic (1991-1992), we attempted to identify the Green function with discrete time invariant models. These kind of models, often called ARX in process science literature, are characterized by discretized ODEs with constant coefficient.
They were shown later (Clément 1995) to be inadequate for the time domain Green function (3) which behaves asymptotically like a *"chirp"* process. This feature results in increasing considerably the model order to maintain a reasonable accuracy as both source point and field points approach the free surface (*i.e* : $\mu \to 0$).
Thus, we were led to adopt a more refined model (4) where the ODE coefficients are themselves function of time.

$$\sum_{i=0}^{i=n} A_i(t) S^{(i)}(t) = \sum_{i=0}^{i=n-1} P_i(t) Q^{(i)}(t) \tag{4}$$

where we use the notation : $S^{(i)}(t) = \dfrac{d^i S(t)}{dt^i}$.
In such a differential model, the causality of the process ensures the right-hand side order to be less than the left-hand side order. This property which is well known when the coefficients are constant, still holds for time-varying models (Zadeh et al. 1963).

2. The auto-regressive terms $A_i(t)$

The left-hand side of (4) is generally referred to as the *auto-regressive* part of the model. It can be obtained from the response of the process to an impulsive input $Q(t) = \delta(t)$.
Here, the impulse response function of the process is, by definition, the Green function itself $F(M,M',t)$.
Taking advantage of the fact that the kernel of the integral (3) can be expressed by an hypergeometric function, an exact fourth order differential equation for F may be derived making use of the general confluent equation :

$$R_1^{\,2} \frac{\partial^4 F}{\partial t^4} + \mu R_1 t \frac{\partial^3 F}{\partial t^3} + \left(\frac{t^2}{4} + 4\mu R_1 \right) \frac{\partial^2 F}{\partial t^2} + \frac{7t}{4} \frac{\partial F}{\partial t} + \frac{9}{4} F = 0 \tag{5}$$

with : $\mu = -(Z+Z')/\sqrt{r^2 + (Z+Z')^2}$. Thus, from (5), the auto-regressive coefficients $A_i(t)$ are found to be polynomials at most of degree two in the time variable. Their coefficients are very simple functions of the geometric parameters μ and R_1. A detailed derivation of (5) will appear in a more lengthy paper (Clément 1997).
As a first step toward computations speed up, one may use this ODE instead of the classical series developments (Newman 1985) for the *in-line* evaluation of the Green function in the numerical computation of the integral (3). To do so, one need also the initial conditions which can be easily deduced from (3) and its time derivatives by using the integral form of Legendre polynomials. After some algebra, we obtain :

$$\begin{cases} F^{(2k)}(r,\zeta,0) = 0 \\ F^{(2k+1)}(r,\zeta,0) = \dfrac{(-1)^k (k+1)!}{R_1^{\,k+2}} \mathrm{P}_{k+1}(\mu) \end{cases} \qquad k = 0,1,\ldots \tag{6}$$

which give the complete set of the time derivatives at the origin ; all the even order derivatives are null. It should be noticed to conclude this section that (5) and (6) are exact analytical results.

3. The forcing terms

The right-hand side of eq.(4) is generally referred to as the forcing term. Its form is a priori unknown, and a direct combination of (2) and (5) would lead to reintroduce convolution integrals in the RHS of the model. Thus, referring to time invariant models for which the property is formally established, we made the hypothesis that the forcing term of the present model can be expressed by a differential form similar to LHS (*i.e* with polynomial coefficients), and we sought it in the form :

$$RHS(4) = \sum_{i=0}^{3} Q^{(i)}(t) \sum_{j=0}^{j=\beta} p_{ij} t^j \tag{7}$$

The determination of the unknown coefficients p_{ij} was made easy by the knowledge of all the Markov parameters of the process through eq.(6). The method consists in expressing the model (4) and its successive time derivatives at the origin of time. At each level of differentiation, one can show that the lowest order unknown parameters p_{ij} may be expressed as a linear combination of the coefficients of (5), and of the Markov parameters $F^{(j)}(.,.,0)$.

4. continuous models of the Green function and its gradient.

The above method was applied first to the Green function itself , and gave :

$$R_1^{\,2} S^{(4)} + \mu R_1 t S^{(3)} + \left(\frac{t^2}{4} + 4\mu R_1\right) S^{(2)} + \frac{7t}{4} S^{(1)} + \frac{9}{4} S = \mu Q^{(2)} + \frac{\mu^2 t}{R_1} Q^{(1)} + \left[\frac{\mu\left(-3\mu^2 + \frac{13}{4}\right)}{2R_1^{\,2}} t^2 + \frac{1+\mu^2}{R_1} \right] Q \tag{8}$$

The maximum order of the polynomials P_i was assumed to be at most equal to the order of the A_i to ensure a stable asymptotic behaviour; whatever the input of the process ; nevertheless, it should be pointed out that the iterative method in §3 could provide higher order polynomials.

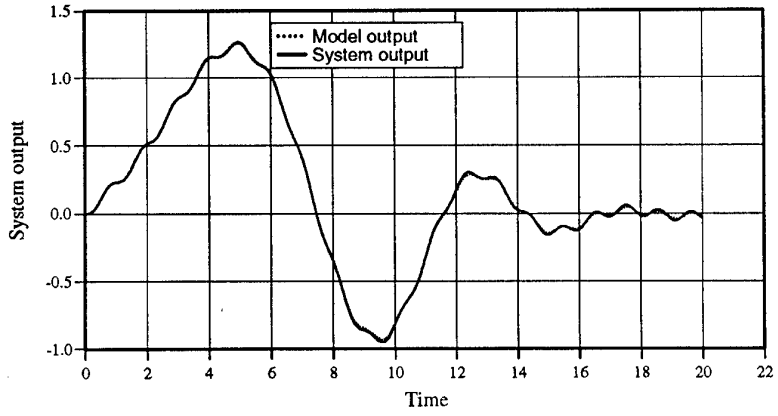

Fig.2 : Output $S(t)$ for input $Q(t)$=sin(6t), computed by both methods. μ =.3714

Results of a simulation of the process output for an harmonic input $Q(t)$=sin(6t) are plotted on Fig.2 . Both methods were applied : a standard trapezoidal integration method using (2) and (3), and the present time-varying model (8). Discrepancies between these two curves appear to remain negligible in this precise case.

Because the solution of the integral equations of time-domain hydrodynamics may require also convolution integrals involving the gradient of the Green function, the present approach was applied to the horizontal and vertical gradient as well.
We simply give below the results after calculations.

Horizontal gradient

$$R_1^2\frac{\partial^4 S}{\partial t^4}+\mu R_1 t\frac{\partial^3 S}{\partial t^3}+\left(\frac{t^2}{4}+6\mu R_1\right)\frac{\partial^2 S}{\partial t^2}+\frac{11t}{4}\frac{\partial S}{\partial t}+\frac{21}{4}S=\frac{-3\sqrt{1-\mu^2}}{R_1}\left\{\mu Q^{(2)}+\frac{\mu^2 t}{R_1}Q^{(1)}+\left[\frac{\mu\left(-5\mu^2+\frac{17}{4}\right)}{2R_1^2}t^2+\frac{1+\mu^2}{R_1}\right]Q\right\} \quad (9)$$

Vertical gradient

$$R_1^2\frac{\partial^4 S}{\partial t^4}+\mu R_1 t\frac{\partial^3 S}{\partial t^3}+\left(\frac{t^2}{4}+6\mu R_1\right)\frac{\partial^2 S}{\partial t^2}+\frac{11t}{4}\frac{\partial S}{\partial t}+\frac{25}{4}S= \quad (10)$$

$$\left(\frac{3\mu^2-1}{R_1}\right)Q^{(2)}+\frac{\mu t}{R_1}\left(\frac{3\mu^2-1}{R_1}\right)Q^{(1)}+\left[\left(-15\mu^4+\frac{75\mu^2}{4}-\frac{13}{4}\right)\frac{t^2}{2R_1^3}+3\mu\frac{\left(\mu^2+1\right)}{R_1^2}\right]Q$$

Numerical simulations were also performed for these two models with the same input, and a comparable accuracy was observed. Thus, the proposed models seem to be useful for our purpose in that frequency range. Nevertheless, the results are not so good as the input frequency decreases, and refining the models of the forcing terms seems to be necessary in that range.

Conclusion The time-domain Green function and its gradient were found to be solutions of fourth order ordinary differential equations with time-varying coefficients. These coefficients functions are low order polynomials of the time variable, and their own coefficients are simple functions of the geometrical parameters of the problem.
These time varying models may be used to compute the convolution integrals in time-domain seakeeping codes without computing the Green function itself (nor its gradient).
The accuracy is excellent for high frequency, but remain to be improved in the low frequency range.

Acknowledgements : This work has been supported by *Direction des Recherches, Études et Techniques* (DRET) of the french Ministry of Defense.

References

R.F BECK, S. LIAPIS (1987) Transient motions of floating bodies at forward speed. *J. Ship Reseach* Vol 31, pp 164-176.

R. BRARD (1948) Introduction à l'étude du tangage en marche. *Bulletin de l'ATMA* Vol 48, PARIS.

A. CLEMENT & L. FOULHOUX (1991) One step ahead in the numerical modelling of transient water waves: the identification of the time-domain Green function. *Computer Modelling in Ocean Engineering 91*. Arcilla et al. Eds. Balkema:Rotterdam.

A. CLEMENT (1992): A discrete time model of the transient hydrodynamics Green function ; Proc. 7th Int. Workshop on Water Waves and Floating Bodies; Val de Reuil, pp 59/62.

A. CLEMENT (1995): Identification de la fonction de Green de l'hydrodynamique transitoire par des modèles continus. *Proc. 5èmes Journées de l'Hydrodynamique*. Rouen. Mars 1995, pp 319/332.

A. CLEMENT (1997): An ordinary differential equation for the Green function of time-domain free-surface hydrodynamics. *(submitted)*.

P. FERRANT (1988) A fast computational method for transient 3D wave-body interactions.*Computer Modelling in Ocean Engineering*. 463-470. Balkema:Rotterdam.

A.B FINKELSTEIN (1957) The initial value problem for transient water waves. *Comm. Pure Appl. Math.*Vol 10, pp 511-522.

A. JAMI (1982) Etude théorique et numérique de phénomènes transitoires en hydrodynamique navale. *Thèse Doctorat ès Sciences* . ENSTA. Paris

A.R MAGEE, R.F BECK (1989): Vectorized computation of the time-domain Green function *4th Workshop on Water Waves and Floating Bodies*. Oystese: Norway.

A.R MAGEE (1991): Large-Amplitude Ship Motions in the Time Domain *PhD Thesis*; Univ. Michigan.

J.N NEWMAN (1985) The evaluation of free surface Green functions. *Proc. Fourth Int. Conf. Num. Ship Hydrodynamics*. Washington.

J.V. WEHAUSEN & E.V. LAITONE (1960) : Surface Waves. *Handbuch Der Physik*. Springer-Verlag Eds.

L.A. ZADEH & C.A. DESOER (1963) : *Linear System Theory*. McGraw-Hill Eds.

DISCUSSION

Newman J.N.: Equation 5 is remarkable. One consequence is that the corresponding frequency-domain Green function integral satisfies a 2nd order ODE with respect to the wavenumber!

Magee A.: I wish to congratulate the author on a truly original contribution on the use of time-domain Green functions. If a more accurate method for the forcing terms can be found, this shortcut should soon supplant all available methods for computing the time-domain Green function, because it will permit a gain of about 80 % in memory requirements for typical calculations. It is clear that equation (5) is exact. Is it possible to find exact solutions for the forcing terms (second part of eqn. 8)? What are the steps necessary to find these terms?

Secondly, you have treated the case applicable to linearised motions at zero forward speed, that is, the positions of the source and field points are not functions of time. However, we already have well-developed frequency-domain calculation methods for this case, at least in infinite depth. The real benefit of the time-domain method is its applicability to more complex cases such as steady forward speed and arbitrary large-amplitude motions because the Green function retains its relatively simple form in these cases as well.

According to my calculations, equation (5) is also valid in a steadily moving coordinate system (linearised problem with steady forward speed U) provided we replace the partial time derivative $\frac{\partial}{\partial t}$ with the total derivative $\frac{\partial}{\partial t}-U\frac{\partial}{\partial x}$ in the steadily moving frame. In this case we would have:

$$R_1^2\left(\frac{\partial}{\partial t}-U\frac{\partial}{\partial x}\right)^4 F+\mu R_1 t\left(\frac{\partial}{\partial t}-U\frac{\partial}{\partial x}\right)^3 F+\left(\frac{t^2}{4}+4\mu R_1\right)\left(\frac{\partial}{\partial t}-U\frac{\partial}{\partial x}\right)^2 F+\frac{7t}{4}\left(\frac{\partial}{\partial t}-U\frac{\partial}{\partial x}\right)F+\frac{9}{4}F=0 \quad (5bis)$$

(1) (2) (3) (4) (5)

where R_1 and μ are functions of time. In order to calculate the Green function in this case, we would need to "simulate" the Green function and its first four x-derivatives, which I have not done here. However, I have tested (5bis) by other means.

The attached figure presents the five terms of equation (5bis) and the sum of the terms, which should equal zero, if the relation holds. The Green function values were calculated using a Romberg method to assure a good precision, and the

derivatives were calculated using finite-difference schemes. The results seem to indicate that the relation holds and this is true for all values of the parameters tested. This calculation is confirmed by an analytical calculation (Maple) using the series expansion of the Green function (up to the order of the truncated series). Furthermore, I believe the same equation should generalise to the case of arbitrary motion of the source and field points (large-amplitude motions case) by using $\frac{\partial}{\partial t} - \vec{V}.\nabla$, where $\vec{V}$ is the relative velocity between M and M' in place of the partial time derivative $\frac{\partial}{\partial t}$ of equation (5). If this is true, then the large-amplitude calculations would be only slightly more time-consuming than linearised ones–a great advance indeed! Could you please comment?

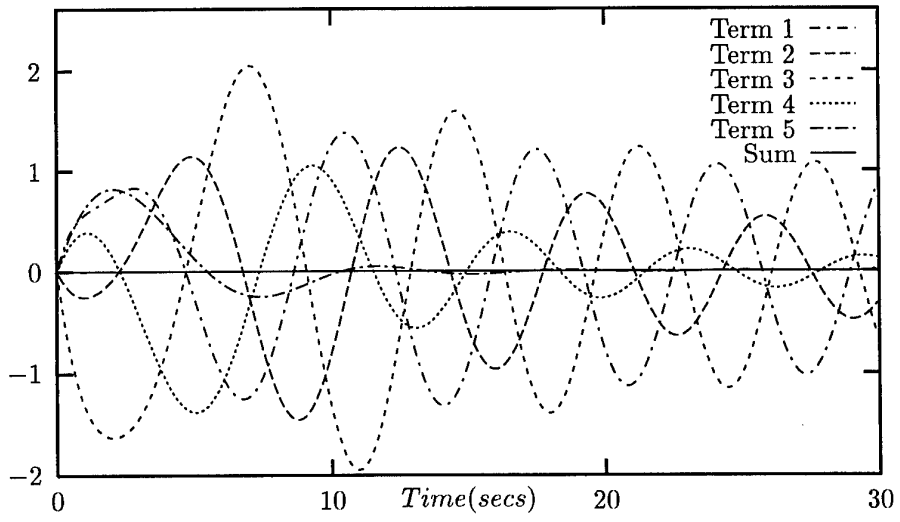

Fig. 1. *The 5 terms of eqn (5bis) and their sum, in the case of steady forward speed* $U = 0.25$, $x = 1$, $y = 0$, $z = -2$

Clément A.: It is indeed possible to find exact solutions for the forcing term. The simplest method consists in differentiating (2) four times using the Leibnitz rule, and then integrating (5) after having multiplied it by $Q(t)$. After a few lines of calculations, the exact forcing term of (4) is obtained. Unfortunately, it contains new convolution integrals, which is exactly what we want to avoid in our model! Thus, we chose the present approximation by a differential form, with no guarantee of convergence.

The Green function F does not depend on the trajectory of the source, due to the impulsive nature of its strength, and then (5) is also valid in that case, expressed in a fixed reference frame, provided R_1 and μ are understood as $R_1(0)$ and $\mu(0)$.

It can be indeed expressed in a moving reference frame by changing the derivative operator as you did, and taking into account the induced dependence of the space parameters on time. Thus, your numerical check of the ODE in these conditions is not surprising. As you mention, it involves higher horizontal derivatives of F. Differential equation similar to (5) could be easily derived for them, from the general lemma established in Clément (1997), to appear shortly.

VISCOUS FREE SURFACE FLOW PAST A SHIP IN STEADY DRIFT MOTION

A. Di Mascio, R. Penna, M. Landrini, E.F. Campana

INSEAN - Italian Ship Model Basin, Via di Vallerano 139, 00128 Roma, Italy

Abstract

The Reynolds averaged Navier–Stokes (RANS) equations with non linear free surface boundary conditions have been solved to simulate the flow field past a ship hull advancing with a drift angle. A Finite Volume technique has been used to discretize the equations, leading to a nonlinear algebraic system solved by a standard multigrid algorithm. Preliminary numerical results obtained for the Series 60 hull have been compared with experimental data.

Introduction

The computation of the unsteady incompressible viscous flow past a ship in maneuvering remains a great challenge. In fact, the general problem is a formidable one. The nonsymmetric flow over the hull is fully three-dimensional, boundary layers are turbulent, flow separation is common and may be followed by reattachment, and large wakes and complicated wave pattern are formed.

In principle, a fully viscous computation allows the prediction of the generation and transport of vorticity in the boundary layer and in the wake, and the coupled free surface and boundary layer interaction. However, the numerical solution of the general problem is in practice still strongly constrained by computer resourches. Reliable simulations of the flow past a manouvering ship are at present only feasible for steady drift motion.

Nevertheless, numerical computations of the RANS equations for the steady problem are particularly important also for the development of improved simplified models. Indeed they may provide useful detailed information on the location of the separation lines and on the evolution of the wake and may be used to calibrate and validate inviscid rotational models. As an example, the influence of an approximate choice of the location of the separation line on the values of the hydrodynamical lateral force and the yaw moment is still to be investigated. In fact, inviscid rotational models give satisfactory results once the separation line is known, as for a flat plate [1] or for a Wigley model. Unfortunately, this can be easily done only when the geometry is such to force the separation (i.e. sharp edges). Furthermore, to define the separation line in the case of 3D ship flows may not be an easy task.

A previous computation of the viscous free surface flow around a yawed Wigley model was attempted by using a domain decomposition approach [2]. In the present paper a large domain solution has been developed.

Mathematical model

We consider the steady flow past a ship hull $\mathcal{B}$ moving in an incompressible viscous fluid. The flow domain is bounded by the free surface $\mathcal{S}$, by the hull surface and extends to infinity. We assume a body-fixed reference frame with the x-axis aligned with the uniform flow and the z-axis positive upwards. The variables have been nondimensionalized by the ship length L and the free stream velocity U.

The velocity field is divergence free

$$\nabla \cdot \mathbf{u} = 0 \qquad \text{in } \mathcal{D} \tag{1}$$

and the momentum equation has to be satisfied

$$\mathbf{u} \cdot \nabla \mathbf{u} + \nabla P = \nabla \cdot \tau \qquad \text{in } \mathcal{D} \tag{2}$$

In the previous equation P is the 'total' pressure, i.e. the sum of the pressure term and the gravity term

$$\nabla P = \frac{\nabla p}{\rho} + \frac{\mathbf{k}}{Fr^2} = \nabla \left[\frac{p}{\rho} + \frac{z}{Fr^2} \right] \tag{3}$$

$\mathbf{k}$ being the unit vector aligned with the z-axis. τ is the stress tensor, including the turbulent stresses

$$\tau = (\frac{1}{Re} + \nu_T)\left[(\nabla \mathbf{u}) + (\nabla \mathbf{u})^T\right] \tag{4}$$

ν_T being the kinematic eddy viscosity. In the present work the Baldwin–Lomax turbulence model has been used.

The boundary conditions to be imposed are the standard ones for Navier–Stokes computations. At the solid wall no slip conditions are enforced, i.e. velocity is set to zero at the boundary (no conditions are required for the pressure). On the free surface $\mathcal{H}(x, y)$, neglecting the effects of surface tension and viscosity, the following kinematic and dynamic (constant pressure on $\mathcal{S}$) boundary conditions are to be satisfied:

$$u\frac{\partial \mathcal{H}}{\partial x} + v\frac{\partial \mathcal{H}}{\partial y} = w \tag{5}$$

$$P = \frac{\mathcal{H}}{Fr^2} \tag{6}$$

Numerical Solution

The Series 60 model (C_b=0.6) has been selected for simulation of this type of flow. In fact, for this model, detailed experimental data are available [3]. Furthermore, we have performed also some comparisons with measured data obtained at INSEAN.

Since the study is devoted to the simulation of the rectilinear motion of a ship advancing with a drift angle, in the numerical solution we cannot exploit the symmetry of the problem about the (x, z)-plane and therefore port and starboard sides are discretized. Hence the computational domain is decomposed into a port and a starboard block, the topology of each block being of H-O type. RANS equations have been written in a pseudo–transient formulation and a Finite Volume technique has been used to discretize the problem. Time integration has been carried out by a Runge–Kutta algorithm, second order accurate in time. The convergence has been accelerated by a FMG–FAS (Full Multigrid–Full Approximation Storage) multigrid technique.

As first test case, we simulate the flow past a Series 60 advancing in a oblique course for a drift angle $\alpha = 5°$ and for $Fr = 0.316$, $Re = 1.5 \times 10^7$. In this computation we have used $128 \times 64 \times 32$ cells in each block (port, starboard) of the fluid domain (streamwise, normal, and girthwise directions respectively).

The wave profile along the hull for both port and starboard side is shown in fig. 1 in comparison with some experimental data obtained by Longo [3]. The wave profile at the bow is dramatically modified with respect to the case $\alpha = 0$, since the different pressure values in that area, between pressure and suction side, imply respectively an increase and a lowering of the wave height. The numerical simulation was able to catch the main features of the flow. The agreement is satisfactory from $x = 0.2$ to $x = 1.2$ (the hull is located between 0 and 1). The flow at the bow ($x < 0.2$) is qualitatively predicted but the maximun free surface elevation in this region are underestimated. The unsufficient longitudinal grid resolution is this area is obviously a major factor in the loss of accuracy of the numerical prediction.

Forces and moments acting on the hull have been also predicted and compared with eperimental data obtained at INSEAN for the fixed hull case. Measurements were made on a model 6.096 m long, following the ASME guidelines [4] for the uncertainty analysis. As a preliminary check, numerical results for the force and moment coefficients for a drift angle $\alpha = 5°$ and for $Fr = 0.316$, $Re = 1.5 \times 10^7$, are compared with the experimental data in Table 1. The computed normal force coefficient C_x shows a satisfactory agreement with the measured data, while the moment coefficient C_{Mz} and the lateral force coefficient C_y are overpredicted.

In fig. 2 the history of the convergence for C_y has been reported as a funtion of the work, defined as the cost of one iteration on the finest grid. The best performance, from the point of view of the CPU time requirements, has been found with a five level computation. C_y values obtained on each level can be easily followed from the coarsest to the finest grid and compared with the reported measured data.

C_x		C_y		C_{Mz}	
$Exp.$	$Num.$	$Exp.$	$Num.$	$Exp.$	$Num.$
-0.0155	-0.0141	0.0222	0.0314	0.0106	0.0133

Table 1: Computed and measured forces and moment coefficients for $\alpha = 5°$, Fr = 0.316, Re = 1.5×10^7

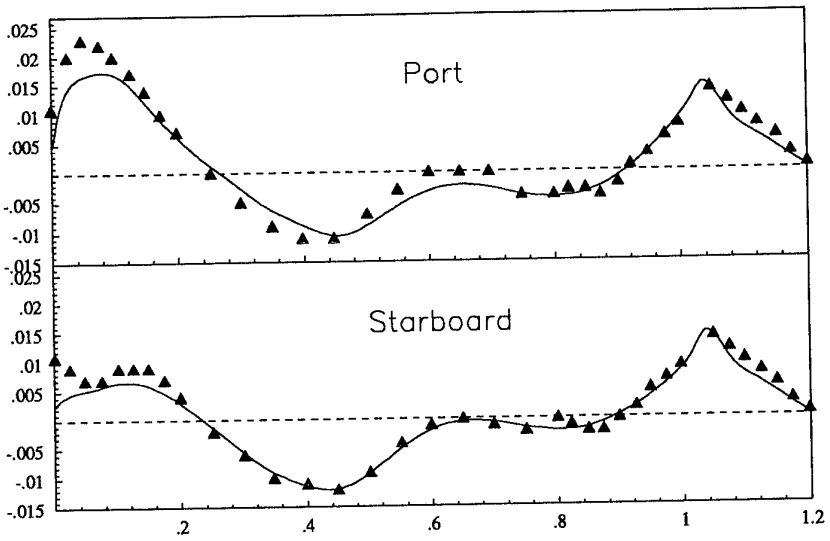

Figure 1: Wave profile along the hull: $Fr = 0.316$, $Re = 5 \times 10^6$, $\alpha = 5°$. Solid lines, numerical simultation ; $\triangle$, experimental data by [3]

A typical wave pattern is depicted in fig. 3 for $Fr = 0.316, Re = 1.5 \times 10^7, \alpha = 5°$ As espected, the free surface elevation in the starboard side is less pronunced, expecially near the bow. The wave pattern is stretched in the port side and spread in the starboard side.

Finally, for the same case as before, the visualization of the computed wake shed from the keel and the stern lines is reported in fig. 4.

Acknowledgment

This research activity was supported by *Ministero dei Trasporti e della Navigazione* through INSEAN Research Program 1994-1996.

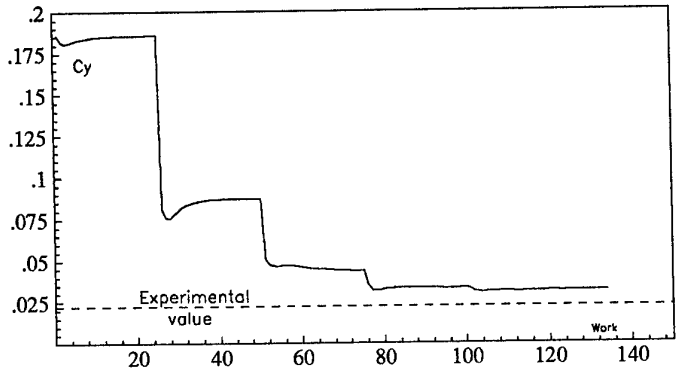

Figure 2: Convergence history for C_y as a function of the work. Five grid levels have been used in the multigrid algorithm. Correspondingly the value of C_y varies from the coarsest grid to the finest one. The experimental value is reported with the dashed line.

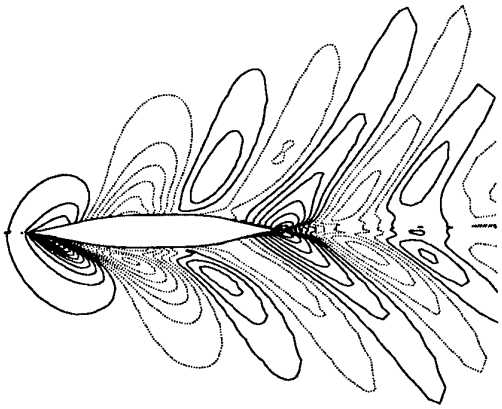

Figure 3: Computed wave pattern for $Fr = 0.316$, $Re = 1.5 \times 10^7$, $\alpha = 5°$

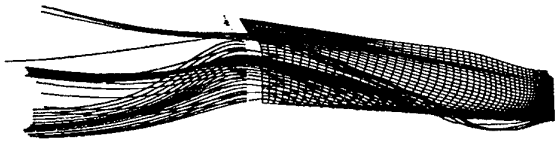

Figure 4: The wake shed from the keel and the stern lines of a Series 60 advancing with a drift angle $\alpha = 5°$

References

[1] Landrini M., Campana E.F., "Steady Waves and Forces About a Yawing Flat Plate", J. Ship Res., Vol. 40, No.3, pp.179–192 (1996).

[2] Campana E.F., Esposito P.G., Penna R., "Numerical Simulation of the Drift Motion of a Ship", Proc. of the 20-th O.N.R. Symposium on Naval Hydrodynamics, Santa Barbara, (1994).

[3] Longo J.,Ph.D. Thesis, Dept. of Mech. Eng., Univ. of Iowa (1996).

[4] ANSI/ASME PTC 19.1-1985, Part 1 "Measurement Uncertainty " (1986).

Solitary waves with algebraic decay

F. DIAS

Institut Non-Linéaire de Nice
UMR 129 - CNRS & UNSA
1361 route des Lucioles, 06560 Valbonne, FRANCE

1 Introduction

The study of capillary–gravity solitary waves is fairly recent. Among these waves, the most relevant from a physical point of view are the waves which bifurcate from a train of infinitesimal periodic waves with the property that their phase and group velocities are equal. These waves exist both in finite and in infinite depth. However, their properties differ with the depth. These waves were first computed numerically in infinite depth by Longuet–Higgins (1989). A physical interpretation was provided simultaneously by Akylas (1993) and Longuet–Higgins (1993). They showed that these waves correspond to stationary solutions of the nonlinear Schrödinger equation that governs slow modulations in space and in time of capillary–gravity waves. In certain regions of parameter space, it is well-known that the nonlinear Schrödinger equation (nlS) admits solutions in the form of wave packets, characterized by two length scales, the length of the envelope and the wavelength of the oscillations inside the envelope. The envelope travels at the group velocity while the oscillations travel at the phase velocity. It is therefore natural to obtain steady wave packets when phase and group velocities are equal. Additional numerical results were provided in infinite depth by Vanden–Broeck & Dias (1992) and in finite depth by Dias, Menasce & Vanden–Broeck (1996).

The important difference between finite and infinite depth comes from the properties of the dispersion relation. Let h denote the depth, k the wave number, g the acceleration due to gravity, c the phase velocity, σ the coefficient of surface tension. In finite depth, the dispersion relation is

$$c^2 = \left(\frac{g}{k} + \sigma k\right) \tanh(kh)\,, \tag{1.1}$$

while in infinite depth it becomes

$$c^2 = \left(\frac{g}{|k|} + \sigma|k|\right)\,, \tag{1.2}$$

which is singular at $k = 0$. This singularity leads to nonlocal terms, which are not present in the nlS equation. In the context of modulated waves, these nonlocal terms represent the interaction between the wave envelope and the induced mean flow. For gravity waves, they were computed first by Dysthe (1979) and recomputed by Stiassnie (1984) by using the so-called Zakharov's equations. Hogan (1985) extended Stiassnie's analysis to capillary–gravity waves. In this abstract, we construct an analytical solution of Hogan's equation which shows that the presence of the nonlocal terms leads to an algebraic decay in $1/x^2$ of the solitary waves. Note that Longuet–Higgins (1989) predicted such a decay purely on physical grounds and that the numerical results of Vanden–Broeck & Dias (1992) also show such a decay.

2 Analytical results

Let the free surface elevation be described by

$$\eta(x,t) = \tfrac{1}{2}\left\{A(x,t)\mathrm{e}^{i(kx-\omega t)} + \text{c.c.}\right\}. \tag{2.1}$$

Using as a basis the so-called Zakharov's equations, Hogan (1985) derived a higher-order nlS equation, similar to Dysthe's equation which was obtained by the method of multiple scales. Dimensionless variables (denoted with primes) are introduced by taking $\sigma/\rho c^2$ as unit length $[L]$ and $\sigma/\rho c^3$ as unit time $[T]$. In addition we introduce a small parameter ϵ (see below) as well as slow variables:

$$(x,z) = [L](x',z'), \quad t = [T]t', \quad A = \epsilon[L]A', \quad \overline{\phi} = \epsilon^2\frac{[L]^2}{[T]}\overline{\phi}', \quad (X,Z,T) = \epsilon(x',z',t').$$

ϕ is the velocity potential, z the vertical coordinate. From now on, the primes will be dropped. The amplitude A satisfies the equation

$$A_T + c_g A_X - \mathrm{i}\epsilon(pA_{XX} + q|A|^2A) + \epsilon^2(rA_{XXX} + uA^2A_X^* + v|A|^2A_X) + \mathrm{i}\epsilon^2 kA\overline{\phi}_X|_{Z=0} = 0, \tag{2.2}$$

where

$$c_g = \frac{\omega}{k}\frac{\alpha+3k^2}{2(\alpha+k^2)}, \quad p = \frac{\omega}{k^2}\frac{3k^4+6\alpha k^2-\alpha^2}{8(\alpha+k^2)^2},$$

$$q = -\omega k^2\frac{8\alpha^2+k^2\alpha+2k^4}{16(\alpha-2k^2)(\alpha+k^2)}, \quad r = -\frac{\omega}{k^3}\frac{(\alpha-k^2)(\alpha^2+6\alpha k^2+k^4)}{16(\alpha+k^2)^3},$$

$$u = \omega k\frac{(8\alpha^2+k^2\alpha+2k^4)(\alpha-k^2)}{32(\alpha-2k^2)(\alpha+k^2)^2}, \quad v = -3\omega k\frac{4k^8+4\alpha k^6-9\alpha^2k^4+\alpha^3k^2-8\alpha^4}{16(\alpha-2k^2)^2(\alpha+k^2)^2},$$

with

$$\omega^2 = k(\alpha+k^2), \quad \alpha = \frac{g\sigma}{\rho c^4}.$$

The potential $\overline{\phi}$ satisfies Laplace's equation

$$\overline{\phi}_{XX} + \overline{\phi}_{ZZ} = 0, \tag{2.3}$$

with boundary conditions

$$\overline{\phi}_Z = \frac{1}{2}\omega\frac{\partial}{\partial X}(|A|^2), \quad (Z=0), \quad \overline{\phi}_Z \to 0, \quad (Z\to-\infty). \tag{2.4}$$

Capillary-gravity solitary waves bifurcate when $\alpha = \alpha_0 = \frac{1}{4}$, $k = k_0 = \frac{1}{2}$, $\omega = \omega_0 = \frac{1}{2}$. The corresponding values of the coefficients are $p_0 = \frac{1}{2}$, $q_0 = \frac{11}{256}$, $r_0 = 0$, $u_0 = 0$, $v_0 = \frac{3}{32}$.

In terms of $\xi = X - c_g T$ and of $\tau = \epsilon T$, the evolution equations for A and $\overline{\phi}$ read

$$\mathrm{i}A_\tau + pA_{\xi\xi} + q|A|^2A + \mathrm{i}\epsilon(rA_{\xi\xi\xi} + uA^2A_\xi^* + v|A|^2A_\xi) - \epsilon kA\overline{\phi}_\xi|_{Z=0} = 0, \tag{2.5}$$

$$\overline{\phi}_{\xi\xi} + \overline{\phi}_{ZZ} = 0, \tag{2.6}$$

with boundary conditions

$$\overline{\phi}_Z = \frac{1}{2}\omega\frac{\partial}{\partial\xi}(|A|^2), \quad (Z=0), \quad \overline{\phi}_Z \to 0, \quad (Z\to-\infty). \tag{2.7}$$

Solutions in the form of envelope solitons can be sought as

$$A = R(\xi)\exp\{\mathrm{i}(\chi\tau + \epsilon f(\xi))\}\,, \tag{2.8}$$

which leads to the following system, correct to order ϵ^2:

$$\begin{aligned} 2pR_\xi f_\xi + pRf_{\xi\xi} + rR_{\xi\xi\xi} + uR^2R_\xi + vR^2R_\xi &= 0\,, & (2.9)\\ pR_{\xi\xi} - \chi R + qR^3 - \epsilon kR\overline{\phi}_\xi|_{Z=0} &= 0\,. & (2.10) \end{aligned}$$

Let us now expand R in powers of ϵ:

$$R = R_0(\xi) + \epsilon R_1(\xi) + \cdots\,.$$

One finds that R_0 satisfies the differential equation

$$pR_{0\xi\xi} - \chi R_0 + qR_0^3 = 0\,, \tag{2.11}$$

which gives

$$R_0 = \frac{a}{\cosh[a(\frac{q}{2p})^{1/2}\xi]}\,, \quad \chi = \tfrac{1}{2}qa^2\,. \tag{2.12}$$

Now we explain the meaning of the small parameter ϵ. The branch of solitary waves bifurcates at $\alpha = \frac{1}{4}$. ϵ measures how far α is from α_0. Let $\mu = \alpha - \alpha_0$. One finds easily that

$$\mu = \frac{11}{256}a^2\epsilon^2\,.$$

Therefore

$$\epsilon R_0 = \frac{16}{\sqrt{11}}\sqrt{\mu}\frac{1}{\cosh[\sqrt{\mu}(x-t)]}\,.$$

The integration of the first equation of the system leads to

$$\epsilon f = -\frac{12}{11}\sqrt{\mu}\tanh[\sqrt{\mu}(x-t)]\,.$$

So far, we have only dealt with the central part of the envelope. Let us now compute the nonlocal term $\overline{\Phi}$:

$$\overline{\Phi} = \tfrac{1}{2}\,\mathrm{i}\,\omega\int_{-\infty}^{+\infty}\mathrm{e}^{iK\xi}\,\mathrm{sgn}\,K\,\widehat{R_0^2}\,\mathrm{d}K = -\tfrac{1}{2}\int_0^{+\infty}\sin(K\xi)\,\widehat{R_0^2}\,\mathrm{d}K\,.$$

One finds that

$$\overline{\Phi} = -\frac{64}{11}\int_0^\infty \frac{K\sin(K\xi)}{\sinh\left(\frac{8\pi}{a\sqrt{11}}K\right)}\,\mathrm{d}K\,.$$

This induced mean flow leads to a change $\overline{\eta}$ of the free surface elevation, given in unscaled variables by

$$\overline{\eta} = -\frac{1}{\alpha}\overline{\Phi}_t = -\frac{1}{22}\left(\frac{16}{\pi}\right)^3\mu^{3/2}\int_0^\infty K^2\,\frac{\cos[\frac{2K}{\pi}\sqrt{\mu}\,(x-t)]}{\sinh K}\,\mathrm{d}K\,.$$

The behavior as $\sqrt{\mu}(x-t)$ becomes large is given by

$$\overline{\eta} \sim \frac{512}{11\pi}\sqrt{\mu}\frac{1}{(x-t)^2}\,.$$

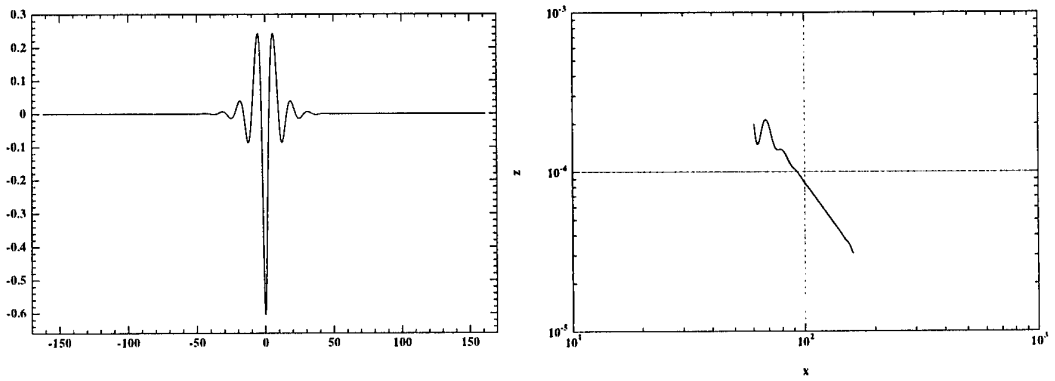

Figure 3.1: Solitary wave for $\mu = 0.02$. Profile and algebraic decay.

It follows that the algebraic tail dominates the exponential tail if

$$(x - t) > -\frac{\ln \mu}{\sqrt{\mu}}.$$

For small amplitude waves, when the algebraic tails starts to dominate, it is already quite small and therefore one can conclude that the effect of the algebraic tail is more pronounced for larger amplitude waves. In the next section, numerical results on the full Euler equations are used to show that it is indeed the case.

3 Numerical results

In this section, we present numerical results for several values of μ. For large values of μ, it is clear that the tail decays algebraically (see plot of $\ln \eta$ versus $\ln x$). The numerical solutions are obtained by using the scheme of Vanden–Broeck & Dias (1992).

ACKNOWLEDGMENTS

This work was done in collaboration with T. Akylas and R. Grimshaw.

REFERENCES

- Akylas T. R. (1993), *Phys. Fluids A* **5**, pp. 789-791.
- Dias F., Menasce D. & Vanden–Broeck J.-M. (1996), *Europ. J. Mech. B* **15**, pp. 17-36.
- Dysthe K. B. (1979), *Proc. R. Soc. Lond.* **A 369**, pp. 105-114.
- Hogan S. J. (1985), *Proc. R. Soc. Lond.* **A 402**, pp. 359-372.
- Longuet–Higgins M. S. (1989), *J. Fluid Mech.* **200**, pp. 451-470.
- Longuet–Higgins M. S. (1993), *J. Fluid Mech.* **252**, pp. 703-711.
- Stiassnie M. (1984), *Wave Motion* **6**, pp. 431-433.
- Vanden–Broeck J.-M. & Dias F. (1992), *J. Fluid Mech.* **240**, pp. 549-557.

Recent progress in dealing with the singular behavior of the Neumann-Kelvin Green function

Y. Doutreleau* and J.-M. Clarisse‡

The Neumann-Kelvin formulation of the linear wave-resistance problem is considered. Due to the singular behavior of the Neumann-Kelvin Green function, special care is required when dealing with surface piercing bodies. Consequently, an element integration technique is proposed as a discretization paradigm. This method, which alleviates the singular behavior of the Green function, is implemented within the frame of a bounded domain formulation for the Neumann-Kelvin problem. Advantages and drawbacks are presented, and possible improvements discussed.

A bounded domain formulation for the Neumann-Kelvin problem

We consider the wave-resistance problem of a body moving at constant speed, $-U_0\,\vec{x}$, in the half space $z \leq 0$ occupied by an ideal fluid at rest. In the Neumann-Kelvin approach, the velocity potential is decomposed, in the co-moving reference frame, as the sum $U_0\,x + \varphi_e$, where φ_e is solution of the Neumann-Kelvin problem.

Panel methods making use of the Neumann-Kelvin Green function, define the perturbation potential φ_e in terms of dipole and source distributions over the body boundary Γ. The potential φ_e, which has then the following integral representation:

$$\varphi_e(M) = \int_\Gamma \left[\varphi_e(P)\,\partial_{\vec{n}_P} G_\nu(M,P) - f(P)\,G_\nu(M,P)\right] d\Gamma_P, \tag{1}$$

where G_ν is the Neumann-Kelvin Green function, $\nu = g/U_0^2$ and $f(P) = -U_0\ (\vec{n}_P \cdot \vec{x})$, is obtained as solution of an integral equation on Γ.

However, rather than solving this integral equation, we here consider a bounded domain problem which is derived using a variational formulation/integral representation coupling method [4]. In addition to its theoretical interest, this approach presents some practical advantages: for example, equation (1) can now be defined on an arbitrary coupling surface Σ thus avoiding the $1/r$ singularities of the Green function. Furthermore, in order to avoid computing second order derivatives of G_ν, the bounded domain formulation is herein modified by introducing a potential $\tilde{\varphi}_i$, solution of a Dirichlet problem in Ω_i, an interior domain of the body (Figure 1-a). Consequently, solving the Neumann-Kelvin problem for a submerged body is shown to be equivalent to finding the solution $(\varphi_e, \tilde{\varphi}_i)$ of the problem:

$$\left\{\begin{array}{ll}
\displaystyle\int_{\Omega_e} \nabla\varphi_e \cdot \nabla\bar{\psi}_e - \frac{1}{\nu}\int_{\widehat{SL}} \partial_x\varphi_e\,\partial_x\bar{\psi}_e\,dS + \mu\int_\Sigma \varphi_e\,\bar{\psi}_e\,d\Sigma & \displaystyle\int_\Gamma f\bar{\psi}_e\,d\Gamma \\
\displaystyle + \int_{\Omega_i} \nabla\left(r_\Gamma^{F_a}(\varphi_e) + \tilde{\varphi}_i\right)\cdot\nabla\overline{\tilde{\psi}_i} & \displaystyle = \quad -\int_\Sigma \bar{\psi}_e \int_\Gamma f(P)\,G_\mu\,d\Gamma_P\,d\Sigma_M \\
\displaystyle - \frac{1}{\nu}\int_\sigma \bar{\psi}_e \int_{\Omega_i} \nabla\left(r_\Gamma^{F_a}(\varphi_e) + \tilde{\varphi}_i\right)\cdot\nabla\left(r_\Gamma^{F_a} + r_{F_a}^\Gamma\right)(G_x)\,d\sigma & \displaystyle + \frac{1}{\nu}\int_\sigma \bar{\psi}_e \int_\Gamma f(P)\,G_x\,d\Gamma_P\,d\sigma_M \\
\displaystyle + \int_\Sigma \bar{\psi}_e \int_{\Omega_i} \nabla\left(r_\Gamma^{F_a}(\varphi_e) + \tilde{\varphi}_i\right)\cdot\nabla\left(r_\Gamma^{F_a} + r_{F_a}^\Gamma\right)(G_\mu)\,d\Sigma &
\end{array}\right. \tag{2}$$

for any test function $(\psi_e, \tilde{\psi}_i)$. In this formulation, the conventions are:

- $G_\mu(M,P) = (\partial_{\vec{n}_M} \cdot + \mu\cdot)G_\nu(M,P)$, where μ is a complex number of non-zero imaginary part so as to avoid irregular frequencies;
- $G_x(M,P) = \partial_{x_M} G_\nu(M,P)\,(\vec{n}' \cdot \vec{x})$, where $\vec{n}'$ is the vector lying in $\widehat{SL}$ and normal to σ at M;
- $r_\Gamma^{F_a}(\psi)$ is such that $r_\Gamma^{F_a}(\psi) = \psi$ on Γ and $r_\Gamma^{F_a}(\psi) = 0$ on F_a, and conversely for $r_{F_a}^\Gamma$.

*Bassin d'Essais des Carènes, Chaussée du Vexin, 27100 Val de Reuil, France
‡CEA/LV, 94195 Villeneuve-St-Georges, France

Unfortunately, because of the singular behavior of $G_\nu(M,P)$ for P downstream of M, the latter being on the free surface (see [7]), the equivalence between the Neumann-Kelvin problem and (2) could not be established for surface piercing bodies. In view of this difficulty, we shall restrict ourselves to the devising of a discretized formulation of (2) for submerged bodies which remains numerically well behaved in the limit of zero depth.

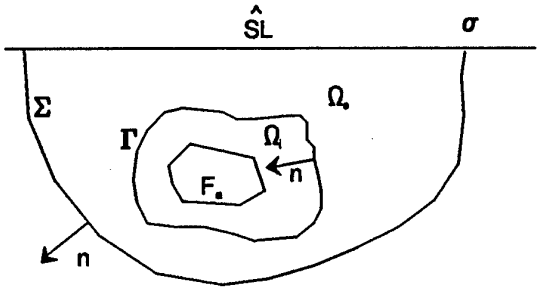

FIG. 1-a: *Coupling method*

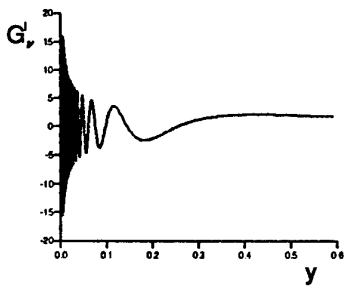

FIG. 1-b: *Singular behavior of* G_ν^l

For this purpose, the bounded domain formulation is solved numerically using a finite element method: the different terms in (2) are discretized with the help of basis functions w_l which depend on the volume discretization of the domains Ω_i and Ω_e, and on the type of interpolation functions being used. The singular behavior of the Green function forbids however the use of classical discretization techniques for the terms of (2) which involves $G_\nu(M,P)$ at its singular regime [1]. Consequently, a specific discretization method must be devised.

An element integration method

The Green function G_ν can be decomposed as the sum of a near-field and a far-field component, G_ν^l, the latter accounting entirely for its singular behavior. The difficulties which arise when discretizing the terms involving G_ν^l in (2), can be circumvented by first, interchanging the orders of integration between the points M and P in (2), then, performing analytically the spatial integration with respect to M. An approach following this principle has also been proposed for the diffraction-radiation problem with forward speed: see [6]. The present procedure leads to computing analytically the integrals:

$$(3) \qquad \int_\sigma \bar{w}_l \, \partial_{x_M} G_\nu^l(x,y,z') \, (\vec{n}'_M \cdot \vec{x}) \, d\sigma_M \quad \text{and} \quad \int_\Sigma \bar{w}_l \, (\partial_{\vec{n}_M} \cdot + \mu \cdot) \, G_\nu^l(x,y,z') \, d\Sigma_M$$

with the notations $x = x_P - x_M$, $y = y_P - y_M$, and $z' = z_P + z_M$. In performing this task, we benefit here from the ability of choosing an arbitrary coupling surface Σ. Hence by imposing Ω_e to be a rectangular prism (Figure 2-a), analytical integration of (3) is only required for M on σ_1 and Σ_1—the portions of σ and Σ directly upstream of the body.

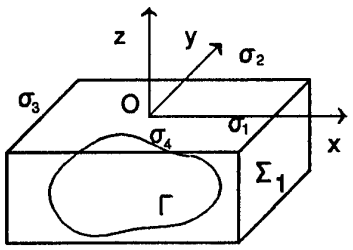

FIG. 2-a: *Particular choice of* Ω_e

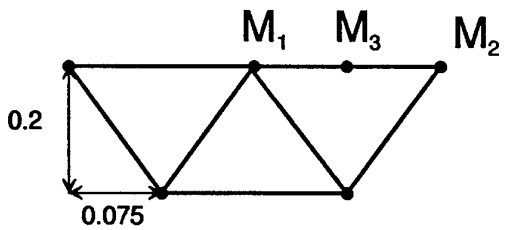

FIG. 2-b: *Discretization of* Σ_1

Based on experience with computations for submerged bodies, Lagrange elements of degree 2 are retained as they provide satisfactory rates of convergence for a limited number of unknowns. Therefore, evaluating the integrals in (3) for a triangular element $\mathcal{T} = (M_1, M_2, M_3)$ of Σ_1 is equivalent to

computing the element integrals:

$$(4)\qquad \begin{cases} T_j = \displaystyle\int_{[M_1,M_2]} w_j\, \partial_{x_M} G^l_\nu(x,y,z')\, d\sigma_M & j = 1,2,3 \\ T^r_j = \displaystyle\int_T w_j\, \partial_{x_M} G^l_\nu(x,y,z')\, d\Sigma_M\,, \quad T^i_j = \displaystyle\int_T w_j\, G^l_\nu(x,y,z')\, d\Sigma_M & j = 1..6\,. \end{cases}$$

For this purpose, we retain the representation of G^l_ν used in [2]. We are thus led to consider the following complex contour integrals:

$$(5)\qquad G_k(r,\alpha,\xi) = \int_{L_+} \frac{\exp\left[-\frac{r}{2}\cosh(2u - i\alpha) + i\xi\cosh u\right]}{(\cosh u)^{k-1}(\sinh u)^{k+1}}\, du\,, \text{ for } k = 0..2,$$

$$(6)\qquad E^q_{k,k'}(r,\alpha,\xi,Q) = \int_{L_+} \frac{\exp\left[-\frac{r}{2}\cosh(2u - i\alpha) + qu + i\xi\cosh u\right]}{(\cosh u)^k\,(z_Q\cosh u - iy_Q\sinh u)^{k'}}\, du\,, \text{ for } \begin{cases} q = -1,0,1 \\ k = 0,1,2 \\ k' = 1,2,3 \end{cases},$$

with $\xi = \nu|x|$, $r = \nu\sqrt{y^2 + z'^2}$, $\alpha = \arctan(-y/z')$, and where L_+ is a path joining $-\infty$ to $+\infty$ and avoiding the poles of the integrand. As the integrals G_k and $E^q_{k,k'}$ are similar to the expression of G^l_ν, the various approximations described in [2] are extended to the present case. Two complementary approximations per integral are thus derived which provide numerical results with an absolute accuracy of at least five significant digits, and this for ξ in a range sufficiently large for the present applications. These approximations consist in: *a)* convergent series expansions for values of the parameter $\mathcal{M} = \xi^2/4r \leq 16$, and *b)* asymptotic expansions along with highly oscillatory integrals when $\mathcal{M} \geq 16$. These oscillatory integrals, similar to that introduced in [8], are evaluated following [5]. The main difference between G^l_ν and the functions G_k and $E^q_{k,k'}$ lies in the fact that the latters are defined and continuous for $\xi > 0$, $r = 0$, $|\alpha| = \pi/2$, whereas the former is singular there.

Applications

Submerged ellipsoid

The present element integration approach has been compared, for the case of a submerged ellispoid, with a classical discretization method as well as with the semi-analytical results of Farell [3]. Wave-resistance results show good agreement between the element integration method and Farell's results for an ellipsoid with an aspect ratio of 5 at a submergence depth of a quarter of the focal distance: see Figures 3-a, b.

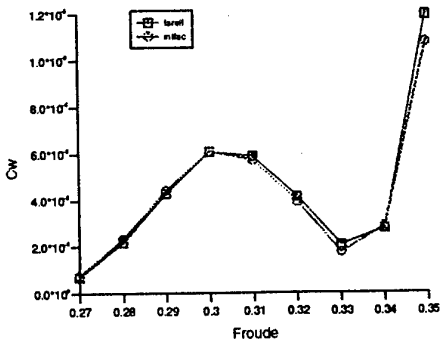

FIG. 3-a: *Small Froude number*

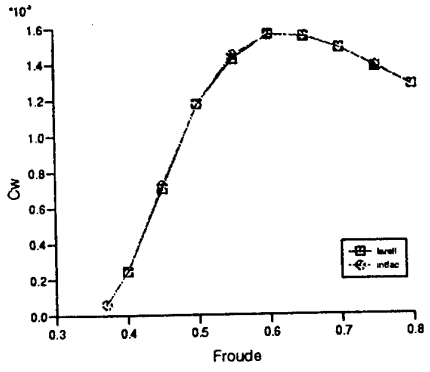

FIG. 3-b: *Large Froude number*

Surface piercing ellipsoid

Computations with the same ellipsoid, but now half submerged, have been performed. Wave-resistance results appear to be strongly unstable with respect to mesh refinements. An analysis of the line and surface integral contributions in (3) furnishes a possible explanation for this behavior. Indeed these contributions present oscillations near the tracks of the discretization points lying on σ_1. These

oscillations, which cannot be resolved with a reasonably fine mesh, render the element integrals T_j acutely sensitive to the location of the point P. This peculiarity is illustrated in Figures 4-a, b for the element integrals T_1 and T_1^r associated to the point M_1 of coordinates $x = 1.4$, $y = z = 0$ (see Figure 2-b): significant peaks are clearly visible about the points $y_P = 0, \pm 0.075$. The fact that these peaks are more pronounced for T_1 than for T_1^r, and that their magnitude increases with the distance ξ, indicates that they are inherent to the highly oscillatory behavior of G_ν^l.

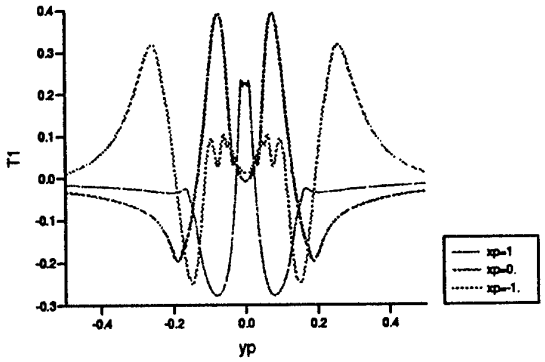

FIG. 4-a: *Behavior of* T_1

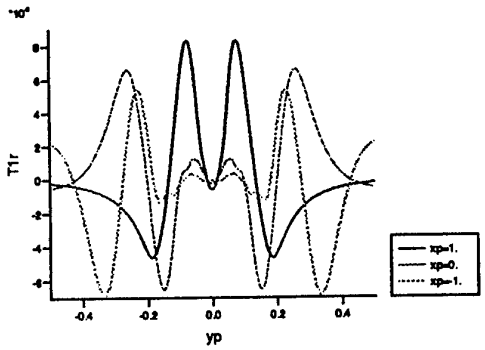

FIG. 4-a: *Behavior of* T_1^r

Discussion

Analytical evaluations of the line and surface integral contributions in (3) has alleviated the singular behavior of G_ν^l, thus resulting in a proper numerical discretization of the bounded domain formulation (2). However, at this stage, numerical results could not be obtained for surface piercing bodies due to the strongly oscillatory behaviors of the element integrals T_j. Such behaviors are associated with the discretization of the boundary Σ_1 and the particular choice of basis functions with discontinuous slopes. Significant improvements could be achieved in several ways, namely:

- by performing analytically the spatial integration with respect to the field point P: while this task does not present further difficulties, the required analytical computations are significantly heavier.
- through the use of C^m elements, $m > 0$: the current finite element procedure based on Lagrange element would need to be taylored to such a case.
- through the use of spectral elements: substantial work would be needed to devise a practical method capable of handling an arbitrary shaped boundary such as Γ.

References

[1] J.-M. Clarisse, "Highly oscillatory behaviors in the Neumann-Kelvin problem", Sixth International Workshop on Water Waves and Floating Bodies, Woods Hole, 1991.

[2] J.-M. Clarisse, J.N. Newman, "Evaluation of the wave-resistance Green function: part 3—the single integral near the singular axis", *J. Ship Res.*, **38**, 1, pp. 1-8, 1994.

[3] C. Farell, "On the wave-resistance of a submerged spheroid", *J. Ship Res.*, **17**, No 1, 1973.

[4] M. Lenoir, A. Jami, "A variational formulation for exterior problems in linear hydrodynamics", *Comp. Meth. in Appl. Mech. and Eng.*, **16**, pp. 341-359, 1978.

[5] J.N. Newman, "Evaluation of the wave-resistance Green function near the singular axis", Third International Workshop on Water Waves and Floating Bodies, Woods Hole, 1988.

[6] F. Noblesse, X.-B. Chen, C. Yang, "Fourier-Kochin theory of free-surface flows", 21-rst Symposium on Naval Hydrodynamics, Trondheim, 1996.

[7] F. Ursell, "On Kelvin's ship-wave pattern", *J. Fluid Mech.*, **8**, pp. 418-431, 1960.

[8] F. Ursell, "On the theory of the Kelvin ship-wave source, asymptotic expansion of an integral", *Proc. R. Soc. Lond.*, **A 418**, pp. 81-93, 1988.

DISCUSSION

Kuznetsov. N.: The finite element method usually leads to tridiagonal matrix while matrices arising from discretization of boundary integral equations are complete. Does the matrix in your coupled approach have the advantage of the FEM to be tridiagonal?

Doutreleau Y., Clarisse J-M.: No, it's not the case because of the coupling terms between the hull Γ and the coupling surface Σ. So we have more unknowns than in boundary integral method, but not so many because in many problems, only one layer of finite elements is needed. The real advantage of the coupling method consists in involving no singularities of Rankine type in the Green function.
The second advantage in the precise problem involved in this talk is that we can decrease the analytical work drastically by choosing an appropriate coupling surface.

Impulsive diffraction by an array of three cylinders

Thomas H. Farstad*

It has recently been discovered that trapped waves are present in an array of cylinders. Frequency-domain work reported by Maniar and Newman [3] and others, includes both analytical solutions and computational results. One of the important questions this phenomenon raises is how long it will take to build up a trapped wave or nearly trapped wave, and how important this will be in the generation of time series. It is also of interest to understand when the interaction between the cylinders occurs.

Impulsive-diffraction analysis by an array consisting of three cylinders has been performed to answer these questions. Results have been reported in the frequency-domain on arrays of the size of 100 cylinders using a B-spline methodology, but the computational expense using a planar, constant strength panel method in the time-domain has so far limited this study to three cylinders. However, the phenomenon found in the frequency-domain are recovered.

During work with arbitrary generalized modes in the time-domain, it was found that a wide variety of problems could be addressed [2]. Generalized modes were therefore used to study the diffraction by the three cylinders. The total potential Φ describing the flow satisfies Laplace's equation. The free surface condition is linearized and the body boundary condition is implied on the mean wetted surface of the global structure. The total potential is decomposed by

$$\Phi = \phi_I + \phi_S + \sum_{j=1}^{J} \phi_j \tag{1}$$

where the incident potential is ϕ_I, the scattered potential is ϕ_S and for all rigid body modes and deformation modes there is an associated radiation potential ϕ_j. If the number of bodies is N then J=6N.

J normal vectors are also defined, in an N body problem such that n_1 is zero on all other bodies except the first. The same is true for n_2 to n_6. The normal vectors n_7 to n_{12} are nonzero on the second body and so on. The diffraction force can then easily be obtained by

$$F_j = \int_{\bar{S}} (\phi_I + \phi_S) n_j \mathrm{dS} \tag{2}$$

where $\bar{S}$ is the mean wetted surface of the global body. The problem is solved using an integral formulation and a free-surface Green function as explained by Bingham et al. [1]. Giving the body an impulsive velocity in a mode, impulse-response functions for the influence on all modes are obtained.

*Aker Norwegian Contractors, Boks 1358 Vika, 0113 Oslo, Norway (thomasfa@chf.mit.edu)

The global problem includes three truncated cylinders in infinite depth of radius and draft a. The separation distance between cylinder centroids is $2d = 4a$. The wave heading is parallel to the array. Each cylinder consists of 240 panels total.

Figure 1 presents the exciting force coefficient vs. nondimensional wavenumber for each of the three cylinders. The exciting force coefficients are found by Fourier transform of the diffraction impulse-response functions. The existence of trapped modes is evident. The results from the time-domain are compared to quantities produced by the frequency-domain code WAMIT, and the comparison confirms the method used. The peak occurring close to $Kd/\pi = 1/2$ is the Neumann trapped wave whereas the peak at $Kd/\pi \approx 1$ is the Dirichlet trapped wave. These names correspond to the boundary conditions for the trapped waves, for further explanation see [3]. Peaks for higher wavenumbers are present as well, all peaks will become sharper in a larger array and with larger draft for each cylinder.

The diffraction impulse-response functions for each of the three cylinders is presented in Figure 2. The response function is compared with the impulsive diffraction of a single cylinder at the same spatial location. To interpret the results it is important to understand that the impulsive wave is a delta function in time at $x = 0$, the same spatial location as the center of the second cylinder. As one would expect, it is found that no interaction is present before the wave-packet is close to the second cylinder. From the time when the majority of this wave-packet is coming close to the second cylinder the interaction is evident from Figure 2-a, where trapped waves are present for $t/(L/g)^{1/2} > 0$. As scattered waves of the second cylinder are becoming important, there is a rapid build-up of a nearly trapped wave-force acting on the first cylinder. The trapped wave has a slow decay rate and when the computation was stopped interaction effects could still be found. Figure 2-a indicates that it takes 4-5 wave periods to dissipate the energy associated with the trapped wave for this geometry.

Figure 2-b indicates that the interaction effects on the second cylinder take place earlier, as can be expected. The sheltering effect is easily seen for $t/(L/g)^{1/2} < 0$, whereas a trapped wave is seen for larger time. The magnitude of the wave is initially about the same as for cylinder one, but the decay rate is faster, of the order of 2-3 wave periods. This might be due to the interaction with the third cylinder, but results reported in the frequency-domain indicate that the separation distance is important as well. The third cylinder experiences a strong sheltering effect, and the trapped wave is not so clearly defined in Figure 2-c. The Fourier transform of the impulse-response function confirms this.

Applying generalized modes theory, the feasibility of computing impulsive diffraction in the time-domain for an array has been demonstrated, and it is shown that frequency-domain results can be reproduced. This gives confidence in the method. For the particular case studied we find that the trapping effect has a fast build-up, but the decay rate is different for each cylinder. This might be connected with the separation distance between the cylinders, and further studies should therefore include variation of the spatial separation. Further work will also be to study this problem in finite depth with bottom-mounted, rigid, cylinders. Interaction effects have been found to be strongest for this case, and by convolving an arbitrary wave-packet with the diffraction impulse-response function one will be able to study the duration of a nearly trapped wave in a random sea. In the generation of a time series this will be of importance.

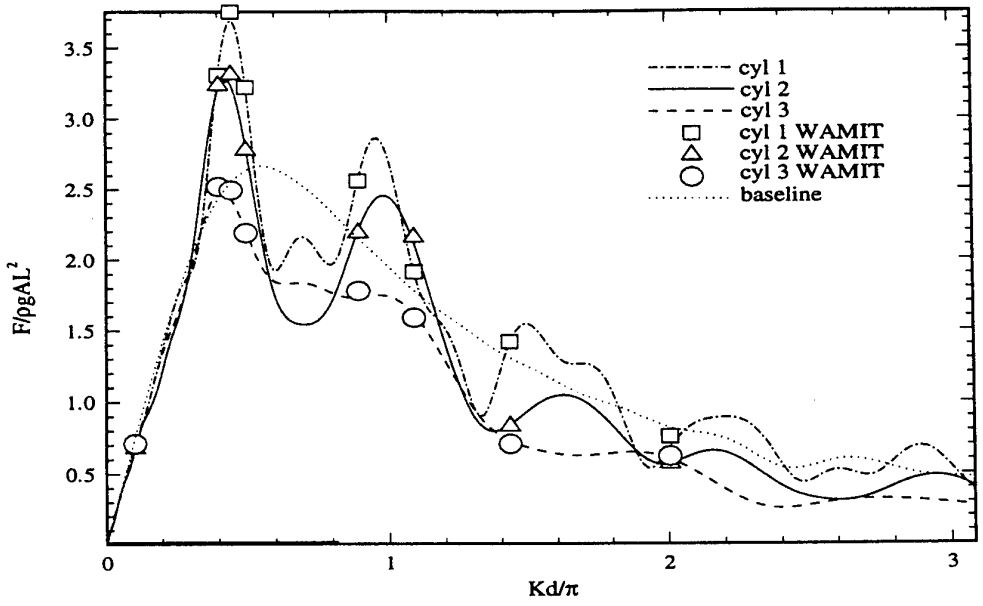

Figure 1: Magnitude of the exciting force coefficient in head seas for an array consisting of 3 truncated cylinders. Cylinder 1 is the first in the row. The separation distance is $2d = 4a$, where a is the radius. The baseline is the force on a single cylinder with no other bodies present.

This work was carried out at the Department of Ocean Engineering, Massachusetts Institute of Technology. Financial support has been received and is acknowledged from the Norway-America Association and the American-Scandinavian Foundation.

References

[1] Bingham, H. B., Korsmeyer. F. T., Newman, J. N., "Prediction of the Seakeeping Charateristics of Ships", *20th Symposium on Naval Hydrodynamics*, 1994.

[2] Farstad, T. H. "Transient seakeeping analysis using generalized modes", M.Sc Thesis, Massachusetts Institute of Technology, 1997.

[3] Maniar, H. D., Newman, J, N., "Wave Diffraction by a Long Array of Cylinders", *11th Workshop on water waves and floating bodies*, 1996.

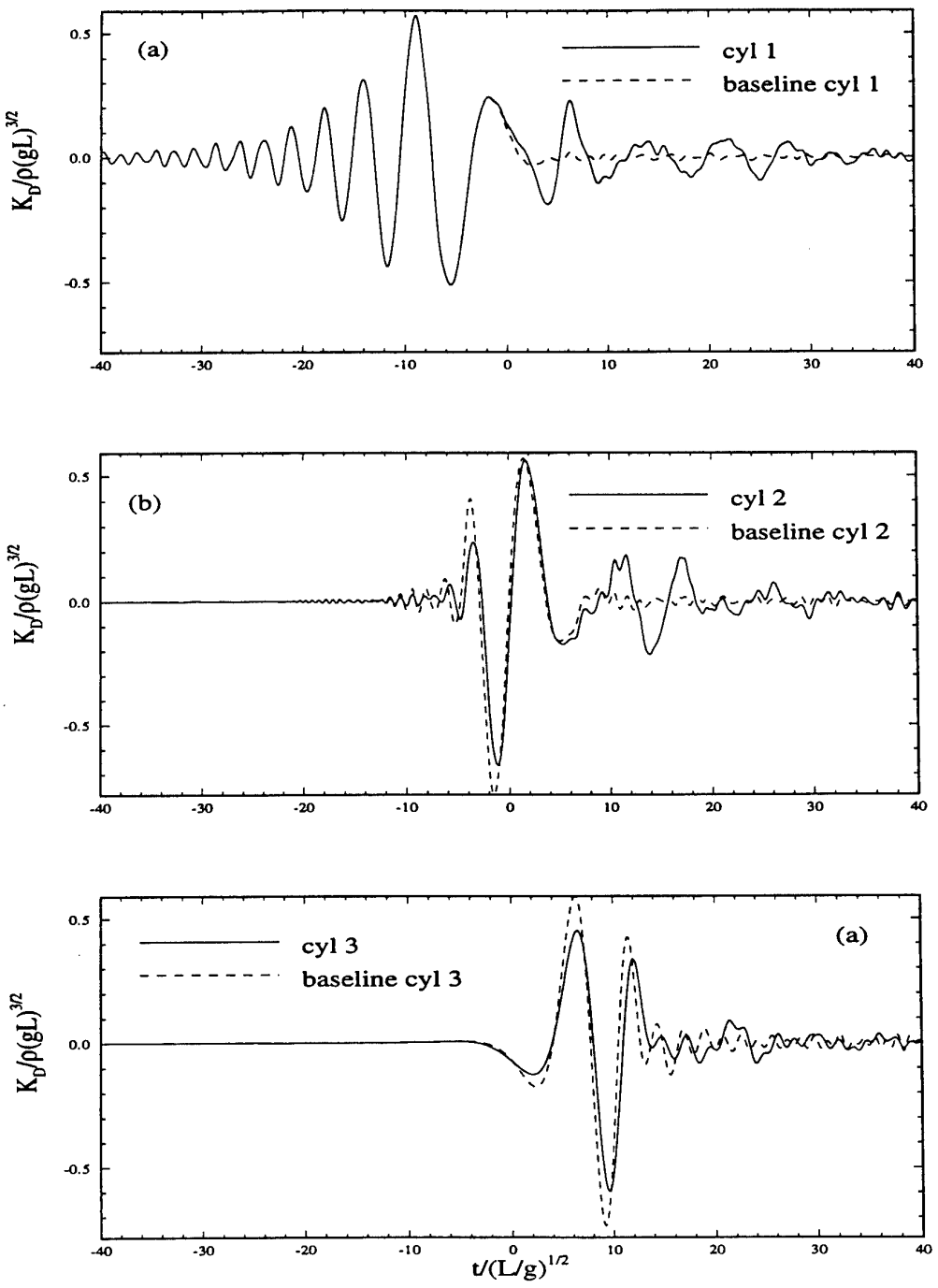

Figure 2: Memory function for the impulsive diffraction problem on an array consisting of three truncated cylinders.

DISCUSSION

Clément A.: Your results are for evenly spaced cylinders; what would happen to the trapped modes in the case of uneven spacing?

Farstad T.H.: I have not studied this problem, but I believe the resonance will disappear if the geometry of the problem is non-symmetric. This can be uneven spacing or cylinders with different diameters, for instance.

Eatock-Taylor R.: Have you encountered any numerical difficulties associated with the high frequency content in the impulsive wave?

Farstad T.H.: The formulation calculating the impulsive wave and performing the water line integral was developed by Bingham, Korsmeyer et. al [1]. The waterline integral is performed at a distance $d/2$ below the free surface, where d is the average height of the panels along the waterline. This attenuates the signal somewhat, and the high frequency problem is avoided.

Molin B.: You seem to hint that one could end up with different design values when using a time domain approach, as compared to the usual frequency domain one. If linearity is assumed, identical values are finally obtained.
On the other hand experiments on TLP like structures show quite different behavior in regular and irregular waves. In regular waves, quasi resonant sloshing motions of the free surface are observed at some frequencies leading to non-linear effects coming into play and ultimately breaking. In irregular waves these resonant sloshing motions get initiated in long wave groups at critical frequencies then disappears. So an aspect of the problem is how many waves it takes for the resonant state to be attained. In this respect your work is quite helpful.

12th WWWFB , Marseille, march 1997 - Revised Version

NONLINEAR WAVE-CURRENT INTERACTIONS IN THE VICINITY OF A VERTICAL CYLINDER

Pierre Ferrant
SIREHNA
1 rue de la Noë, BP 42105
44321 NANTES CEDEX 3 - FRANCE

INTRODUCTION

This paper is dedicated to the analysis of wave-current interactions in the vicinity of a three-dimensional body.

Most recently published numerical methods for the solution of this problem were developed within the frame of frequency-domain analysis, with significant contributions including Nossen *et al* (1991), Emmerhof & Sclavounos (1992), Teng & Eatock-Taylor (1995), Malenica *et al* (1995), among others. The advantage of this first approach is to provide results of interest such as wave forces and runups on the structures in a relatively straightforward manner. On the other hand, the mathematical formulation is significantly more complicated than with zero current speed, with specific problems such as secularity (Malenica 1995). There are also a number of practical limitations, such as regular incoming waves and uniform bottom topography only. At last, the perturbation expansion of boundary conditions with respect to wave steepness and current speed limits the analysis to linear or weakly nonlinear phenomena, and up to the author's knowledge, only linearized formulations have been published to date.

In these conditions, as for a number of other problems (Ferrant 1996b), time domain analysis represents a very attractive alternative. Using a time domain Rankine panel method, it is theoretically possible to implement any level of boundary condition approximation, from linearized conditions to fully nonlinear ones, and there is no limitation on the geometry. Of course, due to their computational demand which may be very important, even for recent workstations, the convergence of the numerical models, their stability and accuracy have not yet been sufficiently studied. Generally speaking, there is a remaining lack of confidence in this class of numerical models which will undoubtedly progressively disappear with their development and validation. The applications of time domain analysis to wave-current interaction problems are still scarce, see for example Kim & Kim (1995), and are restricted to the simulation of problems developed to first order in the wave amplitude parameter ε and in the current speed parameter τ.

In the present paper, we present some results of the application of fully nonlinear time-domain analysis to the wave-current interaction problem in the presence of a three-dimensional body. The incoming flow, including regular waves and current, is modelized using a stream function theory (Fenton & Rienecker 1981), and the problem is formulated in terms of the nonlinear perturbation induced to the incident flow by the body, using a formulation initially developed in Ferrant (1996a) for the capture of higher order diffraction effects in the time domain. The nonlinear free surface boundary conditions are updated using a 4th order Runge-Kutta scheme, the boundary value problem being solved at each step using a linear isoparametric boundary element method. An absorbing layer method is implemented for the absorption of diffracted waves. Results presented at the end of this paper concern the computation of the runup on a vertical cylinder in finite depth due to waves and current.

PROBLEM FORMULATION - NUMERICAL PROCEDURE

The simulation strategy is the same as described in Ferrant (1996a). The incident flow, including here acurrent, is prescribed by a stream function theory (Rienecker & Fenton 1981), and the diffraction problem is solved for the perturbation (Φ_D, η_D) induced by the body, defined by:

$$\Phi(x,y) = \Phi_e + \Phi_D \tag{1}$$

$$\eta(x,y) = \eta_e + \eta_D \tag{2}$$

where the subscript e denotes the pure incident flow. With this definition, we obtain the kinematic and dynamic free surface conditions for the perturbation flow:

$$\frac{d\eta_D}{dt} = -\frac{d\eta_e}{dt} - \vec{grad}(\phi_e + \phi_D).\vec{grad}(\eta_e + \eta_D) + \frac{d(\phi_e + \phi_D)}{dz} \tag{3}$$

$$\frac{d\phi_D}{dt} = -\eta_e - \eta_D - \frac{1}{2}\left[\vec{grad}(\phi_e + \phi_D)\right]^2 - \frac{d\phi_e}{dt} \tag{4}$$

where terms from the incident flow at the right-hand side can be evaluated exactly from the stream function wave model, without influence from time or space discretization. The problem being fully non linear, equations (3) and (3) must be satisfied on the instantaneous free surface position, and thus the incident potential may possibly be evaluated above the undisturbed incident wave. This is possible here because of the continuous prolongation of the incident potential above the incident wave. Of course, the formulation described above is not universal and depends on the availability of an explicit model for the incident wave.

On the body surface, the no-flux condition is written:

$$\Phi_{Dn} = -\beta(t) \cdot \Phi_{en} \tag{5}$$

where b(t) is a scalar function vaying smoothly from 0 to 1 during the first wave period, the simulation starting with Φ_D=0 everywhere in the fluid domain and η_D=0 on the free surface.

A boundary element method is used for the solution of the boundary integral equation formulation of the problem. The method is based on isoparametric triangular elements distributed over the different boundaries. A piecewise linear, continuous variation of the solution over the boundary is thus assumed, and collocation points are placed at panel vertices. Meshes are made of an assembly of different patches, with the assumption of continuous normal on each of them. On intersection lines between two patches, two collocation points are kept at the same geometrical position, and the boundary conditions corresponding to the two surfaces are both satisfied. At the intersection between two solid patches, two Neumann conditions for the two different normals are enforced, whereas at the intersection between solid boundaries and the free surface, both a Neumann (N) condition on the solid surface and a Dirichlet (D) condition on the free surface are satisfied. This discretization scheme reduces the integral formulation to a linear algebraïc system to be solved for the normal velocity on Dirichlet boundaries (free surface) and the potential on Neumann boundaries. This system is made of the influence coefficients of linearly varying distribution of sources on boundary elements. Analytical formulas for the near field, and different approximate formulas for the intermediate and far field of the different panels are implemented. These coefficients are factorized with respect to sources or dipoles density at panel vertices, which are selected as control points. This scheme results in square systems of equations for the singularity distribution on the boundaries of the computational domain, which are solved using a preconditioned GMRES scheme.

After the solution of the boundary value problem and the computation of fluid velocities at the free surface, free surface conditions considered as ODE's for ϕ and η are integrated in time. A fourth order Runge-Kutta method is used for that purpose, requiring four solutions of the boundary value problem per time step.

The radiation condition is enforced by adding dissipative terms in equations (3) and (4) on the outer part of the free surface mesh.

NUMERICAL RESULTS

The numerical scheme has been applied to the simulation of the diffraction of regular waves by a vertical cylinder in water of finite depth, with or without current. The cylinder radius is equal to the water depth, i.e. R/H=1. and the wavenumber is koH=1.0. The wave amplitude is A/H=0.1, and computations have been performed for current speeds U/sqrt(g/H)=-0.1, 0.0, 0.1.

Figure 1 and 2 compare the time series of the wave elevation at the weather side (Fig.1) and at the lee side (Fig. 2), for the three different values of the current speed. Figure 3 compares the maximum runups along the cylinder waterline in the three cases. Present nonlinear results at zero Froude number seem to be close to the second order model of Büchmann *et al* (1997). However, sensible differences in the influence of the current are observed between their approach, which is based on a perturbation analysis up to second order in the wave steepness and to first order in the current speed, and the present fully nonlinear model.

CONCLUSION

Wave-current-body interactions simulations presented in this paper were based on a fully nonlinear model in which no assumptions regarding the relative magnitudes of wave steepness and current speed are necessary. With the present values of the current and wave parameters, we observe sensible differences between the present fully nonlinear approach and the perturbation analysis results of Büchmann *et al* (1997). These differences remain to be clarified, first by comparing both approaches for lower values of the wave amplitude and current speed, but also by comparing numerical results and experimental values. We hope to be able to report on such comparisons in the near future.

Acknowledgments : The development of the code ANSWAVE has been supported by the Direction de la Recherche et de la Technologie, French Ministry of Defense, through successive research contracts. The developments presented in this paper are part of Clarom project on "Large amplitude wave amplifications in the vicinity of offshore structures", with Bureau Veritas, Doris Engineering, Bouyghes Offshore, G.ESIM, Ifremer, Principia and Sirehna as partners.

REFERENCES

B. Büchmann, J. Skourup, K.F. Cheung, 'Runup on a structure due to waves and current', ISOPE'97, Honolulu, 1997

O.J. Emmerhof, P.D. Sclavounos, 'The slow drift motion of arrays of vertical cylinders'. J.F.M., vol.242, pp 31-50, 1992.

P. Ferrant, 'Computation of higher order diffraction effects using a fully nonlinear simulation method', Proc. 11th W.W.W.F.B., Hamburg, 1996a

P. Ferrant, 'Simulation of strongly nonlinear wave generation and wave-body interactions using a 3D MEL model', 21st ONR Symposium on Naval Hydrodynamics, Trondheim, 1996b.

D.J. Kim, M.H. Kim, 'Interaction of a large three dimensional body with waves and currents by THOBEM', Proc. 10th W.W.W.F.B., Oxford, 1995.

S. Malenica, P.J. Clark, B. Molin, 'Wave and current forces on a vertical cylinder free to surge and sway' , Appl. Ocean Res., vol.17, pp 79-90, 1995.

S. Malenica, 'How to remove secularity in the solution of diffraction-radiation problemswith small forward speed', Proc. 10th W.W.W.F.B., Oxford, 1995.

J. Nossen, J. Grue, E. Palm, 'Wave forces on three dimensional flaoting bodies with small forward speed', J.F.M., vol. 227, pp 135-160, 1991.

M.M. Rienecker & J.D. Fenton, 'A Fourier approximation method for steady water waves' - J.F.M., vol.104, pp 119-137, 1981.

B. Teng, R. Eatock-Taylor, 'Application of a higher order BEM in the calculationof wave runup on bodies in a weak current', Int.J. Offshore and Polar Eng., Vol.5, N°3, pp219-224, 1995.

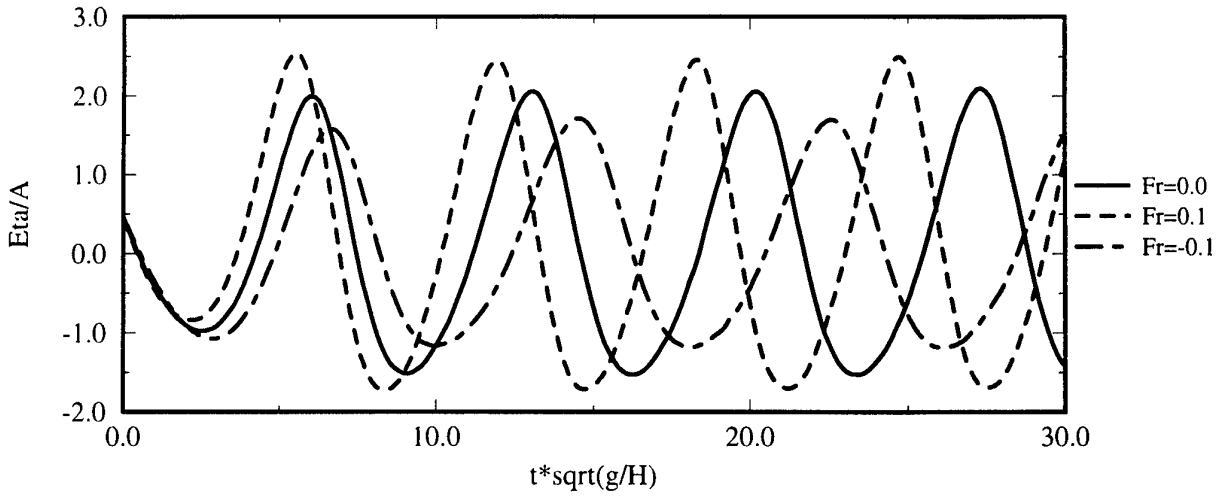

Figure 1: Wave elevation at the weather side. R/H=1.0; A/H=0.1; koH=1.0

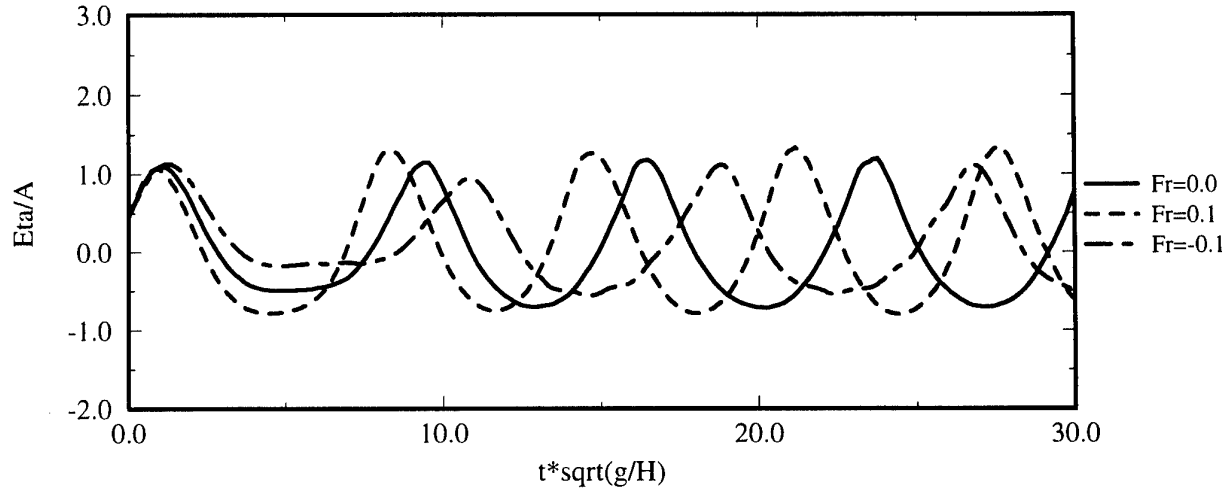

Figure 2: Wave elevation at the lee side. R/H=1.0; A/H=0.1; koH=1.0

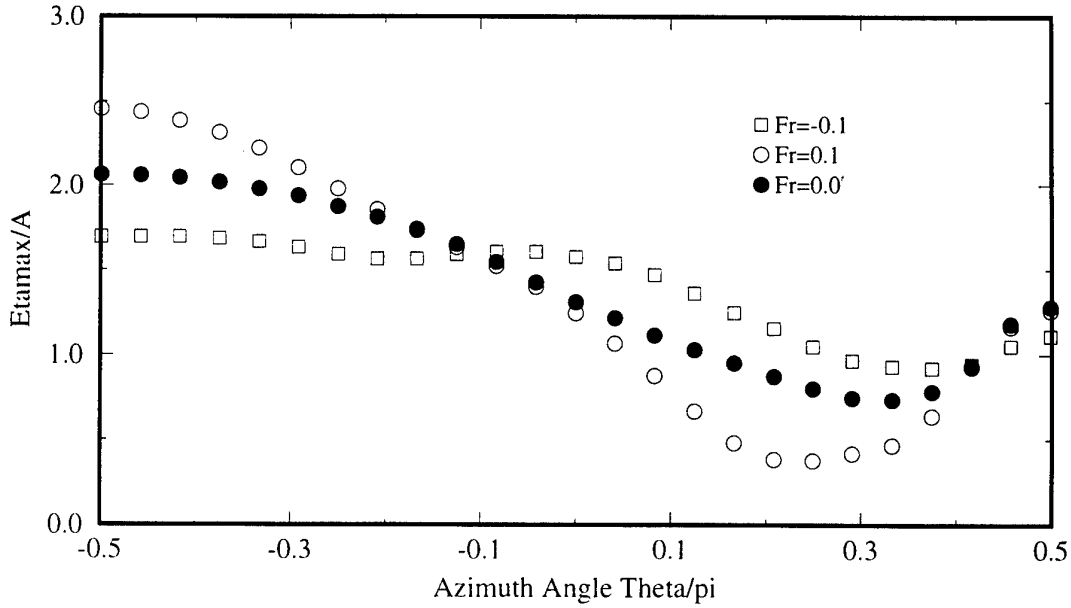

Figure 3 : Maximum wave runup. R/H=1.0; A/H=0.1; koH=1.0

DISCUSSION

Grilli S.: Did I correctly understand that you initialize your computations with a streamfunction, wave everywhere in the domain? Wouldn't this cause initial transient response that may affect the initial oscillation observed in your runup height. These, hence, may not be entirely physical.

Ferrant P.: Yes, the initial conditions correspond to the undisturbed incident wave in the domain, without body. The body is introduced through the Neumann condition which is multiplied by a smooth ramp function going from 0 to 1 during the first wave period.
Of course this procedure produces unphysical transients, but they die out very quickly and a periodic steady state is reached within less than two periods.
Relevant results such as forces and runups are then derived from the steady state part of the solution.

Higher-order wave drift forces on bodies with a small forward speed based on a long wave approximation

S.Finne

Department of Mathematics, Mechanics Division University of Oslo, Norway

1 Introduction

The mean wave force acting on bodies, stationary or moving with a small forward speed in a wave field is considered. This force, the so called wave drift force, has shown to be of great importance within offshore technology. The change in the drift force because of the small speed, the wave drift damping, may be an important damping mechanism.

Calculation of the wave drift forces has traditionally been based on linear theory giving the drift force consistently to second order in the wave amplitude, the mean second order wave force. We here refer to Grue & Biberg (1993), who extended the theory to include a finite depth. In this work we use a long wave approximation to calculate higher order wave drift forces on a vertical cylinder in shallow water, but of interest is also the time-dependent higher order wave force. The latter is among others also considered by Jiang & Wang (1995), for stationary bodies. As a model we use one version of the weakly nonlinear and dispersive Boussinesq equations, see. e.g. Wu (1981), Pedersen (1989). We remark that the Boussinesq equations contain the fully nonlinear hydrostatic equations. The equation set is then modified to include a small current. It is necessary to point out that in many practical problems, the water depth is outside the limit of the long wave approximation. One of the intentions with the present work is however to indicate higher order effects on the wave drift force.

The body is exposed to incoming cnoidal waves, and the wave field around the body is solved numerically in space and time by the finite element method. Then the drift force is computed by first integrating the pressure over the body surface, and then time-averaging the periodic force. The wave drift damping is calculated by numerical differentiation of the drift force with respect to the small current.

2 Mathematical formulation

The problem is considered in a frame of reference (x, y, z) moving with the body, in which there is a small constant current U_0 in the positive x-direction. Assuming potential theory, the velocity field may be expressed by a velocity potential $\Phi(x, y, z, t)$, where t is the time. According to the long wave approximation used here, we then introduce a depth average velocity potential $\psi(x, y, t)$ by

$$\psi(x, y, t) = \frac{1}{h + \eta} \int_{-h}^{\eta} \Phi(x, y, z, t) dz \tag{1}$$

Here $\eta(x, y, t)$ denotes the surface elevation, and the constant h is the mean water depth. We observe that the unknowns ψ and η are only functions of the horizontal coordinates. Furthermore ψ is divided into two parts $\psi(x, y, t) = \phi(x, y, t) + \phi_0(x, y)$ where ϕ and ϕ_0 represent the velocity potential due to the waves and the small current respectively. Typical wave length λ_0, and typical wave height H_0 are then defined, and three important dimensionless parameters α_0, α and ϵ given

by

$$\alpha_0 = \frac{U_0}{\sqrt{gh}}, \qquad \alpha = \frac{H_0}{h}, \qquad \epsilon = \frac{h^2}{\lambda_0^2} \tag{2}$$

will be present in the model. The gravitational acceleration is denoted by g. The actual version of the Boussinesq equations that will be used, and modified to include a small current, has the advantage of containing the unknown velocity potential instead of the two horizontal velocity-components. This reduces the total number of unknowns. The equation set for the unknown potentials ϕ_0 and ϕ, and the surface elevation η is

$$\nabla^2\phi_0 = 0 \tag{3}$$

$$\frac{\partial\phi}{\partial t} + g\eta + \frac{1}{2}(\nabla\phi)^2 - \frac{h^2}{3}\nabla^2\frac{\partial\phi}{\partial t} + \nabla\phi_0\cdot\nabla\phi = 0 \tag{4}$$

$$\frac{\partial\eta}{\partial t} + \nabla\cdot((h+\eta)\nabla\phi) + \nabla\phi_0\cdot\nabla\eta = 0 \tag{5}$$

where neglected terms are $O(\alpha_0^2, \alpha_0\alpha\epsilon, \alpha^2\epsilon, \alpha\epsilon^2)$. Eq. (4) represents conservation of momentum, while eq. (5) represents mass conservation.

The force acting on the body is obtained by integrating the pressure over the body surface. The depth integration is done analytically, and for the time dependent force $\mathbf{F}(t)$ we then obtain the following expression in terms of ϕ_0, ϕ and η

$$\mathbf{F}(t) = \rho h\int_{\Gamma_B}(-\frac{\partial\phi}{\partial t} + \frac{g}{2h}\eta^2 - \frac{1}{2}(\nabla\phi)^2 - \nabla\phi_0\cdot\nabla\phi)\mathbf{n}d\Gamma \tag{6}$$

Here Γ_B denotes the contour line of the body, $\mathbf{n}$ is the normal vector pointing out of the fluid domain and ρ is the fluid density. By time-averaging the force with respect to the wave period, we obtain the drift force $\overline{\mathbf{F}}$

$$\overline{\mathbf{F}} = \rho h\int_{\Gamma_B}\overline{(\frac{g}{2h}\eta^2 - \frac{1}{2}(\nabla\phi)^2 - \nabla\phi_0\cdot\nabla\phi - \frac{1}{6}(\frac{\partial\eta}{\partial t})^2)}\mathbf{n}d\Gamma \tag{7}$$

In this expression neglected terms are $O(\alpha_0^2, \alpha_0\alpha^2\epsilon, \alpha^4\epsilon, \alpha^2\epsilon^2)$, which is consistent with (3) - (5). The wave drift force is then expanded in order of α_0 by $\overline{\mathbf{F}} = \mathbf{F}_0 + \alpha_0\mathbf{F}_1$, where $\mathbf{F}_0$ is the zero speed drift force, and $\alpha_0\mathbf{F}_1$ is the wave drift damping force.

3 Numerical simulation

The numerical solution is performed by using the finite element method, with the ability of easily consider bodies of arbitrary shapes. Differentiation with respect to time is approximated by finite difference. For further details about the numerical method, we refer to Irmann-Jacobsen (1989) where (4)-(5) have been solved numerically when $\phi_0 \equiv 0$.

The model is applicable to an arbitrary fluid domain, but in the present study we want to calculate the drift force on a body in an unbounded fluid, with the incident wave field propagating in positive x-direction. We therefore define the simulating area as a square basin, (see. Fig 1), and solve (3)-(5) with the following initial and boundary conditions.

Eq. (3) for the unknown ϕ_0:

$$\frac{\partial\phi_0}{\partial n} = -U_0, U_0 \quad \text{on} \quad \Gamma_L, \Gamma_R \tag{8}$$

$$\frac{\partial\phi_0}{\partial n} = 0 \quad \text{on} \quad \Gamma_S, \Gamma_B \tag{9}$$

Eq. (4) and (5) for the unknowns ϕ and η:

$$\phi = \eta = 0 \quad t = 0 \tag{10}$$

$$\phi = \phi_I(t), \quad \eta = \eta_I(t) \quad \text{on} \quad \Gamma_L \tag{11}$$

$$\frac{\partial \phi}{\partial n} = 0 \quad \text{on} \quad \Gamma_B, \Gamma_S, \Gamma_R \tag{12}$$

Considering the solution of (4) and (5), (11) is the essential and (12) the natural boundary condition, the latter being the rigid wall condition. The incident waves given by η_I and ϕ_I with given wave length λ, and given wave height H, are the cnoidal wave solution of (4)-(5).

It is necessary to discuss some aspects about the discretization and the choice of boundary conditions. The time-averaging of the force must not be done before the wave field around the body has become nearly periodic in time. We must therefore either impose a radiation condition, or use a very large simulating area. The problem with the first is that it is difficult to ensure that the boundary does not reflect any significant waves, this has been the outcome from simulations where a radiation condition has been applied. In the latter case, one normally need a large number of elements. It is however found, by simulation of solitary waves propagating in one direction, that by increasing gradually and not to fast the element size, reflection because of grid-variation may bee neglected. We therefore use a large basin, with increasing element sizes in the outgoing region (i.e. downstream and to the side of the body see. Fig 1). It is then like wise to use the rigid wall condition on Γ_S and Γ_R. A time-averaging procedure is then established, and the drift force may be computed within a reasonable CPU time. An analytical solution of the second order drift force based on (4)-(5) when $\phi_0 \equiv 0$, has been developed for a circular cylinder. The mean second order wave force has then been computed numerically and convergence-tested with the analytical solution, with very good accuracy.

4 Results

In the first example, the body is a circular cylinder, with radius $R = 5h$, the size of the basin is $110h \times 110h$ with 11745 elements in half of the fluid domain. The body is exposed to an incident cnoidal wave train, and Fig. 2a shows an example of the x-component of $\mathbf{F}(t)$ at two different values of U_0. Fig. 2b and Fig. 2c then shows the x-component of the zero speed drift force and the wave drift damping at different values of the wave height, as a function of the wave length. The numerical differentiation of the drift force is done about $U_0 = 0.0$ with $\Delta U_0 = 0.04\sqrt{gh}$. $H = 0.0$ means second order theory. What is interesting to note is that both the wave drift coefficient $\frac{F_{x0}}{\rho g H^2 2R}$ and the wave drift damping coefficient $\frac{F_{x1}}{\rho g H^2 2R}$ are decreasing with increasing values of $\frac{H}{h}$. In the last example, Fig. 2d, the body is a model of a ship with length $L = 10h$ and beam $B = 1.79h$. In this case we see that the wave drift damping coefficient is not always less for the steepest waves.

References

[1] GRUE, J. AND BIBERG, D. (1993), Wave forces on marine structures with small speed in water of restricted depth. *Appl. Ocean Res.* **15**, 121-135.

[2] IRMANN-JACOBSEN, T. (1989), Finite element solution of the Boussinesq equations. *M.S. thesis in mechanics, University of Oslo.* (in Norwegian)

[3] JIANG, L. AND WANG, K. H. (1995), Hydrodynamic interactions of cnoidal waves with a vertical cylinder. *Appl. Ocean Res.* **17**, 277-289.

[4] PEDERSEN, G. (1989), On the numerical solution of the Boussinesq equations. *University of Oslo, Research Report in Mechanics* **89-1**.

[5] WU, T. Y. (1981), Long waves in ocean and coastal waters. *Proc. ASCE, J. Eng. Mech. Div.* **107**,EM3,501-522

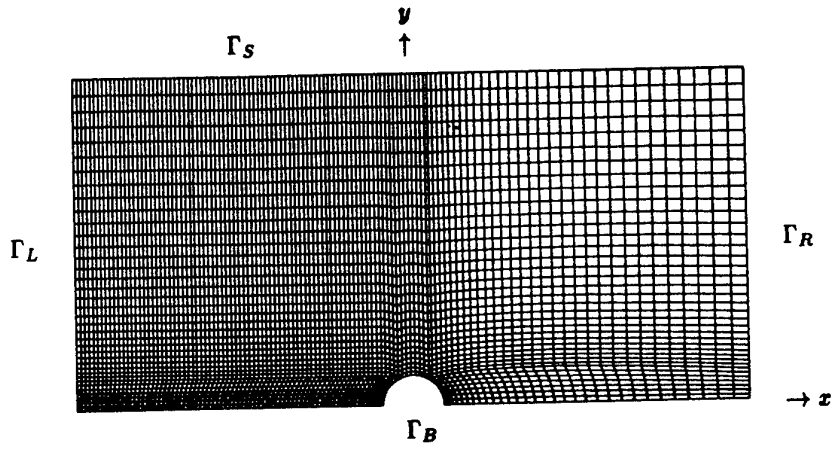

Figure 1: Discretization of half of the fluid domain, for the body being a circular cylinder. 4095 elements.

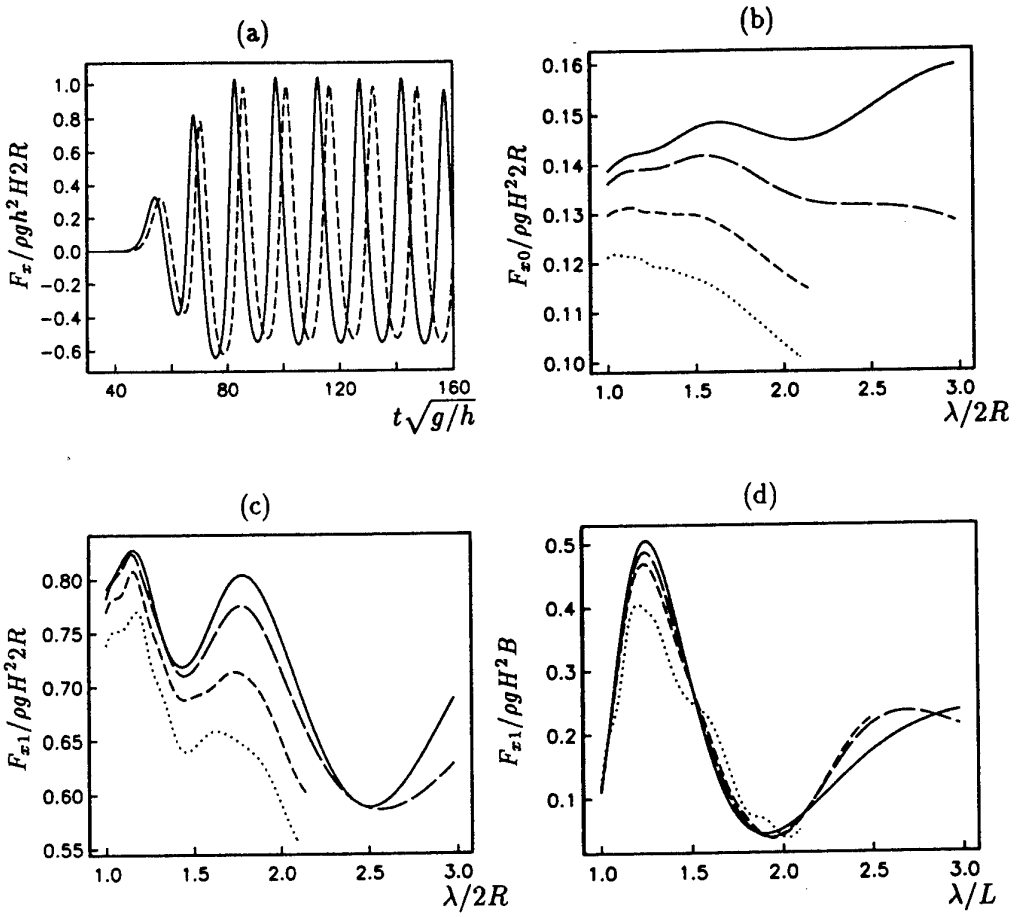

Figure 2: (a): The x-component of $\mathbf{F}(t)$ for the circular cylinder, $H/h = 0.2$, $\lambda/2R = 1.5$, $U_0/\sqrt{gh} = 0.02$ (solid line) and -0.02 (dashed line). (b) and (c): The x-component of $\mathbf{F}_0$ and $\mathbf{F}_1$ for the circular cylinder, $H/h = 0.0$ (solid line), 0.1 (long dashed line), 0.2 (dashed line) and 0.3 (dotted line). (d): F_{x1} for the ship, $H/h = 0.0$ (solid line), 0.1 (long dashed line), 0.15 (dashed line) and 0.3 (dotted line).

STEADY FLOW NEAR A WEDGE SHAPED BOW

E. FONTAINE
Ecole Centrale de Nantes, 1 rue de la Noë, 44072 Nantes Cedex, France.

O.M. FALTINSEN
Division of Marine Hydrodynamics,
Norwegian University of Science and Technology, N-7034 Trondheim, Norway.

1 Introduction

The free surface steady potential flow around a fine wedge shaped bow is studied. The concept of a bow flow solution was first introduced by Ogilvie (1972) and has recently been studied by (among others) Faltinsen & Zhao (1991), Fontaine & Cointe (1997), and Fontaine (1996). When the so called $2D+1/2$ or $2D+t$ theory is used to find the bow solution, good agreement is generally reported between the measured and computed wave profile along the hull. The main differences appear at the "nose" (apex) of the wedge where an initial elevation is observed but is not predicted. To over-come this misfit, a local analysis of the flow in the near-bow domain is performed (see fig. 1). The near-bow solution matches on the one hand to the bow-flow solution and on the other hand to the far-field solution. It also leads to an estimate of the wave elevation at the nose of the bow. Comparison with experiments are given. Extension of the theory to general cross-sections will be discussed in the oral presentation.

2 The near-bow flow

The two non-dimensional parameters describing the wedge shaped bow are $\tan\alpha = b/L$ and $\delta = h/L$. The near-bow domain is based on a length scale equal to the draft h and a velocity scale equal to U. The non-dimensional variables are defined as :

$$\hat{x} = \frac{x}{h}, \quad \hat{y} = \frac{y}{h}, \quad \hat{z} = \frac{z}{h}, \quad \check{\varphi} = \frac{\varphi}{Ub}, \quad \check{\eta} = \frac{\eta}{b}$$

where φ is the velocity perturbation potential and η the free surface elevation. Assuming the ship to be slender or thin ($\alpha \ll 1$, $\delta \ll 1$), the following asymptotic expansions are introduced :

$$\check{\varphi}(\hat{x},\hat{y},\hat{z};\alpha,\delta) = \check{\mu}_1(\alpha,\delta)\,\check{\varphi}_1(\hat{x},\hat{y},\hat{z}) + o(\check{\mu}_1)$$

$$\check{\eta}(\hat{x},\hat{y};\alpha,\delta) = \check{\nu}_1(\alpha,\delta)\,\check{\eta}_1(\hat{x},\hat{y}) + o(\check{\nu}_1)$$

Since there is no dilation of the space variables, the leading order perturbation potential $\check{\varphi}_1$ satisfies the three-dimensional Laplace equation in the fluid domain. Using the non-dimensional variables, the body boundary condition gives :

$$(1+\check{\mu}_1\frac{\partial\check{\varphi}_1}{\partial\hat{x}}) - \frac{\check{\mu}_1}{\delta}\frac{\partial\check{\varphi}_1}{\partial\hat{y}} + o(1) = 0$$

The principle of least degeneracy implies that $\check{\mu}_1 = \delta$. When the ship is thin ($\alpha \ll \delta$), the resulting condition is :

$$\frac{\partial\check{\varphi}_1}{\partial\hat{y}}(\hat{x},0,\hat{z}) = 1 \qquad (1)$$

on the center plane of the hull.
The kinematic free surface condition is imposed on $\hat{z} = (\alpha/\delta)\,\check{\nu}_1\,\check{\eta}_1$ and takes the form :

$$(1+\tan\alpha\frac{\partial\check{\varphi}_1}{\partial\hat{x}})\frac{\partial\check{\eta}_1}{\partial\hat{x}} + \tan\alpha\frac{\partial\check{\varphi}_1}{\partial\hat{y}}\cdot\frac{\partial\check{\eta}_1}{\partial\hat{y}} - \frac{\delta}{\check{\nu}_1}\frac{\partial\check{\varphi}_1}{\partial\hat{z}} + o(1) = 0$$

The principle of least degeneracy implies that $\check{\nu}_1 = \delta$ so that the resulting condition at first order is :

$$\Big[\frac{\partial\check{\eta}_1}{\partial\hat{x}} - \frac{\partial\check{\varphi}_1}{\partial\hat{z}}\Big](\hat{x},\hat{y},0) = 0 \qquad (2)$$

The dynamic free-surface condition is then :

$$\frac{\partial\check{\varphi}_1}{\partial\hat{x}} + \frac{1}{2}\tan\alpha\Big((\frac{\partial\check{\varphi}_1}{\partial\hat{x}})^2 + (\frac{\partial\check{\varphi}_1}{\partial\hat{y}})^2 + (\frac{\partial\check{\varphi}_1}{\partial\hat{z}})^2\Big) + \tan\alpha\frac{gL}{U^2}\check{\eta}_1 + o(1) = 0 \qquad (3)$$

Since $\check{\eta}_1$ is of order $O(1)$, a non-trivial solution can then only be found if :

$$\frac{gL}{U^2} \le O(\frac{1}{\tan\alpha}) \qquad (4)$$

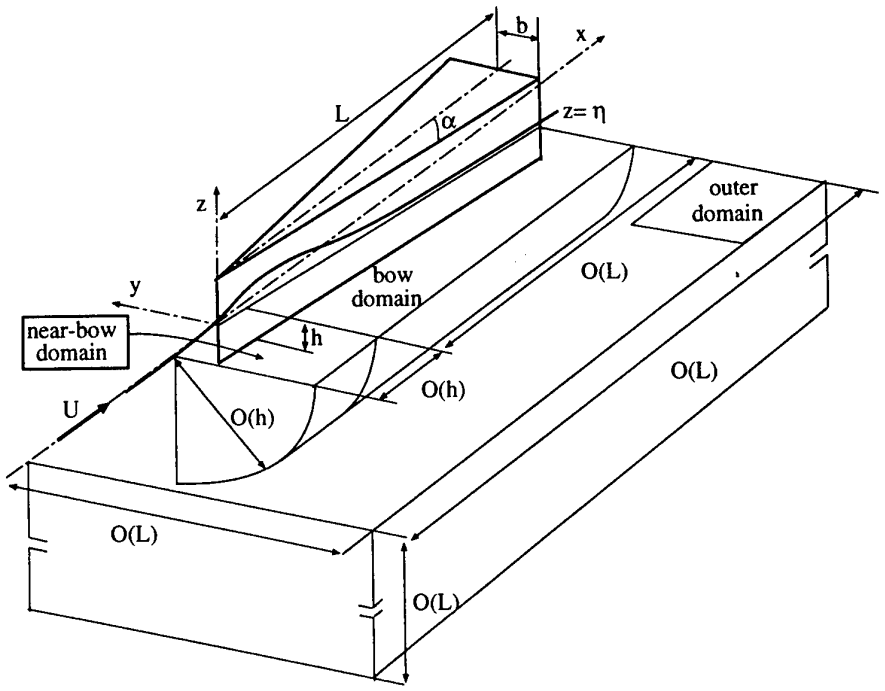

Figure 1: *illustration of the different domains of the composite solution.*

Fontaine & Cointe (1997) obtained a similar condition for the different approximations to be coherent in the bow flow problem :

$$\frac{gL}{U^2} \leq O(\delta) \qquad (5)$$

Since we study both the bow flow and the near-bow flow, we must satify the condition (5) which is the more restrictive. In that case, $2D+t$ theory can be used to compute the bow solution and the previous near-bow approximations remain valid. As a consequence, gravity effect can be neglected at first order in equation (3). Assuming the perturbation potential vanishes at infinity in front of the ship ($\hat{x} \to -\infty$), the resulting condition is :

$$\check{\varphi}_1(\hat{x}, \hat{y}, 0) = 0 \qquad (6)$$

The perturbation potential satisfies the three-dimensional Laplace equation subject to the boundary conditions (1) and (6). The solution of this problem can be expressed in term of a distribution on the center plane of the hull of Rankine sources and mirror sinks above $\hat{z} = 0$:

$$\check{\varphi}_1 = \lim_{\delta \to 0} \frac{1}{2\pi} \int_{-1}^{0} d\zeta \int_{0}^{L/\delta} d\xi \; G(\hat{x}, \hat{y}, \hat{z}, \xi, 0, \zeta)$$

$$\text{with : } \; G = [(\hat{x}-\xi)^2 + \hat{y}^2 + (\hat{z}+\zeta)^2]^{-1/2} - [(\hat{x}-\xi)^2 + \hat{y}^2 + (\hat{z}-\zeta)^2]^{-1/2}$$

Taking the limit and performing the integral leads to :

$$\check{\varphi}_1 = \frac{1}{2\pi} \int_{-1}^{0} ln\Big[\frac{-\hat{x} + \sqrt{\hat{x}^2 + \hat{y}^2 + (\hat{z}-\zeta)^2}}{-\hat{x} + \sqrt{\hat{x}^2 + \hat{y}^2 + (\hat{z}+\zeta)^2}}\Big] d\zeta \qquad (7)$$

3 Matching of the different solutions

Fontaine & Cointe (1997) use the method of matched asymptotic expansions to define an inner solution valid in the bow region, and an outer solution valid far from the ship. Even if the outer solution remains valid in front of the ship, these two solutions are not of same order of magnitude in the near-bow domain so that they do not match at first order (Fontaine, 1996). The introduction of the near-bow domain removes this gap since the near-bow solution matches on the one hand to the bow flow solution and on the other hand to the far-field solution.

Using the following non-dimensional variables :

$$\tilde{x} = \frac{x}{L}, \quad \tilde{y} = \frac{y}{L}, \quad \tilde{z} = \frac{z}{L}, \quad \tilde{r} = \sqrt{\tilde{y}^2 + \tilde{z}^2},$$

the perturbation potential is given by[1] :

$$\frac{\varphi}{Ub} = \begin{cases} \delta\,\check{\varphi}_1(\hat{x},\hat{y},\hat{z}) & \text{in the near-bow domain} \\ \delta\,\hat{\varphi}_1(\tilde{x},\hat{y},\hat{z}) & \text{in the bow domain} \\ \delta^2\,\tilde{\varphi}_1(\tilde{x},\tilde{y},\tilde{z}) & \text{in the far-field domain} \end{cases}$$

The far-field solution is given by a distribution of three-dimensional vertical dipoles on the axis $\tilde{x} \geq 0$. Using $\theta = \tan^{-1}(\tilde{z}/\tilde{y})$, $\tilde{\varphi}_1$ is given by :

$$\tilde{\varphi}_1(\tilde{x},\tilde{r},\theta) = \int_0^\infty \frac{-\mu(s)}{4\,\pi}\frac{\tilde{r}\,\sin(\theta)}{[(\tilde{x}-s)^2+\tilde{r}^2]^{\frac{3}{2}}}\,ds \quad (8)$$

The dipole density is given by the behaviour of the bow flow solution as $\hat{r} \to +\infty$:

$$\lim_{\hat{r}\to\infty} \hat{\varphi}_1(\tilde{x},\hat{r},\theta) = -\frac{\mu(\tilde{x})}{2\pi}\cdot\frac{\sin(\theta)}{\hat{r}} \quad (9)$$

3.1 Matching of the near-bow and bow solutions

In order to match the near-bow flow solution to the bow flow one, we define an intermediate variable $x_\chi = \tilde{x}/\chi(\delta)$ where $\delta \ll \chi(\delta) \ll 1$. x_χ is of order $O(1)$ in the overlap domain and the matching condition at first order is :

$$\lim_{\substack{\delta\to 0 \\ x_\chi>0 \\ x_\chi=O(1)}} \left[\check{\varphi}_1(\frac{\chi(\delta)}{\delta}x_\chi,\hat{y},\hat{z}) - \hat{\varphi}_1(\chi(\delta)x_\chi,\hat{y},\hat{z})\right] = 0$$

This condition states that the behaviour of the bow solution at origin must be the same as the behaviour of the near-bow solution as $\hat{x} \to +\infty$. Taking (7) into account, this condition implies that :

$$\hat{\varphi}_1(0,\hat{y},\hat{z}) = \frac{1}{2\pi}\int_{-1}^{0} \ln\left[\frac{\hat{y}^2+(\hat{z}-\zeta)^2}{\hat{y}^2+(\hat{z}+\zeta)^2}\right] d\zeta \quad (10)$$

This can be recognised as a solution of the bow flow problem. Indeed, this expression satisfies the two-dimensional Laplace equation subject to the body boundary condition and an homogeneous Dirichlet condition on the unperturbed free-surface. As a result, the two solutions match if the initial conditions for the bow flow problem are :

$$\hat{\varphi}_1(0,\hat{y},0) = 0 \quad \text{and} \quad \hat{\eta}_1(0,\hat{y}) = 0$$

These are the same initial conditions as used in the bow flow solution by Fontaine & Cointe (1997) and Faltinsen & Zhao (1991). However, this matching is more precise since the bow flow and the near-bow flow solutions have the same order of magnitude in the overlap domain. As we will see in section 4, it also leads to an initial wave elevation.

[1] where the subscript 1 indicates that the quantity is of order $O(1)$

3.2 Matching of the near-bow and far-field solutions

3.2.1 Bow side matching

The behaviour of the near-bow solution far aside the ship bow (as $\hat{x} = O(1)$ and $\hat{r} \to +\infty$) must be the same as the behaviour of the far-field solution in the vicinity of the ship bow side, i.e. as $\tilde{r} \to 0$. As before, we define an intermediate variable $r_\chi = \tilde{r}/\chi(\delta)$ ($\delta \ll \chi(\delta) \ll 1$) which is of order $O(1)$ in the overlap domain. The matching condition is at first order :

$$\lim_{\substack{\delta\to 0 \\ r_\chi=O(1)}} \left[\check{\varphi}_1(\hat{x},\frac{\chi(\delta)}{\delta}r_\chi,\theta) - \delta\,\tilde{\varphi}_1(\delta\hat{x},\chi(\delta)r_\chi,\theta)\right] = 0$$

When $\delta \to 0$, it follows from (7) and (8) that :

$$\begin{aligned} \check{\varphi}_1(\hat{x},\frac{\chi(\delta)}{\delta}r_\chi,\theta) &= \frac{1}{2\pi}\frac{\delta}{\chi(\delta)}\frac{\sin\theta}{r_\chi} + O[\frac{\delta^2}{\chi(\delta)^2}] \\ \delta\tilde{\varphi}_1(\delta\hat{x},\chi(\delta)r_\chi,\theta) &= -\frac{\mu(0)}{4\pi}\frac{\delta}{\chi(\delta)}\frac{\sin\theta}{r_\chi} + o[\frac{\delta}{\chi(\delta)}] \end{aligned}$$

The dipole density $\mu(0)$ is determined by using equations (9) and (10). This leads to $\mu(0) = -2$ so that the two solutions match.

3.2.2 Matching in front of the bow

The behaviour of the near-bow flow solution far ahead of the bow, as $\hat{r} = O(1)$ and $\hat{x} \to -\infty$ must equal the behaviour of the far-field solution in front of the bow (as $\tilde{x} \to 0^-$). Using an intermediate variable $x_\chi = \tilde{x}/\chi(\delta)$ so that $\delta \ll \chi(\delta) \ll 1$, the matching condition is at first order :

$$\lim_{\substack{\delta\to 0 \\ x_\chi=O(1) \\ x_\chi<0}} \left[\check{\varphi}_1(\frac{\chi(\delta)}{\delta}x_\chi,\hat{r},\theta) - \delta\tilde{\varphi}_1(\chi(\delta)x_\chi,\delta\hat{r},\theta)\right] = 0$$

When $\delta \to 0$, it follows from (7) and (8) that :

$$\begin{aligned} \check{\varphi}_1(\frac{\chi(\delta)}{\delta}x_\chi,\hat{r},\theta) &= \frac{1}{4\pi}\frac{\delta^2}{\chi(\delta)^2}\frac{\hat{r}\sin\theta}{{x_\chi}^2} + o[\frac{\delta^2}{\chi(\delta)^2}] \\ \delta\,\tilde{\varphi}_1(\chi(\delta)x_\chi,\delta\hat{r},\theta) &= -\frac{\mu(0)}{8\pi}\frac{\delta^2}{\chi(\delta)^2}\frac{\hat{r}\sin\theta}{x_\chi^2} + o[\frac{\delta^2}{\chi(\delta)^2}] \end{aligned}$$

As a result, the two solutions match.

4 Composite solution

The composite solution is obtained by adding the near-bow to the bow solution and by substracting the common part (given by eq. (10) for the potential). In front of the bow ($\hat{x} < 0$), the composite solution for the wave elevation is equal to the near-bow solution and can be found by integrating the kinematic free-surface condition (2) :

$$\check{\eta}_1(\hat{x}<0,\hat{y}) = \frac{1}{\pi}\left[\hat{x}\ln\left(\frac{\hat{x}+\sqrt{\hat{x}^2+\hat{y}^2}}{\hat{x}+\sqrt{\hat{x}^2+\hat{y}^2+1}}\right) + \sqrt{\hat{x}^2+\hat{y}^2} - \sqrt{\hat{x}^2+\hat{y}^2+1}\right]$$

The wave elevation in front of the bow is therefore independant of the speed and the wave elevation at the nose is :

$$\eta(0,0) = \frac{\alpha h}{\pi} \qquad (11)$$

These results differ from the results of Sclavounos (1994). He predicted half the value of eq. (11). The theoretical result has been compared with experiments presented by Fontaine (1996). Because of the small size of the tested model, the effect of surface tension is important. The experimental results can be scaled to full scale by introducing a surface tension parameter (see fig. 2). Full scale corresponds to that surface tension parameter goes to zero. The results show that eq. (11) is reasonable.

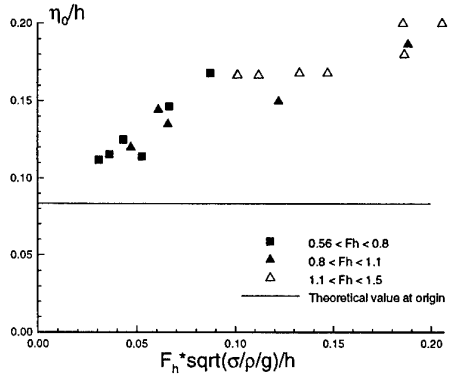

Figure 2: Initial elevation as a function of the surface tension parameter. $\alpha = 15°$, $F_h = U/\sqrt{gh}$, σ = surface tension.

For the wave elevation along the hull ($\hat{x} > 0$), the following three-dimensional correction should be added to the bow flow solution :

$$\Delta\eta = \frac{\alpha h}{\pi}\left[\hat{x}\ln\left(2\hat{x}(-\hat{x}+\sqrt{\hat{x}^2+1})\right) - \hat{x} + \sqrt{\hat{x}^2+1}\right]$$

x/h	0^-	0.05	0.1	0.15	0.2	0.3
$\pi\Delta\eta/(\alpha h)$	1.0	0.83	0.73	0.66	0.6	0.5

x/h	0.4	0.5	1.	2.	5.	∞
$\pi\Delta\eta/(\alpha h)$	0.43	0.38	0.22	0.12	0.05	0

Table 1: Numerical values of the wave profile correction.

However, this three-dimensional correction is not sufficient to completely explain the differences between experiments and the bow solution by Fontaine & Cointe (1997). One reason to this is surface tension effects like in fig. 2. There were not done measurements for the wave elevation along the hull for small surface tension parameter to see any trend for full scale situation. This need futher investigations.

References

[1] FALTINSEN, O.M. and ZHAO, R. (1991) : *"Numerical prediction of ship motions at high forward speed"*, Phil. Trans. of the Royal Society, London (A), Vol. 334, pp. 241-252.

[2] FONTAINE, E. and COINTE, R. (1997) : *"A Slender Body Approach to Nonlinear Bow Waves"*, Phil. Trans. of the Royal Society, London (A).

[3] FONTAINE, E. (1996) : *"Simulation de l'écoulement potentiel engendré par un corps élancé perçant la surface libre à forts nombres de Froude"*, Thèse de Doctorat de l'Ecole Nationale des Ponts et Chaussées, Paris.

[4] OGILVIE, T.F. (1972) : *"The wave generated by a fine ship bow"*, Ninth Symp. Naval Hydrodynamics, Vol. 2, pp. 1483-1525.

[5] SCLAVOUNOS, P. (1994) : *"On the Intersection Near a Fine Ship Bow"*, Twentieth Symp. Naval Hydrodynamics, pp. 934-945.

DISCUSSION

Tuck E.O.: I applaud this study, which corrects a well-known deficiency in the 2.5 D theory, namely absence of a rise in FS at the bow. But I am not sure how it was achieved, since surely matching between the local bow flow and the 2.5 D expansion should have supplied a non-zero initial condition to the latter.

Fontaine E.: Thank you for your comments. The matchings have been performed using the classical technique of matched asymptotic expansions and the details of the procedure will be published soon. It appears that 3D effects arise in the composite solution which is the sum of the 2.5 D expansion and the local bow flow, substracting the common part of the two expansions.

On new mode of wave generation by moving pressure disturbance.

A.M.Frank

Computing Center, Siberian Branch of Russ. Acad. Sci.,
Krasnoyarsk, 660036, RUSSIA
e-mail: frank@sf.krasnoyarsk.su

The problem of waves generation by moving surface pressure disturbance is well known and well enough studied in the works of many authors. Here we present the results of numerical simulation of 2D plain waves generation by negative pressure disturbance, which revealed a new regime when moving with a critical speed disturbance doesn't generate upstreame-advancing solitons.

1. Mathematical model

Numerical model used in computations is the so-called discrete nonlinear-dispersive shallow water model [1]. The essence of this approach is that an incompressible flow with a free surface is simulated by a finite mechanical system of material particles with some holonomic constraints which represent an incompressibility condition. The governing equations are obtained then from Hamilton principle. The main advantage of such models is that they provide exact conservation of mass, momentum, angular momentum and energy even for coarse spatial discretization. So they give, in particular, the numerical solutions which are real solitary waves advancing with constant amplitude, shape and phase speed without any numerical dissipation or radiation. This property seems to be important for long-time calculations and played, in particular, significant role in solving Mach reflection problem [2].

In a shallow water case some additional simplifications can be made which, as in case of usual fluid motion equations, allow to reduce the dimension of a model. A detailed description of the model and the results of numerical testing it's accuracy are given in [1]. There was shown also that for even bottom this model gives a finite-dimensional approximation of well known Green-Naghdi (1976) equations. As far as the problem under consideration deals only with even bottom, one may assume that the discrete model used here is just a kind of difference scheme for Green-Naghdi equations in lagrangian variables, which conserves exactly the horizontal momentum and total energy.

2. Numerical results

An infinite fluid layer of constant depth H with a free surface is considered. The moving surface pressure disturbance is given by

$$p = \begin{cases} p_0 \cos^2(\pi\xi/2L), & \text{if } |\xi| \le L \\ 0, & \text{if } |\xi| > L. \end{cases}$$

where $\xi = x - x_0 - Ut$. Hereafter we assume the depth H, fluid density ρ and gravity acceleration g being unit, and the pressure disturbance being moved with a critical speed $U = 1$. The computational domain moves step by step after disturbance with the boundary conditions corresponding to the quiescent liquid at the right end and a kind of "open" condition at the left one. It is known that for $p_0 > 0$ such disturbance, pushing a fluid ahead, generates periodically upstream-advancing solitons. The wave resistance coefficient always remains positive oscillating near some mean value.

When $p_0 < 0$ the solitons are also generated but the mechanism is different. This rarefaction region first pulls out a wave of large amplitude which, having a large speed, quickly overtakes the pressure source and losing an amplitude becomes a soliton. The wave resistance coefficient periodically changes sign, but the mean value, as far as a radiation of solitons takes place, is usually nonzero. It appeared, however, that the halfwidth L of a rarefaction region can be specially chosen so that a new periodic mode arises when no upstream-advancing soliton are generated. This effect first was observed for the solitons of large amplitude, wich exist only in shallow water approximation but break down in reality. Then it was found to be the case for all amplitudes.

In fig.1 an example of such mode for $p_0 = -0.12$ is given. It is well seen that the pressure disturbance pulls out a wave, which coming to the right end of pressure region loses it's amplitude and dissapears there completely. At this time the next wave appears near the left end of pressure region and so on. The wave resistance coefficient C_d versus time t plot shows periodic behaviour with almost zero mean value. In our calculations this periodic mode took place for some 8-10 periods and then a soliton of small amplitude was emitted (see fig.1 (f)), which probably means that this mode is unstable. Still it seems to be interesting as an example of new nonlinear and nontrivial solutions.

In fig.2 the values of L versus p_0 are plotted for which this mode is realized. Fig.3 shows the maximal values of wave amplitudes which arise in this regime. It can be seen that this mode exists for moderate amplitudes and so it is possible trying to observe it in experiment.

1. *Frank A.M.* Discrete nonlinear-dispersion shallow water model. J. of Appl. Mech. and Techn. Phys.(transl.),1994,v.35,No.1,p.34-42.
2. *Serebrennikova O.A., Frank A.M.* Numerical modeling of Mach reflection for solitary waves. J. of Appl. Mech. and Techn. Phys.(transl.),1993,v.34,No.5, p.610-618.

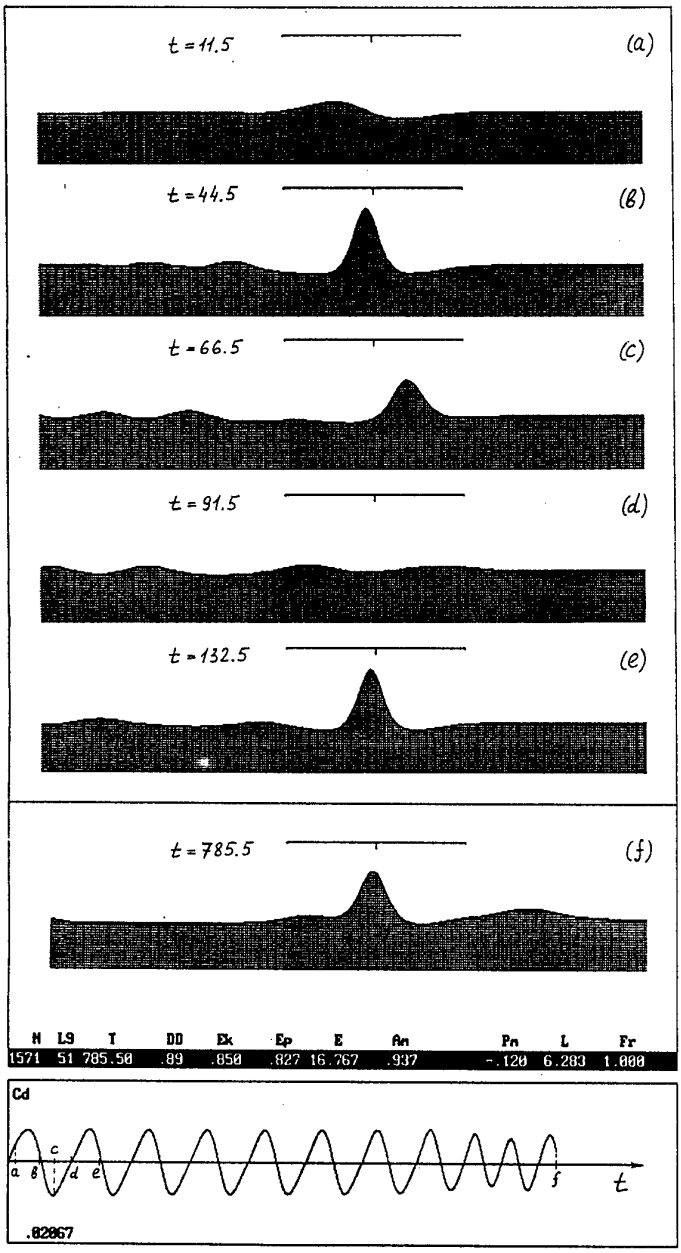

Fig. 1

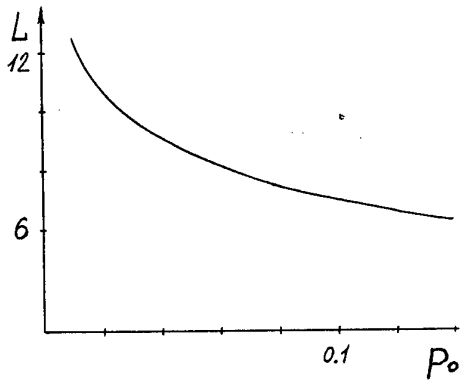

Fig. 2

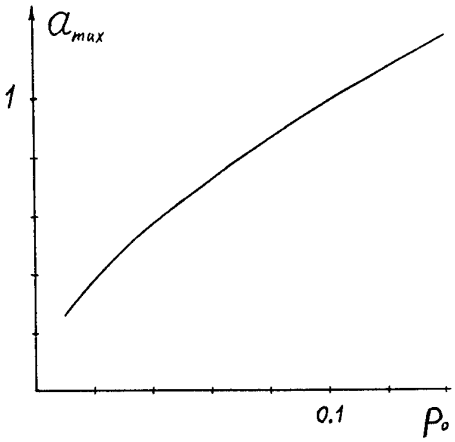

Fig. 3

MOTION SIMULATION OF A TWO-DIMENSIONAL BODY AT THE SURFACE OF A VISCOUS FLUID BY A FULLY COUPLED SOLVER

L. GENTAZ, B. ALESSANDRINI, G. DELHOMMEAU
Laboratoire de Mécanique des Fluides
Ecole Centrale de Nantes B.P. 92101 44321 Nantes Cedex 3
phone : (33) 02 40 37 25 96, fax : (33) 02 40 37 25 23, e-mail : Lionel.Gentaz@ec-nantes.fr

INTRODUCTION

We present here an original solver [1] to compute two-dimensional free surface flows in viscous and incompressible fluid by a finite difference method. In most of the methods used nowadays for solving such problems, free surface elevation is updated at each time step by integration of the kinematic condition after computation of velocity and pressure fields [2] [6]. In these methods non-physical boundary conditions must be introduced to solve linear systems and non-linear free surface boundary conditions cannot be computed accurately. In the method presented here exact non-linear free surface boundary conditions are implemented on the real position of the free surface. At each time step the totally coupled linear system for velocity, pressure and free surface elevation unknowns is solved by a CGSTAB algorithm. Results for a free surface-piercing cylinder in forced heave, sway or roll motion are presented.

EQUATIONS AND NUMERICAL RESOLUTION

Navier-Stokes equations for laminar flows are written under convective form in a cartesian system (x^1, x^2) defining the physical fluid domain. The dependant unknowns are the cartesian components (u^1, u^2) of velocity, the dynamic pressure $p = P + \rho g x^2$ including gravitational effects and the free surface elevation h. A curvilinear system $(\varepsilon^1, \varepsilon^2)$ is used to simplify the implementation of boundary conditions. Here $\varepsilon^1 = 0$ is the equation of the immersed part of the body and $\varepsilon^2 = 0$ the equation of the free surface. A partial transformation of the moving physical space in a fixed curvilinear computational space is then defined.
In classical uncoupled methods a linear system issued from discretisation of transport and continuity equations is solved by weakly-coupled algorithms such as PISO or SIMPLER. Thus new velocity and pressure fields are obtained at each time step. The free surface elevation is updated by integration of the kinematic condition. This method leads to several theorical or numerical problems :
- a free surface boundary condition for velocities is lacking because of the use of kinematic condition for free surface elevation calculation. A supplementary non-physical condition must be used and does not allow an accurate calculation of viscous or surface tension effects. Moreover the normal dynamic condition is used as a Dirichlet condition for the pressure what leads to a poor mass conservation just under the free surface.
- the singularity of the kinematic condition at the intersection of free surface and solid body can be solved by introducing a meniscus. For very refined grids in the vicinity of the body this meniscus can become too important and lead to numerical divergence of the computation.
- the use of the SIMPLER algorithm gives a poor convergence of non-linear residuals (fig. 1) and it is a serious problem to compute unsteady flows.

In the new method proposed here the kinematic condition is used as a free surface boundary condition for velocity. The tangential dynamic condition is the other condition on the free surface for velocities (as in the uncoupled method). The discrete pressure unknowns are yet located at the centre of the cells (velocity unknowns are located at the nodes of the mesh) and no pressure boundary conditions are required. With these choices we have only physical boundaries conditions on the free surface. The normal dynamic condition gives a relation between pressure and free surface and will be used to compute the free surface elevation.
A totally-coupled solution is chosen to ensure mass conservation.
The mass conservation is represented by a pressure equation which is discretised by a Rhie and

Chow procedure to avoid checkerboard oscillations. This procedure is generalised for cells located near the free surface to take free surface effects into account and to make the pressure block invertible. At each iteration the following linear system for discrete velocity, pressure and free surface elevation unknowns (respectively called U, P and H) is solved and inverted by the iterative CGSTAB algorithm [8]:

$$\begin{array}{r} \text{transport equations} \rightarrow \\ \text{pressure equation} \rightarrow \\ \text{normal dynamic condition} \rightarrow \end{array} \begin{bmatrix} M_u & M_p & \\ M_{du} & M_{dp} & \\ & M_{sp} & M_{sh} \end{bmatrix} \begin{pmatrix} U \\ P \\ H \end{pmatrix} = \begin{pmatrix} f_u \\ f_p \\ f_h \end{pmatrix}$$

With the coupled method the convergence of non-linear residuals is very good (fig. 1) compared to the convergence of the uncoupled method. Moreover the total CPU time is decreased by the totally coupled method (two or three twice as fast than the uncoupled method for the same global simulation time).

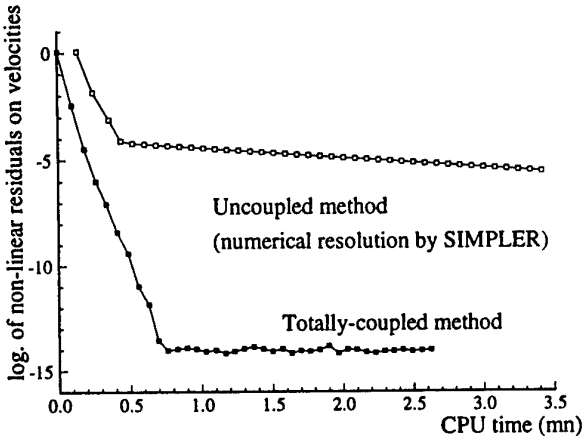

Fig. 1 : Convergence of non-linear residuals with the present method and an uncoupled method

RESULTS

The monoblock structured grids used here are generated by an direct algebraic method.
Heave forced motion has been first computed for a circular cylinder. The flow is supposed to be symmetric and simulated only in half the fluid domain.

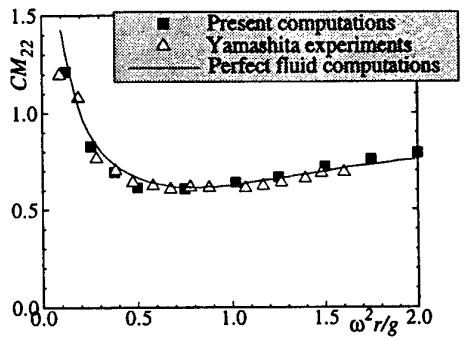

Fig. 2 : Added mass in heaving

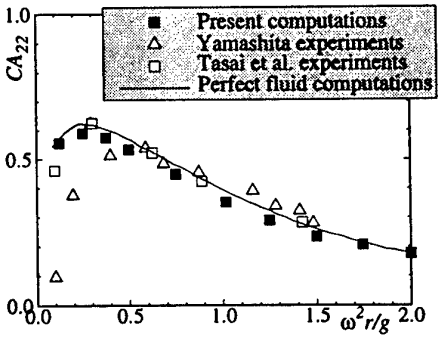

Fig. 3 : Damping coefficient in heaving

A Fourier transform of the computed time series of the hydrodynamic forces acting on the body leads to non-dimensional hydrodynamic coefficients.
Numerical results are in good agrement with Yamashita [10] and Tasaï *et al.* [7] experiments even for the 3rd-order force amplitude [3] and perfect flow computations [5]. Added mass and damping

coefficients are presented on figures 2 and 3.
For numerical simulations of a rectangular cylinder in forced sway or roll motion [4] the fluid domain comprises two free surface boundaries which are not connected. These two interfaces are defined by the equations $\varepsilon^2 = 0$ and $\varepsilon^2 = \varepsilon^2_{max} = 1$ (see fig. 4).

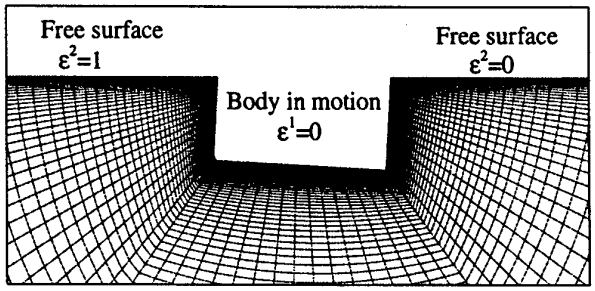

Fig. 4 : Shape of the grid during a computation in roll

For the sway motion the beam-to-draft ratio B/T was 2 (B=0.4 m in the present computation and in Vugts experiments [9]) and the forced motion of the form $y(t) = y_a \sin(\omega t)$ with y_a=0.02 m. The present method leads to a good accordance of the computed added mass with the experimental results or perfect fluid computations of Vugts (fig. 5) but under-estimates the damping coefficient for non-dimensional frequencies upper than 0.75 (fig. 6).

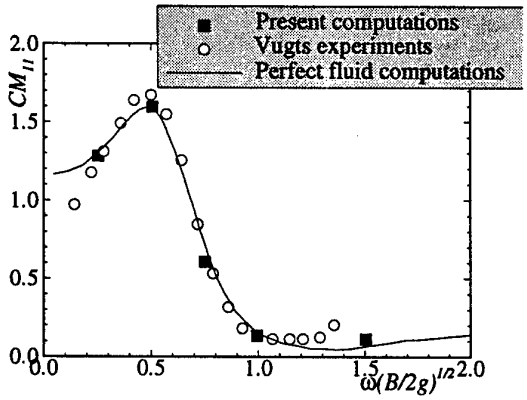

Fig. 5 : Added mass in swaying (for a rectangle)

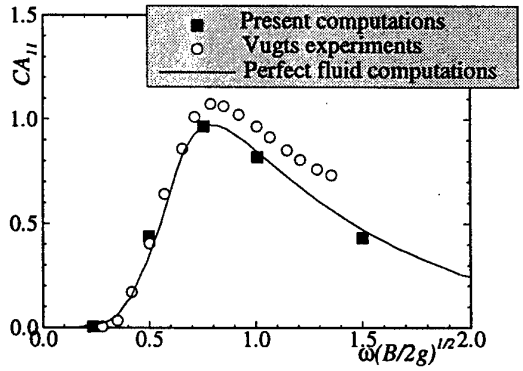

Fig. 6 : Damping coefficient in swaying (for a rectangle)

For roll motion the beam-to-draft ratio B/T was 2 and the forced motion of the form $\phi(t) = \phi_a \sin(\omega t)$ with Φ_a=0.1 rad. Results are compared with viscous flow computations of Yeung *et al.* [11] (made with Φ_a=0.05 rad) based on the Free-Surface Random-Vortex Method and Vugts experiments with Φ_a=0.1 rad (non-dimensional experimental results for Φ_a=0.1 rad and Φ_a=0.05 rad are nearly the same) or inviscid flow computations.
The CM_{ij} and CA_{ij} with i different from j are the mass coupling and the damping coupling coefficients in the i-equation by motion in the j-mode respectively (with 1 for sway motion, 2 for heave motion and 3 for roll around an axis perpendicular to the plane of the flow). The hydrodynamic coefficients are non-dimensionalised according to $CM_{ij} = a_{ij} / \rho A B^2$ and $CA_{ij} = b_{ij} \sqrt{B/2g} / \rho A B^2$. A is the area coefficient. A 10000 nodes-grid (100 on the body) was used for most of the computations with a time step of 0.01 s. For lower motions frequencies a 23000 nodes-grid (230 nodes on the body) was required and the time step was 0.005 s.
Added roll moment of inertia (fig. 7) is well-predicted and close from Vugts experiments. However the damping coefficient in roll is highly over-predicted (fig. 8) for all motion frequencies. On the contrary the mass and damping coupling coefficients are in good agreement with Vugts experiments and perfect fluid computations (fig. 9 and 10) except for the mass coefficient for the lowest computed

frequency.
These first results are satisfying and show the interest of viscous-flow computations for such quite complex flows. However other computations must be undertaken particularly for the calculation of the damping coefficient in sway and roll. More refined grids in the vicinity of the body will be used to try to compute viscous effects (particularly vortices shedding near solid walls and corners of the body in motion) with more accuracy and should improve present results.

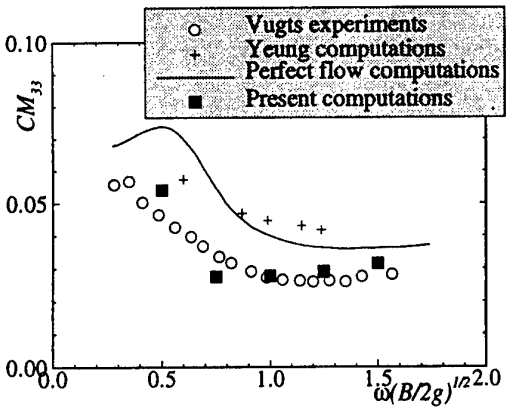

Fig. 7 : Added mass moment of inertia in roll (for a rectangle)

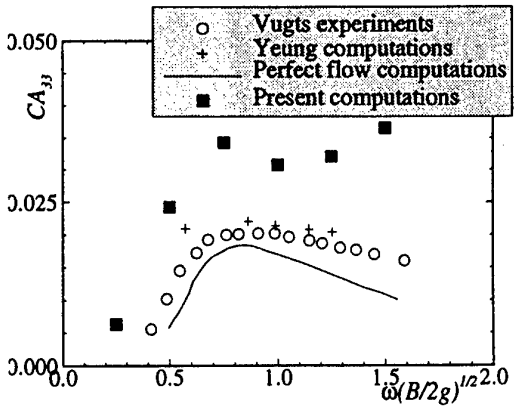

Fig. 8 : Damping coefficient in roll (for a rectangle)

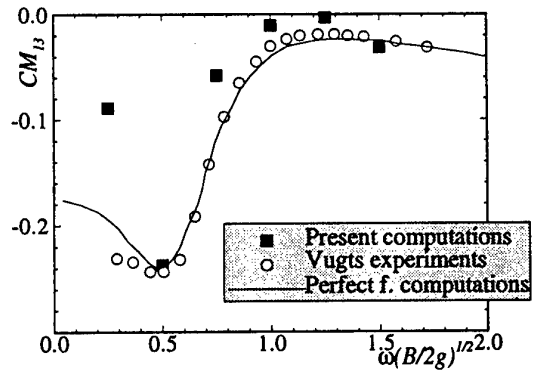

Fig. 9 : Mass coupling coefficient of roll in sway (for a rectangle in roll)

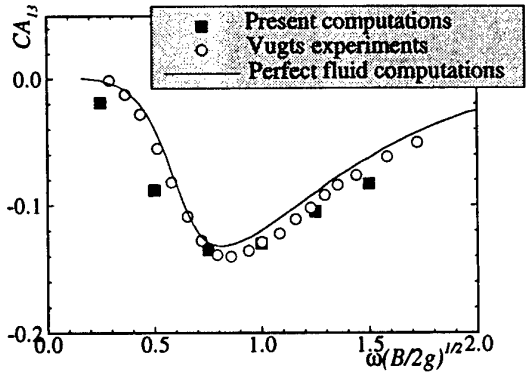

Fig. 10 : Damping coupling coefficient of roll in sway (for a rectangle in roll)

REFERENCES

[1] B. Alessandrini, G. Delhommeau, *Preprints of 21st Symposium on Naval Hydrodynamics (Tuesday Sessions),* Trondheim, Norway, pp. 40-55, 1996.
[2] L. Gentaz, B. Alessandrini, G. Delhommeau, *10th WWWFB,* Oxford, pp. 77-80, 1995.
[3] L. Gentaz, B. Alessandrini, G. Delhommeau, *15th ICNMFD,* Monterey, pp. 112-113, 1996.
[4] P.M. Guillerm, *Rapport de DEA*, Ecole Centrale de Nantes, 1996.
[5] A. Papanikolaou, H. Nowacki, *13th Symp. on Naval Hydrodynamics*, pp. 303-331, 1984.
[6] *Proceedings of CFD Workshop,* Tokyo, 1994.
[7] F. Tasaï, W. Koterayama, *Reports of Research Inst. for Applied Mech.*, Kyushu Univ., vol. 23, no. 77, 1976.
[8] H.A. Van der Vorst, *J. Sci. Stat. Comp.*, vol. 13, 1992.
[9] J.H. Vugts, *International Shipbuilding Progress,* vol. 15, pp. 251-276, 1968.
[10] S. Yamashita, *Journal Society Naval Architecture of Japan*, vol. 141, pp. 61-69, 1977.
[11] R. Yeung, C. Cermelli, S.W. Liao, *Preprints of 21st Symposium on Naval Hydrodynamics (Tuesday Sessions),* Trondheim, Norway, pp. 69-86, 1996.

DISCUSSION

Yeung R.W.: These are encouraging calculations along a boundary-fitted coordinate full N-S solver of Yeung & Ananthakrishnan (1992, J. Eng. Math.). However, I do not believe the calculations you presented have sufficient precision. Fig. 3 shows that the total damping with viscosity is less than the inviscid solution. Our recent FSRVM method (Ref. 11) has been validated by comparing vorticity structures with DPIV measurements. As mentioned in Ref. [11], we have some doubts that Vugt's expt. data for added inertia is correct. Your calculations for CM_{33} may well be off by as much your damping is unreasonably high in Fig. 8. I hope you can be successful in tracking down the problems.

Gentaz L., Alessandrini B., Delhommeau G.: The originality of the present method consists in solving only one fully-coupled linear system for the velocity, pressure and free surface elevation unknowns at each iteration. This method first implemented by B. Alessandrini (1995, Numerical Method in Laminar and Turbulent Flows, Atlanta, vol. IX, part 1, pp. 1173-1184) allows complete free-surface boundary conditions to be taken into account and an efficient and fast convergence during nonlinear process (figure 2) contrary to weakly-coupled methods as this one described by Yeung and Ananthakrishnan in Journal Engineering Mathematics, 1992, or others (1994, proceedings of CFD Workshop, Tokyo).

We do not believe that differences between Navier-Stokes computations and experiments for the figure 3 (damping coefficient for a circular cylinder in forced heave motion) are significant. In this case, part of viscous forces seems negligible. In our opinion, these differences can be explained by Fourier analysis of forces acting on the body or gaps in the manual plot of experimental data but are not due to an insufficient precision in the computation.

Concerning hydrodynamic coefficients for a rectangular cylinder in forced roll motion, damping coefficient is actually largely overestimated and its computation must be improved. For the added inertia coefficient CM_{33} we hope you can provide other experimental data to confirm your hypothesis and computations.

AN INVESTIGATION OF STANDING WAVES USING A FULLY NON-LINEAR BOUNDARY ADAPTIVE FINITE ELEMENT METHOD

D M Greaves[1], A G L Borthwick[2] and G X Wu[1]

[1] Dept of Mechanical Engineering, University College London, Torrington Place, London WC1E 7JE, U.K.
[2] Dept of Engineering Science, University of Oxford, Parks Road, Oxford OX1 3PJ, U.K.

1. INTRODUCTION

This paper describes a quadtree based finite element solver for two-dimensional fully non-linear time-dependent free surface flows. In the scheme, the free surface is allowed to deform, and a new mesh created at each time step. To ensure fast, fully automatic mesh generation, an underlying Cartesian quadtree grid is first created about seeding points at the free surface and on rigid boundaries; the quadtree grid is then triangularised to generate the finite element mesh.

Details of the governing equations and finite element formulation used in this work are given by Wu and Eatock Taylor (1994, 1995). The quadtree-based grid generation is described in detail by Greaves (1995). Numerical results obtained here are for standing waves in rectangular tanks of various aspect ratio. The results show encouraging agreement with analytical solutions and alternative numerical data.

2. RESULTS

The fully non-linear moving boundary finite element method was used to simulate various cases of standing waves in rectangular containers. Mesh size and time step convergence tests were carried out for a steep standing wave profile, taken from Mercer and Roberts (1992). Standing waves generated from sinusoidal initial profiles were also considered. The decrease in non-linear wave frequency with amplitude in deep water, and the corresponding increase in shallow water, noted by Tsai and Jeng (1994) as well as Vanden-Broeck and Schwartz (1981) and Tadjbakhsh and Keller (1960), are observed. Each of the standing wave simulations presented herein has a larger crest amplitude than trough amplitude, which is typical of non-linear wave profiles (Tsai and Jeng, 1994).

The various parameters used in the numerical simulations are non-dimensionalised as follows,

$$\phi = \frac{\phi^*}{h^*(g^*h^*)^{\frac{1}{2}}}, \quad L = \frac{L^*}{h^*}, \quad t = \left(\frac{g^*}{h^*}\right)^{\frac{1}{2}} t^*, \quad \omega = \left(\frac{h^*}{g^*}\right)^{\frac{1}{2}} \omega^* \quad , \qquad (17)$$

where ϕ is the velocity potential, h is the water depth, g is the acceleration due to gravity, L is any length, t is time and ω is the wave frequency. The superscript * represents a dimensional value. All calculations were performed on a SUN SPARC 10 workstation.

In each of the following simulations, the dimensionless height of the container walls is equal to 1.5. Unless otherwise stated, the seeding points are spaced to provide the maximum mesh resolution along the free surface boundary and at the container walls in the region which intersects with the free surface. The seeding point spacing at the free surface is equal to $S_{min}=2^{-M}$, where M is the maximum division level of the underlying quadtree grid. Thus, the resolution of the underlying quadtree grid, and also of the finite element mesh, is finest where velocity potential gradients are likely to be highest, and coarsest at the bottom of the container where gradients are likely to be low.

Standing Waves in a Rectangular Container

Various standing waves were simulated in order to investigate the relationship between water depth, amplitude, and frequency of oscillation. The waves have initial surface elevation profile, $\eta = a\cos(2\pi x/b)$ where x is measured along the length of the tank, b is the length of the tank and a is the wave amplitude.

Figure 1 shows the initial mesh for case A. The dimensionless length of the tank, b, is equal to the dimensionless wavelength 2. The dimensionless wave amplitude, $a = 0.05$. Figure 2 shows the wave surface elevation history at the centre of the tank, plotted with the linear and first plus second order analytical solutions calculated following the method described by Wu and Eatock Taylor (1995), for comparison. The linearised analytical solution does not agree well with the fully non-linear numerical solution as time increases. The inclusion of second order terms, however, leads to much better agreement.

The time period of non-linear oscillation in Figure 2 is greater than that predicted by linear theory. This effect was noted by Tsai and Jeng (1994), Vanden-Broeck and Schwartz (1981), and Tadjbakhsh and Keller (1960). Tsai and Jeng (1994) calculated numerical Fourier solutions of standing waves in finite water depth, and observed that the non-linear wave frequency increases with wave steepness for water depths less than 0.1662 of its wavelength, and decreases with increasing amplitude for depths greater than this value.

Various cases were investigated and the results recorded in Table 1. Figure 3 shows the initial mesh for case D, and the temporal free surface elevation plot is given in Figure 4. In Figure 4, the third trough is higher than those surrounding it, which may indicate the occurrence of double minima in the wave profile at this stage. This effect is recorded by Tsai and Jeng (1994) for shallow water standing waves.

Each simulation was continued over at least five cycles and the non-linear wave frequency, ω, determined, along with the corresponding h/L_o and H/L_o values, where H is the wave height. The corresponding linear wave frequency, ω_o, and linear wave length, L_o, are calculated using linear wave theory. The ratio, ω/ω_o, is given in Table 1 as a function of h/L_o and H/L_o for each of the standing wave calculations and can be seen to agree reasonably with equivalent frequency ratios obtained from Tsai and Jeng's (1994) data. The decrease in non-linear wave frequency with increasing amplitude is evident for cases A and B, in which $h = L_o/2$, and for case C in which $h = L_o/4$. In case D, $h = L_o/10$ and the non-linear wave frequency is greater than the linear value.

Standing Wave Interaction with an Array of Three Submerged Circular Cylinders

In order to demonstrate the flexibility of the mesh generator to model complex geometries, the case of a standing wave in a tank containing three submerged horizontal cylinders was simulated. Figure 5 shows the initial mesh for this case, in which the cylinders each have diameter, $d = 0.35$. The underlying quadtree grid has a maximum of 8 and a minimum of 5 division levels. The wave has an initial cosine elevation of amplitude $a = 0.01$. Figure 6 shows the computed time history of the wave elevation recorded at the centre of the tank. A regular standing wave oscillates above the submerged bodies.

3. CONCLUSIONS

The finite element mesh generator proposed herein produces a mesh of high quality triangular elements without hanging nodes from an underlying quadtree grid. Coupled with the finite element solver, the adaptive grid generator models the moving free surface with a high level of resolution, controlled by the spacing of the seeding points.

The flexibility of the method is demonstrated by the results presented here, which agree well with published data. The predicted deviation of the period of oscillation from the linear value as the wave height is increased corresponds to that described by Tsai and Jeng (1994).

4. ACKNOWLEDGEMENTS

This work forms part of the Uncertainties in Loading on Offshore Structures ULOS programme. It was sponsored by EPSRC through MTD Ltd and jointly funded with: Aker Engineering, Amoco (UK) Exploration Company, BP Exploration Operating Co. Ltd., Brown and Root Ltd., Exxon Production research Company, Health and Safety Executive, Shell UK Exploration and Production, Den Norske Stats Oljeselskap a.s., Texaco Britain Ltd., EPSRC Grant Reference: GR/J23198 (Oxford), GR/J23532 (UCL). The authors would also like to acknowledge the invaluable input provided by Professor R. Eatock Taylor.

5. REFERENCES

Greaves, D.M. (1995) "Numerical modelling of laminar separated flows and inviscid steep waves using adaptive hierarchical meshes", *DPhil thesis*, Oxford University.

Mercer, G.N. and Roberts, A.J. (1992) "Standing waves in deep water: their stability and extreme form", *Physics of Fluids*, Vol. A4(2), pp. 259-269.

Tadjbakhsh, I. and Keller, J. B. (1960) "Standing surface waves of finite amplitude", *Journal of Fluid Mechanics*, Vol. 8, pp. 442-451.

Tsai, C-P. and Jeng, D-S. (1994) "Numerical Fourier solutions of standing waves in finite water depth", *Applied Ocean Research*, Vol. 16, pp. 185-193.

Vanden-Broeck, J-M. and Schwartz, L.W. (1981) "Numerical calculation of standing waves in water of arbitrary uniform depth", *Physics of Fluids*, Vol. 24(5), pp. 812-815.

Wu, G.X. and Eatock Taylor, R. (1995) "Time stepping solutions of the two dimensional non-linear wave radiation problem", *Ocean Engineering*, Vol. 22, pp. 785-798.

Wu, G.X. and Eatock Taylor, R. (1994) "Finite element analysis of two dimensional non-linear Transient water waves", *Applied Ocean Research*, Vol. 16, pp. 363-372.

CASE	h/L_0	H/L_0	(ω/ω_0) present scheme	(ω/ω_0) Tsai and Jeng (1994)
A	0.5	0.05	0.991	0.996
B	0.5	0.13	0.978	0.979
C	0.25	0.10	0.989	0.989
D	0.1	0.02	1.007	1.003

Table 1 Comparison between results predicted by the present method and by Tsai and Jeng (1994) for various combinations of wave steepness and water depth.

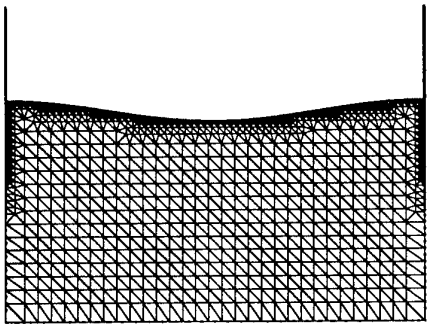

Figure 1 $t = 0$, Case A

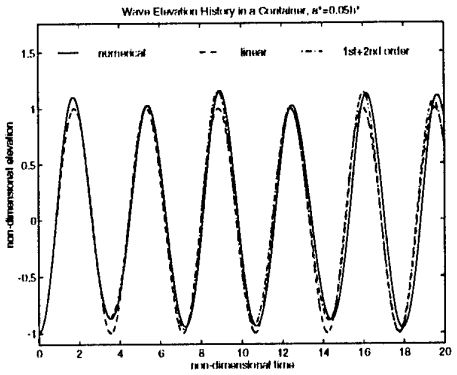

Figure 2 Case A

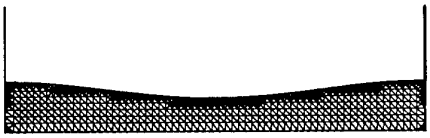

Figure 3 $t = 0$, Case D

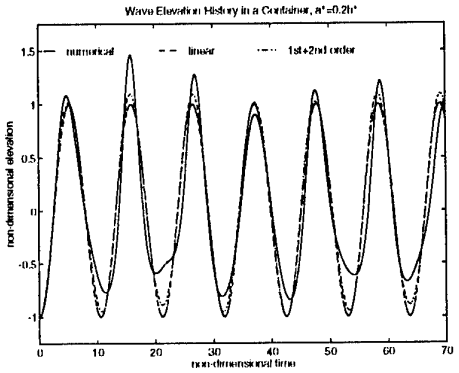

Figure 4 Case D

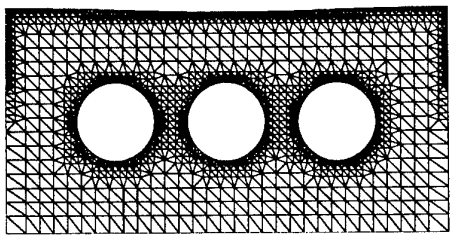

Figure 5 $t = 0$

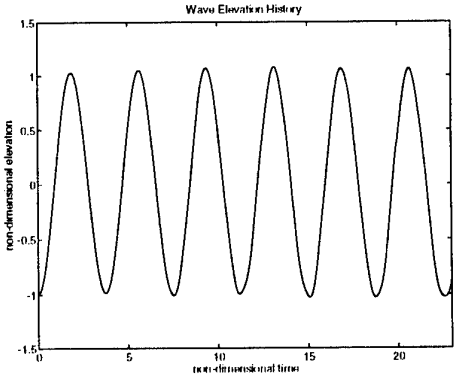

Figure 6 Three submerged circular cylinders

DISCUSSION

Magee A.: Is your gridding scheme appropriate for use in a nonlinear BEM surface grid on a complex (ship) hull form?

Greaves D.M., Borthwick A., Wu G.X.: If a discrete set of seed points can be defined which describe the hull form, then it should be possible to produce a surface mesh using the octree-based method.

Fully nonlinear properties of shoaling periodic waves calculated in a numerical wave tank

Stéphan T. Grilli [1], and Juan Horrillo [2]

In this work, nonlinear properties of finite amplitude shoaling periodic waves are calculated over mildly sloping bottom topographies, using a *numerical wave tank* which combines :

(i) a Boundary Element Model (BEM) solving Fully Nonlinear Potential Flow (FNPF) equations in a domain of arbitrary shape Ω (i.e., in a so-called physical space), up to and including wave overturning (Grilli *et al.*, 1989; Grilli and Subramanya, 1996; Fig. 1);

(ii) a generation of *zero-mass-flux Streamfunction Waves* at the deep water extremity of the tank, Γ_{r1} (i.e., exact periodic wave solutions of FNPF equations superimposed to a mean current equal and opposite to the wave mass transport velocity; Grilli and Horrillo, 1996a); and

(iii) an *Absorbing Beach* (AB) at the far end of the tank, which features both free surface absorption (through applying an external pressure; Cointe, 1990) and active absorption at the tank extremity, Γ_{r2} (using a piston-like condition; Clement, 1996). The beach depth is gradually increased to induce wave de-shoaling and a feedback mechanism adaptively calibrates the absorption coefficient, as a function of time, for the beach to absorb the period-averaged energy of incident waves, computed at the AB entrance, $x = x_l$ (Grilli and Horrillo, 1996a).

Incident waves of various heights H_o and periods T are modeled (covering the range k_oH_o = [0.028 ,0.105]), first over plane slopes s (1:35, 1:50, and 1:70; Fig. 1) and then over "natural beaches" of similar mean slope; in all cases both the AB location and characteristics are adjusted for the waves to shoal up to very close to their breaking point (BP). Due to the low reflection from such mild slopes and from the AB, a quasi-steady state is soon reached in the tank for which both *local and integral properties* of shoaling waves are calculated as a function of depth $h(x)$. These are the shoaling coefficient $K_s = H/H_o$, the phase velocity c, the wave relative height H/h (i.e. a measure of nonlinearity in classical shallow water wave models), the wave steepness $kH = 2\pi H/L$, the mean water level η_m, the radiation stress S_{xx}, the mean Eulerian current U_m, and the energy flux E_f.

For a shallow enough normalized depth ($k_oh < 0.5$ or $kh < 0.77$), significant differences are observed between FNPF results and 1st (LWT), 3rd (CWT), and higher-order steady wave (FSWT; Sobey and Bando, 1991) theories (Fig. 2). For the first two theories, low-order nonlinearity is clearly the main reason for the observed differences in a region where $H/h = \mathcal{O}(1)$; with the latter theory, the lack of skewness in the wave shape and the representation of the bottom by horizontal steps likely explain the observed differences. Despite the significant influence of actual bottom shape on the results, however, for the range of tested mild slopes, FNPF results are found to be

[1]Dept. of Ocean Engng., University of Rhode Island, Narragansett, RI 02881, USA, Ph.Nb.: (401) 874-6636; Fax : (401) 874-6837; email : grilli@mistral.oce.uri.edu; http ://www.oce.uri.edu/~grilli

[2]Graduate research assistant; same address.

fairly similar for the same wave taken at the same normalized depth ($k_o h$ or kh). This is also found true for a mildly sloping bottom with geometry corresponding to a "natural beach" and average slope 1:50. [This "natural beach" has a depth variation defined according to Dean's equilibrium beach profile, $h = A(x^* - x)^{2/3}$, with x^* denoting a constant, function of the location of the toe of the slope in depth h_o, and A depending on the specified average beach slope.] This, hence, allows us to use kh as the *unique parameter* describing a mild bottom variation and to compute additional results on a unique mild slope (1:50). Among these results, when taking all tested waves simultaneously, the normalized wave steepness $kH/k_o H_o$ shows an almost one-to-one relationship with kh in the shoaling region (Fig. 3). Quite surprisingly, due to a partial compensation of nonlinear effects for the wave height and celerity, LWT is found to be quite a good predictor of this parameter (maximum difference is 11%), whereas discrepancies for H and c reach 55 and 85%, respectively.

For the tested waves, the wave set-down (Fig. 4a) is quite well predicted by the first-order perturbation of LWT, except in the shallower region, where it is smaller, following the steep drop in radiation stresses (Fig. 4b). [This could also partly be due to the mean undertow current. More work remains to be done about this.]. Radiation stresses are overpredicted by the first-order theory in the region where wave left/right asymmetry (i.e., skewness) becomes large, confirming the sensitivity of this parameter to wave shape. Otherwise, agreement with the theory is quite good. A Fourier analysis of surface profiles shows, as expected, a continuous transfer of energy from the fundamental to higher-order harmonics in the shoaling region (Fig. 4c); this illustrates nonlinear interactions in the shoaling wave field. The 3rd-harmonic amplitude a_3 is found to be strongly correlated with wave asymmetry/skewness.

More results will be presented at the workshop, including some for barred beaches. Further discussions can also be found in Grilli and Horrillo (1996b).

References

Clément, A. , Coupling of Two Absorbing Boundary Conditions for 2D Time-domain Simulations of Free Surface Gravity Waves. *J. Comp. Phys.*, **126,** 139-151, 1996.

Cointe, R. , Numerical Simulation of a Wave Channel. *Engng. Anal. with Boundary Elemts.*, **7** (4), 167-177, 1990.

Grilli, S.T., and J., Horrillo , Numerical Generation and Absorption of Fully Nonlinear Periodic Waves. *J. Engng. Mech.* (accepted), 1996a.

Grilli, S.T., and J., Horrillo , Nonlinear Properties of Waves Shoaling over Slopes and Natural Beaches. In *Proc. 25th Intl. Conf. on Coastal Engineering* (ICCE25, Orlando, USA, 9/96), ASCE edition, 1996b (in press).

Grilli, S., Skourup, J., and Svendsen, I.A. , An Efficient Boundary Element Method for Nonlinear Water Waves, *Engng. Analysis with Boundary Elements,* **6**(2), 97-107, 1989.

Grilli, S.T. and Subramanya, R. , Numerical Modeling of Wave Breaking Induced by Fixed or Moving Boundaries. *Comp. Mech.*, **17,** 374-391, 1996.

Sobey, R.J. and Bando, K. , Variations on Higher-order Shoaling. *J. Waterway Port Coastal and Ocean Engng.*, **117** (4), 348-368, 1991.

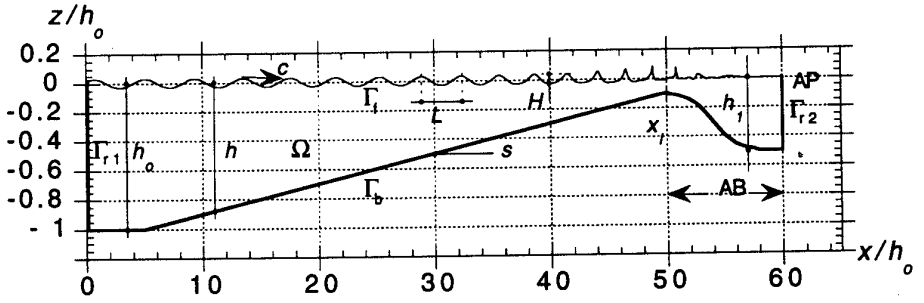

Figure 1: Sketch of "numerical wave tank" for FNPF computations of periodic waves shoaling over a plane slope s.

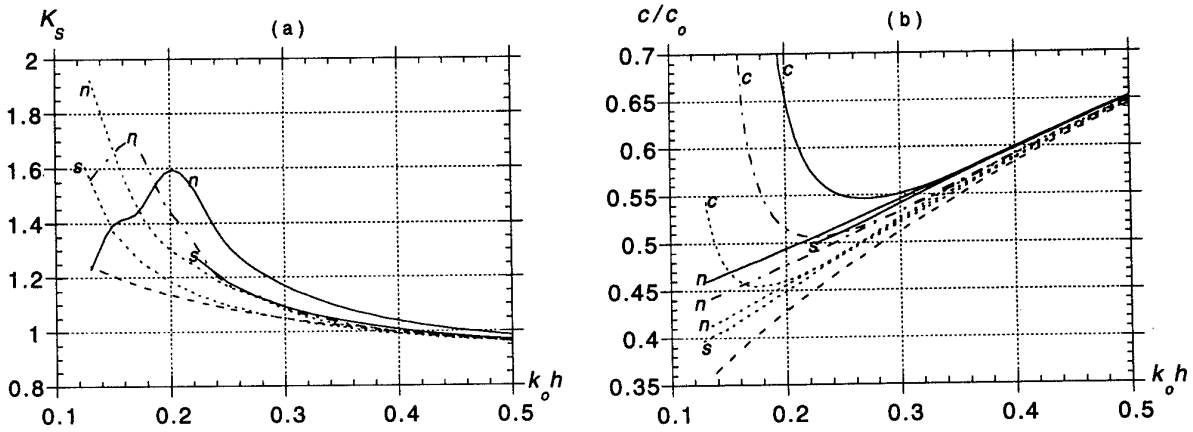

Figure 2: (a) shoaling coefficient $K_s = H/H_o$; and (b) celerity c, for periodic waves shoaling over a 1:50 plane slope, with $H_o' = H_o/h_o =$ (- - - -) 0.04, (— - —) 0.06, and (——) 0.08, and $T' = T\sqrt{g/h_o} = 5.5$: (n) FNPF results; (s) Sobey and Bando's (1991) FSWT results; (– – –) LWT results; (c) CWT results. $c_o = gT/(2\pi)$ is the (linear) deep water celerity.

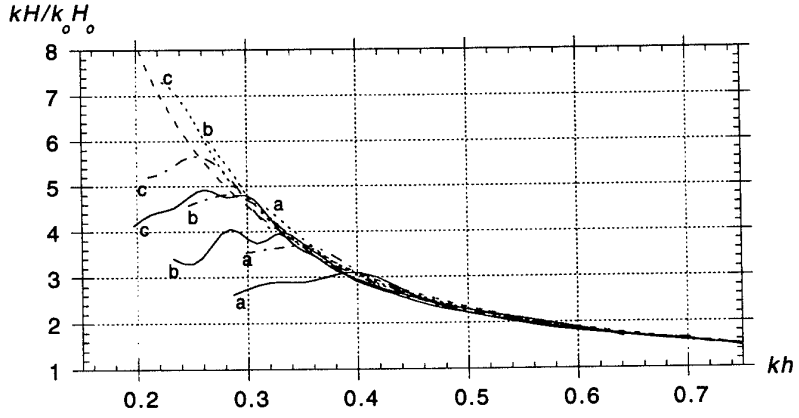

Figure 3: Normalized wave steepness kH/k_oH_o for periodic waves shoaling over a 1:50 slope. $H_o' =$ (- - - -) 0.04, (— - —) 0.06, and (——) 0.08, and $T' =$: 5.5 (curves a); 6.5 (curves b); 7.5 (curves c). (– – –) LWT results.

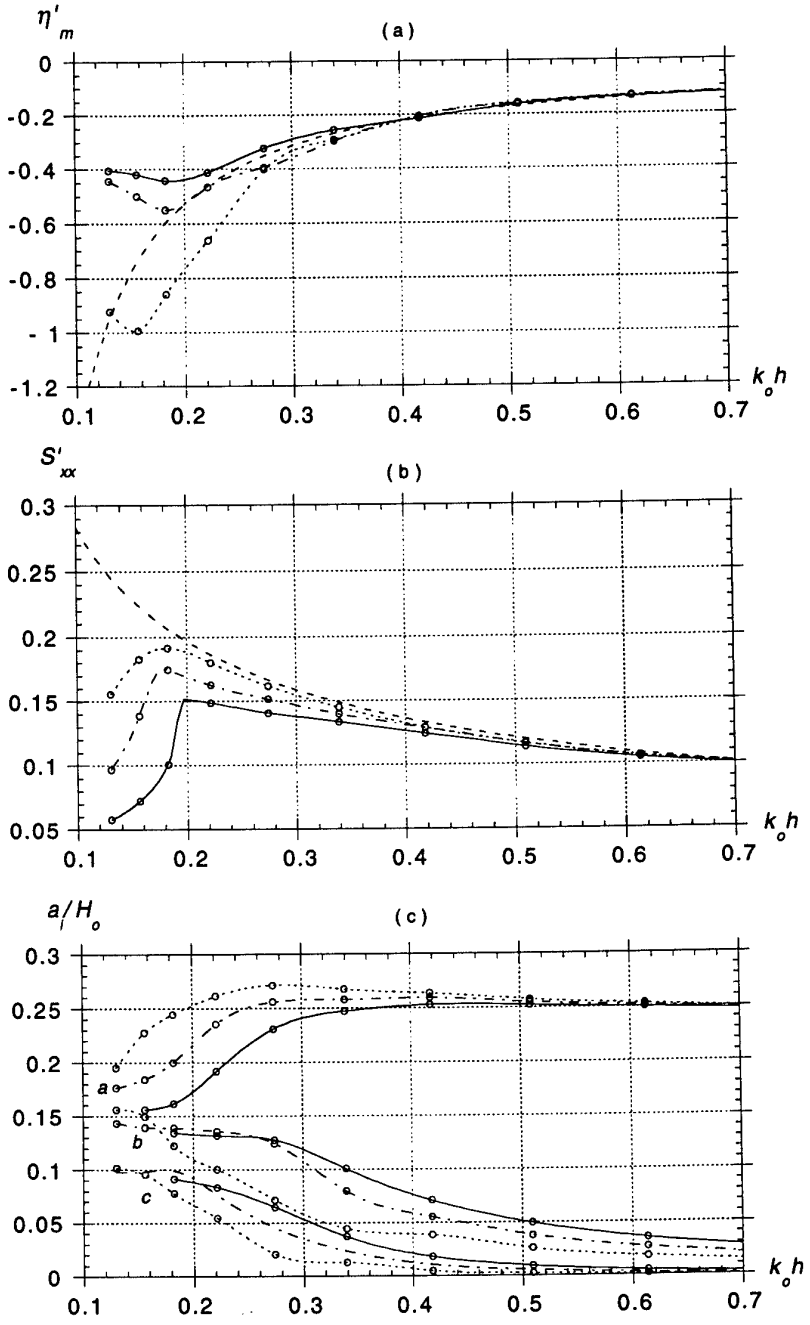

Figure 4: Normalized (a) mean water level $\eta'_m = \eta_m / h_o H_o'^2$; (b) radiation stress $S'_{xx} = S_{xx}/\rho g H_o^2$ (with ρ the fluid density); and (c) first three harmonics amplitudes (a,b,c $\equiv a_i$, i = 1,2,3), for three periodic waves shoaling over a 1:50 slope. Symbols and definitions are as in Fig. 2. Results have been averaged over $3T$ in the quasi-steady regime. Symbols (o) denote locations of "numerical gages". Corrections, $\Delta\eta'_{mo} = -0.0274$ and $\Delta S'_{xxo} = h'_o(\Delta\eta'_{mo}) + (\Delta\eta'_{mo})^2/2$, have been applied to the linear results for η'_m and S'_{xx}, respectively, to account for the actual mean water level in depth h_o in the FNPF results.

(Abstract for the 12th International Workshop on Water Waves and Floating Bodies, Marseilles, 16-19 March 1997)

Modelling of fully nonlinear internal waves and their generation in transcritical flow at a geometry

by

John Grue and Enok Palm

Mechanics Division, Department of mathematics,
University of Oslo, Norway

Introduction

Knowledge of flows due to internal waves, their origin and propagation, is important for many reasons. Relevant examples are flows in fjords and at sills, breaking of internal waves and mixing processes in the ocean, motion in coastal water and sub-surface waves in a layered ocean. An important aspect of the latter relates to oil exploration in deep water, with operation performed from ships or oil platforms floating at the sea surface, connected to subsea drilling or production via long cables. Knowledge of currents in the ocean, which may be induced by internal waves, may be of importance for the design of such concepts, in addition to the wave effects at the ocean surface. Dynamics of internal waves is also important in dimensioning of subwater bridges, which have been proposed across Norwegian fjords. This study is in particular motivated by needs relating to the two latter problems. In this abstract we describe recent efforts at the University of Oslo on this issue, both theoretical and experimental.

Time stepping of the interface

In the two-layer model we study fully nonlinear two-dimensional motion of two fluid layers of infinite horizontal extension under the action of gravity, with the gravitation force along the negative vertical direction. The lower fluid layer has thickness h_1 at rest and constant density ρ_1, and the upper layer has thickness h_2 at rest and constant density ρ_2, where ρ_2 is smaller than ρ_1. Hereafter, index 1 refers to the lower fluid, and index 2 to the upper. A coordinate system $O-xy$ is introduced with the x-axis along the interface at rest and the y-axis pointing upwards. Unit vectors $\mathbf{i},\mathbf{j}$ are introduced accordingly. We assume that the two fluids are homogenous and incompressible and that the motion in each of the layers is irrotational such that the velocities may be obtained by potential theory, i.e.

$$\mathbf{v}_1 = u_1\mathbf{i} + v_1\mathbf{j} = \nabla\phi_1, \qquad \mathbf{v}_2 = u_2\mathbf{i} + v_2\mathbf{j} = \nabla\phi_2, \tag{1}$$

where ϕ_1 and ϕ_2 satisfy the Laplace equation in their respective domains.

We adopt a pseudo Lagrangian method where pseudo particles are introduced on the interface, each with a weighted velocity given by

$$\mathbf{v}_X = (1-\alpha)\mathbf{v}_1 + \alpha\mathbf{v}_2 \tag{2}$$

where $0 \leq \alpha \leq 1$. To determine the position $\mathbf{R} = (X, Y)$ of a pseudo particle we use

$$\frac{D_\times \mathbf{R}}{dt} = \mathbf{v}_\times \tag{3}$$

where a pseudo Lagrangian derivative is introduced by $D_\times/dt = \partial/\partial t + \mathbf{v}_\times \cdot \nabla$. From the dynamic boundary condition at the interface I we find

$$\frac{D_\times(\phi_1 - \mu\phi_2)}{dt} = \mathbf{v}_\times \cdot (\mathbf{v}_1 - \mu\mathbf{v}_2) - \frac{1}{2}(\mathbf{v}_1^2 - \mu\mathbf{v}_2^2) - (1-\mu)gY - \frac{\sigma}{\rho_1 R_I} \quad \text{at} \quad I \tag{4}$$

where $\mu = \rho_2/\rho_1$. The equations (3) and (4) contain sufficient information to integrate $\mathbf{R}$ and $\phi_1 - \mu\phi_2$ forward in time. It is, however, an advantage to apply also higher order derivatives of (3) and (4) in a time stepping procedure for $\mathbf{R}$ and $\phi_1 - \mu\phi_2$.

The Eulerian velocity fields in the layers are obtained by solving the Laplace equation at each time step. It turns out that accurate solution of the Laplace equation is crucial to an algoritm for computing interfacial flows. Earlier works on time evolution of nonlinear interfacial waves have applied singularity distributions directly along the interface to solve the Laplace equation. We have sought a different method, and have chosen to employ Cauchy's integral theorem for this purpose, which is advantageous in avoiding instability.

Invoking complex analysis we introduce complex variable $z = x + iy$ and complex velocities $q_j(z) = u_j - iv_j$, $j = 1, 2$. Since q_j are analytic functions of z we have by use of Cauchy's integral theorem

$$-\pi i q_2(z') = PV \int_I \frac{q_2(z)dz}{z' - z} + \int_I \frac{q_2(z)^* dz^*}{z^* + 2ih_2 - z'} \qquad (z \text{ on } I) \tag{5}$$

$$\begin{aligned} \pi i q_1(z') &= PV \int_I \frac{q_1(z)dz}{z' - z} + \int_I \frac{q_1(z)^* dz^*}{z^* - 2ih_1 - z'} \\ &+ \int_B \frac{q_1(z)dz}{z' - z} + \int_B \frac{q_1(z)^* dz^*}{z^* - 2ih_1 - z'} \qquad (z \text{ on } I) \end{aligned} \tag{6}$$

$$\begin{aligned} \pi i q_1(z') &= \int_I \frac{q_1(z)dz}{z' - z} + \int_I \frac{q_1(z)^* dz^*}{z^* - 2ih_1 - z'} \\ &+ PV \int_B \frac{q_1(z)dz}{z' - z} + \int_B \frac{q_1(z)^* dz^*}{z^* - 2ih_1 - z'} \qquad (z \text{ on } B) \end{aligned} \tag{7}$$

where PV denotes principal value and B denotes the boundary of a geometry in the lower fluid. Only the real part of the principal value integrals in (5)–(7) are singular.

Transcritical flow at a topography. Upstream solitary waves

We apply the model to study transcritical two-layer flow at a bottom topography. There are several questions concerning this subject: Under which conditions is the flow unsteady? Another aspect is upstream influence in stratified flows, which in part can be addressed by the present two-layer model. Furthermore, for which conditions may transcritical flow over topography generate upstream solitary waves? These topics have

been discussed in earlier works exploiting hydraulic nonlinear theory or weakly nonlinear dispersive models. These methods have, however, limited validity with regard to nonlinearity and dispersion and give unrealistic predictions for finite amplitude and moderate wave length.

In the transcritical regime we find that an undular upstream bore is generated when the speed of the geometry, U, is less than a value which slightly exceeds the linear long wave speed, c_0. In the remaining part of the transcritical regime we find that solitary waves propagating upstream are generated by the geometry. We show an example in figure 1, which is due to a half elliptical bottom topography with horizontal half-axis $10h_1$, vertical half-axis $0.1h_1$, moving with speed $U/c_0 = 1.1$ in the lower layer, with $h_2/h_1 = 4$ and $\mu = 0.7873$. We have performed a very long time simulation with this configuration. A depression behind the moving geometry stabilizes at a level of 80% of the initial thickness of the lower fluid. The upstream waves have all the same amplitude, within a variation of 0.3%. The amplitude has same magnitude as the depth of the thinner layer, which means that the nonlinear effect is rather strong. Upon comparing with the solution of a steady profile we find a very good agreement between the computed profiles and wave speeds. Thus, the simulated waves may be regarded as a train of solitary waves.

In several other examples (not shown) we find that a moving geometry generates upstream disturbances with rather large elevation, even for geometries with small height (the volume of the geometry cannot be too small). We also compare our results with weakly nonlinear Korteweg-de Vries, finite depth and Benjamin-Ono theories. Our results indicate that these theories in many cases predict quite unrealistic wave profiles, and that a fully nonlinear method in general is required to investigate stratified transcritical flow at a geometry or bottom topography.

Experiments

We also perform experiments on internal waves with the perposes to determine wave shapes, velocity profiles and compare with theoretical models, such as the interface method. The experiments are carried out in a wave tank, and we use fresh water above salt water with vertical density profiles varying between $\rho_2 = 1.0000 g/cm^3$ and $\rho_1 = 1.0225 g/cm^3$. The velocity field in solitary waves is measured using Particle Tracking Velocimetry, where the fluid is seeded with particles and the motion is recorded onto a video tape. This is later digitized and analyzed by image processing.

The experiments are carried out with different (vertical) density variations, including profiles from rather localized depth variation, to density variations with some vertical extension. We compare the velocity profiles due to solitary waves with approximately corresponding amplitudes obtained by computations and experiments. We find very good agreement between the different methods, see figure 2. In this example $h_1/h_2 = 4$ and $|Y|_{max}/h_2 = 0.68$. This means that the interface method may be applied also to a stratified fluid, as long as a typical wave is much longer than the thickness of the stratification.

This research was supported by The Research Council of Norway through a grant of computing time (Programme for Supercomputing).

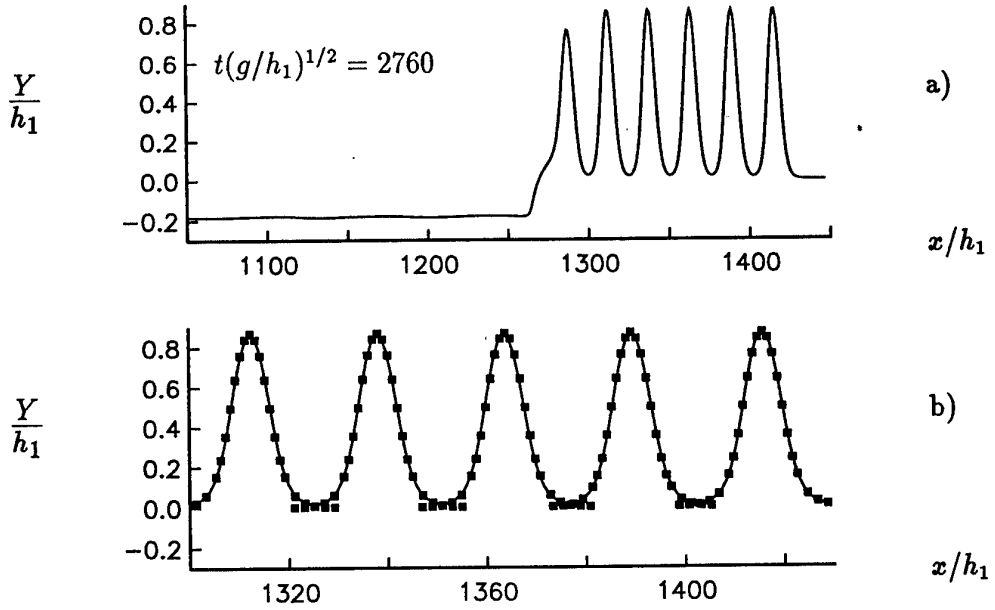

Figure 1: Generation of upstream solitary waves. Moving elliptical bottom topography with major half-axis (horizontal) $10h_1$, minor half-axis (vertical) $0.1h_1$. $U/c_0 = 1.1$, $\mu = 0.7873$, $h_2/h_1 = 4$. (a) Profile after $t\sqrt{g/h_1} = 2760$. (b) Close up of figure (a), black squares mark steady solitary wave solution with $|Y|_{max}/h_1 = 0.869$.

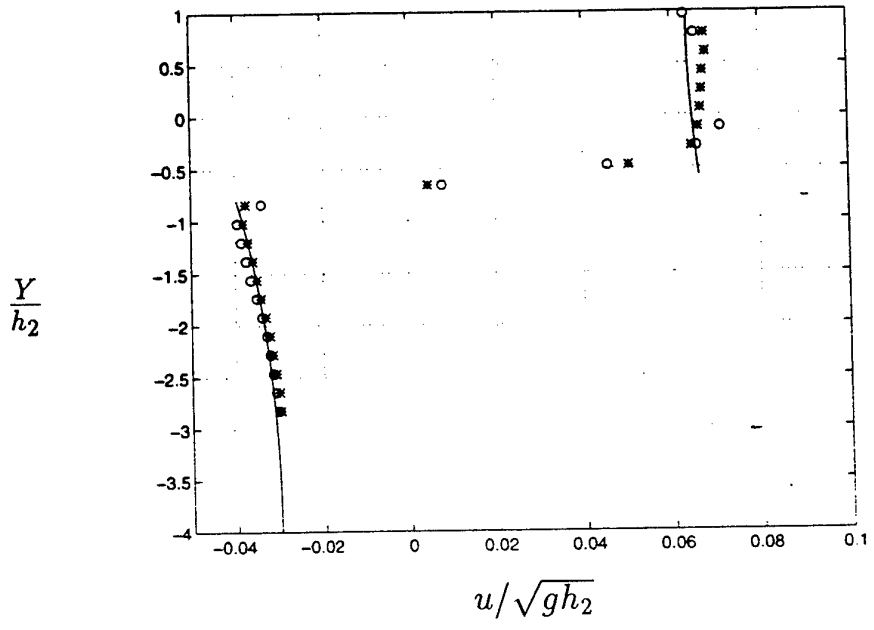

Figure 2: Velocity profile at the crest of a solitary wave. $*$ and o: experiments with different stratification. Solid line: two-layer model (theory). $|Y|_{max}/h_2 = 0.68$, $\mu = 0.978$, $h_1/h_2 = 4$.

DISCUSSION

Grilli S.: What type of boundary conditions did you use on lateral boundaries of your model? Did you translate the model with the mean wave velocity?

Grue J., Palm E.: The lateral boundaries are assumed far away such that the flow there may be considered to be zero. The model is translated with the mean wave velocity–approximately–in the computations.

The excitation of waves in a very large floating flexible platform by short free-surface water waves.

Aad J. Hermans *

1 Introduction

At the eleventh workshop on water waves and floating bodies *Ohkusu* et.al. [2] described recent developments of the design of floating airports. These floating airports consist of a thin mat configuration of very large horizontal size. One must think of dimensions of about several kilometers by several hundred meters, while the thickness of the mat is several meters. For these configurations the natural bending rigidity is relatively small and the elastic deflection due to wave action will be dominant compared with the rigid body motions. This paper treats in principle the same problem as Ohkusu did but with a different mathematical method, a similar approach can be found in *Stoker* [5] for the motion of a floating elastic beam in shallow water. If one looks at the operational conditions of the airport it is expected that in general the deflections are generated by short waves, this means waves with a wavelength short with respect to the horizontal dimensions if the platform, but such that the thickness of the structure is small with respect to this wavelength. This motivates us to treat the mat as an infinite thin plate at the free-surface and to neglect its thickness. In this presentation results for the wave transmission and reflection by a half-plane and a strip will be shown. Finally the propagation of the disturbances due to an accelerating and a decelerating point source are shown, this can be seen as the simulation of the take-off and landing of an airplane.
The problem has some resemblance with the deflection of a floating ice plate. There is a lot of literature about this topic, hence, some more information can be distracted from these sources. The papers of *Schulkes* et. al. [3],[4] and *Meylan* et. al. [1] are mentioned for further reference.

2 Mathematical formulation

We consider the situation that the platform is positioned in an area where no tidal current is present and the incident waves are long crested. The waves will be incident with a arbitrary angle of incidence. To keep the formulae simple we treat the case of infinite water depth, it will be clear from the analysis that the case of finite water depth is a straight forward extension. Viscous effects are neglected as well. In the fluid domain we introduce the velocity potential $V(\boldsymbol{x},t) = \nabla\Phi(\boldsymbol{x},t)$. The incident wave will be written as,

$$\Phi_{inc}(\boldsymbol{x},t) = e^{ik(x\cos\alpha+y\sin\alpha)+kz-i\omega t}, \tag{1}$$

where $k = \omega^2/g$ is the dispersion relation and α the angle of incidence. The waves are short with respect to the length L and the beam B of the platform, i.e. $kB \gg 1$ and $L/B \gg 1$.

*Faculty of Applied Mathematics and Computer Science, TUDelft, Mekelweg 4, 2628 CD Delft, The Netherlands

The wave number k is be the proper large parameter in the asymptotic expansions. Usually in the application of the *ray method* the expansions are made with respect to k, in the final results it becomes evident what dimensionless parameter plays a dominant role. In our case it is expected that in beam seas the parameter kB is essential, while for pure head seas we have to consider kL. So we don't bother about the two large parameters. In the fluid domain we have the potential equation

$$\Delta\Phi = 0 \tag{2}$$

together with the linearized free-surface condition for (x, y) outside the platform

$$\frac{\partial^2\Phi}{\partial t^2} + g\frac{\partial\Phi}{\partial z} = 0 \text{ at } z = 0 \tag{3}$$

The platform is assumed to be a thin layer at the free-surface $z = 0$, this seems to be a good model for a shallow draft platform. The platform is modelled as an elastic plate with zero thickness. To describe the deflection w we apply the thin plate theory, this finally leads to an equation for Φ at $z = 0$ in the platform area

$$\left\{\frac{EI}{\rho g}\left(\frac{\partial^2}{\partial x^2} + \frac{\partial^2}{\partial y^2}\right)^2 + \frac{m}{\rho g}\frac{\partial^2}{\partial t^2} + 1\right\}\frac{\partial\Phi}{\partial z} + \frac{1}{g}\frac{\partial^2\Phi}{\partial t^2} = 0 \tag{4}$$

We now introduce harmonic waves in the form of the ray expansion

$$\Phi(\boldsymbol{x}, t; k) = a(\boldsymbol{x}, k)e^{ikS(\boldsymbol{x})-i\omega t} \text{ with } a(\boldsymbol{x}, k) = \sum_{j=0}^{N}\frac{a_j(\boldsymbol{x})}{(ik)^j} + o((ik)^{-N}) \tag{5}$$

where $S(\boldsymbol{x})$ is the phase function and $a(\boldsymbol{x}, k)$ the amplitude function. Insertion of (5) into the Laplace equation (2) gives

$$-k^2\nabla_3 S\cdot\nabla_3 Sa + ik(2\nabla_3 a\cdot\nabla_3 S + a\Delta_3 S) + O(1) = 0 \tag{6}$$

The subscript 3 is used to indicate the three-dimensional ∇ and Δ operator. If no subscript is used the operators are two-dimensional in the horizontal plane. We compare orders of magnitude in (6). This leads to a set of equations for S and a_0 to be satisfied in the fluid region:

$$O(k^2) : \nabla_3 S\cdot\nabla_3 S = 0, \tag{7}$$

$$O(k^1) : 2\nabla_3 a_0\cdot\nabla_3 S + a_0\Delta_3 S = 0. \tag{8}$$

Next we insert (5) into the free-surface condition (3) outside the platform to get the following :

$$O(k^1) : iS_z = 1 \text{ and } O(k^{-j}) : a_{jz} = 0 \text{ for } j = 0\cdots N \text{ at } z = 0 \tag{9}$$

The next step is to insert (5) into the condition at the platform. At this stage we have to make some estimates of the order of magnitude of the parameters of the platform. We introduce

$$\frac{EI}{\rho g} = \frac{\mathcal{E}}{k^4} \text{ and } \frac{m}{\rho} = \frac{\mathcal{M}}{k}.$$

In this case the elastic properties and the mass of the platform play a role in the diffraction of the waves. The parameters $\mathcal{E}$ and $\mathcal{M}$ are of order one in k, this means they stay finite if k tends to infinity. This sounds like a contradiction, but it makes sense, it will be shown the values of these parameters may be large or small. The first two terms in the asymptotic evaluation of (4) become

$$O(k^1) : \left\{\mathcal{E}(S_x^2 + S_y^2)^2 - \mathcal{M} + 1\right\} iS_z = 1 \text{ at } z = 0 \tag{10}$$

and

$$O(k^0) : a_0 \left[\mathcal{E}\frac{\partial}{\partial z}(S_x^2 + S_y^2)^2 + 2S_z \left\{\frac{\partial}{\partial x}(S_x(S_x^2 + S_y^2)) + \frac{\partial}{\partial y}(S_y(S_x^2 + S_y^2))\right\}\right] + \tag{11}$$
$$a_{0z}\left\{\mathcal{E}(S_x^2 + S_y^2)^2 - \mathcal{M} + 1\right\} + 4a_{0x}S_xS_z(S_x^2 + S_y^2) + 4a_{0y}S_yS_z(S_x^2 + S_y^2) = 0$$

We combine the equations for the phase function at the free-surface with those in the water domain and obtain:

$$S_z = -i \text{ or } S_x^2 + S_y^2 = 1 \text{ outside the platform} \tag{12}$$

$$\left\{\mathcal{E}S_z^4 - \mathcal{M} + 1\right\} S_z = -i \text{ for } 0 < x < L \text{ and } 0 < y < B \tag{13}$$

Equation (13) has four solutions for $S_z : \{r_1, \pm r_2 + ir_3, \pm r_4 + ir_5\}$. Only the values of S_z with negative imaginary part are taken into account.

3 Infinitely long platform

We consider plane waves incident at $y = 0$. For convenience we assume the platform infinitely long, hence the waves are diffracted by a half-plane or a strip of width B. The wave field for $y < 0$ consists of an incident and reflected wave:

$$\Phi(\boldsymbol{x}, t) = e^{ik(x\cos\alpha + y\sin\alpha) + kz - i\omega t} + Re^{ik(x\cos\alpha - y\sin\alpha) + kz - i\omega t} \tag{14}$$

where R is the reflection coefficient.

Let us first solve the problem for the half-plane in other words with $B = \infty$. We then have (14) for $y < 0$ and for $y > 0$:

$$\Phi(\boldsymbol{x}, t) = \sum_{j=1}^{3} a_j e^{ik\left(x\cos\alpha + y\sqrt{n_j^2 - \cos^2\alpha}\right) + kir_j z - i\omega t} \tag{15}$$

where the square root is such it is positive or that its imaginary part is positive. This is to guarantee that the waves are either outgoing or evanescent. In this expression different types of solutions are combined. For all the components the amplitude function is a constant in the whole domain, in the case of a plane incident wave. For instance, for the real $n_1 < 1$ the solution consists, for angles of incidence with $|\cos\alpha| < n_1$ of a transmitted wave. This wave gives rise to reflections at $y = B$, if B is finite. If $|\cos\alpha| > n_1$ we have total reflection at $y = 0$, however the formulation (15) still gives a proper description of the evenescent mode. The angle for wich $|\cos\alpha_c| = n_1$ is called the critical angle α_c. The other two contributions are always of evenescent type, because the arguments of the sin

and cos terms are always complex. The four unknown coefficients $\{R, a_j\}$ for $j = 1, 2, 3$ are completely determined by the boundary conditions at the edge of the platform. We require continuity of the wave elevation and its inclination, hence, we assume platform very flexible. We now obtain

$$\Phi|_{0-} = \Phi|_{0+} \text{ and } \Phi_y|_{0--} = \Phi_y|_{0+} \text{ at } y = 0 \text{ and } z \neq 0, \tag{16}$$

furthermore at the edge of the platform we have the condition of zero moment and zero shear force

$$\frac{\partial^3}{\partial y^3}\left(\frac{\partial \Phi}{\partial z}\right) = \frac{\partial^2}{\partial y^2}\left(\frac{\partial \Phi}{\partial z}\right) = 0 \text{ at } y = 0+ \text{ and } z = 0 \tag{17}$$

We now solve four linear equations for the four unknown coefficients. In the figures 1 and 2 the elevation is shown for several values of the angle of incidence for $\mathcal{E} = 1$ and $\mathcal{M} = 0.5$. For the angle of incidence $\alpha = \pi/3$ we notice a plane wave propagating along the platform and two evanescent modes, while for the small value $\alpha = \pi/8$ total reflection occurs and the deflection of the platform consists of three evanescent modes.

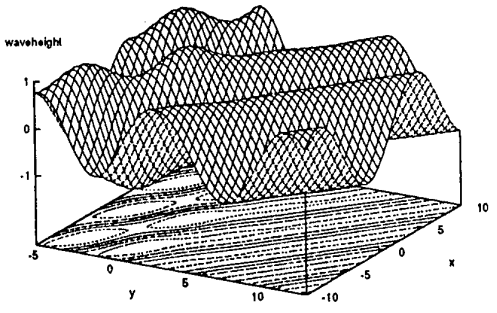

Figure 1: Waveheight for $\alpha = \pi/3$.

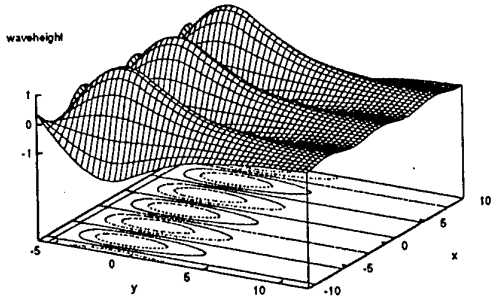

Figure 2: Waveheight for $\alpha = \pi/8$.

References

[1] Meylan, M. and Squire, V.A., The response of ice floes to ocean waves. *J. Geophysical Research*, Vol. 99 No. C1

[2] Ohkusu, M. and Nanba, M., Hydroelastic behavior of a very large floating platform in waves. *Proceedings of the eleventh Workshop on Water Waves and Floating Bodies*, Hamburg, 1996.

[3] Schulkes, R.M.S.M., Hosking, R.J. and Sneyd, A.D., Waves due to a steady moving source on a floating ice plate. Part 2. *J.Fluid Mech.*, Vol. 180, pp. 297-318, 1987.

[4] Schulkes and Sneyd, A.D., Time-dependent response of floating ice to a steadily moving load. *J.Fluid Mech.*, Vol. 186, pp. 25-46, 1988.

[5] Stoker, J.J., *Water Waves*, Interscience Publ., New York, 1957. Springer-Verlag, Berlin, 1960.

Free surface integrals in non-linear wave-diffraction analysis

J. B. Huang[1], R. Eatock Taylor[1] and R. C. T. Rainey[2]

[1] *Department of Engineering Science, University of Oxford, U. K.*
[2] *W. S. Atkins Consultants Ltd, Epsom, Surrey, U. K.*

A difficult problem in frequency-domain analysis of non-linear wave interaction with offshore structures is the evaluation of the two-dimensional free-surface integral, which provides the 'locked wave' component of the diffraction potential. This is usually done by meshing the free-surface of the fluid domain into boundary elements, and carrying out the integration element-by-element. The approach is known to be very time-consuming, especially if needed for computing the third-order forces, where it is necessary to evaluate the second-order potentials over a large domain on the free-surface. This paper proposes an alternative way of performing the free-surface integrations. We first extend the integration domain into the entire free-surface, then subtract out the contribution from the internal water plane occupied by the structures. In this way an efficient semi-analytical method can be developed, and the integrals are reduced to one-dimensional quadratures. The algorithm presented in the paper is relevant to obtaining the 'locked wave' component of the diffraction potential at either second or third order.

1. Semi-analytical method for the free surface integrals

We consider the locked wave component of the potential associated with diffraction by an array of vertical, surface-piercing structures of arbitrary shape. We define a global co-ordinate system (x, y, z) and a number of local cylindrical co-ordinate systems (r_k, θ_k, z) which coincide with the individual structures. The z axis originates from the quiescent free-surface and points upwards. For simplicity we only consider the second-order potential, but the formulation is also valid at third order. In the local coordinate system, the locked wave potential can be expressed as:

$$\phi_p^{(2)}(r_k, \theta_k, z) = \int\int_{S_f} Q^{(2)}(s) G^{(2)}(r_k, \theta_k, z; s) ds \tag{1}$$

where S_f is the entire free-surface of the fluid domain, $Q^{(2)}$ is the forcing function and $G^{(2)}$ the Green function.

We rewrite equation (1) as

$$\phi_p^{(2)}(r_k, \theta_k, z) = \int\int_{S_{fe}} Q^{(2)}(s) G^{(2)}(r_k, \theta_k, z; s) ds - \sum_{j=1}^{N_c} \int\int_{S_{wj}} Q^{(2)}(s) G^{(2)}(r_k, \theta_k, z; s) ds \tag{2}$$

where S_{fe} is the extended region over the whole free-surface, and S_{wj} is the water plane of the jth cylinder. This arrangement implies that we first extend the region of validity for $Q^{(2)}$ into the water planes occupied by the structures, and then subtract the contribution due to the ficticious forcing from the extended region.

We express the forcing function at a point (r_j, θ_j) inside the jth water plane as:

$$Q^{(2)}(r_j, \theta_j) = Q^{(2)}[a(\theta_j), \theta_j] \frac{r_j}{a(\theta_j)} \tag{3}$$

where $a(\theta_j)$ is the radial co-ordinate on the jth waterline at θ_j.

The major computational burden comes from the first integral on the right-hand side of equation (2). For its efficient evaluation, we expand the locked wave potential, the free-surface forcing function and the Green function into Fourier series:

$$\phi_p^{(2)}(r_k,\theta_k,z)=\sum_{n=-\infty}^{\infty}\phi_{pn}^{(2)}(r_k,z)e^{in\theta_k},\ Q_p^{(2)}(r,\theta)=\sum_{n=-\infty}^{\infty}Q_n^{(2)}(r)e^{in\theta} \tag{4}$$

$$G^{(2)}=\sum_{n=-\infty}^{\infty}e^{in(\theta_k-\theta)}\{Z_0^{(2)}(0)Z_0^{(2)}(z)J_n(\kappa r_<)H_n(\kappa r_>)\frac{i}{4}+\frac{1}{2\pi}\sum_{q=1}^{\infty}Z_q^{(2)}(0)Z_q^{(2)}(z)I_n(\kappa_q r_<)K_n(\kappa_q r_>)\} \tag{5}$$

where $r_>=\max(r_k,r)$, $r_<=\min(r_k,r)$. $Z_0^{(2)}(z)$, $Z_q^{(2)}(z)$ are eigenfunctions, and $J_n(x)$, $H_n(x)$, $I_n(x)$, $K_n(x)$ are normal and modified Bessel/Hankel functions respectively.

We remark that the above-defined integrals associated with the Green function are valid in the whole fluid domain, inspite of the fact that $H_n(x)$, $I_n(x)$ possess singularities at $x\to 0$. In fact, as $x\to 0$, we use the asymptotic form of the normal and modified Bessel/Hankel functions, noting that when $r\to 0$, $Q^{(2)}(r,\theta)=rf(\theta)$; and when $r_k\to 0$, we have $Q_n^{(2)}(r)G_n^{(2)}|_{r_k\to 0}=0$. When $r_k>0$, except for the logarithmic singularity at $r\to r_k$, $z=0$, no other singularity is encountered in the Green function. The logarithmic singularity was first discussed by Fenton (1978). When the field point is outside the waterplanes $S_{wj}(j=1,2,\cdots,N_c, j\neq k)$, the nth the Fourier mode of the locked wave potential can be expressed as:

$$\begin{aligned}
\phi_{pn}^{(2)} &= Z_0^{(2)}(0)Z_0^{(2)}(z)\frac{\pi i}{2}\{H_n(\kappa r_k)[S_1(n,r_k)-\frac{1}{2\pi}\int_0^{2\pi}Q^{(2)}(a(\theta))e^{-in\theta}\int_0^{a(\theta)}r^2J_n(\kappa r)drd\theta] \\
&- \phi_{p1}^{(2)}(n,r_k)+J_n(\kappa r_k)S_2(n,r_k)\}+\sum_{q=1}^{\infty}Z_q^{(2)}(0)Z_q^{(2)}(z)\{K_n(\kappa_q r_k)[\int_0^{r_k}Q_n^{(2)}(r)rI_n(\kappa_q r)dr \\
&- \frac{1}{2\pi}\int_0^{2\pi}Q^{(2)}(a(\theta))e^{-in\theta}\int_0^{a(\theta)}r^2I_n(\kappa_q r)drd\theta] \\
&- \phi_{p2}^{(2)}(n,q,r_k)+I_n(\kappa_q r_k)\int_{r_k}^{\infty}Q_n^{(2)}(r)rK_n(\kappa_q r)dr\},
\end{aligned} \tag{6}$$

where

$$\begin{aligned}
S_1(n,r_k) &= \int_0^{r_k}Q_n^{(2)}(r)rJ_n(\kappa r)dr; \\
S_2(n,r_k) &= \int_{r_k}^{\infty}Q_n^{(2)}(r)rH_n(\kappa r)dr;
\end{aligned}$$

$$\begin{aligned}
\phi_{p1}^{(2)}(n,r_k) &= \frac{1}{2\pi}\sum_{j\neq k}^{N_c}\sum_{m=-\infty}^{\infty}\begin{pmatrix}J_m(\kappa r_k)H_{n-m}(\kappa R_{jk})\\ H_m(\kappa r_k)J_{n-m}(\kappa R_{jk})\end{pmatrix}e^{i(n-m)(\alpha_{jk}-\pi)} \\
&\int_0^{2\pi}Q^{(2)}(a(\theta_j))e^{-in\theta_j}\int_0^{a_j(\theta_j)}r_j^2J_n(\kappa r_j)dr_jd\theta_j,\begin{pmatrix}r_k<R_{jk}\\ r_k>R_{jk}\end{pmatrix};
\end{aligned}$$

$$\begin{aligned}
\phi_{p2}^{(2)}(n,q,r_k) &= \frac{1}{2\pi}\sum_{j\neq k}^{N_c}\sum_{m=-\infty}^{\infty}\begin{pmatrix}I_m(\kappa r_k)K_{n-m}(\kappa R_{jk})\\ K_m(\kappa r_k)I_{n-m}(\kappa R_{jk})\end{pmatrix}e^{i(n-m)(\alpha_{jk}-\pi)} \\
&\int_0^{2\pi}Q^{(2)}(a(\theta_j))e^{-in\theta_j}\int_0^{a_j(\theta_j)}r_j^2J_n(\kappa r_j)dr_jd\theta_j,\begin{pmatrix}r_k<R_{jk}\\ r_k>R_{jk}\end{pmatrix}.
\end{aligned}$$

In deriving equation (6), we have used the Bessel addition theorem, R_{jk} being the horizontal distance between the jth and kth coordinate systems. A similiar expression for the nth Fourier mode of the second-order locked wave component in the extended region can also be obtained.

In the case of simple geometry, e.g. for multiple bottom-seated or truncated cylinders, semi-analytical solutions for the 'free-wave' component can be obtained (Huang & Eatock Taylor 1997). Such a solution is adopted in generating the results in the next section.

2 Computation of the one-dimensional free-surface integrals

Let R_J be a large radius, such that when $r > R_J$, the local waves associated with the modified Bessel functions can be neglected, and the asymptotic forms can be used for the normal Bessel or Hankel functions. Thus integrals like $S_2(n, R_J)$ can be carried out analytically. For $r < R_J$ we can derive recurrence formulae such as the following for the free-surface integrals:

$$S_1(n, a) = 0; S_1(n, r_0 + \Delta r) = S_1(n, r_0) + \int_{r_0}^{r_0+\Delta r} r Q_n(r) J_n(\kappa r) dr \tag{7}$$

$$S_2(n, r_0) = S_2(n, r_0 + \Delta r) + \int_{r_0}^{r_0+\Delta r} r Q_n(r) H_n(\kappa r) dr. \tag{8}$$

Algorithms for the integrals associated with the modified Bessel functions are treated in Huang & Eatock Taylor (1997). In a small interval $[r_j, r_j + \Delta r]$, we express the forcing function $Q_n(r)$ and the Bessel/Hankel functions (or modified Bessel functions) as a quadratic function of r, and the quadrature over this interval can then be carried out analytically. A similar approach was taken by Malenica & Molin (1995), using numerical integration over a smaller interval.

3 A numerical example

As a numerical example, we consider the free-surface elevation in the vicinity of four bottom-seated cylinders of radius $a = 15.5m$, in water of depth $h = 300m$. The centre-lines of the cylinders are placed at the corners of a square of side length $L = 80m$. The incident wave is in the same direction as the x axis, which bisects two opposite sides of the square. The non-dimensional wave number is given by $ka = 0.403$; and the wave amplitude $A = 6m$.

Figures 1a and 1b illustrate respectively the linear and maximum non-linear (first order plus second order) free surface elevations around the cylinders. Figure 2 shows the contours of the non-linear free surface elevation at $t = 0$. Figure 3 plots the maximum linear and non-linear wave run-up on the up-wave and down-wave cylinders. Figure 4 presents the maximum linear and non-linear wave elevations along the x axis. From these figures, we note that the maximum wave elevation in this specific case is not at the surface of the up-wave cylinders, but is located a little distance in front of them, on the centre-line. We also see that the non-linear effect can either increase or reduce the local free surface elevation.

4 Concluding remarks

A semi-analytical procedure is proposed for evaluating the free surface integrals associated with the frequency-domain analysis of non-linear wave diffraction by multiple structures of arbitrary shape. A distinguishing characteristic of the procedure is that it is highly efficient for evaluating the non-linear potential at a large number of points. It takes only a few minutes on a Sun Workstation, for the case of a complete second-order analysis of four cylinders. With a fully numerical method, it takes over 20 hours CPU time on the same computer. This method therefore provides an efficient tool for flow visualization of non-linear wave field around multiple structures, and for undertaking third-order analyses.

This work was sponsored by EPSRC through MTD Ltd (Grant GR/L19355) and jointly funded with Den Norske Stats Oljeselskap a.s. and W.S. Atkins Consultants Ltd.

References

[1] Fenton, J. D. (1978) Wave forces on vertical bodies of revolution. *J. Fluid Mech.* **85**, 241-255.

[2] Malenica, S. & Molin, B. (1995) Third harmonic wave diffraction by a vertical cylinder. *J. Fluid Mech.* **302**, 203-229.

[3] Huang, J.B. & Eatock Taylor, R. (1997) Second-order wave diffraction by a group of vertical cylinders. In preparation.

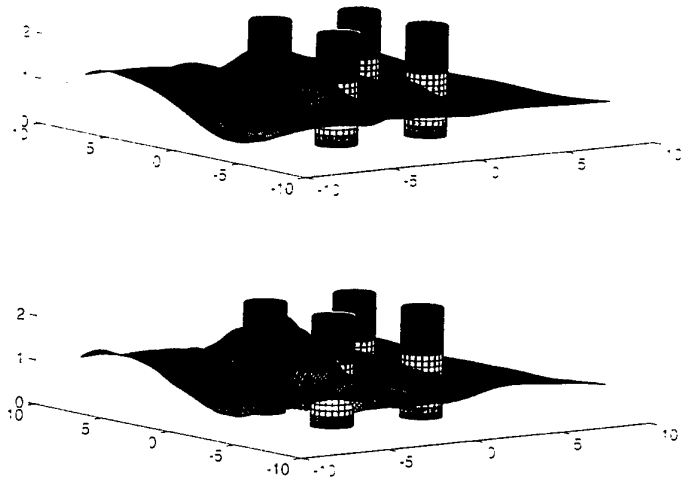

Figure 1. Isometrics of maximum free surface elevation around 4 bottom-seated cylinders: (a) first-order; (b) first-order plus second-order.

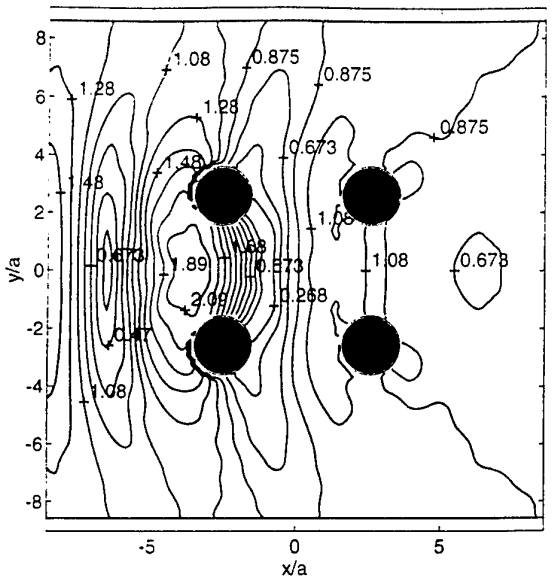

Figure 2. Contours of non-linear wave elevation at $t = 0$.

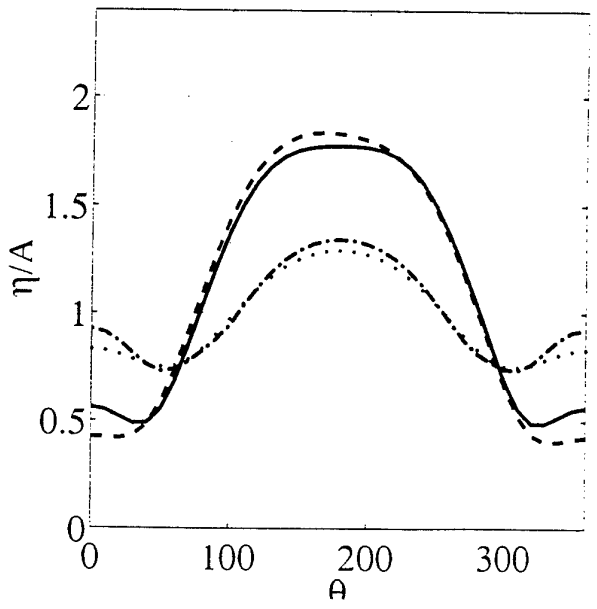

Figure 3. Maximum wave run-up around the cylinders; (———) linear, up-wave cylinder; (– – –) non-linear, up-wave cylinder; (·····) linear, down-wave cylinder; (–·–·–) non-linear, down-wave cylinder.

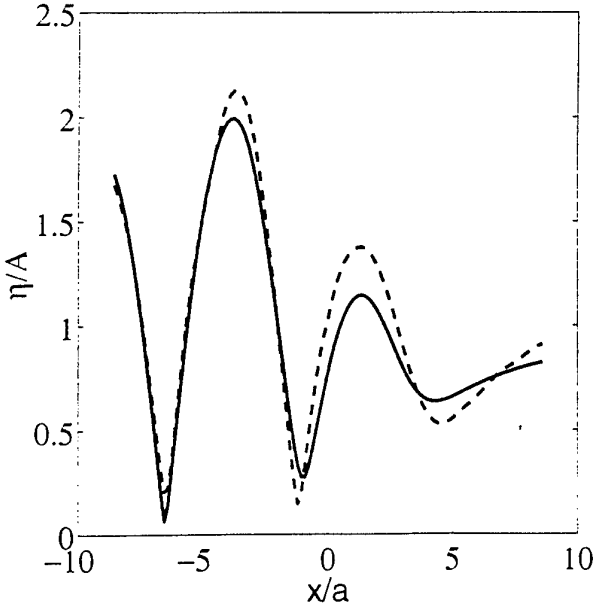

Figure 4. Maximum free surface elevation along the central line $y = 0$. (———) linear; (– – –) nonlinear.

(Abstract for the 12^{th} International Workshop on Water Waves & Floating Bodies, March 1997)

Nonlinear Ship Wave Simulations by a Rankine Panel Method

Yifeng Huang and Paul D. Sclavounos

Department of Ocean Engineering
MIT, Cambridge, Massachusetts 02139, U.S.A.

1 Introduction

Nonlinear hydrostatics, Froude-Krylov and hydrodynamic effects have been found in many experimental and numerical studies to be important for the accurate prediction of the ship motion responses in waves. In this article, a linear, time-domain, three-dimensional Rankine Panel Method has been extended, on the basis of a Weak-Scatterer Hypothesis, to treat the nonlinear motions of realistic ship hulls in steep ambient waves.

The Rankine Panel Method (RPM) has enjoyed a great deal of success in recent years, for the treatment of both the steady wave resistance and unsteady seakeeping problems, owing to its flexibility to different types of free surface conditions and simplicity in using the Rankine source as the Green function in the boundary integral formulation. The time-domain treatment of the surface wave disturbance has been adopted here and demonstrated in the linear case (cf. [3][5]) to be stable, convergent and accurate. The time marching is carried out by a so-called Emplicit Euler scheme, which integrates explicitly the kinematic free surface condition and implicitly the dynamic condition. The method is able to obtain accurate and convergent ship wave patterns and ship response predictions. Building upon this solid foundation, the solution of nonlinear ship wave problems is outlined in this article.

According to the Weak-Scatterer theory, the ship wave disturbance is linearized about the instantaneous position of the ambient wave profile. The resulting boundary value problem is derived and the rationale of the hypothesis is discussed. The numerical framework of the solution is presented, along with computations of motion responses of realistic ship hulls in steep ambient waves which demonstrate a marked improvement over linear theory in waves of even moderate steepness.

2 Formulation and Numerical Method

The Weak-Scatterer hypothesis, first proposed by Pawlowski [4], relaxes two restrictions in classical linear ship motion theory: the amplitude of the incoming waves and ship motions. In contrast to linear theory, both amplitudes are allowed to be large as long as the ship radiation and diffraction disturbance is sufficiently small, and thus linearizable. Ambient waves are driven by the environment, and their amplitude is therefore not dependent on the hull shape or ship speed. The ship wave disturbance, on the other hand, is often seen in experimental studies and

full scale observations to be relatively small. An extreme example is that of a thin ship moving with large amplitude in steep incident waves. This vessel is evidently not going to generate large disturbances, hence justifying the Weak-Scatterer linearization. Most ships are designed to be slender, and thus, are expected to generate wave disturbances which are not as large as steep ambient waves. Moreover, in the course of their interaction with ambient waves ships behave as compliant rigid bodies in heave and pitch which often induce small wave disturbances due to their tendency to contour the ambient waves.

The present theory allows the ambient wave amplitude and ship motions to be arbitrary and linearizes the ship wave disturbance about the incident wave profile. The hull geometric non-linearity is therefore treated more accurately than in linear theory, and is found to be essential for the accurate predictions of ship motions, especially for ships with prominent counter-top sterns and flared bows.

Within potential flow theory, the free surface conditions in the ship-fixed coordinate system are stated as follows,

$$\left[\frac{\partial}{\partial t}-(\vec{U}-\nabla\Psi)\cdot\nabla\right]\eta=\frac{\partial\Psi}{\partial z}, \qquad \text{on the exact free surface,} \tag{1}$$

$$\left[\frac{\partial}{\partial t}-(\vec{U}-\nabla\Psi)\cdot\nabla\right]\Psi=\frac{1}{2}\nabla\Psi\cdot\nabla\Psi-g\eta, \qquad \text{on the exact free surface,} \tag{2}$$

where ζ is the wave elevation. The total disturbance potential Ψ and free surface wave elevation ζ is decomposed as follows,

$$\Psi(\vec{x},t)=\Phi(\vec{x},t)+\phi(\vec{x},t)+\varphi_0(\vec{x},t)+\varphi(\vec{x},t), \tag{3}$$

$$\eta(x,y,t)=\zeta_0(x,y,t)+\zeta(x,y,t). \tag{4}$$

The basis flow Φ is the solution of a ship moving through a wavy solid ($\Phi_n = 0$) free surface boundary that is prescribed by incoming wave. The time-local flow ϕ represents the instantaneous fluid response to the ship motion and is the solution of a pressure release boundary value problem ($\phi = 0$) on the free surface. A thorough numerical stability study [3] shows that no convergent results can be obtained without separating the time-local flow ϕ from the total disturbance potential Ψ. φ_0 denotes the incident wave potential and ζ_0 is the incident wave elevation. φ and ζ stand for the remaining part of the total disturbance quantities: wave disturbance velocity potential and wave elevation, respectively. ζ records the history of the wave flow and takes the form of an initial boundary value problem.

In accordance with the Weak-Scatterer model, it is assumed that, $\Phi \sim \mathcal{O}(1); \varphi_0 \sim \mathcal{O}(1); \phi \sim \mathcal{O}(1); \varphi \sim \mathcal{O}(\epsilon)$ and $\zeta_0 \sim \mathcal{O}(1); \zeta \sim \mathcal{O}(\epsilon)$. The problem is linearized accordingly. After plugging the decompositions (3),(4) into the free surface conditions (1),(2) and performing a Taylor expansion to transfer the free surface conditions from $z = \zeta$ to $z = \zeta_0$, with the omission of high order terms $\mathcal{O}(\epsilon^2)$, the following free surface conditions are obtained,

$$\begin{aligned}[\frac{\partial}{\partial t}-(\vec{U}-\nabla\Phi-\nabla\phi-\nabla\varphi_0)\cdot\nabla]\zeta &= -[\frac{\partial}{\partial t}-(\vec{U}-\nabla\Phi-\nabla\phi-\nabla\varphi_0)\cdot\nabla]\,\zeta_0+\frac{\partial\varphi_0}{\partial z}\\ &+\frac{\partial\Phi}{\partial z}+\frac{\partial\phi}{\partial z}+\frac{\partial\varphi}{\partial z}-\nabla\varphi\cdot\nabla\zeta_0+[\frac{\partial^2\Phi}{\partial z^2}+\frac{\partial^2\varphi_0}{\partial z^2}-\nabla(\frac{\partial\Phi}{\partial z}+\frac{\partial\varphi_0}{\partial z})\cdot\nabla\zeta_0]\,\zeta, \quad z=\zeta_0(x,y,t),\end{aligned} \tag{5}$$

$$[\frac{\partial}{\partial t}-(\vec{U}-\nabla\Phi-\nabla\phi-\nabla\varphi_0)\cdot\nabla]\varphi=-[\frac{\partial}{\partial t}-(\vec{U}-\nabla\Phi-\nabla\phi-\nabla\varphi_0)\cdot\nabla]\,\varphi_0+\frac{1}{2}\nabla\varphi_0\cdot\nabla\varphi_0-g\zeta_0$$
$$-[\frac{\partial}{\partial t}-(\vec{U}-\nabla\Phi)\cdot\nabla]\,\Phi+\frac{1}{2}\nabla\Phi\cdot\nabla\Phi-[\frac{\partial}{\partial t}-(\vec{U}-\nabla\Phi-\nabla\phi)\cdot\nabla]\,\phi+\frac{1}{2}\nabla\phi\cdot\nabla\phi-g\zeta$$
$$-[\frac{\partial}{\partial t}-(\vec{U}-\nabla\Phi-\nabla\phi-\nabla\varphi_0)\cdot\nabla]\,\frac{\partial\Phi}{\partial z}\zeta-[\frac{\partial}{\partial t}-(\vec{U}-\nabla\Phi-\nabla\phi-\nabla\varphi_0)\cdot\nabla]\,\frac{\partial\phi}{\partial z}\zeta$$
$$-[\frac{\partial}{\partial t}-(\vec{U}-\nabla\Phi-\nabla\phi-\nabla\varphi_0)\cdot\nabla]\,\frac{\partial\varphi_0}{\partial z}\zeta, \qquad z=\zeta_0(x,y,t). \quad (6)$$

On all solid boundaries, the no-flux condition is imposed over the instantaneous submerged surfaces. Φ governs the steady translation, ϕ accounts for the rigid body oscillatory motions and φ represents the incident wave diffraction. The radiation condition is enforced by the application of a dissipative beach, which resembles the absorbing beach in a wave tank.

The resulting boundary value problems are solved by a thoroughly tested time-domain Rankine panel method. The method uses plane quadrilateral panels, but applies bi-quadratic spline representation of the unknown over their surface, with continuity in the value and slope of the unknown across panels. The time matching is carried out by the Emplicit Euler scheme and the nonlinear rigid body equation of motion is solved by a fourth-order Adams-Bashford-Moulton scheme, using a fourth-order Runge-Kutta scheme for the first four time steps. The numerical algorithm is rationally shown , (cf. [3][5]), to be stable and computationally efficient.

Unlike pure linear theory, the present method solves the boundary value problems on an incident-wave-prescribed free surface and the instantaneous submerged hull surface. Figure 1 shows a computational grid, with the free surface panel elevated at the position of the incoming wave profile and the submerged ship surface determined by the instantaneous position of the ship. The whole ship is outlined by the bold line to illustrate how much/little the ship surface could actually be submerged during the course of traveling. Figure 2 presents computed results of the heave and pitch motion responses for the S7-175 ship over a range of incident wave frequencies. In comparison with experimental measurements documented in [1], this nonlinear method is seen to offer a substantial improvement over linear theory and its nonlinear variation, which accounts for the nonlinear hydrostatic and Froude-Krylov exciting forces coupled with linear hydrodynamics. More results will be presented at the Workshop.

References

[1] Dalzell, J.F., Thomas III, W.L. and Lee, W.T., (1986) " Correlations of model data with analytical load predictions for three high speed ships", *Department Report*, Ship Hydrodynamics Department, Naval Surface Warfare Center.

[2] Huang, Y., (1996) "Nonlinear ship motions by a Rankine Panel Method", PhD Thesis, MIT, Cambridge, MA.

[3] Kring, D.C. and Sclavounos, P.D., (1995) "Numerical Stability Analysis for Time Domain Ship Motion Simulations", *Journal of Ship Research*, Vol. 39, No. 4, pp 321-327.

[4] Pawlowski, J., (1992) "A nonlinear theory of ship motions in waves", Proceedings of the *19th Symposium on Naval Hydrodynamics*, Seoul, Korea.

[5] Vada, T. and Nakos, D.E., (1993) "Time-marching schemes for ship motion simulations", Proceedings of the *8th International Workshop on Water Waves and Floating Bodies*, St. John's, Newfoundland, Canada.

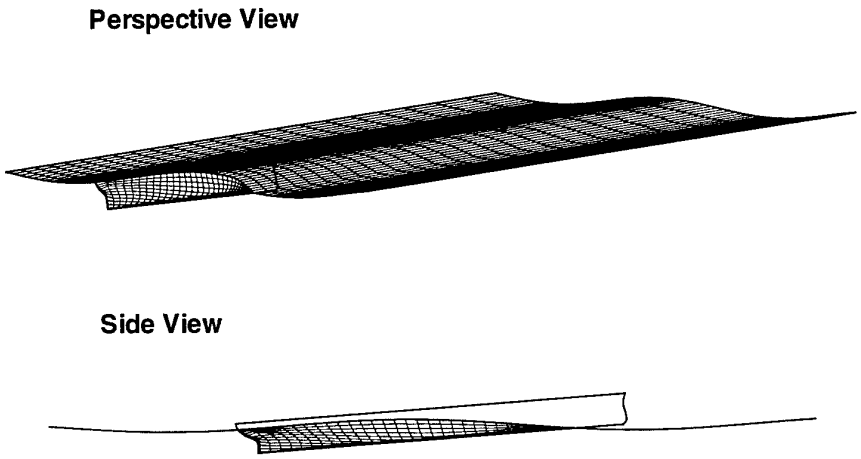

Figure 1: Typical Rectangular Computational Grid

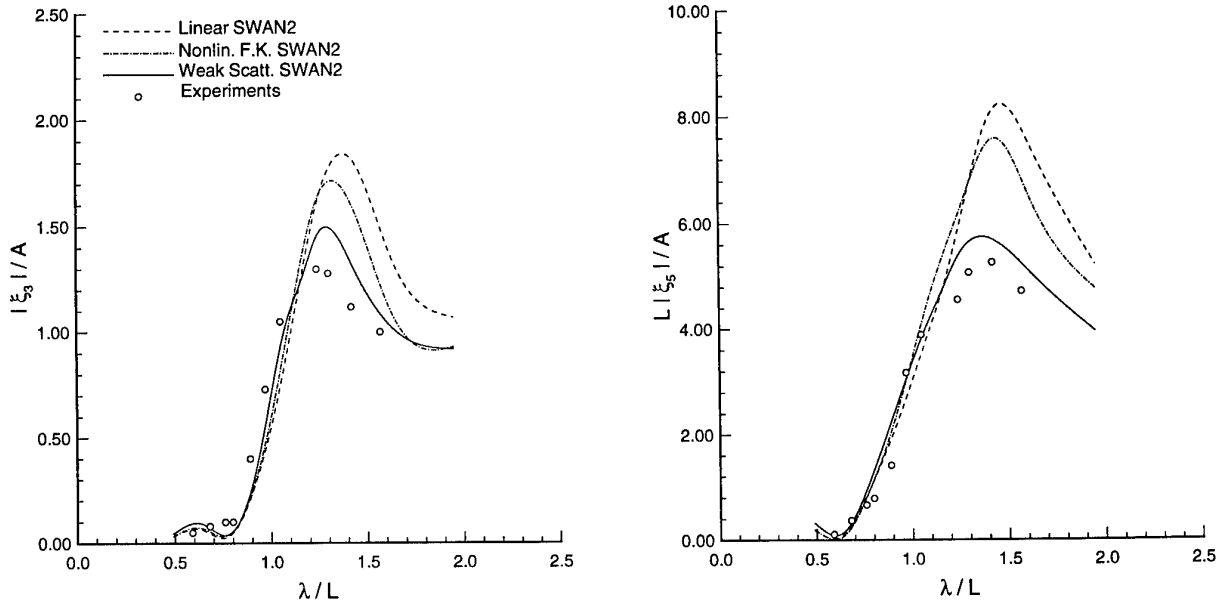

Figure 2: Amplitude of the heave and pitch response amplitude operator (RAO) for the S7-175 Containership at $\mathcal{F} = 0.275$ in head seas, with the incoming wave amplitude at $A/L = 0.015$.

Numerical Study on the Influence of the Steady Flow Field in Seakeeping

Hidetsugu IWASHITA
Engineering Systems, Hiroshima University
Kagamiyama 1-4-1, Higashi-Hiroshima 739, JAPAN
Volker BERTRAM
Institut für Schiffbau, Universiät of Hamburg
Lämersieth 90, 22305 Hamburg, GERMANY

1 Introduction

3-D methods for estimating seakeeping of ships have become popular with the wide availability of high-speed computers and sophisticated numerical techniques. Some finite element analyses of the ship structure require improved estimations of the unsteady wave forces on the hull. Especially fatigue analysis involving repeatedly imposed unsteady forces is quite interesting for ship yards. In this respect, computations should take into account forward-speed effects and three-dimensional effects. Two-dimensional computations, e.g. strip methods, are insufficient for this purpose. [1], [2].

Forward-speed effects include more than just the change of the frequency of encounter, [3]. The degree of approximation for the steady flow is important in the unsteady calculations. Iwashita et al. applied their 3-D Green function method to a blunt tanker, [1], and a catamaran, [2], demonstrating this not only for the unsteady hydrodynamic forces, but also for the unsteady pressures on the hull. These calculations included the steady disturbance effect through the body boundary condition approximating the steady flow by double-body flow. This approximation is adequate if the steady waves generated by the ship are small. The validity of this approximation should be confirmed by investigating how the steady wave field affects the unsteady wave field. The discrepancy between experimental and computational pressure distributions near the bow of the tanker in [1] suggests a significant effect of the steady wave field in some cases and motivated the present numerical study.

We study numerically the influence of the steady flow to the unsteady wave field, using a 3-D Green function method (GFM) and a Rankine panel method (RPM) taking the steady disturbance effect into account. Three approximations of the steady flow are employed for the input of the unsteady problem: uniform flow ignoring the steady disturbance, double-body flow, and linear (Kelvin) wave field. m-vector, steady velocity field and its derivatives evaluated from those steady flows are commonly used both in the GFM and the RPM. The GFM includes the steady flow only through the body boundary condition and the free-surface boundary condition by necessity includes only the uniform flow. The RPM can include the steady flow both in the body boundary condition and the free-surface boundary condition. We can therefore observe the influence of the body boundary condition and the free-surface boundary condition separately or together. Results are shown here for a Series-60($C_b = 0.6$) for the hydrodynamic forces and the unsteady pressures on the hull.

2 Boundary Conditions

We consider a ship advancing at constant forward speed U in oblique regular waves encountered at angle χ, Fig.1. The ship motion $\xi_j e^{i\omega_e t}(j = 1 \sim 6)$ around its equilibrium position and the wave amplitude A of the incident wave are assumed to be small. ω_0 is the circular frequency and K the wave number of the incident wave. The encounter circular frequency is $\omega_e (= \omega_0 - KU\cos\chi)$. The linear theory is employed for this problem assuming ideal (potential) flow.

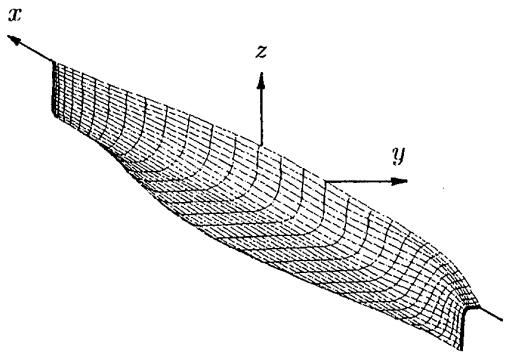

Fig.1 Coordinate system

The velocity potential Φ governed by Laplace's equation can be expressed as

$$\Phi(x,y,z;t) = U[-x+\phi_s(x,y,z)] + \Re[\phi(x,y,z)e^{i\omega_e t}] \tag{1}$$

where

$$\phi = \frac{gA}{\omega_0}(\phi_0+\phi_7) + i\omega_e\sum_{j=1}^{6}\xi_j\phi_j\,, \quad \phi_0 = ie^{Kz-iK(x\cos\chi+y\sin\chi)} \tag{2}$$

ϕ_s is the steady potential, ϕ the unsteady velocity potential including the incident wave potential ϕ_0, scattering potential ϕ_7 and radiation potential $\phi_j(j=1\sim 6)$.

The linearization of the free-surface boundary condition and the body boundary condition yields two set of the boundary condition for ϕ_s and $\phi_j(j=1\sim 7)$.

$$\frac{\partial^2\phi_s}{\partial x^2} - \mu\frac{\partial\phi_s}{\partial x} + K_0\frac{\partial\phi_s}{\partial z} = 0 \quad \text{on } z=0\,, \qquad \frac{\partial\phi_s}{\partial n} = n_1 \quad \text{on } S_H \tag{3}$$

$$\left.\begin{aligned} &\Big[\Big(i\omega_e - U\frac{\partial}{\partial x}\Big)^2 + \mu\Big(i\omega_e - U\frac{\partial}{\partial x}\Big) + g\frac{\partial}{\partial z}\Big]\phi_j = 0 && \text{on } z=0 \\ &\frac{\partial\phi_j}{\partial n} = n_j + \frac{U}{i\omega_e}m_j \quad (j=1\sim 6)\,, && \frac{\partial\phi_7}{\partial n} - \frac{\partial\phi_0}{\partial n} \quad \text{on } S_H \end{aligned}\right\} \tag{4}$$

where

$$\begin{aligned} &(n_1,n_2,n_3) = \boldsymbol{n}\,, && (m_1,m_2,m_3) = -(\boldsymbol{n}\cdot\nabla)\boldsymbol{V}\,, \\ &(n_4,n_5,n_6) = \boldsymbol{r}\times\boldsymbol{n}\,, && (m_4,m_5,m_6) = -(\boldsymbol{n}\cdot\nabla)(\boldsymbol{r}\times\boldsymbol{V})\,, \\ &\boldsymbol{r} = (x,y,z)\,, && \boldsymbol{V} = \nabla(-x+\phi_s)\,, \quad K_0 = g/U^2 \end{aligned}$$

μ in the free-surface boundary conditions is the Rayleigh's artificial viscosity introduced to satisfy the radiation condition at infinity, and $\boldsymbol{n}$ is a normal vector inward to fluid. ϕ_s and ϕ_j also subject to the condition at infinite depth.

3 Solution Methods

The GFM using the spline element described in [1] and [2] is applied to solve the unsteady problem subject to (4). The direct method solves the integral equation to avoid the irregular-like solutions and the steepest descent integration method proposed by Iwashita & Ohkusu [4] evaluates the wave term of the Green function.

The unsteady pressure distribution on the hull is estimated by an expression derived by Timman and Newman [5]:

$$p(x,y,z) = -\rho(i\omega_e + U\boldsymbol{V}\cdot\nabla)\phi - \rho\frac{U^2}{2}\sum_{j=1}^{6}\xi_j(\beta_j\cdot\nabla)(\boldsymbol{V}\cdot\boldsymbol{V})\,, \quad \beta_j = \begin{cases} \boldsymbol{e}_j & (j=1,2,3) \\ \boldsymbol{e}_{j-3}\times\boldsymbol{r} & (j=4,5,6) \end{cases} \tag{5}$$

ρ is the density of the fluid, $\boldsymbol{e}_j(j=1,2,3)$ are the unit vectors of x,y,z axes.

The right hand second term of eq.(5) indicates the dynamical restoring force due to the unsteady motion in the steady flow. The second derivatives of the steady flow in this term are determined by solving the steady problem (3). We solve the steady problem by using the RPM explained in the subsequent paragraph. For the double-body flow, the same method can be applied omitting the second derivative of ϕ_s in the free-surface boundary condition in (3).

The hydrodynamic forces are calculated by integrating the unsteady pressure (5) over the hull up to the calm-water level.

The RPM described in [6] is used. The unsteady velocity potential is represented by source distributions on the hull and the free surface. The radiation condition is numerically satisfied by the staggered grid technique which is approximately equivalent to the condition $\phi_x = \phi_{xx} = 0$ at upstream. This method therefore is applicable only for $\tau > 1/4$.

Several kinds of free-surface boundary condition are possible by the RPM. Among them we employed the following unsteady free-surface boundary condition derived under the assamption of the small unsteady disturbance of the free surface, [6]:

$$-\omega_e^2\phi + 2i\omega_e B\phi + 2\overline{\nabla}\phi_s\overline{\nabla}\phi + (B\overline{\nabla}\phi_s + \boldsymbol{a}^{(0)} + \boldsymbol{a}^g)\overline{\nabla}\phi + \overline{\nabla}\phi_s(\overline{\nabla}\phi_s\cdot\overline{\nabla})\overline{\nabla}\phi = 0 \quad \text{on } z=\zeta_s \tag{6}$$

where

$$\boldsymbol{a}^{(0)} = (\overline{\nabla}\phi_s\overline{\nabla})\overline{\nabla}\phi_s\,, \quad \boldsymbol{a}^g = \boldsymbol{a}^{(0)} - (0,0,g)^T\,, \quad B = -\frac{1}{a_3^g}\frac{\partial}{\partial z}(\overline{\nabla}\phi_s \cdot \boldsymbol{a}^g)$$

This free-surface boundary condition is satisfied on the steady wave surface $z = \zeta_s$. It includes the influence of the steady flow completely.

4 Results

Fig.1 shows the grid system of Series-60($C_b = 0.6$) container ship employed in this calculation. 990 elements are used on the body surface and 1500 elements on the free surface in the RPM.

Fig.2 shows the distributions of the m_3-vector on the hull calculated assuming the double-body flow and the linear (Kelvin) solution for the steady flow. We can see an influence of the Kelvin wave near the free surface. Two different computations, based on a desingularized constant strength panel and a higher-order panel, were previously tested for a half-immersed prolate spheroid in double body flow and we found good agreement with the analytical solution for both approaches. A significant difference between them, however, was observed at the bow and stern parts when we applied them for the Series-60. Then the higher-order panel was adopted in Fig.2 and following calculations, as the computed results appeared more plausible.

Fig.3 shows the wave pressure distribution on some hull sections at $F_n = 0.2$, $\lambda/L = 0.3$, $\chi = 180°$. The influence of the steady flow seems remarkable especially in the bow part. It is confirmed that the approximation of the exact steady flow tends to underestimate the wave pressure.

Fig.4 shows heave exciting force and pitch exciting moment obtained by integrating this pressure over the hull surface. The influence of the steady flow is less significant here due to the integration effect.

Calculations for a tanker with blunt bow are in progress and should be finished in time for the workshop.

References

[1] Iwashita, H., Ito, A., Okada, T., Ohkusu, M., Takaki, M., Mizoguchi, S.: Wave Forces Acting on a Blunt Ship with Forward Speed in Oblique Sea (3rd Report), J. Soc. Naval Arch. Japan 176 (1994) (in Japanese)

[2] Iwashita, H., Kataoka, S.: 3-D Analysis of the Hydrodynamic Interaction between Steady and Unsteady Flows for a Catamaran, 3rd Korea-Japan Joint Workshop on Ship & Marine Hydrodynamics, Seoul (1996)

[3] McCreight, W.: Ship Motions with Nonlinear High Speed Effects, 6th WWWFB, Woods Hole (1991)

[4] Iwashita, H., Ohkusu, M.: Hydrodynamic Forces on a Ship Moving with Forward Speed in Waves, J. Soc. Naval Arch. Japan 166 (1989) (in Japanese)

[5] Timman, R., Newman, J.N.: The Coupled Damping Coefficients of a Symmetric ship, JSR 5/4 (1962)

[6] Bertram, V.: A 3-D Rankine Panel Method to Compute Added Resistance of Ships, IfS-report 566, Univ. of Hamburg (1996)

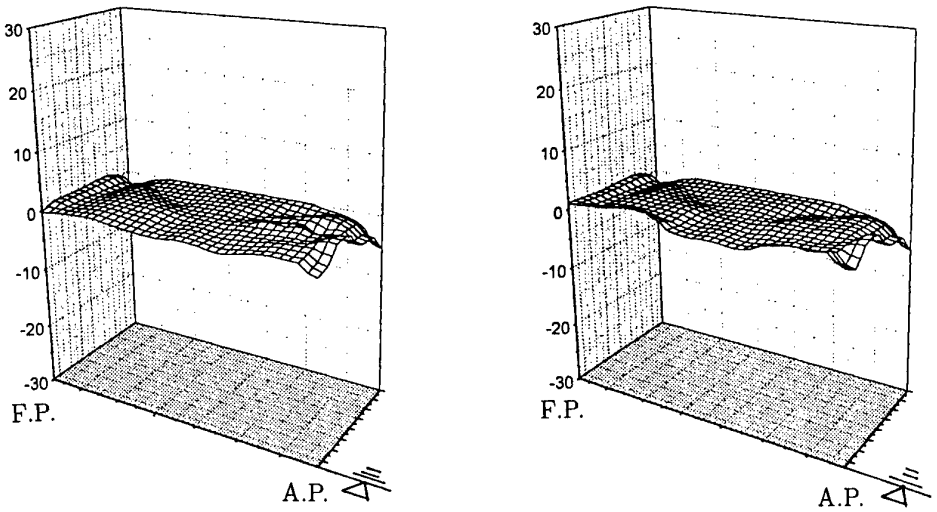

Fig.2 Comparison of m_3 distribution on the ship hull surface
[left: Double body flow, right: Linear Kelvin wave($F_n = 0.2$)]

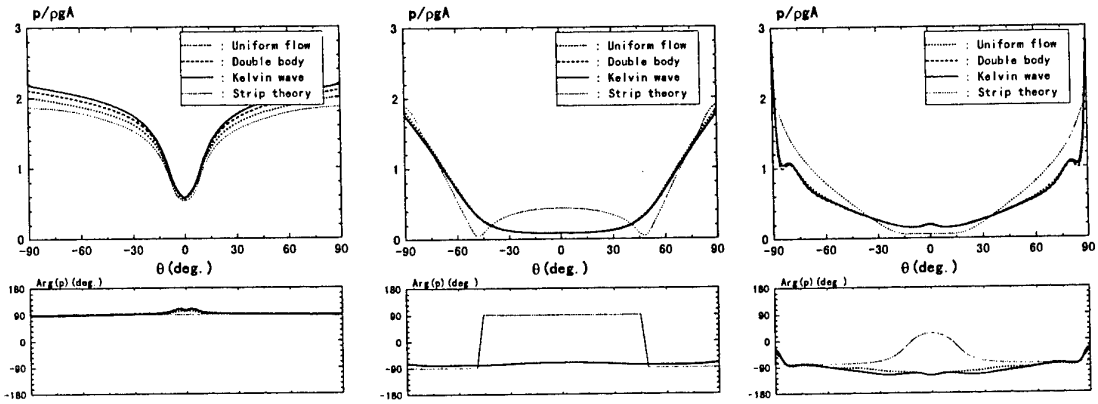

Fig.3 Wave pressure distribution at $F_n = 0.2$, $\lambda/L = 0.3$, $\chi = 180$(deg.)
[left: Ord.9.5, middle: Ord.5, right: Ord.3]

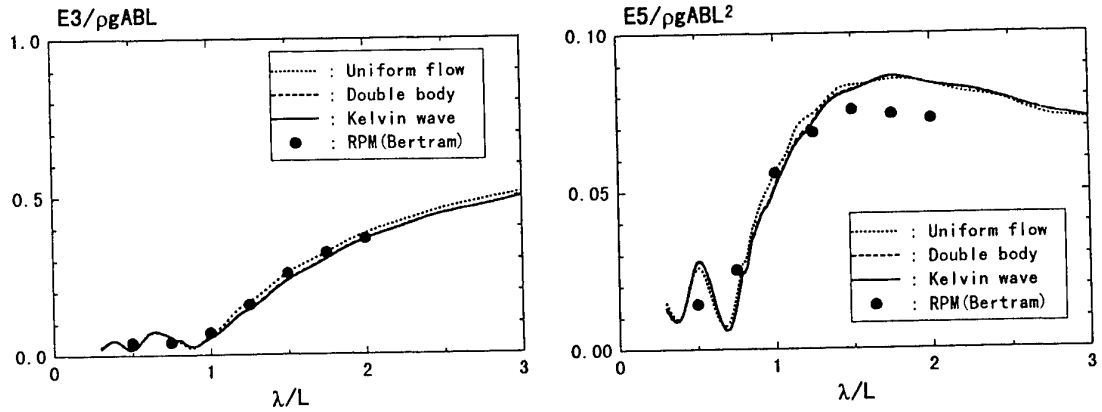

Fig.4 Wave exciting force for heave and pitch at $F_n = 0.2$, $\chi = 180$(deg.)

DISCUSSION

Yeung R.W.: I think this is a nice investigation to understand the role played by the steady flow potential. From the results your showed, it is not surprising that the diffraction potential does not have a strong dependence on $\varphi^{(s)}$. Afterall, the only role that $\varphi^{(s)}$ plays is in the convective derivative of the pressure equation. The much stronger dependence of radiation potentials on $\varphi^{(s)}$ is however to be expected because of the m_j terms.

Iwashita H., Bertram V.: The influence of the steady flow field is concluded to be important only on the estimation of the wave pressure near the bow part for the diffraction problem, and to be always strong for the radiation problem not only on the force estimation but pressure estimation, due to the m_j-term on the body boundary-condition.

Ohkusu M.: You did not discuss your results in terms of the experimental data of the pressure distribution at the bow of a ship presented in your second slide. Your results on Kelvin wave field seem not to agree with the measured pressure distribution close to the free surface in particular.

Iwashita H., Bertram V.: The measurement of the wave pressure along the water line includes some error relating ot the experimental analysis. Near the bow part the pressure gage is sometimes exposed outside the free surface due to large steady waves and Fourier analysis breaks down. The numerical results therefore should be compared with experiments excluding such points near the free surface. Then we can see an improvement of the numerical results by taking the Kelvin wave field into account.

Rainey R.C.T.: I believe this work is of great practical importance, and deserves every encouragement. The authors' conclusion that steady-flow effects are seen mainly at the bow is consistent with the long history of ship structural failures in this region. A ship Classification Society not a million miles from the Institut für Schiffbau, for example, will be familiar with the case of the 100,000 tonne tanker *"Kirki"*, whose whole bow section fell off in the Indian Ocean, in 1991. See my discussion of Faulkner and Williams' paper *The Design for Abnormal Waves*, in the Transactions of the Royal Institution of Naval Architects, Vol 139, 1997.

A Comparison of Two Rankine-source Panel Methods for the Prediction of Free-surface Waves

Carl-Erik Janson

Chalmers University of Technology, Dept. of NAOE, S-412 96 Gothenburg, Sweden
FLOWTECH International AB, S-400 22 Gothenburg, Sweden

Introduction

Dispersion (wavelength error) and damping (amplitude error) have been investigated analytically for two Rankine-source panel methods in two dimensions. The flow is assumed steady incompressible and the Kelvin free-surface boundary condition is applied. The first method uses an upwind four-point operator (Dawson operator) on the free-surface for the velocity derivative in the streamwise direction and to enforce the radiation condition (Kim, K. J. 1989) and (Janson, C. E. 1996A), while the second method uses an analytical expression for the velocity derivative together with a collocation point shift one panel length upstream to satisfy the radiation condition (Jensen, P. S. 1987), (Jensen, G., et. al 1988), (Kim, B. K. 1990) and (Janson, C. E. 1996A). Both first order panels (flat panels, constant source strength) and higher order panels (parabolic panels, linearly varying source strength) have been investigated for the first method while the analysis is restricted to first order panels for the analytical method. The source panels are allowed to be positioned either on the free-surface (standard method) or at a distance above the free-surface (raised panel method). The collocation points on the free-surface may be located at the same longitudinal position as the panel centres (standard method) or they may be shifted upstream relative to the panel centres.

The two methods have also been compared numerically for a three-dimensional flow using the Series 60 CB=0.60 hull to verify the conclusions from the two-dimensional analysis. A grid dependence study for the free-surface was performed for non-linear computations and the grid convergence is compared for the wave profile at a longitudinal cut. The residual of the free-surface boundary condition is also compared for the two methods.

Analysis of Dispersion and Damping

Numerical dispersion and numerical damping occur when the continuous potential flow problem is discretized in a numerical method. Both the discretization of the free-surface source distribution and the introduction of numerical operators to compute the velocity derivative in the free-surface boundary condition introduce errors to the method. A systematic methodology for this type of analysis is described in detail in (Sclavounos, P. D. and Nakos, D. E. 1988) and in (Raven, H. C. 1996) and it is used for the present analysis. The method investigates the properties of the numerical method after transformation to the Fourier space.

A two-dimensional continuous source distribution is assumed at a distance z_{fs} above the undisturbed free-surface level and the Fourier transforms of the induced velocity and velocity derivative at a point on the undisturbed free-surface due to the source distribution are introduced into the Kelvin free-surface boundary condition. The Kelvin free-surface boundary condition can then be formulated to include an operator that relates the induced vertical velocity on the free-surface to the right hand side of the equation which is assumed to be known.

The source distribution is for the first order numerical method discretized into flat panels of uniform size Δx having a constant source strength and the velocity derivative in the streamwise direction is computed using an upwind four-point numerical operator. The source panels are located a distance $z_{fs} = \alpha\Delta x$ above the undisturbed free-surface level and all collocation point are allowed to be shifted a distance $\gamma\Delta x$ upstream of the panel centres. The Fourier transform of the induced velocities at a collocation point on the free-surface and the Fourier transform of the four-point operator are introduced into the Kelvin free-surface boundary condition and as in the continuous case an operator for the vertical velocity can be formulated.

For the first order analytical method the Fourier transform of the analytical expression for the velocity derivative in the streamwise direction replaces the Fourier transform of the four-point numerical operator in the Kelvin condition and an operator for the vertical velocity can again be formulated.

The operator for the higher order numerical method is similar to the first order numerical method but it includes contributions from the curvature of the panel and from the linear source variation.

The dispersion and damping for the discretized method can now be investigated from plots of the real and imaginary parts of a function $Lh(s)$ which is included in the non-dimensionalized form of the operator for the vertical velocity. The difference between the operators for the discretized methods and the operator for the continuous source distribution is shown as the difference between the non-dimensional wave number s and the function $Lh(s)$. The principle for the analysis is shown in figure 1A where on the abscissa $s = 0$ means an infinite number of panels per wavelength and $s = 0.5$ means two panels per wavelength. The intersection between a horizontal line $1/(2\pi \cdot Fn_{\Delta}{}^2)$ where Fn_{Δ} is the panel Froude number and the real part of the function $Lh(s)$ gives the principal far-field wave number found by the discretized method and the difference between this wave number and s gives the dispersion for the method. The intersection between the imaginary part of $Lh(s)$ and a vertical line at the principal far-field wave number indicates the damping of the discretized method. A spurious wave numbers may in some cases be found by the discretized method if a second intersection between the real part of $Lh(s)$ and the horizontal line exists.

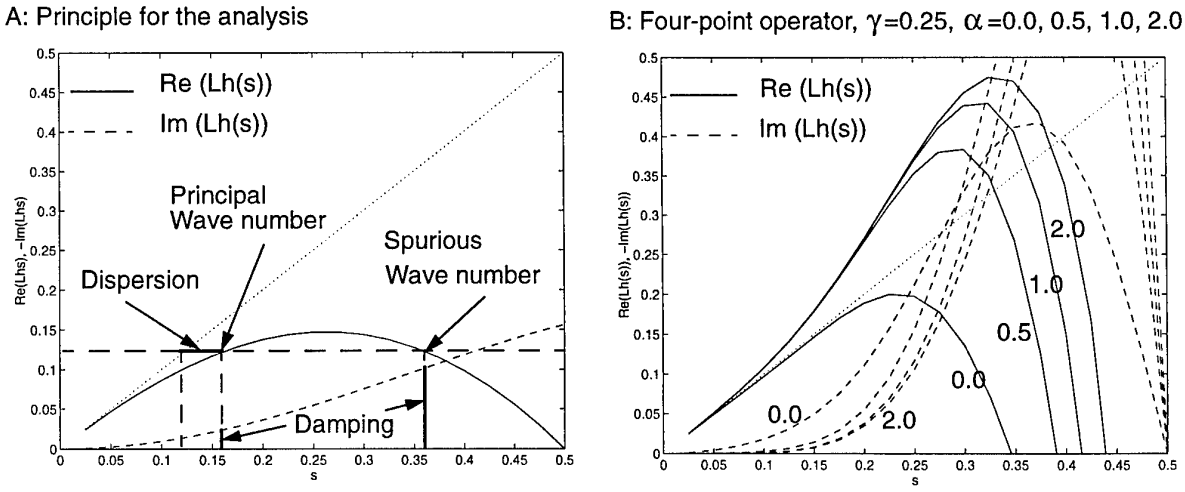

Figure 1 Interpretation of the real and imaginary parts of $Lh(s)$

Different positions of the source panels and the collocations points were investigated and as one example figure 1B shows the influence of the distance between the source panels and the free-surface, α, for a collocation point shift, γ, of one quarter of a panel length and the four-point operator. It can be seen that the damping is reduced as the distance, α, is increased and that the dispersion is small for the principal wave number. The analytical method, figure 2A, shows very small dispersion in a large wave number range as the distance, α, is increased. No damping is present for the analytical method. The analysis shows that there is only a very small difference between first and higher order panels if the source panels are raised a distance above the free-surface. Details of the present analysis are described in (Janson, C. E. 1996B).

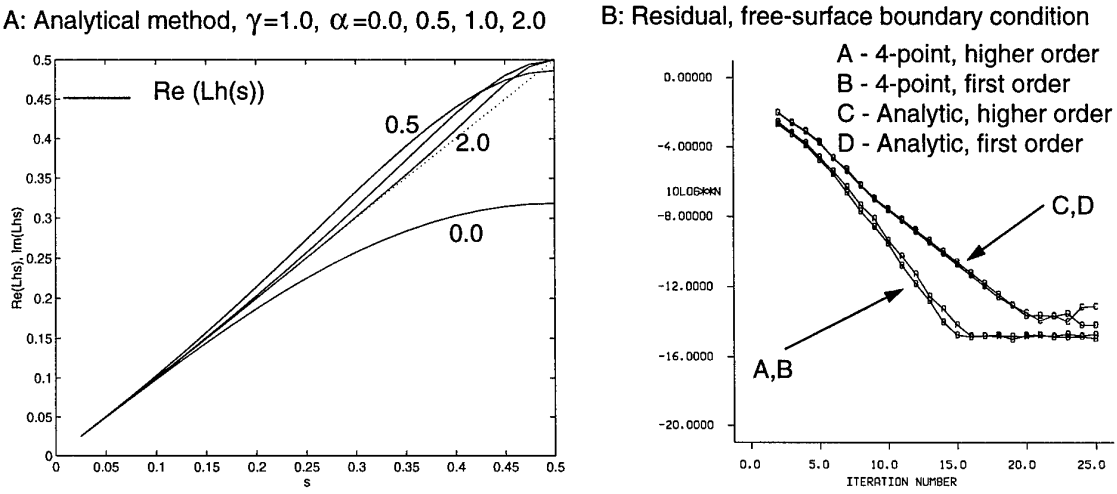

Figure 2

Numerical comparison for the Series 60 hull, Fn = 0.316

Non-linear computations were carried out for the Series 60 hull using both the four-point operator and the analytical method. The solution method for the non-linear problem is to linearize the free-surface boundary condition around a known base solution and solve the problem in an iterative manner. In each iteration the problem is linearized with respect to the solution from the previous iteration. The first iteration is started from a zero Froude number flow where a Neuman condition is applied on the free-surface. In the first linear solution the linearized free-surface boundary conditions are applied on the undisturbed free-surface and are in the following iterations moved to the wavy free-surface computed in the previous iteration. The source panels were raised about one panel length above the wavy free-surface.

The iteration history of the max residual for the combined free-surface boundary condition is in figure 2B shown for the four-point operator and the analytical method both for first and higher order panels using 25 panels per fundamental wave length. It can be seen that the residuals are reduced to very small values for both methods but the analytical method shows a slightly slower convergence. Note the logarithmic scale for the residual. There is only a very small difference between first and higher order panels.

A grid dependence study was carried out for the number of panels on the free-surface using higher order panels. In figure 3 the wave profile is plotted at 0.0755*Lpp aside of the centre line for 5, 10, 15, 20, 25 and 30 panels per fundamental wave length and as can be seen the wave profile converges towards the measured profile as the number of panels is increased. A slightly faster convergence is noted for the analytical method but the solution is still not grid independent for 30 panels per wave length.

It is interesting to note that the same conclusions can be made from the Fourier analysis in two dimensions and the numerical computation in three dimensions. In both cases the analytical method shows smaller dispersion than the four-point operator and the amplitude converges faster due to smaller damping. But, for the large number of panels used in applied computations there is only a small difference between the analytical method and the four-point operator. Only a minor difference was obtained between first and higher order panels in the Fourier analysis and this very small difference occurred for the wave profile also in the numerical computations.

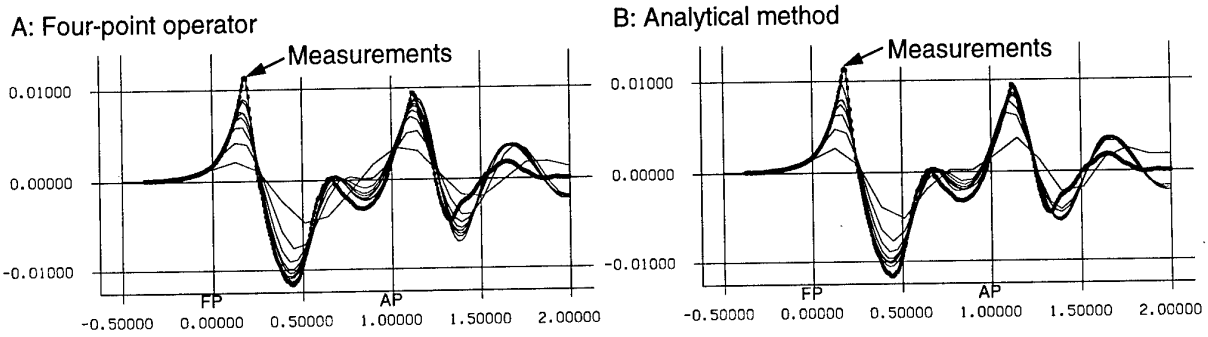

Figure 3 Wave profile 0.0755*Lpp aside of the centre line

References

Janson, C. E. 1996A A Comparison of Non-linear Rankine-source Methods for the Prediction of Free-surface Waves. Department of Naval Architecture and Ocean Engineering, Report 96:44, Chalmers University of Technology, Gothenburg.

Janson, C. E. 1996B Damping and Dispersion of Rankine-source Free-surface Panel Methods. Department of Naval Architecture and Ocean Engineering, Report 96:46, Chalmers University of Technology, Gothenburg.

Jensen, G., Bertram, V., Söding, H. 1988 Ship Wave-Resistance Computations. Proceedings of the 5th International Conference on Numerical Ship Hydrodynamics, Hirochima, Japan.

Jensen, P. S. 1987 On the Numerical Radiation Condition in Steady-State Ship Wave Problem. Journal of Ship Research, Vol. 31, No 1, pp 14-22.

Kim, B. K. 1990 Derivation of Second derivatives of the Velocity Potential for First and Higher Order Rankine Source Panels. Flowtech Internal Report No 1.

Kim, K. J. 1989 Ship Flow Calculations and Resistance Minimisation. PhD Thesis, Chalmers University of Technology, Gothenburg.

Raven, H. C. 1996 A Solution Method for the Nonlinear Ship Wave Resistance Problem. PhD Thesis, MARIN, Netherlands.

Sclavounos, P. D. and Nakos, D. E. 1988 Stability Analysis of Panel Methods for Free-surface Flows with Forward Speed. Proceeding of the 17th Symposium on Naval Hydrodynamics, The Hague, Netherlands, pp. 173 - 193.

Capillary ripples on standing water waves

Lei Jiang, William W. Schultz, and Marc Perlin

Department of Mechanical Engineering and Applied Mechanics
Department of Naval Architecture and Marine Engineering
University of Michigan, Ann Arbor, Michigan 48109 USA

The dynamics of capillary-gravity standing waves strongly impact remote sensing. Satellite images obtained by SAR (Synthetic Aperture Radar) exhibit brighter radar returns near ocean features such as currents, shelves, and slicks. The backscatter of microwaves by these surface features is sensitive to the curvature and periodicity of the sea surface on centimeter scales. Dynamics of wave reflection in these regions and hence the dynamics of standing waves are critical in interpreting SAR images. Jiang *et al.* (1996) generated Faraday waves in laboratory experiments and compared to fully-nonlinear numerical simulations. New dynamics of harmonic interaction and interesting steep waves were discovered. In particular, triply-periodic breaking are discussed in Jiang *et al.* (1997). Herein, we present results on even shorter wavelengths, 2 cm to 15 cm, and on the formation of superharmonic waves (ripples) in the ensuing wave forms.

Numerical methods and experimental techniques

The flow is assumed to be irrotational, spatially periodic, and infinitely deep. Capillary number $\kappa = \sigma k^2/\rho g$ represents the effect of surface tension, where σ is the surface tension, k is the wavenumber, ρ is the water density, and g is the gravitational acceleration. The fully-nonlinear free surface problem is solved by a spectral Cauchy-integral method, based on the kernel desingularization of Roberts (1983). As shown in Schultz *et al.* (1994), this method gives exponentially accurate solutions. When vertical forcing is provided, a term proportional to ϕ_{xx} is added to the dynamic free surface condition to simulate the free-surface boundary-layer damping and to provide an energy sink to balance the wave forcing.

The standing wave excited by vertical oscillation (Faraday resonance) is subharmonic (Benjamin & Ursell 1954). Herein Faraday resonance is used as a "clean" experimental method to generate two-dimensional steep standing waves. We use a rectangular glass tank 105 mm long and 300 mm deep. The testing water depth is 150 mm in the experiments. An aspect ratio of $6.2:1$ in the third dimension is chosen to eliminate cross waves and maintain a two-dimensional wave field. The wave profile is recorded with a laser-sheet technique and a high-speed intensified imager/recorder. The vertical oscillation is provided by a mechanical shaker with computer control.

Parasitic ripple generation

We first validate our numerical method by calculating parasitic ripple formation on the forward face of traveling gravity waves (Cox 1958, Longuet-Higgins 1963). A linear Stokes wave is used as the initial condition with wavelengths of 6.5 cm ($\kappa = 0.07$) and 5 cm ($\kappa = 0.119$). The wave first becomes spatially asymmetric with the crest tilting forward (wave steepness ka=0.20). Then larger curvature is found on the forward face and ripples are excited after one wave period, as shown in figure 1. The number of ripples and their large steepness agree with the experiments by Perlin *et al.* (1993) and the viscous simulation of Dommermuth (1994). These computations prove that neither viscous damping nor vorticity is required for the ripple formation, even though damping may be needed to describe the subsequent evolution of these parasitic ripples and the underlying vortex structure (Longuet-Higgins 1992, Mui & Dommermuth 1995). Demonstrating ripple formation requres only 64 free-surface nodes per wave length in our computation; much more efficient than Dommermuth's full-field computation.

Ripple formation can be interpreted as higher-order resonance between the fundamental mode and its superharmonics at critical capillary numbers $\kappa = 1/N$ (Wilton 1915) where N is an integer. Longuet-Higgins (1963) explained parasitic ripples on a traveling wave as the result of a capillarity-induced pressure

disturbance at the wave crest, analogous to ripple generation on a *steady* stream. Because the group velocity for capillary waves is faster than the phase velocity of the underlying wave, the ripples appear on the front face of the wave crest. Ripple formation cannot be confirmed by Longuet-Higgins' theory for standing waves, as the standing wave is *unsteady* and the background flow can no longer be transformed into a *steady* stream. However, the high-order resonance condition: $\kappa = 1/N$ should be equally valid for traveling waves and standing waves, therefore predicting ripple formation on standing waves.

Our numerical simulation for free standing waves uses a high-order gravity standing wave solution as the initial condition. A large-amplitude 6.5-cm wave (ka=0.57) evolves into a waveform with many ripples on the surface. Shown in figure 2, the number of ripples is about 15 ($\approx 1/\kappa$). The ripple growth can be explained in terms of interaction between short waves and a long wave as follows: Curvature variations first appear at the crest during its ascending phase. When the crest motion reverses, small ripples are carried by the orbital velocity of the underlying wave to the two troughs with their wavelength stretched and their steepness reduced. Because capillary waves propagate faster, these ripples reach the two troughs before the orbital velocity reverses. The ripples then encounter an opposing velocity field and are shortened and steepened. This *intermittent* growth occurs within one half wave cycle. Compared to traveling waves, the ripple growth is slower and the average ripple steepness is much smaller, although the initial wave steepness is three times larger. The ripples are generally shorter and steeper at the trough of a standing wave (figure 2b), in contrast to the behavior of short waves on a long traveling wave.

In reality, water waves are accompanied by a free-surface boundary layer that provides a viscous damping proportional to the square of wavenumber. The higher harmonics experience much larger damping than the fundamental harmonic. Therefore, the already weak parasitic ripples can be suppressed by viscous damping. We model both vertical forcing (acceleration) and viscous damping (ϕ_{xx} term) to simulate Faraday waves. A periodic wave solution is achieved with the same wave steepness and the same κ as shown in figure 2. However, due to the viscous damping, ripples form and decay quickly before significant ripple steepness is reached.

Using Faraday resonance, we generate 10.5-cm Faraday waves (κ=0.0265) in laboratory experiments. These waves reach a maximum steepness of ka=1.32 with a rounded crest and very steep slope without parasitic ripples (figure 3). This large wave steepness and the corresponding wave profile agree with the calculations of Schultz & Vanden-Broeck (1990) for free standing waves. More extensive experiments on wavelengths from 5 cm to 10 cm are required to further confirm our numerical findings on the parasitic ripples and the effect of viscous damping.

Wilton ripples under Faraday resonance

Internal resonance occurs at the critical capillary number $\kappa = 1/N$, leading to the existence of a family of solutions (Wilton ripples). Only limited modes participate in the resonance when N is a small integer. Generalized Wilton ripples are usually referred to as triad interactions (Perlin *et al.* 1990). For standing waves with $\kappa = 1/2$, two solutions are found for moderate wave amplitude by Vanden-Broeck (1984). Both the first and the second harmonics are retained at first order in his analysis. However, such solutions are limited by the weakly-nonlinear assumption, leaving the behavior of capillary-gravity standing waves at large wave steepness unexplored.

We calculate standing waves generated by Faraday resonance at these critical capillary numbers. The wavelength is fixed at 2.44 cm ($\kappa = 1/2$). With small forcing amplitude, we obtain a periodic wave with low wave steepness (ka=0.06) in figure 4(a). Either one crest or two crests appear at different phases of a wave cycle, similar to the two solutions of Vanden-Broeck (1984). As we increase the forcing amplitude and therefore increase the wave steepness to ka=0.35 (figure 4b), three or four crests appear in the wave profile at different phases of a periodic wave cycle. A frequency spectrum of wave elevation demonstrates that the second, the third, and the fourth harmonics are equally significant (the fundamental harmonic is 9.8 Hz). This behavior is not described by the two-mode model of Henderson & Miles (1991) for 2:1 resonance in Faraday waves.

The appearance of higher harmonics is even more evident for $\kappa = 1/3$. With a fixed forcing amplitude and forcing frequency in our numerical calculations, shorter and shorter ripples appear in a cascade on the

free surface, and a periodic state is never reached. If the forcing frequency is slightly different from twice the linear natural frequency, we observe quasi-periodic and chaotic motions in the surface elevation. The cascade to higher wavenumbers eventually leads to a wavelength on the scale of the node spacing and our computation fails.

This proliferation of superharmonics for capillary-gravity waves appears to be not studied in detail in the literature. Perlin & Ting (1992) noted multiple crests in traveling Wilton ripples directed excited by a wavemaker. The importance of small-scale wave forms to remote sensing applications warrants a more in-depth study of these phenomena.

This research was supported by the Office of Naval Research partially under contract number N00014-93-1-0867 and partially under the University Research Initiative Ocean Surface Processes and Remote Sensing at the University of Michigan, contract number N00014-92-J-1650.

References

Benjamin, T. B. & Ursell, F. 1954 The stability of the plane free surface of a liquid in vertical periodic motion.*Proc. R. Soc. Lond.* A **225**, 505–515.

Cox, C. S. 1958 Measurements of slopes of high-frequency wind waves. *J. Mar. Res.* **213**, 95–109.

Dommermuth, D. G. 1994 Efficient simulation of short and long-wave interactions with applications to capillary waves. *ASME J. Fluid Eng.* **116** (1), 77–82.

Henderson, D. M. & Miles, J. W. 1991 Faraday waves in 2:1 internal resonance. *J. Fluid Mech.* **222**, 449–470.

Jiang, L.,Ting, C.-L., Perlin, M. & Schultz, W. W. 1996 Moderate and steep Faraday waves: Instabilities, modulation and temporal asymmetries. *J. Fluid Mech.* **329**, 275–307.

Jiang, L., Perlin, M. & Schultz, W. W. 1997 An experimental study of breaking standing waves: period tripling and breaking-wave dissipation. Submitted for publication.

Longuet-Higgins, M. S. 1963 The generation of capillary waves by steep gravity waves. *J. Fluid Mech.* **16**, 138–159.

Longuet-Higgins, M. S. 1992 Capillary rollers and bores. *J. Fluid Mech.* **240**, 659–679.

Mui, R. C. Y. & Dommermuth, D. G. 1995 The vortical structure of parasitic capillary waves. *ASME J. Fluid Eng.* **117** (3), 355–61.

Perlin, M., Henderson, D. & Hammack, J. 1990 Experiments on ripple instabilities. 2. Selective amplification of resonant triads. *J. Fluid Mech.* **219**, 51–80.

Perlin, M., Lin, H. & Ting, C. 1993 On parasitic capillary waves generated by steep gravity waves: an experimental investigation with spatial and temporal measurements. *J. Fluid Mech.* **255**, 597–620.

Perlin, M. & Ting, C.-L. 1992 Steep gravity-capillary waves within the internal resonance regime. *Phys. of Fluids A* **4** (11), 2466–2478.

Roberts, A.J. 1983 A stable and accurate numerical method to calculate the motion of a sharp interface between fluids *IMA J. Appl. Math.* **31**.

Schultz, W. W., Huh, J. & Griffin, O. M. 1994 Potential energy in steep and breaking waves. *J. Fluid Mech.* **278**, 201–228.

Schultz, W. W. & Vanden-Broeck J. M. 1990 Computations of nonlinear standing waves. *Bull. Amer. Phys. Soc.* **35**, 2290.

Schultz, W. W., Vanden-Broeck J. M., Jiang, L. & Perlin, M. 1996 Nonlinear standing waves: singularity formation and small surface tension effect. Submitted for publication.

Vanden-Broeck, J. M. 1984 Nonlinear gravity-capillary standing waves in water of arbitrary uniform depth. *J. Fluid Mech.* **139**, 97–104.

Wilton, J. R. 1915 On ripples. *Phil. Mag.* **29** (6), 688–700.

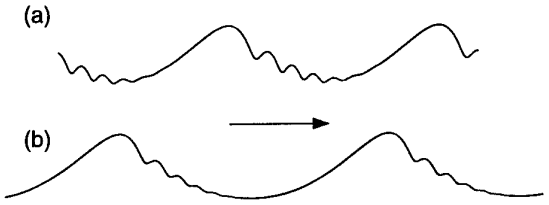

Figure 1: Calculated parasitic ripples on traveling wave (ka=0.20) with wavelengths (a) 5 cm, (b) 6.5 cm.

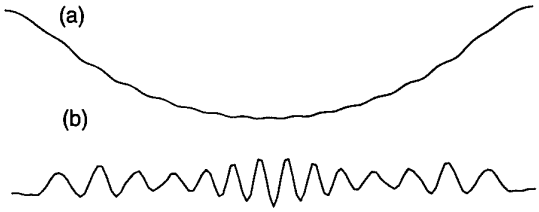

Figure 2: Calculated 6.5-cm standing wave (ka=0.57) with parasitic ripples, (a) elevation, (b) curvature.

Figure 3: Laser-sheet image of steep (ka=1.23) Faraday wave of 10.5-cm wavelength.

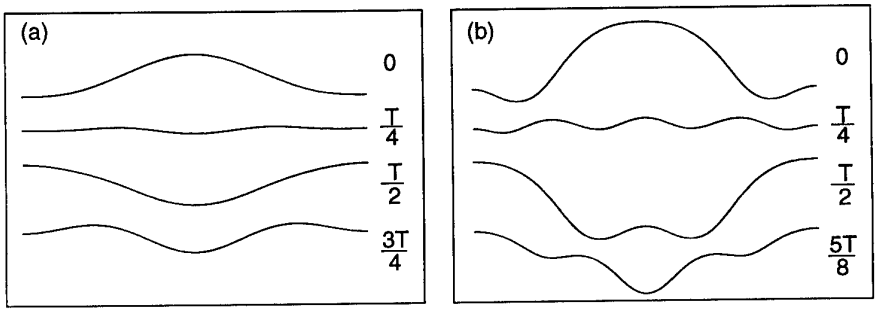

Figure 4: Calculated Faraday wave at different phases of the wave period T for $\kappa = 1/2$ (wavelength: 2.44 cm). (a) ka=0.06, forcing amplitude: 0.045 mm; (b) ka=0.35, forcing amplitude: 0.12 mm.

DISCUSSION

Grilli S.: You mentioned that to model laboratory experiments, you used a φ_{xx} damping term. Would this be also applicable to the real ocean?

Jiang L., Schultz W., Perlin M.: We use the φ_{xx} damping term to model open ocean where free-surface boundary layer is the dominant source of dissipation. Damping measured in laboratory experiments is dominated by the sidewall boundary layer and contact-line damping. A good model that consider all these effects has not yet been found.

Wu T.Y.: Taylor seems to have objected to the 90-degree conjecture.

Jiang L., Schultz W., Perlin M.: Yes, Taylor (1953) questioned the derivations for the 90-degree conjecture, even though he did not say the conjecture was wrong. However, his experiments did not disapprove the conjecture. We have found a crest angle smaller than 90 degrees in calculation. In the experiments where period-tripled breaking occurs, the sharp-crest mode has a crest angle much less than 90 degrees.

WAVE IMPACT ON ELASTIC PLATES

T.I.Khabakhpasheva, A.A.Korobkin

Lavrentyev Institute of Hydrodynamics,
Novosibirsk, 630090, RUSSIA

The plane unsteady problem of wave impact onto an elastic beam of finite length is considered. Initially a wave crest touches the beam at its central point (central impact) or at its edge (edge impact). Then the liquid hits the beam from below at a constant velocity. The impact process can be divided into two stages: in the first stage (impact stage) the beam is wetted only partially, in the second stage (penetration stage) the beam is totally wetted and continues to interact with the liquid. The impact stage is considered here only. At this stage the hydrodynamic loads are very high and are dependent on both the velocity of contact region expansion and the beam deflection. The problem is coupled. The dimension of the contact region is unknown in advance and has to be determined together with the liquid flow and the beam deflection. Here the beam deflection is of main interest that is why the numerical method to treat the problem is designed in such a way that the elastic characteristics can be effectively evaluated, but not the hydrodynamic ones.

We shall determine the beam deflection, the bending stresses in the beam and the duration of the impact stage under the following assumptions: (1) the beam deflection is governed by the Euler beam equation; (2) the beam is connected with the main structure bu rotatory springs at the beam ends; (3) the liquid is ideal and incompressible; (4) the air influence on the impact, and both external mass forces and surface tension, are negligibly small; (5) the wave profile near impact point can be approximated by parabolic contour with the initial radius of curvature at the top R; (6) the beam length $2L$ is much less then R; (7) dimension of the contact region grows with time. Assumption (6) implies that the deformations of both the wave profile and the beam are of $O(\varepsilon)$ as $\varepsilon = L/R \to 0$ at the impact stage. Moreover, in the leading order the boundary conditions and the equations of the liquid motion can be linearized with the relative accuracy $O(\varepsilon)$.

1 Formulation of the problem

The central impact is considered in this section only, the edge impact is treated in a similar way. In order to formalize the derivation of the model describing the first stage of the impact, the following scales are introduced: L as the length scale, $L^2/(RV)$ as the time scale, L^2/R as the displacement scale, V as the velocity scale, $\rho V^2(R/L)$ as the pressure scale, where ρ is the liquid density. The original equation of liquid flow, the boundary and initial conditions and the Euler beam equation, which are written in the non-dimensional variables, contain three parameters $\varepsilon, \alpha, \beta$ where $\alpha = M_B/(\rho L)$, $\beta = (EJ)/(\rho L R^2 V^2)$. Here M_B is the beam mass per unit length, E is the elasticity modulus, J is the inertia momentum of the beam cross-section. The parameter ε can be referred to as the parameter of linearization.

Taking formally $\varepsilon = 0$ in the original equations and the boundary conditions, we obtain the following boundary-value problem with respect to velocity potential $\varphi(x, y, t)$ and the beam deflection $w(x, t)$:

$$\varphi_{xx} + \varphi_{yy} = 0 \qquad (y < 0), \tag{1}$$

$$\varphi_y = -1 + w_t(x, t) \qquad (y = 0, |x| < c(t)), \tag{2}$$

$$\varphi = 0 \qquad (y = 0, |x| > c(t)), \tag{3}$$

$$\varphi \to 0 \qquad (x^2 + y^2 \to \infty), \tag{4}$$

$$p(x, y, t) = -\varphi_t(x, y, t), \tag{5}$$

$$\alpha \frac{\partial^2 w}{\partial t^2} + \beta \frac{\partial^4 w}{\partial x^4} = p(x, 0, t) \qquad (|x| < 1, t > 0), \tag{6}$$

$$w = 0, \qquad w_{xx} \pm k w_x = 0 \qquad (x = \pm 1), \tag{7}$$

$$w = w_t = 0 \qquad (|x| < 1, t = 0), \tag{8}$$

The bending stress distribution $\sigma(x,t)$ is given in the dimensionless variables as $\sigma(x,t) = w_{xx}(x,t)$, with its scale $Eh/(2R)$, where h is the maximal thickness of the beam. The positions of the contact points are described in the symmetrical case by the only function $c(t)$. Despite the fact that both the equations of motion and the boundary conditions are linearized, the problem remains nonlinear as $c(t)$ is unknown. The 'spring' conditions (7) were introduced by Kvålsvold and Faltinsen (1993), k is the nondimensional spring stiffness.

The formulation of the problem (1) - (8) is not complete. It must be added by an equation for the dimension of the contact region. Usually the equation derived by Wagner (1932) is used, but this equation is difficult to incorporate into a numerical scheme. We use here the equation suggested by Korobkin (1996). The equation is, in fact, a modification of the classical Wagner condition. It is

$$\int_0^{\pi/2} y_b[c(t)\sin\theta, t]d\theta = 0, \tag{9}$$

where the function $y_b(x,t)$ describes the shape of the beam with respect to the initial position of the free surface. In the present case, $y_b(x,t) = x^2/2 - t + w(x,t)$, equation (9) gives

$$t = \frac{1}{4}c^2 + \frac{2}{\pi}\int_0^{\pi/2} w[c(t)\sin\theta, t]d\theta. \tag{10}$$

The problem (1) - (10) is solved with the help of the normal mode method. This method leads to infinite system of ordinary differential equations with respect to the principal coordinates of the beam deflection $w(x,t)$.

2 Normal mode method

Within the framework of this method the beam deflection $w(x,t)$ is sought in the form

$$w(x,t) = \sum_{n=1}^{\infty} a_n(t)\psi_n(x). \tag{11}$$

Here $\psi_n(x)$ are non-trivial solutions of the homogeneous boundary-value problem

$$\frac{d^4\psi_n}{dx^4} = \lambda_n^4 \psi_n \qquad (|x| < 1),$$

$$\frac{d^2\psi_n}{dx^2}(\pm 1) \pm k\frac{d\psi_n}{dx}(\pm 1) = 0, \qquad \psi_n(\pm 1) = 0,$$

where λ_n are the corresponding eigenvalues. Moreover, the eigenfunctions $\psi_n(x)$ satisfy the orthogonality condition

$$\int_{-1}^{1} \psi_n(x)\psi_m(x)\,dx = \delta_{nm},$$

where $\delta_{nm} = 0$ when $n \neq m$ and $\delta_{nn} = 1$. Substitution of equations (11) into (6) - (8) and solution of the hydrodynamical part of the problem (1) - (5) provide the following system of ordinary differential equations

$$\frac{d\vec{a}}{dt} = (\alpha I + \kappa S)^{-1}(\beta D\vec{d} + \vec{f}), \tag{12}$$

$$\frac{d\vec{d}}{dt} = -\vec{a}. \tag{13}$$

Here $\vec{a} = (a_1, a_2, a_3, \ldots)^T$, $\vec{d}$ is the vector $\vec{d} = (d_1, d_2, d_3, \ldots)^T$, $d_n = (\beta\lambda_n^4)^{-1}(\alpha\dot{a}_n + b_n)$, $\vec{f} = (f_1(c), f_2(c), f_3(c), \ldots)^T$, I is the unit matrix, D is the diagonal matrix, $D = \mathrm{diag}\{\lambda_1^4, \lambda_2^4, \lambda_3^4, \ldots\}$. The right-hand side of the system (12), (13) depends on $\vec{a}$, $\vec{d}$, c, but not on t. Therefore, it is convenient to take c as a new independent variable, $0 \leq c \leq 1$. Differential equation for $t = t(c)$ follows from (10) and has the form

$$\frac{dt}{dc} = Q(c, \vec{a}, \dot{\vec{a}}), \tag{14}$$

where

$$Q(c, \vec{a}, \dot{\vec{a}}) = \frac{c + (4\kappa/\pi)(\vec{a}, \vec{\Gamma}_c(c))}{2 - (4\kappa/\pi)(\dot{\vec{a}}, \vec{\Gamma}(c))}, \tag{15}$$

$$\Gamma_n(c) = \int_0^{\pi/2} \psi_n(c\sin\theta)d\theta, \qquad \Gamma_{nc}(c) = \int_0^{\pi/2} \psi_n'(c\sin\theta)\sin\theta d\theta.$$

Multiplying equations of system (12), (13) by dt/dc and taking (14) into account, we get

$$\frac{d\vec{a}}{dc} = \vec{F}(c, \vec{d})Q(c, \vec{a}, \vec{F}(c, \vec{d})), \tag{16}$$

$$\frac{d\vec{d}}{dc} = -\vec{a}Q(c, \vec{a}, \vec{F}(c, \vec{d})), \tag{17}$$

where $\vec{F}(c, \vec{d}) = (\alpha I + \kappa S(c))^{-1}(\beta D\vec{d} + \vec{f}(c))$. The initial conditions are

$$\vec{a} = 0, \qquad \vec{d} = 0, \qquad t = 0 \qquad (c = 0). \tag{18}$$

The system (16), (17) is suitable for numerical evaluation. Indeed, for small times we have $c(t) = O(t^{1/2})$, $w(x,t) = O(t^{3/2})$, $w_t = O(t^{1/2})$, $w_{tt} = O(t^{-1/2})$, and therefore, one cannot start numerical calculations for system (12) - (14) with homogeneous initial conditions. Difficulties with initial conditions for system of differential equations with respect to principal coordinate $a_n(t)$ and their derivatives $\dot{a}_n(t)$, where the time t is taken as the independent variable, are described by Kvålsvold end Faltinsen (1993). On the other hand, $t = O(c^2)$, $w = O(c^3)$, $w_t = O(c)$, $w_{tt} = O(c^{-1})$ as $c \to 0$, and there are no problems with initial conditions for system (14) - (17).

Initial value problem for the edge impact is similar to (14) - (18) but elements of the system are different. Moreover, the derivative dt/dc can become large (the speed of contact region expansion is small) at some moment t_1 of the impact stage. In this case we need to return to system (12), (13) as $t \approx t_1$.

3 Numerical results

The initial-value problem (14) - (18) is solved numerically by the fourth-order Runge-Kutta method with uniform step Δc. The condition that the numerical scheme is stable was derived. The step Δc has to decrease as $O(N^{-2})$ if the number of modes N taken into account increases.

Main part of the calculations were performed for simply supported beam ($k = 0$). Central impact was analysed for the case $L = 0.5$m, $R = 10$m, $h = 2$cm, $E = 21 \cdot 10^{10}$H/m^2, $V = 3$m/s, $\varrho = 1000$kg/m^3, $\varrho_b = 7850$kg/m^3, $b = 0.5$m, where ϱ_b is the beam density and b is the beam width. This gives $\alpha = 0.314$, $\beta = 0.311$. The number of 'dry' modes N taken into account is equal to 15. The speed of the contact region expansion was found to be positive and bounded as $c > 0$. Numerical results are compared with both the Wagner approach and the Karman approach for the estimation of the wetted size of the beam. It was found that the simplified approaches do not provide appropriate approximations of the speed of the contact region expansion. Bending stress peaks close to the end of the impact stage and its maximum value is 140N/mm^2. One-mode approximation, $N = 1$, does not give correct information about evolution of the bending stresses, but maces it possible to estimate their maximal value.

Edge impact is analysed for $\alpha = 0.157, \beta = 0.04$. It was revealed that the speed of the contact region expansion is not uniform and takes its minimal positive value at distance $1.2L$ from the impact point. After that the speed grows beyond all bounds before the beam is totally wetted. This means that acoustic effects have to be taken into account at the final phase of the impact stage. The hydrodynamic force tends to infinity as $dc/dt \to \infty$, where $c(t)$ is the dimension of the contact region. This effect, which was not revealed for central impact, is referred to as blockage. It is assumed that the parameter β, which is the dynamical rigidity of the beam, is responsible for this effect. The calculations were performed for $\beta = 0.02, \beta = 0.04$ and $\beta = 0.06$. It was found that small variations of β lead to significant changes of the process evolution. When a half of the beam is wetted, the speed dc/dt becomes negative and the wetted area starts to decrease for $\beta = 0.02$. This phenomenon may be responsible for cavitation effects and the beam ventilation. In the case $\beta = 0.06$ the speed dc/dt is positive and bounded as $c > 0$, and the hydrodynamic force is bounded at the impact stage. Comparison of central impact and edge impact for the same values of the parameters α, β shows that at the end of the impact stage the beam deflections and the distributions of the bending stresses differ significantly.

If $k \neq 0$ the calculations were performed for the central impact only. It is shown that the conditions of simply supported beam, $k = 0$, can be used to estimate bending stresses near the beam centre.

The numerical results demonstrate that at least five modes have to be taken into account to derive the initial data for the penetration stage of the impact. It should be noted that the present approach does not require supercomputers. The computer program, which was used for the calculations with 15 modes, takes about 30 minutes of computer time in a PC-486(66MHz) computer.

References

Korobkin A. A. Water impact problems in ship hydrodynamics // Advances in Marine Hydrodynamics (ed. M. Ohkusu), Southampton: Computational Mechanics Publications, 1996, P. 323 - 371.

Kvålsvold J., Faltinsen O. M. Hydroelastic modelling of slamming against wetdecks // 8th Intern. Workshop on Water Waves and Floating Bodies, Saint Johns, Canada, 1993.

Wagner H. Über Stoss- und Gleitvorgänge an der Oberfläche von Flüssigkeiten// Z. Angew. Math. Mech. 1932. V. 12. H. 4. S. 193 - 215.

The Computation of the Second-Order Hydrodynamic Forces on a Slender Ship in Waves

Yonghwan Kim, P.D. Sclavounos

Massachusettes Institute of Technology

1 Introduction

The accurate prediction of the mean and slow-drift force on a ship is necessary for the reliable simulation of slow-drift response and design of a positioning system. The slow-drift problem, in particular, becomes important for the ship with no forward speed, like a drilling ship or shuttle tanker. In contrast to a floating off-shore platform, the ship is a slender body. Therefore, slender-body theory is applicable to reduce the effort which comes from full 3-dimensional discretization. In the present study, strip and unified theory are applied to predict the second-order mean drift forces and moment and wave drift damping coefficient.

2 Application of Slender-Body Theory

Consider a ship at zero-forward speed in regular monochromatic waves. When the ship is slender, slender-body theory allows an accurate linear solution for the radiation and diffraction problems. Especially, unified theory provides excellent accuracy for not only diffraction problem but also the heave and pitch radiation problem. For the transverse motions, strip theory is adequate.

2.1 Strip Theory with NIIRID

NIIRID[1] is a computer code developed at MIT for the computation of the radiation and diffraction forces on a 2-dimensional section. This code adopts the 2-dimensional wave source potential as the Green function, and provides the complete linear solution of the radiation and diffraction problems. In this study, NIIRID is integrated into a strip theory code based on the Salvesen, Tuck and Faltinsen(STF) method[2].

2.2 Unified Theory

Newman[3], Sclavounos[4] developed an excellent slender-body theory which carries out the solution of the zero-speed seakeeping problem in the frequency domain. Unified theory adds a 3-dimensional correction to the sectional solution of strip theory. In this theory, the radiation potential is obtained by the superposition of the strip theory solution(particular solution) and the longitudinal wave interaction(homogeneous solution). The diffraction potential has an analogous form which can be related to the radiation solution in not very

short waves. The most important task in unified theory is to solve the integral equations for the three-dimensional sectional strength, q_j. For example, the integral equation for the radiation problem is

$$q_j(x) - \frac{1}{2i\pi}(\frac{\sigma_j}{\bar{\sigma}_j} + 1)L(q_j) = \sigma_j(x) \qquad j = 3(\text{heave}), 5(\text{pitch}) \tag{1}$$

with

$$\begin{aligned} L(q_j) \;=\; & q_j(x)\,(\gamma + \pi i) \;+\; \int_L d\xi\, \{\frac{1}{2} + sgn(x-\xi)\, ln(2\nu|x-\xi|)\, \frac{d}{d\xi} q_j(\xi) \\ & -\frac{\pi\nu}{4}\,(Y_o(|\nu(x-\xi)|) + 2iJ_o(|\nu(x-\xi)|) + H_o(|\nu(x-\xi)|))\; q_j(\xi)\} \end{aligned} \tag{2}$$

where σ_j is the two-dimensional strength obtained from strip theory. All other notations are the same with Ref.4. The added mass, a_{ij}, and damping coefficient, b_{ij}, can be derived from the equation,

$$\omega^2 a_{ij} - i\omega b_{ij} = -i\omega\rho \int\int n_i \psi_j ds - i\omega\rho \int\int n_i \frac{q_j - \sigma_j}{\sigma_j + \bar{\sigma}_j}(\psi_j + \bar{\psi}_j) ds \tag{3}$$

where ψ_j is the strip theory potential. The wave exciting forces and moments can be obtained from the Haskind relation. The far-field formula derived by Sclavounos(1985) has been adopted in the present study.

$$X_i = \frac{i\rho g A}{2\omega} \int_L q_j(x) e^{i\nu x \cos\beta} dx \tag{4}$$

where A is the wave amplitude and β is the heading angle of the wave relative to the ship axis.

2.3 Mean Drift Forces and Moment

Maruo(1960) derived a far-field formula for the surge and sway mean forces,

$$\bar{F}_{x,y} = \frac{\rho\nu^2}{8\pi} \int_0^{2\pi} |H(\theta)|^2 \left\{ \begin{array}{c} (\cos\theta + \cos\beta) \\ (\sin\theta + \sin\beta) \end{array} \right\} d\theta \tag{5}$$

The far-field equation for mean yaw moment was derived by Newman(1967),

$$\bar{M}_z = -\frac{\rho\nu}{8\pi} Im \int_0^{2\pi} \bar{H}(\theta) \frac{\partial H}{\partial\theta}(\theta) d\theta - \frac{1}{2\nu L}\, Im\{\frac{\partial H}{\partial\theta}(\pi + \beta)\} \tag{6}$$

where $H(\theta)$ is the Kochin function. In the present study, the following form of the Kochin function is found to generate the most accurate results for the drift forces and moment[5].

$$H(\theta) = \int_L \sum_{j=0}^{7} \sigma_j^*(x) e^{-i\nu x \cos\theta} dx \tag{7}$$

where the sectional source strength (heave & pitch) or horizontal dipole moment (roll, sway & yaw) are defined as follows

$$\sigma_j^*(x) = \int_{C_m(l)} \left[\frac{\partial}{\partial n}\phi_j(x_m, y, z) - \phi_j(x_m, y, z) \frac{\partial}{\partial n} \right] e^{\nu(z - iy\sin\beta)} dl \tag{8}$$

where $C_m(l)$ denotes the ship section at station $x = x_m$.

2.4 Wave Drift Damping

The drift damping is also an important quantity in the slow-drift oscillation problem. Aranha[6] suggested a formula for the wave drift damping which is adopted in the present study although there is some doubt about its accuracy in the radiation problem.

3 Computational Results

Fig.1 shows the added mass and damping coefficient of the heave motion and Fig.2 shows the heave and pitch RAO. Both are for the Series 60(C_B = 0.7) hull. As expected, unified theory is in very good agreement with WAMIT. Fig.3 shows the pitch component of the Kochin function. The accurate computation of the Kochin function is the key to the drift force computation. Some minor discrepancy with WAMIT's is found, and the accumulation of this discrepancy produces the difference of the total drift force and moment. However, the agreement is generally favorable. Fig.4 shows the mean drift force for the surge of a parabolic hull with beam/length=0.15. The longitudinal drift force is more important than others since the ship will change her position to be parallel to the wave direction. This figure shows the effect of the number of stations in unified theory. Fig.5 shows the lateral mean force on the Series 60 hull. Since the fore and aft body of this hull is not symmetric, the longitudinal component doesn't vanish. Sway, roll, and yaw components contribute to the second-order quantities in headings other than head seas. Fig.6 shows the wave drift damping coefficients. Aranha's formula is applied to the mean forces obtained by strip theory, unified theory and WAMIT. The primary difference of these curves is the difference of the slopes of mean forces with respect to the wave heading angle and wave frequency.

4 Acknowledgement

This work is supported by the Joint Industry Project, SWIM, at MIT.

References

[1] P.D. Sclavounos, 1980, *Users Manual of NIIRID,* MIT Report

[2] Salvesen, N., Tuck, E.O., and Faltinsen, O., 1970, *Ship Motions and Ship Loads,* Trans. of SNAME, Vol.78

[3] J.N. Newman, 1978, *The Unified Theory of Ship Motions,* Advances in Applied Mechanics, Vol.18

[4] P.D. Sclavounos, 1981, *The Interaction of an Incident Wave Field with a Floating Slender Body at Zero Speed,* Proc. of the 3rd Int. Conf. on Numerical Shiphydrodynamics

[5] Y. Kim, and P.D. Sclavounos, 1996, *Users Manual of SWIM Version 4.0,* MIT Report

[6] J.A.P. Aranha, 1994, *A Formula for Wave Damping in the Drift of a Floating Body,* Jour. of Fluid Mechanics, Vol.272

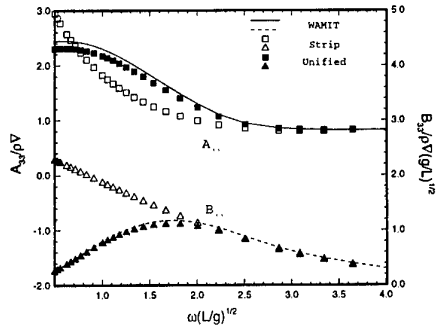

Figure 1: Added-Mass and Damping Coefficient : Heave, Series 60($C_B = 0.7$) Hull

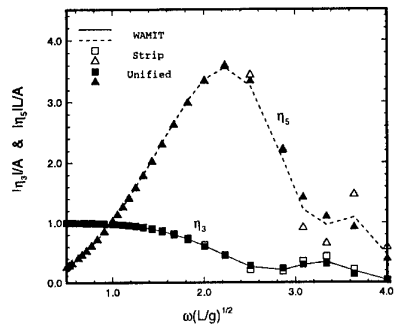

Figure 2: Heave and Pitch RAO : Series 60($C_B = 0.7$) Hull, Head Sea

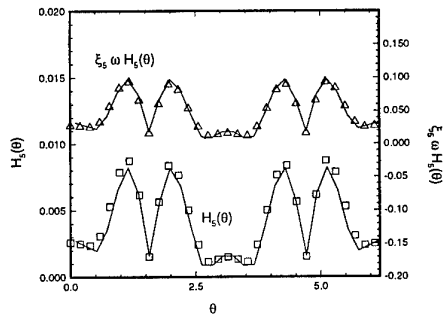

Figure 3: The Pitch Component of the Kochin Function : Series 60($C_B = 0.7$) Hull, $\omega(L/g)^{1/2} = 3.34$, Head Sea

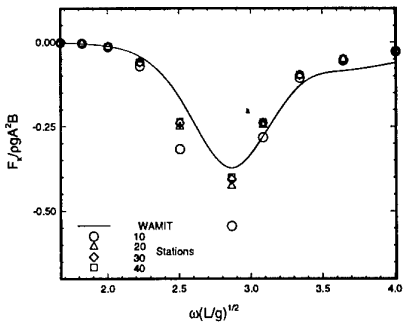

Figure 4: The Convergence of Drift Force : Parabolic Hull($B/L = 0.15$), Head Sea

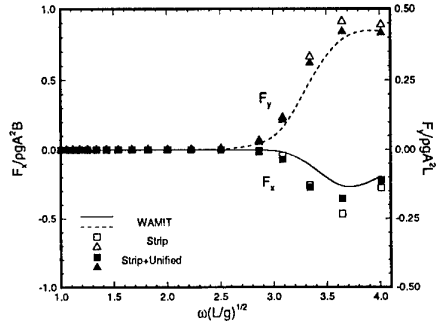

Figure 5: The Drift Forces : Series 60($C_B = 0.7$) Hull, Beam Sea

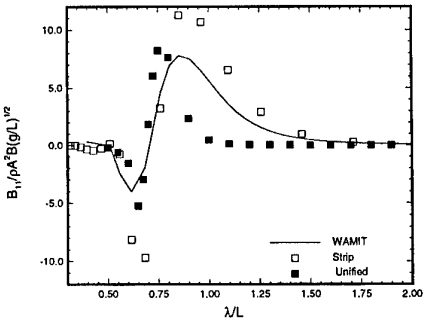

Figure 6: The Wave Drift Damping : Parabolic Hull($B/L = 0.15$), Head Sea, Surge-Surge Component

Wave Breaking Simulation Around a Lens-shaped Mast By a V.O.F. Method

O. Laget, C. de Jouëtte, J.M. Le Gouez, S. Rigaud
Principia R.D., Port de Brégaillon, 83507 La Seyne Sur Mer cedex, France.

Abstract

Using the CFD code EOLE, described in [3], numerical computations of steady waves around a partially immersed vertical lens-shaped mast have been done. These computations were realized using a "Volume of Fluid" method coupled with the Euler or Reynolds-averaged Navier-Stokes equations. The V.O.F. technique is often used to modelize unsteady phenomena. In [3], this technique was adapted to treat steady problems as non-linear waves induced by a submerged hydrofoil placed in a uniform flow. The purpose of this paper is to expose the way the V.O.F method was extended to compute fluid flows in body fitted grids, and to highlight the interesting features of this method applied to a strong non linear wave pattern around a 3D lens-shaped mast.

1 Introduction

Nowadays, as shown in [5], two major groups of methods are used to determine the wave resistance of structures moving at a constant speed. First, potential methods, based on a Dawson technique are more and more used by shipyards or tank facilities as industrial tools. However, the limits of the potential theory do not allow to treat viscous interactions, nor high non linear free surface. Therefore, important attention is payed to implement free surface algorithm in general Navier-Stokes or Euler solvers. A common feature of these methods is to follow the free surface evolutions by mean of mesh deformation. As the general evolution of ship goes to high speed vehicule, this method may be unadapted to deal with bow waves where wave breaking occur or whith transom stern flows. In the EOLE code , developed since 1990, the resolution of Euler or Navier-Stokes equations is coupled with the "Volume of Fluid" method for the tracking of the interface. This technique is very efficient for very complicated free surface unsteady phenomena like jets, bubble collapse, sloshing, cavitation. It is expected that this method may be used efficiently for steady problems like the wave resistance one. The algorithm, initialy developed for unsteady flows has been adapted to steady problems and its application in curvilinear coordinates is presented. A first serie of results around a vertical lens-shaped mast moving at Froude numbers between 0.4 and 1.2 is presented, and shows the interest of the method.

2 Theory

The steady Euler equations for incompressible fluids are solved using a pseudo-compressibility method [2]. This is an iterative method which consists in introducing derivatives with respect to a fictitious time called pseudo-time τ, into the continuity and the momentum equations as follows :

$$\frac{\partial \tilde{\rho}}{\partial \tau} + \rho \,\mathrm{div}\, \vec{u} = 0, \qquad \frac{\partial \tilde{\rho}\vec{u}}{\partial \tau} + \mathrm{div}\left(\rho \vec{u} \otimes \vec{u} + p\bar{I}\right) = \vec{0}$$

Where $\tilde{\rho}$ is a pseudo-density, ρ the fluid density, $\vec{u}$ the fluid velocity, p the pressure and $\bar{I}$ the identity tensor. This system is closed using a relation linking the pressure and the pseudo-density and called pseudo-law of state : $p = G(\tilde{\rho})$. The steady solution is obtain as the asymptotic limit of the pseudo-transient solution of this pseudo-unsteady system (PUS) when the pseudo-time goes toward infinity. The main features of the numerical method for pseudo-time integration are a finite-volume method based on a space-centered scheme, second and fourth order artificial viscosity terms, five stages Runge-Kutta pseudo-time stepping and implicit residual smoothing.

2.1 Steady VOF method

The V.O.F. method implemented in the EOLE code is based on the technique, previously proposed by Hirt and Nichols [4]. The fraction of fluid in each cell of the discretization mesh is represented by a function F whose value can vary from zero to one while the cell is respectively empty or full of fluid. The free surface is contained by the cells with F values between zero and one. For a steady problem, the evolution of the F field is governed by the following transport equation in which the time is replaced by the pseudo-time τ :

$$\frac{\partial F}{\partial \tau} + \frac{\partial uF}{\partial x} + \frac{\partial vF}{\partial y} + \frac{\partial wF}{\partial z} = 0 \tag{1}$$

where (x, y, z) is the cartesian system, (u, v, w) the cartesian components of the velocity. The evolution of the F function is made from fluxes calculations (based on "donor-acceptor method" [4]) through all the faces of each cell. This algorithm is implemented in curvilinear system (ξ, η, ζ) via a coordinates transformation of jacobian $J = \frac{\partial(\xi,\eta,\zeta)}{\partial(x,y,z)}$. The last equation (1), for a cell Ω (of faces $\delta\Omega_{\xi+}$, $\delta\Omega_{\xi-}$, $\delta\Omega_{\eta+}$, $\delta\Omega_{\eta-}$, $\delta\Omega_{\zeta+}$, $\delta\Omega_{\zeta-}$ and volume V_Ω) in the new coordinates system (ξ, η, ζ) is given by :

$$\frac{dF}{d\tau} + \frac{1}{\Delta\xi\Delta\eta\Delta\zeta}\left(\int_{\delta\Omega_{\xi+}} f\hat{u}d\eta d\zeta - \int_{\delta\Omega_{\xi-}} f\hat{u}d\eta d\zeta + \right.$$
$$\left. \int_{\delta\Omega_{\eta+}} f\hat{v}d\xi d\zeta - \int_{\delta\Omega_{\eta-}} f\hat{v}d\xi d\zeta + \int_{\delta\Omega_{\zeta+}} F\hat{w}d\xi d\eta - \int_{\delta\Omega_{\zeta-}} f\hat{w}d\xi d\eta\right) = 0 \tag{2}$$

where $f(\xi, \eta, \zeta, \tau)$ is a continue fonction defined at each point (ξ, η, ζ, τ) of the fluid domaine and whose values are contained between 0 and 1. $\hat{u}$, $\hat{v}$ and $\hat{w}$ are the modified contravariant velocity components which can be expressed as follow :

$$\hat{u} = \vec{U}.\vec{grad}\xi\frac{J}{\bar{J}}\ , \quad \hat{v} = \vec{U}.\vec{grad}\eta\frac{J}{\bar{J}}\ , \quad \hat{w} = \vec{U}.\vec{grad}\zeta\frac{J}{\bar{J}}\ .$$

where $\bar{J}$ is the jacobian of the coordinates transformation estimated at each face of the cell. For example at the face $\delta\Omega_{\xi+}$:

$$\vec{n}\,dS = \frac{1}{\bar{J}}\overrightarrow{\text{grad}}\xi d\eta d\xi$$

where $\vec{n}\,dS$ is the normal vector of the face in the cartesian coordinates. The expression for the calculation of the fluxes originaly proposed by Hirt and Nichols [4] is now written, in the curvilinear system, as follow :

$$\Delta F = \min(F_{AD}|\hat{U}|\Delta\tau + CF, F_D V_\Omega) \quad \text{with} \quad CF = \max[(1 - F_{AD})|\hat{U}|\Delta\tau - (1 - F_D)V_\Omega, 0]$$

where F_A and F_D are the volumes of fluid contained in the "acceptor" and the "donor" cell respectively (see figure 1). F_{AD} can be both F_A or F_D depending of the mode "donor" or "acceptor" determined by the slope of the free surface which is calculated in the curvilinear system using the gradient of the V.O.F. The "acceptor" mode is adapted to the case of a free surface moving parallel to its normal vector, and the "donnor" mode is adapted to the case of a free surface moving perpendicular to its normal vector. Writing all the V.O.F. algorithm in curvilinear coordinates allow fluid computations to be realized in body-fitted grids.

As the scheme used to discretize the previous equation (2) is explicit in pseudo-time, a CFL criteria is added to the one of the conservative equations (continuity and momentum equations) to force the free surface not move throught more than a part of a cell during a pseudo-time step :

$$\frac{U_j\Delta\tau}{\Delta x_j} < CFL_{Vof}$$

where x_j and U_j are respectively x, y, z and u, v, w for $j = 1, 2, 3$. The pseudo-time step value is determined by taking the minimum value between the one given by the previous relation and the value calculated with the CFL criteria on the conservative equations.

3 Numerical results

Some numerical results about the wave generation induced by a 3D lens-shaped vertical mast (length : 0.3375 m and maximum thickness : 0.045 m) partially immersed (0.4 m) are presented. Computations were realized for several values of the Froude number from 0.4 to 1.4 in order to observe the evolution of the wave resistance, and to make comparisons with existing results. On figure (2) the values of the wave resistance obtained using EOLE, are compared with the ones measured during the experiments (performed at "Ecole Centrale de Nantes" [1]) and those computed with the Dawson method (REVA code, potential linear and non linear theory) by Delhommeau *et al* [1]. At intermediate values of the Froude Number (between 0.4 and 1) EOLE's results are closer to the experimental ones than those given by the REVA code. The better representation of the non-linear free surface arround the body is the explanation. For higher values of the Froude number (between 1 and 1.4) the wave resistance values of both codes are in agreement with the experiments because the free surface deformation along the body is smoother. For the free surface location, the experiments show that breaking appears when the Froude number value is larger than 0.5. Such phenomenon can be qualitatively represented by steady Volume of Fluid computations. On figures 3, 4 and 5, the free surface position along the body and the plane of symmetry obtained with EOLE are compared to the one given by REVA for the values of the Froude number equal to 0.4, 0.6 and 1 respectively. Note that the free surface calculated by the V.O.F. method is represented by the line V.O.F. = 0.5, using the post-prossessing logiciel Tecplot (Amtec Engineering, Inc.). A more precise representation should be preferable. The extrema computed with EOLE have a larger amplitude than the ones given by REVA but their locations along the body are in agreement with each other. As the pseudo-time is a non-physical iterative variable, the free surface instabilities (like droplets) appearing on the figures (4) and (5) give qualitative informations about the breaking (for example the Froude number of transition), but can not represent the unsteady evolution of the interface. To be more accurate in representing such phenomenon some unsteady computations can be performed, but they need more CPU time. The calculations presented here, were done on half a domain (because of symmetry reasons) discretized by a 230000 cells mesh on 2000 pseudo-time iterations. This kind of computations have been realized on a Digital DEC ALPHA 600/266 station (428 SPECfp92) in 37 hours.
All the results presented here, show the ability of the V.O.F. method to describe non linear free surface phenomena. Further developments, especially to improve the representation of the free surface, will be carried on.

4 Acknowledgments

The authors wish to thanks the "Direction de la REcherche et de la Technologie" (DGA/DRET), Research Agency of Ministery of Defense, which is supporting this work.

References

[1] **G. Delhommeau, C. Couchman, L. Jeannaud, H. Doyer,** *"Etude théorique et numérique des non linéarités dans les problèmes d'écoulement stationnaires à surface libre et validation experimentale."* Contrat DRET 92/142, Rapport de synthèse finale, 1994.

[2] **C. de Jouëtte,** *"Développement d'une méthode de pseudo compressibilité pour le calcul des écoulements de fluide incompressible - Applications aux écoulements instationnaires en présence d'une surface libre."* Thèse de doctorat, Université de Nice - Sophia Antipolis, 12 décembre 1994.

[3] **C. de Jouëtte, J.M. Le Gouez, O. Put (Laget), S. Rigaud,** *"Volume of Fluid Method (VOF) Applied to Non-Linear Wave Problems on Body-Fitted Grids."* 11th International Workshop on Water Waves and Floating Bodies, Hamburg, Germany, 17-20 March 1996.

[4] **C.W. Hirt and B.D. Nichols,** *"Volume of fluid (VOF) method for the dynamics of free boundaries."* J. of Computational Physics, vol. 39, pp. 201-225,1981.

[5] Proceedings of C.F.D. Workshop, Tokyo, Japan, 1994.

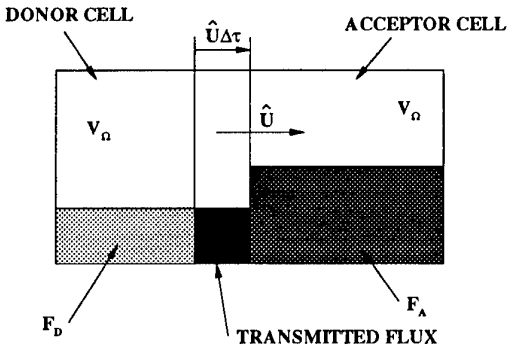

Figure 1: V.O.F. method : donor and acceptor cells.

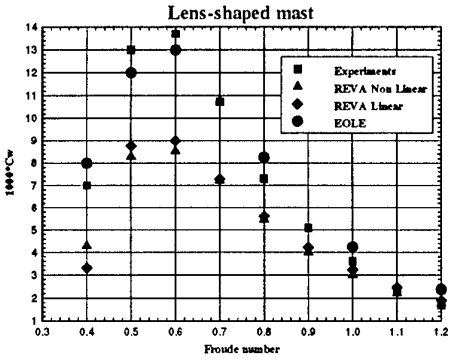

Figure 2: Lens-shaped mast : wave resistance coefficients.

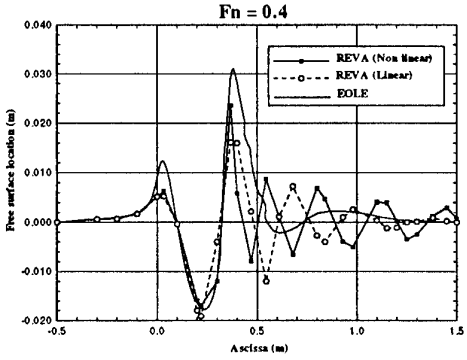

Figure 3: Lens-shaped mast : free surface elevation $Fn = 0.4$.

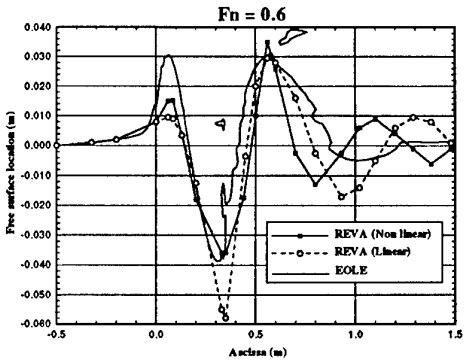

Figure 4: Lens-shaped mast : free surface elevation $Fn = 0.6$.

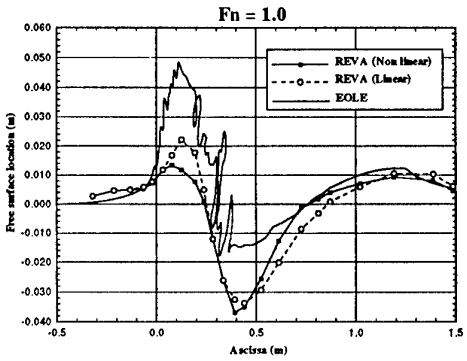

Figure 5: Lens-shaped mast : free surface elevation $Fn = 1$.

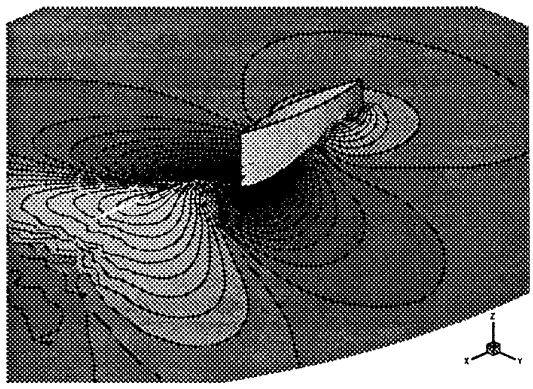

Figure 6: Lens-shaped mast : wave pattern $Fn = 0.6$

Twelfth International
WORKSHOP ON WATER WAVES AND FLOATING BODIES

VISCOUS EFFECTS IN WAVE–BODY INTERACTION

M. Landrini †, M. Ranucci §, C.M. Casciola §, G. Graziani §
† INSEAN, Via di Vallerano 139, 00128 Roma (Italy)
§ Dipartimento di Meccanica e Aeronautica, Università di Roma *La Sapienza*

1 Introduction

The flow of an incompressible viscous fluid about a circular cylinder beneath a regular Stokes wave train is a typical problem in marine structures hydrodynamics and several theoretical and experimental results are available.

The accurate experimental analysis by Chaplin [5] confirms that the vertical mean value of the hydrodynamic force as well as the second and third harmonics of the fluctuating components are well explained in terms of the inviscid diffraction of the incident wave field as is described by weakly nonlinear models [7, 8], and by fully nonlinear computations [6]. However, the potential theory fails to capture exhaustively the entire phenomenon. Actually, Chaplin's results revealed a significant reduction in the amplitude of the fundamental harmonic of the loading which cannot be related to the purely inviscid diffraction of the incoming waves.

For a cylinder with small submergence, the nonlinear dynamics of the wave system is crucial and tightly coupled to the dynamics of the vorticity field about the body. In these conditions, we have to consider the full Navier–Stokes equations for a free surface flow. To this purpouse, a particle method which account for viscous effects and flow separation near the body is deviced and the nonlinear behaviour of the free surface is fully considered (see also Yeung [9] for a similar approach in the context of roll motion of ship cross–sections).

2 Description of the mathematical problem

We consider a circular cylinder $\mathcal{B}$ immersed beneath a regular wave train on the free surface $\mathcal{F}$. The water depth is assumed infinite and the fluid domain $\mathcal{D}$ is unbounded in the horizontal direction. The motion of the viscous incompressible fluid within $\mathcal{D}$ is described by the Navier–Stokes equations. The standard no–slip condition must be satisfied on the solid boundary $\partial\mathcal{B}$ and the kinematic and dynamic conditions hold at the free surface. Actually, we neglect the effects of the free surface boundary layer and assume the support of the body–generated vorticity to be confined away from the free interface. Consistently the dynamic boundary condition on $\mathcal{F}$ simply requires the fluid pressure to be atmospheric. Under such hypothesis, for finite times and far from the body, the fluid motion reduces to an irrotational wave system. In particular, we consider the corresponding Stokes wave field as a basis flow and solve for the correction which describes both viscous and diffraction effects.

In order to analyze the vortical flow around the body and its interaction with the free surface, a vorticity–velocity formulation is considered, and an operator splitting approach is adopted for the numerical solution. The algorithm approximates the flow evolution by a sequence of diffusive and convective steps according to the Stokes and Euler equations, respectively. In particular, the diffusion of the vorticity is described through the solution of the heat transfer equation, the advection step consists in evaluating the Lagrangian motion of the vortical particles, while the free surface evolves according to a purely inviscid dynamics. To enforce the no–slip boundary condition, following Chorin [1], a vortex sheet is inserted on the body contour after each convective step. This vortex sheet is furtherly lumped in order to obtain the circulation of the discrete vortices which are diffused together with those already existing within the flow field. The solution of the problem is effectively achieved by means of a fast vortex method coupled to an integral representation of the velocity field.

In order to describe the diffusion of the vorticity, a deterministic approach based on the integral representation for the diffusion problem is adopted as discussed in [2] for flows without a free surface. Consistently with this particle scheme, the evolution of the free surface is described through the motion of markers distributed on $\mathcal{F}$ by using kinematic and dynamic evolution equations expressed in terms of velocity components [4].

Finally, the perturbation velocity field in the fluid domain is expressed in terms of the Poincaré representation formula [3]. At each convective–step, a boundary integral equation is first solved to determine the normal velocity

component on $\mathcal{F}$ and the tangential velocity component on $\partial\mathcal{B}$ and then the velocity field in $\mathcal{D}$ is explicitely computed through the integral representation.

3 Computational results

The above described algorithm is used to analyze the interaction of a Stokes wave train with a submerged circular cylinder in order to enlight the role of the viscosity. The solutions of the Navier–Stokes equations are compared with those provided by an inviscid model which usually fully captures the nonlinear dynamics of wave–body interactions as well as with the experiments reported in [5]. In particular, Chaplin's Case–E ($kR = 0.206$, $h/R = 2.0$) is considered in detail since non–linear diffraction effects are expected to be more pronounced for shallow submergences of the cylinder.

By examining the wave patterns reported in figure 1 for $t/T_S = 10$ and $K_c = 0.75$, a first comparison between the viscous (black line) and inviscid (red line) solutions is possible. Qualitatively, the wave diffraction dynamics appears to be unaltered by the vorticity generated at the body boundary: however, although the two solutions appear to be coincident for low values of K_c, an increasingly pronounced difference can be detected for larger values, the amplitude of the emitted shorter wavelenghts appearing to be reduced in the viscous solution. Consistently, the wave induced loading predicted by the viscous and by the inviscid model coincides for the smaller K_c and show significant discrepancies for the largest value. In particular, the time evolution of the two force components F_x, F_y is reported in figure 2 for $K_c = 1.0$. In this figure, after an initial transient of about one wave period during which the viscous (black lines) and the inviscid solutions (red lines) are substantially superimposed, the viscous loads oscillate with different amplitudes with respect to the inviscid ones. In both cases the time behavior of the force displays an apparent non–sinusoidal shape which manifests the non–linear effects in the wave–body interaction.

Since the detected differencies between the two solutions are related to the generation and to the following evolution of the vorticity, it is worthwhile to discuss the dynamics of the rotational field. A typical vorticity distribution is shown in figure 3 where cyan–blue region denote the positive values (*i.e.* clockwise) and red–yellow region the negative ones. Two intense vorticity layers of opposite sign which are driven by the rotating flow induced by the waves may be observed. Then, due to the diffusion, the vorticity is furtherly spread away from the cylinder, a thickened structure is generated and new vortex layers, of opposite sign, possibly appear on the body. Finally, the interaction of opposite signed layers takes place, originating the well defined structure observed in the figure above the cylinder. Near the body the vorticity field becomes periodic soon after the beginning of the flow evolution while the *far* field dynamics does not significantly affect the forces acting on the body.

A quantitative assessment of this behaviour can be gained through the analysis of the mean value over a period of the circulation along circles concentric with the cylinder, figure 4. In particular the black, red and green lines refer to $t/T_s = 18$, 19 and 20, respectively. A steady mean circulation is estabilished about the cylinder while farther from the body the dynamics of the far field vorticity still maintains a considerable time dependance. In his analysis of the nonlinear behaviour of wave induced loads, Chaplin pointed out the mean circulation about the cylinder as the key feature to explain the marked decreasing of the actual inertia coefficient with respect to the potential flow prediction. This difference emerges from figure 5, where the present inviscid solution (black line) always exceeds Chaplin's experimental data. The correct behaviour is fully recovered by the viscous solution shown in the same plot (red symbols), thus confirming the relevance of the diffusion for this force components.

References

[1] Chorin A. J. (1973): Numerical study of slightly viscous flow. *J. Fluid Mech.*, **57**, 785-796.

[2] Graziani G., Ranucci M., Piva R. (1995): From a Boundary Integral Formulation to a Vortex Method for Viscous Flows, *Comput. Mech.*, **15**, 4, 301-314.

[3] Bassanini, P., Casciola, C. M., Lancia, M. R. & Piva R. 1991 A boundary integral formulation for the kinetic field in aerodynamics. Part I. *Europ. J. Mech.*, B/Fluids, **10**(6), 605-627.

[4] Casciola, C. M. & Landrini, M. 1996 Nonlinear long waves generated by a moving pressure disturbance *J. Fluid Mech.*, **325** 399–418.

[5] Chaplin., J.R. 1984 Nonlinear forces on a horizontal cylinder beneath waves. *Journal of Fluid Mechanics*, **147**,pp 449–464.

[6] Y. Liu, D.G. Dommermuth, D.K.P. Yue. A high–order spectral method for nonlinear wave–body interactions. *Journal of Fluid Mechanics*, 245:115–136, 1992.

[7] T. F. OGILVIE. First and second order forces on a circular cylinder submerged under a free surface. *Journal of Fluid Mechanics*, 16:451-472, 1963.

[8] T. VADA. A numerical solution of the second-order wave-diffraction problem for a submerged cylinder of arbitrary shape. *Journal of Fluid Mechanics*, 174:23-37, 1987.

[9] R. W. YEUNG, C. CERMELLI, S. W. LIAO Vorticity fields due to rolling bodies in a free surface - Experiment and Theory. 21^{st} Symposium on Naval Hydrodynamics, Trondheim, Norway, 1996.

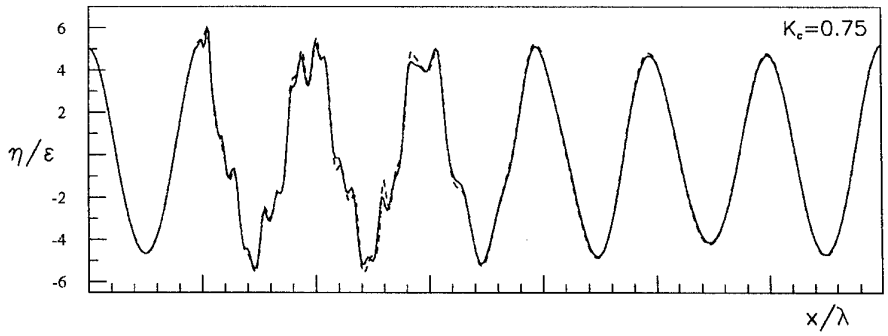

Figure 1: Free surface profiles for $K_c = 0.75$ and $t/T_S = 10$. Comparison of viscous (solid line) and inviscid (dashed line) solutions.

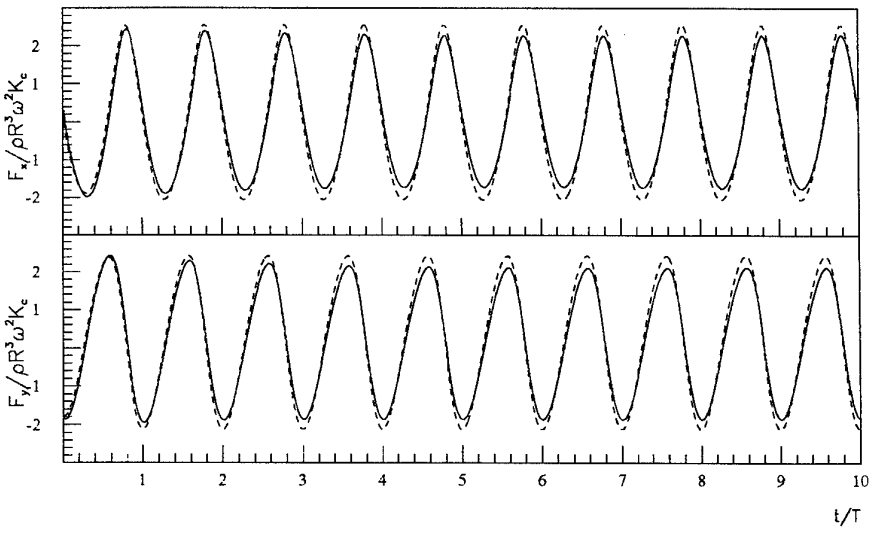

Figure 2: Evolution in time of horizontal (upper plot) and vertical (lower plot) force components ($K_c = 0.75$). Comparison of the viscous (solid lines) and inviscid (dashed lines) solutions.

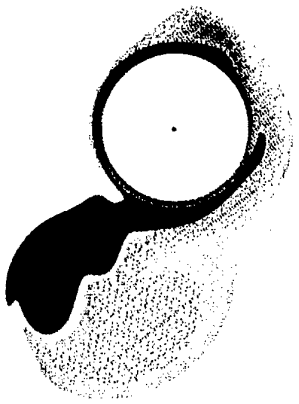

Figure 3: Vorticity field around the circular cylinder at $t/T_S = 10$, $K_c = 0.75$.

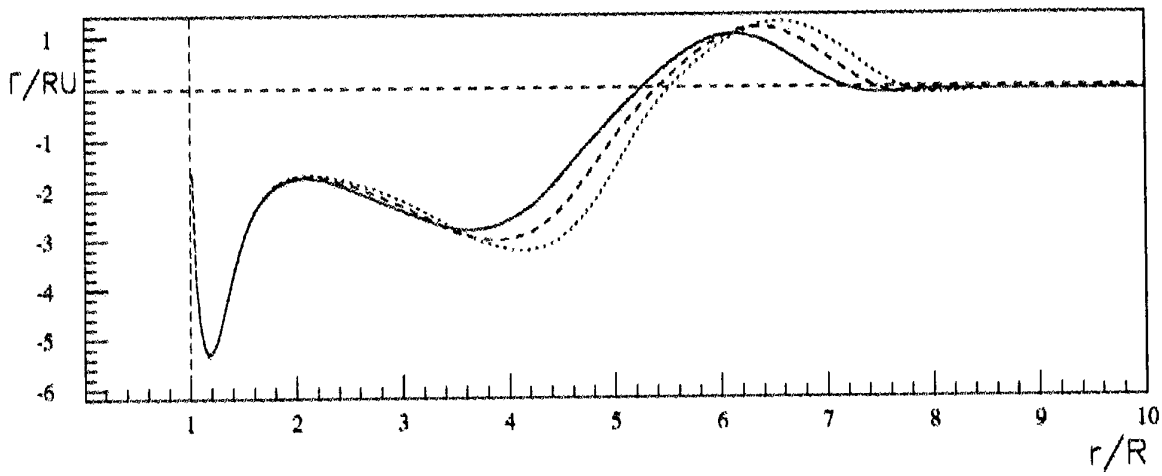

Figure 4: Total mean circulation about circles of increasing radius r ($K_c = 0.75$). The three curves refer to $t/T_S = 18, 19, 20$ (solid, dashed and dotted lines respectively).

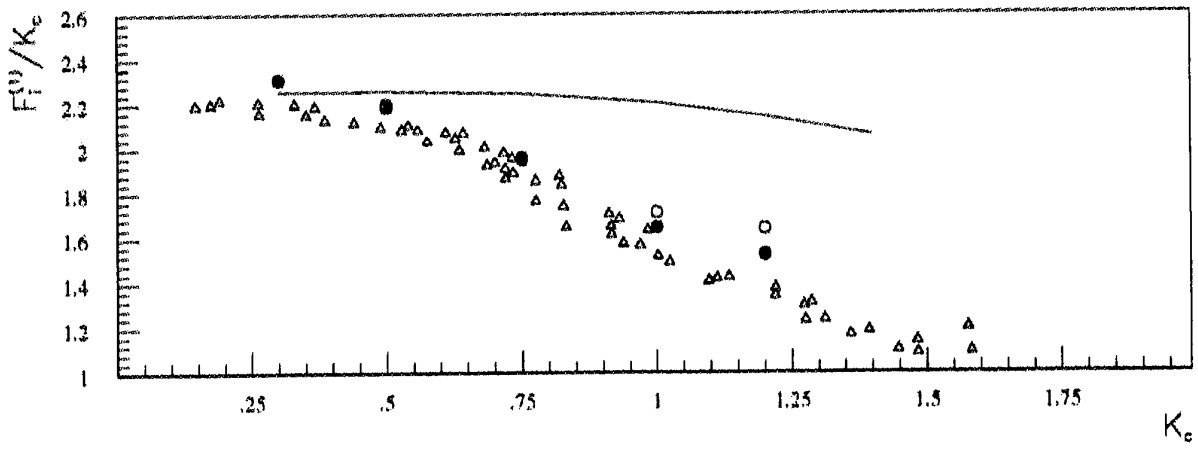

Figure 5: Fundamental spectral component of horizontal and vertical forces on the cylinder. (triangles: Chaplin's data, circles: present viscous solution, solid line: present inviscid solution)

Numerical investigations into non-uniqueness in the two-dimensional water-wave problem

by C.M. Linton
Department of Mathematical Sciences, Loughborough University,
Leicestershire, LE11 3TU, UK

Introduction

The proof, by McIver (1996), of the existence of eigenvalues (trapped modes) in the two-dimensional water-wave problem has answered the general question of uniqueness in the negative but has created many new and interesting questions for investigation. For example, given a particular geometry for which there is no uniqueness proof, we have no general method for determining whether or not eigenvalues exist.

In this work we will consider a class of geometries, namely pairs of symmetrically-placed surface-piercing angled barriers in water of infinite depth, and use an integral equation approach to investigate the existence or otherwise of eigenvalues. This particular class of geometries has been chosen for three reasons. First the problem is not known to be unique, though recent results of N. Kuznetsov (Linton and Kuznetsov 1997) provide ranges of the frequency parameter for which uniqueness is assured. Secondly it is sensible to choose a geometry which shares as many of the characteristics of those computed numerically by McIver (1996) as possible, and her results were for pairs of surface-piercing bodies. Thirdly we must choose a geometry for which mathematical progress can be made. The problem of wave scattering by a single surface-piercing angled barrier has been solved using hypersingular integral equations by Parsons and Martin (1994) and it is their approach that has been followed here.

Formulation

We consider the case of an inclined surface-piercing barrier next to a vertical wall. By symmetry any eigenvalues for this problem will correspond to trapped modes for a pair of symmetrically-placed surface-piercing barriers. The geometry is illustrated in Figure 1. Following Parsons and Martin (1994) we set the problem up as a hypersingular integral equation. Trapped modes then correspond to non-trivial velocity potentials ϕ for which the discontinuity across the plate, $[\phi]$, satisfies

$$\oint\!\!\!\!\!\!-_{\Gamma} [\phi(q)] \frac{\partial^2 G(p,q)}{\partial n_p \partial n_q} \mathrm{d}s_q = 0, \qquad p \in \Gamma,$$

where p and q are points on the plate, Γ, the integral is a Hadamard finite-part integral and $G(P,Q)$ is the standard free-surface Green's function. The free-surface boundary condition satisfied by G is $KG + \partial G/\partial y = 0$ on $y = 0$ and if a trapped mode exists for a particular Ka ($\equiv \omega^2 a/g$) then Ka is the corresponding eigenvalue.

The unknown function $[\phi]$ is approximated as a finite sum of Chebyshev polynomials of the second kind leading to an equation of the form

$$\sum_{n=1}^{N} A_{mn}(Ka, b/a, \theta) c_n = 0, \qquad m = 1, \ldots, N.$$

Eigenvalues correspond to values of Ka for which the determinant of the matrix $\boldsymbol{A}$ with elements A_{mn}, $m, n = 1, \ldots, N$, vanishes in the limit as $N \to \infty$. It is clear that with

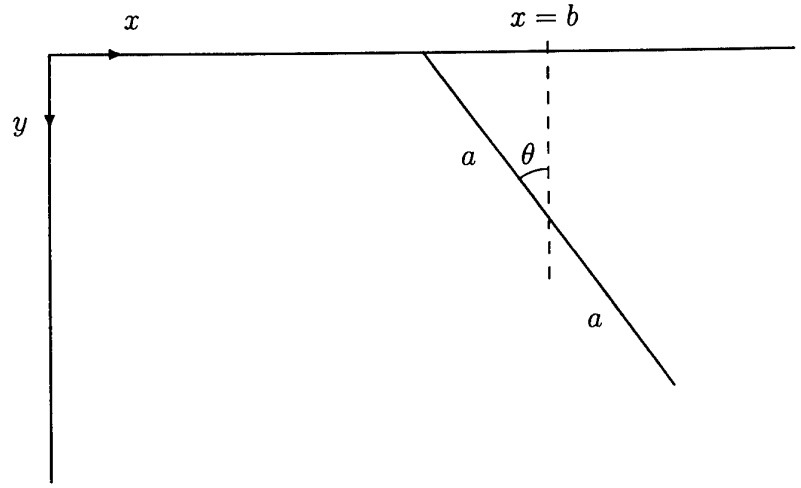

Figure 1: Definition sketch

this approach we are unlikely to be able to *prove* the existence or otherwise of eigenvalues. However we are able to provide strong numerical evidence for the existence of eigenvalues and also to show that if the eigenvalues do indeed exist then they are unstable to perturbations in the geometry in a sense which will be made precise. Even if eigenvalues do not exist, we can show that there are values of Ka in the vicinity of which a related scattering problem has qualitatively different behaviour from that at more typical values.

Results and discussion

A number of results will be presented, both illustrating the powerful evidence for existence of eigenvalues and computations of the eigenvalues themselves. A key point is that the elements of $\boldsymbol{A}$ are complex and so, in general, is its determinant. One way of looking at the problem is to find zeros of the real and imaginary parts of the determinant, which is numerically straightforward as each is a real-valued function which passes through zero, and then to see if these zeros occur at the same point.

For a particular example we fix the inclination of the barrier at $\theta = \pi/4$. The values of Ka at which zeros of the real and imaginary parts of the determinant occur are plotted in Figure 2 for a range of values of b/a. The solid line represents a zero of the real part and the dotted lines represent zeros of the imaginary part. We see that the real part of the determinant has a zero for all values of b/a in the range shown in the figure whereas the imaginary part has a pair of zeros which coalesce and disappear near $b/a = 2.21$. An eigenvalue exists if the lower dotted line actually touches the solid line. The qualitative behaviour shown in the figure is typical.

Numerical results suggest that eigenvalues, if they exist, are *unstable* in the sense that it is possible that an arbitrarily small change to the geometry will cause the eigenvalue to be lost. This is in contrast to previously discovered trapped-mode phenomena in water waves. For example, in the case of a submerged horizontal cylinder, edge waves exist whatever the cross-section and so the geometry can be changed arbitrarily without the eigenvalue disappearing. However in the problem considered here arbitrarily small perturbations to the geometry can lead to the disappearance of an eigenvalue. It is possible, however, to vary b/a and θ at the same time in such a way as to retain the eigenvalue. In other words the numerical evidence suggests that eigenvalues exist on curves in $(b/a, \theta)$ space.

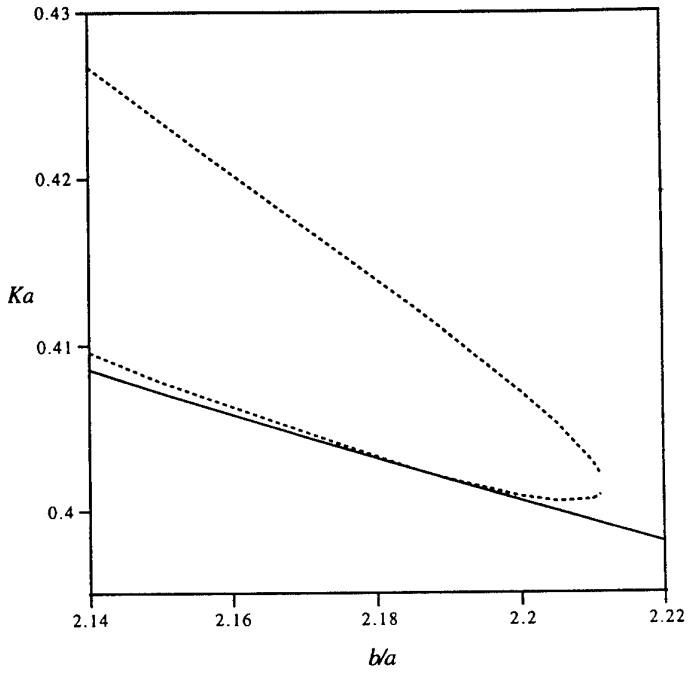

Figure 2: Values of Ka at which the real part (—) and the imaginary part $(\cdots)$ of the determinant vanish.

Simple continuity considerations show that the unstable nature of the eigenvalues is related to the tangential nature of the contact in Figure 2 and to the need to consider a complex-valued determinant rather than a real one (which would be more convenient). This is illustrated schematically in Figure 3. In diagrams a) and b), which are to be compared with Figure 2, the solid curves represent the value of Ka at which the real part of the determinant vanishes and the dotted curves the value at which the imaginary part vanishes. Diagram b) (top) shows the situation as we find it in Figure 2 whereas diagram a) (top) shows the situation where the curves intersect at a non-zero angle. In the lower figures we see the possible effect of a small perturbation. The fact that we observe behaviour like that in case b) suggests that arbitrarily small perturbations exist which totally destroy the eigenvalues.

Diagram c) represents the situation where we are looking for a zero of a real-valued determinant. The horizontal line represents zero and the curve is the value of the determinant. Here again the figures illustrate that provided the determinant passes through zero, sufficiently small perturbations will not destroy the eigenvalue. In our problem this is not the case and diagram d) shows why finding the zero of a complex-valued determinant is then appropriate. The curve again represents the value of the determinant, now plotted in the complex plane, with Ka varying as we move along the curve. In this case the determinant can be displaced from the origin by an arbitrarily small perturbation.

We can also shed light on the situation by considering a circular cylinder on the centreline of a two-dimensional parallel-plate waveguide, as considered by Callan, Linton, and Evans (1991) who showed that trapped modes, antisymmetric about the centreline of the guide, exist for such a geometry. If we impose the antisymmetry the problem reduces to one of finding the zeros of a real determinant and the eigenvalues are stable (in the sense we have used the word in this paper), always remembering that we cannot consider perturbations which

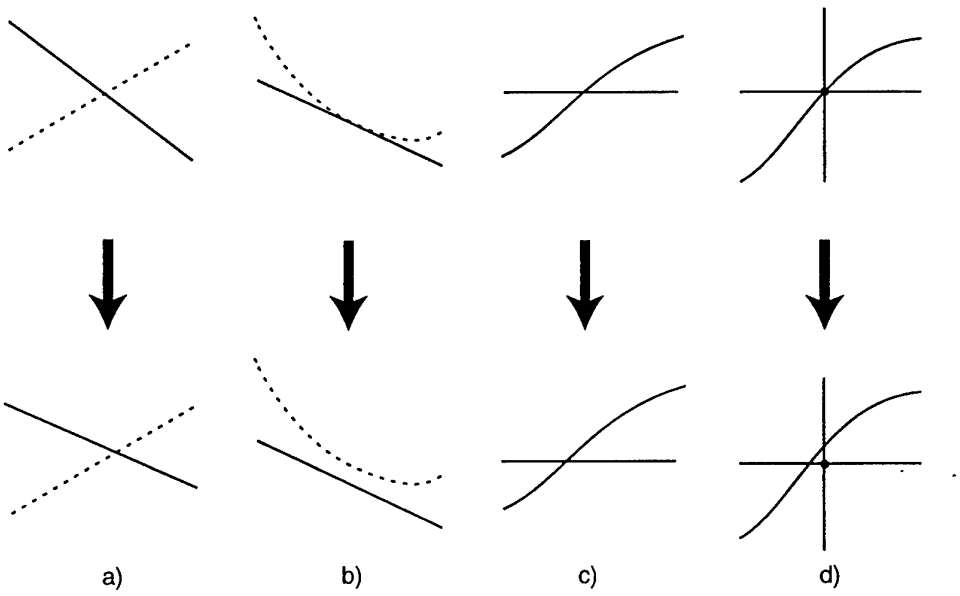

Figure 3: Unstable nature of eigenvalues. See text for details.

destroy the symmetry. This is what we would expect since Evans, Levitin, and Vassiliev (1994) have shown that trapped modes exist for bodies of any shape (subject to some mild restrictions) on the centreline of a waveguide provided the geometry is symmetric about this line. However if we make no assumptions about symmetry, thus allowing us to consider arbitrary perturbations in the geometry, we find that we must consider a complex-valued determinant. Again this is expected since an arbitrarily small displacement of the cylinder from the centreline (a perturbation which destroys the symmetry) causes the eigenvalue to disappear.

References

CALLAN, M. A., LINTON, C. M., & EVANS, D. V. (1991). Trapped modes in two-dimensional waveguides. *J. Fluid Mech.*, **229**, 51–64.

EVANS, D. V., LEVITIN, M., & VASSILIEV, D. (1994). Existence theorems for trapped modes. *J. Fluid Mech.*, **261**, 21–31.

LINTON, C. M., & KUZNETSOV, N. G. (1997). Non-uniqueness in two-dimensional water-wave problems: numerical evidence and geometrical restrictions. Submitted.

MCIVER, M. (1996). An example of non-uniqueness in the two-dimensional linear water wave problem. *J. Fluid Mech.*, **315**, 257–266.

PARSONS, N. F., & MARTIN, P. A. (1994). Scattering of water waves by submerged curved plates and by surface-piercing flat plates. *Applied Ocean Research*, **16**(3), 129–139.

DISCUSSION

Tuck E.O.: Your instability argument is very interesting. However, it is possible that small perturbations might change the "touching" phenomenon in the opposite direction. That is, instead of eliminating the non-uniqueness at a particular wavenumber $k = k_o$, it might create non-uniqueness at two neighbouring frequencies $k = k_o \pm \varepsilon$.

Linton C.M.: Whilst this is true the fact that the eigenvalue also corresponds to a complex-valued function passing through zero suggests that a transition to zero eigenvalues rather than to two is more likely.
Also in other fields, notably quantum mechanics, eigenvalues embedded in the continous spectrum (as those considered in this paper are) are known to be unstable to small perturbations.

Finite Element Analysis of Non-linear Transient Waves in a Three Dimensional Long Tank

Q.W. Ma+, G.X. Wu+ and R.Eatock Taylor++

+ Department of Mechanical Engineering, University College London, Torrington Place, London WC1 7JE, UK

++ Department of Engineering Science, University of Oxford, Parks Road, Oxford OX1 3PJ, UK

Numerical simulation of propagating waves in a tank has been mainly based on the boundary element method (BEM), see for example Cointe[1], Contento *et al* [2], Dold & Peregrine[3].Grilli *et al* [4] and Lin *et al*[5]. Although BEM has many known advantages, its storage and CPU requirement increase at a rate proportional to the square of the number of nodes. Because of this, most analyses based on BEM provided results only for a short tank. Wang *at al* [6] combined a multi-subdomain approach with BEM and dealt with the problem of two dimensional waves in a long tank. It appears, however, that the effectiveness of this approach in three dimensions is less certain.

The finite element method (FEM) has recently been used in the nonlinear transient water wave problem [7,8]. It has been observed that FEM has several advantages for this problem. In particular, its matrix is banded and its influence coefficients can be obtained from the volumes of the elements when the linear shape function is used. It has been noticed [7,8] that FEM normally requires far less CPU and memory than BEM. However when the computational domain increases, these requirements of FEM are still excessive as reported by the authors [8], who adopted domain decomposition to reduce the memory requirement. Since that work, the authors have invested considerable efforts to improve the methodology and the CFD code. Changes are made mainly in two areas. Firstly we have replaced the Gaussian elimination method for solving the matrix equation with an iterative method. In the former method, all the coefficients within the band width have to be stored even if they are zero. In the latter method, however, only those non-zero terms have to be kept. The number of non-zero terms is usually less than one tenth of the band width. Thus the iterative method requires far less memory. Furthermore, zero operations have been eliminated in the iterative method, which makes the computation far more efficient. Also when the iteration is used in the time domain, the initial solution can be taken from that at the last step. All these have improved the efficiency of the computation significantly.

The second change we have made is based on the fact that the wave created by the wavemaker propagates towards the far end gradually. This means that the computational domain can be divided into disturbed and undisturbed domains as shown in Figure 1. In the undisturbed region, the free surface is considered as unchanged and as a result the coefficients corresponding to the nodes in this region can be kept constant.

When these changes were made, the CPU and memory requirement were significantly reduced. We calculated a case with about 203,520 elements and 1,000 time steps in the last ONR conference [8]. It took about 193 hours CPU time. The same job now takes about 10 hours on the same machine.

For the cases considered below, various parameters have been nondimensionalised as follows

$$(x,y,z) \rightarrow d(x,y,z) \quad f \rightarrow (\rho g R_0^2 d) f$$

$$t \rightarrow (d/g)^{1/2} t \qquad \omega \rightarrow (g/d)^{1/2} \omega$$

where d is the water depth, ρ is the density, g is the acceleration due to gravity, ω is the frequency, R_0 is the radius of the cylinder and f is the force acting on the cylinder

The first case considered is the transient wave generated by a wavemaker. The length of the tank is $L = 100d$. The motion of the wave maker is governed by

$$U(t) = a\omega \sin(\omega t)$$

with the frequency $\omega = 1.45$ and the amplitude a=0.016. The total number of elements used in the 3D model is 2,127,943 and the calculation is over 14,400 steps ($\Delta t = 0.021666$). A numerical beach is applied at the far end. The total CPU for this case is about 147 hours on a DEC ALPHA 255^{233}. Figure 2 gives the wave history at the centre point of the tank (x=L/2). It can be seen that the calculated wave remains steady over a long period of time, which means that the reflection has no significant effect on the result yet. Figure 3 provides the wave profiles at two different time steps. The solid line corresponds to t=59T and the dashed line to t=72T (where T is the period of the wavemaker). They coincide with each other very well. However, as can be seen, the amplitude becomes smaller and smaller away from the wavemaker. This may be due to numerical dissipation but it requires further investigation.

The second case considered is a vertical cylinder in a wave tank with length $L = 40.5d$ while the water depth and the motion of the wavemaker are the same as above. The cylinder is placed at the centre of the tank and its diameter is $.05d$. 649,728 elements are used and the calculation is made over 10,000 time steps. The total CPU is 103 hours. Figure 4 gives the horizontal force on the cylinder.

Figure 5 shows the nonlinear effects on the force acting on the cylinder. All parameters are the same as those in figure 4 except the length of the tank has now been taken as 16.5d. The results correspond to three different motion amplitudes of the wavemaker: $a = 0.004, 0.016, 0.032$. The nondimensionalised forces defined above have been here divided by the nondimensionalised amplitude. The figure shows that when the amplitude is 0.032, the non-linear effects on the force become evident. Further results and discussions will be given in the workshop.

Acknowledgements

This work was sponsored by EPSRC through MTD Ltd (Grant ref GR/K80372) and jointly funded with Brown & Root Ltd.

References

[1] Cointe, R. 1990, "Numerical simulation of a wave channel," Eng. Anal. Bound. Elem. Vol.7, pp167-177.

[2] Contento, G. and Casole S., 1995," On the generation and propagation of waves in 2D numerical wave tanks," ISOPE'95, Vol.3 pp10-18.

[3] Dold, J.W. and Peregrine, D.H. 1984, "Steep unsteady waves: an efficient computational scheme," Proc 19th Int Conf. Coastal Eng., ASCE, Houston, I, pp955-967.

[4] Grilli, S.T. , Skourup, J. and Svendsen, A., 1989, "An efficient boundary element method for nonlinear water waves," Eng. Anal. Bound. Elem. Vol.6 pp97-107.

[5] Lin, W.M., Newman, J.N. & Yue, D.K., 1984, " Nonlinear forced motion of floating bodies," Proc. 15th Symp on Naval Hydrodynamics, Hamburg, Germany, pp33-49.

[6] Wang, P., Yao, Y. and Tulin, M.P., 1995, "An efficient numerical tank.for non-linear water waves, based on the multi-subdomain approach with BEM," International Journal for Numerical Method in Fluids, Vol.20, pp1315-1336.

[7] Wu, G.X. and Eatock Taylor, R., 1995, "Time stepping solutions of the two dimensional non-linear wave radiation problem," Ocean Engng, Vol. 22, No. 8, pp 785-798.

[8] Wu, G.X. Ma, Q.W., and Eatock Taylor, R. 1996 "Analysis of interactions between non-linear waves and bodies by domain decomposition", 21st Symposium on Naval Hydrodynamics, Norway.

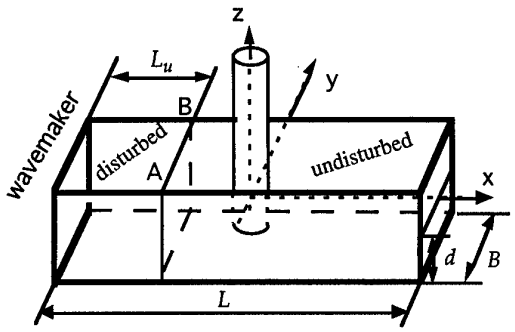

Figure 1 The division of disturbed and undisturbed regions

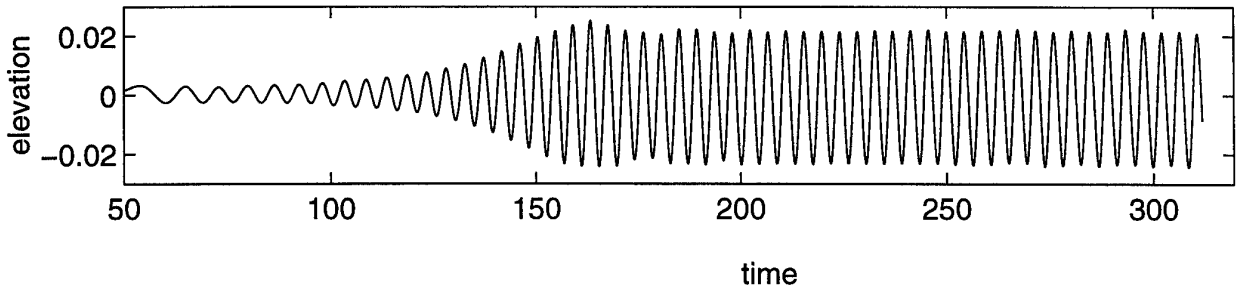

Figure 2. The wave history at the middle point of the tank

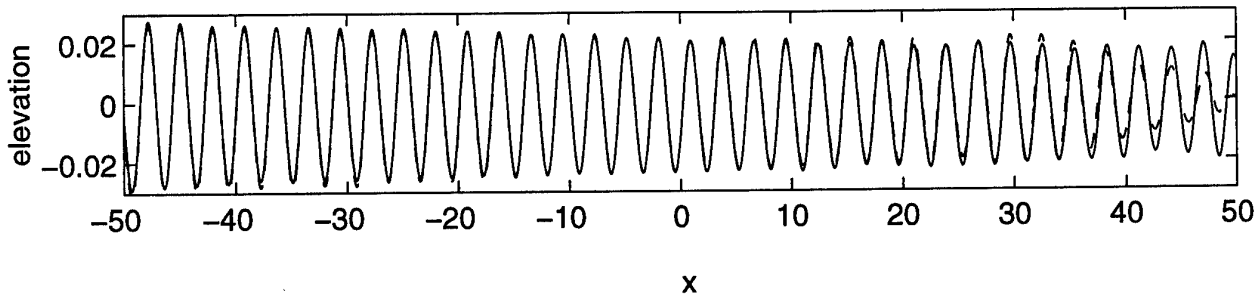

Figure 3 The wave profiles in the longitudinal plane y=0 at two particular time steps
(dashed line: t=59T ; Solid line: t=72T)

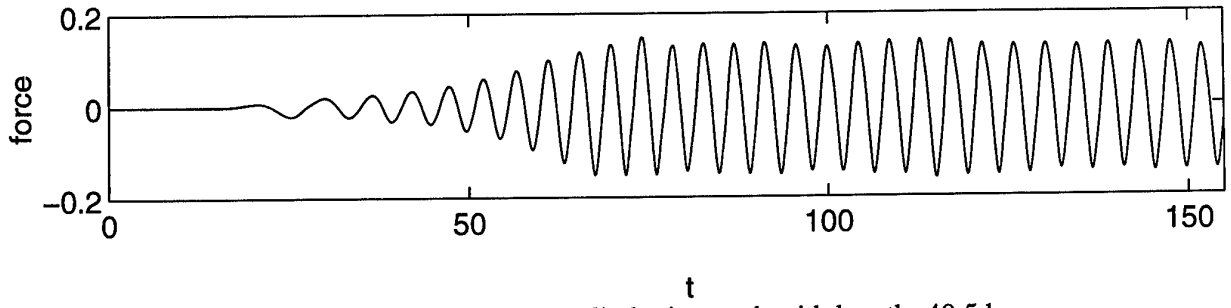

Figure 4 The force history acting on a cylinder in a tank with length=40.5d

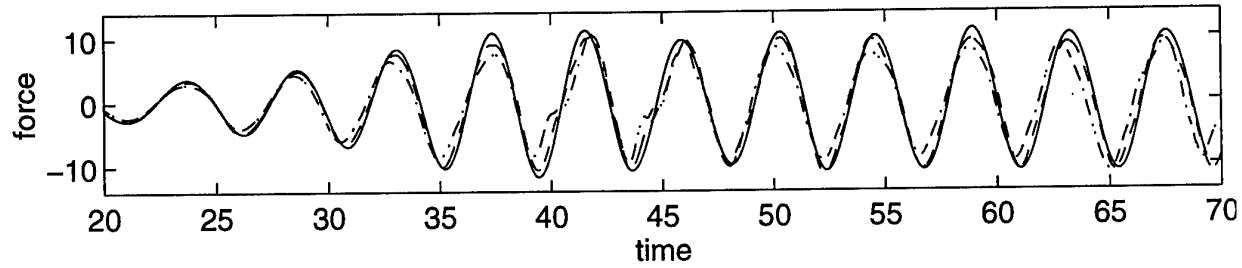

Figure 5 The force history on a cylinder at different motion amplitudes

of the wavemaker(——— a=.004; — — — a=.016; —·—·— a=.032)

DISCUSSION

Molin B.: Aren't you concerned by wall effects in your numerical tank, which seems to be rather narrow?

Ma Q.W., Wu G.X., Eatock Taylor R.: Yes, we would be concerned if these results were intended to simulate the open sea. The wall effects can be reduced by using a wider tank or by applying appropriate lateral beaches (the beach at the far end has been implemented in our work). Our future work will be investigating simulations of the open sea. At this stage we are more concerned by the other challenges of long time simulations. Our current set up is of course similar to what is done in many physical experiments.

Schultz W.: You indicate that regridding is quite dissipative. Have you tried various interpolating schemes during this process?

Ma Q.W., Wu G.X., Eatock Taylor R.: Yes, we have also tried higher order interpolation but the improvement did not meet our expectations, particularly in the case of steep waves. Reducing the amount of remeshing does reduce the dissipation but it may cause numerical instability. Further investigation is needed to find the optimum between remeshing and dissipation.

Grilli S.: I am surprised by your preliminary observation that FEM solutions are more efficient than BEM solutions for a Laplace's equation in 3D. It is my experience and there are results in the literature showing just the opposite, i.e., when comparing similarly accurate solution of a benchmark problem, using two similarly optimized FEM and BEM codes, the BEM method is always faster, sometimes by up to an order of magnitude, than the FEM method. And I am not even talking about multipole expansions that may be used in BEM.
Hence I think you might not have used a properly optimized BEM code in your comparisons (In particular, just dividing the domain in sub-regions with artificial matching boundaries may speed up BEM solutions by a factor equal to the number of sub-regions). Another advantage of the BEM vs FEM is that it is exact inside the domain, due to Green's identity. Can you comment on this?

Ma Q.W., Wu G.X., Eatock Taylor R.: We made our conclusion based on our own experience with BEM and FEM. We made clear that our BEM is not optimised and there might be better ways of programming the BEM code. To the best of our knowledge, however, it has yet to be shown that BEM can achieve the same efficiency as we achieved here. The only work we have seen, which used the multi-subdomain approach, is by Wang, Yao and Tulin (1995) for the 2D long wave tank problem. When the domain decomposition is optimised, the total number of coefficients is about $6M(2N+1)$, where M and N are total numbers of nodes on the free surface and the wave maker, respectively. This is comparable with the 2D version of our FEM, which has about $7MN$ coefficients. There are, however, several important points here:

(1) In our FEM code, the total number of coefficients is always linearly proportional to the total number of nodes, no matter how complicated the fluid domain is. In BEM, it very much depends on the shape of the domain. For example, it will be interesting to see how optimisation can be applied to a square shape or indeed to an arbitrary shape. Similarly, the efficiency of this technique is also uncertain for an arbitrary 3D domain, even for a 3D square wave tank.

(2) Even when the number of coefficients of BEM and FEM becomes comparable, the calculation of FEM coefficients is far more efficient. This is particularly important when millions of nodes are used.

(3) This work is part of our research effort in CFD. We are currently also undertaking research into viscous flows with a free surface. BEM is not applicable in this case.

APPLICATIONS USING A SEAKEEPING SIMULATION CODE

by

Allan Magee
Bassin d'Essais des Carènes

The computer code RATANA has been developed in order to simulate nonlinear and large–amplitude effects in ship motions. (See King, 1990). The present paper reports on progress in the continuing development of this package. The kernel of the code solves a coupled system of equations in body–fixed coordinates (Euler's equation). Various subroutines compute the forces required to solve the equations of motion. In principle, any type of force can be included, for example, Froude–Krylov and hydrostatics, linearised time–domain radiation and diffraction, nonlinear roll damping and active stabilisers. The use of a time–domain solver greatly eases the modeling of nonlinear external forces.

In the large–amplitude approach, adopted here, Froude-Krylov and hydrostatic forces are computed on the instantaneous hull position while the time–domain radiation and diffraction forces are computed using the linearised mean body position. The method is similar to that utilised by Adegeest, 1995 and appears to offer a good compromise between computational time and accuracy of the results produced. In order to use the instantaneous wetted surface in the calculations, the entire hull up to the highest waterline to be immersed must be paneled. The pressure due to the incident wave (Froude-Krylov pressure) is modified by so-called Wheeler stretching (Wheeler, 1970)

$$p_I(x,y,z,t) = \rho g \sum_n A_n e^{k_n(z-\eta_I)} e^{-ik_n(x\cos\beta_n + y\sin\beta_n)} e^{i\omega_n t} \qquad -\infty < z < \eta_I$$

where the incident wave elevation is taken as

$$\eta_I(x,y,t) = \sum_n A_n e^{-ik_n(x\cos\beta_n + y\sin\beta_n)} e^{i\omega_n t}$$

To calculate radiation forces, the impulse response functions can be entered directly if available, or can be obtained by Fourier transform of the added mass and damping coefficients obtained from a frequency–domain code such as DIODORE. A harmonic analysis is employed as a post–processor to decompose the temporal signals of motion, forces or other responses into mean values and harmonics of the fundamental frequency.

Using the mean body position for all the forces and linearising the equations of motion leads to a strictly linear time–domain simulation model. After transients have died out, the linear time–domain model yields purely sinusoidal responses, and the results should be identical to those obtained from frequency–domain calculations as well as to the fundamental component obtained from the large–amplitude model in the limit of vanishing wave amplitude.

Large–amplitude effects become important in roll motion in oblique seas. The effects of separation on active stabilisers with large incidence angles can be modeled. The large–amplitude formulation also appears to give good results for phenomena which are dominated by synchronous pitch motion in head seas. The calculation of drift forces (vertical for submarines, the hydrostatic term for added resistance of surface ships), has been treated with success. Treatment of the slamming problem, where relative motions and velocities in the bow region are important has recently been discussed, Fontaine, *et al.*, 1996.

As an example of calculations using the large–amplitude approach, a typical Naval vessel at 15 knots forward speed in head seas was chosen. A number of simulations in regular waves of varying frequency and amplitude were performed. Figures 1 and 2 show the heave

and pitch transfer functions obtained from the harmonic analysis of the motion signals. The coefficients presented in the figures are the amplitudes of the various harmonic components of the signals normalised by the incident wave amplitude to the appropriate power. For example, for the heave transfer functions the mean, first, second, and third harmonics are denoted η_3^0/A^2, η_3^1/A, η_3^2/A^2, η_3^3/A^3, respectively. Thus normalised, the coefficients vary only slightly as functions of the wave-amplitude. For reasons of confidentiality, the values have been divided by a reference value, denoted $_{max}$, which is dimensionless constant.

The effects of large amplitude motion are strongest at frequencies near the peak of the pitch transfer function corresponding to a wavelength $\lambda = 130m$, or about 1.15 times the ship length, but the heave and pitch motions do not show very strong nonlinearities. For example, at this frequency there is a slight reduction (about 4%) of the peak of the fundamental pitch transfer function for the maximum value of the parameter $\lambda/A = 30$ shown in the figure, corresponding to a wave amplitude of $4.2m$. The mean heave displacement coefficient attains its maximum positive value of approximately 0.035 of the maximum where the coefficient of the fundamental is about 0.5 times the maximum. The mean heave displacement would thus reach less than 30% of the fundamental oscillatory component. The results obtained using the linearised version of the code (denoted 'LIN') are also shown for comparison along with the frequency–domain results. These latter two are in agreement to graphical accuracy.

Recent applications of the large–amplitude method include the calculation of shear forces and bending moments which show nonlinear effects even in moderate seas. Figure 3 shows the contribution of the Froude-Krylov and hydrostatic forces to the vertical shear force at various stations along the hull as functions of time. The frequency chosen corresponds to the maximum of the second harmonic shear force coefficient. The values of the shear forces in still water have been subtracted off, so only the contributions due to unsteady effects are presented. Only the last two periods of the simulation, those used in the harmonic analysis, are shown.

While the heave and pitch motions themselves are not found to be very nonlinear, the shear forces do contain strong mean, double-frequency and higher-order components at all the stations. These are clearly evident for the top figure ($\lambda/A = 30$), but much less so in the bottom figure where the signals appear much more sinusoidal, because of the small wave amplitude.

In figures 4 and 5 the results of the harmonic analysis of the signals at station 5 (solid line in figure 3) are shown. Note that the peak of the second harmonic response (shown in figure 5) is about 23% of the fundamental at the corresponding frequency. Thus, for the same $4.2m$ wave amplitude, the second harmonic component is approximately equal to the fundamental. Experiments are currently being performed on a segemented model of this ship. Comparisons with numerical results will allow assessment of the importance of nonlinenearities in structural loadings and the validition of the present model. If they can be made available, results will be presented at the workshop.

This work is the result of research supported partly by DGA/DRET, under contract number 95/2011 J. This support is gratefully acknowledged.

References

[1] Adegeest, L.J.M. 1995. Nonlinear hull girder loads in ships. Ph.D. Diss. Technical University of Delft.

[2] Fontaine E., L. Boudet, J.F. Leguen and A. Magee, 1996. Impact hydrodynamique d'un corps allongé et plat : Application au tossage. *Sixième Journées de l'Hydrodynamique*, Nantes.

[3] King, B.K. 1990 A Fast numerical solver for large–amplitude ship motions simulations, *The Fourth International Conference on Stability of Ships and Ocean Vehicules*, 299-306, Naples.

[4] Wheeler, J.D. 1970. Method for calculating forces produced by irregular waves, *Journal of Petroleum Technology*, 359-370.

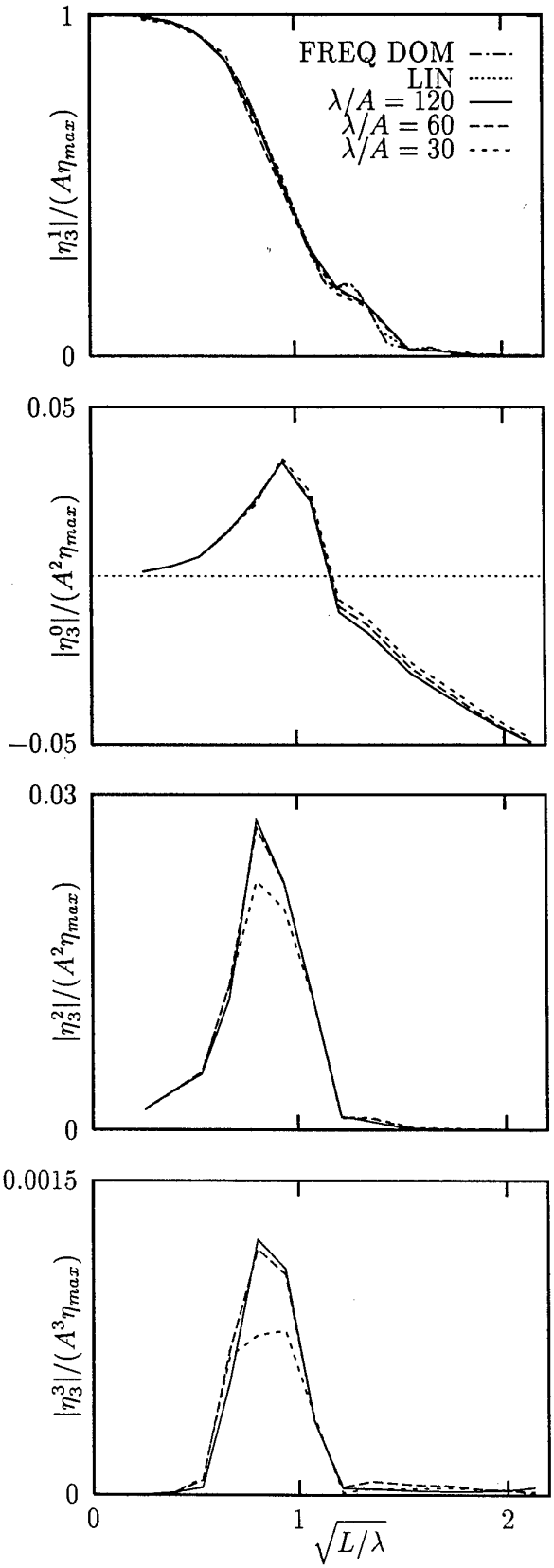

Figure 1: Heave motion transfer functions in head seas at 15 knots

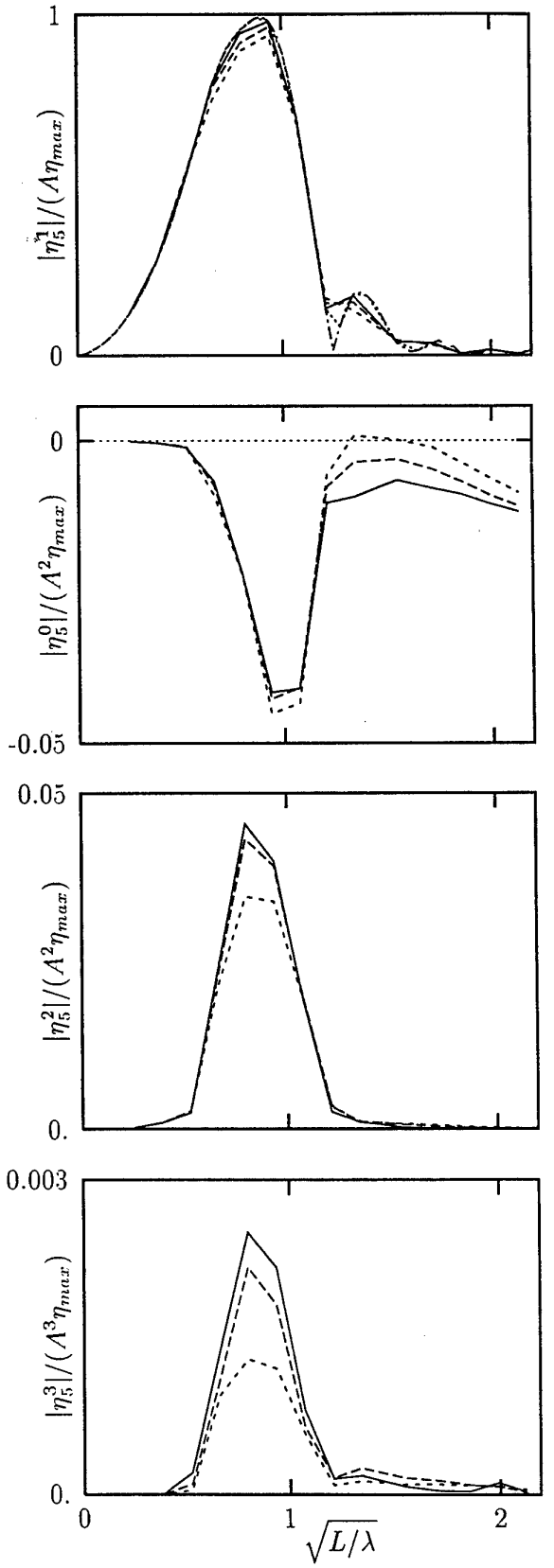

Figure 2: Pitch motion transfer functions in head seas at 15 knots

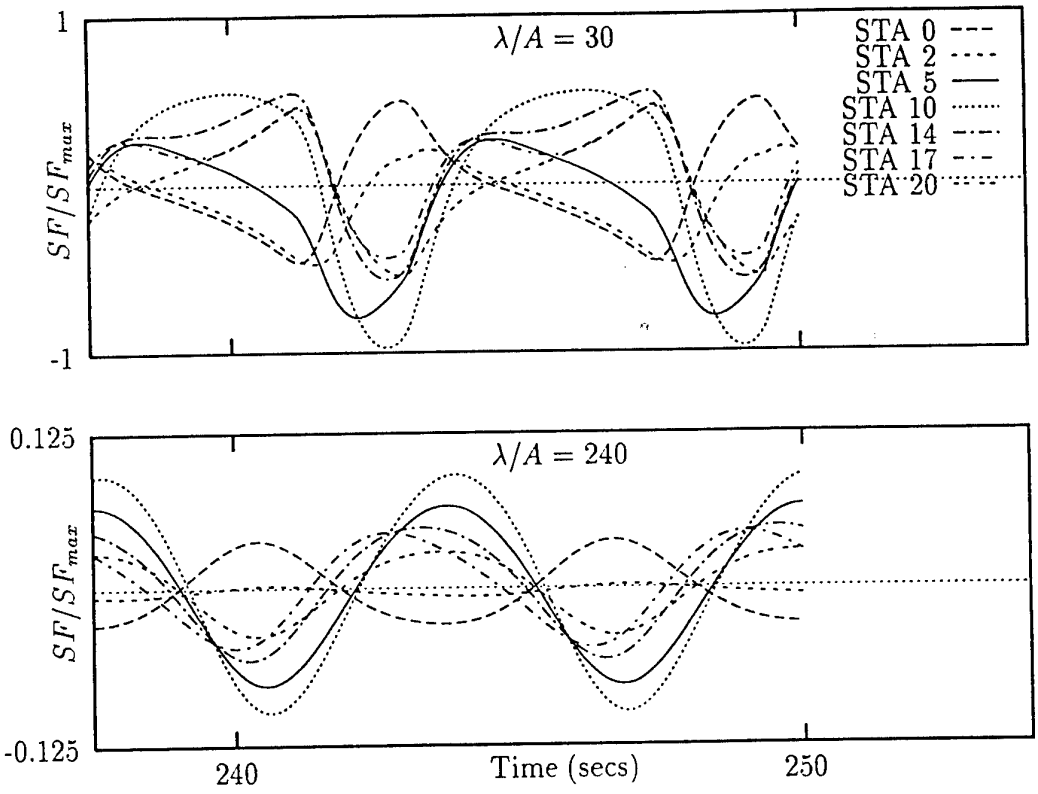

Figure 3: Shear forces versus time at various stations in head seas at 15 knots at two wave amplitudes

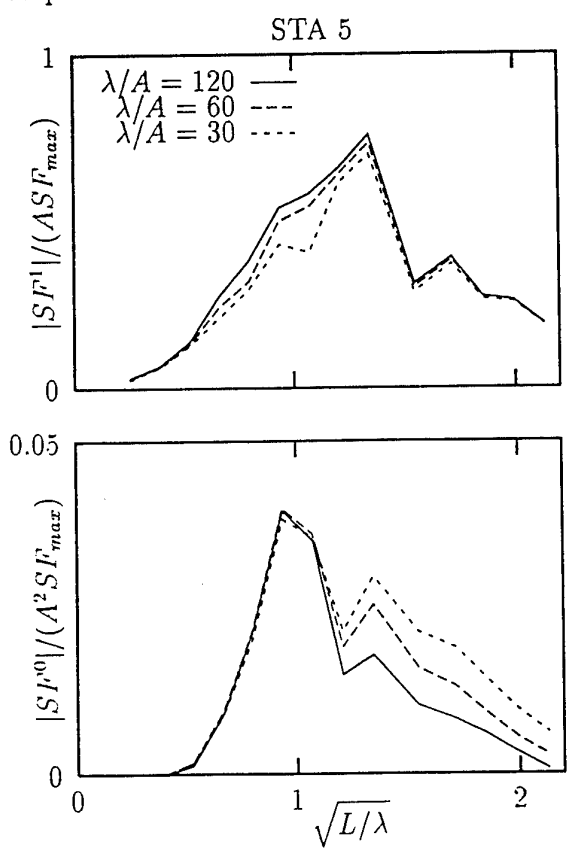

Figure 4: Amplitudes of the mean and first harmonics of the shear force at station 5

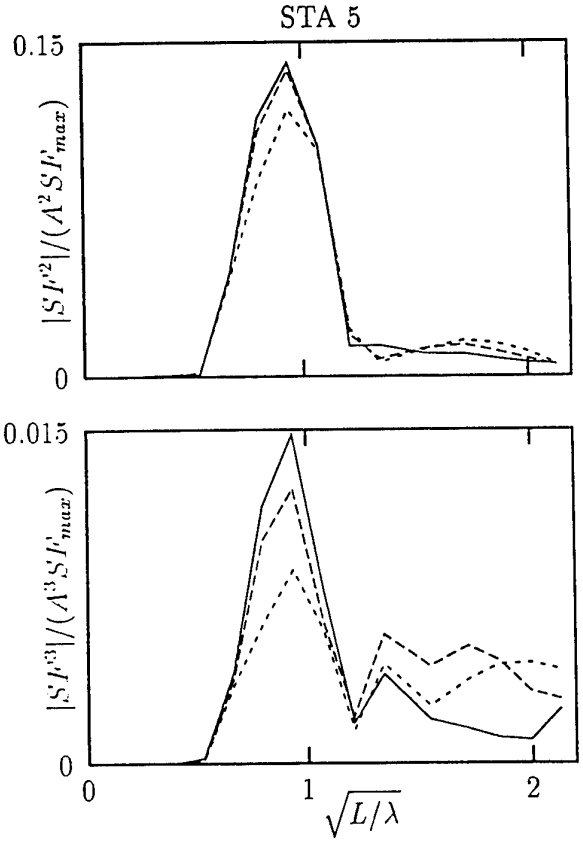

Figure 5: Amplitudes of the second and third harmonics of the shear force at station 5

Higher order wave diffraction of water waves by an array of vertical circular cylinders

Šime MALENICA
Bureau Veritas - CRD, 10 rue Jacques Daguerre
92565 Rueil Malmaison, FRANCE

It is well known that the wave forces exerted on a multicolumn offshore structure (TLP, semi-sub, GBS, ...) can be seriously affected by the effects of interaction between cylinders. The calculation of forces by simply summing the forces for isolated cylinders is usually wrong. As far as the linear theory is considered, there exist today numerous numerical models which calculate these interaction effects correctly. However, at second order there is only few of them and the calculations involved are very time consuming. That is the reason why some authors try to seek for semianalytical solutions, in idealized configurations, which are considerably less expensive and more precise. At first order, this was done by different authors but the most complete methodology was presented in [2]. At second order there are two approachs recently proposed [3,5]. Even if these two methods are similar there are some important differences in the methodology and in the numerical implementation. The purpose of this paper is to discuss more in detail the method proposed in [3] and to give some clarifications about the numerical implementation which has to be adopted in order to support eventual third order calculations.

General methodology

The main difficulty associated with higher order problems is the treatement of the free surface integral which is involved in the solution. The free surface condition, which is the main difficulty of the problem, at higher order is given by :

$$-\alpha\psi+\frac{\partial\psi}{\partial z}=Q \tag{1}$$

and use of any method involves the evaluation of an integral over the entire free surface in order to take account for the forcing term Q. The method that we use to solve this problem is the combination of the Linton and Evans method [2] for first order diffraction for an array of vertical cylinders, and the semi-analytical solution for the second order diffraction by a single cylinder [1,4].
All notations correspond to the following configuration :

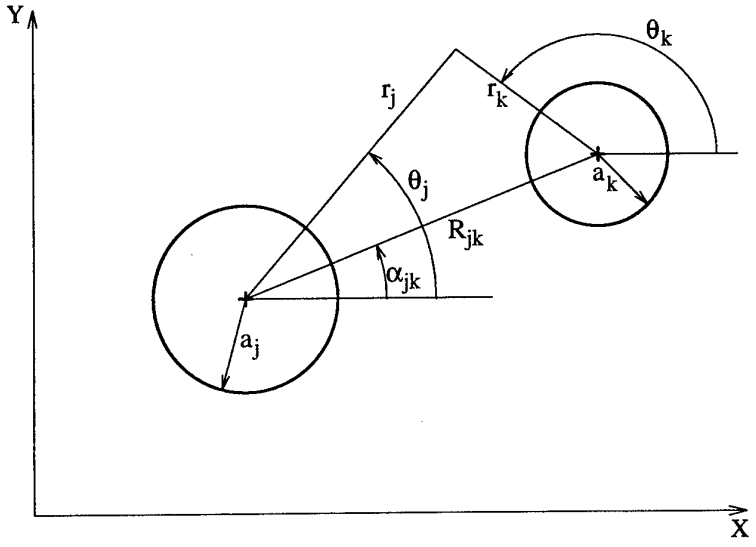

Figure 1. Basic configuration.

The well known Green's identity for one point outside of the fluid domain, can be written (for the sake of clarity we consider homogeneous Neuman boundary condition on the body) :

$$-\iint_{S_{B0}} \psi \frac{\partial G}{\partial n}\, dS = -\iint_{S_F} G\, Q\, dS \tag{2}$$

where ψ is the higher order potential, Q is its forcing term on the free surface and G is the Green function which, in the coordinate system of the k-th cylinder, can be written as :

$$G(r_k,\theta_k,z_k;\rho_k,\upsilon_k,\zeta_k) = \sum_{m=-\infty}^{\infty} \left\{ -\frac{i}{2} C_0 \begin{bmatrix} H_m(\kappa_0 r_k) J_m(\kappa_0 \rho_k) \\ J_m(\kappa_0 r_k) H_m(\kappa_0 \rho_k) \end{bmatrix} f_0(z) f_0(\zeta) \right.$$

$$\left. - \frac{1}{\pi} \sum_{n=1}^{\infty} C_n \begin{bmatrix} K_m(\kappa_n r_k) I_m(\kappa_n \rho_k) \\ I_m(\kappa_n r_k) K_m(\kappa_n \rho_k) \end{bmatrix} f_n(z) f_n(\zeta) \right\} e^{im(\theta_k - \upsilon_k)} \quad ; \quad \begin{bmatrix} r_k > \rho_k \\ r_k < \rho_k \end{bmatrix} \tag{3}$$

where $\kappa_0 \tanh\kappa_0 H = -\kappa_n \tan\kappa_n H = \alpha$, H being the water depth, and :

$$f_0(z) = \frac{\cosh\kappa_0(z+H)}{\cosh\kappa_0 H} \quad ; \quad f_n(z) = \frac{\cos\kappa_n(z+H)}{\cos\kappa_n H} \quad ; \quad C_0 = [2\int_{-H}^{0} f_0^2(z)dz]^{-1} \quad ; \quad C_n = [2\int_{-H}^{0} f_n^2(z)dz]^{-1} \tag{4}$$

We develop now the potential on the k-th cylinder in the eigenfunction expansion as follows :

$$\psi^k = \sum_{m=-\infty}^{\infty} [B_{m0}^k f_0(\zeta) + \sum_{n=1}^{\infty} B_{mn}^k f_n(\zeta)]\; e^{im\upsilon_k} \tag{5}$$

After writing the equation (2) for one point inside the cylinder $k \rightarrow (r_k = a_k - \delta\,,\ 0 < \delta \le a_k)$, carrying out the integration by ζ, using the orthogonality of the functions $f_n(z)$, using the Graff's addition theorem for Bessel functions, exploiting the orthogonality of the functions $e^{im\theta}$ and rearranging the different terms we obtain for the part associated with the B_{m0}^k coefficients :

$$B_{m0}^k + \sum_{j\neq k} \frac{a_j}{a_k} \sum_{n=-\infty}^{\infty} B_{n0}^j \frac{J_n'(\kappa_0 a_j)}{H_m'(\kappa_0 a_k)} H_{n-m}(\kappa_0 R_{jk}) e^{i(n-m)\alpha_{jk}}$$

$$= -\frac{C_0}{\pi a_k \kappa_0 H_m'(\kappa_0 a_k)} \int\int_{S_F} H_m(\kappa_0 \rho_k) e^{-im\upsilon_k} Q(\rho_k,\upsilon_k) dS \quad , \quad k=1,N \quad ; \quad m=-\infty,\infty \tag{6}$$

This expression represent the final system of equations for the unknown coefficients B_{m0}^k.
Similarly the expression for the coefficients B_{mn}^k can be obtained :

$$B_{mn}^k + \sum_{j\neq k} \frac{a_j}{a_k} \sum_{l=-\infty}^{\infty} B_{ln}^j \frac{I_l'(\kappa_n a_j)}{K_m'(\kappa_n a_k)} (-1)^l K_{l-m}(\kappa_n R_{jk}) e^{i(l-m)(\alpha_{jk}-\pi)}$$

$$= -\frac{C_n}{\pi a_k \kappa_n K_m'(\kappa_n a_k)} \int\int_{S_F} K_m(\kappa_n \rho_k) e^{-im\upsilon_k} Q(\rho_k,\upsilon_k) dS \quad , \quad k=1,N \quad ; \quad m=-\infty,\infty \tag{7}$$

Second order diffraction

The main difficulty in solving the above equations is the evaluation of the free surface integrals which should exclude the cylinder surfaces. In order to minimize the 2D integration the following procedure can be adopted for 4 equaly spaced cylinders :

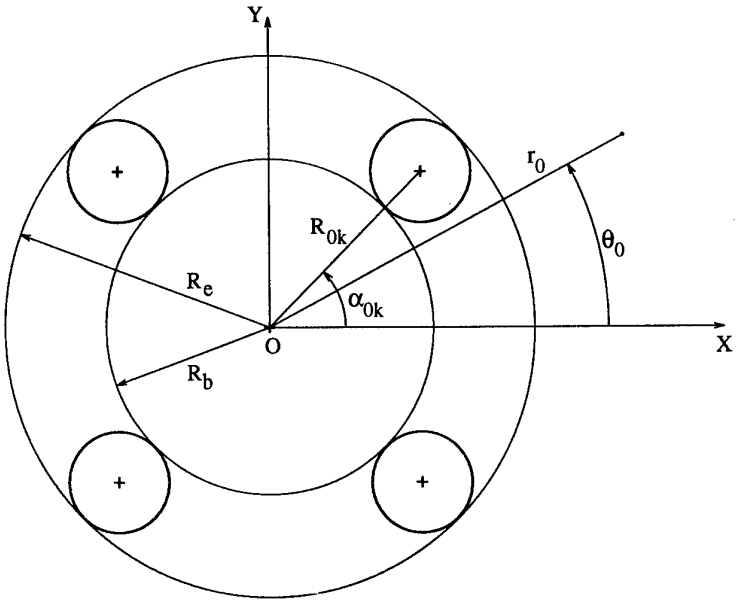

Figure 2. Differents regions for integration.

We recall the first order solution [2] :

$$\phi_I = -\frac{igA}{\omega} f_0(z) \sum_{m=-\infty}^{\infty} e^{im(\pi/2-\beta)} J_m(k_0 r_0) e^{im\theta_0} \quad ; \quad \phi_D = f_0(z) \sum_{k=1}^{N} \sum_{m=-\infty}^{\infty} A_m^k Z_m^k H_m(k_0 r_k) e^{im\theta_k} \tag{8}$$

and the expression for the forcing term Q in the second order diffraction problem :

$$Q_D^{(2)} = \frac{i\omega}{2g}(3\nu^2 - k_0^2)(\phi_D\phi_D + 2\phi_I\phi_D) + \frac{i\omega}{g}(\nabla_0\phi_D\nabla_0\phi_D + 2\nabla_0\phi_I\nabla_0\phi_D) \tag{9}$$

Using the Graff's theorem we can write the first order diffraction potential ϕ_D in the global coordinate system (X,Y) i.e. in terms of (r_0,θ_0) :

$$\phi_D = f_0(z) \sum_{m=-\infty}^{\infty} \left\{ \sum_{k=1}^{N} \sum_{n=-\infty}^{\infty} A_n^k Z_n^k H_{n-m}(k_0 R_{0k}) e^{i(n-m)(\alpha_{0k}-\pi)} \right\} J_m(k_0 r_0) e^{im\theta_0} \qquad r_0 \le R_b \tag{10}$$

$$\phi_D = f_0(z) \sum_{m=-\infty}^{\infty} \left\{ \sum_{k=1}^{N} \sum_{n=-\infty}^{\infty} A_n^k Z_n^k J_{n-m}(k_0 R_{0k}) e^{i(n-m)(\alpha_{0k}-\pi)} \right\} H_m(k_0 r_0) e^{im\theta_0} \qquad r_0 \ge R_e \tag{11}$$

This allows us to write the forcing term $Q_D^{(2)}$ in the form (in the regions $r_0 \le R_b$ and $r_0 \ge R_e$) :

$$Q_D^{(2)} = \sum_{m=-\infty}^{\infty} Q_{Dm}^{(2)}(r_0) e^{im\theta_0} \tag{12}$$

At the same time we write the term $H_m(\kappa_0\rho_k)e^{-im\upsilon_k}$ [eqn. (6)] in terms of (ρ_0,υ_0) [similar procedure apply for $K_m(\kappa_n\rho_k)e^{-im\upsilon_k}$ in eqn. (7)]:

$$H_m(\kappa_0\rho_k)e^{-im\upsilon_k} = \sum_{n=-\infty}^{\infty} H_{m-n}(\kappa_0 R_{0k}) e^{i(m-n)(\pi-\alpha_{0k})} J_n(\kappa_0\rho_0) e^{-in\upsilon_0} = \sum_{n=-\infty}^{\infty} \alpha_{mn}^k J_n(\kappa_0\rho_0) e^{-in\upsilon_0} \qquad \rho_0 < R_{0k} \tag{13}$$

$$H_m(\kappa_0\rho_k)e^{-im\upsilon_k} = \sum_{n=-\infty}^{\infty} J_{m-n}(\kappa_0 R_{0k}) e^{i(m-n)(\pi-\alpha_{0k})} H_n(\kappa_0\rho_0) e^{-in\upsilon_0} = \sum_{n=-\infty}^{\infty} \beta_{mn}^k H_n(\kappa_0\rho_0) e^{-in\upsilon_0} \qquad \rho_0 > R_{0k} \tag{14}$$

The free surface integral in (6) is now divided into three parts :

$$\iint_{S_F} = \int_0^{2\pi}\int_0^{R_b} + \iint_{S_d} + \int_0^{2\pi}\int_{R_e}^{\infty} \tag{15}$$

where S_d is the surface between R_b and R_e without cylinder surfaces.
In the first and third integral, the integration by υ can be carried out explicitely :

$$\int_0^{2\pi}\int_0^{R_b} H_m(\kappa_0\rho_k)e^{-im\upsilon_k} Q_D^{(2)}\rho_0 d\rho_0 d\upsilon_0 = 2\pi \sum_{n=-\infty}^{\infty} \alpha_{mn}^k \int_0^{R_b} J_n(\kappa_0\rho_0)Q_{Dn}^{(2)}(\rho_0)\rho_0 d\rho_0 \tag{16}$$

$$\int_0^{2\pi}\int_{R_e}^{\infty} H_m(\kappa_0\rho_k)e^{-im\upsilon_k} Q_D^{(2)}\rho_0 d\rho_0 d\upsilon_0 = 2\pi \sum_{n=-\infty}^{\infty} \beta_{mn}^k \int_{R_e}^{\infty} H_n(\kappa_0\rho_0)Q_{Dn}^{(2)}(\rho_0)\rho_0 d\rho_0 \tag{17}$$

In this way we reduced the 2D integration to 1D and, in the same time, the most difficult integral (from R_e to ∞) is put in the same form as in the single cylinder case and the same method can be used for its evaluation. So the only "real" 2D integral evaluation needed is over the surface S_d, and since this surface is relatively small, this integration can be done with little computational effort.
Knowing the second order potential on the surfaces of the cylinders, the second order potential at any point in the fluid can be calculated by using the Green's theorem :

$$\psi_D^{(2)} = \sum_{j=1}^{N} 2\pi a_j \sum_{m=-\infty}^{\infty} [B_{m0}^j \frac{i\kappa_0}{4} J_m'(\kappa_0 a_j) f_0(z) H_m(\kappa_0 r_j) + \sum_{n=1}^{\infty} B_{mn}^j \frac{\kappa_n}{2\pi} I_m'(\kappa_n a_j) f_n(z) K_m(\kappa_n r_0)] e^{im\theta_j} - \iint_{S_F} G Q_D^{(2)} dS \tag{18}$$

The reduction to the global coordinate system (r_0,θ_0), in the free surface integral, can again be very useful.

What about third order ?

The task seems to be very difficult, but not hopeless. If we are interested only in the forces we can use the well known Haskind relations to avoid the explicit calculation of the third order potential :

$$F_{3j}^{(3)} = \iint_{S_B} \psi_D^{(3)} N_j dS = -\iint_{S_B} \frac{\partial \psi_I^{(3)}}{\partial n} dS + \iint_{S_F} \phi_j Q_D^{(3)} dS \tag{19}$$

where $F_{3j}^{(3)}$ is the part of the third order forces induced by the third order diffraction potential $\psi_D^{(3)}$, $\psi_I^{(3)}$ is the third order incident potential, ϕ_j is the assisting radiation potential and $Q_D^{(3)}$ is the third order forcing term [4].
The main problem in the evaluation of this forces is the calculation of the free surface integral which requires the knowledge of the second order potential and some of its derivatives over the entire free surface. Even if the expression (18) can be used directly for the calculation of the potential $\psi_D^{(2)}$, some important numerical problems (treatement of the logaritmic singularity at the free surface, calculation of the derivatives, problems of convergence, ...) should be solved, and this is a rather complicated task.

References

[1] CHAU F.P., EATOCK TAYLOR R., 1992. : "Second order wave diffraction by a vertical cylinder", J.Fluid Mech., Vol.240, pp. 571-599.

[2] LINTON C.M., EVANS D.V., 1990. : "The interaction of waves with arrays of vertical circular cylinders", J.Fluid Mech., Vol.215, pp. 549-569.

[3] MALENICA S., 1995. : "Second order wave diffraction for an array of vertical cylinders", Note Bureau Veritas 95-10c.

[4] MALENICA S., MOLIN B., 1995 : "Third harmonic wave diffraction by a vertical cylinder", J.Fluid Mech., Vol. 302, pp. 203-229.

[5] HUANG J.B., EATOCK TAYLOR R., 1996. : "Second-order interaction between waves and multiple bottom-mounted vertical circular cylinders", 11th WWWFB, Hambourg, Germany.

Wave tank simulations using a fractional-step method in a cell-centered Finite Volume Implementation

Stefan Mayer, Antoine Garapon and Lars Sørensen
International Research Centre for Computational Hydrodynamics (ICCH),
Agern Allé 5, DK-2970 Hørsholm, Denmark, e-mail: icch@dhi.dk

Introduction. Many attempts have been made in the past to solve the unsteady incompressible Euler or Navier Stokes equations with full nonlinear free surface description, without the assumption of irrotational flow and use of the Bernoulli type dynamic boundary condition. Unfortunately, it seems that these methods usually have suffered from relatively large numerical errors and especially numerical damping, which did not allow accurate long term simulations of travelling gravity waves, see e.g. Tsai and Yue (1996) [4].

Here, an attempt is made to extend the application range of free surface Euler equations, so that unsteady wave problems can be simulated with accuracies, which are comparable to those of potential flow methods. In the present paper, the method has been applied to travelling waves in channels with submerged bars, and results are compared to experimental data. Furthermore, steady currents are introduced and wave current interaction is described, including wave blocking conditions.

Method. The two-dimensional Euler equations,

$$\nabla \cdot \boldsymbol{u} = 0, \tag{1}$$

$$\frac{\partial \boldsymbol{u}}{\partial t} + \boldsymbol{u} \cdot \nabla \boldsymbol{u} = -\nabla p, \tag{2}$$

are solved for the Cartesian velocity $\boldsymbol{u} = (u_x, u_y)$ and dynamic pressure p. The usual inviscid dynamic boundary conditions are imposed,

$$p = \rho g \eta\ , \quad \nabla \boldsymbol{u} \cdot \boldsymbol{n} = 0, \tag{3}$$

η denoting the free surface elevation and $\boldsymbol{n}$ being the surface normal vector. The kinematic boundary condition is expressed in terms of the local volume flux $f = \boldsymbol{u} \cdot \boldsymbol{n}$ through the free surface

$$\frac{d\eta}{dt} = \frac{df}{dn_y}. \tag{4}$$

A finite volume code employing a cell-centered variable layout on general curvilinear grids has been extended by the arbitrary Lagrangian Eulerian (ALE) formulation [1] expressing the discretized mass and momentum balance equations on a time-varying grid in a conservative formulation. The elevation η is discretized at every grid cell face along the free surface, and (4) is then integrated in time by an explicit Adam Moulton third order multistep method. An adaptive curvilinear grid is generated algebraically and the time integration of the fluid motion is performed by a second order fractional step method, to some extend following Zang et al. (1994) [5]. Assuming that solutions for velocity and pressure exist up to time step t^n, and grid and boundary conditions have been set for t^{n+1}, the velocity field at time t^{n+1} is split into a predictor velocity field $\boldsymbol{u}^*$ and an irrotational correction $\nabla\phi$,

$$\boldsymbol{u}^{n+1} = \boldsymbol{u}^* + \nabla\phi. \tag{5}$$

$\boldsymbol{u}^*$ is updated by time-integrating to second order the momentum equations (2)

$$\begin{aligned} \frac{\boldsymbol{u}^* - \boldsymbol{u}^n}{\Delta t} &+ \frac{1}{2}((\boldsymbol{u}_g(\nabla \boldsymbol{u}^*) + \boldsymbol{u}_g(\nabla \boldsymbol{u}^n)) \\ &= \frac{3}{2}\nabla p^n - \frac{1}{2}\nabla p^{n-1} \\ &- \frac{3}{2}(\boldsymbol{u}(\nabla \boldsymbol{u}))^n - \frac{1}{2}(\boldsymbol{u}(\nabla \boldsymbol{u}))^{n-1}, \end{aligned} \tag{6}$$

employing QUICK interpolation for the convective terms. The grid velocity $\boldsymbol{u}_g$ reflects the motion of grid lines from time step n to $n+1$ according to the ALE approach. The correction $\nabla\phi$ is determined by restricting $\boldsymbol{u}^{n+1}$ to satisfy the continuity equation (1), hence

$$\nabla^2\phi = -\nabla \boldsymbol{u}^*. \tag{7}$$

The pressure is computed by the divergence of the momentum equation (2)

$$\nabla^2 p^{n+1} = -\nabla \cdot (\boldsymbol{u} \cdot \nabla \boldsymbol{u})^{n+1}, \tag{8}$$

together with boundary condition (3). While the implicit part of the discretized momentum equation (6) is solved iteratively by either point- or line-relaxation, the Poisson equations (7) and (8) are solved by a standard multigrid method.

Waves are generated by imposing second order Stokes velocity profiles at one side of the fluid domain of the form

$$u_x = (U_1(y)\sin(\varphi) + U_2(y)\sin(2\varphi)), \qquad (9)$$

with $\varphi = \omega t + \theta$. At the opposite end both the elevation η and the fluid velocity $\boldsymbol{u}$ are relaxed at every timestep towards prescribed values, η_p and $\boldsymbol{u}_p$, respectively, by following procedure

$$\eta = (1-\alpha)\eta + \alpha\eta_p\ ,\ \ \boldsymbol{u} = (1-\alpha)\boldsymbol{u} + \alpha\boldsymbol{u}_p. \quad (10)$$

α denotes a relaxation parameter, which increases softly as the waves are entering into the numerical sponge layer.

Results. The method has been tested for standing and travelling waves in both deep and shallow water. With numerical resolutions in time and space of $L/\Delta x >= 50$ and $T/\Delta t >= 50$, respectively, the linear dispersion relation is fulfilled to an accuracy better than 1%. Errors in mass conservation can be neglected in all cases, because the kinematic condition is expressed in terms of the local volume flux and the discretization of the transport equations is conservative. However, since in contrast to potential flow methods, no energy equation is solved, but energy balance has to emerge out of the numerical solution of mass and momentum transport equations, the main problem are errors in energy conservation. With a resolution of $L/\Delta x \approx 50$ and $T/\Delta t \approx 50$ about 0.5% of the energy of a deep water standing wave is dissipated during a wave period. Using $L/\Delta x \approx 50$ and $T/\Delta t \approx 100$ that number is decreased to about 0.1%.

The method has been used to study the propagation of regular incident waves with period $T = 2.02$ s and height $H = 0.02$ m over a submerged bar on a horizontal bottom, see Fig. 1, this test being investigated experimentally by Luth et al. (1994) [2]. On the upward slope the incoming waves are shoaling, nonlinearity hereby generating bound higher harmonics, which travel phase locked to the primary wave. On the downward slope these harmonics are released as free waves resulting in an irregular wave pattern.

In the simulation waves are generated for 80 s in fluid initially being at rest. The computed elevation history and its Fourier transform has been compared to measurements at selected locations, see Figs. 2 and 3. On the upward slope good agreement with measurements is found, the nonlinear shoaling process being well described even with rather coarse discretization. On the lee side of the bar fine spatial discretization is required to resolve the released higher harmonic waves, which are otherwise damped by numerical dissipation. However, given sufficient discretization, the model describes phase accurate the resulting irregular wavetrain behind the bar.

In a channel with a submerged bar a steady current is introduced by modifying the sponge layer and the wave generating boundary condition, see Fig. 4. The local Froude number on top of the bar takes values of about $Fr \approx 0.4$. Waves of height $H = 0.005$ m and with periods $T = 2$ s and $T = 1$ s, respectively, are generated during 100 s and propagate against the mean flow direction. In the case, $T = 2$ s waves travel in close agreement with linear theory with regard to amplitude and wave number, almost recovering to their initial shape after the bar, see Fig. 5.

In the case of $T = 1$ s, however, waves are blocked on the upward slope, since the current velocity exceeds the group velocity of the wave. The blocking point agrees precisely to the location estimated by linear wave theory. In order to resolve more closely the blocking process, discretization is refined to $\Delta t = 0.005$ s and $\Delta x \approx 0.01$ m around the blocking point and waves with initial heights of both $H = 0.001$ m and $H = 0.005$ m are generated. The elevation profile clearly shows the incoming wave to be superposed by short reflected waves, with wavelength being shortened with increasing depth and dissipated by numerical damping, see Fig. 6.

Integral mass and energy equations can be solved to estimate the mean velocity U and the mean elevation η_m as function of the horizontal position x. The expression for the apparent frequency

$$\sigma = \omega + kU\ ,\ \ \sigma = 2\pi/T, \qquad (11)$$

can then be solved together with the linear dispersion relation,

$$\omega^2 = gk\tanh k(h+\eta_m), \qquad (12)$$

having two solutions for k, the smaller k_i being the wave number of the Doppler shifted incident wave, and the greater k_r being the wave number of the reflected wave, if blocking occurs, see e.g. [3].

By identifying the wave crests in the computed elevation profile $\eta(x)$, or the vertical fluid velocity $u_y(x)$, respectively, the wave number of the reflected wave is estimated as function of x, see Fig. 8. The estimated wave numbers are seen to be scattered, but found in average to follow quite closely the theoretical estimate. The scattering increases with the increasing initial height of the generated wave, and seems to be due to the Doppler shift, by which the incident waves influence the shorter reflected waves.

Conclusion A finite volume code employing a modified fractional step method has been applied to

unsteady, incompressible free-surface flow. The numerical damping characteristics are not good compared to state of the art potential flow methods using equivalent resolution in time and space. However, the numerical accuracy in the present method is sufficiently good to allow phase-accurate simulation of nonlinear 2D waves within $O(100)$ wave lengths or wave periods, which we believe is an improvement compared to results in the past. Both steady and non steady rotational currents can be introduced directly, the example of wave blocking being a demonstration of the special capabilities of the present method.

The method is intended to be a supplement for investigation of interaction of wave motion with other processes as wave-current interaction, interaction with laminar and turbulent bottom boundary layers, etc. Finally, we believe that the present method is a good basis on which models describing the effect of wave breaking on wave driven currents, turbulence, etc., can be developed.

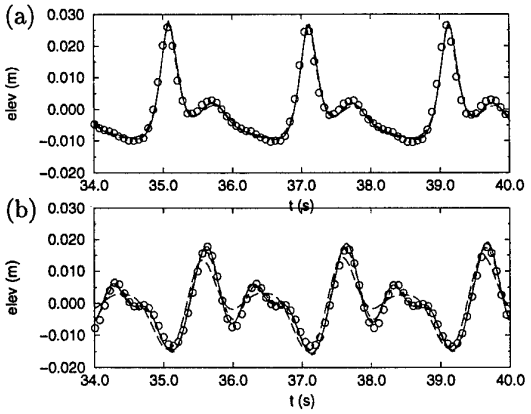

Figure 2: Surface elevations as funtion of time of waves propagating over submerged bar, see Fig. 1. (a) $x = 13.5$ m (top of bar), (b) $x = 21$ m, (behind bar). (o) meas., Luth et al. (1994), (----) comp., $\Delta x = 0.015$ m, $\Delta t = 0.01$ s, (- - - -) comp., $\Delta x = 0.03$ m, $\Delta t = 0.02$ s, (-- -- --) comp., $\Delta x = 0.06$ m, $\Delta t = 0.04$ s.

References

[1] R. K. C. Chan. *J. Comput. Phys.*, 17:311–331, 1975.

[2] H. R. Luth, G. Klopman, and N. Kitou. Technical Report H1573, Delft Hydraulics, 1994.

[3] D. H. Peregrine. *Adv. in Appl. Mech.*, 16:10–117, 1976.

[4] W. Tsai and D. K. P. Yue. *Ann. Rev. Fluid. Mech.*, 28:249–78, 1996.

[5] Y. Zang, R. L. Street, and J. R. Koseff. *J. Comput. Phys.*, 114:18–33, 1994.

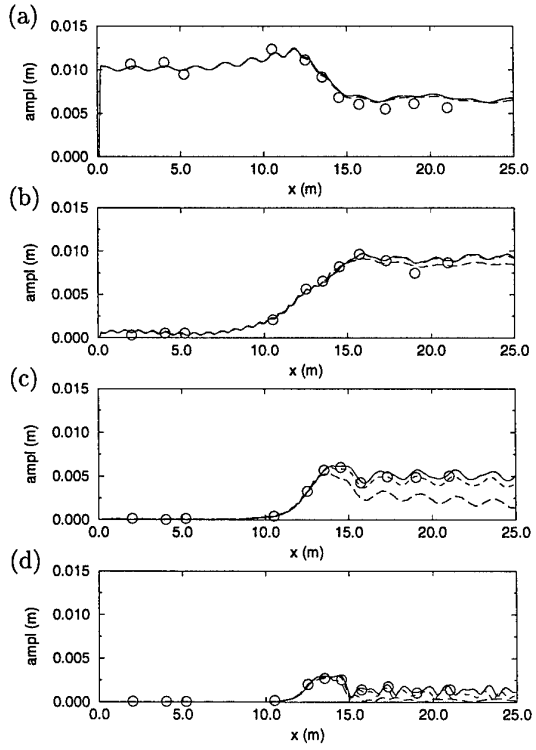

Figure 3: Propagation of regular waves over a submerged bar, see Fig. 1. (a-d) Amplitudes of 1^{st} to 4^{th} harmonic, respectively, as function of x-location along the channel. (o) measurements by Luth et al. (1994), (----) $\Delta x = 0.015$ m, $\Delta t = 0.01$ s, (- - - -) $\Delta x = 0.03$ m, $\Delta t = 0.02$ s, (-- -- --) $\Delta x = 0.06$ m, $\Delta t = 0.04$ s.

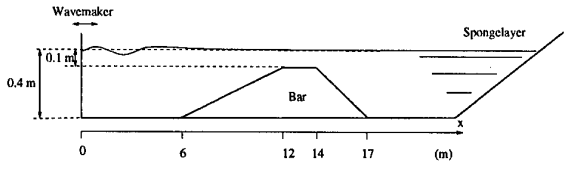

Figure 1: Wave Flume with submerged bar on horizontal bottom. Waves are generated with inital height $H = 0.02$ m and period $T = 2.02$ s.

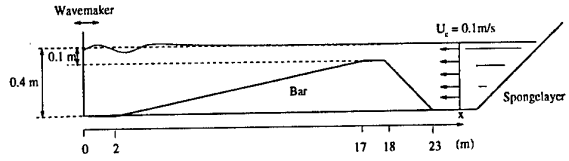

Figure 4: Wave Flume with submerged bar on horizontal bottom for studying wave current interaction.

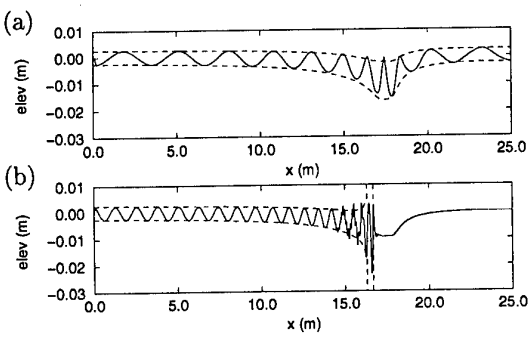

Figure 5: Propagation of waves over a submerged bar with opposing current, see Fig. 4. Elevation profiles at 5 phases within a period at $t = 95$ s. Initial wave height, $H = 0.005$ m, and current $U_c = 0.1$ m/s at 0.4 m depth. (a) Wave period $T = 2$ s. (b) Wave period $T = 1$ s. (- - - -) envelope according to linear wave theory.

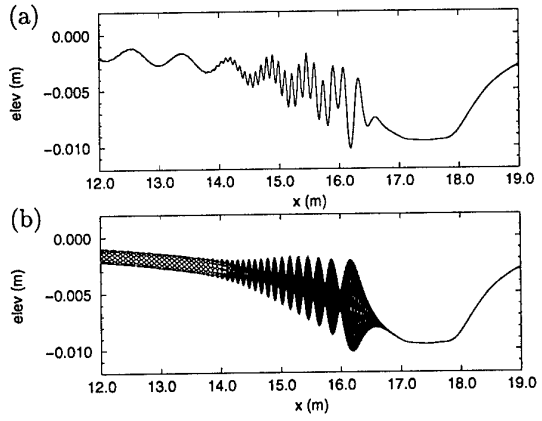

Figure 6: Wave with period $T = 1$ s and initial height $H = 0.001$ m propagating against steady current, see Fig. 4. (a) Elevation at $t = 95$ s. (b) Elevation profiles at 10 phases within a period bewteen $t = 95$ s and $t = 96$ s.

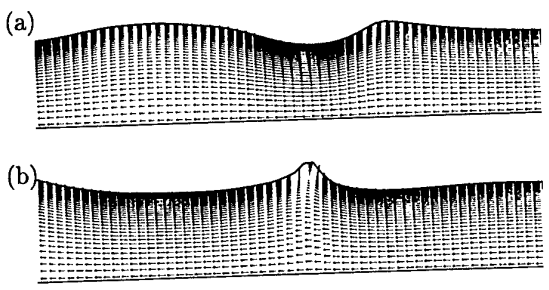

Figure 7: Fluid domain and velocity vectors around blocking point of waves with period $T = 1$ s and initial height $H = 0.005$ m propagating against steady current, see Fig. 4. (a) $t = 95.00$ s, (b) $t = 95.50T$ s.

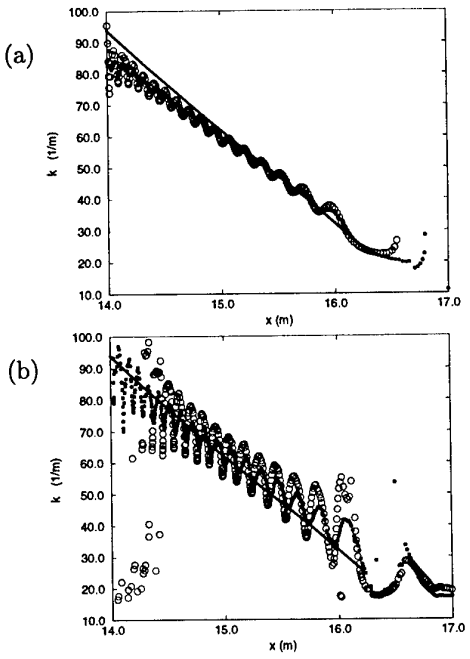

Figure 8: Estimate of wavenumber of wave, being reflected by current, as function of the location x. (a) initial wave height $H = 0.001$ m, (b) initial wave height $H = 0.005$ m. (o) estimate based on surface elevation, (·) estimate based on vertical surface velocity, (----) theoretical value based on (11) and (12).

DISCUSSION

Borthwick A.: Is the algebraically generated curvilinear grid essentially the same as a sigma transformed mesh? If so, could not additional savings in computer time be gained by using the sigma transformed approach given that the mapped equations would be simpler?

Mayer S.: Since the code is derived from a general purpose CFD code, the Finite Volume discretization scheme is implemented for general non-orthogonal grids, including cross derivative terms in both the interior of the grid and along grid boundaries.
However, the automatic grid generation algorithms used in the present work are almost equivalent with the use of sigma transformed meshes, since the considered geometries are simple and, in particular, the channel side walls are vertical. In general, both memory requirement and CPU-consumption could probably be reduced quite a lot, if our algorithm would be written specifically for the numerical wave flume application. This is not only due to the possible simplification of grid generation and discretization schemes, but also because the solution algorithm for the algebraic equation systems could take advantage of the simple grid structure.

Schultz W.W.: Does most of your numerical dissipation come from the Euler prediction step or the potential correction step?

Mayer S.: Generally, most numerical damping comes from the predictor step, in particular, from the QUICK upwind schemes, which we employ for the convective terms. Additionally, some dissipation is introduced in the spatial discretization of the kinematic boundary condition. For time steps, used here, the dissipation due to the potential correction is negligible. (However, for very small timesteps - 1000 time steps or more per wave period - it may become significant).

Resonance in the unbounded water wave problem

Maureen McIver
Loughborough University, Loughborough, Leicestershire, LE11 3TU, U.K.

Introduction

In recent work, McIver (1996) demonstrated that there exist configurations of bodies in two dimensions for which the linearised water wave problem does not have a unique solution at a certain frequency. Non-uniqueness was proved by establishing the existence of a non-zero solution to the homogeneous boundary value problem at the relevant frequency. Such a solution, which decays at infinity and has finite energy, is called a *trapped mode.* In this work, it is shown that for such bodies the solution to certain forced boundary value problems, such as the heave problem, do not exist at the trapped mode frequency. The non-existence of the heave potential means that there is no steady state solution to the problem in which the bodies are forced to make small vertical oscillations about their mean position and similar interpretations may be made of the non-existence of other potentials. In related problems in waveguides, Werner (1987) has shown that trapped modes are closely related to resonances in certain initial value problems. By investigating the solution to a specific initial value problem in which an oscillatory pressure forcing is given to the free surface, it is shown that the steady state potential does not exist because resonance occurs. Work is currently underway to investigate the links between trapped modes and resonances in the more general initial value problem, using the spectral theory techniques of Goldstein (1969).

Construction of the trapped mode potential

An example of a system of bodies for which non-uniqueness occurs is found by constructing a potential which decays to zero at infinity and interpreting some of its streamlines as body boundaries. The potential is constructed by placing two infinite depth wave sources in the free surface, separated by a distance of half a wavelength. (Other suitable potentials may be constructed from sources placed any odd number of half wavelengths apart or a source and a sink placed an even number of wavelengths apart.) Thus the potential is given by

$$\phi = \int_0^\infty \frac{e^{-ky}}{k-K}\cos k(x-a)\,dk + \int_0^\infty \frac{e^{-ky}}{k-K}\cos k(x+a)\,dk, \qquad (1)$$

where the contour of integration passes below the pole in each integral and $Ka = \pi/2$. Coordinate axes are chosen so that the origin is in the mean free surface and the $y-$axis points vertically downwards. The distance between the sources is $2a$ and $K = \omega^2/g$, where ω is the angular frequency and g is the acceleration due to gravity. As the sources are half a wavelength apart, the waves produced by each source cancel at either infinity and the potential decays to zero. In addition, the contributions to the integrals arising from the integration below the poles cancel and so the potential is purely real. The streamlines for the potential are illustrated in figure 1, where the variables have been nondimensionalised so that $x' = Kx$ and $y' = Ky$ and so the sources are at the positions $(\pm\pi/2, 0)$.

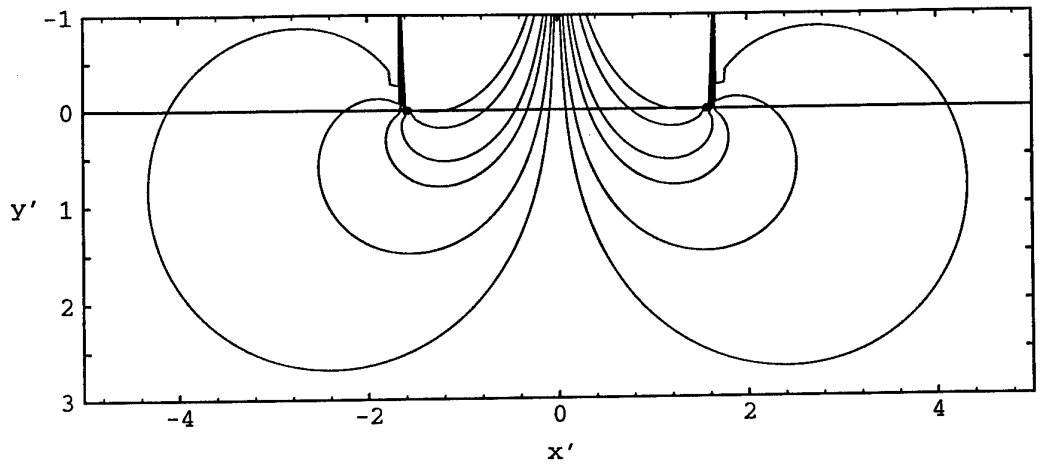

Figure 1 - The streamline pattern for two wave sources a nondimensional distance π apart

The half-plane $y' < 0$ represents the region above the free surface and so the potential has no physical meaning there but the continuation of the streamlines into that region has been included to illustrate how the streamlines cross the free surface. Any parts of streamlines which remove the singularities from the fluid may be chosen to represent body boundaries and an example of such bodies is given in figure 2.

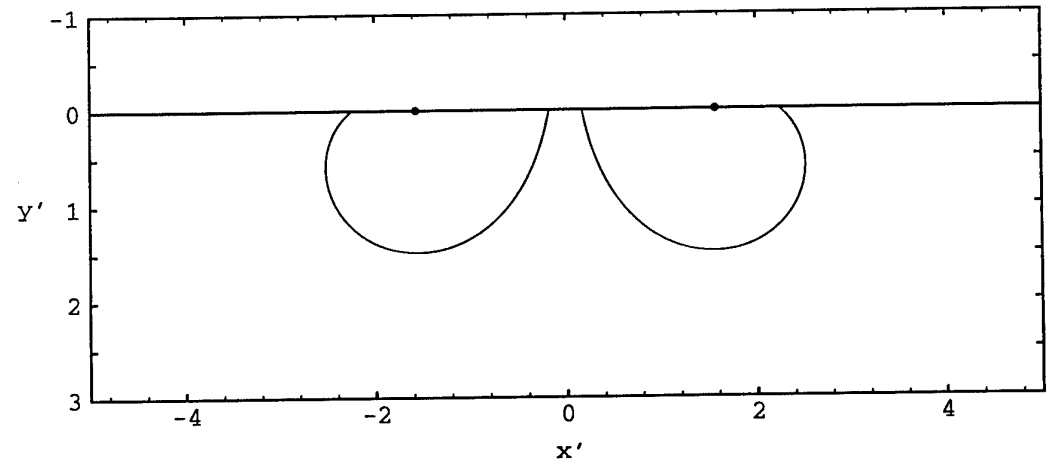

Figure 2 - Two surface-piercing bodies for which non-uniqueness occurs

For the remainder of this work attention will be confined to a pair of bodies such as those given in figure 2 for which a trapped mode exists at frequency $\omega = \omega_0$ (wavenumber $K = K_0$). The trapped mode potential will be denoted by $\phi_0(x, y)$.

Non-existence of the heave potential

The boundary value problem for the heave potential $\phi_h(x, y)$ at frequency ω_0 is the same as that for the trapped mode potential ϕ_0 except that ϕ_h produces outgoing waves at

infinity and the normal derivative of ϕ_h on the bodies is given by

$$\frac{\partial \phi_h}{\partial n} = n_y, \tag{2}$$

where n_y denotes the component of the inward normal to the bodies in the vertical direction. Under the assumption that ϕ_h exists, an application of Green's theorem to ϕ_0 and ϕ_h in the fluid region outside the bodies gives

$$\int_{\text{bodies}} \phi_0 \, n_y \, dS = 0. \tag{3}$$

Thus equation (3) is a necessary condition for the existence of ϕ_h. (It is equivalent to the orthogonality condition which appears in the Fredholm alternative.) However, an application of Green's theorem to ϕ_0 and $u = y - 1/K_0$ in the fluid region outside the bodies, closed by a large semicircle, shows that

$$\int_{\text{bodies}} \phi_0 \, n_y \, dS = -\pi K_0 p_1. \tag{4}$$

where p_1 is the coefficient of the vertical dipole in ϕ_0 at a large distance from the origin. For the particular trapped mode given by the potential in (1), $p_1 = -2/K_0 \neq 0$ and so the heave potential does not exist at the trapped mode frequency for the pair of bodies illustrated in figure 2.

Existence of the diffraction potential

Once the incident wave has been subtracted out from the diffraction potential the remaining scattered potential satisfies

$$\frac{\partial \phi_d}{\partial n} = -\frac{\partial}{\partial n}[e^{iK_0 x - K_0 y}] \tag{5}$$

on the bodies, assuming that the wave is incident from large negative x. Under the assumption that the diffraction potential exists an application of Green's theorem to ϕ_0 and ϕ_d in the fluid region outside the bodies gives

$$\int_{\text{bodies}} \phi_0 \frac{\partial}{\partial n}[e^{iK_0 x - K_0 y}] \, dS = 0, \tag{6}$$

which is a necessary condition for the existence of ϕ_d. However, an application of Green's theorem to ϕ_0 and $e^{iK_0 x - K_0 y}$ shows that (6) is true when ϕ_0 is *any* trapped mode potential. Under the assumption that the Fredholm alternative applies this is sufficient for the diffraction potential to exist.

Resonance in a specific initial value problem

In order to investigate the physical significance of the non-existence of a steady-state potential, an initial value problem in which the fluid is given an oscillatory pressure forcing

on the free surface is investigated. Let $\Phi_p(x,y,t)$ satisfy Laplace's equation, have zero normal derivative on the bodies, decay to zero at large depths and satisfy the condition

$$\frac{\partial^2 \Phi_p}{\partial t^2} - g\frac{\partial \Phi_p}{\partial y} = \phi_0(x,0)\cos\omega_0 t, \quad t > 0, \tag{7}$$

on the free surface outside the bodies with initial conditions

$$\Phi_p(x,0,0) = \frac{\partial \Phi_p}{\partial t}(x,0,0) = 0. \tag{8}$$

If a steady state solution to this problem were sought in the form $\Phi_p = Re[\phi_p(x,y)e^{-i\omega_0 t}]$, a boundary value problem for ϕ_p would be obtained which does not have a solution. (The necessary condition for the existence of $\phi_p(x,y)$ is $\int \phi_0^2(x,0)\,dx = 0$, where the integral is taken over the whole free surface outside the bodies. As ϕ_0 is real and not equal to zero everywhere on $y = 0$, this condition is not satisfied.) However, from the equations and boundary conditions satisfied by the trapped mode potential ϕ_0 it is straightforward to show that the solution to the initial value problem is given by

$$\Phi_p = \frac{t}{2\omega_0}\phi_0(x,y)\sin\omega_0 t. \tag{9}$$

Clearly the amplitude of the oscillation of the resulting fluid motion grows with time and resonance occurs. Physically the problem may be interpreted as a situation in which energy is continually fed into a local oscillation and is not carried away from the vicinity of the body through any wave motion.

Conclusion

An example has been given which shows that resonance can occur in the two-dimensional, linear, water wave problem in an unbounded region when there is at least one trapped mode solution of the related frequency domain problem. The more general initial value problem in which the free surface condition (7) is replaced by

$$\frac{\partial^2 \Phi_p}{\partial t^2} - g\frac{\partial \Phi_p}{\partial y} = Re[f(x)\,e^{-i\omega_0 t}], \quad t > 0, \tag{10}$$

where $f(x)$ is square integrable, is currently under investigation. In particular, it is hoped to extend the results of Goldstein (1969) for waveguides and expand $f(x)$ as an integral over all scattering potentials plus a sum over all trapped mode potentials and then derive an explicit expression for Φ_p with the use of a Laplace transform in time.

References

Goldstein, C. I. 1969 'Eigenfunction expansions associated with the Laplacian for certain domains with infinite boundaries. I' *Transactions American Mathematical Society*, Vol. 135, pp 1 - 31.

McIver, M. 1996 'An example of non-uniqueness in the two-dimensional linear water wave problem.' *J. Fluid Mechanics*, Vol. 315, pp 257 - 266.

Werner, P. 1987 'Resonance phenomena in cylindrical waveguides' *J. Mathematical Analysis and Applications*, Vol. 121, pp 173 - 213.

DISCUSSION

Evans D.V.: What are the implications of your non-uniqueness on, say, the heave added mass of a catamaran having hull cross-section precisely of the form which gives your non-uniqueness?

McIver M.: The heave added mass doesn't actually exist at the exact frequency at which non-uniqueness occurs. Although I haven't done the computations, in the corresponding case for a body in a channel, the added mass tends to plus or minus infinity either side of the trapped mode frequency. I would expect the same thing to happen in this case.

Schultz W.: To apply the Fredholm alternative theorem as you have described requires the solution to be self-adjoint. What new insights could be found if this constraint were dropped? Could asymmetric solutions be found?

McIver M.: I agree that the operator in this case is self-adjoint. However, I don't think that you need to have a non-self-adjoint operator in order to obtain an asymmetric configuration of bodies. In the example I presented you could construct 2 bodies of different size by taking parts of different streamlines.

Tuck E.O.: If non-uniqueness occurs at some particular wavenumber $k = k_o$, this means that output quantities like added mass do not exist at $k = k_o$. An interesting question is what then happens at $k = k_o \pm \varepsilon$ where ε is arbitarily small. Can one make the output as large as one likes by choosing ε sufficiently small? That is, on a graph, does the output appear to "go to infinity" as $k \to k_o$?

McIver M.: I think this is correct. Certainly when you get trapped modes about a cylinder in a channel the added mass goes to plus or minus infinity either side of the trapped mode frequency.

On uniqueness and trapped modes in the water-wave problem for a surface-piercing axisymmetric body

P. McIver[1] and N. Kuznetsov[2]

[1]Department of Mathematical Sciences, Loughborough University, UK

[2]Russian Academy of Sciences, St Petersburg, Russia

1 Introduction

The problem of uniqueness of the frequency-domain solution to the linearised water-wave problem is fundamental, as was recently highlighted by Ursell (**1**) who placed it first in his list of (at the time) unsolved problems. A number of uniqueness results have been established for specific geometries. In particular, John (**2**) proved the most widely known theorems for surface-piercing obstacles in two and three dimensions. Simon & Ursell (**3**) generalised John's 2D theorem to cover a wider class of obstacles including totally submerged ones. The first uniqueness theorem for a 2D obstacle separating a portion of the free surface from infinity was obtained by Kuznetsov (**4**). Simon & Kuznetsov (**5**) generalised this result to the case of a toroidal surface-piercing body. However, there is no general theorem giving necessary and sufficient criteria for either two- or three-dimensional geometries. The fact that some necessary conditions must be fulfilled for uniqueness follows from the recent achievement of M. McIver (**6**) who constructed the first examples of non-uniqueness for the two-dimensional water-wave problem. These 'trapped modes' were constructed from two equal-strength wave sources placed in the free surface and positioned so that the waves radiated to each infinity by one source are cancelled by the other. She proved that there exist families of stream-line pairs surrounding the sources that can be interpreted as two surface-piercing structures. The corresponding three-dimensional problem was considered by McIver & McIver (**7**) who constructed solutions from a ring source with a vertical axis of symmetry placed in the free surface. The radius of the ring is chosen to eliminate the radiated wave; this results in a standing-wave motion that decays more quickly in the radial direction than any propagating wave solution. The stream surfaces of the flow correspond to toroidal structures floating in the free surface.

The present work extends the work of McIver & McIver (**7**) in two ways. First of all it is shown that, for certain toroidal structures, uniqueness for any mode of the fluid motion may be established over particular ranges of frequency. Secondly, trapped mode solutions are constructed numerically for non-axisymmetric modes in the presence of an axisymmetric structure.

2 Formulation

An inviscid, incompressible fluid occupies the half-space $y \geq 0$ with Cartesian coordinates (x, y, z) chosen so that $y = 0$ corresponds to the free surface and y is directed vertically downwards. Horizontal polar coordinates (r, θ) are defined by $x = r\cos\theta$, $z = r\sin\theta$. A structure, axisymmetric about the y axis and with submerged volume D and wetted surface S, floats in the free surface. The fluid domain is denoted by W and the free surface by F. The structure is toroidal in shape so that the free surface is in two distinct parts; the outer free surface is denoted by F_+ and the inner free surface of radius b is denoted by F_-. The geometry is sketched in Fig. 1.

Within the framework of the linearised theory, a time-independent potential ϕ corresponding to a trapped wave motion must satisfy

$$\nabla^2\phi = 0 \quad \text{in} \quad W, \tag{1}$$

the free-surface condition

$$K\phi + \frac{\partial\phi}{\partial y} = 0 \quad \text{on} \quad F = F_- \cup F_+ \tag{2}$$

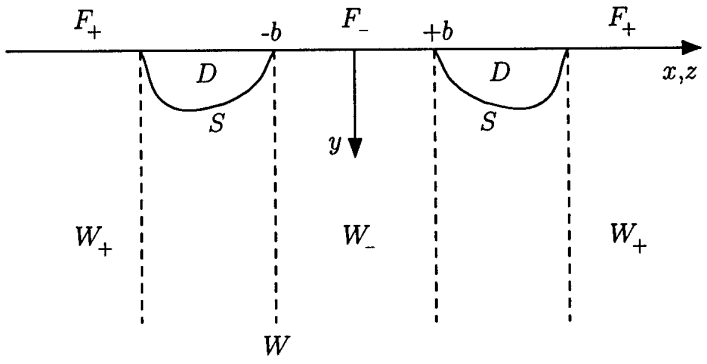

Figure 1: Sketch of geometry

and the body boundary condition

$$\frac{\partial \phi}{\partial n} = 0 \quad \text{on} \quad S, \tag{3}$$

where $\partial/\partial n$ indicates differentiation in a direction normal to the surface S of the structure. Here $K = \omega^2/g$, where g is the acceleration due to gravity. The radiation condition requires that ϕ and $\nabla\phi$ decay at infinity in such a way that the energy of a trapped fluid motion is finite and therefore

$$\int_W |\nabla\phi|^2 \,\mathrm{d}x\,\mathrm{d}y\,\mathrm{d}z + \int_F |\phi|^2 \,\mathrm{d}x\,\mathrm{d}z < \infty. \tag{4}$$

3 A uniqueness theorem

For modes of the form

$$\phi = \phi_n(r,\theta,y) = \phi^{(n)}(r,y)\cos n\theta, \quad n = 0, 1, \ldots, \tag{5}$$

energy arguments related to those used by John (**2**) and Simon & Ursell (**3**) may be used to obtain the following:

Theorem *Consider the axisymmetric fluid domain W illustrated in Fig. 1 where the torus D is strictly bounded by two vertical cylinders that intersect D at the free surface F (the so called 'John' condition); the inner cylinder has radius b. For a given azimuthal mode number n, suppose that for some value of the non-dimensional frequency parameter Kb*

$$j_{n,m} \le Kb \le j'_{n,m+1}, \tag{6}$$

where $j_{n,m}$ denotes the m-th zero of the Bessel function J_n and $j'_{n,m}$ denotes the m-th zero of J'_n. If $n = 0$, then $m \in \{1, 2, \ldots\}$. If $n \ge 1$, then $m \in \{0, 1, \ldots\}$ with $j_{n,0} = 0$. Then, for this value of Kb, the boundary-value problem (1-4) has only trivial solutions in the form (5).

In other words, for toroidal geometries satisfying the John condition, the solution of the water wave problem with azimuthal mode number n is unique provided that (6) is satisfied.

4 Trapped mode solutions

Trapped mode solutions to the problem (1-4) are sought in the form (5) where $\phi^{(n)}$ is taken as the potential of a ring source of radius c in the free surface. The potential for such a source (**8**, equation 3.10) singular on $(r, y) = (c, 0)$ is

$$\begin{aligned} R_n(r,y;c) &= 4\pi^2 iKc\,\mathrm{e}^{-Ky} J_n(Kr_<)H_n^{(1)}(Kr_>) \\ &\quad + 8c\int_0^\infty (\nu\cos\nu y - K\sin\nu y) I_n(\nu r_<)K_n(\nu r_>)\frac{\nu\,\mathrm{d}\nu}{\nu^2+K^2}, \end{aligned} \tag{7}$$

where $r_> = \max\{r, c\}$, $r_< = \min\{r, c\}$, and J_n, I_n, K_n and $H_n^{(1)}$ denote standard Bessel, modified Bessel and Hankel functions of order n. In general, at large radial distances the ring source gives outgoing waves as a result of the Hankel function in the first term. It may be shown that the integral term decays like r^{-3} as $r \to \infty$. Radiating waves in $r > c$ are annulled by taking c to satisfy $J_n(Kc) = 0$; that is Kc is chosen to be a zero of the Bessel function J_n. Any surface in the fluid domain that is always parallel to the local velocity may be interpreted as the surface of a structure.

The purely axisymmetric case $n = 0$ was considered by McIver & McIver (**7**). It was proved using the Stokes' stream function that for a given non-radiating ring source a family of corresponding toroidal structures can be constructed that exclude the source from the fluid domain, thus establishing the existence of trapped mode solutions. For $n \geq 1$ no stream function is available so here the evidence given for the existence of trapped modes is purely numerical.

On the surface of any structure it is required that there is no flow in the normal direction. For axisymmetric structures, surfaces independent of θ are sought in the form $r = r(y)$ and the condition of no flow in the direction of the local normal $\mathbf{n}$ may be written

$$\frac{\mathrm{d}r}{\mathrm{d}y} = \frac{\phi_r}{\phi_y}. \tag{8}$$

This differential equation may be solved numerically using standard procedures. A typical calculation is given in Fig. 2 for the case of azimuthal mode number $n = 1$, the radius of the ring source is chosen as its smallest possible value $Kc = j_{1,1}$. The figure shows typical stream surfaces; any surface, or combination of surfaces, for which the singularity is enclosed may be interpreted as a structural surface. It should be noted that these stream surfaces do not satisfy the John condition required by the theory of §3.

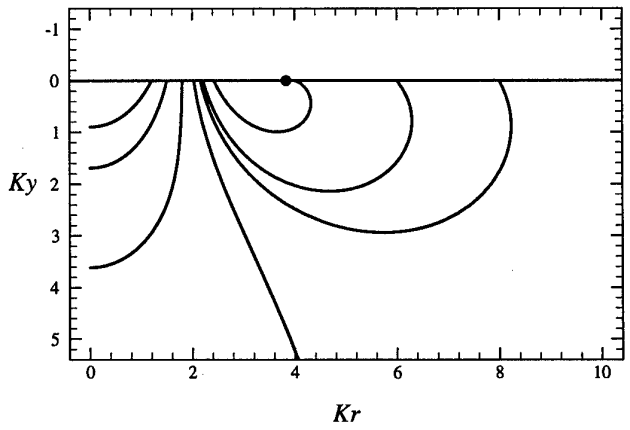

Figure 2: Axial plane cross section of stream surfaces for mode number $n = 1$. The source position $Kc = j_{1,1}$ is marked •.

5 Discussion

Fig. 3 shows numerical calculations of the values of Kb corresponding to the intervals of existence for trapped modes that may be constructed using a single ring source. Also shown are the intervals for uniqueness given in (6). These intervals are complementary despite the fact that the trapped mode solutions violate the conditions under which the uniqueness theorem was derived.

It is apparent from that there are intervals in Kb for which there may be uniqueness for all modes (disregarding for the moment the requirement that John condition must be satisfied). For example, for $n = 1$ no trapped modes have been found for $Kb \in (2.51, 3.05)$ while uniqueness of the

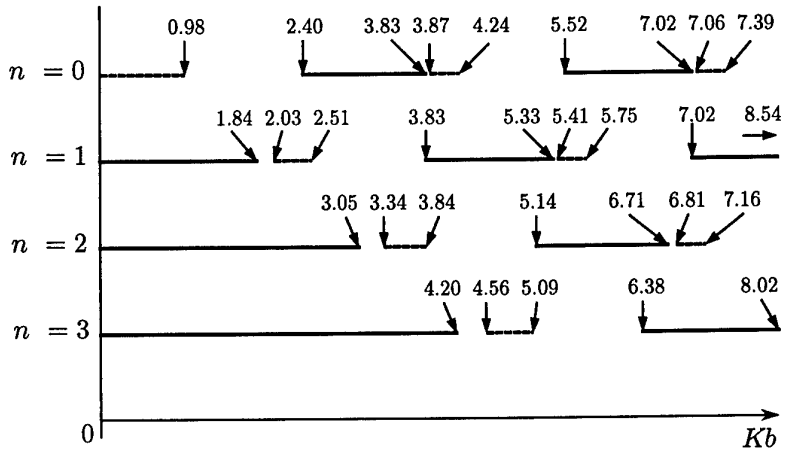

Figure 3: Values of the inner radius Kb for which uniqueness has been established (———), provided the structure satisfies the John condition, and values of Kb for which trapped modes may be constructed (– – – – –) using a single ring source. The integer n is the azimuthal wave number.

solution has been established in this interval for all other modes. However, it should be pointed out that in the equivalent two-dimensional problem of two-surface piercing bodies, Linton & Kuznetsov (**9**) have found evidence of modes trapped by bodies violating the John condition within the region for which uniqueness is predicted by the theory that requires the John condition.

6 Conclusion

The uniqueness of the solution to linear water-wave problems with axisymmetric floating bodies has been considered. Uniqueness of the solution has been established for a restricted class of body geometries over certain ranges of frequency. Further, examples of non-uniqueness, or trapped modes, have been constructed numerically for geometries that do not satisfy the restrictions required by the uniqueness theorem but, nevertheless, the frequency ranges where they occur are entirely consistent with that theorem. Further work is required to extend the uniqueness theorem to a wider class of geometries and to explore the range of trapped mode solutions that are possible.

References

1. F. Ursell, In *Wave Asymptotics*, ed. P. A. Martin & G. R. Wickham. Cambridge University Press (1992).
2. F. John, *Commun. Pure Appl. Maths* **3** (1950) 45-101.
3. M. J. Simon & F. Ursell, *J. Fluid Mech.* **148** (1984) 137-154.
4. N. G. Kuznetsov, *Math. Notes Acad. Sci. USSR* **44** (1988) 685-690.
5. M. J. Simon & N. G. Kuznetsov, *Applied Mathematics Internal Report* 96/1. Department of Mathematics, University of Manchester (1996).
6. M. McIver, *J. Fluid Mech.* **315** (1996) 257-266.
7. P. McIver & M. McIver, *Q. J. Mech. Appl. Math.* to appear.
8. A. Hulme, *J. Fluid Mech.* **128** (1983) 387-412.
9. C. M. Linton & N. G. Kuznetsov, submitted for publication.

DISCUSSION

Clark P.: When engineers hear about uniqueness and trapped modes they instinctively think that these are issues of concern to mathematicians only. Could the axisymmetric wave trap described in your paper be the basis of an effective wave power device, where the energy in the trapped modes would be extracted by, say, a Well's turbine? This woul be of great interest to engineers.

McIver P., Kuznetsov N.: Resonance will occur when forcing is applied at a trapped mode frequency. Whether the bandwidth around a trapped mode frequency is substantially different from that for the near-resonant motions already familiar to designers of wave-power devices is still an open question, but one that we will investigate in the near future. There is certainly a possibility that improved oscillating water column devices may result from this work.
Another reason the existence of pure (as opposed to leaky) trapped modes should be of concern to engineers is because standard numerical methods will fail at, or very close to, a trapped mode frequency.

Eatock Taylor R.: Is it significant that these bulbous shapes are not "wall-sided" at the water line? Is the trapped modes "industry" interested in wall-sided bodies which are concave below the water-line? Such structures can presumably experience cancellation in the vertical wave force.

McIver P., Kuznetsov N.: In the water-wave problem, there is still a great deal to be understood about the circumstances under which trapped modes can occur. In particular, it is not known whether the first examples of "open-sea" trapped modes presented at this workshop have geometries which are in some way typical; their particular character may be just a result of the method of construction. We certainly cannot rule out the existence of trapped modes for the type of wall-sided bodies you describe.

On the Non-Uniqueness in the 2D Neumann–Kelvin Problem for a Tandem of Surface-Piercing Bodies

by Oleg Motygin and Nikolay Kuznetsov

Laboratory on Mathematical Modelling in Mechanics,
Institute of Problems of Mechanical Engineering, Russian Academy of Sciences

1. Introduction

The present note is concerned with a tandem of horizontal cylindrical bodies moving forward with constant velocity U in the free surface of an inviscid, incompressible fluid under gravity. The resulting fluid motion is described by the linearized water-wave theory (the corresponding boundary value problem is usually referred to as the Neumann–Kelvin problem). For a totally submerged body in the fluid of infinite depth Kochin (1937) and Vainberg & Maz'ya (1973) had given almost exhaustive mathematical theory of this problem. The case of surface-piercing bodies is much more complicated. A number of significant results have been obtained for this case by Ursell (1981), Lenoir (1982), Kuznetsov & Maz'ya (1989), Kuznetsov & Motygin (1995), but a lot of questions still remains unsolved for it.

Treating the special case of semi-submerged circular cylinder Ursell (1981) found that the Neumann–Kelvin problem has a two-parameter set of solutions. He proposed two conditions complementing the original problem to make it well-posed (uniquely solvable for all values of U with possible exception for a sequence tending to zero). The corresponding "least singular" solution gives a bounded velocity field near corner points. This result was generalized by Kuznetsov & Maz'ya (1989), who proved that the least singular statement is well-posed for an arbitrary contour having non-acute angles with the free surface. A number of other supplementary conditions appeared in Lenoir (1982), Kuznetsov & Maz'ya (1989), Motygin & Kuznetsov (1995) and Kuznetsov & Motygin (1995). The "resistanceless" supplementary conditions considered in the last paper provide that the total resistance (a sum of wave resistance and spray resistance) vanishes for a surface-piercing tandem.

Recently McIver (1996) demonstrated the existence of a non-uniqueness example for the 2D sea-keeping problem. She applied the so-called inverse procedure for simultaneous construction of two surface-piercing bodies and of the potential of mode trapped by these bodies. Here we use the same method for the Neumann–Kelvin problem. Actually, our example delivers non-uniqueness to two statements of the problem, namely, to the least singular and to the resistanceless statements for a surface-piercing tandem.

2. Statement of the problem

The geometrical notations are given in figure 1.

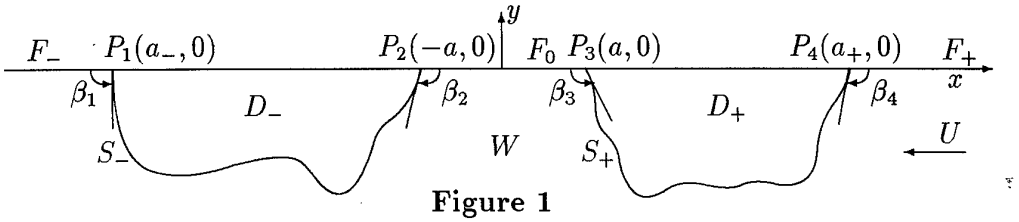

Figure 1

Assuming that the fluid motion is steady-state in a coordinate system attached to the tandem we describe it by a velocity potential u, which must satisfy the boundary value problem:

$$\nabla^2 u = 0 \text{ in } W, \quad u_{xx} + \nu u_y = 0 \text{ on } F_0 \cup F_+ \cup F_-, \quad \partial u/\partial n = U\cos(n,x) \text{ on } S_+ \cup S_-, \quad (1)$$

$$\lim_{x\to+\infty} |\nabla u| = 0, \qquad \sup\{|\nabla u| : (x,y) \in W \setminus E\} < \infty, \quad \int_{W\cap E} |\nabla u|^2 \,\mathrm{d}x\,\mathrm{d}y < \infty. \quad (2)$$

Here $\nu = g\,U^{-2}$, where g is the acceleration due to gravity; $S_\pm$ denotes an open arc lying in $\mathbb{R}^2_-$ and E is a compact set in $\overline{\mathbb{R}^2_-}$, containing $D_- \cup D_+$ with contiguous parts of F_0, F_+ and F_-.

The last condition in (2) allows to avoid strong singularities at the corner points P_k, $k = 1,2,3,4$, because according to Kuznetsov & Maz'ya (1989)

$$u = \begin{cases} C + B\rho^{\pi/2\beta}\sin(\pi\theta/2\beta) + A\rho\cos(\theta-\alpha) + O(\rho^{1+\delta}) & \text{when } \beta > \pi/2, \\ C + B[\rho\log\rho\sin\theta - \rho(\theta-\pi/2)\cos\theta] + A\rho\cos(\theta-\alpha) + O(\rho^{1+\delta}) & \text{when } \beta = \pi/2, \\ C + A\rho\cos(\theta-\alpha) + O(\rho^{1+\delta}) & \text{when } \beta < \pi/2. \end{cases} \tag{3}$$

as $\rho \to 0$. Here (ρ_k, θ_k) are polar coordinates with a pole at P_k and $(-1)^k \cdot \mathbf{i}$ directed along the polar axis. The angles $\theta_{1,3}$ ($\theta_{2,4}$) are measured counterclockwise (clockwise) and $0 \le \theta_k \le \beta_k$. The subscript k indicating the dependence of variables, coefficients and $\delta > 0$ on P_k is omitted.

If $\beta_k \ge \pi/2$ and $B_k \ne 0$, then the velocity vector ∇u is singular when approaching P_k along all non-horizontal directions. However, u_x has finite limits along the x-axis which will be denoted by $u_x(P_k)$. Following Ursell (1981) we say that u satisfying (1), (2) is the *least singular* solution (solution to Problem (L)) if every $B_k = 0$ in the asymptotics (3) for u.

Let us turn to the resistanceless statement of the Neumann–Kelvin problem for a tandem. We remind that any solution to (1), (2) has the following asymptotics as $|z| \to \infty$:

$$u(x,y) = C + Q\log(\nu|z|) + H(-x)\mathrm{e}^{\nu y}(\mathcal{A}\sin\nu x + \mathcal{B}\cos\nu x) + \psi(x,y). \tag{4}$$

Here $z = x + iy$, C is an arbitrary constant, H is the Heaviside function, and the estimates $\psi = O(|z|^{-1})$, $|\nabla\psi| = O(|z|^{-2})$ hold. The constants Q and $\mathcal{A}$ are determined by

$$\pi\nu Q + \sum_{\pm}[u_x(P_{3\pm1}) - u_x(P_{2\pm1})] = \nu\int_S \frac{\partial u}{\partial n}\,\mathrm{d}s,$$

$$-\frac{\mathcal{A}}{2} = \int_S\Big[u\frac{\partial}{\partial n}(\mathrm{e}^{\nu y}\cos\nu x) - \frac{\partial u}{\partial n}\mathrm{e}^{\nu y}\cos\nu x\Big]\,\mathrm{d}s + \sum_{\pm}\pm[\nu^{-1}u_x(x,0)\cos\nu x + u(x,0)\sin\nu x]_{x=\pm a}^{x=a_\pm},$$

where $\sum_\pm$ means summation of two terms. The last formula with cos and sin replaced by $-\sin$ and cos respectively gives the coefficient $\mathcal{B}$.

Let u satisfy (1), (2), and let the following supplementary conditions $\mathcal{A} = 0$, $\mathcal{B} = 0$, $u_x(P_1) = u_x(P_2)$, $u_x(P_3) = u_x(P_4)$ hold. Then we say that u is the *resistanceless* potential (solution to Problem (R)). The term *resistanceless* becomes clear if we take into account the formula expressing the total resistance to forward motion (see Motygin & Kuznetsov (1995)):

$$R = -\frac{\rho\nu}{4}(\mathcal{A}^2 + \mathcal{B}^2) - \frac{\rho}{2\nu}\Big\{[u_x^2(x,0)]_{x=a_-}^{x=-a} + [u_x^2(x,0)]_{x=+a}^{x=a_+}\Big\},$$

where ρ is fluid's density.

Using the source method proposed by Kuznetsov & Maz'ya (1989) one can prove that *problems (L) and (R) (with an arbitrary right hand side in the Neumann condition) are solvable for all $\nu > 0$ with possible exception for a discrete sequence of values (own for each problem).*

3. Non-uniqueness examples

For construction of examples we use the inverse procedure, which replaces finding a solution to a given problem by determining physically reasonable fluid region for a given solution. We define the latter with the help of Green's function

$$G(z,\zeta) = -\frac{1}{2\pi}\log(\nu^2|(z-\zeta)(z-\bar{\zeta})|) - \frac{1}{\pi}\int_0^\infty \frac{\cos k(x-\xi)}{k-\nu}\,\mathrm{e}^{k(y+\eta)}\,\mathrm{d}k - \mathrm{e}^{\nu(y+\eta)}\sin\nu(x-\xi),$$

which describes the forward motion of a source placed at $\zeta = \xi + i\eta$. Putting

$$u(z) = (\pi/\nu)\,[G_x(z,\pi/\nu) - G_x(z,-\pi/\nu)]\,, \tag{5}$$

we obtain a solution to the problem (1), (2) for a surface-piercing tandem if at least one of the streamlines of the flow connects the x-axis on either side of a dipole point and another streamline similarly surrounds the other dipole point (we interpret these streamlines as contours of two bodies). The streamlines are level lines of the stream function v, which is a harmonic conjugate to u. We use the following representations:

$$\begin{aligned} v(z) &= \int_0^\infty \frac{\cos k(x+\pi/\nu) - \cos k(x-\pi/\nu)}{k-\nu} \mathrm{e}^{ky} \,\mathrm{d}k \\ &= \mathrm{Re}\left\{\mathrm{e}^{-i\nu z}\left[\mathrm{Ei}(i\nu(z-\pi/\nu)) - \mathrm{Ei}(i\nu(z+\pi/\nu))\right]\right\}, \end{aligned} \tag{6}$$

where the second formula in terms of the exponential integral follows from 8.212.5, Ryzhik & Gradshteyn (1980) *Table of Integrals*. The asymptotics of Ei implies that $v(z) \sim \pm \log|z \pm \pi/\nu|$ as $z \to \mp\pi/\nu$. Thus, the streamlines enclosing the dipoles do exist for sufficiently large values of v, and these lines are close to semicircles which are the level lines of $\log|z \pm \pi/\nu|$.

The particular combination of dipoles (5) is chosen to cancel wave terms in the asymptotics of u. The latter fact is an immediate consequence of the following formula

$$G(z;\zeta) \sim -\pi^{-1}\log(\nu|z|) - 2\mathrm{e}^{\nu(y+\eta)}\sin\nu(x-\xi) \text{ as } x \to -\infty.$$

Therefore, u delivers a solution to Problem (R), because the second pair of supplementary conditions in the definition of this problem is also fulfilled. Really, the direct calculation based on (6) shows that $v_y - \nu v = 0$ when $y = 0$ and $x \neq \pm\pi/\nu$, and hence, the derivatives $v_y = u_x$ have the same value at both end-points (belonging to the x-axis) of any streamline enclosing one of the dipoles.

Actually, u has no singular points on the x-axis except for $\pm\pi/\nu$. Hence, if $\beta_k \geq \pi/2$, $k = 1,2,3,4$ (see fig. 1 for definition of β_k) for the streamlines which we interpret as bodies, then u delivers a solution to Problem (L) as well. The latter is the case because we have

$$\tan\beta_k = (-1)^k u_y(P_k)/u_x(P_k) = (-1)^{k+1} v_x(P_k)/v_y(P_k).$$

From this and from the behavoiur of derivatives shown on figure 3(a) one obtains that all angles β_k are non-acute for the streamlines given by (6).

4. Discussion

A new type of non-uniqueness for the Neumann–Kelvin problem is described. The well-known non-uniquness (see Introduction) is a consequence of sub-definiteness of this boundary value problem for surface-piercing bodies, and occurs for all such bodies and all values of ν. The

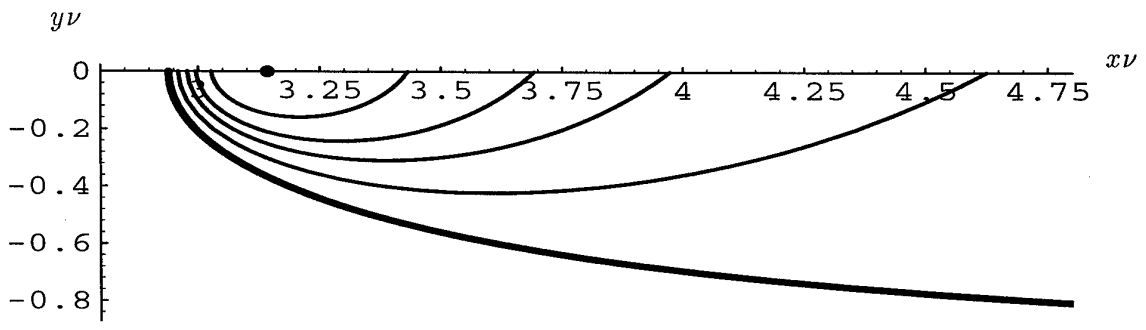

Figure 2. Streamlines for $v = 0$ (bold line), 0.2, 0.4, 0.6, 1.0.

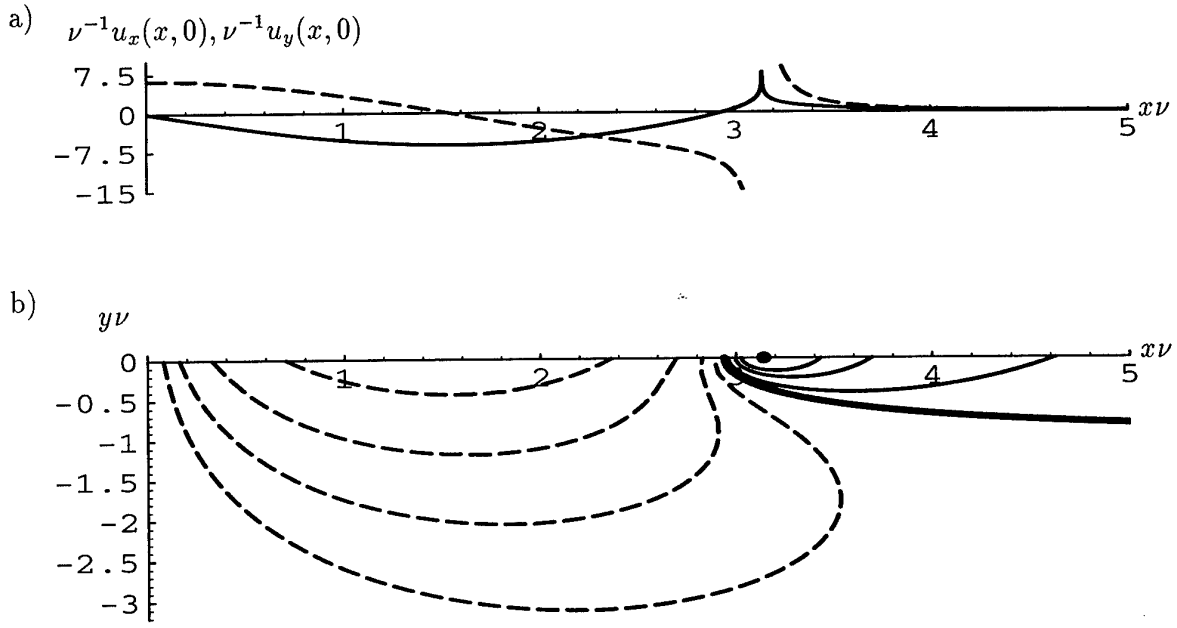

Figure 3. a) $\nu^{-1}u_x(x,0)$ and $\nu^{-1}u_y(x,0)$ (dashed line) are plotted against $x\nu$; b) shows streamlines for $v = -0.5, -1.0, -2.0, -4.0$ (dashed lines), $v = 0$ (bold line) and $v = 0.2, 0.6, 1.0$.

new type of non-uniqueness takes place only for special values of ν depending on the geometry. These values are point eigenvalues corresponding to modes of finite energy (known as trapped modes) embedded in the continuous spectrum of the relevant pseudo-differential operator. The latter spectrum is known to be $(0, +\infty)$.

We use a pair of horizontal dipoles for obtaining trapped modes, whereas McIver (1996) applies a pair of sources in her construction. The reason is that dipoles deliver an example for two statements simultaneously. The potential generated by two sources gives an example of non-uniqueness only for the least singular statement and cannot satisfy the second pair of supplementary conditions in Problem (R).

There is no unique set of supplementary conditions vanishing the total resistance to the forward motion of more than two surface-piercing bodies. At the same time, the least singular solution can be naturally defined for any number of bodies. The corresponding non-uniqueness examples can be easily constructed. In particular, the potential (5) delivers examples of non-uniqueness for Problem (L) with 3 and 4 cylinders (see fig. 3(b) for the corresponding streamlines).

References

KOCHIN, N.E. 1937 English translation: *SNAME Tech. & Res. Bull.* No **1–8** (1951).

KUZNETSOV, N.G. & MAZ'YA, V.G. 1989 *Math. USSR Sbornik.* **63**, 425–446.

KUZNETSOV, N.G. & MOTYGIN, O.V. 1995 *A.M. Basin Memorial Conf. on Ship Hydrodynamics.* St. Petersburg, pp. 154–162 (in Russian).

LENOIR, M. 1982 *ENSTA Rapport de Recherche.* No **164**. Paris.

MOTYGIN, O. & KUZNETSOV, N. 1995 *The 10th Int. WWWFB.* Oxford, pp. 181–185.

MCIVER, M. 1996 *J. Fluid Mech.* **315**, 257–266.

URSELL, F. 1981 *The 13th Symp. on Naval Hydrodynamics.* Tokyo, pp. 245–251.

VAINBERG, B.R. & MAZ'YA, V.G. 1973 *Trans. Moscow Math. Soc.* **28**, 33–55.

DISCUSSION

Tuck E.O.: Could you explain why you are studying the Neumann-Kelvin problem? This is a serious question, since there are matters raised in the paper such as singularities at the body-FS junction points, which relate directly to the question of the practical relevance of the N-K problem. Although my own opposition to the N-K problem is well known, it is possible that critics like me could be converted to believe in it, if studies like this were motivated to explain these singularities, or to use them as an outer expansion is a systematic approximation.

Motygin O., Kuznetsov N.: We consider the N-K problem as a phenomenological model. The so-called full non linear problem is also only a model, because it involves the assumption that the fluid motion is irrotational everywhere. However, this is hardly true near body-FS junction points. Since the linear N-K problem requires supplementary conditions, their choice can be used for an appropriate phenomenological description of fluid motion near junction points. Different supplementary conditions could be good for different ranges of the Froude number.

Abstract for the 12th International Workshop on Water Waves and Floating Bodies, Marseille, France, March 1997.

STEADY WAVE SYSTEMS IN A TWO-LAYER FLUID OF FINITE DEPTH

Thai Nguyen and Ronald W. Yeung
Naval Architecture and Offshore Engineering
University of California at Berkeley, Berkeley, CA 94720-1780, USA.

1. Introduction

Density stratification occurs frequently in the open oceans. Surface or sub-surface marine vehicles can operate in such an environment. This gives rise to some hydrodynamic problems of intrinsic interest. If the pycnocline thickness is small, a common model is to treat the medium as a two-layer fluid. A review of this subject indicates that existing derivations of the source potential in a two-layer fluid usually assume the lower fluid to be infinitely deep [1-3] or upper fluid bound by a rigid lid [2]. A more recent formulation [4] does allow each fluid layer to have finite depth but requires the density difference between the two layers to be small. Under this latter assumption, the surface and internal wave systems are only weakly coupled. In this paper, the translating source potential for a two-layer fluid of finite depth is derived in a form amenable to numerical evaluation. The source is restricted, for illustration purpose, to the upper layer, but the density difference between the two layers can be finite. Surface and internal wave patterns are computed for a density difference large enough so that some coupling between the surface and internal wave systems exists and their intertwined behavior is observed and illustrated.

2. Mathematical Formulation

Let's define a rectangular coordinate system moving with a point source at a constant speed U along the positive x-axis. The (x, y) plane of this system coincides with the undisturbed interface between the two fluid layers, and the z-axis is positive upward. Let ρ_1, h_1 and ρ_2, h_2 denote the densities and depths of the upper and lower layers, respectively. If the velocity potential in each layer is given by $G^{(m)}(\xi, \eta, \zeta; x, y, z)$, where (ξ, η, ζ) is the location of the source and $m = 1, 2$ refers to the upper and lower fluid layer, respectively, then the governing equations for $G^{(m)}$'s are

$$\nabla^2 G^{(1)} = \delta(x - \xi, y - \eta, z - \zeta) \qquad \nabla^2 G^{(2)} = 0 \tag{1}$$

The linearized boundary conditions on the free surface $z = h_1$, the interface $z = 0$, and the rigid bottom $z = -h_2$ are:

$$k_o G_z^{(1)} + G_{xx}^{(1)} - \mu G_x^{(1)} = 0 \qquad z = h_1 \tag{2}$$

$$\gamma(k_o G_z^{(1)} + G_{xx}^{(1)} - \mu G_x^{(1)}) = k_o G_z^{(2)} + G_{xx}^{(2)} - \mu G_x^{(2)} \qquad z = 0 \tag{3}$$

$$G_z^{(1)} = G_z^{(2)} \qquad z = 0 \tag{4}$$

$$G_z^{(2)} = 0 \qquad z = -h_2 \tag{5}$$

where $k_o = g/U^2$ and $\gamma = \rho_1/\rho_2$. The fictitious viscosity μ, introduced in the above formulation to facilitate the satisfaction of the radiation condition, will be taken to zero in the final results. Finally, the radiation or asymptotic condition is given by

$$\lim_{x \to +\infty} \sqrt{R} \nabla G^{(m)} = o(1), \qquad \lim_{x \to -\infty} \sqrt{R} \nabla G^{(m)} = O(1). \tag{6}$$

where $R = \sqrt{(x - \xi)^2 + (y - \eta)^2}$.

3. Solution of the Source Functions

The solutions for $G^{(m)}$'s are assumed to have the following forms

$$G^{(1)} = \frac{1}{r} + G_o^{(1)} \qquad G^{(2)} = G_o^{(2)} \tag{7}$$

where $r^2 = (x-\xi)^2 + (y-\eta)^2 + (z-\zeta)^2$ and $G_o^{(m)}$'s are some harmonic functions in their respective domains. Using Fourier transform, represented here by the symbol $\mathcal{F}\{\}$, we can express $\mathcal{G}_o^{(m)}(k,\theta,z) = \mathcal{F}\{G_o^{(m)}(x,y,z)\}$ as

$$\mathcal{G}_o^{(m)}(k,\theta,z) = A^{(m)}(k,\theta)e^{kz} + B^{(m)}(k,\theta)e^{-kz} \tag{8}$$

where $A^{(m)}$ and $B^{(m)}$ are unknown functions of k and θ. Substituting the above expression of $\mathcal{G}_o^{(m)}(k,\theta,z)$ into the Fourier transforms of Eqns. (2)-(5), and (7), we obtain a system of linear equations which can be solved for $A^{(m)}$ and $B^{(m)}$. Once $A^{(m)}$ and $B^{(m)}$ are known, $\mathcal{G}_o^{(m)}(k,\theta,z)$ can be inverted to the (x,y,z) space, and by using Eqn. (7) again, we obtain the following expressions for the $G^{(m)}$'s.

$$\begin{aligned} G^{(1)} &= \frac{1}{r} - \frac{1}{2\pi}\int_{-\pi}^{\pi}\int_0^{\infty} \{2\epsilon ab e^{-kd}\cosh[k(z-\zeta)] + 2a(a+\gamma b)e^{-kh}\cosh[k(z-\zeta)] - \epsilon b^2 e^{k(h-z-\zeta)} \\ &\quad + \epsilon a^2 e^{-k(h-z-\zeta)} - b(a+\gamma b)e^{k(d-z-\zeta)} + a(\gamma a+b)e^{-k(d-z-\zeta)}\}\frac{e^{ik\omega}}{\Delta}dkd\theta \end{aligned} \tag{9}$$

$$G^{(2)} = \frac{\gamma}{2\pi}\int_{-\pi}^{\pi}\int_0^{\infty} \{b(a+b)[e^{k(h+z-\zeta)} + e^{k(d-z-\zeta)}] - a(a+b)[e^{-k(h+z-\zeta)} + e^{-k(\delta-z-\zeta)}]\}\frac{e^{ik\omega}}{\Delta}dkd\theta$$

where $\epsilon = 1-\gamma$

$d = h_1 - h_2$ $\qquad$ $h = h_1 + h_2$

$a = k + k_o\sec^2\theta + i\mu\sec\theta$ $\qquad$ $b = k - k_o\sec^2\theta + i\mu\sec\theta$

$\omega = (x-\xi)\cos\theta + (y-\eta)\sin\theta$ $\qquad$ $\Delta(k,\theta) = 2\epsilon ab\cosh(kd) + b(\gamma a+b)e^{kh} + a(a+\gamma b)e^{-kh}$

It is possible to show that if we let h_2 in Eqn. (9) goes to infinity, we will recover the two-layer Green function for the case of infinitely deep lower fluid layer as given in [2]. In another scenario, $G^{(1)}$ and $G^{(2)}$ can be reduced to the potential of a source moving in a uniform fluid of depth h by letting $\rho_1 = \rho_2$. Alternatively, $G^{(1)}$ can be reduced to the same uniform source potential of depth h_1 when we take $\gamma = 0$, or $h_2 = 0$.

To obtain the final results for $G^{(m)}$'s, we will now take the limit of the expressions in Eqn. (9) with μ goes to zero . The θ integration in Eqn. (9) can be redefined to range from $(-\frac{\pi}{2}, \frac{\pi}{2})$ by taking advantage of some symmetry properties of the integrand. We can therefore write $G_o^{(m)}$ as

$$G_o^{(m)} = \lim_{\mu\to 0}\Re e\left\{\int_{-\frac{\pi}{2}}^{\frac{\pi}{2}}\int_0^{\infty} H^{(m)}(k,\theta)\frac{e^{ik\omega}}{\Delta}dkd\theta\right\} \tag{10}$$

where $\Re e\{\}$ represents the real part of the complex expression inside the $\{\}$, and $H^{(m)}(k,\theta)$'s are some known functions. The roots of the equation $\Delta = 0$ are of critical importance. They are given implicitly by:

$$k_n = k_o\sec^2\theta\frac{t_1+t_2+(-1)^{n+1}[(t_1+t_2)^2 - 4\epsilon t_1 t_2(1+\gamma t_1 t_2)]^{\frac{1}{2}}}{2(1+\gamma t_1 t_2)} - i\mu\sec\theta, \qquad n = 1,2 \tag{11}$$

where $t_1 = \tanh(k_n h_1)$, $t_2 = \tanh(k_n h_2)$. The roots k_1 and k_2 can be assigned to be associated with the surface wave mode and internal wave mode, respectively. Note that Eqn. (11) does not always yield a solution for k_n for all values of θ. A useful way of characterizing this complex relation is to define the following two critical Froude numbers Fr_1 and Fr_2 corresponds to the maximum phase velocity c_1 of the surface wave mode and c_2 of the internal wave mode, respectively:

$$Fr_n^2 = \frac{c_n^2}{gh} = \frac{1}{2} + (-1)^{n+1}\left(\frac{1}{4} - \epsilon\frac{h_1 h_2}{h^2}\right)^{\frac{1}{2}}, \qquad n = 1,2 \tag{12}$$

By definition, $Fr_2 < Fr_1$. It can be shown that when $Fr = U/\sqrt{gh} > Fr_n$, a "supercritical" case, k_n does not exist for $|\theta| < \theta_n = \cos^{-1}(Fr_n/Fr)$. By contrast, when $Fr < Fr_n$, the "subcritical" case, k_n exists for all values of θ within the range of integration. Note that $k_1 > k_2$, and as μ approaches zero, both roots approach the positive real axis from the lower half of the complex plane. The inner $(k-)$ integral of Eqn. (10) can now be evaluated using one of the contours as shown in Figs. 1 and 2 depending on whether $\omega > 0$ or $\omega < 0$ (see, e.g. [5]). In the limit of $R \to \infty$, the integrals along the path Γ_2 and Γ_4 vanish. Cauchy's residue theorem can be applied to yield:

$$G_o^{(m)} = \Re e\left\{-\int_{-\frac{\pi}{2}}^{\frac{\pi}{2}}\int_{\Gamma_3} H^{(m)}(\sigma,\theta)\frac{e^{i\sigma\omega}}{\Delta(\sigma,\theta)}d\sigma d\theta\right\} + 2\pi\sum_{n=1}^{2}\Im m\left\{\int_{-\frac{\pi}{2}}^{\frac{\pi}{2}-\psi} H^{(m)}(k_n,\theta)\frac{e^{ik_n\omega}}{\Delta'(k_n,\theta)}d\theta\right\} \tag{13}$$

where $\Delta' = \partial\Delta/\partial k$ and $\psi = \tan^{-1}[y/(-x)]$. The integrals along Γ_3 and Γ_5 are complex conjugates of each other and have been combined to obtain this final expression, which is amenable to numerical treatment. Note that when $Fr > Fr_n$, k_n does not exist for all θ, and the range of integration of the single integral should be modified accordingly. For example, if $\frac{\pi}{2} - \psi > \theta_n > 0$, the range of integration is actually $(-\frac{\pi}{2}, -\theta_n)$ and $(\theta_n, \frac{\pi}{2} - \psi)$.

4. Surface Waves and Internal Waves

The surface waves and internal waves due to a translating point source can now be calculated as follows

$$\zeta^{(1)}(x,y) = \frac{U}{g} G_x^{(1)}\Big|_{z=h_1} \qquad \zeta^{(2)}(x,y) = \frac{U}{g\epsilon}(G_x^{(2)} - \gamma G_x^{(1)})\Big|_{z=0} \tag{14}$$

If we restrict our analysis of the wave patterns to the far field of the source, then we only need to focus on the single integrals in Eqn. (13). In the far field, $\zeta^{(m)}$ can be written as

$$\zeta^{(m)}(x,y) \sim \sum_{n=1}^{2} \Re e \left\{ \int_{-\frac{\pi}{2}}^{\frac{\pi}{2}-\psi} P^{(m)}(k_n,\theta) e^{ik_n\omega} d\theta \right\} \tag{15}$$

According to Eqn. (15), both surface and internal waves contain contributions from the poles k_1 and k_2, where, as mentioned earlier, we associate the contribution from k_1 with the surface wave mode and the contribution from k_2 with the internal wave mode. The method of stationary phase can be applied to Eqn. (15) in the usual manners. The term $e^{ik_n\omega}$ can be rewritten as $e^{i\bar{R}f_n(\theta,\psi)}$, where $\bar{R} = \sqrt{(x-\xi)^2 + (y-\eta)^2}/h$ and $f_n(\theta,\psi) = -hk_n\cos(\theta+\psi)$. The number of stationary points of f_n depends on the values of ψ and Fr.

When $Fr < Fr_n$, the function f_n has two stationary points for $\psi < \psi_n$. Each of these can be identified with a system of transverse or divergent waves. The half-angle of the wave pattern, ψ_n, increases from $19°28'$ to $\frac{\pi}{2}$ as Fr goes from zero to Fr_n. This angle then decreases as $\sin^{-1}(Fr_n/Fr)$ when $Fr > Fr_n$. Also, when $Fr > Fr_n$, there exists only one stationary point which corresponds to the divergent waves. In this case, the source is travelling faster than the fastest waves of the n mode, and transverse waves are not possible for this steady-state problem. Since $Fr_1 > Fr_2$, the surface and internal wave patterns can be classified into three different regimes with respect to Fr. When $Fr < Fr_2$, the wave system due to each mode contains both transverse and divergent waves. When $Fr_2 < Fr < Fr_1$, the wave system due to the surface wave mode still contains both transverse and divergent waves, but the wave system due to the internal wave mode has only divergent waves. As Fr increases past Fr_1, both wave systems now contain only divergent waves.

As an example, Figs. 3-8 illustrate how the surface and internal wave patterns vary as Fr increases from a value less than Fr_2 to a value greater than Fr_1. The physical parameters are: $h_1/h = 0.5$, $\gamma = 0.5$, and corresponding to these parameters, $Fr_1 = 0.924$ and $Fr_2 = 0.383$. The source is located in the middle of the upper layer, i.e., $\zeta/h = 0.25$. In these figures, the scales in the vertical direction are stretched for clarity, and the scale factors are given in the captions. Also, the nondimensional $\bar{\zeta}^{(m)}$ is defined as $\zeta^{(m)}/h$. Figs. 3 and 4 show the surface and internal waves for $Fr = 0.37 < Fr_2$. In this case, both the surface and internal wave modes contain transverse and divergent waves, and the coupling effect can be clearly seen on the free surface where the amplitude of the surface waves due to the internal wave mode are comparable to that due to the surface wave mode. Figs. 5 and 6 show the surface and internal waves for $Fr_2 < Fr = 0.5 < Fr_1$. At this Froude number, the internal wave mode only has divergent waves. The transverse waves on the interface in Fig. 6 are due to the surface wave mode. Figs. 7 and 8 show the surface and internal waves for $Fr = 1.3 > Fr_1 > Fr_2$. Here, only divergent waves are present since the Froude number is greater than the critical Froude numbers of both modes. These and other features of the flow will be further discussed at the Workshop.

References

[1] Hudimac, A. A., "Ship Waves in a Stratified Ocean," Journal of Fluid Mechanics, Vol. 11, 1961.

[2] Sabunçu, T., "The Theoretical Wave Resistance of a Ship Travelling Under Interfacial Wave Conditions," Norwegian Ship-Model Experiment Tank, Trondheim, Pub. No. 63, 1961.

[3] Sturova, I. V., "Effect of Internal Waves on the Hydrodynamical Characteristics of a Submerged Body," Izvestiya RAN, Fizika Atmosfery i Okeana, Vol. 29, No. 6, 1993 (in Russian).

[4] Miloh, T., Tulin, M. P., and Zilman, G., "Dead-Water Effects of a Ship Moving in Stratified Seas," Proceedings of the 11th Intl. Conf. on OMAE, Vol. 1, Part A, 1992.

[5] Yeung, R. W., "Sinkage and Trim in First-Order Thin Ship Theory," J. of Ship Reseach, Vol. 16, No. 1, 1972.

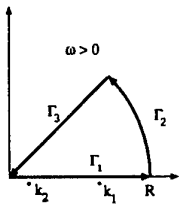

Figure 1: Integration Contour for $\omega > 0$

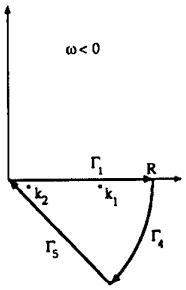

Figure 2: Integration Contour for $\omega < 0$

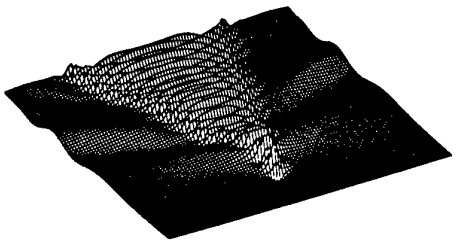

Figure 3: Surface Waves,$4E4 \times \bar{\zeta}^{(1)}, Fr = .37$

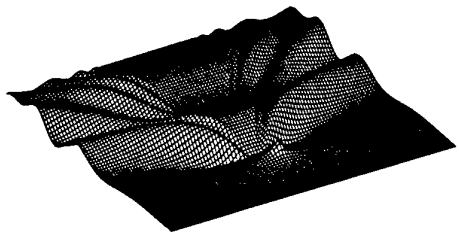

Figure 4: Internal Waves,$3E4 \times \bar{\zeta}^{(2)}, Fr = .37$

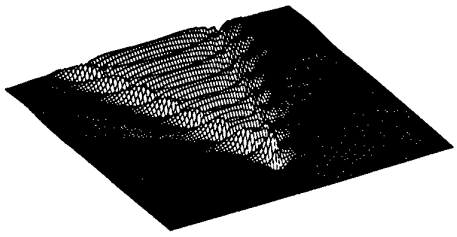

Figure 5: Surface Waves,$4E4 \times \bar{\zeta}^{(1)}, Fr = .5$

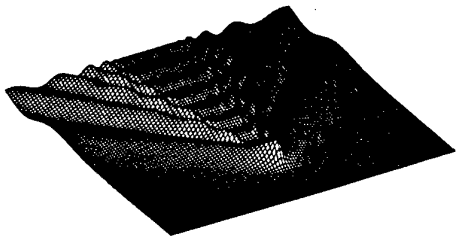

Figure 6: Internal Waves,$6E4 \times \bar{\zeta}^{(2)}, Fr = .5$

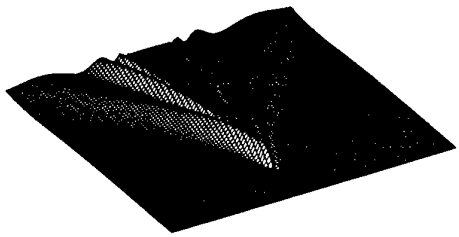

Figure 7: Surface Waves,$7E4 \times \bar{\zeta}^{(1)}, Fr = 1.3$

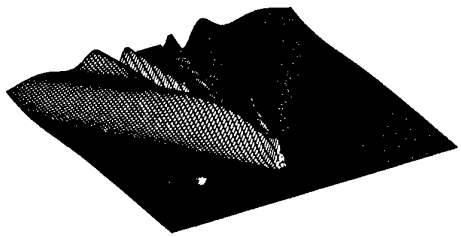

Figure 8: Internal Waves,$3E5 \times \bar{\zeta}^{(2)}, Fr = 1.3$

DISCUSSION

Kuznetsov N.: Have you any physical explanation of phase shift for internal waves?

Nguyen T., Yeung R.W.: The amplitudes of the surface waves and internal waves due to the surface wave mode are in phase, but the amplitudes are 180° out-of-phase for the internal wave mode. This situation is similar to the oscillations of two point masses connected by linear, elastic springs and suspended in a vertical plane. In the first mode of vibration at the natural frequency ω_1, the masses move together and their oscillations are in phase. In the second mode of vibration at frequency ω_2, the masses move in opposite directions and their displacements are 180° out-of-phase.

Wavelet and spline methods for the solution of wave-body problems

by

Jens Olav Nygaard and John Grue
Mechanics Division, Department of mathematics,
University of Oslo, Norway

1 Introduction

Integral equation methods represent powerful alternatives in computation of potential flow around geometries and bodies, where an important example is interaction between water waves and floating bodies. Numerical implementation of the integral equation has often been based on a low-order method, where the boundary of the geometry is subdivided into piecewise straight lines in two dimensions or quadrilaterals in three dimensions. The unknown potential or source-strength is assumed to be constant over each subdivision of the boundary. For complex geometries like e.g. the wetted part of an oil platform, this method leads to a large number of unknowns (n), if a reasonable accuracy of the potential and the flow shall be obtained.

The rather extensive applications of the low-order method illustrate its power. It is, however, desirable to investigate higher order integral methods which have features not included in a low-order method: possibility of finding derivatives of the potential, reduction of the number of unknowns and thereby the size of the matrices, fast convergence of the method, and adaptivity. Another aspect relates to geometrical design. Most practical geometries today are designed by advanced mathematical procedures, e.g. using splines. It is therefore desirable to make available wave analysis tools which are based on the same mathematical procedures as in the modelling of the geometry. The purpose is to integrate efficient and accurate computations of the flow and forces in the design process.

We investigate wavelet and spline methods, which have rather different properties, see Nygaard *et al.* (1996). One of the advantages of the wavelet method is the possibility of performing compression of the coefficient matrix of the system. According to Beylkin, Coifman and Rokhlin (1991), it is possible to devise an $\mathcal{O}(n)$ algorithm for certain integral operators, where n is the number of unknowns. We test the methods on Fredholm integral equations of the second kind. Preliminary results for the wavelet method show that the order of convergence for the present integral operator depends on the geometry. We compare the wavelet and spline methods. The latter method has, in the context of wave analysis, been discussed by Lee *et al.* (1996).

For simplicity we assume two-dimensional motion and consider a half-immersed rectangular cylinder floating in a free surface, responding to incoming waves. Coordinates (x, y) are introduced, with x being horizontal and y vertical. Assuming time harmonic motion with frequency ω, the potential is on the form $\Phi = \mathrm{Re}(\hat{\chi} e^{i\omega t})$, where $\hat{\chi}$ satisfies the Laplace equation in the fluid domain, $\partial\hat{\chi}/\partial y = K\hat{\chi}$ at $y = 0$ ($K = \omega^2/g$), radiation conditions in the far field and $\partial\hat{\chi}/\partial n = V_n$ at the contour S of the cylinder, n is the inward pointing normal vector. From Green's theorem we obtain the usual integral formulation

by

$$\int_S \left(\hat{\chi}(\boldsymbol{\xi}) \frac{\partial G(\boldsymbol{\xi}, \boldsymbol{x})}{\partial n_\xi} - \frac{\partial \hat{\chi}(\boldsymbol{\xi})}{\partial n_\xi} G(\boldsymbol{\xi}, \boldsymbol{x}) \right) dS_\xi = \begin{cases} -\pi \hat{\chi}(\boldsymbol{x}) & \text{on } S \\ -2\pi \hat{\chi}(\boldsymbol{x}) & \text{in the fluid} \end{cases} \tag{1}$$

where $r, r' = [(x-\xi)^2 + (y \mp \eta)^2]^{1/2}$,

$$G(\boldsymbol{\xi}, \boldsymbol{x}) = \ln r - \ln r' + 2\mathrm{Re}\left(\mathrm{e}^Z \int_\infty^Z \frac{\mathrm{e}^{-w}}{w} dw \right) + 2\pi i \mathrm{e}^Z$$

and $Z = -iK(\xi - x) + K(\eta + y)$, $-3\pi/2 < \arg Z < -\pi/2$.

2 The wavelet method - multiresolution analysis

The wavelet method is a Galerkin scheme with a basis which decomposes functions into pieces of different frequency content locally in space. We expand a function f as

$$f = f_0 + g_0 + g_1 + \cdots = \sum_k c_k^0 \phi_k^0 + \sum_k d_k^0 \psi_k^0 + \sum_k d_k^1 \psi_k^1 + \cdots \tag{2}$$

where the basis consists of the functions ϕ_k^0 and ψ_k^j. The subscript indices denote a translation in space (k), and the superscript indices give the location of the frequency (j). The translation in space is uniform, so the function is defined on a uniform grid. Where the function is reasonably smooth, the frequency content will be concentrated. This means that the coefficients corresponding to this particular localization in space will be dominant for a few frequencies. Correspondingly, frequencies which are not so dominating will have small coefficients. Depending on the regularity of the function and necessary accuracy of approximation, a number of these coefficients may be discarded. This makes it feasible to design an adaptive procedure for the solution of our problem, based on a hierarchical structure of *multiresolution analysis.* In short, the term *multiresolution analysis* is coined for the collection of nested approximation spaces spanned by the functions ϕ_k^0 and ψ_k^j. For details on the multiresolution analysis, see e.g. Jawerth and Sweldens (1994). We use the Daubechies wavelet basis indexed by the number N, as in Daubechies (1992). We use $N = 3$ and $N = 8$. The scaling and wavelet functions for $N = 3$ is depicted in fig. 1.

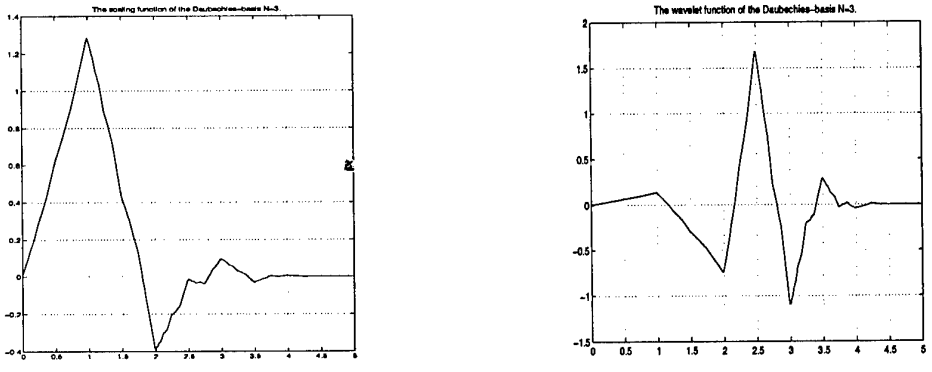

Figure 1: Scaling and wavelet function

3 Spline method

Using splines, we get the simplicity of piecewise polynomials, and for many applications, the geometry will also naturally be defined by splines. This is the case for our examples. The potential is represented by the linear combination of a number of B-splines B_i, for $i = 1, \ldots, m$. In our case, the knot-vector will always be a refinement of the knot vector for the geometry, but that is no requirement. A number of projection schemes are appropriate to use, and we start by inserting the expansion $\chi(t) = \sum_{i=1}^{m} \chi_i B_i(t)$ into the parameterized integral equation. **Collocation** with five collocation points between each knot gives an overdetermined system which is solved by a least-squares method. For the **Galerkin** case we use the B-splines both as trial and test functions, and multiply (1) (after parameterization and application of the spline-expansion,) by $B_i(t)$ for all i, and integrate along the contour. This leads to a square system of exactly m equations.

4 Numerical results

We have implemented the methods and compared them with respect to accuracy (L^2-error) and the corresponding number of non-zero matrix elements of the linear systems. The problems are well conditioned, and the systems can be solved by an iterative method utilising only matrix-vector multiplications, with a constant number of iterations.

Our results show that

- The wavelet method results in a matrix which may easily be compressed, resulting in a very sparse system yielding an accurate solution.
- For smaller problems, or when high accuracy is not needed, a spline implementation will be both simple and efficient.
- For larger problems, e.g. when the geometry is complicated or a high degree of accuaracy is needed, an efficient implementation of the wavelet method will be able to outperform the spline method.

We show an example for the case of a square cylinder in the long wave approximation ($K = 0$) in fig. 2. The figure illustrates that large parts of the coefficient matrix in the wavelet method may be discarded, and that a higher accuracy is obtained in the wavelet case than in the spline case. In this particular example we also compare with analytical results by using the Schwarz-Christoffel transform. We find convergence, also at the corners of the square cylinder. Further results, for different wave frequencies, will be presented at the workshop.

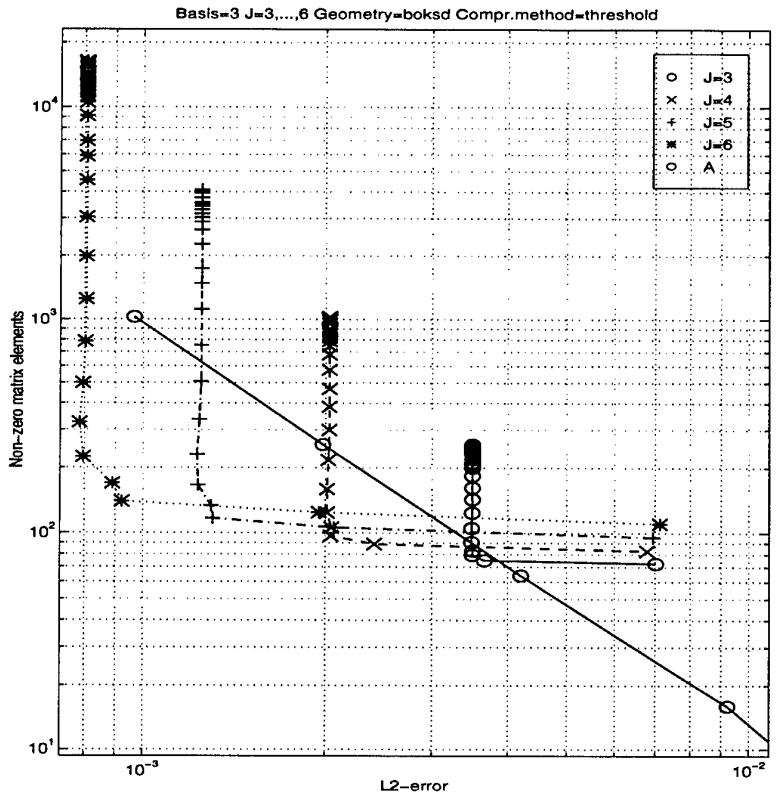

Figure 2: Accuracy of potentials for half-immersed square cylinder, surge motion, no incoming waves. $K=0$. Solid line: spline-Galerkin solution with quadratic splines. Dashed and dotted lines: wavelet solutions, basis $N=3$, varying degrees of matrix-compression. The number of unknowns before compression is 2^{J+1}, $J = 3,4,5,6$. Horizontal axis: L^2 error (accuracy). Vertical axis: Number of non-zero matrix elements in the linear system.

References

BEYLKIN, G., COIFMAN R. AND ROKHLIN, V. Fast wavelet transforms and numerical algorithms i. *Communications on Pure and Applied Mathematics,* XLIV:141-183, 1991.

DAUBECHIES, I. Ten Lectures on Wavelets. *CBMS-NFS Regional conference series in applied mathematics.* SIAM, Philadelphia, Pennsylvania, 1992.

JAWERTH, B. AND SWELDENS, W. An overview of wavelet based multiresolution analyses. *SIAM Review* , **2**, 36(3):377-412, Sept. 1994.

LEE, C.-H., MANIAR, H., NEWMAN, J. AND ZHU, X. Computations of Wave Loads Using a B-Spline Panel Method. *21st Symp. on Naval Hydrodynamics* , Trondheim, Norway, 1996.

NYGAARD, J. O., GRUE, J., LANGTANGEN, H. P., AND MØRKEN, K. On adaptive spline and wavelet methods for an integral formulation of inviscid flow. *To be published,*, 1996.

DISCUSSION

Huang J.:

1) Normally, when a function $f(x)$ is expanded in wavelet space, it is expanded in one wavelet space $\{V_m\}$, i.e. at scale m. Why did you expand $f(x)$ (as shown in eq. 2) using different $\{V_m\}$ and superimpose them?

2) You showed the results of potential derivative, did you involve the direct evaluation of wavelet in your computation? The derivative of Daubechies wavelet is highly oscillated.

Nygaard J.O., Grue J.:

1) The functions decomposed into multiresolution analyses are indeed decomposed only in one space V_J (a space spanned by translates of the *scaling function* ϕ,) but it is then decomposed further into the *wavelet spaces* (spanned by translates and dilations of the actual *wavelet* ψ) W_j, for $j = J_o, \ldots, J-2, J-1$, together with a remainder in V_o. Here, $V_J = U_{j=0}^{J-1} W_j \cup V_0$. (Note that V_0 is just a convenient way of denoting the coarsest space where the sequence of nested spaces is truncated.)

2) No, the direct evaluation of the scaling function ϕ or the wavelet function ψ were not used at any stage. The Daubechies wavelets (and scaling functions) are indeed highly oscillating for large N, and they are not very smooth for small N. This carries over to the derivatives of the functions, but we note that there are Daubechies bases with arbitrarily smooth scaling functions avd wavelets, and therefore also arbitrarily smooth derivatives. However, there is a connection between the smoothness and the oscillatory behaviour. (As well as length of support, length of discrete filters and so on, so any choice of N will be a compromise.)

When, for final plots and other uses of the functions expanded in the wavelet bases, evaluations are needed, the recursive refinement scheme (also denoted the *pyramid scheme*,) gives a stable and efficient way of obtaining large numbers of evaluations of the functions. This applies also to the more irregular of the Daubechies bases.

Magee A.:

1) In the compression method, you must search through the matrix to find the smallest value. Is this a significant computational burden?

2) Your results for the spline method seem to indicate that the results are improved with higher discretization (that is, the irregular behaviour is reduced for finer discretization). But is the exact (theoretical) irregular frequency equal to one of those used in the calculations? Have you checked frequencies nearby to be sure you are not missing the most irregular behavior of the numerical solutions which may change as a function of the discretization?

Nygaard J.O., Grue J.:

1) Yes, this is a burden in our implementation. However, this is done in this particular way because we have wanted to investigate whether or not the wavelet method will be able to compete with methods based on splines before putting effort into developing more efficient code. For an efficient implementation, larger portions of the elements to be discarded in the compression process have to be predicted without their actual computation.

2) Irregular frequencies are always present in the formulation, however, for a successively finer discretization of the spline knot vector, we find that the ill-behaved frequency domain is reduced. We shall look into more detail regarding the dependence of the observed irregular frequencies on the discretization.

Hydroelastic Response of a Floating Thin Plate in Very Short Waves

M. Ohkusu & Y.Nanba

Research Institute for Applied Mechanics, Kyushu University, Japan

1.Introduction

A thin membrane with small bending rigidity floating on the water surface is a model of a floating structure with huge horizontal size as large as several kilometers and very small draft of a few meters; this configuration is a recent conceptual design of floating airport. We present a theoretical method to predict hydroelastic response of such membrane to the wave action of incident wave at a constant frequency ω.

2.Formulation

The dynamic condition and the kinematic condition for the velocity potential $\phi(x,y,z)e^{i\omega t}$ of the flow to be satisfied underneath the membrane occupying the part of $z=0$ surface represented by Ω_M in Fig.1 are :

$$\left[\frac{D}{\rho g}\left(\frac{\partial^2}{\partial x^2}+\frac{\partial^2}{\partial y^2}\right)^2-\frac{\omega^2}{g}d+1\right]\frac{\partial\phi}{\partial z}-\frac{\omega^2}{g}\phi=0 \quad \text{at} \quad z=0 \quad \text{on} \quad \Omega_M \tag{1}$$

$$w=\frac{1}{i\omega}\frac{\partial\phi}{\partial z} \qquad \text{at} \quad z=0 \quad \text{on} \quad \Omega_M \tag{2}$$

where D is the bending rigidity, d the draft of the membrane, ρ the density of water and $w(x,y)e^{i\omega t}$ the vertical displacement of the membrane from the equilibrium position (Ohkusu & Namba (1996)). Notice that those conditions are imposed at $z=0$ because the draft d is negligibly small. Obviously the free surface condition on the water surface Ω_W, $z=0$ plane other than Ω_M, is given by

$$\frac{\partial\phi}{\partial z}-\frac{\omega^2}{g}\phi=0 \quad \text{at} \quad z=0 \quad \text{on} \quad \Omega_W \tag{3}$$

Our problem is to solve a boundary value problem of

$$\nabla^2\phi=0 \tag{4}$$

with the boundary conditions (1) and (3) and other condtions such as radiation condition and the edge condition of the membrane when a wave is incident on the membrane. Once ϕ is known we compute the deflection w of the membrane by using (1) and (2).

This problem may be considered as a problem of the wave propagation on two different media Ω_M and Ω_W, whose characteristics are represented by a quasi-free surface condition (1) and a free surface condtion (3) respectively. The "wave" elevation on the surface Ω_M is given by equation (2). The wave elevation on the real water surface Ω_W is also written similar way.

Dispersive relation corresponding to the quasi-free surface condition (1) will be written in the form

$$\left(\frac{D}{\rho g}k_*^4-\frac{\omega^2}{g}d+1\right)k_*-\frac{\omega^2}{g}=0 \quad \text{on} \quad \Omega_M \tag{5}$$

where k_* is the wave number of the "waves" occuring in the region Ω_M. One of five roots of equation (5) is a real number k_Λ. Two of other roots are complex numbers corresponding to the evanescent waves prevailing at the edge of the membrane. Another two roots have negative real part and not legitimate for our problem of deep water because the wave motion increases infinitely as z approches $-\infty$.

The wave number $k=\omega^2/g$ on the Ω_W is not equal to k_Λ on the Ω_M. This means the waves incident on the membrane are refracted following Snell's law when they propgate from the water surface into the membrane surface. Since $k>k_\Lambda$ generally, the incident waves do not penetrate into the membrane when the incident angle is less than a critical angle.

Let us consider the case when the wave length of the incident waves coming from the positive x is very small compared with B the breadth and L the length of the membraneas. It is a natural situation because the horizontal size of the structure is huge. So we assume $kL >> O(1)$ and $kB >> O(1)$. The waves penetrating through the edge EF at $x = 0$ into the region Ω_M at $0 << y << B$ will be approximately two dimensional waves uniform to the y direction, which would occur if the membrane extended from $y = -\infty$ to $y = +\infty$ without any edge. This is because the waves in that location many wavelengths away ffrom the edges is hardly affected by the existence of the edges at $y = 0, B$. Ohkusu & Nanba (1996) gave this 2D solution.

The velocity potential ϕ_{2D} of the 2D wave with uniform crest along the y direction and propagating into the positive x will be written in the form

$$\phi_{2D} = \bar{\phi}_{2D}(x, z)e^{-ik_\Lambda x} \tag{6}$$

when it propagates deep at $x >> O(1)$ into Ω_M. We can assume k_Λ is large and

$$\frac{\partial \bar{\phi}_{2D}}{\partial x} << k_\Lambda \tag{7}$$

in this location. The wave elevation near the edge FG ($y \sim 0$) and HE ($y \sim B$) on Ω_M must have a component matched with the form (6), which will be expressed in the form

$$\phi_\Lambda = \psi_\Lambda(x, y, z)e^{-ik_\Lambda x} \tag{8}$$

Another component of the wave elevation to occur near $y = 0$ or $y = B$ will be

$$\phi_0 = \psi_0(x, y, z)e^{-ikx} \tag{9}$$

This will be a penetrated wave through the edge FG at $y = 0$ or HE at $y = B$ from the water surface into the Ω_M. Nevertheless the incident waves e^{-ikx} are travelling into the direction paralel to both the edges and their incidence angle to the edges is zero, much less than the critical angle; since the progressing waves can not penetrate into the region Ω_M and the wave (9) must be the evanescent wave significant only near the edges, at $y = O(k^{-1})$ or $y = B - O(k^{-1})$.

Our final solution for the velocity potential ϕ is a summation of k_Λ component (8) and k component (9).

3. k_Λ-component

ϕ_Λ of (8) will be derived as follows. $\partial\psi_\Lambda/\partial x << k_\Lambda$ transforms $\nabla^2\phi_\Lambda$ to

$$\left(\frac{\partial^2}{\partial y^2} + \frac{\partial^2}{\partial z^2} - k_\Lambda^2\right)\psi_\Lambda = 0 \tag{10}$$

The condition (1) on Ω_M is approximated by

$$\left[\frac{D}{\rho g}\left(-k_\Lambda^2 + \frac{\partial^2}{\partial y^2}\right)^2 - \frac{\omega^2}{g}d + 1\right]\frac{\partial\psi_\Lambda}{\partial z} - \frac{\omega^2}{g}\psi_\Lambda = 0 \quad \text{at} \quad z = 0 \quad \text{on} \quad \Omega_M \tag{11}$$

The edge conditions of the membrane will be given by

$$\left(\frac{\partial^3}{\partial y^3} - (2-\nu)k_\Lambda^2\frac{\partial}{\partial y}\right)\frac{\partial\psi_\Lambda}{\partial z} = 0$$
$$\left(\frac{\partial^2}{\partial y^2} - k_\Lambda^2\nu\right)\frac{\partial\psi_\Lambda}{\partial z} = 0 \qquad \text{at} \quad y = 0 \tag{12}$$

Here ν is Poisson's ratio but we assume $\nu = 0$ in the article for simlicity.

The free surface condition on Ω_W is equation (3). It is straightforward to find radiation condition on the water surface side, which is

$$\psi_\Lambda \sim Ae^{ik\sqrt{1-(k_\Lambda/k)^2}y} \quad \text{at} \quad y \to -\infty \tag{13}$$

The solution should match with (6) on the Ω_M side when it is away from the edge of $y = 0$:

$$\psi_\Lambda \sim \bar{\phi}_{2D}(x,z) \quad \text{at} \quad y = Y \quad (0 << Y << B) \tag{14}$$

The solution ψ satisfying all the conditions (10) to (13) is given by

$$\psi_\Lambda(x,y,0) = f(x)\bar{\psi}_\Lambda(y,0) \tag{15}$$

Here $\bar{\psi}_\Lambda$ is a solution of a linear Fredholm integral equation

$$\bar{\psi}_\Lambda(y,z) = e^{k_\Lambda z} + k_\Lambda \int_0^Y \left(\bar{\psi}_\Lambda(y',z) - \frac{k}{k_\Lambda}\int_0^Y g(y',\eta)\bar{\psi}_\Lambda(\eta,0)d\eta\right) S(y,z;y',0)dy' \quad \text{at} \quad z = 0 \tag{16}$$

where $S(y,z;y',z')$ is wave source function of the Helmoholtz equation satisfying (10) and the radiation (13) which has been extensively studied. One expression of the wave source function is

$$S(y,0;y',0) = -\frac{k_\Lambda}{\pi}\int_0^\infty \frac{\mu K_1(k\sqrt{(y-y')^2+\mu^2})}{\sqrt{(y-y')^2+\mu^2}}d\mu + \frac{i}{\sqrt{1-(k_\Lambda/k)^2}}e^{-ik_\Lambda|y-y'|} \tag{17}$$

The Green function $g(',\eta)$ in the equation (16) is a solution of

$$\left(\frac{D}{\rho g}\frac{d^4}{dy^4} - 2\frac{D}{\rho g}k_\Lambda^2\frac{d^2}{dy^2} + \frac{D}{\rho g}k_\Lambda^4 - \frac{\omega^2}{g}d + 1\right)g(y,y') = \delta(y-y') \tag{18}$$

with the boundary conditions (12) ($\nu = 0$ is assumed) and

$$g = \frac{\partial g}{\partial y} = 0 \quad \text{at} \quad y = Y \tag{19}$$

The condition (11) is readily transformed into an integral form using $g(y,y')$ as

$$\frac{\partial\bar{\psi}_\Lambda}{\partial z} = k\int_0^Y g(y,y')\bar{\psi}_\Lambda(y',0)dy' \tag{20}$$

which was used in deriving the integral equation (16) from the Green's second identity.

The unknown $f(x)$ will be determined with the condition (14) and given by

$$f(x) = \bar{\phi}_{2D}(x,0)/\bar{\psi}_\Lambda(Y,0) \tag{21}$$

4. k-component

ϕ_0 of equation (9) is the effect due to the wave penetration through the edge $y = 0$ from the water surface side ($y < 0$) is significant only close to the edge. It is obtained as a solution when head seas are incident on a slender membrane; the method is given in Ohkusu & Nanba (1996). The solution is written as

$$\psi_0(x,y,z) = F(x)[e^{-kz} + \bar{\psi}_0(y,z)] \tag{22}$$

where $\bar{\psi}_0$ is a solution of an integral equation

$$\bar{\psi}_0(y,0) = \int_0^B kG(y,,0;y',0)\left[(\bar{\psi}_0(y,0)+1) - \int_0^B f(y',\eta)(\bar{\psi}_0(\eta,0)+1)d\eta\right]dy' \tag{23}$$

$G(y,z:y',z')$ is a wave source function not increasing exponentially at $|y| \to \infty$ given by Ursell (1968).

Unknown $F(x)$ is determined such that the outer approximation of (22) will match with the inner approximation of the outer potential. The matching condition is:

$$1 - \frac{1+i}{2\sqrt{\pi k}}\int_0^x \frac{d\xi Q(\xi)}{\sqrt{x-\xi}} = F(x) \tag{24}$$

$$Q(x) = F(x)k^2 \int_0^B \left[(\bar{\psi}_0(y,0) + 1) - \int_0^B f(y',\eta)(\bar{\psi}_0(\eta,0) + 1)d\eta \right] dy' \tag{25}$$

in those expressions $f(y,y')$ is the Green function similar to $g(y,y')$. $f(y,y')$ is a solution of (18) with k_Λ replaced by k satisfying the boundary conditions (12) at $y = 0$ as well as $y = B$ with k substituted in h_Λ.

5. Numerical example

One example of numerical results by the present method is illustrated in Fig.1. This picture shows the deflection of the membrane at one time instant. Feature of the combined effect due to k and k_Λ components is seen. Details of numerical calculation and another results will be presented at the Workshop.

References

Ohkusu,M. and Nanba,Y. (1996): Hydroelastic behavior of a very large floating platform in waves, 11th WWWFB, Hamburg

Ursell,F. (1968): On head seas travelling along a horizontal cylinder, J.of Inst.Maths. Applics. 4

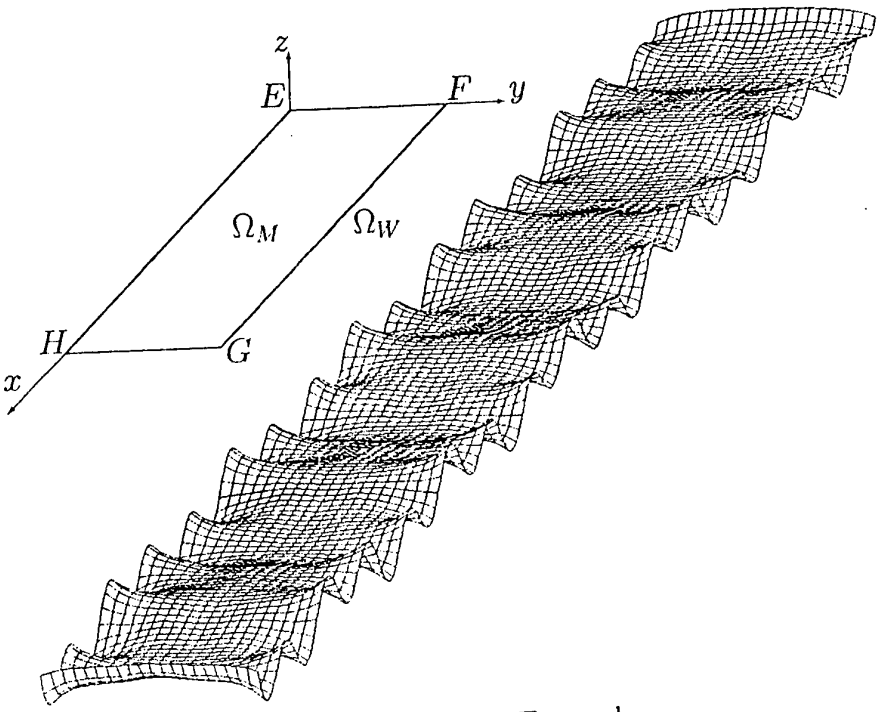

Fig.1 Numerical Example

Recent results on trapped modes and their influence on finite arrays of vertical cylinders in waves

R. Porter and D. V. Evans
School of Mathematics, University of Bristol, Bristol, BS8 1TW, UK

Introduction

At the last Workshop in Hamburg, Maniar & Newman showed that at particular frequencies the in-line first-order exciting forces on those cylinders near the centre of a large number of identical bottom-mounted vertical circular cylinders in a linear array become extremely large, compared to the force on an isolated cylinder. These frequencies coincide with those associated with certain trapped modes around a corresponding cylinder on the centre-plane of a wave channel. These trapped modes are of two types. The Neumann trapped modes, satisfying Neumann conditions on all solid boundaries and a Dirichlet condition on the centre-plane, were discovered by Callan *et al* (1991) and have been proved to exist for all values of $0 < a/d < 1$ where $2a$ is the cylinder diameter and $2d$ is the width of the channel. See Evans *et al* (1994). Numerical computations by Callan *et al* (1991) indicate that there is just one such trapped mode having a unique wavenumber, k^N, satisfying $k^N < \pi/2d$ where the angular velocity ω^N is given by $\omega^N = (gk^N \tanh k^N h)^{1/2}$ with h the depth of the channel. Physically the Neumann trapped mode describes an antisymmetric sloshing motion about the centre-plane of the channel which is confined to the vicinity of the cylinder and decays rapidly down the channel. Mathematically, the value $(k^N)^2$ is an eigenvalue of the Laplacian operator in the unbounded region contained between one channel wall, the centre-plane of the channel and one half of the cylinder, and $(k^N)^2$ lies below the continuous spectrum which for this problem is $[\pi^2/4d^2, \infty)$.

The second type, discovered by Maniar & Newman (1996) and described as Dirichlet trapped modes, satisfy a Neumann condition of no normal flow through the cylinder surface but Dirichlet conditions on both the channel walls and the centre-plane. They have no obvious physical interpretation in the context of water waves but are well-known in the acoustical literature where they are termed acoustic resonances. For a review, see Parker & Stoneman (1989).

In contrast to the Neumann trapped modes, the Dirichlet trapped modes only appear to exist for a restricted range of a/d. Thus the computations of Maniar & Newman (1996) suggest that a Dirichlet trapped mode exists provided $0 < a/d \lesssim 0.677$, a figure which the present authors have refined to 0.6788 using the same method.

Convincing experimental evidence for the Neumann trapped modes have been given recently by Retzler (private communication, 1996). Maniar & Newman (1996) pointed out that long finite periodic arrays of identical bottom-mounted cylinders have applications to structures such as long bridges or proposed designs for offshore airports. In practice, however, it is clear that at least a double array of supporting cylinders will be needed so that it is important to predict the corresponding trapped mode frequencies for *more* than a single cylinder on the centre-line. In fact we have solved the problem of determining all the trapped modes which can occur when any number of rigid bottom-mounted vertical circular cylinders are placed on the centre plane of a channel. The cylinders can have any radii and can be spaced arbitrarily and the trapped modes are antisymmetric about the centre plane and satisfy either Neumann or Dirichlet conditions on the channel walls.

The method is based on the multipole method, in which singular solutions of the Helmholtz equation satisfying an antisymmetry condition on the channel centre plane are modified to include the boundary conditions on the channel walls. The total potential about any cylinder may then be expressed as a Fourier-type sum over all relevant multipoles and the total potential anywhere in the channel as the sum over all cylinders. The remaining condition to be satisfied, that of no-flow on

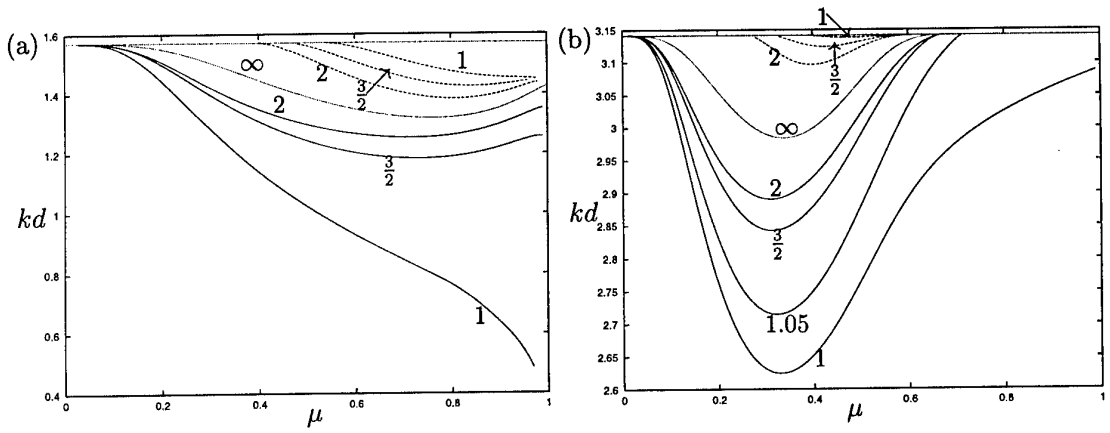

Figure 1: Variation of (a) Neumann and (b) Dirichlet trapped mode frequencies as μ varies in the case of two cylinders for different values of the spacing parameter λ (shown against the curves). Symmetric modes (——), antisymmetric modes (– – –).

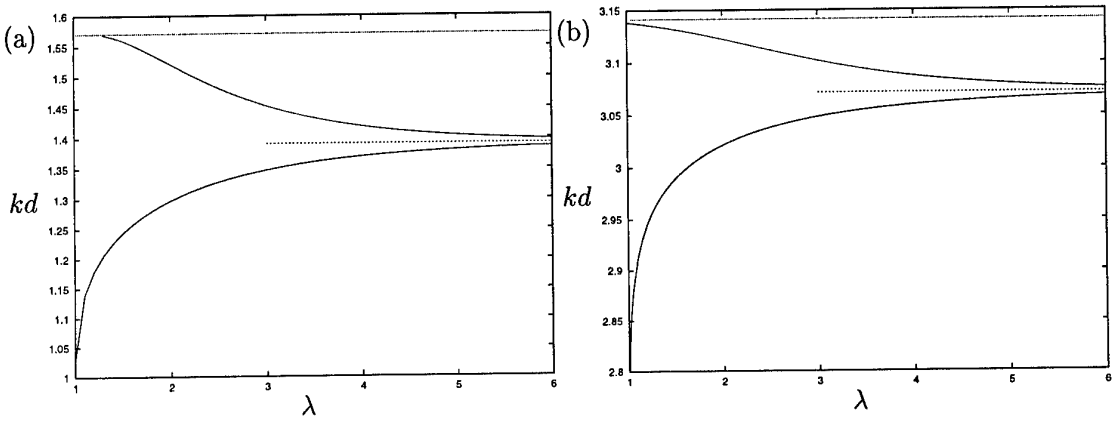

Figure 2: Variation of (a) Neumann and (b) Dirichlet trapped mode frequencies for two cylinders, both $\mu = \frac{1}{2}$ as the spacing parameter, λ, varies.

the cylinder surfaces, is achieved by use of a Bessel function addition theorem, as in Linton & Evans (1990), yielding a homogeneous determinant system whose non-trivial solutions correspond to the trapped mode frequencies. The same method has recently been used by Linton & McIver (1996) to determine the scattering properties of any number of circular cylinders of arbitrary size and position in a channel. The method is an extension of that used by Callan *et al* (1991) for the single cylinder.

The number of possible configurations of cylinders we could consider to illustrate the results is of course limitless so we shall concentrate mainly on the case of two identical cylinders because of its connection with *finite* double arrays of cylinders which occur in offshore structures. The non-dimensional trapped mode wavenumber kd is in this case a function of two dimensionless parameters μ and λ describing the size and spacing of the centres of the cylinders. We choose $\mu = a/d$ and let the centres of the cylinders be located at $(\pm\lambda a, 0)$ so that λ is a spacing parameter being the ratio of cylinder separation to cylinder diameter. When $\lambda = 1$ the cylinders are touching and as $\lambda \to \infty$ we would expect results for the trapped modes to approach the single cylinder results as the interaction between them diminishes. This proves to be the case as figure 1 illustrates. Here, Neumann and Dirichlet trapped mode wavenumbers kd are plotted against μ for different λ. Also shown is the unique curve for both the Neumann and Dirichlet trapped modes for an isolated cylinder which we label $\lambda = \infty$. We consider the Neumann modes first, all of whose wavenumbers satisfy $kd < \pi/2$. The solid curves are symmetric Neumann trapped modes whilst the dashed curves above the $\lambda = \infty$ curve are all antisymmetric Neumann trapped modes. We can draw the following conclusions about the Neumann modes from figure 1. For sufficiently large μ there exist *two* trapped modes, a low frequency symmetric mode and a higher frequency antisymmetric mode, for each value of λ. However, for fixed

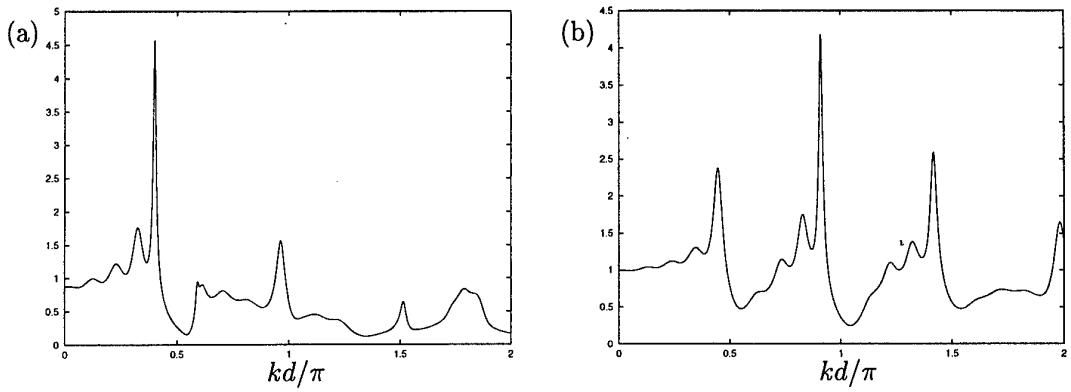

Figure 3: Maximum exciting force against non-dimensional wavenumber kd in the case of head seas interacting with a double array of 2×9 cylinders all of radius a. The two rows are $4a$ apart and in each row the centres are $2d$ apart. (a) $a/d = \frac{1}{2}$, (b) $a/d = \frac{1}{4}$.

λ, as μ decreases a value is reached at which the antisymmetric mode disappears.

It appears from figure 1 that, as expected, the curves for increasing λ approach the single cylinder results. This is more clearly seen in figure 2 which plots kd against λ for $\mu = \frac{1}{2}$. Both the Dirichlet and the Neumann curves rapidly approach the corresponding single cylinder trapped mode frequency as λ increases. Notice how the antisymmetric Neumann mode cuts off below a certain value of $\lambda > 1$ whilst the antisymmetric Dirichlet mode persists down to touching at $\lambda = 1$. This behaviour can also be seen from figure 1 by considering the intersection of $\mu = \frac{1}{2}$ with curves of different λ. However it is also clear from figure 1 that in general the behaviour of the Dirichlet modes is more complicated than the Neumann modes.

It is possible to remove the channel walls and regard both types of trapped modes as oscillations between adjacent pairs of cylinders in a doubly-infinite row, the Neumann modes having an antinode at each mid-plane between pairs of cylinders and the Dirichlet modes a node. Following the discussion of Maniar & Newman (1996) that a *finite* single row containing many cylinders could experience large forces and at frequencies close to the Neumann and Dirichlet trapped modes for a single cylinder in a channel, or its equivalent *infinite* row of cylinders, we should expect that the peaks in figures 3(a) and 3(b) which give the maximum in-line exciting force on the middle pair of cylinders in a double row of 2×9 cylinders due to head seas to be close to the corresponding symmetric trapped modes. In figures 3(a),(b) the distance between two cylinders in a pair is $4a$ so that in both figures the corresponding doubly-infinite row requires $\lambda = 2$. It is clear from figure 1 at $\lambda = 2$ that this is indeed the case. Thus the computed values of the symmetric Neumann and Dirichlet trapped mode wavenumbers for $\mu = \frac{1}{2}$ are $kd = 1.29771$ and $kd = 3.02157$ respectively compared to the peaks at 1.256 and 3.024 in figure 3(a) whilst for $\mu = \frac{1}{4}$ the trapped modes at $kd = 1.46567$ and 2.90894 compare to the peaks at 1.400 and 2.856 respectively in figure 3(b). The other peaks in figures 3(a),(b) correspond to nearly-trapped waves. However, recent careful numerical calculations have confirmed, using two independent methods that it is possible to find a pure trapped mode of both Neumann and Dirichlet type, at the very precise values of $a/d = 0.3520905$ with $k^N d = 1.488884\pi$ and for $a/d = 0.2670474$ with $k^D d = 1.991867\pi$ respectively. Notice that these trapped modes are embedded in the continuous wavenumber spectrum. Surface elevations for each trapped mode are presented in figure 4.

The effect of increasing the number of cylinders in a channel is generally to increase the number of trapped mode frequencies to be equal to the number of cylinders. It can be anticipated that the exciting force on cylinders in the centre of an array consisting of four lines of periodically-spaced identical cylinders would show large values at the four wavenumbers corresponding to the equivalent trapped modes.

Finally it is not necessary to have large numbers of cylinders to obtain large forces. As a result of near-trapping effects it is possible for as few as four bottom-mounted cylinders to manifest large forces, in this case, 50 times that on a single cylinder, when excited by a particular incident wave

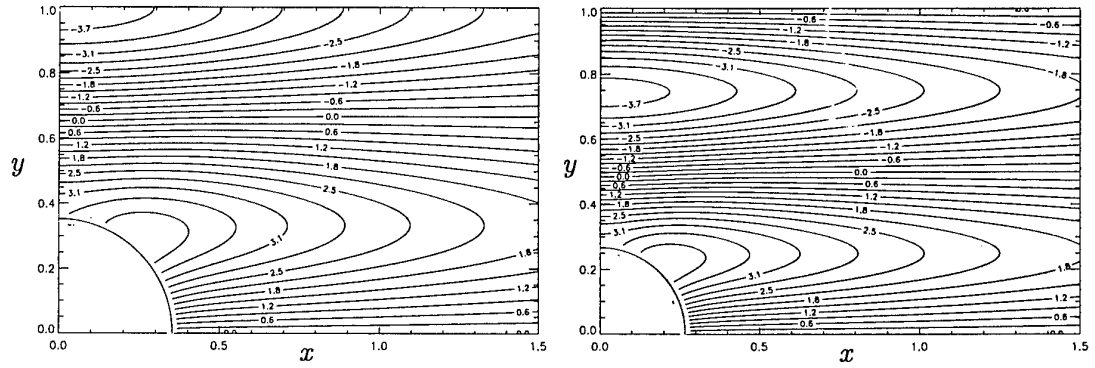

Figure 4: Surface elevation for Neumann and Dirichlet trapped modes embedded in the continuous spectrum.

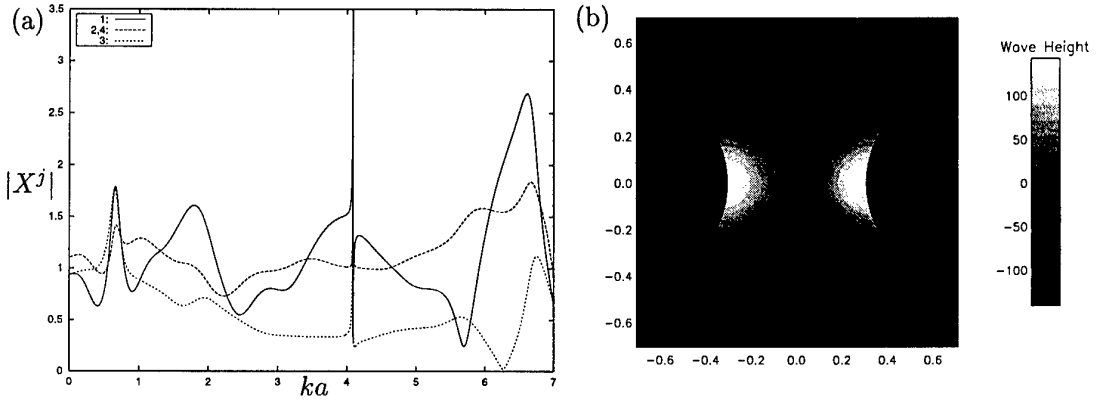

Figure 5: (a) Non-dimensional forces on four cylinders arranged in a square in head seas as wavenumber ka varies; (b) Free surface elevation at near-trapping ($ka = 4.08482$).

frequency, as shown in figure 5(a) using the interaction theory of Linton & Evans (1990). Notice from figure 5(b), which describes the free surface at near-trapping that the force acts radially and alternates in sign from one cylinder to the next.

Conclusion

We have illustrated the importance of an understanding of trapped modes in order to anticipate possible large forces on finite arrays of bottom-mounted cylinders. We have derived results for any number of cylinders in a wave channel and shown how these affect a finite double array of cylinders. We have also shown how near-trapping can account for large forces for as few as four cylinders when the spacing is sufficiently small, and we have presented results for pure trapped modes which are embedded in the continuous spectrum. Further results will be described at the Workshop.

References

CALLAN, M., LINTON, C. M. & EVANS, D. V. 1991 Trapped modes in two-dimensional waveguides. *J. Fluid Mech.* **229**, 51–64.

LINTON, C. M. & EVANS, D. V. 1990 The interaction of waves with arrays of vertical circular cylinders. *J. Fluid Mech.* **215**, 549–569.

LINTON, C. M. & MCIVER, P. 1996 The scattering of water waves by an array of circular cylinders in a channel. *J. Eng. Maths.* **30** 661–682.

MANIAR, H. D. & NEWMAN, J. N. 1996 Wave diffraction by a long array of cylinders. *Submitted for publication in J. Fluid Mech.*

PARKER, R & STONEMAN, S. A. T. 1989 The excitation and consequences of acoustic resonances in enclosed fluid flow around solid bodies. *Proc. Instn. Mech. Engrs.* **203**, 9–19.

VIOLENT SURFACE MOTION AROUND VERTICAL CYLINDERS IN LARGE, STEEP WAVES - IS IT THE RESULT OF THE STEP CHANGE IN RELATIVE ACCELERATION?

R.C.T.RAINEY

Centre for non-linear dynamics, University College London, and WS Atkins London

Abstract

Violent surface motions are seen around fixed vertical cylinders in large, steep waves. They are also predicted, by the small-time expansion method, when a vertical cylinder moving horizontally in still water undergoes a step change in its horizontal acceleration. But a sharp (classically 120 degree) crest, which is the defining feature of steep waves, necessarily implies a step change in horizontal particle acceleration in the incident wave (since surface slope = $a_x/(g + a_z)$ where a_x and a_z are horizontal and vertical components of particle acceleration).This observation suggests that the violent surface motion is *the result of a step change in the relative cylinder acceleration.*

The leading-order small-time expansion result on the moving cylinder is derived and discussed below. Despite the violence of the surface motion, it is noteworthy that the hydrodynamic force per unit length on the cylinder actually *reduces* near the surface. In terms of slender body theory, the total effect of the free surface is of a higher order in slenderness than the other forces acting.

1. Background

There is considerable current interest in the oil industry in the violent motion of the water surface produced around a vertical cylinder by a wave which is relatively large (height/diameter = 2, say) and also very steep (height/length = 0.1, say). Figures 1, 2 and 3 illustrate the effect at realistic scales. Its importance is not only in the potentially damaging effect on the superstructures of offshore oil platforms, but also in the "ringing" vibration produced by the associated sudden load fluctuations. From a theoretical point of view, the interest in the phenomenon is that it is highly non-linear (the vibration can be at ten times the wave frequency), and that Stokes expansion methods widely employed (see e.g. Malenica & Molin, 1995) for calculating wave loads are probably irrelevant, see Chaplin, Rainey & Yemm, 1997.

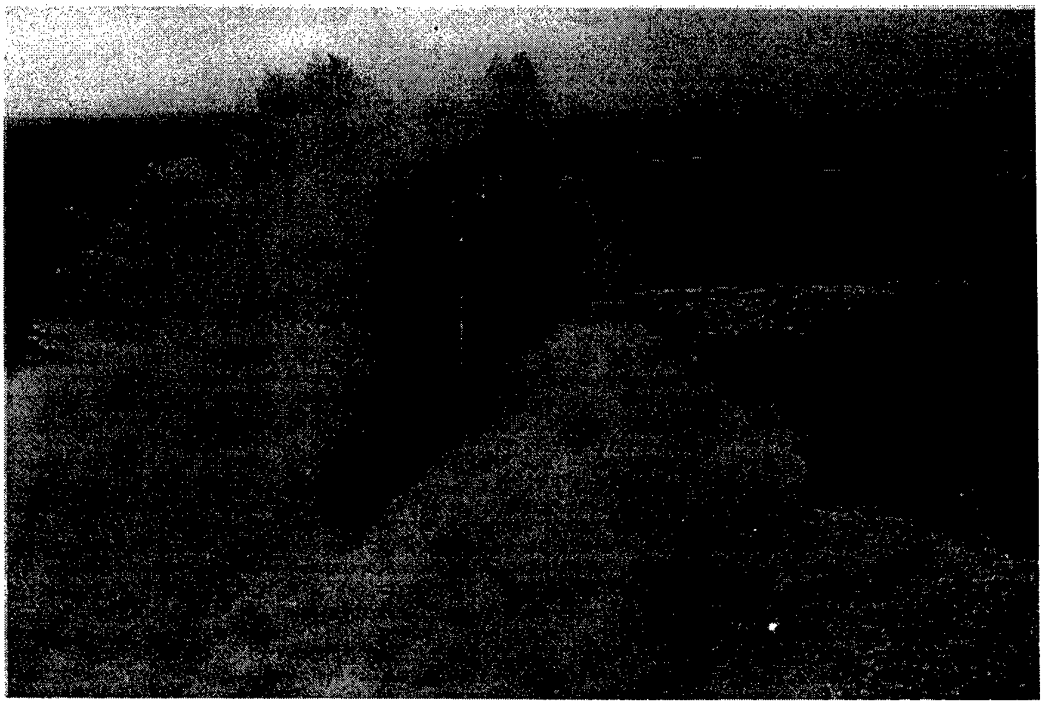

Figure 1. Large wave at the AR-MEN lighthouse, Brittany; diameter approximately 8m

Figure 2. Focused wave at the large flume at De Voorst; cylinder diameter 0.5m

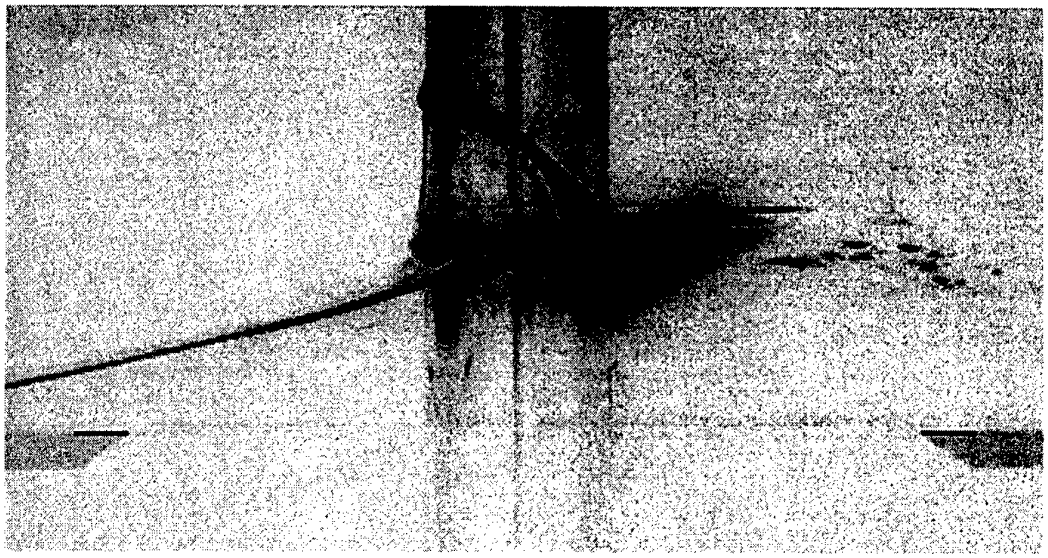

Figure 3. Focused wave passing a cylinder of diameter 0.1m in recent experiments on "ringing" (after Chaplin, Rainey & Yemm, 1997)

2. The small-time expansion solution for a vertical cylinder moving horizontally from rest in still water

In the well-known small-time expansion scheme, which has recently been applied to this problem by Wang and Chwang (1989), the velocity potential φ and surface elevation η are expanded as power series thus:

$$\phi = \phi_1 t + \phi_2 t^2 + \phi_3 t^3 + \ldots. \qquad \eta = \eta_1 t + \eta_2 t^2 + \eta_3 t^3 + \ldots. \qquad (1)$$

By Taylor series expansion of ϕ about the still-water position ($z = 0$), the free-surface boundary conditions can then be applied at $z = 0$, as a series of conditions of successively higher order in the time t. The process is closely analogous to Stokes' expansion, with t replacing the Stokes expansion parameter. The leading-order boundary conditions are:

$$\phi_1 = 0 \qquad \eta_1 = 0\,, \quad 2\eta_2 = \partial\phi_1 / \partial z \tag{2}$$

This potential-flow problem can be easily solved, for finite depth in the case of Wang and Chwang, and for infinite depth here. We simply observe (see e.g. Bland (1961) p.108-9) that there are solutions of the form:

$$\phi = \phi_1 t = at[kK_1'(kb)]^{-1} K_1(kr)\cos\theta \sin kz \tag{3}$$

where the cylinder velocity is at (i.e. a step change in acceleration from zero to a), b is its radius, and r, θ, z are the usual cylindrical co-ordinates, with $\theta = 0$ being the direction of motion and z being positive upwards. Rather than the required normal velocity on the cylinder surface of $at\cos\theta$, these solutions have a velocity of $at\cos\theta\sin kz$; they must therefore be combined by means of the Fourier sine transform:

$$\frac{2}{\pi}\int_0^\infty \frac{\sin kz}{k} dk = \mathrm{sgn}(z) \tag{4}$$

to give the required solution as:

$$\phi_1 = \frac{-2}{\pi}\int_0^\infty \frac{aK_1(kr)\cos\theta \sin kz}{k^2 K_1'(kb)} dk \tag{5}$$

so that the leading-order expression for the free surface elevation is:

$$\eta = \frac{-1}{\pi}\int_0^\infty \frac{at^2 K_1(kr)\cos\theta}{kK_1'(kb)} dk \tag{6}$$

This is readily plotted with MATHCAD and is shown (out to a distance $10b$ from the axis) in Figure 4 below.

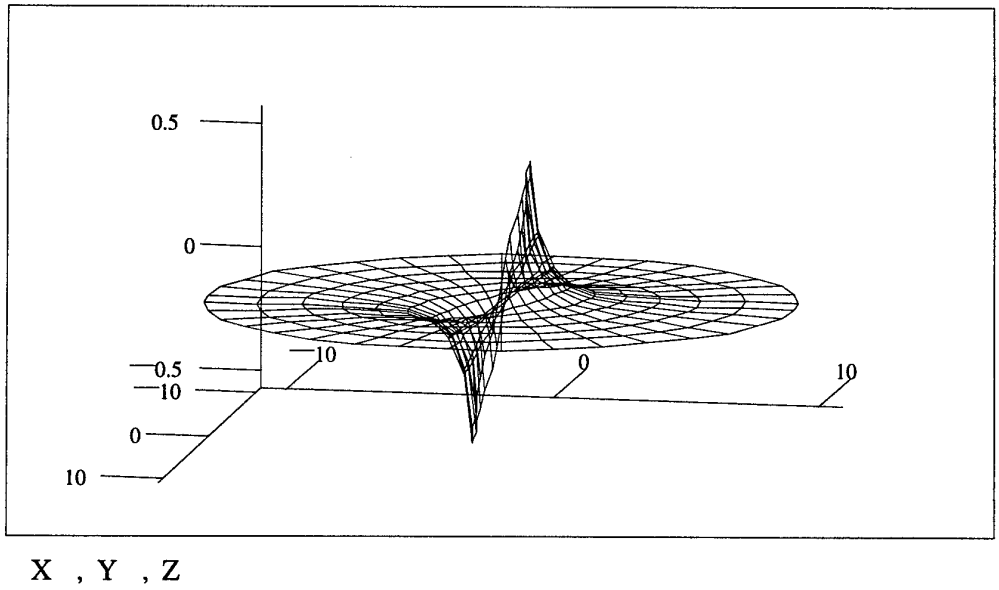

Figure 4. Free surface around a vertical cylinder accelerating from rest in still water

For present purposes the striking feature is the singularity at the cylinder surface, reminiscent of the flows in Figures 1-3. This feature has long been recognised in earthquake engineering, as occurring next to dams (Westergaard 1933) and cylindrical piers (Jacobsen 1949) undergoing impulsive motions. In this literature the surface boundary conditions (2) appear to be taken as axiomatic, without any formal justification by a small-time expansion. Indeed, the dam or pier motion is taken as a continuous vibration, from which the impulsive motion is later synthesised.

Perhaps no less interesting is the force per unit length on the cylinder, which is readily obtained to leading order, by integrating the transient pressure $-\rho\phi_t = -\rho\phi_1$ from (5), around the cylinder, to give:

$$2\rho b \int_0^\infty \frac{aK_1(kb)\sin kz}{k^2 K_1'(kb)} dk \qquad (7)$$

in the sense opposing the acceleration a of the cylinder, i.e. as an "added mass force". This expression can also readily be evaluated with MATHCAD, as shown (from $z = -10b$ to $z = 0$) in Figure 5 below.

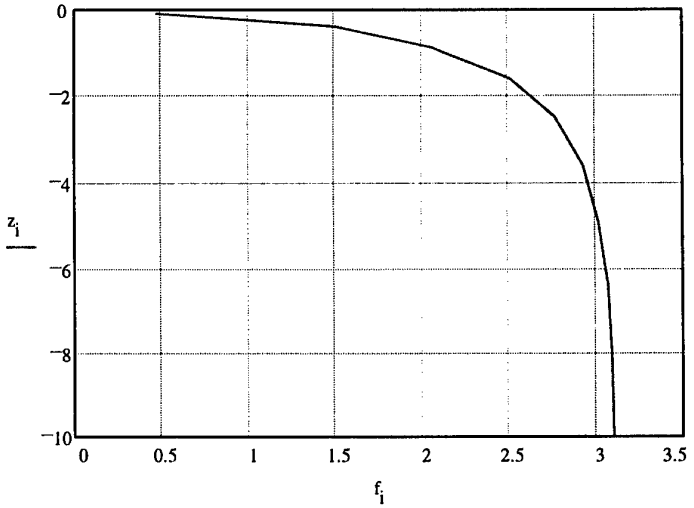

Figure 5. Variation of force per unit length f (normalised w.r.t. $\rho b^2 a$) with depth z

As expected, it converges to $\pi\rho b^2 a$ at large depth (i.e. the 2-D "Morison" result), but tends to *zero* as the surface is approached. Thus the violent surface motion of Figure 4 is associated, somewhat surprisingly, with a *reduction* of the hydrodynamic load, compared with the 2-D result. The difference in the total load can be obtained by integrating the above curve with depth - according to MATHCAD the result is about $\pi\rho b^3 a$. In terms of slender-body theory, the dependence on b^3 makes the effect of higher order in slenderness than other "end effects". There is thus no contradiction with the "end effect" discussed by the author at the 10th Workshop (Rainey, 1995) - that was of lower order in slenderness, but evidently only important when the flow remains smooth (i.e. the Stokes' expansion case of small wave steepness), as indeed suggested then.

This work was supported by EPSRC through MTD Ltd (grant GR/J23198), and jointly funded by the managed programme on uncertainties in loads on offshore structures.

References

Bland, D.R., 1961 *Solutions of Laplace's Equation* London: Routledge & Kegan Paul

Chaplin, J.R., Rainey, R.C.T. & Yemm, R.W. 1997 Ringing of a vertical cylinder in waves *JFM (submitted April 96, and in revised form December 96)*

Malenica & Molin, 1995 Third harmonic wave diffraction by a vertical cylinder *JFM* ***302*** *203-229*

Rainey, R.C.T. 1995 The hydrodynamic load at the intersection of a cylinder with the water surface

Wang, K-H & Chwang, A.T. 1989 Non-linear free-surface flow around an impulsively moving cylinder *J.Ship Res.* ***33*** *no.3 194-202*

Westergaard, H.M. 1933 Water pressures on dams during earthquakes *Trans ASCE* ***98*** *418-433*

Jacobsen, L.S. 1949 Impulsive hydrodynamics of fluid inside a cylindrical tank and of a fluid surrounding a cylindrical pier *Bulletin of the Seismological Society of America* ***39*** *189-204*

DISCUSSION

Schultz W.: The small time expansion is non-uniformly valid near the contact line (Joo, Schultz, Messitor 1991?; King & Needham 1995). A local expansion no longer has the $\phi_0 = 0$ free surface condition and modifies the *ln tanh* singularity. It is likely that this modification might have negligible effect on a slamming force, based on your results. Any comment?

Rainey R.C.T.: Indeed. In 1994, in the *Journal of Fluid Mechanics*, Vol 268 pp 89-101, King and Needham treat the 2-D "wavemaker" problem rigorously, and I understand from Howell Peregrine that their methods ought to be applicable in the present case of a vertical cylinder. Such a rigorous treatment might show that the surface motion remains violent, and the slamming force is little changed, as you suggest. If you, or they, were to investigate this matter further, I would be delighted!

Grilli S.: Two dimensional computations using fully nonlinear potential flow equations have shown that very large upward vertical accelerations can be created for certain types of so-called flip-through wave impacts on vertical structures. I would think that a similar phenomenon could occur for vertical cylinders, assuming some sort of wave focusing ensuring quasi-2D conditions. This hence could explain the violent upward motions you observed. We of course have to wait for the 3D codes to be efficient enough to get a more definite answer. Can you comment on this?

Rainey R.C.T.: I assume you mean the type of "flip-through" impact described in the paper by Peregrine and Cooker at the 1990 WWWFB in Manchester, and subsequently e.g. in *Coastal Engineering (1992)*. This is a very interesting suggestion, but actually I am not aware of it having been seen in model tests on cylinders. The phenomenon I am describing occurs well before wave breaking, and there is no vertical wall of water approaching the cylinder and "flipping through".

Two-Dimensional Inviscid Transom Stern Flow

S. M. Scorpio and R. F. Beck
University of Michigan, USA

Introduction

Two-dimensional fully nonlinear transom stern flow is investigated using the Desingularized Euler - Lagrange Time-domain Approach or DELTA method. Mixed Euler-Lagrange time stepping is due to Longuet-Higgins and Cokelet (1976). The field equation is solved using the desingularized boundary integral method described in Beck et al. (1994). The flow is unsteady in that the problem is started from rest and accelerated up to steady forward speed. The purpose of this study is to compare with previous steady calculations and to provide a starting point for extending to unsteady fully nonlinear three-dimensional transom stern flows.

The cases studied herein correspond to those in Vanden-Broeck and Tuck (1977) and Vanden-Broeck (1980). They compute nonlinear waves behind a transom stern using a series expansion in the Froude number. The problem is solved in an inverse manner in which the coordinates x and y are the dependent variables and the velocity potential and stream function ϕ and ψ are the independent variables. The series expansions in x and y are everywhere divergent but can be summed by standard methods. Integro-differential equations with nonlinear boundary conditions are solved in the inverse space to obtain the expansion coefficients.

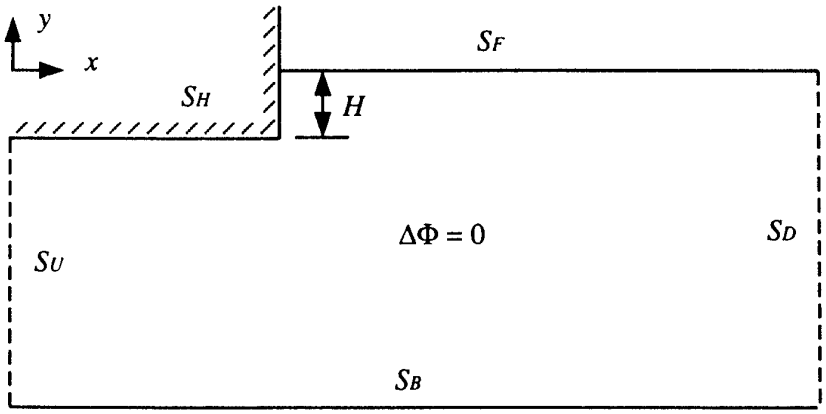

Figure 1: Problem configuration

Problem Formulation

Figure 1 shows the problem configuration. The $x - y$ coordinate system is translating with speed U_b in the negative x direction. Laplace's equation governs in the fluid domain and the velocity potential is $\Phi = U_b x + \phi$. The surfaces which bound the fluid are: S_F = Free Surface; S_H = Body Surface; S_U = Upstream Truncation Surface; S_D = Downstream Truncation Surface; S_B = Bottom Surface.

The boundary conditions are:

$$\left.\begin{aligned} \frac{D\eta}{Dt} &= \frac{\partial \phi}{\partial z} \\ \frac{D\phi}{Dt} &= -g\eta + \tfrac{1}{2}|\nabla\phi|^2 \end{aligned}\right\} \qquad \vec{x} \in S_F$$

$$\frac{\partial \phi}{\partial n} = -U_b n_1 \qquad \vec{x} \in S_H$$

$$\nabla\phi \to 0 \quad \text{as} \quad y \to -\infty \qquad \vec{x} \in S_B$$

where $\frac{D}{Dt} = \frac{\partial}{\partial t} + \nabla\Phi \cdot \nabla$ is the material or Lagrangian derivative, $\vec{n} = (n_1, n_2, n_3)$ is the unit normal on the body pointing out of the fluid, g is the acceleration of gravity, η is the free surface elevation, and ϕ is the perturbation potential. The boundaries S_U and S_D are unspecified. We have run cases with S_U and S_D prescribed to satisfy continuity and saw very little difference in the results as long as S_U and S_D are far enough up and downstream respectively. We placed the trunction boundaries about twelve wavelengths away from the transom for these calculations.

Results

Vanden-Broeck (1980) suggested that two realistic solutions exist for the steady flow behind a transom stern. For small values of the Froude number, the flow rises up the transom to a stagnation point. The free surface separates from the transom at the stagnation point creating waves downstream which increase in steepness with increasing Froude number. We'll call this solution A. This solution is physically unreasonable for large values of Froude number because the ratio of stagnation height to transom depth goes to infinity as the Froude number goes to infinity. For large Froude numbers a second, more physically realizable solution exists in which the flow separates cleanly from the bottom of the transom. We'll call this solution B. This solution reduces to the uniform stream as Froude number tends to infinity and the downstream waves steepen as Froude number becomes small. In fact, Vanden-Broeck (1980) found a minimum Froude number (= 2.26) below which the downstream waves would exceed the theoretical breaking wave steepness limit ($2A/\lambda = 0.141$).

The problem is started from rest and the hull is accelerated up to steady forward speed. Using the DELTA method, the inviscid solution *always tends towards configuration A* as the hull reaches steady forward speed, regardless of the Froude number. In a viscous fluid, we know that the flow behaves like solution B for high Froude numbers. As the hull speed increases from rest, the flow separating from the bottom of the transom becomes turbulent, resulting in the "dead water" region commonly observed behind transom sterns. Consequently the pressure behind the transom is lowered. Eventually the falling pressure causes the free surface to drop to the bottom of the transom resulting in the solution B flow. Once the flow is separating cleanly from the transom, the turbulence is confined to the thin boundary layer (for high speeds) and viscous wake. Using an inviscid flow model, it appears to be impossible to proceed from transom wetted to transom dry. However, we did find two techniques which resulted in solution B.

The first was to start the problem at steady forward speed with the transom out of the water. The hull is then lowered slowly into the water. As the hull is lowered, the free surface remains separated from the bottom of the transom and solution B results. This

technique will not work for a problem starting from rest with the transom immersed. In order to obtain solution B for the problem starting from rest we tried a second technique in which we attempt to mimic the effect of the dead water region by artificially lowering the stagnation pressure on the transom. This pressure drop can be modeled in the inviscid flow code by modifying the boundary condition on the transom. The condition,

$$\frac{\partial \phi}{\partial n} = -U_b n_1$$

causes the stagnation pressure. We reduce the stagnation pressure by modifying the transom boundary condition to:

$$\frac{\partial \phi}{\partial n} = -U_b n_1 \left(2e^{-\beta t^2} - 1\right)$$

As the hull accelerates up to speed, the pressure on the transom drops until the free surface drops down to the bottom of the transom. When the hull reaches steady speed, solution B is recovered.

The general numerical details are similar to those outlined in Beck et al. (1994). There is a double node where the free surface meets the transom in the solution A flow. One node satisfies the body boundary condition while the other satisfies the free surface boundary condition. Treating the intersection in this manner has consistently worked well in the desingularized method. There is one additional constraint (or Kutta condition) at the bottom of the transom in the solution B flow. The free surface nodes are allowed to move downstream with the fluid velocity during the intermediate time steps (we're using 4^{th} order Runge-Kutta). At the end of a major time step the free surface nodes are regrided back to their original positions by interpolating elevations and potentials. The Kutta condition is imposed by regriding the first free surface node back to the bottom of the transom. The potential at this point is computed from the source strengths.

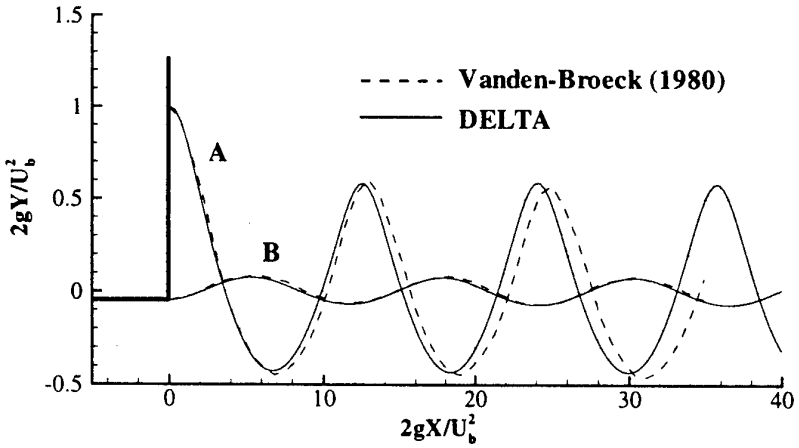

Figure 2: Solutions A and B at $F_H = 6.3$

Figure 2 shows the waves generated by the transom stern at Froude number based on transom depth of $F_H = U_b/\sqrt{gH} = 6.3$. The fully nonlinear solution starting from rest is compared with Vanden-Broeck's 1980 results which are also fully nonlinear. Both steady state solutions A and B are compared. The solutions agree quite well except there is a noticeable difference in wavelength for solution A.

	a^*	λ^*	$2a^*/\lambda^*$	λ_0^*	λ_4^*
Vanden-Broeck	0.53	12.1	0.088	12.6	11.5
DELTA	0.51	11.6	0.088	12.6	11.6

Table 1: Comparison of downstream wave characteristics for solution A

Table 1 shows downstream wave characteristics for the Vanden-Broeck (1980) and DELTA solution A. Here, $a^* = a2g/U_b^2$ is the nondimensional wave amplitude found by subtracting the minimum wave elevation from the maximum and dividing by two for the downstream waves and $\lambda^* = \lambda 2g/U_b^2$ is the nondimensional wavelength. Since the phase speed of the waves equals U_b, we can use the deep water dispersion relation to estimate the wavelength. The linear wavelength is $\lambda_0^* = \lambda_0 2g/U_b^2 = 4\pi = 12.6$. Using the 5^{th} order dispersion relation for deep water Stokes waves ($U_b^2 = g/k(1 + (ka)^2 + 5/4(ka)^4)$) and the computed wave amplitude (a) we can solve for the wave number (k) and get an estimate for the nonlinear wavelength ($\lambda_4^* = \lambda_4 2g/U_b^2$). Although both computations show waves with the same steepness, Vanden-Broeck's waves do not satisfy 5^{th} order dispersion.

Conclusions

For two-dimensional transom stern flow, the transition from transom wetted to transom dry at high Froude number is accomplished in the inviscid flow model by modifying the transom boundary condition. Perhaps a more appropriate transom boundary condition could be contrived which allows solution A for low Froude numbers and transitions appropriately to solution B as the Froude number increases through the critical value ($F_H = 2.26$). Presumably this technique may be applied to the unsteady three-dimensional problem. Of course flow behind a three-dimensional transom is much more complex and requires further study.

Acknowledgments

This research was funded by the Office of Naval Research and the University of Michigan/Sea Grant/Industry Consortium on Offshore Engineering. The computations were made in part using a CRAY allocation at the San Diego Supercomputer Center.

References

1. Beck, R.F., Cao, Y., Scorpio, S.M. and Schultz W.W., (1994). Nonlinear ship motion computations using the desingularized method. 20^{th} *Symposium on Naval Hydrodynamics*, Santa Barbara, California.

2. Longuet-Higgins, M.S. and Cokelet, C.D., (1976), The deformation of steep surface waves on water: I. A numerical method of computation. In *Proceedings of the Royal Society of London*, vol. **A350**, pp. 1-26.

3. Vanden-Broeck, J.-M. and Tuck, E.O., (1977), Computation of near-bow or stern flows, using series expansion in the Froude number. In *Proceedings of the* 2^{nd} *International Conference on Numerical Ship Hydrodynamics*, Berkeley.

4. Vanden-Broeck, J.-M., (1980). Nonlinear stern waves. *Journal of Fluid Mechanics*, vol. **96**, part 3, pp. 603-611.

DISCUSSION

Tuck E.O.: Can you explain why the particular form of the body boundary condition was chosen, with the property that the RHS exactly changes sign as t goes from 0 to ∞. As $t \to \infty$, since no part of this boundary is wet, it surely doesn't matter what the limiting boundary condition is.

Scorpio S., Beck R.: The boundary conditions was: $\frac{\partial \phi}{\partial n} = -U_b n_1 \left(2e^{-\beta t^2} - 1\right)$.

At $t = 0$, $\frac{\partial \phi}{\partial n} = -U_b n_1$, as $t \to \infty$, $\frac{\partial \phi}{\partial n} \to +U_b n_1$.

Initially we tried $\frac{\partial \phi}{\partial n} = -U_b n_1 \, e^{-\beta t^2}$ but $\frac{\partial \phi}{\partial n} \to 0$ as $t \to \infty$ was not strong enough to suck the free surface down to the bottom of the transom. $\frac{\partial \phi}{\partial n}$ had to change sign in order to generate the necessary drop in pressure. Professor Tuck is absolutely correct in that there is no significance in $\frac{\partial \phi}{\partial n} \to +U_b n_1$ as $t \to \infty$.

In fact, the form of the boundary condition was arbirarily chosen to provide a smooth transition from transom wetted to dry. Surely there are many choices of boundary condition which would produce the same result.

Yeung R.W.: In a recent work (Yeung, 1991, Math. Approaches to Hydrodynamics, SIAM Publ.) a number of "time-dependent" solutions were worked out in the context of "solution A". There was basic agreement with Van-den-Broeck's results. In the same article (see also Yeung & Ananthakrishnan, 1992, 19th ONR Symposium), a solution with viscosity is given to illustrate how an entrained vortex is first formed at the "sharp stern", leading eventually to its "sheering off". Presumably, at sufficiently large time, the drop in water level in the stern will approach the keel point. These references may serve to explain what is happening at the stern physically.

Scorpio S., Beck R.: We would like to thank Professor Yeung for his comments and for the references that we are sure will be most helpful. The mechanisms that cause the transom stern flow to proceed from wetted to dry as the ship accelerates from rest are very interesting. We think there is a good qualitative understanding of this process already. Perhaps some careful physical experiments, or numerical experiments as cited by Professor Yeung, can give us a better quantitative understanding of this process.

The 12st International Workshop on Water Waves and Floating Bodies, Marseilles, 1997

Stability Analysis of the 2D linearized unsteady free-surface condition

Lisette M. Sierevogel and Aad J. Hermans
Department of Applied Mathematics, Delft University of Technology, The Netherlands

Introduction

In recent years, many studies have been carried out to describe unsteady ship motions. These motions are important to predict the seakeeping behaviour of a ship, which includes the interaction between waves and the velocity of the ship. Prins (1995) has developed a two- and three-dimensional time-domain algorithm to compute the behaviour of a cylinder, a sphere and a commercial tanker in current and waves. Since the results were satisfactory, we have extended this method by including a frequency-independent absorbing boundary condition, see Sierevogel (1996a), and apply it to a LNG carrier at higher speed, see Sierevogel (1996b).
The increase in the speed causes some numerical instabilities on the free surface. However, the instabilities disappear by using upwind discretization instead of central discretization for the x-derivative. In this abstract, we carry out a theoretical study of the numerical dispersion and damping, and the stability. We follow the work of Raven (1996) and Nakos (1990). The analysis is restricted to the two-dimensional (2D) case for simplicity, while we did also computation in 3D.

1 The time-domain algorithm

In this abstract, we consider the 2D problem we described in Sierevogel (1996a): A cross-section of a horizontal circular cylinder with radius R, floating in water of infinite depth. A uniform stream flows with velocity U in the positive x-direction and regular waves are travelling in the positive or negative x-direction. The coordinate system is chosen such that the undisturbed free surface coincides with $z = 0$. We consider a potential flow with the velocity potential Φ, satisfying the Laplace equation. By using the dynamic and kinematic conditions and by dividing the potential into a steady ϕ and an unsteady $\overline{\phi}$ part, we get an linearized free-surface condition on the undisturbed free surface. We approximate the unsteady potential $\overline{\phi}$ by the undisturbed flow potential Ux. In Sierevogel (1996a), we don't do this approximation, but in this analysis it is done for simplicity. Now the linearized free-surface condition becomes

$$\phi_{tt} + g\phi_z + 2U\phi_{xt} + U^2\phi_{xx} = 0 \quad \Rightarrow \quad \phi_z = -\frac{1}{g}\phi_{tt} - \frac{2U}{g}\phi_{xt} - \frac{U^2}{g}\phi_{xx} \qquad \text{at } z = 0\,, \tag{1}$$

To solve the problem, we introduce a Green function, G, satisfying the Laplace equation and we use Green's second theorem. We can use this Green's theorem to calculate the potential on every time step and every panel. Knowing the potential, we are able to calculate the first- and second-order forces and motions. However, in this abstract we are only interested in the stability of the potential on the free surface. Therefore, we are looking at Green's theorem for the potential on the free surface. When both $\boldsymbol{x}$ and $\boldsymbol{\xi}$ are on the free surface, then $G_\zeta = 0$ and the principal value of the integral along ∂S_{fs} becomes zero. Combining equation (1) and Green's theorem, we get

$$\frac{1}{2}\phi(x,t) - \int\limits_{\partial S_{fs}} \left(\frac{1}{g}\frac{\partial^2}{\partial t^2} + \frac{2U}{g}\frac{\partial^2}{\partial\xi\partial t} + \frac{U^2}{g}\frac{\partial^2}{\partial\xi^2}\right)\phi(\xi,t)G(x-\xi)\,\mathrm{d}\xi = RHS \qquad \text{at } z,\zeta = 0\,. \tag{2}$$

with the right hand side, which includes all integrals over the rest of the boundary,

$$RHS = \int\limits_{\partial S\setminus\partial S_{fs}} (\phi G_\zeta - G\phi_\zeta)\,\mathrm{d}\Gamma := \int\limits_{\partial S_{fs}} f(\boldsymbol{\xi})G(\boldsymbol{x},\boldsymbol{\xi})\,\mathrm{d}\xi\,.$$

In practice errors will also be introduced by the discretization of the potential on the hull surface. However, in this abstract we only look at the errors due to the discretization of the free-surface.

2 Continuous Fourier Transform

The Fourier transform of the continuous free-surface equation (2) is derived using the 2D Fourier Transform of the function $\phi(x,t)$ and its inverse are defined by the following pair of equations

$$\tilde{\phi}(k,\omega) = \int_{-\infty}^{+\infty}\!\!\int \phi(x,t)e^{-i(\omega t - kx)}\,\mathrm{d}x\,\mathrm{d}t \quad \text{and} \quad \phi(x,t) = \frac{1}{(2\pi)^2}\int_{-\infty}^{+\infty}\!\!\int \tilde{\phi}(k,\omega)e^{i(\omega t - kx)}\,\mathrm{d}\omega\,\mathrm{d}k\ ,$$

with k the Fourier wave number in the x-direction and with ω the frequency in Fourier space. By using Lighthill's (1959) definition of the Fourier Transform of a log function, we derive the Fourier Transform of the Green function. By using the convolution theorem, we get the Fourier Transform of equation (2). Next we can write continuous Fourier Transform of the potential as follows

$$\tilde{\phi}(k,\omega) = \frac{\tilde{F}(k,\omega)\tilde{G}(k)}{\frac{1}{2} + \left(\frac{\omega^2}{g} - \frac{2U\omega k}{g} + \frac{U^2k^2}{g}\right)\tilde{G}(k)}\ .$$

Transforming the solution back to physical space, leads to

$$\phi(x,t) = \frac{1}{4\pi^2}\int_{-\infty}^{+\infty}\int_{-\infty}^{+\infty} \frac{\tilde{F}(k,\omega)}{\tilde{\mathcal{W}}(k,\omega)}\,e^{i(\omega t - kx)}\,\mathrm{d}\omega\,\mathrm{d}k\ , \quad \text{with} \quad \tilde{\mathcal{W}}(k,\omega) = -|k| + \frac{\omega^2}{g} - \frac{2U\omega k}{g} + \frac{U^2k^2}{g}\ .$$

with $\tilde{\mathcal{W}}$ the continuous spectrum In section 4, we evaluate the continuous and discrete spectrums, we compare the dispersion relation for the continuous problem with that of the discrete problem. The dispersion relation of the continuous problem is the polar $\tilde{\mathcal{W}}(k,\omega) = 0$.

3 Discrete Transformations

In the discrete problem, the solution $\phi(x,z,t)$ is discretized over a free-surface grid of uniform spacing Δx in the x-direction. The collocation point is in the centre of the panel. The solution $\phi(x,z,t)$ is discretized in the time using a uniform time step Δt. To find the discrete form of the free-surface condition, we write equation (2) as follows

$$\frac{1}{2}\phi(x_i,t_n) - \sum_{j=-\infty}^{+\infty}\left(\frac{1}{g}\frac{\partial^2}{\partial t^2} + \frac{2U}{g}\frac{\partial^2}{\partial\xi_j\partial t} + \frac{U^2}{g}\frac{\partial^2}{\partial\xi_j^2}\right)\phi(\xi_j,t_n)\int_{\xi_j-\frac{\Delta x}{2}}^{\xi_j+\frac{\Delta x}{2}} G(x_i-\xi)\,\mathrm{d}\xi = RHS$$

We derive the Fourier Transforms of respectively the integral over the Green function, the x- and t-derivatives, and the free-surface condition, using the 2D Discrete Fourier Transform, and its inverse , which are defined as

$$\hat{\phi}(k,\omega) = \Delta x\Delta t\sum_{m=-\infty}^{+\infty}\sum_{n=-\infty}^{+\infty}\phi(x_m,t_n)e^{-i\theta} \quad \text{and} \quad \phi(x_m,t_n) = \frac{1}{4\pi^2}\int_{-\frac{\pi}{\Delta x}}^{+\frac{\pi}{\Delta x}}\int_{-\frac{\pi}{\Delta t}}^{+\frac{\pi}{\Delta t}}\hat{\phi}(u,s)e^{i\theta}\,\mathrm{d}k\,\mathrm{d}\omega\ ,$$

where $\theta = \omega n\Delta t - km\Delta x$, and using the discrete convolution theorem. For the first- and second-order x-derivative we use either a central difference scheme or an upwind scheme. By introducing the non-dimensional wave number $\hat{k} = \frac{k\Delta x}{2\pi}$ and frequency $\hat{\omega} = \frac{\omega\Delta t}{2\pi}$, which can been seen as one over the number of step per wavelength or period, the discrete dispersion relation can be written as

$$\begin{aligned}
\hat{W} = {} & -|k|\frac{\pi\hat{k}}{\sin\left(\hat{k}\pi\right)} - \frac{\omega^2}{g}\frac{1}{4\pi^2\hat{\omega}^2}\left(2 - 5e^{-2\pi i\hat{\omega}} + 4e^{-4\pi i\hat{\omega}} - e^{-6\pi i\hat{\omega}}\right) - \\
& \frac{2U\omega k}{g}\frac{1}{16\pi^2\hat{\omega}\hat{k}}\left(3 - 4e^{-2\pi i\hat{\omega}} + e^{-4\pi i\hat{\omega}}\right)\left(d_1^{(x)}e^{-2\pi i\hat{k}} + d_0^{(x)} + d_{-1}^{(x)}e^{2\pi i\hat{k}} + d_{-2}^{(x)}e^{4\pi i\hat{k}}\right) - \\
& \frac{U^2k^2}{g}\frac{1}{4\pi^2\hat{k}^2}\left(d_1^{(xx)}e^{-2\pi i\hat{k}} + d_0^{(xx)} + d_{-1}^{(xx)}e^{2\pi i\hat{k}} + d_{-2}^{(xx)}e^{4\pi i\hat{k}}d_{-2}^{(xx)}e^{6\pi i\hat{k}}\right) = 0\ . \qquad (3)
\end{aligned}$$

4 Evaluation of the discretization schemes

The evaluation is done first for the zero-speed case, and then the complete dispersion relation, first for waves travelling with the current to the right and then for waves travelling to the right. We compare the the roots of the dispersion relation computed by the continuous and discrete spectrums. We analyse the errors, try to find the wiggles and give some stability criterions. We follow the work of Raven (1996) and Nakos (1990), but our dispersion relation is more complex than theirs. Their continuous and discrete operator, applying linear Kelvin free-surface condition and considering a source contribution, are linear in the wave number. Therefore, the intersection of real part of $Lh(\hat{k})$ with the line $1/Fn_\Delta^2$ indicates the wave number of the discretized case and the imaginary part of $Lh(\hat{k})$ is proportional to the numerical damping. In our case we have the analyse the discrete wave number itself

$$k_d = k_c \{1 + C_R(\omega, \Delta\omega, \Delta x) + iC_I(\omega, \Delta\omega, \Delta x)\} \ . \tag{4}$$

When k_c is negative the wave is travelling to the left and when k_c is positive the wave is travelling to the right. The discrete wave numbers are the roots of the discrete dispersion relation $\hat{W}$. The term C_R indicates numerical dispersion, an increase ($C_R < 0$) or decrease ($C_R > 0$) of the characteristic length of the associated waves. The term C_I indicates numerical damping ($C_I < 0$) or numerical amplification ($C_I > 0$). Usually one root is nearly the continuous wave number. Any secondary root away from the continuous wave number indicates a spurious wave number. If the imaginary part of this root is positive, wiggles will appear.

In figure 1 and 2, we show the numerical dispersion C_R and damping C_I of the first wave numbers, calculated with equation (3) for downstream waves, as function of $\hat{k}$. We see that for both discretizations for $\hat{k} < 0.08$ the both the numerical dispersion and damping are small, but there is more numerical damping using the upwind scheme. We also notice that the wave number decreases for $U > .1$ using upwind discretization, while it increases using central discretization.

Using central discretization, the dispersion relation sometimes has two roots for one frequency, see figure 3. The solid lines are the wave number of the continuous dispersion relation. The root far from the continuous wave number has a very large imaginary part, this means that the short waves with that wavelength will amplify rapidly, these numerical instabilities are called wiggles. Figure 3 shows, for instance, that when $\hat{k} = 0.10$ and $U = 0.2$, there are wiggles for $\omega \geq 8$, and no wiggles for $\omega < 8$. In figure 4, we show the critical grid Froude number $Fn_{\Delta x} = U/\sqrt{g\Delta x}$ as function of U. This grid Froude number is used by Nakos (1990) and Raven (1996) in their analysis. In our analysis, we can say that the central discretization is stable that $Fn_{\Delta x} < 0.15$, however it seems that there is still a dependence of the grid size or $\hat{k}$. More calculations for smaller $\hat{k}$ show the conditions remains $Fn_{\Delta x} < 0.15$.

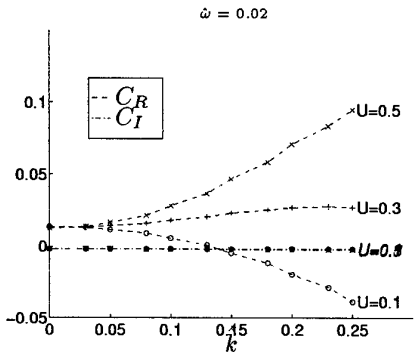

Figure 1: *The numerical dispersion C_R and damping C_I for the first root, as in equation (4), as function of $\hat{k}$, for different speed U, using central discretization*

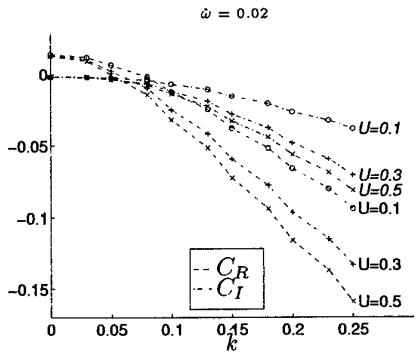

Figure 2: *The numerical dispersion C_R and damping C_I for the first root, as in equation (4), as function of $\hat{k}$, for different speed U, using upwind discretization*

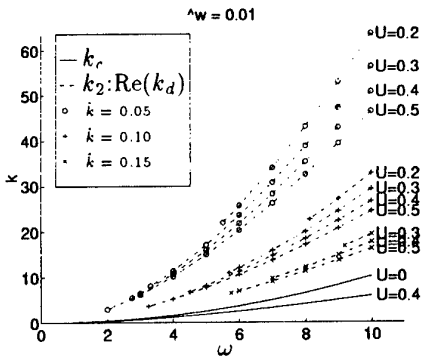

Figure 3: *The spurious wave number, as function of the frequency, for different $\hat{k}$, for $\hat{\omega} = 0.01$ and for different speed U, using central discretization*

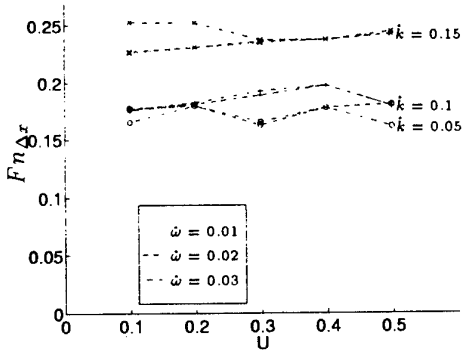

Figure 4: *The maximum value of the grid Froude number as function of U, $\hat{k}$ and $\hat{\omega}$, for which the central discretization is stable*

5 Conclusions

In this abstract, we developed a theoretical model for a stability analyse of the unsteady 2D linearized free-surface condition. The stability analyse shows us that the numerical method used in Prins(1995) and Sierevogel (1996a) is accurate if we use minimum 20 panels per wavelength and 50 time steps per period. We compare central and upwind discretization, and it turns out that downstream with both discretizations the numerical damping and dispersion is less than 1%. The disadvantage of central discretization is the numerical instability which appear when the grid Froude number $Fn_{\Delta x} > .15$. Upstream is the numerical dispersion using upwind discretization larger than using central discretization, but central discretization causes numerical instabilities. Therefore we need more time steps per period.

An other possibility to eliminate the numerical instabilities is a upstream shift of the collocation point, see Raven (1996). A more accurate scheme using less panels can be obtain using higher-order basis functions on the panels, for example quadratic splines, see Nakos (1990). It is possible to evaluate the 3D linearized free-surface condition the same way as we presented in this abstract, only the problem two times three unknowns: x, Δx, y, Δy, t, Δt, and therefore complex to evaluate.

In our numerical program we use the double body potential instead of the undisturbed potential flow. We also use a Green's function which satisfies the bottom condition. These points may change the stability condition a little.

References

Lighthill, M.J. (1959). *Introduction to Fourier analysis and generalised functions.* University Press, Cambridge.

Nakos, D.E. (1990). *Ship wave patterns and motions by a three dimensional Rankine panel method.* PhD thesis, Massachusetts Institute of Technology, USA.

Prins, H.J. (1995). *Time-domain calculations of the drift forces and moments.* PhD thesis, Delft University of Technology, The Netherlands.

Raven, H.C. (1996). *A solution method for the nonlinear ship wave resistance problem.* PhD thesis, Delft University of Technology, The Netherlands.

Sierevogel, L.M. and Hermans, A.J. (1996a). Absorbing boundary condition for floating two-dimensional objects in current and waves. *Journal of engineering mathematics 30, 573-586.*

Sierevogel, L.M. and Hermans, A.J. (1996b). Time-domain calculations of first- and second-order forces on a vessel sailing in waves. *Proc. of the 21st symp. on naval hydrodynamics, Trondheim.*

DISCUSSION

Kim Y.:

1) In the unsteady problem, temporal stability is also important. Could you explain your temporal stability criteria?

2) Could you show that the limiting case of numerical dispersion when $\Delta x, \Delta t \to 0$ goes to continuous dispersion relation?

Sierevogel L. + Hermans A.: The authors are grateful to Y. Kim for giving a copy of an unpublished article [1].

1) To examine the temporal stability we follow Kim, Kring & Sclavounos [1] and write the discrete dispersion relation as a third-order complex relation

$$\frac{1}{g(\Delta t)^2}Z^3+\left(\frac{-4}{g(\Delta t)^2}+\frac{-U}{2g\Delta t\Delta x}D^{(x)}\right)Z^2+\left(\frac{5}{g(\Delta t)^2}+\frac{4U}{2g\Delta t\Delta x}D^{(x)}\right)Z$$
$$+\frac{\Delta x}{2\hat{G}}+\frac{-2}{g(\Delta t)^2}+\frac{-3U}{2g\Delta t\Delta x}D^{(x)}-\frac{U^2}{g(\Delta x)^2}D^{(xx)}=0,$$

where $Z=e^{-i\omega\Delta t}$ is the growth factor for each time step. When one of the three roots of this dispersion relation is outside the unit circle in the complex plane, the numerical scheme is temporal unstable. Satisfying the conditions in the paper, the numerical scheme seems to be temporal stable, but this case is too complex to derive a condition analytical, the way Kim, Kring & Sclavounos [1] did.

2) The consistency of the discrete dispersion relation can be examined through using Taylor polynomials when $lim_{\Delta x\to 0}$ and $lim_{\Delta t\to 0}$, then follows

$$\hat{W}=\tilde{W}+\mathrm{O}\left((\Delta x,\Delta t)^2\right)$$

---

[1] Kim Y., Kring D.C., & Sclavounos, P.D. (1997). Linear and nonlinear interactions of surface waves with bodies by a three-dimensional Rankine panel method. *Submitted for publication.*

(12th Int. Workshop on Water Waves and Floating Bodies, Marseille, France, 16-19 March 1997)

A Second Order 3D BEM for Wave-Structure Interaction

Jesper Skourup[1] , Bjarne Büchmann[2] & Harry B. Bingham[1]

INTRODUCTION

At the previous workshop a 3D Boundary Element Model with active absorption at the open boundaries was presented. The model was formulated correct to second order in the free surface conditions but only the linear part of it was implemented. The tests involved regular waves on a fixed structure and forced linear motions of a floating structure. Further details can be found in Skourup and Bingham (1996).

The present abstract considers some of the extensions to the model, which have been implemented since the last workshop. The second order free surface conditions have now been implemented and active absorption is used at the lateral boundaries for both the first order scattered waves and for the second order scattered waves. Numerical results to second order of the run-up on a fixed vertical circular cylinder are presented and they agree well with the analytical second order results by Kriebel (1992). Results are also presented using first order irregular waves incident on a freely floating ship. The computed motions of the ship compare well with linearized frequency domain calculations using the well verified frequency domain code WAMIT.

MATHEMATICAL FORMULATION

A potential flow is assumed, with boundary conditions expanded up to second order and applied on the mean positions of the free surface and body boundaries (see Isaacson and Cheung, 1992, or Skourup, 1996). The total velocity potential is separated into a known incident potential ϕ_I, and a scattering potential ϕ_S representing the effects of the body and its motions,

$$\phi(\vec{x},t) = \varepsilon\left[\phi_I^{(1)}(\vec{x},t)+\phi_S^{(1)}(\vec{x},t)\right] + \varepsilon^2\left[\phi_I^{(2)}(\vec{x},t)+\phi_S^{(2)}(\vec{x},t)\right] + \ldots \quad (1)$$

where ε is the perturbation parameter, $\vec{x}$ is an observation point, t is the time and the superscripts denote the order of the expansion. By formulating the boundary value problem for the scattered field alone all waves in the domain are outgoing waves, and all lateral boundaries can thus be formulated as absorbing boundaries.

The active wave absorption method used here is similar to the one used at the Danish Hydraulic Institute for wave absorption in physical flumes. The motion of a wave absorber is a function of the time history of the wave absorber position and of the free surface elevation at the wave absorber. These are transformed to an updated wave absorber position by use of a digital filter designed to match a theoretically determined transfer function (see Schäffer et al., 1994, for details). The same technique may also be used in a 3D model by considering a finite number of 2D wave absorbers placed next to each other and working independently. Each absorber is then governed by the same digital recursive filter and by the local time history of the position of the absorber and the elevation there. An extension to a fully 3D active absorption method is given in Schäffer and Skourup (1996), but it has not yet been implemented

[1] International Research Centre for Computational Hydrodynamics, Danish Hydraulic Institute, Agern Allé 5, DK-2970 Hørsholm, Denmark, e-mail:icch@dhi.dk

[2] Department of Hydrodynamics and Water Resources, Building 115, Technical University of Denmark, DK-2800 Lyngby, Denmark, e-mail:buchmann@isva.dtu.dk

into the present version of the program. In the numerical simulations the absorbers all work in the piston mode, but digital filters are also available for hinged flap wave absorbers. The wave absorber boundary condition is of the Neumann type.

To compute the potential, the boundary value problem is re-cast as a boundary integral equation via Green's 2nd identity

$$\alpha(\vec{x})\phi(\vec{x},t) = \int_{\Gamma} \phi(\vec{\xi},t)G_n(\vec{x},\vec{\xi}) - G(\vec{x},\vec{\xi})\phi_n(\vec{\xi},t)\, d\Gamma \tag{2}$$

where $\vec{\xi} = (\xi_1,\xi_2,\xi_3)$ is the position vector of an integration point situated at the boundary Γ of the domain, subscript n indicates differentiation along the outwards normal vector at $\vec{\xi}$, and the factor $\alpha(\vec{x})$ depends on the position of the observation point ($\alpha(\vec{x}) = 2\pi$ for $\vec{x}$ situated at a smooth part of the boundary). Equation (2) is discretized using a panel method with the kernel function $G(\vec{x},\vec{\xi}) = 1/|\vec{x} - \vec{\xi}|$, and the variation over a panel of both the potential and the geometry is taken to be linear. Collocation is performed at the corners of each panel, and the resulting linear system of equations is solved by LU factorisation at the first time level (i.e. at $t=0$) and then by back-substitution at each time step. The free surface boundary conditions are integrated using 4th order Adams-Bashforth and Adams-Moulton schemes. Further details concerning the numerical solution can be found in Skourup (1996).

NUMERICAL EXAMPLES

Two numerical examples are given in this abstract. The first example considers second order wave run-up on a fixed vertical circular cylinder. The numerical wave tank is square with a side length equal to about 3.5 times the length of the regular waves used in each test. The cylinder is situated with the centre at the symmetry line of the wave tank, and a Green's function accounting for the symmetry and satisfying the impermeability condition at the horizontal sea bed is used. Thus, the calculation domain can be reduced to half of the original domain and the sea bed can be excluded. For these tests the boundary of the domain is discretized using about 3500 nodes and a simulation covering 10 wave periods is performed using 2000 time steps. The computing time for one simulation is 40 CPU minutes on an IBM RS6000 computer.

The maximum run-up on the cylinder is determined as the average value of the wave crest height during a few wave cycles. The linear solution is well known and straightforward to compute (cf. MacCamy and Fuchs, 1954), while the second order solution is by no means simple to determine (see Kriebel, 1990). Kriebel (1992) gave results correct to second order for wave run-up on a vertical circular cylinder covering a range of ka and kh values (where k is the wavenumber, a is the cylinder radius and h is the water depth). These results are reproduced using the present second order Boundary Element Method. In Fig. 1 ka=0.271, kh=0.750 and the wave steepness is kH=0.215 (where H is the wave height). The agreement with the second order run-up curve from Kriebel (1992) is very good. Another example with ka=0.684, kh=1.894 and kH=0.391 is depicted in Fig. 2. Again the agreement with the results by Kriebel (1992) is excellent. A more comprehensive comparison with Kriebel's results will be given at the conference.

As a second example we consider a Series 60 C_b=0.7 hull exposed to a sum of first order waves (corresponding to an irregular wave time series) incident from ahead. In order to minimize wave reflections (i.e. by generating waves in the optimal frequency range of the active absorber), and to retain an adequate spatial discretization for all wave components, eight waves distributed in the range $1.29 < \omega' < 2.48$ are used (where $\omega' = \omega\sqrt{h/g}$ is the non-dimensional radian wave frequency). The boundary of the domain is discretized with 2000 nodes and a simulation covering 2048 timesteps takes about 15 CPU minutes on the IBM RS6000 computer. Figures 3, 4 and 5 show the response amplitude operators (RAO) and phases for the ship in the surge, heave and pitch modes. These results have been computed as the Fourier transform of the body motion relative to the Fourier transform of the incident wave elevation at the centre of the ship. The simulation results compare well with calculations made using the well verified frequency-domain code WAMIT (1995). The small discrepancies at the higher frequencies are attributed to a sparse discretization of the corresponding wave lengths.

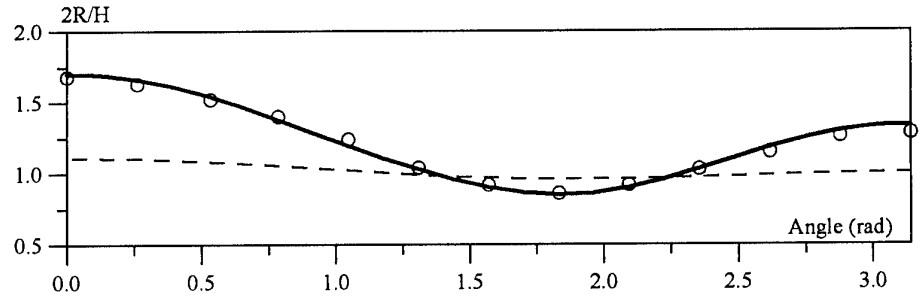

Figure 1. Wave run-up on fixed vertical circular cylinder. ka=0.271, kh=0.750, kH=0.215. Linear solution (dashed), second order solution (solid). The analytical results by Kriebel (1992) are depicted by circles.

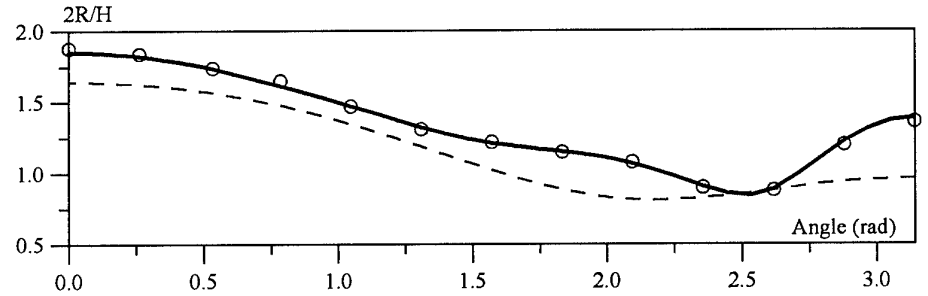

Figure 2. Wave run-up on fixed vertical circular cylinder. ka=0.684, kh=1.894 and kH=0.391. Linear solution (dashed), second order solution (solid). The analytical results by Kriebel (1992) are depicted by circles.

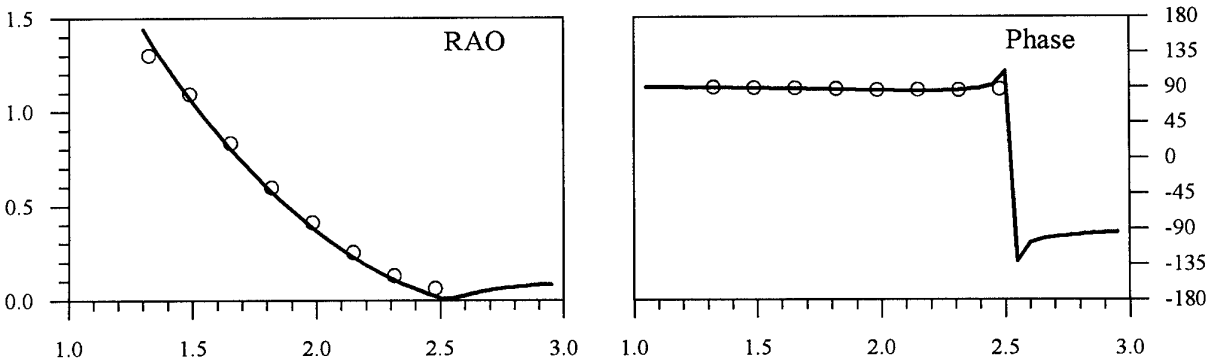

Figure 3. Surge RAO and phase (in degrees) for a Series 60 hull (C_b=0.7) exposed to irregular waves. The non-dimensional radian wave frequency ω' is depicted on the x-axis, the WAMIT results are shown with a solid line and the present numerical results are depicted by circles.

CONCLUSIONS

A second order 3D Boundary Element Model for the interaction between waves and structures has been developed. For a fixed structure (vertical circular cylinder) the wave run-up correct to second order has been computed, and the numerical results agree well with the analytical solution by Kriebel (1990,1992). The interaction between irregular waves and a freely floating ship has been simulated using the linear part of the model and good agreement with the theoretical RAOs and phases are found.

The interaction between waves, a current and a structure is also implemented and can be simulated by the present model. Results with the interaction of waves, current and a structure will be shown at the conference, but published elsewhere (see Büchmann et al., 1997).

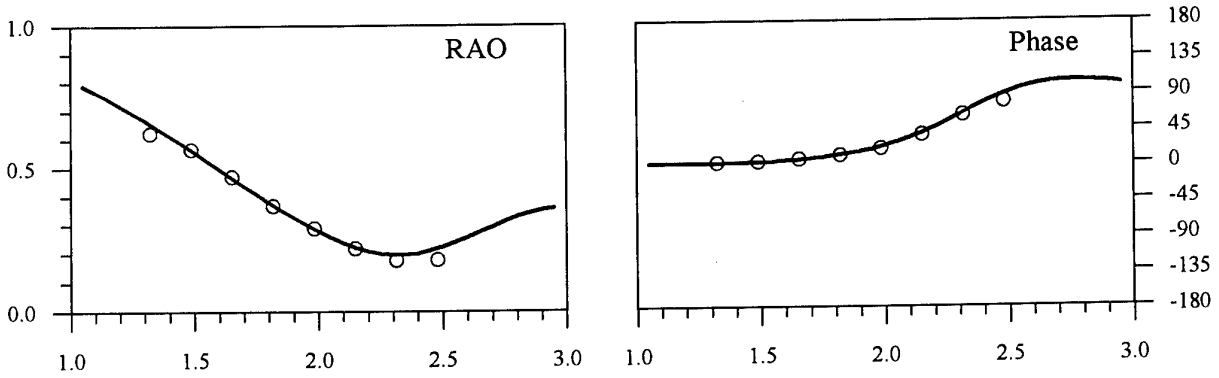

Figure 4. Heave RAO and phase (in degrees) for a Series 60 hull (C_b=0.7) exposed to irregular waves. The non-dimensional radian wave frequency ω' is depicted on the x-axis, the WAMIT results are shown with a solid line and the present numerical results are depicted by circles.

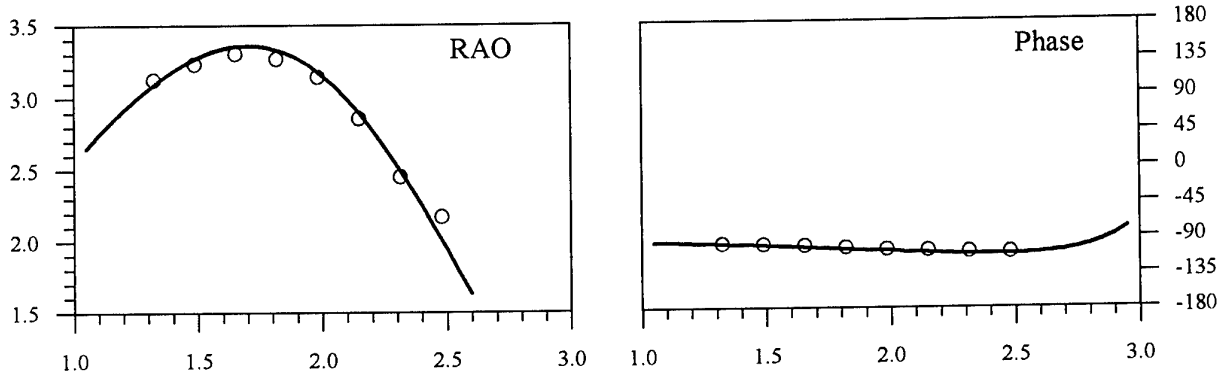

Figure 5. Pitch RAO and phase (in degrees) for a Series 60 hull (C_b=0.7) exposed to irregular waves. The non-dimensional radian wave frequency ω' is depicted on the x-axis, the WAMIT results are shown with a solid line and the present numerical results are depicted by circles.

ACKNOWLEDGEMENTS

The present work was funded by the Danish National Research Foundation. Their support is greatly appreciated. David L. Kriebel is thanked for sending us the analytical second order runup data.

REFERENCES

Büchmann, B., Skourup, J. and Cheung, K.F. (1997). Runup on a structure due to waves and a current. To be presented at the 7th Int. Offshore and Polar Engineering Conf. (ISOPE-97), Honolulu, Hawaii, USA.

Isaacson, M. and Cheung, K.F. (1992). Time-domain second-order wave diffraction in three dimensions. *Journal of Waterway, Port, Coastal and Ocean Engineering*, ASCE, **118**(5), 496-515.

Kriebel, D.L. (1990). Non-linear wave interaction with a vertical circular cylinder. Part I: Diffraction theory. *Ocean Engineering*, **17**(4), 345-377.

Kriebel, D.L. (1992). Non-linear wave interaction with a vertical circular cylinder. Part II: Wave run-up. *Ocean Engineering*, **19**(1), 75-99.

MacCamy, R.C. and Fuchs, R.A. (1954). Wave forces on piles: a diffraction theory. U.S. Army Corps of Engineers, *Beach Erosion Board*, Tech. Memo. No. 69, Washington D.C.

Schäffer, H.A., Stolborg, T. and Hyllested, P. (1994). Simultaneous generation and active absorption of waves in flumes. Proc. of the Int. Symp.: WAVES - Physical and Numerical Modelling, Vancouver, Canada, 90-99.

Schäffer, H.A. and Skourup, J. (1996). Active absorption of multi-directional waves. Proc. of the 25th Int. Conf. on Coastal Engineering. Orlando, Florida, USA.

Skourup, J. (1996). Active absorption in a numerical wave tank. Proc. of the 6th Int. Offshore and Polar Engineering Conf. (ISOPE-96), Los Angeles, USA, vol. 3, 31-38.

Skourup, J. and Bingham, H.B. (1996). Active absorption of radiated waves in a 3D boundary element model. Proc. of the 11th Int. Workshop on Water Waves and Floating Bodies. Hamburg, Germany.

WAMIT (1995). User Manual. Department of Ocean Engineering, Massachusetts Institute of Technology.

(Abstract for the 12th International Workshop on Water Waves and Floating Bodies, March 1997)

A study on wave-drift damping by fully nonlinear simulation

Katsuji Tanizawa † and Shigeru Naito ‡

† Ship Research Institute, Tokyo, Japan
‡ Osaka University, Osaka, Japan

1 Introduction

The low-frequency motion of floating marine structures such as moored ships and oil platforms are one of the main concern in ocean engineering. The low-frequency motions are excited by slowly oscillating second-order wave forces and the resonance causes large amplitude horizontal motions. The accurate estimation of the amplitude is very important for the design of mooring system. The conventional damping force due to viscous effect and wave radiation are small and wave-drift damping, resulting from the interaction between an incident wave and low-frequency oscillatory motion of a floating body, is dominant. Therefore the accurate estimation of wave-drift damping is indispensable.

Wave-drift damping has been studied experimentally and theoretically by Wicheres and Slujis [1], Saito, Takagi, Ohkubo and Hirashima [2], Faltinsen [3], Hearn and Tong [4], Nossen, Grue and Palm [5], Zhao and Faltinsen [6], Eatock Taylor and Teng [7], Sunahara [9] and others. In their approach, wave-drift damping is analyzed in a quasi-steady manner, based on the rate of change of the added resistance in waves, with respect to small steady forward velocity. Newman [8] outlines a procedure for the more direct derivation of wave-drift damping from a perturbation analysis and extracted it from second order radiation force at low-frequency.

In this study, a numerical approach is taken for the fully nonlinear analysis of the interaction between an incident wave and low-frequency oscillatory motion of a floating body. Using the fully nonlinear simulation method [12], three motions of a moored two-dimensional body are simulated in presence of a regular wave field and the hydrodynamic force due to the interaction is extracted from horizontal hydrodynamic force act to the body. Based on this numerical study, added mass and damping coefficient due to the interaction are analyzed and a rational explanation of wave-drift damping is proposed. The relation between this explanation and the conventional explanation based on quasi-steady analysis is discussed.

2 Target of the numerical simulation

Motions of a moored two dimensional floating body in a regular wave is considered. Fig.1 shows the target of the simulation. The ideal fluid is bounded by free surfaces, a piston wave maker, a flat bottom, a vertical wall and a floating body. The fluid motion is described by velocity potential and acceleration potential. Motion of the floating body coupled with the fluid motion is solved in the acceleration filed using the implicit body surface boundary condition. All three degrees of freedom are simulated.

Following a preceding work of Cointe et al. [10], artificial damping zones are applied to prevent wave reflection from both ends of wave basin. Inside of the damping zones, damping terms are added to both dynamic and kinematic free surface boundary conditions to give damping effect to free surface. These damping zones effectively work as a wave breaker and an absorbing wave maker. The motions of floating body can be simulated for long time without affected much by reflection waves.

The detail of this simulation method with damping zone is presented in reference paper [12].

3 The interaction between incident wave and low-frequency body motion

To study the interaction between incident wave and low-frequency body motion, the hydrodynamic force purely due to the interaction is extracted from following four nonlinear simulations presented in §3.1, §3.2, §3.3 and §3.4.

3.1 Simulation of moored body motions in still water

To obtained the basic characteristic of the mooring system in still water, free oscillatory motion is simulated. Fig.2 shows the simulated velocity of the body and the horizontal hydrodynamic force acts to the body. Fourier analysis of the simulated results gives following information.

- The natural frequency of the moored body motion in still water is $\tilde{\omega}_o = 0.384\ rad/s$.
- The added mass of the motion is $m_{sd}(\tilde{\omega}_o) = 155.75\ kg$.
- The damping coefficient of the motion is $c_{sd}(\tilde{\omega}_o) = 0.1091\ N/(m/s)$.

Since the radiation wave length correspond to $\tilde{\omega}_o$ is about $390m$ and more than 520 times wider than body breadth, these hydrodynamic coefficients

are similar equal to the limit values $m_{sd}(0) = 148.56\ kg$, $c_{sd}(0) = 0$ when $\omega_o \to 0$.

3.2 Simulation of the moored body motions in a regular wave

Next, free motion is simulated in the presence of a regular incident wave (wave length $\lambda = 2.7\ m$, wave amp. $\zeta_a = 5\ cm$, wave period $T_W = 1.316\ s$). Fig.3(a) shows the simulated sway motion and swaying force act to the body. For the analysis of the slow motion, low-frequency components are extracted by FFT from swaying velocity and swaying force. These are plotted in Fig.3(b) as U and F_X . Two differences exist between Fig.2 and Fig.3(b).

- The natural frequency of slow oscillatory motion in the regular wave is $\tilde{\omega} = 0.420\ rad/s$ and different from that of in still water.
- The significant damping is observed in the regular wave meanwhile damping is weak in still water.

F_X in Fig.3(b) is composed of steady wave-drift force $\bar{F}_X$ and slowly varying component $\tilde{F}_X$, which is considered to be the main cause of the differences.

3.3 Simulation of forced oscillation of the body in still water

To obtain the hydrodynamic force purely due to the interaction between incident wave and slow oscillatory motion, we have to remove the conventional hydrodynamic force F_{sd} due to low-frequency oscillation from F_X . F_{sd} can be obtained from the simulation of forced oscillated body motion in still water. The bottom raw of Fig.4 shows the simulated F_{sd} . The added mass and damping coefficient for $\tilde{\omega}$ can be obtained from Fourier analysis of this force. Then F_{sd} for arbitrary motions is given as

$$F_{sd} = m_{sd}(\tilde{\omega})\dot{U} + c_{sd}(\tilde{\omega})U \ . \qquad (1)$$

Theoretically, F_{sd} can be removed from F_X in Fig.3(b). But for quantitative study, the simulation of transient motion is not adequate and periodically steady state of low-frequency oscillation should be simulated.

3.4 Simulation of the moored body motions oscillated by a low-frequency external force in the regular wave

An external low-frequency force G_X , which is synchronized to $\tilde{\omega}$, is added to the body to oscillate the periodically steady low-frequency motion in the presence of the regular wave. The results are plotted in Fig.5. The amplitude of G_X is set to $|G_X| = 1.8\ N \approx 0.2\bar{F}_X$ in this simulation.

The top row of Fig.5 shows simulated sway motion from $t = 0$ to $250\ T_W$, the 2nd to the 4th row show sway motion, swaying velocity and horizontal hydrodynamic force magnified in time from $t = 150\ T_W$ to $200\ T_W$ and the 5th to the 6th row show low-frequency components of them extracted by FFT. Since the amplitude and the phase of forced oscillating motion shown in Fig.4 are equally set to those of low-frequency motion in Fig.5, the hydrodynamic force due to the interaction is simply given as $F_{wd} = F_X - F_{sd}$. Here, we call F_{wd} as wave-drift force, which is composed of steady wave drift force $\bar{F}_{wd} = \bar{F}_X$ and unsteady force $\tilde{F}_{wd}$. The bottom row of Fig.5 shows F_{wd}

3.5 Interaction between incident wave and slow oscillatory motion

Using F_{wd} and U presented in Fig.5, the interaction can be quantitatively studied. Fourier analysis of F_{wd} and U gives following information.

- The amplitude of F_{wd} is $|F_{wd}| = 1.814\ N$
- The amplitude of U is $|U| = 0.0551\ m/s$
- The phase between F_{wd} and U is $\theta = 2.712\ rad.$

When the simulation converges to the periodically steady state, the damping force balances with the exciting force. Above results, obtained from independent simulation shown in Fig.4 and Fig.5, well satisfy this condition $|F_{wd}| = |G_X|$ and that demonstrate the accuracy of these simulations.

Next, here we write

$$U = |U| \sin \tilde{\omega} t \qquad (2)$$

and decompose F_{wd} into sin and cos components

$$F_{wd} = |F_{wd}| \cos\theta \sin \tilde{\omega} t + |F_{wd}| \sin\theta \cos \tilde{\omega} t \ . \qquad (3)$$

Then added mass and damping coefficient due to the interaction are written as

$$A_X = -\frac{|F_{wd}| \sin\theta}{\tilde{\omega}|U|} \qquad (4)$$

$$B_X = -\frac{|F_{wd}| \cos\theta}{|U|} \ . \qquad (5)$$

Substituting the values of $|F_{wd}|, |U|$ and θ in these equations, we have $A_X = -32.65\ kg$, $B_X = 29.93\ N/(m/s)$. We should not confuse A_X, B_X with the conventional hydrodynamic coefficient m_{sd}, c_{sd} due to the oscillatory motion. A_X and B_X do not exist without incident wave.

Using A_X , the difference between $\tilde{\omega}_o$ and $\tilde{\omega}$ can be explained. The spring constant of the mooring $51.07N/m$, the body mass $191.79kg$ and the added mass in still water $155.75kg$ gives the estimation of the natural frequency in still water $0.383rad/s \approx \tilde{\omega}_o$. Taking the added mass reduction A_X into account, the natural frequency in the wave field becomes $0.403rad/s \approx \tilde{\omega}$.

3.6 Wave-drift damping

B_X is considered to be wave-drift damping for frequency $\tilde{\omega}$. On the other hand, in the theoretical studies, wave-drift damping is defined in quasi-steady manner as

$$\bar{B}_X = -\frac{\partial \bar{F}_X}{\partial U}\bigg|_{U=0} . \tag{6}$$

The relation between B_X and $\bar{B}_X$ can be clearly shown as follows.

Using eq.(2), eq.(3) can be written as

$$F_{wd} = \frac{|F_{wd}|\cos\theta}{|U|}U + \frac{|F_{wd}|\sin\theta}{\tilde{\omega}|U|}\dot{U} . \tag{7}$$

When the slow drift motion is in periodically steady state, $|F_{wd}|$ and $|U|$ are constant. Therefore, partial derivative of F_{wd} with respect to U is given as

$$\frac{\partial F_{wd}}{\partial U} = \frac{|F_{wd}|\cos\theta}{|U|} + \frac{|F_{wd}|\sin\theta}{\tilde{\omega}|U|}\frac{\partial \dot{U}}{\partial U} . \tag{8}$$

Taking the relation

$$\frac{\partial \dot{U}}{\partial U} = -\tilde{\omega}^2\frac{U}{\dot{U}} \tag{9}$$

into account, $\partial\dot{U}/\partial U$ becomes zero at $U = 0$ and we have formula

$$\frac{\partial F_{wd}}{\partial U}\bigg|_{U=0} = \frac{|F_{wd}|\cos\theta}{|U|} . \tag{10}$$

Therefore, Eq.(5) is finally written as

$$B_X = \frac{\partial F_{wd}}{\partial U}\bigg|_{U=0} . \tag{11}$$

This definition of wave-drift damping is valid for $\tilde{\omega} \geq 0$. When $\tilde{\omega}$ tends to zero, $F_{sd} \to 0$ and $F_{wd} \to \bar{F}_X$ can be substituted to eq.(11) to have the conventional definition eq.(6).

4 Conclusion

The hydrodynamic force purely due to the interaction between incident wave and low-frequency body motion is extracted by following nonlinear simulations

1. Free motions of the moored body in still water is simulated to obtain the natural frequency $\tilde{\omega}_o$ in still water.
2. Free motions of the moored body in a regular wave is simulated to obtain the natural frequency $\tilde{\omega}$ in the regular wave field.
3. Forced oscillatory body motions in still water in frequency $\tilde{\omega}$ is simulated to obtain the conventional hydrodynamic force F_{sd} due to the low-frequency oscillation.
4. The moored body motions oscillated by a low-frequency external force in frequency $\tilde{\omega}$ in the regular wave field is simulated to obtain the hydrodynamic force $F_{wd} = F_X - F_{sd}$ purely due to the interaction,

and the rational explanation of added mass A_X and the damping coefficient B_X due to the interaction is given. This explanation reflects the dynamics of the interaction. Series of simulations with different $\tilde{\omega}$ will teach us the frequency dependency of A_X and B_X.

References

1) Wicheres,J.E.W. and Slujis,M.F.: The influence of wave on the low frequency hydrodynamic coefficients of moored vessels, *Proc. of Offshore Tech. Conf. No.3625*,pp2313-2324, (1979)
2) Saito,K., Takagi,M., Ohkubo,H. and Hirashima,M. : On the low-frequency damping forces acting on a moored body in waves, *J. Kansai Soc. Narval Arch. Japan, Vol.195*, pp51-59, (1984)
3) Faltinsen,O.M. : Slow-drift damping and responses of moored ship in irregular waves, *5th OMAE Symp.*, Tokyo, (1986)
4) Hearn,G.E. and Tong,K.C. : A comparative study of experimentally measured and theoretically predicted wave drift damping coefficients, *Proc. OTC, No.6136*, (1989)
5) Nossen,J., Grue,J and Palm,E. : Wave forces on three-dimensional floating bodies with small forward speed, *JFM, Vol.227*, (1991)
6) Zhao,R. and Faltinsen,O.M. : Interaction between current, waves and marine structures, *Proc. 5th Int. Conf. on Num. Ship Hydro.*, Hiroshima, (1989)
7) Eatock Taylor,R. and Teng,B. : The effect of corners on diffraction/radiation forces and wave drift damping, *Proc. OTC, No.7187*, (1993)
8) Newman,J.N. : Wave-drift damping of floating bodies, *JFM, Vol.249*, (1993)
9) Sunahara : A study on wave drift damping acting on multiple floating cylinders, *Ph.D Thesis, The Univ. of Tokyo*, (1994)
10) Cointe,R., Geyer,P., King,B., Molin,B. and Tramoni,M. : Nonlinear and linear motions of a rectangular barge in a perfect fluid, *Proc. 18th Symp. Naval Hydro.*, (1990)
11) Tanizawa,K. : A Nonlinear Simulation Method of 3-D Body Motions in Waves, *J. Soc. Naval Arch. Japan, Vol.178*, (1995)
12) Tanizawa,K. : Long time fully nonlinear simulation of floating body motions with artificial damping zone, *J. Soc. Narval Arch. Japan, Vol.180*, (1996)

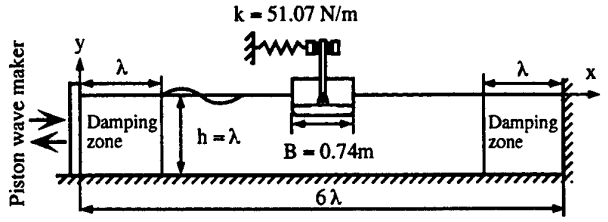

Incident wave $\lambda = 2.7$ m, $h_w = 2\zeta_a = 10$ cm
Floating body Weight 191.8 kg

Fig.1 Model of the simulation

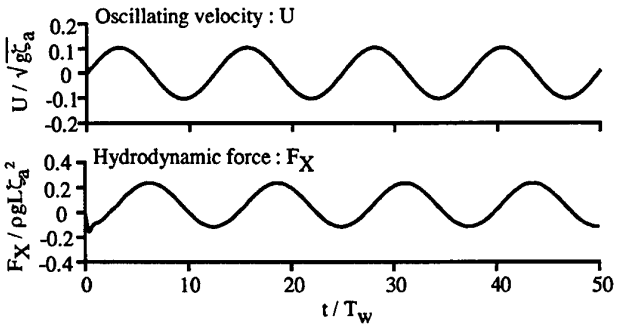

Fig.2 Simulated free oscillatory motion and hydrodynamic force in still water

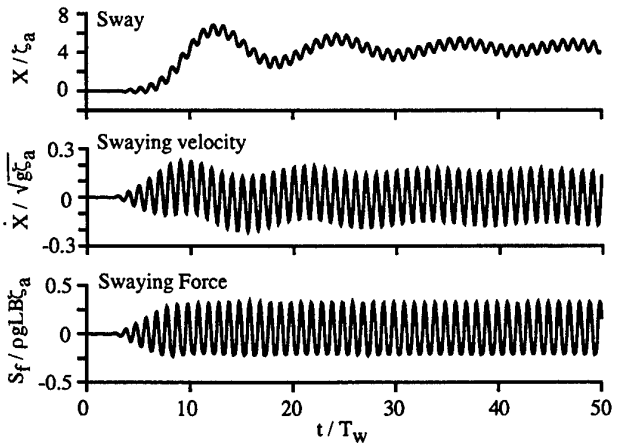

(a) Simulated sway motion and swaying force

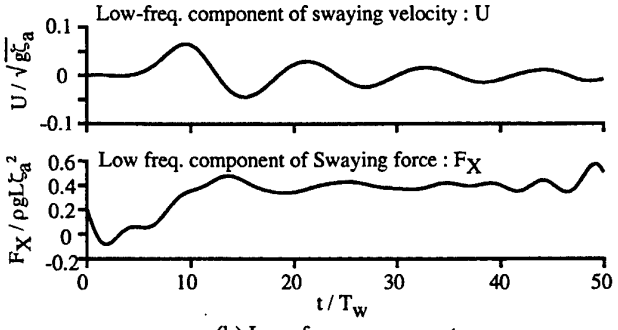

(b) Low-freq. components

Fig.3 Simulated free oscillatory motion and hydrodynamic force in the regular wave

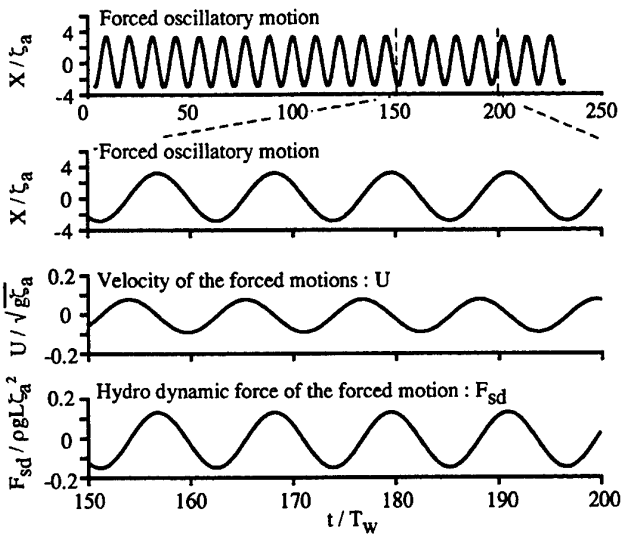

Fig.4 Simulated hydrodynamic force by forced oscillation in still water

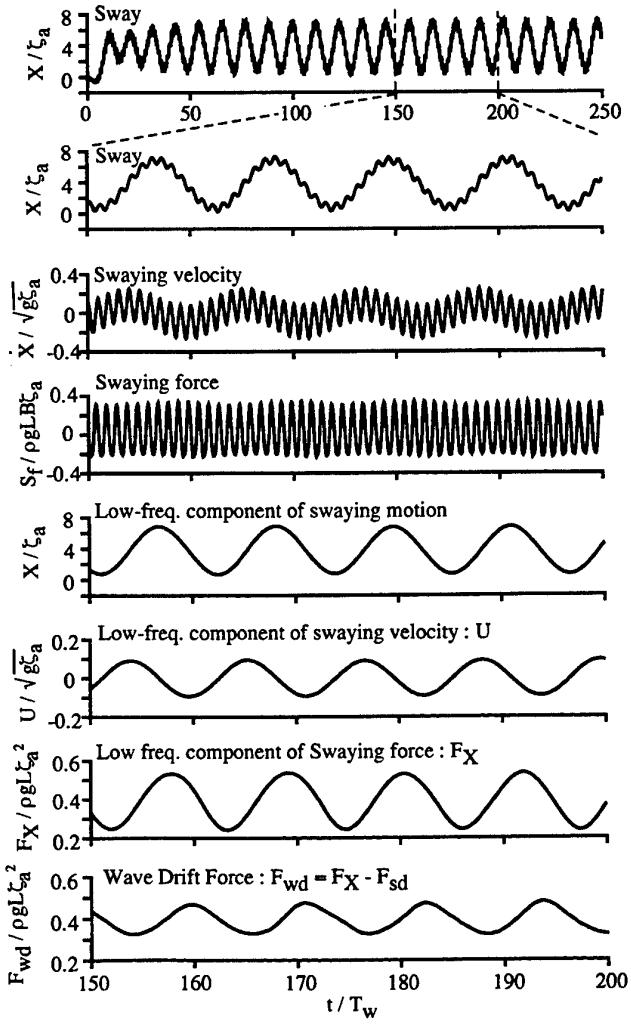

Fig.5 Simulated free oscillatory motion and hydrodynamic force excited by external low-frequency force in the regular wave

DISCUSSION

Molin B.:
1) It seems to me that your procedure to determine wave drift damping is a lot more complicated than what one usually does in a wave tank (i.e. decay tests in still water and regular waves). Can you comment why?
2) Have you made comparisons with published experimental or numerical results?
3) I want to comment that the often observed change in low frequency added mass has more to do with viscous effects than with potential effects.

Tanizawa K. + Naito S.:
1) For the estimation of the wave drift damping, free decay tests are not accurate enough because they are transient phenomena and affected by viscous force. What we usually do is low speed towing test in regular waves based on the conventional definition of the wave drift damping (i.e. the rate of change of the added resistance in waves with respect to small steady forward velocity). But, since this definition is derived from quasi-steady analysis, I proposed dynamic definition of wave drift damping and introduce series of fully nonlinear numerical simulations to determine the wave drift damping based on this dynamic definition.
2) No, not yet.
3) Thank you very much for you comment. Of course viscous effects may affect to the added mass change. What I explain in my talk is pure potential effect to the added mass change.

Newman J.N.: Your approach seems analogous to the rationale in my 1993 paper except that I used a perturbation expansion in powers of the wave amplitude *(A)* and you use a fully nonlinear simulation. I ignored the $O(A^2)$ added mass since it seemed unimportant compared to $O(1)$ conventional added mass. This suggests that your shift in the natural period of slow drift motions is $O(A^2)$. Do you have any results to confirm this?

Tanizawa K. + Naito S.: I simulated the slow drift motions for various wave heights and checked the dependency of the natural frequency to the wave amplitude. The simulated results in Table A show that the change of natural frequency is almost proportional to $O(A^2)$ and this can be a confirmation of your analysis. So, when wave amplitude is small, the change of frequency is not significant. But for larger amplitude wave, the change is not negligible.

Table A: Natural frequency of slow drift motion in regular waves

A/B	$\tilde{\omega}/\tilde{\omega}_0$
0.0	1.0
0.0169	1.0052
0.0338	0.9948
0.0507	1.0182
0.0676	1.0938
0.0845	1.1901

A : Wave amplitude

B : Body breadth 0.74 *m*

$\tilde{\omega}_0$: The natural frequency in still water 0.384 *rad/s*

λ : Wave lenghth 2.7 *m*

Third-harmonic Diffraction Force on Axisymmetric Bodies

Bin Teng
Dalian University of Technology, CHINA
Shunji Kato
Ship Research Institute, Ministry of Transport,JAPAN

1 Introduction

It was observed in model tests and prototype experiments that tension leg platforms(TLPs) and gravity base structure(GBSs) experience sudden bursts of highly amplified resonant activities (ringing) during storms. The ringing phenomenon will induce extreme stress in tethers, end even tethers breaking. It was found that ringing occurs at low frequency and ringing periods are about 3-5 times of the period of the corresponding incident waves. Thus, the calculation of third order force will be significant in predicting ringing phenomenon.

Nonlinear problems are characterized by forcing term in their boundary conditions. For the third order potential, the forcing term on the free surface includes both first and second order potentials. The difficulty in calculating third order force is that second order potential can not be expressed in an explicit form efficiently. Usually, it is represented by an integral equation and an infinite integration has to be carried out on the whole free surface. The present work proposed a one-step forward prediction method to calculate the second order potential on the free surface. Special concerns are also given to the treatment for the logarithmic singularity in the ring Green functions. Then, the third order forces are calculated by an indirect method, which is analogous to the indirect method for second order force.

The method has been implemented for axisymmetric bodies, and no difficulty has been found for extending it to arbitrary bodies, like TLPs. For axisymmetric bodies, a novel integral equation is also proposed.

2 Free Surface Condition

We assume the incident monochromatic waves have an incident frequency ω. Then , the first, second and third order harmonic potentials with the frequencies of $\omega_1 = \omega, \omega_2 = 2\omega$ and $\omega_3 = 3\omega$ are considered for the present interest. We separate the time dependencies explicitly, and write potentials at each order of ϵ as

$$\Phi^{(j)}(x,y,z,t) = \Re[\phi^{(j)}(x,y,z)e^{-i\omega_j t}] \tag{1}$$

Then, we can write the free surface conditions for each velocity potentials as

$$\begin{aligned} \nu_j\phi^{(j)} + \phi_z^{(j)} &= q^{(j)} \quad j = 1,2,3,\cdots \quad \text{on } z = 0 \\ \nu_j &= \omega_j^2/g \end{aligned} \tag{2}$$

where the forcing terms [2] at each order of ϵ are

$$q^{(1)} = 0 \tag{3}$$

$$q^{(2)} = -\frac{i\omega}{2g}\phi^{(1)}(-\frac{\omega^2}{g}\phi_z^{(1)} + \phi_{zz}^{(1)}) + \frac{i\omega}{g}\nabla\phi^{(1)}\cdot\phi^{(1)}$$

$$\begin{aligned} q^{(3)} &= \frac{3i\omega}{g}\nabla\phi^{(1)}\cdot\phi^{(2)} - \frac{i\omega}{2g}\phi^{(1)}(\phi_{zz}^{(2)} - 4\nu\phi_z^{(2)}) - \frac{i\omega}{g}\phi^{(2)}(\phi_{zz}^{(1)} - \nu\phi_z^{(1)}) \\ &- \frac{1}{8g}\nabla\phi^{(1)}\cdot\nabla(\nabla\phi^{(1)}\cdot\nabla\phi^{(1)}) - \frac{\nu}{g}\phi^{(1)}\nabla\phi^{(1)}\cdot\nabla\phi_z^{(1)} \\ &+ \frac{1}{g}(\frac{\nu}{4}\phi^{(1)}\phi_z^{(1)} + \frac{1}{8}\nabla\phi^{(1)}\cdot\nabla\phi^{(1)})(\phi_{zz}^{(1)} - \nu\phi_z^{(1)}) \end{aligned} \tag{4, 5}$$

3 Integral Equation

We separate velocity potentials and forcing terms into incident and diffraction components as

$$\phi^{(j)} = \phi_I^{(j)} + \phi_D^{(j)}, \quad q^{(j)} = q_I^{(j)} + q_D^{(j)}$$

Expanding the diffraction potential and the Green function into the following series

$$\phi_D^{(j)}(\mathbf{x}) = \sum_{m=0}^{\infty} \epsilon_m \phi_{Dm}^{(j)}(r)\cos m\theta \tag{6}$$

$$G(\mathbf{x},\mathbf{x}_0) = \sum_{m=0}^{\infty} \epsilon_m G_m(r,z;r_0,z_0)\cos m(\theta-\theta_0) \tag{7}$$

for axisymmetric body, we can derive the integral equation for the mth mode of jth order potential as

$$\begin{aligned}&[\frac{1}{2\pi} - \nu_j \int_{\Gamma_W} G_0 r dr]\phi_{Dm}^{(j)}(r_0) - \int_{\Gamma_B} [\frac{\partial G_0}{\partial n}\phi_{Dm}^{(j)}(r_0) - \frac{\partial G_m}{\partial n}\phi_{Dm}^{(j)}(r)]r dl \\ = &\int_{\Gamma_B} G_m \frac{\partial \phi_{Im}^{(j)}}{\partial n} r dl + \int_a^{\infty} G_m q_{Dm}^{(j)}(r) r dr\end{aligned} \tag{8}$$

after using a technique to weaken the singularity, where G_m is well known as the ring Green function and G_0 is the simple Green function which satisfies only the fixed free and bottom surface conditions.

4 Numerical Implement

For second order potential in fluid domain, two integrations have to be carried out both on body surface and on free surface when applying integral equation method.

4.1 Integral on the free surface

$$I_{Fm}(r_0,\theta_0,0) = -\int_a^{\infty} r dr q_{Dm}^{(2)}(r)[i\pi C_0 H_m(k_2 r_>)J_m(k_2 r_<) + 2\sum_{n=1}^{\infty} C_n K_m(\kappa_n r_>)I_m(\kappa_n r_<)] \tag{9}$$

Defining L_{mn} term as

$$L_{mn} = 2C_n K_m(\kappa_n r_>)I_m(\kappa_n r_<)Z_n(\kappa_n z) \tag{10}$$

The limitation of L_{mn} term for large n is L_{mn}^s, and its infinite sum is L_m^s, which has a logarithmic singularity when the field point is close to the source point.

To remove the logarithmic singularity, we rewrite the integral as

$$\begin{aligned}&\sum_{n=1}^{\infty}\int_a^{\infty} L_{mn}(r)q_{Dm}^{(2)}(r)r dr \\ \approx &\sum_{n=1}^{N}\int_a^{\infty} L_{mn}(r)q_{Dm}^{(2)}(r)r dr - \sum_{n=1}^{N}\int_{r_0-\Delta r}^{r_0+\Delta r} L_{mn}^s(r)q_{Dm}^{(2)}(r)r dr + \int_{r_0-\Delta r}^{r_0+\Delta r} L_m^s(r)q_{Dm}^{(2)}(r)r dr\end{aligned} \tag{11}$$

For large modes, inside the range $(r-\Delta r, r+\Delta r)$ the first two terms can be canceled each other; outside the range the difference can be neglected. For the third term, a transform is used to remove the singularity. Then the integration can be represented as

$$I_{Fm}(r_0,0) = -[\sum_{n=0}^{N} C_n T_{mn}(r_0) - \sum_{n=1}^{N} V_{mn}(r_0) + V_{m0}(r_0)] \tag{12}$$

where

$$V_{m0}(r_0) = -\frac{1}{2\pi}\int_{r_0-\Delta r}^{r_0+\Delta r} q_{Dm}^{(2)}(r) ln[1-\exp(-\frac{\pi}{d}|r-r_0|)]\sqrt{\frac{r}{r_0}}dr \tag{13}$$

$$V_{mn}(r_0) = \frac{1}{2n\pi}\int_{r_0-\Delta r}^{r_0+\Delta r} q_{Dm}^{(2)}(r)\exp(-\frac{\pi}{nd}|r-r_0|)\sqrt{\frac{r}{r_0}}dr \tag{14}$$

$$T_{m0}(r_0) = S_{m01}(r_0)J_m(k_2 r_0) + S_{m02}(r_0)H_m(k_2 r_0) \tag{15}$$

$$T_{mn}(r_0) = S_{mn1}(r_0)e^{-\kappa_n r_0}I_m(\kappa_n r_0) + S_{mn2}(r_0)e^{\kappa_n r_0}K_m(\kappa_n r_0) \tag{16}$$

where

$$\begin{aligned}S_{m01}(r_1) &= \frac{i\pi}{2}\int_{r_1}^{\infty} q_{Dm}^{(2)}(r)H_m(k_2 r)r dr = S_{m01}(r_0) - \frac{i\pi}{2}\int_{r_0}^{r_1} q_{Dm}^{(2)}(r)H_m(k_2 r)r dr \\ S_{m02}(r_1) &= \frac{i\pi}{2}\int_a^{r_1} q_{Dm}^{(2)}(r)J_m(k_2 r)r dr = S_{m02}(r_0) + \frac{i\pi}{2}\int_{r_0}^{r_1} q_{Dm}^{(2)}(r)J_m(k_2 r)r dr\end{aligned}$$

$$S_{mn1}(r_1) = \int_{r_1}^{\infty} q_{Dm}^{(2)}(r)K_m(\kappa_n r)rdr = S_{mn1}(r_0)e^{\kappa_n(r_1-r_0)} - \int_{r_0}^{r_1} q_{Dm}^{(2)}(r)K_m(\kappa_n r)rdre^{\kappa_n r_1}$$

$$S_{mn2}(r_1) = \int_{a}^{r_1} q_{Dm}^{(2)}(r)I_m(\kappa_n r)rdr = S_{mn2}(r_0)e^{-\kappa_n(r_1-r_0)} + \int_{r_0}^{r_1} q_{Dm}^{(2)}(r)I_m(\kappa_n r)rdre^{-\kappa_n r_1}$$

4.2 Integration on the body surface

For those points not close to body surface, we write the body integration as

$$I_{Bm}(r_0,0) = \int_{\Gamma_B} [\phi_{Dm}^{(2)}(r,z)\frac{\partial G_m}{\partial n} + \frac{\partial \phi_{Im}^{(2)}(r,z)}{\partial n}G_m]rdl = U_{m0}H_m(k_2 r_0) + \sum_{n=1}^{\infty} U_{mn}K_m(\kappa_n r_0) \tag{17}$$

where U_{m0} and U_{mn} are determined by the body integration. When the point is close to the body surface, a technique is also used to weaken the near singularity.

5 Hydrodynamic Force

We divide the third order force into three terms

$$F^{(3)} = \Re[(f_1^{(3)} + f_2^{(3)} + f_3^{(3)})e^{-3i\omega t}] \tag{18}$$

where $f_1^{(3)}, f_2^{(3)}$ and $f_3^{(3)}$ are

$$f_1^{(3)} = -\frac{i\omega}{8g}\rho \int_{C_B} [\phi^{(1)}\nabla\phi^{(1)} \cdot \nabla\phi^{(1)} + \nu^2(\phi^{(1)})^3]\mathbf{n}dc \tag{19}$$

$$f_2^{(3)} = -\frac{1}{2}\int\int_{S_B} \rho\nabla\phi^{(1)} \cdot \nabla\phi^{(2)}\mathbf{n}ds - \rho\nu \int_{C_B} \phi^{(1)}\phi^{(2)}\mathbf{n}dc \tag{20}$$

$$f_3^{(3)} = \int\int_{S_B} 3i\omega\rho[\phi_D^{(3)} + \phi_I^{(3)}]\mathbf{n}ds \tag{21}$$

Similar to the second order force, the third order diffraction force can be further divided as

$$f_{3j}^{(3)} = 3i\omega\rho\int\int_{S_B} [\phi_I^{(3)}n_j + \psi_j\frac{\partial\phi_I^{(3)}}{\partial n}]ds + 3i\omega\rho\int\int_{S_F} \psi_j q_D^{(3)}ds \tag{22}$$

by using an auxiliary radiation potential ψ_j at triple frequency of incident wave.

Dividing the third order forcing term $q^{(3)}$ into two terms, $q_A^{(3)}$(consisting of only the first order potential) and $q_B^{(3)}$ (consisting of the first and second order potentials), the most difficult integral on the free surface, i.e. $\int\int \psi_j q_{BD}^{(3)}ds$, can be represented as

$$\begin{aligned}\int\int_{S_F} \psi_j q_{BD}^{(3)}ds &= \int\int_{S_F} [\psi_j(W - W_I - \frac{i\omega}{2g}\phi_D^{(1)}\phi_{Izz}^{(2)} - \frac{i\omega}{2g}(2\nabla_0\phi^{(1)} \cdot \nabla_0\phi_D^{(2)} - \phi_D^{(2)}\phi_{zz}^{(1)}))\\ &- \frac{i\omega}{2g}\psi_{jzz}\phi^{(1)}\phi_D^{(2)}]ds + \frac{i\omega}{2g}\oint_{C_B} [\phi^{(1)}\phi_D^{(2)}n_j + \psi_j\phi^{(1)}\frac{\partial\phi_I^{(2)}}{\partial n}]dl\end{aligned} \tag{23}$$

using some transforms, where $\nabla_0 = (\frac{\partial}{\partial r}, \frac{1}{r}\frac{\partial}{\partial\theta})$ and

$$W = \frac{i\omega}{g}[3\nabla_0\phi^{(1)} \cdot \nabla_0\phi^{(2)} + 5\nu\phi^{(1)}\phi_z^{(2)} - \phi^{(2)}(\phi_{zz}^{(1)} - \nu^2\phi^{(1)})]$$

6 Numerical results

As the first step, a case of uniform cylinder with radius of a in a water depth of $d/a = 10$ is considered. Figure 2 shows the comparison of third order surge force of the present calculation with the Malenica and Molin's (M & M's), Faltinsen, Newman and Vinje's (FNV's) analytical solutions and experimental results. It can be seen that the present calculation agrees well with M & M's results except for f_{33} component.

Figure 3 shows the comparison of third order pitch moment about the free surface with experimental results. The experimental results are very scattered, and no conclusion can be found. From the calculation results it can be seen that there is a peak at low frequency. This maybe is the exciting source of ringing phenomenon on TLP and GBS. At that frequency, the corresponding force is not very high. The reason for this peak is the acting point of third order surge force is low.

References

1) Faltinsen, O.M., Newman, J.N. & Vinje,T.: Nonlinear loads on a slender vertical cylinder, *J.Fluid Mech.*, Vol.289, pp.179-198, 1995.

2) Malenica, S and Molin,B.: Third -harmonic wave diffraction by a vertical cylinder, *J. Fluid Mech.*, Vol.302, pp.203-229, 1995.

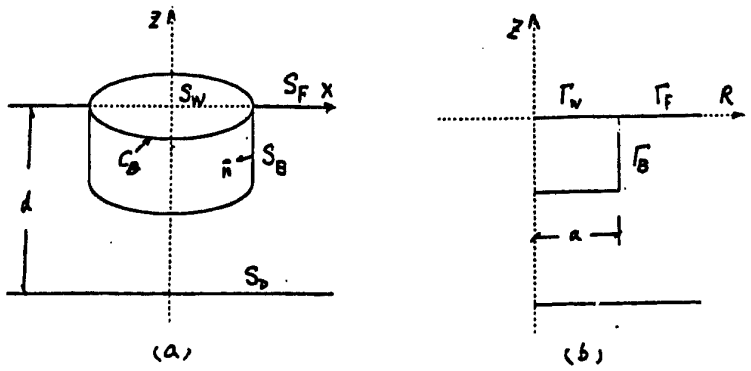

Fig 1 Definition of Sketch

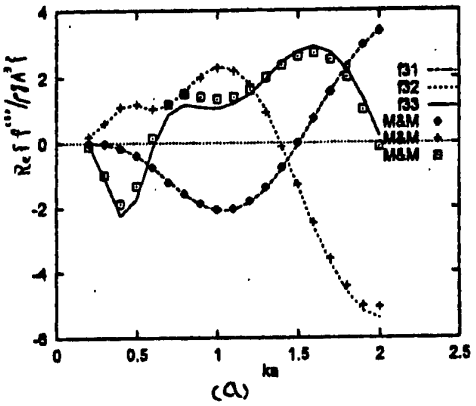

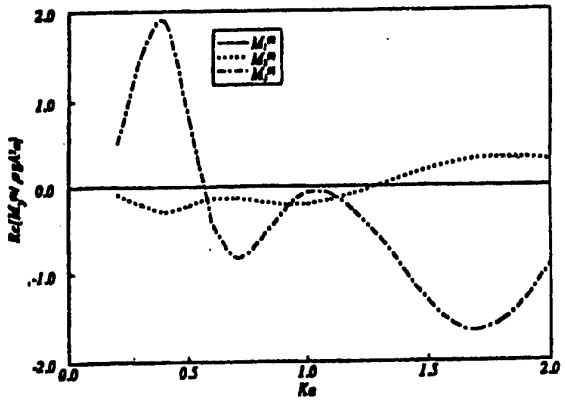

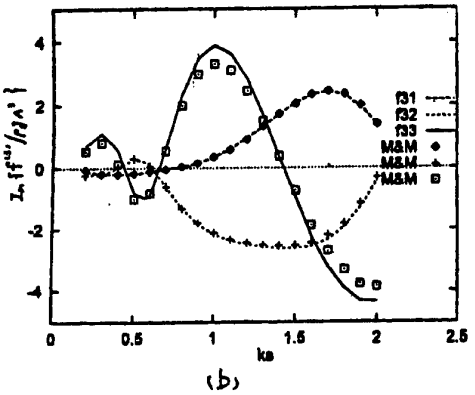

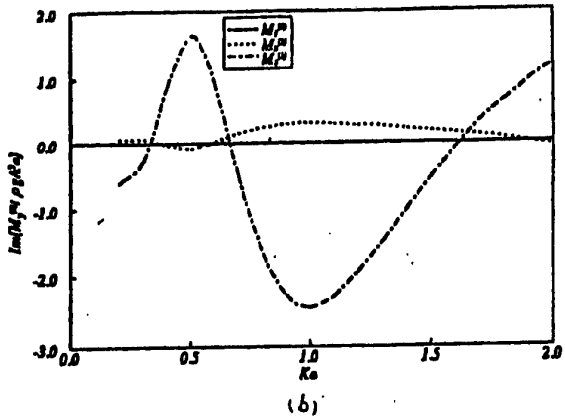

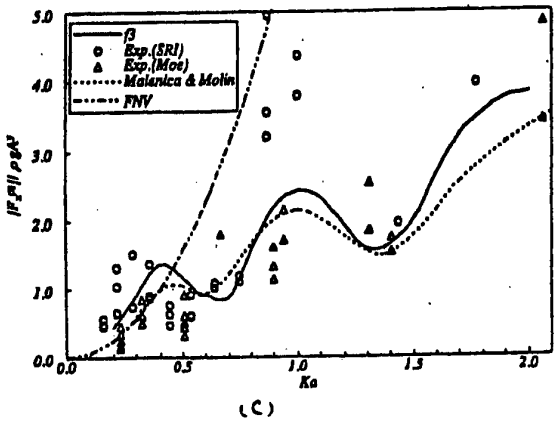

Figure 2 Third order surging force on a uniform cylinder (*d/a=10*)

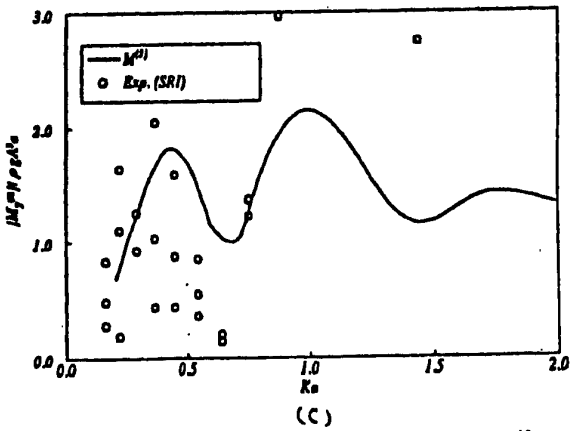

Figure 3 Third order pitching moment about Zc=0 on a uniform cylinder (d/a

DISCUSSION

Kim M.H.: The convergence test of the second-order diffraction computation is very complicated and cumbersome because of multiple parameters to be tested. Have you done any systematic convergence tests for the 3rd order diffraction problem?

Teng B., Kato S.: We did make systematic convergence tests for the 3rd order diffraction problem. At first I found our results were not correct. Then I spent a lot of effort on the examination of its convergence. Firstly, I examined the convergence of each terms. After having gotten their convergence, I made convergence test for the whole system.

Rainey R.C.T.: The authors are to be commended on the skill of their investigation of the difficult topic of 3rd order diffraction. However, I dispute its relevance to "ringing" because:
1) in waves big enough to cause "ringing", the ratio (wave height)/(cylinder diameter) is generally greater than 1, so that Stokes's expansion has diverged.
2) "ringing" can be at much higher frequencies than the 3rd harmonic, e.g. at 10 times the wave frequency.
See the forthcoming paper by J. Chaplin et al. (*Journal of Fluid Mechanics, 1997*).

Teng B., Kato S.: This study deals with the estimation method of 3rd harmonic forces on axisymmetric floating bodies by means of straight forward perturbation technique.
We do not claim that the cause of ringing of a uniform cylinder is due to 3rd harmonic wave forces.

Abstract for 12th International Workshop on Water Waves and Floating Bodies
Marseilles, France, March 1997

STEADY SPLASHING FLOWS

by

E. O. Tuck, S. T. Simakov and L. H. Wiryanto[1]
The University of Adelaide, Australia

Summary

We consider steady two-dimensional free-surface flows involving a jet or splash which rises then falls under gravity. First we examine a stream which is uniform far upstream in a channel of finite constant depth that ends abruptly with a barrier in the form of a vertical or inclined wall, which first forces the flow upward, then either lets it continue in the same direction or bounce back. The resulting splash then falls forever as if into a bottomless chasm. The second configuration examined may be described as a very wide ship bow in water of infinite depth. Namely, we consider a flow past a semi-infinite flat-bottomed body of finite draft, terminated by a plane front face inclined at a prescribed angle. There is a submerged stagnation point on the front face, to which is attached a bifurcating streamline originating far upsteam, such that all of the fluid lying above that streamline is drawn into the splash, whereas all of the fluid below it passes beneath the body. In each case, depending on input parameters such as the angle and height of the front face or barrier, and the value of the far-upstream Froude number, the splash may fall either before or beyond the barrier. The problem is solved via an integral equation formulation, and results are presented in the form of graphs and video images.

Mathematical formulation

To derive the integral equations, we transform the physical plane $z = x + \mathrm{i}y$ into the plane of the complex potential $f(z)$ and then map it into a lower half plane of an artificial variable $\zeta = \xi + \mathrm{i}\eta$. The relation between f and ζ is given by $f = -\log\zeta$ for the channel flow and $f = \zeta - \log\zeta$ for the bow flow.

We introduce for both flows a positive constant $a < 1$ such that $\zeta = a$ is the image of the point where separation of the splash from the barrier occurs. The intervals $-\infty < \xi < 0$ and $0 < \xi < a$ are the transformed free streamlines and $\zeta = 0$ corresponds to the jet far downstream. The point $\zeta = 1$ corresponds to the corner of the barrier for the channel flow, and to the submerged stagnation point for the bow flow. For the latter flow we also introduce a constant $b > 1$ to mark the image $\zeta = b$ of the point where the front face of the bow meets the flat bottom surface of the ship.

The flow problem is solved with the logarithmic hodograph

$$\Omega = \tau(\zeta) - \mathrm{i}\theta(\zeta) = \log f'(z)$$

as a dependent variable. In the numerical solution we reduce the problem to an integral equation for the unknown $\theta(\xi)$ on the interval $(-\infty, a)$, that is, on the free surface, observing that θ is wholly known on the interval $\xi > a$, i.e. on the body.

[1]Permanent address: Mathematics Department, Institut Teknologi Bandung, Indonesia

The free-surface boundary condition is constancy of pressure, or from Bernoulli's equation,

$$\frac{1}{2}e^{2\tau} + gy = \frac{1}{2}, \tag{1}$$

where it is assumed that the far-upstream free-surface level is $y = 0$, and that the upstream uniform flow is of unit magnitude. Representing τ and y in terms of θ in equation (1), we turn it into an integral equation for $\theta(\xi)$. To do so we note first that $\tau(\xi)$ is the Hilbert transform of $\theta(\xi)$. The expression for the $y-$coordinate is found from

$$\frac{dy}{d\xi} = \frac{df}{d\xi}e^{-\tau}\sin\theta, \tag{2}$$

valid for real $\zeta = \xi$, where $df/d\xi = -\xi^{-1}$ for the flow in the channel and $df/d\xi = (1 - \xi^{-1})$ for the flow past the ship. In both cases, equation (2) must be integrated separately in two intervals $\xi \in (-\infty, 0)$ and $\xi \in (0, a)$, as the singularity representing the ultimate fate of the jet does not permit integration through the origin $\zeta = 0$. The initial condition is $y(-\infty) = 0$ for the integration in the interval of negative ξ. Detachment at the junction point between body and free surface is in the present paper assumed to be smooth, with continuous slope and finite non-zero velocity. The appropriate initial condition at $\zeta = a$ for use in the interval $(0, a)$ must be found by integrating (2) from a to 1 for the flow in the channel and from a to b for the flow past the ship.

Results

The integral equations so obtained can be solved numerically by reduction to a finite system of nonlinear equations as in Tuck & Goh (1985) or Tuck (1987). An alternative approach based on a semicircular parametrization and series truncation was used in Vanden-Broeck & Keller (1987), Dias & Tuck (1991), Dias & Christodoulides (1991) and Dias & Vanden-Broeck (1993). For the channel flow, Dias and Christodoulides (1991) solved the limiting problem for a very high vertical barrier where the detachment is via a stagnation point, producing a splash falling before the barrier. Dias and Tuck (1991) reduced the height of the vertical barrier and allowed smooth detachment from its top edge as in the present work, causing the splash to fall beyond the barrier. Vanden-Broeck and Dias (1993) solved a similar problem for a flow past a high vertical ship bow, again with stagnant detachment. Wiryanto and Tuck (1996) recomputed Dias and Christodoulides' solution using the integral equation method, obtaining somewhat more accurate results.

Figures 1 and 2 are typical for the channel flow, showing two possible types of interaction of the stream with the barrier. A backward-diverted jet is observed when the barrier's angle to the horizontal is less than $\pi/2$, but not too small, and the barrier is reasonably high; otherwise the jet falls beyond the barrier. For high walls, the present program fails just before the height of the topmost point of the free surface reaches the stagnation level, with some indication that this point is moving toward the junction point, as in the solutions of Dias and Christodoulides (1991) and Wiryanto and Tuck (1996). In those cases where the jet falls beyond the barrier, the height of the topmost point of the upper free surface increases as we decrease the angle or increase the height of the wall. The program then fails just before this point reaches stagnation level, with some indication that there would as usual be a 120° angle at that point if the limiting solution could be reached.

Figures 3 and 4 exhibit computed flows past a ship bow and we can observe the same tendencies here as with the channel flow. Again there is a domain of parameter values where numerical solution was not achieved, and it may be that no solution exists with the assumed topology. For instance, by changing the slope of the front face, we move from a flow with a

backward-diverted splash "into the stream", to a splash falling forward "into the ship", but are confronted in between by an interval of angles at which the algorithm does not converge. This interval may contain a sub-interval in which the splash rises to a stagnation level, where it divides into two streams, one backward and one forward in a fountain-like manner, as in Vanden-Broeck (1993), but we have not yet computed such flows.

REFERENCES

Dias, F. and Christodoulides, P., "Ideal jets falling under gravity", *Phys. Fluids* A **3** (1991) 1711–1717.

Dias, F. and Tuck, E.O., "Weir flows and waterfalls", *J.Fluid Mech.* **230** (1991) 525–539.

Dias, F. and Vanden-Broeck, J.-M., "Nonlinear bow flows with spray", *J.Fluid Mech.* **255** (1993) 91–102.

Goh, M. K. and Tuck, E. O., "Thick waterfalls from horizontal slots", *J. Engng. Maths.*, **19** (1985) 341–349.

Tuck, E. O., "Efflux from a slit in a vertical wall", *J.Fluid Mech.* **176** (1987) 253–264.

Vanden-Broeck, J.-M., "Two-dimensional jets aimed vertically upwards", *J. Austrl. Math. Soc. B* **34** (1993) 393-400.

Vanden-Broeck J.-M. and Keller, J. B., "Weir flows", *J.Fluid Mech.* **176** (1987) 283–293.

Wiryanto, L. H. and Tuck, E. O., "A back-turning jet formed by a uniform shallow stream hitting a vertical wall", Proc. Int. Conf. on Differential Equations, October 1996, Bandung, Indonesia.

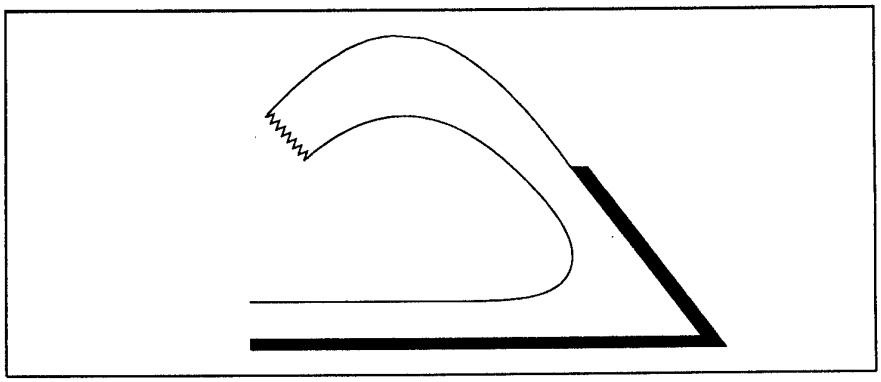

Figure 1:

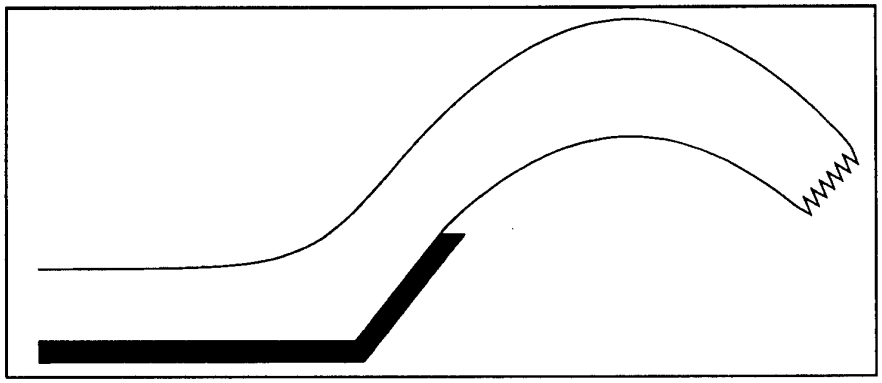

Figure 2:

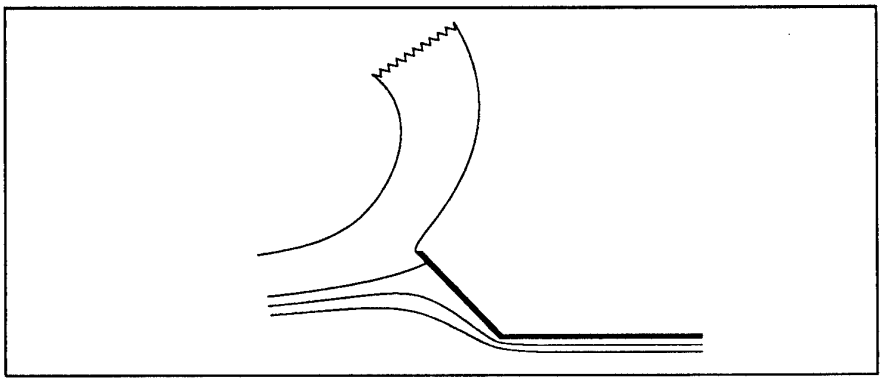

Figure 3:

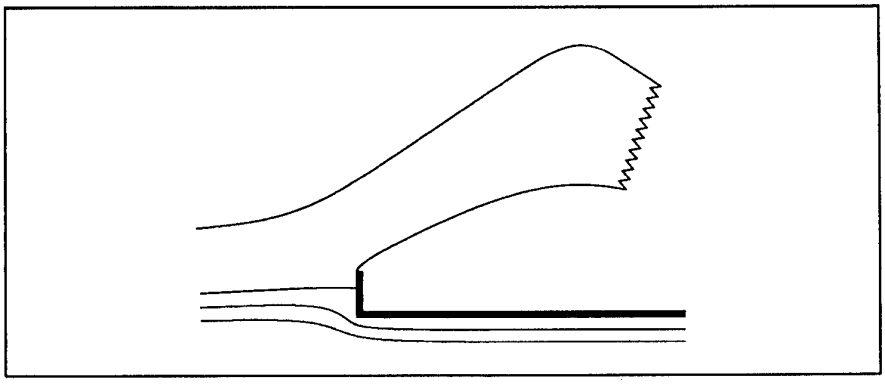

Figure 4:

DISCUSSION

Grilli S.: Did you calculate dynamic pressures induced by jets on solid boundaries?

Tuck E., Simakov S., Wiryanto L.: Not yet. We hope to do this later.

Catamaran Seakeeping Predictions

Riaan van 't Veer, Delft University of Technology

1 Introduction

To solve the motions of a vessel sailing in waves the strip theory is a widely used method. The results are in most cases satisfactory. However, the method becomes less accurate if 3D effects become more important.

By research work done in the past [6] it became clear that for catamaran vessels at low and moderate forward speed the strip theory over predicts the heave and pitch motions if the interaction between the two hulls is included in the calculations. When a catamaran is sailing at high forward speed, the interaction between the two hulls will vanish since the waves generated by one hull can not reach the other hull of the catamaran. It was found that in that case the strip theory could predict the motions of the vessel with more satisfactory results.

Thus, to take interaction effects between the two hulls of a catamaran correctly into account a 3D method is needed.

2 The Boundary conditions

A Rankine panel method has been designed for monohull and catamaran vessels. In this method the hull surface and still water free surface are discretised using flat quadrilateral panels with a constant source strength singularity $(1/r)$ in the collocation point of the panel.

The total velocity potential is written as $\Psi(\vec{x},t) = \Phi(\vec{x}) + \phi(\vec{x}) + \varphi(\vec{x},t)$, where Φ is the double body potential, ϕ is the steady velocity potential and φ is the unsteady velocity potential. The assumption is made that the steady and unsteady potential are independent so that the steady and unsteady problem can be solved separately.

The exact free surface boundary condition on the unknown free surface is linearised to the still water free surface, assuming that the wave elevation from the double body potential allows such a linearisation. The free surface boundary condition for the steady and unsteady problem read, respectively:

$$\begin{aligned} &g\frac{\partial\phi}{\partial z} + \frac{1}{2}\nabla\cdot\phi\nabla(\nabla\Phi\cdot\nabla\Phi) + \nabla\Phi\cdot\nabla(\nabla\Phi\cdot\nabla\phi) - \Phi_{zz}\nabla\Phi\cdot\nabla\phi + \\ &\frac{1}{2}\nabla\Phi\cdot\nabla(\nabla\Phi\cdot\nabla\Phi) - \frac{1}{2}(\nabla\Phi\cdot\nabla\Phi - U^2)(\Phi_{zz} + \phi_{zz}) = 0 \end{aligned} \tag{1}$$

and,

$$\begin{aligned} &g\frac{\partial\varphi_k}{\partial z} - \omega_e^2\varphi_k + 2i\omega_e\nabla\Phi\cdot\nabla\varphi_k + \nabla\Phi\cdot\nabla(\nabla\Phi\cdot\nabla\varphi_k) + \frac{1}{2}\nabla\varphi_k\cdot\nabla(\nabla\Phi\cdot\nabla\Phi) - \\ &\Phi_{zz}(i\omega_e\varphi_k + \nabla\Phi\cdot\nabla\varphi_k) - \frac{1}{2}(\nabla\Phi\nabla\Phi - U^2)(g\varphi_{kzz} + \varphi_{kztt}) = 0 \qquad k = 1,..,7 \end{aligned} \tag{2}$$

where k is the mode of oscillation with $k = 7$ being the diffraction potential.

The hull boundary condition for each potential is that no water can penetrate the hull, thus:

$$\begin{aligned} &\frac{\partial\Phi}{\partial n} = 0, \qquad \frac{\partial\phi}{\partial n} = 0, \\ &\frac{\partial\varphi_k}{\partial n} = i\omega_e n_k + m_k \quad k = 1,..,6, \qquad \frac{\partial\varphi_7}{\partial n} = -\frac{\partial\varphi_0}{\partial n} \end{aligned} \tag{3}$$

where n is the normal vector pointing into the fluid domain. The incoming wave potential is given by φ_0. The m-terms in the unsteady hull boundary condition are calculated analytical,

using Newman [3] and de Koning Gans [1]. The m-terms contain second order derivatives and especially the rotation terms are sensitive for errors in these derivatives due to the length factors with which they are multiplied. In equation (4) the m-terms are written out:

$$\begin{aligned}(m_1, m_2, m_3) &= -(\vec{n} \cdot \nabla)\nabla\Phi == -(n_1\Phi_{xx} + n_2\Phi_{xy} + n_3\Phi_{xz}, \\ &\quad n_1\Phi_{yx} + n_2\Phi_{yy} + n_3\Phi_{yz}, n_1\Phi_{zx} + n_2\Phi_{zy} + n_3\Phi_{zz}) \\ (m_4, m_5, m_6) &= -(\vec{n} \cdot \nabla)(\vec{x} \times \nabla\Phi) = (ym_3 - zm_2 - n_2\Phi_z + n_3\Phi_y, \\ &\quad zm_1 - xm_3 - n_3\Phi_x + n_1\Phi_z, xm_2 - ym_1 - n_1\Phi_y + n_2\Phi_x)\end{aligned} \tag{4}$$

3 Solving the steady or unsteady potential

The Green's identity is used to solve the steady or unsteady potential. That is for the unsteady potential:

$$2\pi\varphi_k(p) - \iint_{FS,H} \varphi_k(q)\frac{\partial G(p,q)}{\partial n_q}dS + \iint_{FS,H} \frac{\partial \varphi_k(q)}{\partial n_q}G(p,q)dS = 0 \tag{5}$$

and a similar expression for the steady problem.

Equation (5) is discretised using N number of flat quadrilateral panels. The unknown variables are discretised using a spline representation, as was presented by Nakos [2]. The spline function is a C-2 function, thus upto the second derivative can be discretised.

4 Some details of the Rankine panel method

A typical free surface panel discretisation for a catamaran problem is presented in Figure (1). The free surface grid is divided into three different grid area's, called `FS1`, `FS2` and `TR`. The transom grid is only pressent if the hull has a transom stern.

Most catamaran vessels have a transom stern to install the waterjet units for propulsion. However, the flow around a transom is typical nonlinear if the transom ends below the still water free surface. Due to the linearisations carried out before, the depth of the transom below $z = 0$ must be limited.

In solving the problem the different grid area's must be connected with each other using physical values at the connection lines. The extra conditions are introduced by assuming an extra set of unknowns, virtually positioned near each border panel of a grid area.

The disturbance due to the vessel are assumed to vanish upstream of the vessel. Practily this means that in the unsteady problem the reduced frequency τ must be greater than 0.25. Thus for the steady and the unsteady problem the conditions $\zeta = 0$ and $\partial\zeta/\partial x = 0$ are discretised at the instream side of the grid.

At the outer-border of the grid the second derivative of the potential in y direction is set to vanish.

Since the problem is symmetric around the x-axis no flow is going through the xOz plane. This means that at $y = 0$ the velocity V_y must be zero.

The continuity of the flow must be satisfied going from one grid to the other grid. This is carried out by discretising the potential itself and the normal vector of the velocity in the y direction and using these two conditions at the intersection. The same conditions are applied between the hull surface and the free surface grid.

If a transom stern is present it is assumed that the flow is leaving the hull surface smoothly, thus the condition $\partial\zeta/\partial x = \alpha$ where α is the transom edge angle, is prescribed in the extra collocation point of the transom sheet. The wave elevation itself is also fixed by the transom edge depth. Using the transom edge angle the wave elevation in the first collocation point aft of the transom becomes $\zeta = \frac{1}{2}h_x \tan\alpha$ where h_x is the first transom sheet panel length in the x direction.

5 Results

In Figure (2) the steady seascape is given for a Wigley catamaran at Fn = 0.30. The stern and bow wave system are clearly spotted. Where the two bow waves meet each other a high peak in the wave system is found.

In Figure (3) the heave and pitch motions of a wigley catamaran vessel are compared with data from experiments [5]. The 3D calculations are refered to as SEASCAPE. The strip theory calculations are performed with the program ASAP, in which ASAP 0 indicates that the interaction between the two hulls is not included in the calculations and ASAP 2 indicates that the 2D interaction between the hulls is taken into account.

The added mass and fluid damping results are presented in Figure (3) as well. A reasonable comparison is found over almost the whole frequency range.

To obtain an indication for the transom stern wave profile calculations, a comparison is presented, Fig. (4), between a non-linear calculation by Raven [4] and the linear calculation from SEASCAPE.

References

[1] H. J. de Koning Gans. *Numerical Time Dependent Sheet Cavitation Simulations using a Higher Order Panel Method.* PhD thesis, Delft University of Technology, January 1994. Delft University Press.

[2] D. E. Nakos. *Ship Wave Patterns and Motions by a Three Dimensional Rankine Panel Methos.* PhD thesis, Massachusetts Institute of Technology, June 1990.

[3] J. N. Newman. Distributions of sources and normal dipoles over a quadrilateral panel. *Journal of Engineering Mathematics*, 20(1):113–126, 1986.

[4] H. C. Raven. *A Solution Method for the Nonlinear Ship Wave Resistance Problem.* PhD thesis, Delft University of Technology, June 1996.

[5] F. R. T. Siregar. Experimental results of the wigley hull formm with advancing forward speed in head waves. Technical Report 1024, Delft University of Technology, Ships Hydrodynamics Laboratory, February 1995.

[6] A. P. Van 't Veer. Catamaran seakeeping prediction. Technical Report 980-S, Delft University of Technology, October 1993.

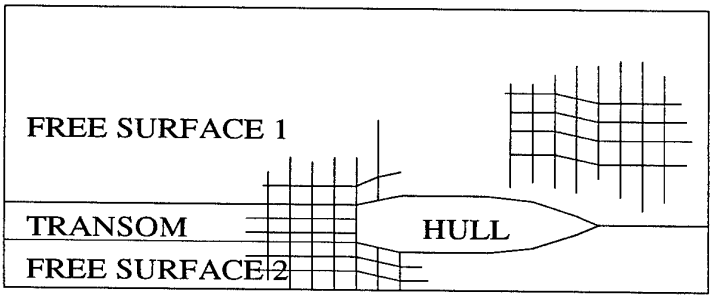

Figure 1: Calculation grid for a catamaran with transom

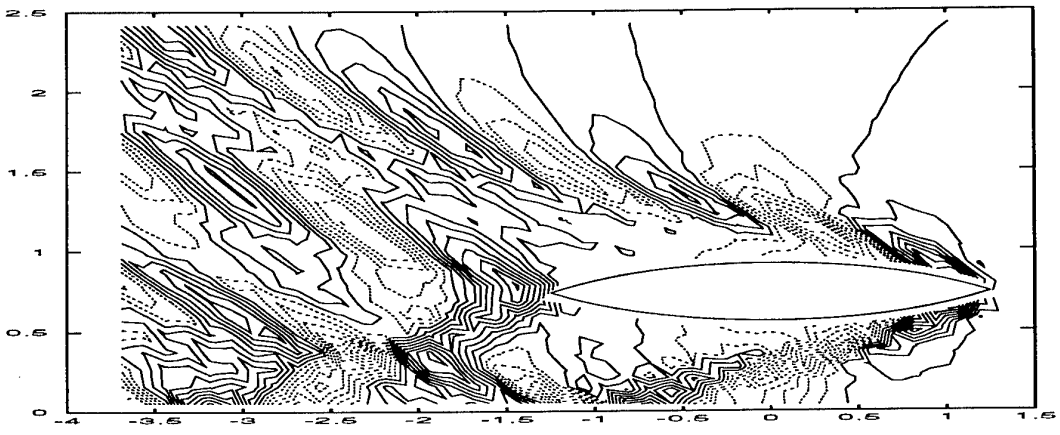

Figure 2: Steady Seascape, Wigley Cat L/B = 7, Fn = 0.30

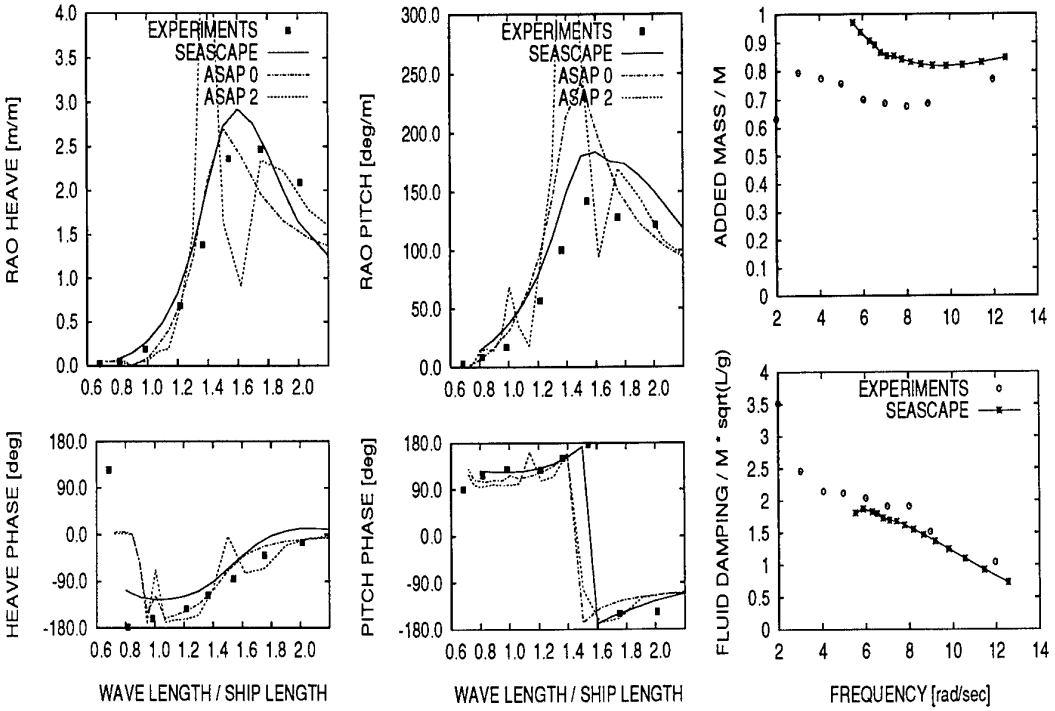

Figure 3: Heave, Pitch, and Added mass and fluid damping results
Wigley Catamaran, L/B = 7, Fn = 0.45

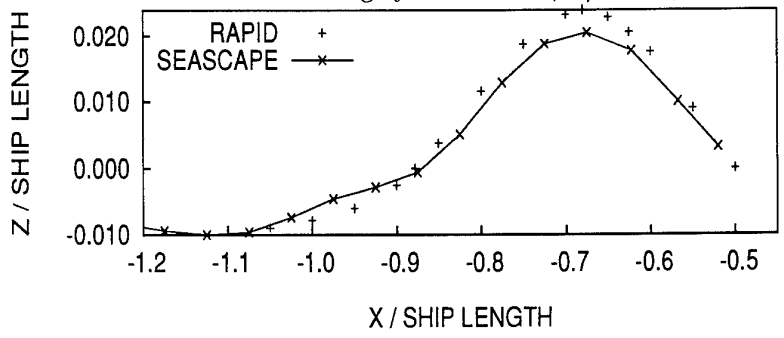

Figure 4: Transom stern wave, Fn = 0.40, RAPID results from Raven [4]

DISCUSSION

Newman J.N.: The highly-tuned heave resonance at $U = 0$ is not really due to wave interactions between the hulls, but to a Helmholtz "pumping" mode in 2D or a longitudinal standing wave in 3D. Do you have any ideas about how this resonant mode is affected by forward velocity?

Van't Veer R.: Thank you for your interesting question about interaction phenomena.
At zero forward speed the added mass and damping coefficients are measured for several heaving twin cylinder configurations by Lee et. al (1971). In most of the measurements the heave added mass drops to negative values where at the same time the fluid damping value goes to zero. This 2D resonance frequency is indeed related to the Helmholtz pumping mode, or can be seen as the behaviour of a moonpool. The resonance frequency can be approximated using the horizontal watercolumn between the two hulls extended with half a circular cylinder underneath. Which yields $\omega = \sqrt{\rho g h / \left(\rho h T + \pi h^2/8\right)}$ where h is the distance between the two hulls and T is the draft of the hull.
With increasing forward speed the moonpool effect will decrease since the watercolumn is not bounded at the fore and aft side. In experiments lately carried out with a catamaran vessel, added mass values close to zero were measured at $Fn = 0.30$ at low frequencies. This indicates in my opinion that a weakened moonpool effect can exist in 3D, if forward speed is not to high. At higher Froude numbers the added mass values became more or less constant over the tested frequency range, indicating no profound interaction effects.
Lee, C.M., Jones, H. and Bedel, J.W.: 1971, Added mass and damping coefficients of heaving twin cylinders in a free surface, *Technical Report 3695*, Departement of the Navy Naval Ship Research and Development Center, Bethesda.

Rainey R.C.T.: Standing on the extreme aft deck of the high-speed catamaran *"Hoverspeed France"*, during her sea trials in Hobart (a harbour discovered by your countryman and my ancestor Abel Tasman, incidentally), I was much struck by the beautiful transom-shaped "groove" cut in the water behind the ship. Its effects appeared to dominate the wave pattern left behind. You mention this in connection with Figures 1 and 4. Can you tell me how the wave resistance of a catamaran compares with the simplest effects of this "groove", i.e. with the

horizontal hydrostatic force that would be felt on the transom at zero speed in still water (and thus is felt, in the opposite sense, by the rest of the hull)? Catamaran designers always appear to minimise the draught of the transom, at the expense of its breadth, which is consistent with minimising this hydrostatic force (since it is proportional to breadth X draught^2).

Van't Veer R.: Thank you for your question in relation to the wave resistance.
The flow around a transom stern is an interesting topic and rather challenging since viscous effects can play an important role. This is especially the case at low Froude number where the transom flow does not leave the transom edge smoothly and a 'dead water' region behind the stern exists. Minimising the transom stern draught (or area) is expected to decrease the resistance since the flow separation will decrease and less energy is lost in the wake pattern.
At higher forward speed or when the transom stern draught is decreased the flow is likely to detach smoothly at the transom edge leaving a nicely shaped 'groove' cut in the water behind. Since the transom stern remains dry there is no horizontal hydrostatic pressure present at the transom. I expect that to obtain a smooth flow detachment it is not always necessary to minimize the transom edge draught, but that it is more important to obtain a smooth hull curvature with a small buttock curvature.

A level set technique for computing 2D free surface flows

Mathias Vogt

Dept. of Naval Architecture and Ocean Engineering, Chalmers University of Technology,Sweden

Kuk-Jin Kang

Korea Research Institute of Ships and Ocean Engineering, Korea

Introduction

The free surface boundary conditions in viscous flow problems can be used in conjunction with basically two different kinds of grid arrangements at the surface. In the fixed grid approach the free surface is tracked and the cells through which the free surface pass include fractions of both fluids. In the moving grid approach a curvilinear grid is fitted to the free surface at every time step. A drawback with the moving grid method is its inability of handling breaking and merging. Due to this shortcoming a new fixed grid method, the level set technique, Sussman et al. (1993), is here used to solve the Navier-Stokes equations for the flow over a bottom bump and around a submerged hydrofoil. Results from numerical simulations with the level set technique are compared to results from moving grid calculations, Kang (1996) and experiments.

Level set method

The level set is a scalar function defined in both fluids with opposite signs in the two fluids. Each level is a subset of the level set function and the subset with a value of zero, the zero level set, is here the free surface. Initially, the function is set equal to the distance from the interface and for later times the value is obtained by setting its material derivative equal to zero. Depending of the sign of the level set function the density and the viscosity are given appropriate values. To smooth the jump at the interface the physical properties are smoothed in a band around the zero level set. One nice feature with this technique is that the interface does not have to be found explicitly but is stored in the information of the level set function. It is also straightforward to extend the formulation to three dimensions.

Simulations presented elsewhere include: a rising air bubble in water, a falling water drop in air and a water drop hitting a pool of water, Sussman et al. (1993). Zhou and Chomiac investigated the Rayleigh-Taylor instability occurring when a light fluid supports or accelerates a heavier one.

Numerical formulation

Equations of motion

The equations of motion are given by the dimensionless Navier-Stokes equations and the incompressible continuity equation. These are solved with the equation for the level set function, ϕ and the following system of equations is obtained

$$\bar{u}_t = -\bar{u}\cdot\nabla\bar{u} + \frac{\zeta^2\nabla^2\bar{u}}{Re\zeta^1} - \frac{\nabla\psi}{\zeta^1}$$

$$\nabla\cdot\bar{u} = 0$$

$$\phi_t = -\bar{u}\cdot\nabla\phi$$

where

$$\psi = p - \frac{y}{Fn^2}$$

$$Fn = \frac{U_0}{\sqrt{gL}}, \qquad Re = \frac{\rho_w \cdot LU_0}{\mu_w}$$

$$\zeta^i = \begin{cases} 1 & if \quad \phi < -\alpha \\ \zeta_a{}^i / \zeta_w{}^i & if \quad \phi > \alpha \\ \bar{\zeta}^i - \Delta\zeta^i \sin\left\langle \frac{\pi\phi}{2\alpha} \right\rangle & otherwise \end{cases}$$

$$\bar{\zeta}^i = (\zeta_a{}^i + \zeta_w{}^i)/(2\zeta_w{}^i), \qquad \Delta\zeta^i = (\zeta_w{}^i - \zeta_a{}^i)/(2\zeta_w{}^i)$$

and $\bar{u} = (u, v)$ is the velocity, p is the pressure, U_o is the uniform flow velocity, L the chord length of the hydrofoil or the channel depth in the bottom bump case and g is the gravitational acceleration. ζ_a^i and ζ_w^i are the density (i=1) and dynamic viscosity (i=2) for air and water, respectively. α is half the prescribed width of the band where the physical properties change.

Solution procedure

The fluid domain is discretized by a finite-volume formulation and the velocity and pressure are defined on a staggered grid system. The method used to update the velocity and pressure is a time splitting fractional step method combined with a velocity and pressure simultaneous iteration method. Convection terms are approximated by a third order upwind scheme and other spacial derivatives are discretized by second order differences, see Kang (1996). When the velocity has been computed within a time step the level set equation is solved. This moves the free surface according to the computed velocity field. Before updating the density and the viscosity the level set function is reinitialized by iterating

$$\phi_t = 1 - |\nabla\phi|$$

to steady state. This ensures that the gradient of the level set function is one, which means that the bandwidth is constant in time.

Boundary conditions

For the level set function the Neumann condition is used at the inflow boundary and at the outflow boundary and linear extrapolation is used at the bottom boundary and at the top boundary. On bodies the no-slip condition, $\bar{u} = \bar{0}$ is imposed, i.e. it is used at the bottom in the bottom bump case and on the foil surface in the submerged hydrofoil case. In the moving grid approach boundary conditions are applied on the free surface, Kang (1996). A uniform flow, $u = 1$, $v = 0$ and zero pressure, $p = 0$ is used as boundary condition at the bottom in the hydrofoil case and when using the level set technique also at the top surface. The same conditions are imposed at the inflow boundary. At the outflow the velocity and the pressure are linearly extrapolated. To avoid reflections of waves at the outflow boundary the level set function is damped with an artificial wave damping function γ in a damping zone as follows;

$$\phi_t = -\bar{u} \cdot \nabla\phi - \gamma(x)\phi|_{y=0}$$

where

$$\gamma(x) = \begin{cases} A\left(\frac{x - x_d}{x_o - x_d}\right)^2 & if \quad x_d \le x \le x_o \\ 0 & otherwise \end{cases},$$

A is a constant, x_o is the x-coordinate at the outflow boundary and x_d is defined as

$$x_d = x_o - 2\pi Fn^2.$$

Since the initial free surface not necessarily coincides with a node the level set function at $y = 0$, $\phi|_{y=0}$ is calculated with linear interpolation. Both the level set function at $y = 0$ and the damping function are calculated once and stored.

Numerical examples

Two different cases have been numerically studied. A submerged NACA 0012 hydrofoil and a bottom bump with the topography described by

$$y = \frac{27E}{4l^3} x(x-l)^2$$

where E denotes the maximum height of the bump, l its length and x is the distance from the leading edge. Initially the flow was accelerated sinusoidally one time unit. The grid used for the bottom bump case was a single-block grid and for the hydrofoil case a two-block H-grid. Computations were carried out for different Froude numbers and the results are in good agreement with the measurements for both methods of determining of the free surface. Results for the foil case are shown in fig. 1. For low enough Froude numbers the generated wave downstream of the bottom bump starts to overturn and break. This phenomenon can be captured with the level set technique, see fig. 2. The result is only qualitative since the resolution is insufficient, but it shows that this method is capable of handling changes in topology.

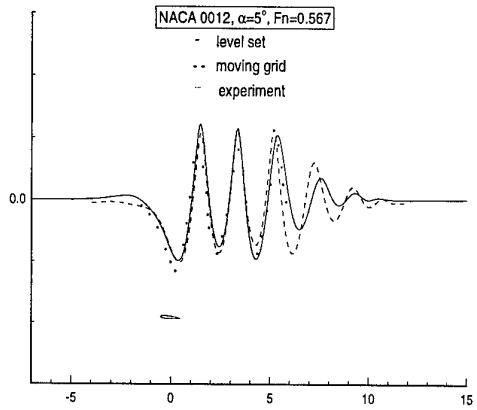

Fig 1. Comparison between numerical methods and experiment.

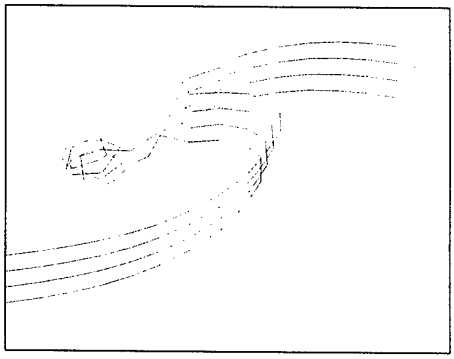

Fig 2. Overturning wave and the break-off of a water drop predicted by the level set technique. Four time steps are shown.

References

Sussman M., Fatemi E., Smareka P. (1993) "A level set approach for computing solutions to incompressible two-phase flow" *J. of comp. Phys.*, vol 114, nr 1, 146-159

Zhou G. & Chomiak J.(1995) "Numerical simulation of three-dimensional compressible/incompressible Rayleigh-Taylor instabilities of stationary and propagating density interface" *Numerical methods in laminar and turbulent flow '95*, vol 9, part 2, 1281-1293

Kang K-J. (1996) "Numerical simulation of nonlinear waves about a submerged hydrofoil" WWWFB '95, Hamburg

DISCUSSION

Wu T.Y.: I would like to encourage the authors to further develop this interesting method for it seems to provide a great deal of potential to future applications to stratified flow motions. In this regard I wish to know:

1) Have the authors applied this method to evaluate the interactions between sheared wind and ocean waves?

2) Have you seriously pursued an error estimate of your computational method?

3) Compared to your levelset equation $d\phi/dt = 0$, which is physically clear upon neglecting mass diffusion, your reinitiating condition seems artifical, empirical at best. To diffuse sharp transitions accross an interface for facilitating computations is fine but don't throw away its capability of predicting, e.g., when a sheared wind separates from an ocean wave.

Vogt M., Kang K-J.:

1) No

2) No

3) The numerical method cannot handle the steep gradients in the density that is present when the two fluids are water and air. The physical properties are therefore smoothed in a band around the interface. This is unphysical unless the band is extreemely thin. The reinitialization procedure itself does nothing but sets the gradient of the levelset function in the normal direction of the interface to one, without changing the position of the interface.

Application of pressure-impulse theory to water wave impact beneath a deck and on a vertical cylinder.

D.J.Wood and D.H. Peregrine
School of Mathematics, University of Bristol, Bristol BS8 1TW, UK
e-mail:deb.wood@bristol.ac.uk, D.H.Peregrine@bristol.ac.uk

Introduction

The impact of water waves on structures can result in very violent motion, in particular if the waves are breaking or near breaking. Many of the studies of wave impact are of impact on a vertical wall or breakwater structure. Here we present results for two slightly different geometrical shapes. Many coastal and offshore structures have openings, overhangs and projections which are open to impact by incident water waves. The first case we consider is the wave impact on the underside of a projecting surface. The example discussed is that of a flat deck close to the mean water level. Secondly, many structures at sea, are supported by circular cylinders, hence we consider wave impact on a circular cylinder. A pressure-impulse approach is used for both cases.

Bagnold (1939) in considering wave impact on a wall, was the first to note that although pressure measurements show great variability between nominally identical wave impacts the integral of pressure over the duration of the impact, the pressure-impulse, is a more consistent measure of wave impact. Cooker and Peregrine (1990 a,b, 1992, 1995) exploited this theoretically to show that the pressure-impulse and its distribution is insensitive to the shape of the impacting water except in a region very close to the structure. Chan (1994) and Losada, Martin and Medina (1995) show good agreement with experiment for wave impact on a wall.

The pressure-impulse satisfies Laplace's equation, with relatively simple boundary conditions. Thus for simple shapes there are standard solution methods which can be used. Further, once one solution has been found the pressure-impulse contours give solutions for other related 'wave' shapes.

Pressure-impulse beneath a deck

We present pressure-impulse calculations for an impact on a horizontal surface near the surface of water of finite depth. For convenience we refer to the rigid surface as a deck. For simplicity, the deck is taken to be at water level and the water is chosen to hit the deck with a uniform vertical velocity component.

The boundary conditions for this problem have a square root singularity where the end of the deck meets the free surface. This singularity causes problems for many solution methods. However, one way to eliminate the problem of the singularity is to map the original problem using conformal maps as follows. First map to a half-space, then use another conformal map to perform a shift and stretch so that by using a final conformal map we can bend the problem back to a semi-infinite strip but with the boundary conditions shifted round to a convenient position, i.e. shift the boundary conditions on the deck round to the vertical wall. This means that the singularity is now eliminated by being mapped to a corner. As we only use conformal maps the pressure-impulse, P, continues to satisfy Laplace's equation, and so we solve using separation of variables. We have made the problem dimensionless by choosing units for which the length of the plate and velocity of the body of water before impact, are both unitary. Figure 1 shows the distribution of pressure-impulse in the water beneath the deck for depth to deck width ratio of 2.0 where the density, deck length and velocity of impact define the units.

The value of total impulse on the deck as a function of a, (water depth)/(deck length), is given in figure 2. This trend is for the impulse from impact of a given velocity and area to increase as

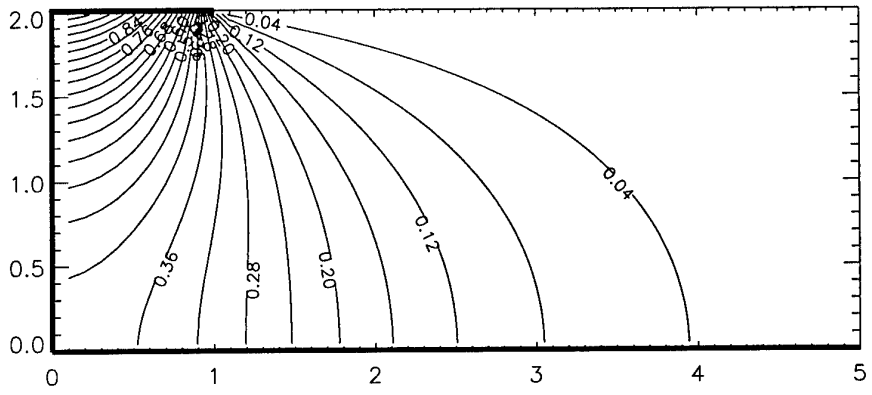

Figure 1: Pressure-impulse contours with $a = 2.0$. Total pressure-impulse on the deck and wall respectively are 0.81 and 1.02

the body of impacting water becomes more confined. The same trend is described by Cooker and Peregrine (1995) for impact on the wall of a rectangular box and by Topliss (1994) for impact within a circular cylinder. Consideration of flow in the most confined circumstances, as a becomes small, has given the concept of 'filling flows' (Peregrine and Kalliadasis, 1995), which is more appropriate for large overhangs. Further, in Peregrine and Thais (1996), an estimate of how the compressibility of dispersed air bubbles, such as those entrained in waves during breaking, may soften wave impact is given.

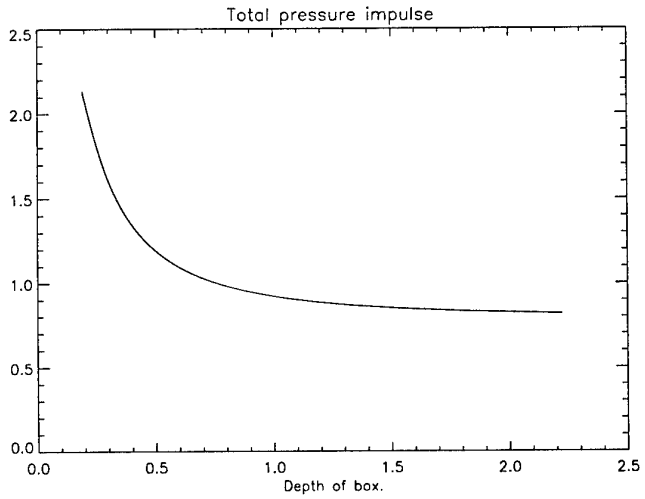

Figure 2: Total impulse on deck against depth a, where a = (water depth)/(deck length).

Impact on a cylinder

We now consider the pressure-impulse acting on a vertical cylindrical structure. For a first approximation in impact problems the water-hammer pressure-impulse is sometimes used. However, Cooker and Peregrine (1990) showed that predicted pressures are reduced significantly due to the effect of the free surface, where the pressure is atmospheric. Cooker and Peregrine (1995) noted that unless the thickness of the impacting water is quite small the actual shape of the wave away from the impact region is relatively unimportant. Hence, for simplicity, the shape of a wave impacting on a cylinder is considered to have a horizontal free surface.

Again we use pressure-impulse theory, and solve Laplace's equation, this time in cylindrical coordinates, by separation of variables. Figure 3 shows the pressure-impulse contours on the cylinder in an infinite body of water with the impact on a patch of the cylinder just below water level. Figure 4 shows the pressure-impulse contours in a wall of water impacting on the cylinder. In both these cases, which are chosen for mathematical convenience, the impact velocity is taken to be unidirectional. The angle ϕ is angle in radians, where $\phi = 0$ is at the centre of the impact region. The velocity V will vary with position. However, for demonstration, it is adequate to choose a simple velocity field. For example, a typical velocity in a breaking wave in deep water would be about $1.4c$, where c is the phase velocity of the linear wave of the same period. For simplicity of analysis the velocity of impact is scaled to unity in the present analysis.

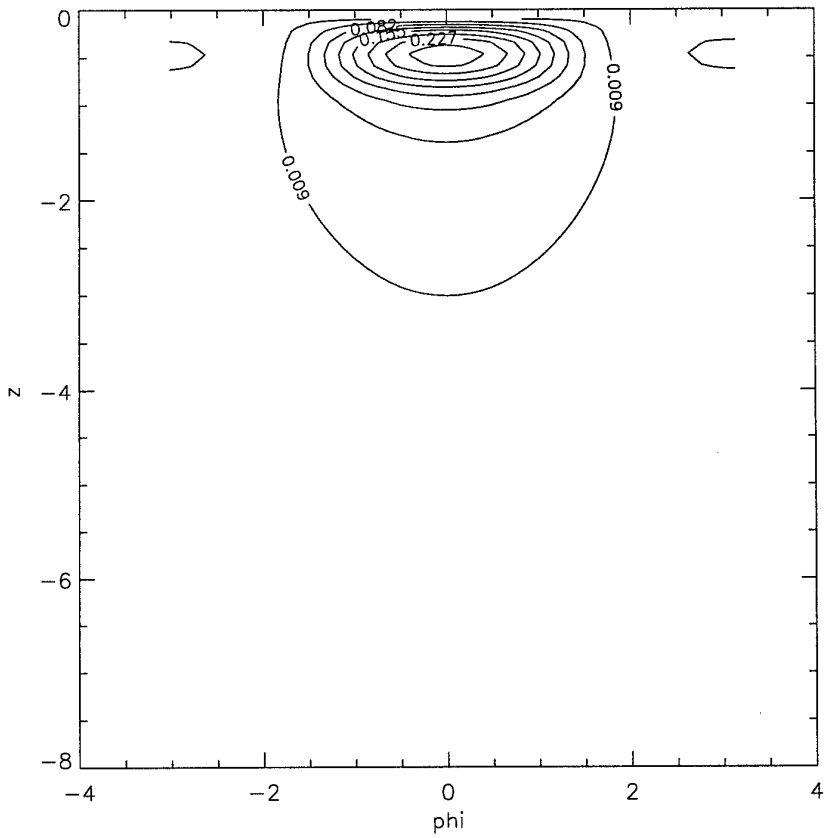

Figure 3: Distribution of pressure-impulse on a cylinder (unwrapped) with the wave impact on half of the top 10 % of the cylinder

There is a high pressure gradient towards the top of the cylinder/wedge, giving a strong impulse away from the point of high pressure acting on any projections. The method of direct solution of

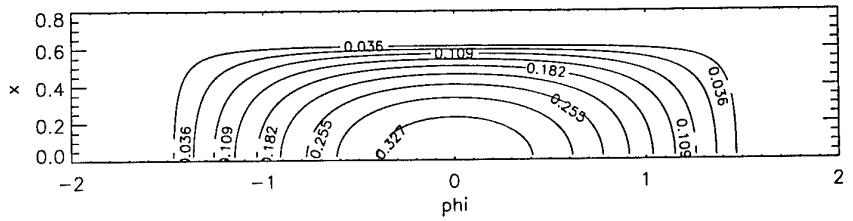

Figure 4: Distribution of pressure impulse on a cylinder (unwrapped) with the wave impact from a wall of water.

Laplace's equation by separation of variables used here is mathematically simple. However in practice it may be better to use a boundary integral method.

Conclusion

A readily evaluated solution is found for the pressure-impulse from waves hitting a deck from below. It is found that the impulse is greater if the water is shallow. Pressure-impulse theory can also give a model of impact on a cylinder. The total impulse for 2D impact on a wall of the same projected cross-sectional area is 1.016, on a cylinder it is 0.250 when the impact is surrounded by water and 0.263 for the 'wedge' of angle π bounded below by a fixed bed. We can compare this with the water hammer approach, which is dependent on how long the wave crest is. For example, if the wave crest has width l, with the unit density, velocity, and cylinder radius we are using, it gives an impulse due to momentum in the wave of $2l$. This is much bigger than the above case where l = 1=radius of the cylinder.

We intend to compare the pressure-impulse model of impact on a cylinder with experimental data given in Chaplin, Greated, Flintham and Skyner (1992).

Acknowledgements

Support of the U.K. EPSRC, M.T.D. Ltd. ULOS programme, and the European Commission, Directorate General XII, Science, Research and Development, contract number MAS3-CT95-0041, is gratefully acknowledged.

References

BAGNOLD, R.A. (1939). Interim report on wave pressure research. *J. Inst. Civil Engrs* **12**, 201-226.
CHAN, E.S. (1994). Mechanics of deep water plunging-wave impacts on vertical structures. *Coastal Engng* **22**, 115-133.
CHAPLIN, J.R., GREATED, C.A., FLINTHAM, T.P., & SKYNER, D.J. (1992) *U.K. Dept. of Energy Report OTH-90-324*
COOKER, M.J. & PEREGRINE, D.H. (1990a). Violent water motion at breaking wave impact. *Proc. 22nd Internat. Conf. Coast. Engng., ASCE* 164-176.
COOKER, M.J. & PEREGRINE, D.H. (1990b). A model for breaking wave impact pressures. *Proc. 22nd Internat. Conf. Coast. Engng., ASCE* 1473-1486.
COOKER, M.J. & PEREGRINE, D.H. (1992). Wave impact pressure and its effect upon bodies lying on the sea bed. *Coastal Engng.* **18**, 205-229.
COOKER, M.J. & PEREGRINE, D.H. (1995). Pressure-impulse theory for liquid impact problems. *J. Fluid Mech.* **297**, 193-214.
LOSADA, M.A., MARTIN, F.L. & MEDINA, R. (1995). Wave kinematics and dynamics in front of reflective structures. *Wave forces on inclined and vertical wall structures. ASCE,* editors N. Kobayashi & Z. Demirbilek, 282-310
PEREGRINE, D.H. & KALLIADASIS, S. (1996). Filling flows, coastal erosion and cleaning flows. *J. Fluid Mech.* **310**, 365-374.
PEREGRINE, D.H. & THAIS, L. (1996). The effect of entrained air in violent water wave impacts. *J. Fluid Mech.* **325**, 377-397.
TOPLISS, M.E. (1994). Water wave impact on structures. Ph.D. dissertation, University of Bristol.

DISCUSSION

Grilli S.: Knowing the pressure impulse acting on a very rigid structure (i.e. for which elasticity can be neglected), how would you estimate the impact duration, in order to obtain pressures and forces?

Wood D., Peregrine H.: The pressure impulse technique is aimed at getting relatively simple solutions for complex events. Thus a simple time profile, a triangle, may be assumed, with an estimate of duration that depends on the actual physical scale. Wave impact studies indicate that, for the laboratory scale, durations around a milli-second occur for the most violent impacts. At larger scales 0.01 to (0.5) seconds may be appropriate. There are clear indications that at larger scales both air trapped by the impact, and air bubbles dispersed in the water are important.

Kim Y.: I think it is not difficult to include simple compressibility model to pressure Poisson equation. Do you have any idea to consider the compressibility of fluid with simplified method?

Wood D., Peregrine H.: The simplest model of air trapped by an impact is to include a rebound velocity. We have just started such work.
The effect of bubbles dispersed in the water as the cause of compressibility has been studied for a different but related flow in Peregrine & Thais (1996) "The effect of entrained air in violent water impacts", Journal of Fluid Mech. 325, pp 377-397.

Resonant Interactions of Kelvin Ship Waves With Ambient Ocean Waves

Qiang Zhu, Yuming Liu & Dick K.P. Yue

Department of Ocean Engineering
Massachusetts Institute of Technology
Cambridge, Massachusetts 02139, USA

1 Summary

In recent field experiments, Brown *et al.* (1989) observed that inside the Kelvin wake of a moving ship, there can be two soliton-like envelopes which extend to a long distance behind the ship. It is known that such solitary waves are not predicted by the steady ship-wave theory even with the inclusion of free-surface nonlinearity (*e.g.*, Newman 1971; Akylas 1987). Upon including unsteady waves, Mei (1991) suggested that oscillations of an advancing ship may be the possible source for the generation of oblique solitary waves in the Kelvin wake. Despite a speculation of high-frequency heave and pitch oscillations of a ship moving in ambient sea waves, his theory gives qualitative predictions of only partial solitary features observed in field experiments.

In this work, we provide an alternate mechanism for the generation of observed solitary waves in the ship wake by considering nonlinear resonant interactions of steady Kelvin waves and unsteady ambient waves in the spirit of Phillips (1960). We show that a new progressive wave along a particular ray inside the ship wake can be created due to third-order resonant interactions of Kelvin waves with an ambient incident wave. The wavenumber and propagation direction of the generated wave and the resonance-ray location, which depend on ship speed and ambient-wave wavenumber, are determined by the resonant conditions which we derive explicitly. To understand the development of the new wave, we derive the evolution equations for interaction wave components by a multiple-scale analysis. It is found that the generated wave has a solitary envelope in the lateral direction, and the envelope itself grows with the distance from the ship in the near wake while slowly oscillates in the far wake. Such theoretical predictions are confirmed in the near wake by direct time-domain simulations of a moving point source in an ambient incident wave field.

2 Resonant conditions

For a ship moving in an ambient incident wave field, let us examine the possibility of resonant interactions between the Kelvin ship wave and the incident wave. For convenience, let vector wavenumber $\mathbf{k_s}$ represent the Kelvin ship wave and $\mathbf{k_i}$ the incident wave. According to Phillips (1960), third-order interaction of the Kelvin wave and the incident wave, with the incident wave counted twice, can become resonant so that a new progressive wave can be generated if the following condition is satisfied:

$$\cos(\theta_i - \theta_s) = 2\eta^{-1/2} + 8\eta^{1/2} - 3\eta - 6 \tag{1}$$

where $\eta = |\mathbf{k_i}|/|\mathbf{k_s}|$ and θ_i and θ_s respectively denote propagation directions of the Kelvin wave and the incident wave relative to the ship velocity U. The generated free wave possesses

a wavenumber $\mathbf{k_r}=2\mathbf{k_i}-\mathbf{k_s}$ and a frequency $\omega_r=2\omega_i-\omega_s$ with ω_i and ω_s representing frequencies of the incident wave and the Kelven wave respectively.

Under the condition (1), the resonant interaction between the Kelvin wave and the incident wave occurs along a particular ray inside the ship wake since Kelvin wave wavenumber $\mathbf{k_s}$ is constant on each ray. Once the new (free) wave is created, it propagates at its own group velocity, $\mathbf{V_g}=\omega_r\mathbf{k_r}/2|\mathbf{k_r}|^2$. Meanwhile, the ray itself moves forward at speed $\mathbf{U}$ as the ship advances. In general, the new wave and the resonance ray will propagate away each other so that no significant energy built-up for the new free wave can be resulted except for the case where the normal component of $\mathbf{V_g}$ on the resonance ray is identical to the normal velocity of the resonance ray, i.e.

$$\mathbf{V_g}\cdot\mathbf{n}=\mathbf{U}\cdot\mathbf{n} \tag{2}$$

where $\mathbf{n}$ denotes the unit normal of the resonance ray. Under the condition (2), the generated free wave propagates along the resonance ray and remains on the ray at any time as the ship moves forward. This leads to an energy built-up for the generated free wave along the resonance ray.

We remark that unlike resonant interactions among plain waves for which only the condition (1) is required, the occurrence of (third-order) resonant interactions between the Kelvin ship wave and an plain incident wave requires the satisfaction of both conditions (1) and (2). For a given incident wave ($\mathbf{k_i}$), we can determine the ship speed ($\mathbf{U}$) for the occurrence of resonances and the orientation of the resonance ray (α), from (1) and (2). Figure 1 shows the result as a function of the propagation angle (θ_i) of ambient incident waves (for the interaction with the transverse wave).

Note that if $\mathbf{k_s}$ and $\mathbf{k_i}$ exchange their positions in (1), it follows that the resonance may also occur for third-order interactions with the Kelvin wave counted twice.

3 Multiple-scale analysis

To understand the development of the new progressive wave in the ship wake, we carry out a multiple-scale perturbation analysis to obtain evolution equations for envelopes of interaction wave components in the vicinity of the resonance ray. Referring to a coordinate system fixed with the ship, the evolution equation at steady state for the amplitude of the generated wave, A_r, for example, can be written in the form:

$$\sigma_1\frac{\partial A_r}{\partial\xi}+i\left(\sigma_2\frac{\partial^2}{\partial\xi^2}+\sigma_3\frac{\partial^2}{\partial\xi\partial\zeta}+\sigma_4\frac{\partial^2}{\partial\zeta^2}\right)A_r+i\left(C_1A_sA_s^*+C_2A_iA_i^*+C_3A_rA_r^*\right)A_r=C_4A_s^*A_i^2$$

where $*$ denotes the complex conjugate, and A_s and A_i are amplitudes of the Kelvin wave and the incident wave, respectively. Here ξ are ζ are coordinates along and perpendicular to the resonance ray. The coefficients $\sigma_{1,2,3,4}$ and $C_{1,2,3,4}$ are given in terms of wavenumbers and frequencies of the interaction waves.

After imposing proper boundary conditions in the lateral direction, the evolution equations can be easily solved by the use of numerical integration. Figure 2 shows a typical result for the envelope of the generated wave near the resonance ray. As expected, the generated wave grows by absorbing energy from the primary waves in the near wake while slowly oscillates due to an energy exchange with the primary waves in the far wake.

4 Direct numerical simulation

To verify the theory, we perform a nonlinear time-domain simulation of a moving point source in an ambient incident wave field using a high-order spectral method (Liu, Dommermuth & Yue 1992). Simulation results confirm the theoretical prediction that nonlinear resonant interaction of the Kelvin wave and the incident wave can generate a soliton-like free wave in the ship wake. In particular, quantitative comparisons for the growth rate of the solitary wave in the near wake are obtained, which are shown in figure 3.

5 References

AKYLAS, T.R. 1987 Unsteady and nonlinear effects near the cusp lines of the Kelvin ship-wave pattern. *J. Fluid Mech.*, **175**, 333–342.

BROWN, E.D., BUCHSBAUM, S.B., HALL, R.E., PENHUM, J.P., SCHMITT, K.F., WATSON, K.M. & WYATT, D.C. 1989 Observation of a nonlinear solitary wave packet in the kelvin wake of a ship. *J. Fluid Mech.*, **204**, 263–293.

LIU, Y., DOMMERMUTH, D. G. & YUE, D. K. P. 1992 A high-order spectral method for nonlinear wave-body interactions. *J. Fluid Mech.* **245**, 115-136.

MEI, C.C. & NACIRI, M. 1991 Note on ship oscillations and wake solitons. *Proc. R. Soc. Lond.*, A**432**, 535–546.

NEWMAN, J.N. 1971 Third order interactions in the Kelvin ship wave systems. *J. Ship Res.*, **15**, 1–10.

PHILLIPS, O.M. 1960 Unsteady gravity waves of finite amplitude. Part I. The elementary interactions. *J. Fluid Mech.*, **9**, 193–217.

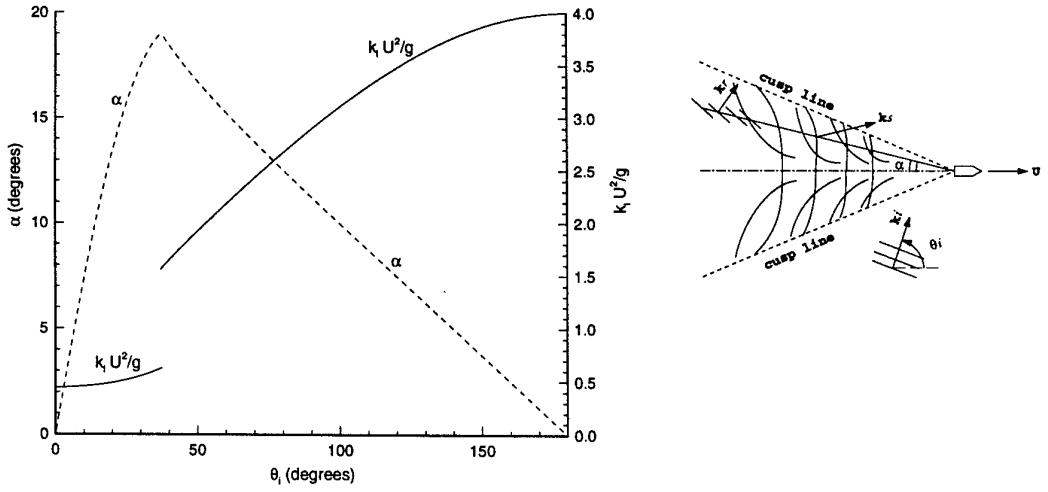

Figure 1: The resonance-ray location (α), and ship forward speed ($\mathbf{U}$) and incident wave wavenumber ($\mathbf{k_i}$) for wave resonances as a function of incident angle (θ_i).

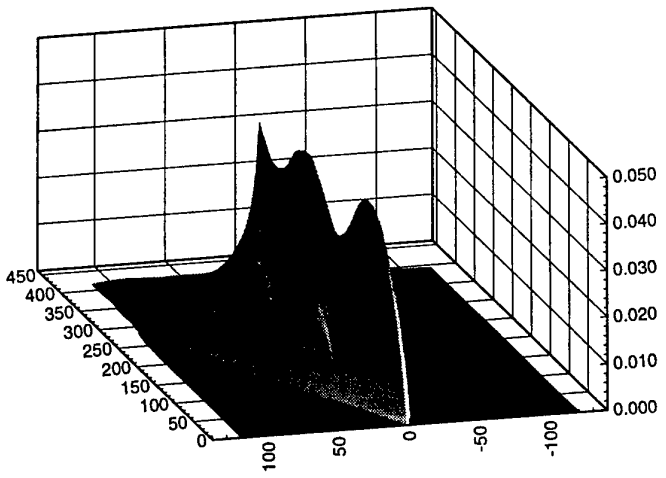

Figure 2: The envelope of the generated progressive wave in the neighbourhood of the resonance ray (α=7.5^o) in the Kelvin wake. (Incident-wave steepness $|\mathbf{k_i}|A_i$=0.15; incident angle θ_i=120^o; ship forward speed U=1.86$(g/|\mathbf{k_i}|)^{1/2}$; and Kelvin-wave steepness $|\mathbf{k_s}|A_s$=0.75$U(gr)^{-1/2}$ with r the distance from the ship.)

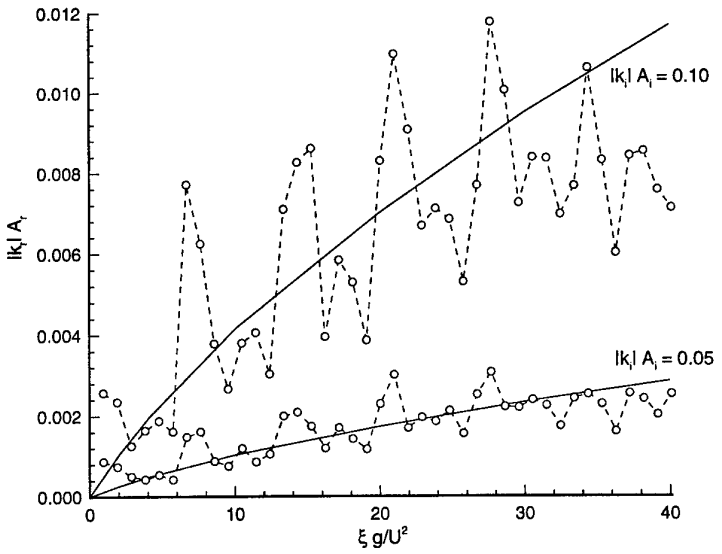

Figure 3: The comparisons between the theoretical solution by a multiple-scale analysis (———) and the direct simulation result (- -⊙- -) for the initial growth of the generated progressive wave on the resonance ray (α=7.5^o) in the Kelvin wake of a moving point source. (θ_i=120^o; U=1.86$(g/|\mathbf{k_i}|)^{1/2}$; and $|\mathbf{k_s}|A_s$=0.75$U(gr)^{-1/2}$.)

DISCUSSION

Peregrine H.:

a) This talk assumes considerable coherence in the ambient waves;

b) Another explanation is that these features are due to the waves from the ship's stern passing through the wake and shear layer due to boundary layers (Peregrine, 1971 J.F.M.)

Zhu Q., Liu Y., Yue K.P.:

a) Our theory shows that third-order quartet resonant interactions between steady ship waves and unsteady ambient incident waves can generate soliton-like progressive waves inside the Kelvin wake of a ship. Accordingly, the generated resonant wave becomes comparable in magnitude to the local ship wave over an interaction distance $L \sim O(\varepsilon^{-2})$, where ε is the steepness of the incident or steady ship waves. This is confirmed by our numerical results. For the case of Brown *et al.* (1989), L is estimated to be $O(150 \sim 200)$ m (corresponding to the ship forward speed of $\sim 7.7 m/s$). Such distances are not unreasonably large to assume some coherence of the dominant ambient wave component which we assume to be present.

b) Peregrine (1971) found that as a result of the presence of a ship wake, the stern waves diverge at an angle to the center-line of the ship smaller than that for the bow waves. However, this is unlikely to be the mechanism responsible for the observation of Brown *et al.* (1989) since the stern waves decay with distance R from the ship as $R^{-1/2}$ which is much faster than the observed solitary wave decay rate (which is slower than $R^{-1/3}$).

Schultz W.: Your solutions do not appear to be symmetric behind the ship. Are they? [answer: beach reflection, etc]. This seems to be more far fetched than the ambient waves exciting the ship and analyzing the unsteady wave pattern as in the last presentation by Chen and Noblesse. Any comments?

Zhu Q., Liu Y., Yue K.P.: For a single monochromatic incident wave, our theory predicts the generation of a soliton-like progressive wave on one side of the ship wake. In order for two soliton-like waves to be observed inside the Kelvin wake, the theory requires the presence an additional incident wave component. Since Brown *et al.* (1989) did not measure/report on the ambient wave environment of

the field experiments, the presence of additional ambient wave components can neither be ruled out nor confirmed.

If the unsteady wave due to ship motions is considered, its cusp line angle, wavenumber and propagation direction depend on $\tau = \omega U/g$, where ω is the oscillation frequency and U the forward speed of the ship, and g the gravitational acceleration. From the aerial photograph of Brown *et al.* (1989) (cf. figure 2), the solitary wave appears at an angle of 13° ~ 14° (measured from the ship track) which requires τ to be 0.5 ~ 0.7. At these values of τ, the propagation direction and wavenumber of the unsteady wave should be close to those of the steady waves near the Kelvin cusp line. These are not supported by the field observations.

Georg Weinblum Special Meeting

19-20 March 1997

A Special Meeting was held after the Twelfth Workshop to celebrate the 100th anniversary of the birth of Georg Weinblum. Professor Weinblum was an international leader in ship theory. He inspired a generation of colleagues, including several who are still active participants in the Workshops. For this reason it was felt that the anniversary celebration should be held in conjunction with the Twelfth Workshop.

Since Weinblum's death in 1974, a series of Memorial Lectures have been presented on an annual basis (the list is given at the end of this volume). All of the former Lecturers were invited to participate in the Special Meeting, and to present lectures. Thirteen among them contributed. Titles of their presentations and short written abstracts are given in the following pages.

Georg Weinblum
22-01-1897 - 04-04-1974

Georg Weinblum Special Meeting

List of contributions

Stagnation Points

K. J. Bai[1], C. W. Dawson[2], J.W.Kim[3], and J. V. Wehausen[3]

A rectilinear potential flow about a circle in the plane or about a sphere in three dimensions results in two stagnation points, one at each end of a diameter. For any bounded simply connected region in the plane it follows from Riemann's Mapping Theorem that there is an analytic function mapping the exterior of the unit circle into the exterior of the region and behaving like a rectilinear flow at infinity. Hence there are only two stagnation points on the boundary of the region in question. Although harmonic functions in three dimensions share many properties with analytic functions in the plane, there is no analogue of the Riemann theorem. In fact, there is only a very restricted set of transformations that preserve the property of being harmonic (see, e.g., Kellogg, *Foundations of Potential Theory* , 1929, pp. 235-236). It is natural to ask whether there can be more than two stagnation points in a potential flow about a bounded simply connected body in three dimensions. The question is raised in Kellogg (ibid., pp. 273-277) but not really answered. It is shown in Kellogg (p. 273) that there cannot be a continuous surface distribution of stagnation points (unless, of course, the potential function is constant). On the other hand, one knows that there can be continuous linear distributions of stagnation points if Laplace's equation can be separated in a particular coordinate system, as in $\Phi(x,y,z) = \varphi(x,y)Z(z)$ with $Z(z) = \text{const.}$ or $\Phi(r, \theta, z) = R(r)\Theta(\theta)Z(z)$ with $\Theta = \text{const.}$ One might be led to conjecture that any continuous line of stagnation points must be associated with a coordinate system in which Laplace's equation may be separated. However, the following is a counterexample (JWK) to this conjecture:

$$\Phi(x,y,z) = (1/2)x^2 y^2 - (1/2)(x^2 + y^2)z^2 + (1/6)z^4,$$

for both the x-axis and the y-axis are lines of stagnation points.

A discussion by one of us (JVW) with Charles Dawson in June 1978 concerning the possibilities of multiple stagnation points resulted in a letter from him dated 28 June 1978 describing his investigation of a 3-dimensional body generated by two dipoles of equal moment situated on a line perpendicular to an oncoming steady rectilinear flow. As is well known, when the separation of the dipoles is zero, one streamline will generate a sphere with stagnation points at opposite ends of a diameter. Dawson correctly predicts the dipole separation at which each of the two stagnation points will begin to separate into three stagnation points, and also the

---

[1] Seoul National University, [2] Formerly, David Taylor Model Basin,
[3] University of California at Berkeley

(further) separation at which the single body will divide into two bodies. In addition, he computed the positions of the stagnation points lying on the central streamline as long as there is only one body.

Dawson died in January 1980 without having published any details concerning his calculations. In the present paper we present not only the analysis and computation necessary to substantiate Dawson's results, but also other relevant details accessible by exploiting modern computational capabilities, especially *Mathematica*. In addition to the 3-dimensional problem, we also treat the analogous 2-dimensional problems for two dipoles and for two vortices. The analysis and the computation for these are simpler than for three dimensions, in particular, because of the presence of a stream function, but the results are relevant both for their similarities to and their differences from the 3-dimensional case.

The qualitative difference between two and three dimensions is chiefly a result of the following facts. Let Φ be the velocity potential, in either two or three dimensions, of the rectilinear flow in direction Ox about two dipoles at a distance $2a$ apart and perpendicular to the oncoming flow. In two dimensions Φ_{xx} and Φ_{yy} vanish together at the two stagnation points associated with the largest separation a before a single closed stream body splits into two bodies, with, of course, two stagnation points on each. In three dimensions, however, $\Phi_{yy} = 0$ at a stagnation point associated with a *smaller* value of a than that at which $\Phi_{xx} = 0$, which again occurs at the largest value of a before the single closed stream body divides into two bodies. It is shown, however, that $\Phi_{yy} > 0$ is associated with the presence of two further stagnation points with $y \neq 0$, so that there exists an interval of dipole separations for which there is only one closed stream body but three stagnation points on each side. Furthermore, there exists an interval of separations for which $\Phi_{yy} \geq \Phi_{xx} > 0$, and this implies that the single body is not smooth at the waist, i. e. at the intersection of the stream body with the plane perpendicular to and bisecting the line joining the two dipoles. In two dimensions this nonsmooth behavior can occur only at the "last" single body when $\Phi_{xx} = \phi_{yy} = 0$, the only separation at which Φ_{xx} and Φ_{yy} are equal.

The following two pages show graphs illustrating the differing behaviors for different separations, both for two-dimensional vortex and dipole pairs and for three-dimensional dipole pairs.

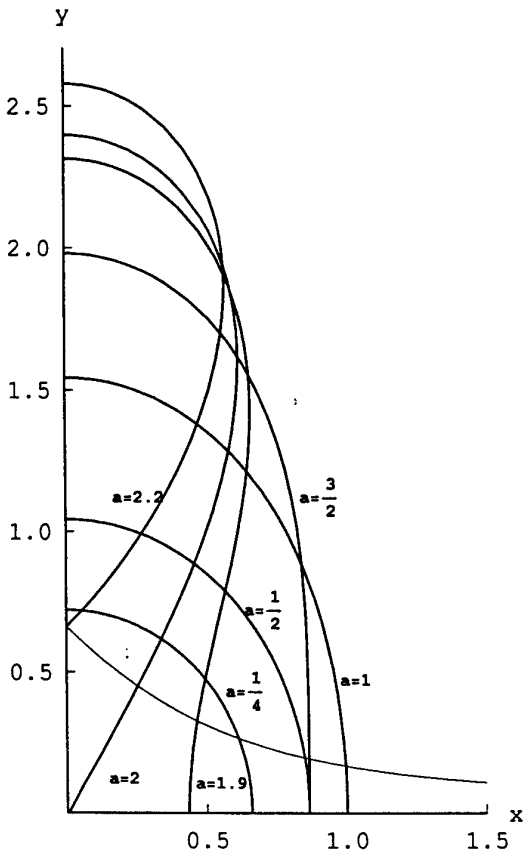

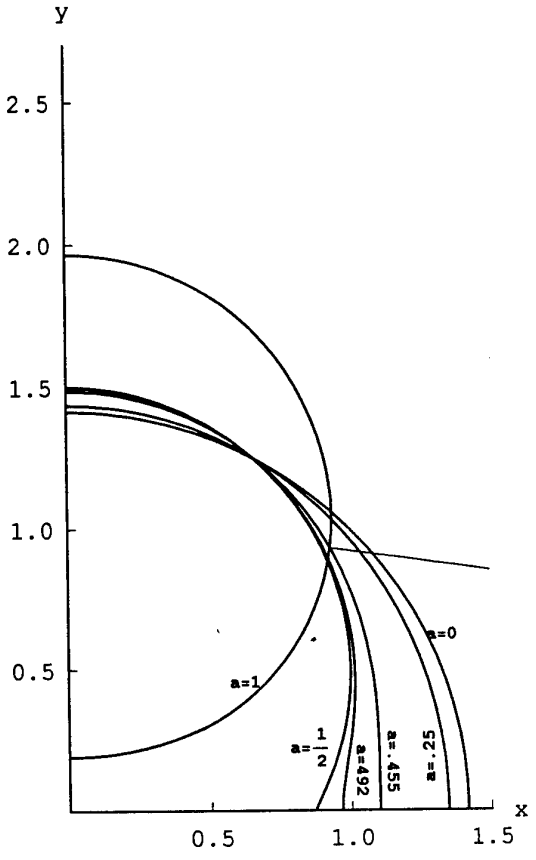

Two vortices in the plane **Two dipoles in the plane**

Traces in the first quadrant are shown for the closed streamlines generated by two vortices (on the left), all of the same strength, and by two dipoles (on the right), all of the same moment, but at different spacings, indicated in each case by the value of a. For the vortex pair the largest value of a before two separate bodies are formed is $a = 2$, for the dipole pair this value is $a = 1/2$. In each case this is the value of a associated with $\Phi_{xx} = 0$. The value of a at the boundary between convex and concave behavior at the stagnation point is $a = 3/2$ for the vortices and $a = 0.455 = [(2^{1/2} - 1)/2]^{1/2}$. In each case this is the value of a associated with $\Phi_{xyy} = 0$ at the stagnation point.

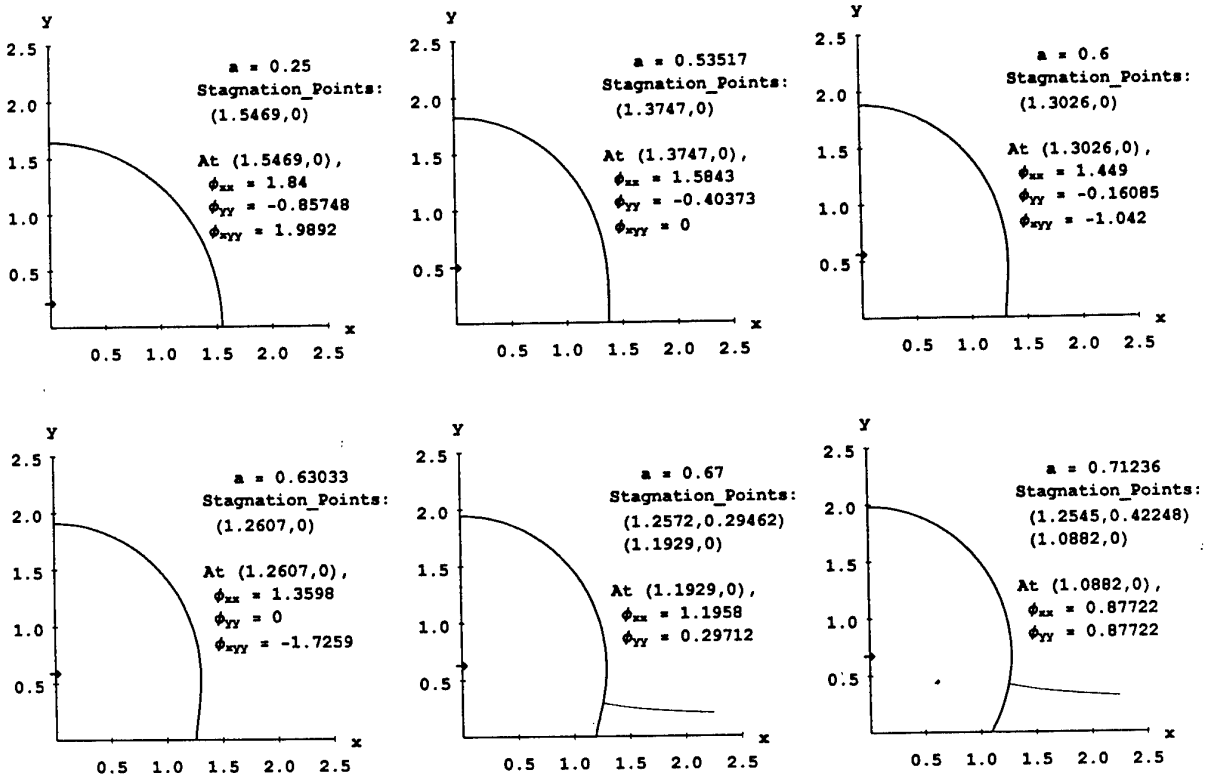

Two dipoles in space

Traces in the first quadrant of the (x, y)-plane of the streambodies generated by two dipoles, all of equal moment but with different spacings, as shown by the value of a. All streambodies are bodies of revolution about the y-axis and are symmetric about the (x, z)-plane.

In the first four traces there is a single stagnation point, on the x-axis, in the quadrant shown, and hence one on each side of the streambody. The separation $a = 0.63033$, corresponding to $\Phi_{yy} = 0$, is the largest value of a for which there is only one such stagnation point. The value $a = 0.53517$, corresponding to $\Phi_{xyy} = 0$ at the stagnation point, is the boundary between convex and concave behavior of the streamsurface at the stagnation point. The last four traces, for which $0.63033 < a \leq 0.73972$, all show a second stagnation point at $y > 0$, hence three on each side. At $a = 0.71236$ $\Phi_{xx} = \Phi_{yy}$ at the stagnation point, and the streamsurface has a corner at the (x ,z)-plane. For $a > 0.71236$ this corner becomes an inward-pointing cusp. The largest value of a before the streambody splits into two is $a = 0.73972$.

An Integral Representation of a Wave Function in the Theory of Wave Resistance of Ships

By Masatoshi Bessho

The kernel function of a singurality in the theory of wave resistance of ships is usually represented by a double integral, but it was shown in the memoirs by the author that the kernel function has a single integral representation which faciliates numerical works exeedingly[3].

However, the analysis of the memoirs is somewhat obscure and may have some errors. In fact some authors have indicated the errors in the formulas in the memoirs[2),4),5)].

In the present paper the integral representation of a wave function is reanalyzed and revised.

A function which is treated here is as follows ;

$$P_{-1}(x,y,z) = Re.\left[\frac{1}{2}\int_{-\infty}^{\infty} e^{f(t)}dt\right], \tag{1}$$

where

$$\begin{aligned} f(t) &= ix\cosh t - iy\sinh t\cosh t - z\cosh^2 t, \\ &= ix\cosh t - \rho\cosh t\cosh(t+i\alpha), \end{aligned} \tag{2}$$

and $\rho = \sqrt{y^2+z^2}$, $\quad \tan\alpha = y/z.$

Then, since we have an integral

$$e^{-\rho\cosh^2(t+i\alpha/2)} = \frac{1}{2\sqrt{\pi\rho}}\int_{-\infty}^{\infty} e^{-\frac{v^2}{4\rho}-iv\cosh(t+i\alpha/2)}dv, \tag{3}$$

inserting this in equation (1) and shifting the path of the integration in the t-plane yields

$$P_{-1}(x,y,z) = \frac{e^{(\rho-z)/2}}{4\sqrt{\pi\rho}}\int_{-\infty}^{\infty} e^{-\frac{v^2}{4\rho}}dv\int_{-\infty}^{\infty} e^{iR\cosh(t+i\alpha/2-i\psi)}dt, \tag{4}$$

where

$$R = \sqrt{x^2+v^2-2xv\cos(\alpha/2)}, \quad \tan\psi = \frac{x\sin(\alpha/2)}{x\cos(\alpha/2)-v}. \tag{5}$$

Making use of the integral representation of Bessel function of the second kind

$$Y_0(R) = -\frac{1}{\pi}\int_{-\infty}^{\infty} e^{iR\cosh u}du, \tag{6}$$

We obtain the following formula :

$$P_{-1}(x,y,z) = -\frac{e^{(\rho-z)/2}}{4\sqrt{\rho/\pi}} \int_{-\infty}^{\infty} e^{-\frac{v^2}{4\rho}} Y_0(R) dv = I_1. \tag{7}$$

This formula is correct in the following special cases, that is,

$$P_{-1}(0,y,z) = \frac{1}{2} e^{-z/2} K_0(\rho/2), \tag{8}$$

$$P_{-1}(x,0,0) = -\frac{\pi}{2} Y_0(x), \tag{9}$$

but does not contain a divergent wave component and is not correct in general. Moreover, equations (8) and (9) are special cases of the following expansions[3].

$$P_{-1}(x,y,z) = \frac{1}{2} e^{-z/2} \sum_{n=0}^{\infty} (-1)^n \epsilon_n K_n(\rho/2) J_{2n}(x) \cos n\alpha, \tag{10}$$

$$P_{-1}(x,y,z) = -\frac{\pi}{2} e^{-z/2} \sum_{n=0}^{\infty} \epsilon_n I_n(\rho/2) Y_{2n}(x) \cos n\alpha, \tag{11}$$

Equation (10) is convergent and gives a correct value in the range of a moderate $x^2/(4\rho)$ value but it is not convergent numerically when the value largely increases.

On the other hand, equation (11) is not convergent but is an asymptotic one. Some authors have discussed its defect which does not give a divergent wave component.

In these circumstances, the present paper aims to revise equation (7).

Now, we evaluate equation (4) using the path of the integration in the t-plane as shown in Fig.1 where the angle ψ takes zero at negative infinity of v and tends to π at positive infinity.

However, the horizontal line $i\pi/2$ in the t-plane is singular for the integrand of the integral, so the pass cannot cross the line $i\pi/2$ which causes the error.

Hence, the absolute value of this angle ψ must be confined within $\pi/2$ in order to correct this point.

Now, if the value of v is complex in equation (4), the argument of the potential term of the integral becomes as follows refering to Fig. 2.

$$R\cosh(t + i\alpha/2 - i\psi) = Re^{i\gamma} \cosh(\tau + t + i\alpha/2 - i\psi), \tag{12}$$

where

$$R = \sqrt{r_1 r_2}, \quad e^{\tau} = \sqrt{r_1/r_2}, \tag{13}$$

$$\frac{\theta_1 + \theta_2}{2} = \gamma, \quad \frac{\theta_1 - \theta_2}{2} = \psi, \tag{14}$$

Moreover, if we choose the path of the integration as shown in Fig.3 where γ takes zero from negative infinity of v to the point B and takes $-\pi$ from B to positive infinity, the dotted line in Fig.1 becomes the solid line which has a jump at A,B,C.

Thus, we obtain the same form as equation (4), but the argument of Bessel function of the second kind in the integrand must be multiplied by $exp(-i\pi)$.

Since we have the relation [1]

$$Y_0(Re^{-i\pi}) = Y_0(R) - 2iJ_0(R), \tag{15}$$

The real part becomes the same as the integral (7) but we must add the integral on the path A,B,C in Fig.3 where Y_0 cancels out with each other but J_0 remains.

Therefore, equation (4) can be rewritten in the following form.

$$P_{-1}(x,y,z) = I_1 + I_2 \tag{16}$$

where I_1 denotes equation (7) and I_2 is the term to be added. Making use of equation (12) through (15), we obtain I_2 as follows ;

$$I_2 = Re.\left[-\frac{i}{2}\sqrt{\pi/\rho} \times e^{(\rho-z)/2}\int_A^B e^{-\frac{v^2}{4\rho}} J_0(R)dv\right], \tag{17}$$

where $\quad A = x\cos(\alpha/2) \quad , \quad B = xe^{i\alpha/2},$

or

$$I_2 = Re.\left[\frac{1}{2}\sqrt{\pi/\rho}e^{(\rho-z)/2}x\sin\frac{\alpha}{2}\int_0^1 e^{-\frac{v^2}{4\rho}} J_0(R)du\right], \tag{18}$$

where $\quad v = x\cos(\alpha/2) + iux\sin(\alpha/2) \quad , \quad R = x\sqrt{1-u^2}\sin(\alpha/2),$

Now, we examine the result equations (16) and (17) in the following manner. Firstly, when x becomes zero, then I_2 vanishes clearly, and when both y and z tends to zero, then I_2 vanishes owing to the exponential term of the integrand of (14) or (15). Therefore, the formulas (8) and (9) are correct.

Secondly, let us consider an asymptotic character of the integral. We can integrate asymptotically as follows.

$$\int_a^\infty e^{-\frac{v^2}{4\rho}}dv \longrightarrow \frac{2\rho}{a}e^{-\frac{a^2}{4\rho}}, \quad for \ \ |\frac{a^2}{4\rho}| \gg 1, \tag{19}$$

Then, we can evaluate the integral approximately for small ρ as follows.

$$I_2 \longrightarrow Re.\left[\frac{\sqrt{\pi\rho}}{4x}e^{\frac{\rho-z}{2}-\frac{x^2}{4\rho}e^{i\alpha}+\frac{i(\pi-\alpha)}{2}}\right]. \tag{20}$$

References

[1] Abramowitz, M. , and Stegun, I, A., : Handbook of Mathematical Functions Dover, New York 1964

[2] Baar, J.J.M., and Price, W.G., :"Evaluation of the wavelike disturbance in the Kelvin wave source potential" Journal of Ship Research, Vol.32,1,pp. 44-53, 1988

[3] Bessho, M. :"On the fundamental function in the theory of wave-making resistance of ships" Memoirs of the Defense Academy of Japan, Vol.4,2,pp. 99-119, 1964

[4] Newman, J. N. :"Evaluation of the wave resistance Green function near the singular axis" Third International Workshop on Water Waves and Floationg Bodies, Woods Hole, U.S.A. ,pp. 17-20, April 1988

[5] Ursell, F. :"On the theory of the Kelvin ship-wave source : asymptotic expansion of an integral" Proc. Roy. Soc. London, A 418 ,pp. 81-93, 1988

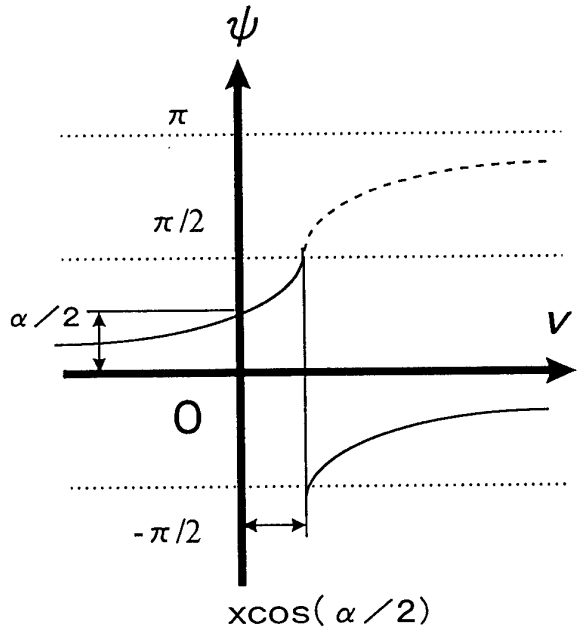

Fig. 1 The value of ψ

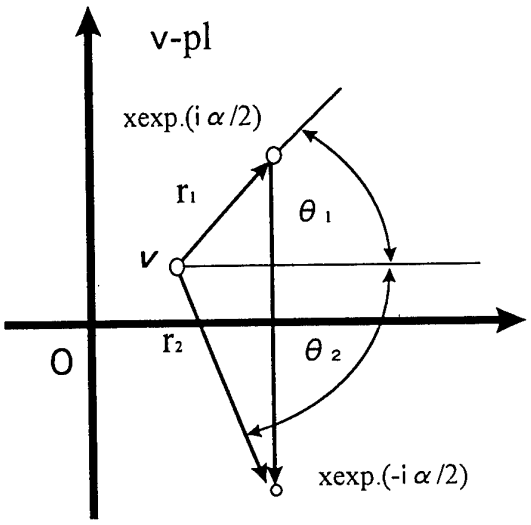

Fig. 2 Complex v-plane

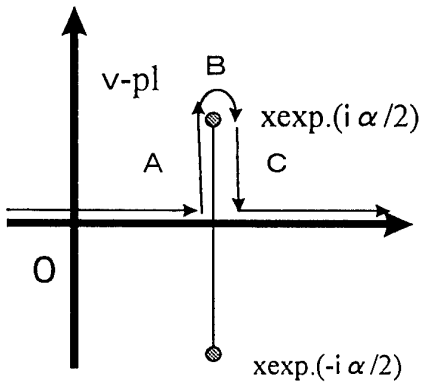

Fig. 3 Path of integration in v- plane

SOME UNEXPLORED ASPECTS

OF HYDROFOIL WAVE DRAG

J. P. Breslin

A brief recounting of the milestones in the development of hydrofoil craft from the end of the last century and ending with the vessels built by the US Navy is given. An account of the evolution of theory for invicid flow about hydrofoil sections and the extension to finite aspect ratios is followed by three applications of lifting line theory to a foil tested at in a model basin.

The wave resistance of an aspect ratio 10 hydrofoil as inferred from analysis of lift and drag measurements is compared with results of lifting-line theory for infinitely deep water, for the depth of the towing tank and for a channel of the same width and depth of the test basin. The poorest correlation is obtained for the latter condition. Suggestions for additional work on hydrofoil lift and drag are given.

SLOSHING IN TWO-DIMENSIONAL TANKS

O.M. Faltinsen
Division of Marine Hydrodynamics
Norwegian University of Science and Technology
N-7034 Trondheim, Norway

F. Solaas
MARINTEK, P.O.box 4125 Valentinlyst
7002 Trondheim, Norway

1. INTRODUCTION

Environmental concern has lead to requirements about double bottoms and skin in new tankers. Since it is desirable to save steel, this has lead to wide oil tanks that can be smooth inside. This increases the danger of occurrence of sloshing and large slamming loads inside the tanks. The most violent fluid motions occur in the vicinity of the lowest natural period for the fluid motion inside the tank. When the tank is smooth, viscous effects are not important and potential flow theory can be used. Nonlinear free surface effects are significant. However, ship motions exciting sloshing are often not large. This means that the external hydrodynamic loads can be approximated by linear theory. However, the coupling between the external linear flow and the internal nonlinear flow should be considered.

There exist commercial CFD codes based on Navier-Stokes Equations and nonlinear free surface conditions that are used to simulate sloshing. A difficulty occurs in describing simultaneously the slamming loads inside the tank. A reason is the much smaller time scale of slamming relative to the characteristic sloshing period. Hydroelasticity may also complicate the simultaneous solution of sloshing and slamming loads.

The complexity of the sloshing flow can easily lead to inaccuracies in the numerical solution. Good verification procedures is therefore of great importance. This paper describes a verification procedure of a nonlinear numerical method for sloshing.

2. THEORY

The method is based on Moiseev's (1958) perturbation method. Details are described by Solaas (1995) and Solaas and Faltinsen (1997). The forced sway or roll motion of the tank is $0(\varepsilon)$ and the fluid response is $0(\varepsilon^{1/3})$. Here ε is a small parameter and a measure of the ratio between the tank motions and the horizontal dimensions of the tank. Non-shallow water depth and two-dimensional flow are assumed. The tank oscillates with frequency ω and a steady-state solution is found. The lowest natural frequency σ_1 for the fluid motion is related to ω by

$$\omega^2 = \sigma_1^2 + \varepsilon^{2/3}\alpha \tag{1}$$

where $\alpha = 0(1)$. The total velocity potential for the fluid motion is expressed as

$$\Phi_T = \phi_1\varepsilon^{1/3} + \phi_2\varepsilon^{2/3} + \phi_3\varepsilon + \phi_c(x,y)\cos\omega t \tag{2}$$

where ϕ_c is of $0(\varepsilon)$, satisfies the body boundary condition, but not the free surface condition. Further t is the time variable. The solution of ϕ_1 can be written as $\psi_1(x,z)N\cos\omega t$, where ψ_1 is the

eigenfunction for the fluid motion corresponding to the natural frequency σ_1. N is determined by a secularity condition in the 3.order solution. ψ_1 (and ϕ_2 and ϕ_3) are determined by a low order panel method based on representing the velocity potential by Green's second identity. The second order potential ϕ_2 satisfies an inhomogeneous free surface condition which is a function of ϕ_1 and follows by the perturbation scheme. The normal derivative of ϕ_2 on the mean position of tank surface is zero. The solution can be written as

$$\phi_2 = \alpha_0 t + \sum_{n=1}^{\infty} \psi_n(x,z) d^{(n)} \frac{N^2}{2} \sin(2\omega t) \tag{3}$$

Here ψ_n are eigenfunctions for the fluid motion corresponding to eigenfrequency number n. α_0 is a constant and determined by conservation of fluid mass. It follows from this requirement that the perturbation scheme is only possible with vertical walls at the mean waterline. The third order potential ϕ_3 satisfies an inhomogeneous free surface condition which is a function of ϕ_1, ϕ_2 and ϕ_c. The normal derivative of ϕ_3 on the mean position of the tank surface is zero. The right hand side of the free surface includes a term proportional to $\psi_1 \cos\omega t$. This leads to a secularity condition that determines N as the solution of

$$a_1 N^3 + \alpha N + e_1 = 0 \tag{4}$$

This means that up to three solutions of N is possible for any frequency ω.

3. VERIFICATION

Faltinsen (1974) derived an analytical solution for a rectangular tank based on Moiseev's procedure. This was used by Solaas (1995) and Solaas and Faltinsen (1997) to compare all details of the first, second and third order solution. It was found that many elements were needed in the low order panel method. For instance with 500 elements evenly distributed on the mean free surface, the third order potential oscillating with frequency 3ω have relative error of $0(10^{-3})$ on the free surface element closest to the intersection between the near body surface and the mean free surface. This verification of the numerical method demonstrates that great care has to be shown in the numerical analysis.

4. CONCLUDING REMARKS

High numerical accuracy is needed in a numerical method describing sloshing in a tank.

A perturbation solution based on Moiseev's procedure can only be used for tanks with vertical walls at the mean waterline.

A perturbation solution based on Moiseev's procedures seems difficult to generalize to irregular sea.

Sloshing and sloshing induced slamming have very different time scales, which makes an integrated analysis difficult. A possibility may be to generalize the hydroelastic slamming theory described by Faltinsen (1997).

REFERENCES

Faltinsen, O.M., 1974, A nonlinear theory of sloshing in rectangular tank, Journal of Ship Research, Vol. 22, No. 3, September, pp. 193-202.

Faltinsen, O.M., 1997, The effect of hydroelasticity on ship slamming, Phil. Trans. R. Soc., A, 355, 1-17.

Moiseev, N:N., 1958, On the Theory of nonlinear vibrations of a liquid of finite volume, Applied Mathematics and Mechanics (PMM), Vol. 22, No. 5.

Solaas, F., 1995, Analytical and numerical studies of sloshing in tanks, Dr.Ing.thesis, Division of Marine Hydrodynamics, The Norwegian Institute of Technology, NTH, MTA-Report 1995:107.

Solaas, F., Faltinsen, O.M., 1997, Combined numerical and analytical solution for sloshing in two-dimensional tanks of general shape, Journal of Ship Research, Vol. 41, No. 2, June.

The CHAPMAN Project

Development of a New Navier-Stokes Solver with a Free Surface

Prof. Lars **Larsson**
Chalmers Univ. of Technology
Dept. of Naval Architecture and Ocean Engineering

As shown in the 1990 and 1994 Workshops on hydrodynamics CFD the CFD technique may now be used for many practical purposes in ship design. Several obstacles remain however, as explained in the 18th Weinblum memorial lecture by the present author. The accuracy needs to be improved in resistance prediction and in the computation of the details of the wake field. To accomplish this, improvements may be necessary in the following areas: grid generation, turbulence modelling, free surface boundary conditions and numerics.

CHAPMAN is a cooperative project between Chalmers and FLOWTECH International for developing a new Navier-Stokes solver with improvements in all four areas above. The method uses a structured multi-block overlapping grid generator CHALMESH, developed within the project. Thin curvilinear component grids are employed near the hull and all appendages, and these component grids are embedded into a global Cartesian grid. CHALMESH takes care of the interpolation in the overlapping regions. Singularities are avoided by introducing separate component grids around singularity lines. The propeller is represented in a cylindrical component grid, which rotates inside the hull grid and this will enable the blade flow to be computed when the propeller rotates in the behind condition.

The solver has a free surface capability based on the level set approach, which is capable of handling overturning waves and changes in topology, like when the wave breaks. The Reynolds-averaged Navier-Stokes equations are solved with an advanced turbulence model, and several alternatives for this model are now being tested for some generic test cases. A mixed explicit/implicit temporal solution scheme is under develoment where the implicit technique is used only in the normal direction in the thin curvilinear grids.In this way the small time steps required in the explicit technique due to the very thin cells close to the hull surface are avoided. To minimize numerical dissipation central differencing is used for all terms and the minimum amount of artificial dissipation needed to stabilise the solution for the given grid spacing is computed from a theory for the smallest scales by Henshaw and Kreiss. Alternatively, the theory may be used for finding the required grid spacing for stability without artificial dissipation.

50 YEARS OF YOKOHAMA NATIONAL UNIVERSITY SHIP HYDRODYNAMICS LABORATORY

BY
HAJIME MARUO
YOKOHAMA NATIONAL UNIVERSITY

Foreword

In the occasion of the 100th anniversary of the late Professor Georg Weinblum, 50 years of the research activities at Ship Hydrodynamics Laboratory of Yokohama National University, of which I have been in charge since 1947 until my retirement in 1988, is reviewed briefly.

This topic has much relevance to the memory of Prof.Weinblum, because most of the projects carried out in this laboratory have been motivated or stimmulated more or less by his work, especially at their earlier stage. I studied one of his earliest paper published in 1930 on ZAMM[1] in 1944,when I was a student of University of Tokyo, and I was much impressed by his work. This experience had become obviously the motivation of my first work on the study of planing hulls. Another example of his influence is through the work on the hull form of minimum wave resistance which was seemingly the subject of Weinblum's main interest.

The first time when I met Prof.Weinblum was in 1963 in the occsion of International Seminar on Theoretical Wave Resistance at Ann Arbor Michigan. My great surprise at that moment was that he had already known my earlier work. I still remember his encouragement through the work on the wave resistance of slender ships, which I was engaged in at the moment. Since that time, I was able to keep contact with him through the technical committee of ITTC until his death. Therefore the influence from him may appear throughout the period.

The Ship Hydrodynamics Laboratory

Ship Hydrodynamics Laboratory of Yokohama National University belongs to the Department of Naval Architecture and Ocean Engineering, which was founded in 1930 as a part of Yokohama College of Engineering founded in 1920. The College was shifted to Yokohama National University in 1949 by the reformation of the educational system. The university moved to a new campus in1976. Main research facilities of the department is as follows.

Towing Tank:

Old Campus (1933 - 1976) $L \times B \times D = 50.4m \times 3.6m \times 2.75m$

New Campus (1976 - - -) $L \times B \times D = 110m \times 8.0m \times 3.5m$

Other Facilities:

Circulating Water Channel

Wind Tunnel

On my retirement from Yokohama National University in 1988, Prof. Mitsuhisa Ikehata has succeeded to the position in charge of the laboratory.

Outline of Research Projects

Subjects of the research projects carried out at the Ship Hydrodynamics Laboratory since 1947 are listed below in time sequence. Numbers in parentheses indicate the year when the first paper on the subject in each project was published, and the superscript gives the corresponding literature.

Hydrodynamics of Planing Hulls:

Two Dimensional Problem

Theory of Resistance Components, Spray and Wave (1947)[2]

Pressure Distribution , Analytical Solution (1951)[3]

Three Dimensional Problem

Resistance Components (1949)[4)]

High Aspect Ratio Approximation (1953)[5)]

Low Aspect Ratio Approximation (1962)[6)]

Nonlinear Phenomena in Shallow Water:

Aerodynamic Analogy (1952)[7)]

Sinkage and Change of Trim (1981)[8)]

Detection of the Boundary Layer Transition:

Hot Wire Anemometry in the Towing tank (1953)[9)]

Flow Visualization in the Towing Tank (1954)[10)]

Motion of Bodies under Free Surface:

Hydrofoil of Finite Span (1953)[11)]

Non-uniform Motion of a Submerged Body (1955)[12)]

Wave Force on an Obstacle:

Submerged Cylinder (1954)[13)]

Vertical Cylinder (1956)[14)]

Drift Force of a Floating Body (1960)[15)]

Added Resistance in Waves:

Regular Waves (1957)[16)]

Irregular Waves (1960)[17)]

Theory of Slender Ships:

Wave Resistance in Steady Forward Motion (1962)[18)]

Seakeeping Problems (1966)[19)]

Hull Pressure Distribution in Waves (1974)[20)]

Ship Wave Pattern (1983)[21)]

Hull Form Research:

Minimum Wave Resistance Hull Forms (1963)[22)]

Semi-submerged Hull of Minimum Wave Resistance (1964)[23)]

Application of the Theory to Hull Form Design (1966)[24)]

Mathematically Wave Free Form (1969)[25)]

Application of the Nonlinear Optimization Technique (1979)[26)]

Experimental Separation of Resistance Components:

Implementation of the Wave Pattern Analysis in theTank Test Practice (1967)[27)]

Decomposition of Resistance by the Wake Survey (1976)[28)]

Ship Waves and Wave resistance in Viscous Fluid:

Effect of the Wake on Waves (1972)[29]

Ship Waves and Wave Resistance of a Thin Ship in Viscous Fluid (1973)[30]

Full Hull Forms at Low Froude Numbers:

Double Body Linearization (1977)[31]

Bow Flow Phenomena (1983)[32]

Effect of Surface Tension to the Model Bow Flow (1985)[33]

Waves and Wave Resistance with Nonlinear Free Surface Condition (1985)[34]

Marine Propellers:

Propeller Characteristics in Turbulent Wake (1981)[35]

Unsteady Propellers in Non-uniform Wake (1984)[36]

Turbulent Flow in Ship's Wake:

Turbulence Measurement in the Ship Model Wake (1982)[37]

Modelling of Turbulent Boundary Layer and Wake (1985)[38]

Two Dimensional Computation of Nonlinear Free Surface:

Application to Slender Ships at Forward Speed (1994)[39]

Water Entry and Hydrodynamic Impact, Experimental Validation (1996)[40]

Concluding Remarks

Half a century has passed since the Hydrodynamic Laboratory of Yokohama National University started. One may observe its research activities to have covered various field of ship hydrodynamics. On arranging research projects, it has been intended to keep an even share between theory and experiment. This criterion seems to have been nearly attained. Another idea is that the practical usefulness, especially in the field of shipbuilding, of theoretical findings has been taken seriously. This concept may match the spirit of Prof. Weinblum.

References

1) G.Weinblum: Wellenbildener Widerstand von Schiffen, ZAMM 10 (1930)
2) H.Maruo: A contributionto the theory of the gliding plate on the surface of water, Journal of the Society of Naval Architects of Japan (JSNA) 78 (1947)*
3) H.Maruo: On the solution of the integral equation in the two dimensional theory of the gliding plate, Bull. Faculty of Eng. Yokohama National University (BEYNU) 1 (1951)*
4) H.Maruo: On the theory of wave resistance of a body gliding on the surface of water, JSNA 81 (1949)*
5) H.Maruo: Theory of the hydroplane with broad and short planing surface, BEYNU 2 (1953)
6) H.Maruo: The lift of low aspect ratio planing surfaces, 9th Japan National Conference for Theoretical and Applied Mechanics (NCTAM) 1962
7) H.Maruo: On the shallow water effect, JSNA 84 (1952)*
8) H.Maruo, T.Tachibana: An investigation into the sinkage of a ship at the transcritical speed, JSNA 150 (1981)
9) H.Maruo: Application of the hot wire measurement to water current, BEYNU 2 (1953)
10) H.Maruo: Document for the contribution to 7th ITTC (1954)

11) H.Maruo: The effect of the surface of water on a submerged wing, JSNA 86(1953)*
12) H.Maruo: Fundamental formula for wave motion caused by moving bodies, JSNA 87 (1955)
13) H.Maruo: Force of water waves on an obstacle, JSNA 95 (1954)
14) H.Maruo: The force of water waves upon a fixed obstacle, BEYNU 5 (1956)
15) H.Maruo: The drift of a body floating on waves, Journ.Ship Res. 4-3 (1960)
16) H.Maruo: The excess rsistance of a ship in rough seas, Internat. Shipbuild. Progr. 4-35 (1957)
17) H.Maruo: On the increase of the resistance of a ship in rough seas II, JSNA 108 (1960)*
18) H.Maruo: Calculation of the wave resistance, the draught of which is as small as the beam, JSNA 112 (1962)
19) H.Maruo: An application of the slender body theory to the ship motion in head seas, JSNA 120 (1966)*
20) H.Maruo, N.Sasaki: On the wave pressure acting on the surface of an elongated body, JSNA 136 (1974)*
21) H.Maruo, M.Ikehata, Y.Takizawa, T.Masuya: Computation of ship wave pattern by the slender body approximation, JSNA 154 (1983)*
22) H.Maruo, M.Bessho: Ships of minimum wave resistance, JSNA 114 (1963)*
23) H.Maruo, M.Ishii: Semi-submerged ship with minimum wave-making resistance, JSNA 116 (1964)*
24) H.Maruo: How to apply the wave resistance theory to the hull form design, Bulletin of the Soc. of Naval Arch. of Japan 438, 439 (1966)*
25) H.Maruo: Theory and application of semi-submerged ships of minimum wave resistance, Japan Shipbuilding & marine Engineering 4 (1969)
26) M.Higuchi, H.Maruo, K.Suzuki, O.Kanagawa: Fundamental studies on hull form design by means of non-linear programming, JSNA 145 (1979)*
27) M.Ikehata, K.Nozawa: Determination of wave-making resistance of a ship by the method of wave analysis, JSNA 121 (1967)*
28) H.Maruo: Separation of resistance components, Internat. Seminar on Ship Technology, Seoul (1976)
29) H.Maruo, K.Hayasaki: On the transfiguration of water waves propagating into a uniform wake, JSNA 132 (1972)*
30) H.Maruo, J.Matsumura: Ship waves and wave resistance in a viscous fluid, JSNA 134 (1973)*
31) H.Maruo, K.Suzuki: Wave resistance of a ship of finite beam predicted by the low speed theory JSNA 142 (1977)
32) H.Maruo: On the breaking of waves at the bow, Symposium on New Developments of Naval Architecture and Ocean Engineering, Shanghai (1983)
33) H.Maruo, M.Ikehata: On the free surface flow around a model bow, JSNA 158 (1985)*
34) H.Maruo, S.Ogiwara: A numerical method of non-linear solution for steady waves around ships JSNA 157 (1985)*
35) M.Ikehata, H.Maruo, M.Ando, M.Ito: The effects of non-uniformity and turbulence of flow on hydrodynamic characteristics of propeller, JSNA 150 (1981)*
36) M.Ikehata, M.Ando, H.Maruo: Theoretical analysis of unsteady characteristics of marine propeller in ship's wake, JSNA 156 (1984)*
37) H.Maruo: Measurements of near-field turbulent flow field in the towing tank, 4th Symposium on turbulent flow, Tokyo (1982)*
38) M.Ikehata, H.Maruo: Investigation into turbulence model for stern flow around the bow, Osaka Colloquium on ship viscous flow, Osaka (1985)
39) H.Maruo, W.S.Song: Nonlinear analysis of bow wave breaking and deck wetness of a high speed ship by the parabolic approximation, 20th Symp. on Naval Hydro. Santa Barbara (1994)
40) W.S.Song, H.Maruo: Numerical simulation of nonlinear water waves due to wedge entry, 2nd International. Conference on Hydrodynamics, Hong Kong (1996)
* Written in Japanese

"There is no theorem like the Lagally theorem." "The Ellipsoid is God's gift to naval architects."

T. Miloh
School of Engineering, Tel-Aviv University, 699 78 Ramat-Aviv, ISRAEL

Georg P. Weinblum (1897-1974) was born about the same time when John H. Michell (1863-1940) had already completed writing his seminal work on the wave resistance of thin ships (Michell 1898) - some hundred years ago. Thus, it was not a coincidence that G.P.W. chose to write his doctoral dissertation (submitted in 1929) on ships of minimum wave resistance using Michell's theory. It is also well known that Michell's famous article did not get the proper attention (at least from the naval architects community) for over 25 years, although it was published in one of the most prestigious journals (Philosophical Magazine). Indeed it was Sir Thomas Havelock, probably the leading theoretician working on ship hydrodynamics at the beginning of the century, who rediscovered Michell's paper 25 years after it had appeared (Havelock 1923). The first reference to Michell's work in Havelock's paper appeared only as a side comment "On the other hand, Michell, in an extremely interesting paper, gave a general expression for wave resistance, but it suffers from serious limitations, in that the surface of the ship must be everywhere inclined at only small angle to its vertical meridian plane". A more well deserved credit to Michell's theory was given in a paper by Wigley (1926). It is believed that by that time Weinblum became acquainted with Michell's work and since then he became a strong advocate and promoter for using the Michell's wave resistance formula. Weinblum also tried to bridge the gap between theoreticians and naval architects practitioners and provided in his papers sample computations and comparisons between theory and experiments. As an example, we mention his joint paper with Graff & Kracht on the wave resistance of a conventional merchant-ship hull which includes a comparison of drag measurments with numerical evaluations of the Michell integral (Graff et al. 1964). In his continuous efforts to exploit relevant theories to find how they can help ship designers, he has introduced, during the four year period (1948-1952) that he spent at the DTMB, the important paper of Lagally (1923) to the U.S. community of ship hydrodynamicists. In this context we cite a paragraph from Landweber's paper (1967) who wrote "About 20 years ago Georg Weinblum succeeded in convincing his incredulous colleagues at the David Taylor Model Basin that THERE IS NO THEOREM LIKE THE LAGALLY THEOREM ... and pointed out the power of the LAGALLY theorem and new fields of research to many of us". Yet another off-repeated statement of Weinblum is "THE ELLIPSOID IS GOD'S GIFT TO NAVAL ARCHITECTS" (Newman 1972). Weinblum suggested to use the concept of equivalent ellipsoids for approximating real ship forms (Weinblum 1936). He was definitely inspired by the theoretical work of Havelock and was probably the first worker in ship theory to study and apply the hydrodynamics of spheroids and ellipsoids to more general bodies of revolution. The same citation regarding ellipsoidal forms, which is attributed to Weinblum, is also mentioned in Wu & Chwang (1974) and Miloh (1979). Stimulated by these two Weinblum quotations, we intend to present here an historical account of some theoretical methods for calculating potential flows about 3-D ellipsoidal shapes. Also presented is the development of the Lagally method for calculating hydrodynamic loads on 3-D arbitrary rigid and defformable moving bodies.

Ellipsoid Theorem

In order to determine the hydrodynamical loads on a moving body by using the Lagally theorem, it is necessary first to find the image singularity system within the body of the exterior potential flow field. For a general body this procedure usually involves solving numerically an integral equation of a Fredholm type. However, for the class of symmetric separable quadratic surfaces (i.e. spheres, spheroids and ellipsoids), the image singularity system can be found analytically using harmonic analysis. The idea is to analytically continue the exterior flow across the surface inside the body and to find the interior ultimate (minimal) singularity system.
Let us first consider a spherical coordinate system (R, μ, ψ) defined by

$$x = R\mu, \quad y + iz = R(1-\mu^2)^{\frac{1}{2}} e^{i\psi}, \tag{1}$$

where (x, y, z) is a cartesian system. An arbitrary exterior potential flow field about a sphere which vanishes at infinity $R \to \infty$, can be represented by a Neumann series of exterior spherical harmonics. Following Hobson (1955) a typical term of such a series can be written as

$$R^{-(m+1)} P_n^m(\mu) e^{i\psi} = \frac{(-1)^n}{(n-m)!} \left(\frac{\partial}{\partial x}\right)^{n-m} \left(\frac{\partial}{\partial y} + i\frac{\partial}{\partial z}\right) (x^2+y^2+z^2)^{-\frac{1}{2}}, \tag{2}$$

where $P_n^m(\mu)$ denotes the Legendre polynomial. Thus, the ultimate system of singularities for exterior spherical harmonics consists of a system of multipoles at the origin. A similar theorem for spheroidal exterior harmonics has

been given without proof by Havelock (1952). A proof was provided later on by Miloh (1974). The orthogonal transformation between a cartesian and a spheroidal coordinate system (ξ, μ, ψ) is

$$x = \xi\mu, \quad y + iz = (\xi^2 - 1)^{\frac{1}{2}}(1 - \mu^2)^{\frac{1}{2}} e^{i\psi}, \tag{3}$$

where the distance between the two foci is taken to be 2. Havelock theorem can then be written as

$$Q_n^m(\xi) P_n^m(\mu) e^{im\phi} = \frac{1}{2}\left(\frac{\partial}{\partial y} + i\frac{\partial}{\partial z}\right)^m \int_{-1}^{1} \frac{(\xi^2 - 1)^{\frac{m}{2}} P_n^m(\xi)\ d\xi}{\sqrt{(x - \xi)^2 + y^2 + z^2}}, \tag{4}$$

where Q_n^m represents the Legendre polynomial of the second kind. Thus, the ultimate image singularity system for an exterior spheroidal harmonic can be represented as a multipole distribution along the axis between the two foci. The axisymmetric case which corresponds to $m = 0$, renders a source distribution $P_n(x)$ on $1 > |x|$. The most general separable quadratic surface is the triaxial ellipsoid.

$$\frac{x^2}{a^2} + \frac{y^2}{b^2} + \frac{z^2}{c^2} = 1; \quad a > b > c. \tag{5}$$

The orthogonal transformation between the cartesian (x, y, z) and the ellipsoidal coordinate system (ρ, μ, ν) is given by

$$x = \frac{\rho\mu\nu}{hk}, \quad y^2 = \frac{(\rho^2 - h^2)(\mu^2 - h^2)(h^2 - \nu^2)}{h^2(k^2 - h^2)}, \quad z^2 = \frac{(\rho^2 - k^2)(k^2 - \mu^2)(k^2 - \nu^2)}{k^2(k^2 - h^2)}, \tag{6}$$

where $h^2 = a^2 - b^2$, $k^2 = a^2 - c^2$ and $-h < \nu < h < \mu < k < \rho < \infty$. An arbitrary potential flow field past an ellipsoid can be represented in terms of ellipsoidal exterior harmonics $F_n^m(\rho)E_n^m(\mu)E_n^m(\nu)$ where E_n^m and F_n^m denote the Lame polynomials of the first and second kind respectively. There exist four different types of Lame polynomials of the first kind; class K and L (both even in z) and class M and N (both odd in z). The ellipsoidal theorem (Miloh 1974) then states that exterior ellipsoidal harmonics of class K and L may be generated by a source distribution $\sigma(x, y)$ such that

$$F_n^m(\rho)E_n^m(\mu)E_n^m(\nu) = -\int_{S_0} \frac{\sigma(x', y')\ dx'\ dy'}{\sqrt{(x - x')^2 + (y - y')^2 + z^2}}, \tag{7}$$

where (x', y') are the rectangular points in the (x, y) plane within the focal ellipse (the ultimate image system)

$$S_0 \equiv \frac{x^2}{a^2 - c^2} + \frac{y^2}{b^2 - c^2} = 1, \quad z = 0. \tag{8}$$

and $\sigma(x', y')$ is given by

$$\sigma(x', y') = -\frac{(2n + 1)E_n^m(\mu')E_n^m(\nu')}{2\pi k E_n^m(k)\sqrt{(k^2 - h^2)}}\left(1 - \frac{x^2}{k^2} - \frac{y^2}{k^2 - h^2}\right)^{-\frac{1}{2}}. \tag{9}$$

In a similar manner, one can express an exterior ellipsoidal harmonic of class M or N as a normal doublet distribution

$$F_n^m(\rho)E_n^m(\mu)E_n^m(\nu) = \frac{\partial}{\partial z}\int_{S_0} \frac{\delta(x', y')\ dx'\ dy'}{\sqrt{(x - x')^2 + (y - y')^2 + z^2}}, \tag{10}$$

where

$$\delta(x', y') = \frac{(2n + 1)E_n^m(\mu')E_n^m(\nu')}{2\pi k \bar{E}_n^m(k)\sqrt{(k^2 - h^2)}}, \quad \bar{E}_n^m(k) = \frac{E_n^m(k)}{\sqrt{\rho^2 - k^2}}. \tag{11}$$

Finally, solving general potential flow problems past ellipsoidal bodies requires the expansion of the Green function $\frac{1}{r_{PQ}}$ (i.e. the inverse of the distance between two points $P(\rho, \mu, \nu)$ and $Q(\rho', \mu', \nu')$ where $\rho' > \rho$) in terms of ellipsoidal harmonics. Such an expansion has been given in Miloh (1973)

$$\frac{1}{r_{PQ}} = \sum_{n=0}^{\infty}\sum_{m=1}^{s(n)} \frac{2\pi}{(2n + 1)\gamma_n^m} F_n^m(\rho')E_n^m(\mu')E_n^m(\nu')E_n^m(\rho)E_n^m(\mu)E_n^m(\nu), \tag{12}$$

where

$$\gamma_n^m = \int_{-h}^{h}\int_{h}^{k} \frac{(\mu^2 - \nu^2)(E_n^m(\mu)E_n^m(\nu))^2\ d\mu\ d\nu}{\sqrt{(\mu^2 - h^2)(\mu^2 - k^2)(\nu^2 - h^2)(\nu^2 - k^2)}} \tag{13}$$

and $s(n)$ is defined below for the four classes of Lame polynomials;

$$\begin{array}{cccccc} & K & L & M & N & * \\ s(n) = & 1 + \frac{n}{2} & \frac{n}{2} & \frac{n}{2} & \frac{n}{2} & \text{for } n \text{ even} \\ & \frac{1}{2}(n + 1) & \frac{1}{2}(n + 1) & \frac{1}{2}(n + 1) & \frac{1}{2}(n - 1) & \text{for } n \text{ odd} \end{array} \tag{14}$$

Lagally Theorem

Once the image singularity system of the exterior flow field past the body is known, one can directly compute the hydrodynamical loads experienced by the body in terms of these singularities. The so-called Lagally theorem is valid for both $2-D$ and $3-D$ deformable or rigid surfaces and for a line, surface, volume or discrete singularity distribution. Using this technique avoides the computation of the pressure distribution and its integration over the body surface. In many respects it is more direct and accurate than the method of pressure integration and may be also considered as an extension of the $2-D$ Blasius method for $3-D$ flows. Lagally (1922) gave only an expression for the force acting on a source of output m and on a doublet $\mathbf{d}$ both placed in a potential steady stream $\mathbf{v}$. The corresponding Lagally force is $-4\pi\rho[m\mathbf{v}+(\mathbf{d}\cdot\nabla)\mathbf{v}]$ where ρ is the density of the fluid. It is also interesting to note that the particular expression for a point source has been derived earlier by Munk (1921). The so-called steady Lagally method has been revised by Betz (1932) who also provided a simpler derivation. Extensions for unsteady flows and multipoles have been first proposed by Cummins (1953, 1957). Further work on the subject of rigid body hydrodynamics is due to Landweber & Yih (1956) and Landweber (1967). The case of deformable bodies and the appropriate generalization of the Lagally theorem have been discussed and presented by Landweber & Miloh (1980). More recent applications for the case of a moving deformable body embedded in a non-uniform ambient flow field are given in Galper & Miloh (1994, 1995). Let the equation of the deformable surface in a body-fixed coordinate system be given by $S(\mathbf{r},t)$. Then the deformable potential is found from the following Neumann boundary condition on S

$$\frac{\partial\phi_d}{\partial n}=-\frac{\partial S}{\partial t}\frac{1}{|\nabla S|}. \tag{15}$$

Assume next that the image singularity system consists of multipoles m_q of order $q=\alpha+\beta+\gamma$ located at (x_s,y_s,z_s) where the internal flow field is given by

$$\phi=-m_qD_q(\frac{1}{R}),\quad D_q=\frac{\partial^q}{\partial x_s^\alpha\partial y_s^\beta\partial z_s^\gamma}\quad ,R^2=(x-x_s)^2+(y-y_s)^2+(z-z_s)^2. \tag{16}$$

The Lagally force acting on the deformable body is then given by

$$\frac{\mathbf{F}}{\rho}=\frac{d}{dt}\left(v(t)\mathbf{V}_c-4\pi\sum_s^{(d)}m_qD_q(\mathbf{r})_s+\mathbf{K}_d\right)-4\pi\sum_s m_qD_q(\nabla\phi)_s, \tag{17}$$

where $v(t)$ is the volume of the body, $\mathbf{V}_c$ is the instantaneous velocity of its centroid and $\mathbf{K}_d$ is the deformation Kelvin impulse defined by

$$\mathbf{K}_d=-\int_S\phi_d\,\mathbf{n}\,dS. \tag{18}$$

Also $\sum_s$ denotes the sum of all singularities and $\sum_s^{(d)}$ excludes those due to ϕ_d. The above formulation can be applied to the problem of self-propulsion of a deformable body which was first discussed in Benjamin & Ellis (1966, 1990), Saffman (1967), Wu (1976) and Miloh (1983). It has been demonstrated in these papers that a deformable body can propel itself persistently starting from rest in an inviscid and incompressible fluid by applying a periodic surface deformation with zero-mean. The collinear velocity of self-propulsion U_s can be expressed in terms of the deformation Kelvin-impulse K_d, the body mass M_b and its added-mass T as

$$(M_b+T)U_s+K_d=0. \tag{19}$$

It is shown that the persistent self-propulsion motion arises from a non-linear interaction between symmetric and skew-symmetric surface deformation modes. Extension for the case of a maneuvering body (i.e. including auto-rotation) and self-propulsion in an ambient non-uniform stream, are given in Miloh & Galper (1993) and Galper & Miloh (1995). It is demonstrated that the presence of a flow non-uniformity may considerably amplify the order of magnitude of the self-propulsion velocity, as a result of parametric resonant interactions between surface deformations and flow non-uniformity. Applications to bubble dynamics including the problem of bubble coalesce in a cloud are discussed within the same framework in Galper & Miloh (1994, 1995). The same methodology can be also used for estimating the hydrodynamical loads on slender ocean structures in a non-uniform wave field (Galper & Miloh (1996, 1997)).

References

1. Benjamin T.B. & Ellis A.T.,Phil. Trans. Vol.260, (1966) p.221
2. Benjamin T.B & Ellis A.T., J. Fluid Mech. Vol.212, (1990) p.65
3. Betz A.,Ing. Arch. Vol.3, (1932)
4. Cummins W.E., DTMB Rep.708 (1953)
5. Cummins W.E., J. Ship Res. Vol.1, (1957) p.7
6. Galper A.R. & Miloh T., Proc. Roy. Soc. Lon. Vol. A446, (1994) p.169
7. Galper A.R. & Miloh T., J. Fluid Mech. Vol. 295, (1995) p. 91
8. Galper A.R & Miloh T. App. Ocean Res. Vol. 18, (1996) p.29
9. Galper A.R. & Miloh T., JOMAE Vol.119, (1997) p.42
10. Graff W.,Kracht A. & Weinblum G.P., Trans. Soc. Naval Arch. & Marine Eng. Vol.72 (1964) p.374
11. Havelock T.H., Proc. Roy. Soc. A. Vol.103, (1923) p.199
12. Havelock T.H., Proc. Roy. Soc. A. Vol.131, (1931) p.275
13. Havelock T.H., QJMAM Vol.5, (1952) p.129
14. Hobson E.W., "The theory of spherical and ellipsoidal harmonics" Chelsea (1955)
15. Lagally M., ZAMM. Vol.2, (1922) p.409
16. Landweber L., Schiffstechnik Vol.14, (1967) p.19
17. Landweber L. & Miloh T., J. Fluid Mech. Vol. 96 (1980) p.33
18. Landweber L. & Yih C.S., J. Fluid. Mech. Vol.1. (1956) p.319
19. Michell J.H., Phil. Mag. Vol.45. (1898) p.106
20. Miloh T. & Galper A.R. Proc. Roy. Soc. Lon. Vol. A442 (1993) p.273
21. Miloh T., Israel. J. Tech. Vol.11 (1973) p.63
22. Miloh T., SIAM J. App. Math. Vol.26 (1974) p.334
23. Miloh T., J. Ship Res. Vol.23 (1979) p.66
24. Miloh T., J. Ship Res. Vol.27 (1983) p.145
25. Munk. M., NACA Rep.114 (1921)
26. Newman J.N., J. Ship Res. Vol.14 (1972) p.41
27. Saffman P.G., J. Fluid. Mech. Vol 1. (1956) p.249
28. Weinblum G.P., Ing. Arch. Vol.7 (1936) p.104
29. Weinblum G.P., DTMB Rep.886 (1955)
30. Wigley W.C.S., Trans. Inst. Naval Arch. Vol.68 (1926) p. 124
31. Wu T.Y., Schiffstechnik Vol.23 (1976) p.229
32. Wu T.Y & Chwang A.T., Proc. 10th ONR Sym. Naval Hydrodynamics (1974)

(Special Weinblum Meeting, Carry-le-Rouet, 26-27 March 1997)

Resonant Diffraction Problems

By J. N. Newman

Department of Ocean Engineering, MIT, Cambridge, MA 02139, U.S.A.

Resonant motions of floating bodies are particularly important when the damping is small. Familiar examples include rolling of ships, and the heave response of slender spar buoys. In cases such as these the resonant motion is associated solely with the body dynamics, that is to say with the force or moment coefficients of the radiation problem where the body is oscillating in otherwise calm water. The resonant frequency is determined from the condition that the inertial force due to the body mass and hydrodynamic added mass is equal and opposite to the hydrostatic restoring force; the amplitude at resonance is inversely proportional to the damping.

Resonant motions of the free surface can occur independently of the body motions for certain special types of diffraction problems. Well known examples include moon pools, and wave-power devices with oscillating water columns, where an enclosed internal region of the fluid exists with a free surface, coupled to the exterior domain via a submerged opening. The lowest resonant frequency is associated with the Helmholtz mode, where the motion of the internal fluid is similar to a heaving rigid body with the same mass and waterplane area.

The case of a moon pool is particularly important for certain types of offshore platforms. Computations are presented to illustrate the amplitude of free-surface elevation at the center of the moon pool, for a generic family of axisymmetric cylinders. The Helmholtz resonance is a prominent feature in the diffraction solution, with increasing peak amplitude and decreasing bandwidth as the moon pool radius is reduced. In the case where the body is free to heave in the presence of incident waves, we find from careful computations that there is no amplification of the moon pool response at the original resonant frequency of the diffraction problem, apparently because the free motions of the body adapt to and cancel out any large forcing pressure at the bottom of the moon pool. Instead, the moon pool resonance occurs at a slightly higher frequency and wavenumber. This is due to the occurrence of a second heave resonant frequency, which in turn is caused by the rapid variation of the heave added mass with respect to frequency.

Complete enclosure of the internal free surface is not necessary. Resonant motions, including the Helmholtz mode, can occur when there is an opening between the interior and exterior fluid regions, as in the case of a harbor with a small entrance (Mei, 1977). Another interesting example is where two vessels are close together in a catamaran configuration or, equivalently, a single vessel is close to a parallel wall (quay). In the long narrow interior domain resonant standing waves can occur with large amplitude, provided the frequency is such that the nodes of the standing wave coincide with the openings to the exterior domain at the ends of the two vessels. Numerical results to illustrate this phenomenon were presented by Newman and Sclavounos (1988).

At the last Workshop Maniar & Newman (1996) showed that resonant motions can occur in the gaps between adjacent circular cylinders in a long periodic array, although there is no clear distinction between the interior and exterior domains of the free surface. More extensive results and analysis are described by Maniar & Newman (1997). These resonant modes are associated with trapped waves which exist for diffraction past a single cylinder in a channel, but the connection with that problem is essentially mathematical and cannot be explained on a simple physical basis. This phenomenon is important even for small numbers of cylinders, as in the case of a tension-leg platform, but it is remarkably large for longer arrays with peak wave loads acting on individual cylinders which are more-or-less proportional to the total number of cylinders in the array.

Both 'Neumann' and 'Dirichlet' trapped modes exist in correspondence with the boundary conditions imposed on the walls in the channel problem. The results for long arrays of cylinders also display secondary peaks and intermediate minima, just below these critical frequencies. In recent work Maniar has shown that the secondary features can be explained in terms of superposing end-to-end the diffraction fields of smaller arrays with one-half, one-third, one-quarter, etc. of the total number of cylinders.

Porter and Evans (1997) have shown that analogous resonant modes can occur in the case of a circular array, especially when the gaps between adjacent cylinders are small. At first glance one might suppose that this phenomenon is more analogous to the case of a harbor with a small entrance, where the resonance is associated with the interior fluid domain and free surface. However the correspondence of their modes and wavenumbers with those found for the linear array suggests that the resonance is due to the gaps between the cylinders and not to the interior domain. Indeed, their findings help to explain why this phenomenon is relevant to tension-leg platforms.

References

Maniar, H. D. & Newman, J. N., 1996 'Wave diffraction by a long array of circular cylinders,' 11th International Workshop on Water Waves and Floating Bodies, Hamburg.

Maniar, H. D. & Newman, J. N., 1997 'Wave diffraction by a long array of cylinders,' Journal of Fluid Mechanics, **339**, 309-329.

Mei, C. C. 1977 *The Applied Dynamics of Ocean Surface Waves*, Wiley (also World Scientific Publishing, 1989).

Newman, J. N., & Sclavounos, P. D. 1988 'The computation of wave loads on large offshore structures,' Conference on the Behaviour of Offshore Structures (BOSS '88), Trondheim.

Porter, R. & Evans, D. V. 1997 'Recent reults on trapped modes and their influence on finite arrays of vertical cylinders in waves,' 12th International Workshop on Water Waves and Floating Bodies, Carry-le-Rouet.

ON SHIP WAVES AT TRANSCRITICAL SPEEDS

Som D. Sharma
Institute of Ship Technology
Mercator University, D-47048 Duisburg, Germany

Summary

In a historical review extending back to the memorable International Symposium on Ship Theory held at Hamburg in 1962 to celebrate Georg Weinblum's 65th birthday it was shown how efficiently modern shallow-water ship-wave theory, developed largely by several Weinblum Memorial Lecturers attending this present meeting, has succeeded in explaining various exciting transcritical flow phenomena, originaly observed at full scale more than a century ago and repeatedly verified in ship model tanks. These include the dramatic rise and fall of wave resistance, reversal of squat, metamorphosis of wave pattern, and generation of forward solitons, all occurring as ship speed rises through its critical value in shallow water, particularly in a narrow channel. Systematic model experiments initiated by Weinblum at the Shallow Water Towing Tank in Duisburg (VBD) more than 35 years ago have proved invaluable for validating recent theoretical computations. New wave pattern, side force and yaw moment measurements have corroborated the calculations in more detail. Further development of the theory by this Speaker's group at Duisburg has culminated in the discovery of "superconductive" channels and catamarans, characterized by zero wave resistance at a chosen supercritical design speed. This is achieved, in principle, by mutual cancelation of bow and stern waves, a bit akin to the classical Busemann's biplane proposed for hypersonic flight some 60 years ago. The superconductive catamaran, rendered independent of channel sidewalls by use of suitably cambered hulls, would, besides saving propulsive power by virtue of its vanishing wave resistance, have the additional environmental benefit of being a "no-wash" vehicle. Ongoing research is concerned with the conception of a cambered air-cushion catamaran, ideally eliminating the local wave also.

References (in chronological order)

CHEN, X.-N.; SHARMA, S. D. (1992 = 1995): A slender ship moving at a near-critical speed in a shallow channel, J. of Fluid Mech., vol. 291, pp. 263-285.
CHEN, X.-N.; SHARMA, S. D. (1994): Nonlinear theory of asymmetric motion of a slender ship in a shallow channel, Proc. 20th Symp. on Naval Hydrodynamics, Santa Barbara/CA, USA, pp. 386-407.
JIANG, T.; CHEN, X.-N.; SHARMA, S. D. (1994): Numerical and experimental study of lateral force and yaw moment on a slender ship moving at high speed in shallow water, Proc. MCMC '94, Southampton, UK, pp. 361-374.
CHEN, X.-N.; SHARMA, S. D. (1994): A slender ship moves in a shallow channel, Proc. ICHD '94, Wuxi, China, pp. 158-165.
JIANG, T.; SHARMA, S. D.; CHEN, X.-N. (1995): On the wavemaking, resistance and squat of a catamaran moving at high speed in a shallow water channel, Proc. FAST 1995, Travemünde, Germany, pp. 1313-1325.
CHEN, X.-N.; SHARMA, S. D. (1995 = 97): Zero wave resistance for ships moving in shallow channels at supercritical speeds, J. of Fluid Mech., vol. 335, pp. 305-321.
CHEN, X.-N.; SHARMA, S. D. (1996): On ships at supercritical speeds, Proc. 21st Symp. on Naval Hydrodynamics, Trondheim, Norway.
CHEN, X.-N.: Elimination of wave resistance by a cambered twin-hull at supercritical speed, Ship Technology Research (Schiffstechnik), Band 44, Heft 1, Feb. 1997, pp. 13-21.
SHARMA, S. D.; CHEN, X.-N. (1997): Novel cambered-hull catamaran for high speed in shallow water, Proc. FAST '97, Sydney, Australia, pp. 125-132.

MULTIHULLS

E. TUCK

University of Adelaide, Applied Math. Dept.

A discussion of various problems involving one or more bodies at or near a free surface is given. The general problem of multihull wave resistance is discussed, including the generalised Michell integral and Krein's zero-drag caravans. Some work done at Adelaide over the past two years on minimising the total (viscous plus wave) drag of multihull ships using the genetic algorithm technique is summarised. Recent work on a pair of tandem submerged cylinders is also discussed, including identification of configurations having zero drag on each separate body.

Remarks on Energy Transport in Waves

Marshall P. Tulin
Director, Ocean Engineering Laboratory
University of California, Santa Barbara

Preface *In 1950 I arrived at the Taylor Model Basin in Washington, age 24, to begin work in naval hydrodynamics. George Weinblum was 53 then. He had arrived there 2 years earlier after a stay in England, and was to return to Hamburg two years later. He was a large man, with a very large head and twinkly eyes, of immense charm and diplomacy and talent, of great sharp wit, and with an international view of life. He seemed somewhat the bohemian.*

He had already made a large impact on the very talented people there, including John Wehausen, Manley St. Denis, Lou Landweber (our Boss), Phil Eisenberg, Bill Cummins, John Breslin, Dick Couch, and others. He loved young people, and he went out of his way to encourage us. His deep faith in the necessity to treat naval architecture problems in a scientific way made a deep and lasting impression on us all, especially considering that he was a man of practical experience.

Despite the tentativeness of life away from his family and homeland, and without a fixed position, I believe that during this period his life was a very happy one. He was well liked by everyone and loved by more than a few persons.

In tribute to him I want to point out that he had a very considerable positive influence on people there, who themselves went on to have a great effect on naval architecture and naval hydrodynamics in our country, and on education in those fields.

Remarks

Is it possible to say anything new about this subject, which is in all relevant texts covered by introduction of the notion of group velocity? Now it is true that the subject of the group velocity includes puzzling aspects. For example, the connection between the parallel and separate treatments of group velocity via kinematical and/or dynamical demonstrations, leading in the case of linear waves to identical results.

And, beyond that, the question as to the proper treatment and results in the case of finite amplitude waves.

The present remarks are however not concerned directly with these questions. Our concern is even more basic. It can be put in this question: What is it that physically propagates at the group velocity? Obviously the difficulty in answering lies in the fact that the energy in surface waves is compartmented in two parts: kinetic and potential. It has been customary to treat these as a sum, and it is the sum of these which demonstrations suggest are propagated at the group velocity. Furthermore, the kinetic energy has been treated not only as averaged in time, but also in the vertical direction.

Unfortunately, this customary treatment hides from our view the real mechanisms of energy transport in water waves, and obscures the real meaning of group velocity, which in actuality is an arithmetic mean. The answer to the question underlined above is: only the modulated wave envelope propagates physically at the group velocity.

Proper understanding of the subject requires consideration of the kinetic energy flux vector at all points in the wave, and separate consideration of the surface energy, which itself consists of two parts, gravitational and surface tension. It is also necessary to conceptualize the waves not as a uniform Stokes wave, but as a wave whose amplitude is changing in space and time. It is only when these things are done that the actual mechanisms of wave energy transport reveal themselves clearly.

Then it can be shown that in the case of monochromatic gravity waves, the time averaged kinetic energy at every depth below the wave trough propagates horizontally at speeds between one and two times the phase speed of the wave, depending on the water depth. In a frame moving with the wave speed, the kinetic energy at each point can be seen to propagate along flux lines which extend beneath the surface from one point to another on the wave surface. these lines are arranged in four cells per wavelength, Figure 1, and in shallow water the cells containing flux in the wave propagation direction are more dominant, resulting in a net forward flux relative to the moving wave.

For all waves, the time averaged gravitational potential energy does not propagate at all, while the (linearized) surface tension energy propagates at twice the wave phase velocity. The net result is that the transport speed calculated as a weighted average of the transport of the separate components of energy yields the familiar group velocity.

In the case of a modulating gravity wave the kinetic energy propagates vertically as well as horizontally and in this way provides the potential energy at the surface to the forward face of a wave group and extracts it from the surface in the opposite case, Figure 2. It is due to this mechanism of exchange between gravitational and kinetic energies that the modulation is allowed to propagate, and the speed of propagation for weak waves is precisely the group velocity.

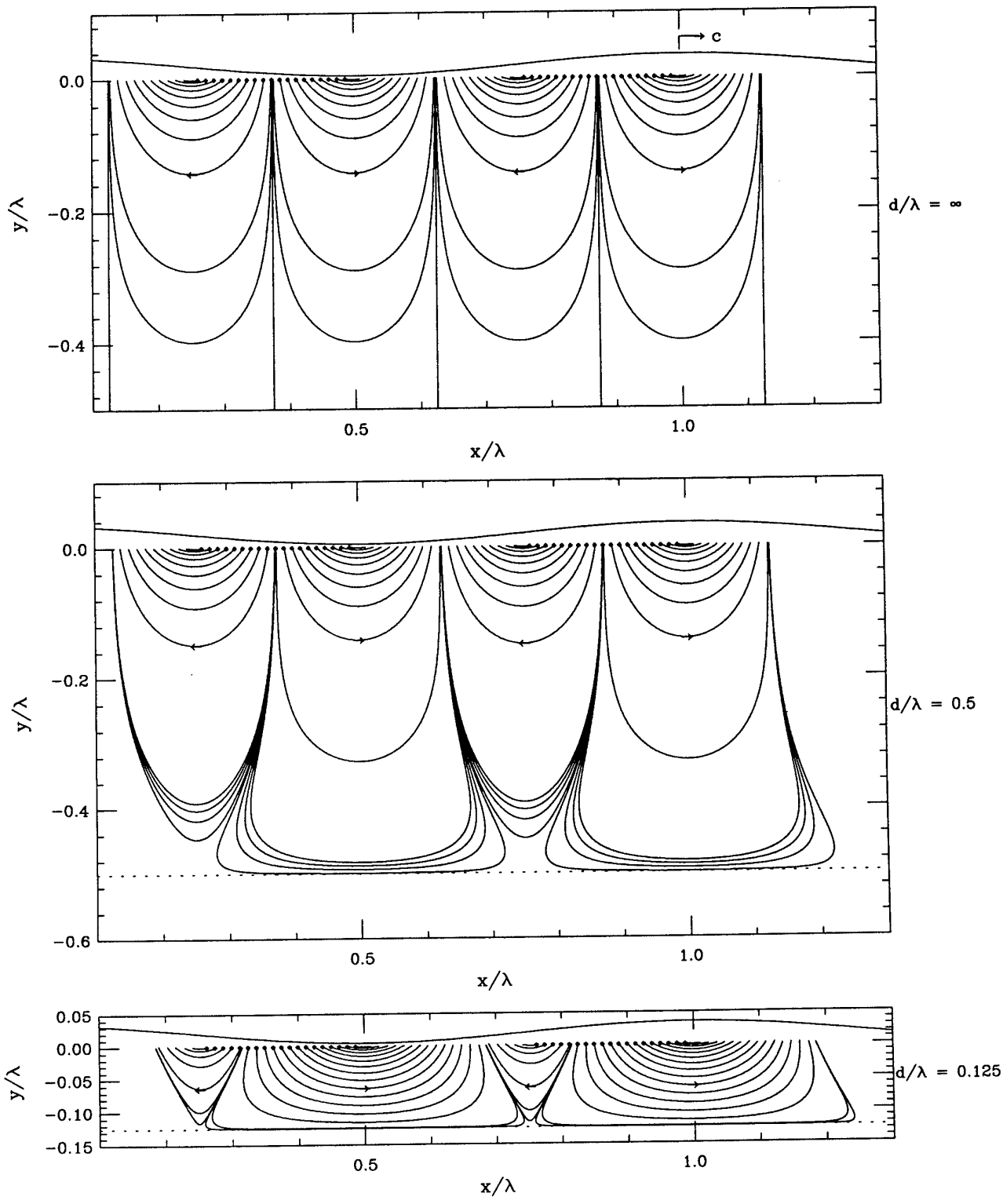

Kinetic Energy Flux under Monochromatic Waves

Figure 1

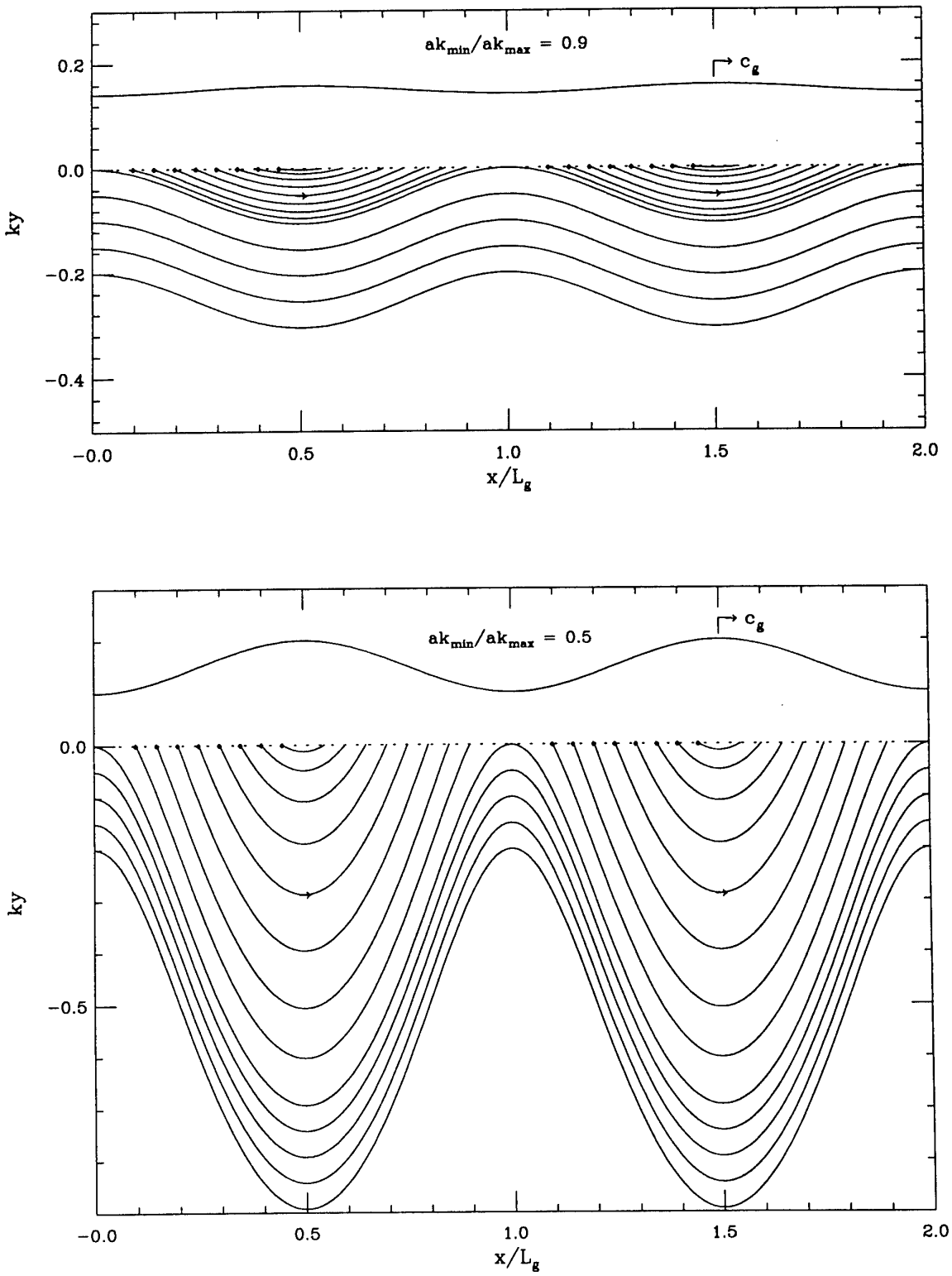

Kinetic Energy Flux in Wave Groups

Figure 2

NOTES ON WAVE MOTION NEAR A SPHERE BETWEEN PARALLEL WALLS

BY F.URSELL

DEPARTMENT OF MATHEMATICS,
MANCHESTER UNIVERSITY, M13 9PL, U.K.

1 Introduction

The following problem was proposed to me by G.X. Wu at the 1996 Workshop in Hamburg . A submerged sphere of radius a is placed with its centre at depth f midway between parallel vertical walls $x = \pm\ell$, where $\ell > a$, and performs prescribed simple harmonic oscillations of angular frequency ω and small amplitude. How can the motion be calculated ? Problems of this type in two dimensions are well understood , how can the methods be generalized ? It will be seen that the three-dimensional solution involves much mathematical analysis, and only an outline will be given here.

Rectangular cartesian axes (x, y, z) are taken with the origin O in the mean free surface $y = 0$, where y increases with depth. Let the corresponding velocity potential be denoted by $\phi(x, y, z)\exp(-i\omega t)$. (The time-factor $\exp(-i\omega t)$ will henceforth be omitted.) Then the governing equation is

$$\left(\frac{\partial^2}{\partial x^2} + \frac{\partial^2}{\partial y^2} + \frac{\partial^2}{\partial z^2}\right)\phi(x, y, z) = 0, \tag{1.1}$$

with the boundary condition

$$K\phi + \frac{\partial\phi}{\partial y} = 0 \text{ on } y = 0, \tag{1.2}$$

where $K = \omega^2/g$, and the boundary condition

$$\frac{\partial\phi}{\partial x} = 0 \text{ on } x = \pm\ell. \tag{1.3}$$

We take spherical polar coordinates (r, θ, α) about the centre $(0, f, 0)$ of the sphere, such that

$$x = r\sin\theta\sin\alpha, y = f + r\cos\theta, z = r\sin\theta\cos\alpha, \text{ where } r^2 = x^2 + (y - f)^2 + z^2. \tag{1.4}$$

The boundary condition on the sphere $r = a$ is assumed to be of the form

$$\frac{\partial\phi}{\partial r} = U(\theta, \alpha) = \sum_{n=0}^{\infty}\sum_{m=0}^{n} U_n^m \mathrm{P}_n^m(\cos\theta)\cos m\alpha, \text{ say }, \tag{1.5}$$

where $U(\theta, \alpha)$ is a prescribed even function of α, and the coefficients U_n^m are therefore assumed known. (Odd functions of α can be treated in the same way.) The functions P_n^m are the usual associated Legendre functions, see [Bateman, I, 1953]. There is also a radiation condition at infinity: the waves travel outwards towards $z = \pm\infty$.

2 Outline of the solution

The solution will make use of the method of multipoles. A typical solution of Laplace's equation singular at the centre of the sphere is $r^{-n-1}\mathrm{P}_n^m(\cos\theta)\cos m\alpha$. In the absence of side walls the multipole potential (including the image in the free surface) can be shown to be

$$\begin{aligned}(G_n^m)_\infty &= G_n^m(x, y, z; 0, f, 0; \infty) \\ &= \frac{\mathrm{P}_n^m(\cos\theta)}{r^{n+1}}\cos m\alpha + \frac{(-1)^n}{(n-m)!}\int_0^\infty \frac{k + K}{k - K}\, k^n\, e^{-k(y+f)} J_m(k\rho)\, dk \cos m\alpha,\end{aligned} \tag{2.1}$$

where $J_m(Z)$ is the usual Bessel function of order m, see [Bateman, II, 1953], and where the radiation condition is satisfied if the contour of integration passes below the pole $k = K$. When side walls are present then each multipole (2.1) has an image potential $(G_n^m)_{image}$ in the side walls. We write

$$(G_n^m)_\ell = (G_n^m)_\infty + (G_n^m)_{image},$$

Evidently near the centre of the sphere the image potential $(G_n^m)_{image}$ must have an expansion of the form

$$\sum_{N=0}^{\infty} \sum_{M=0}^{N} a(n,m;N,M)\, r^N\, \mathrm{P}_N^M(\cos\theta)\, \cos M\alpha. \tag{2.2}$$

For the solution of our boundary-value problem the coefficients $a(n,m;N,M)$ in (2.2) must be known explicitly, and our recent work has shown that the coefficients in this expansion can actually be found in a form involving single and double integrals. We shall now assume (and it should not be difficult to prove) that the solution of our problem can be expressed as the sum

$$\phi(x,y,z) = \sum_{n=0}^{\infty} \sum_{m=0}^{n} C(n,m) a^{n+1} (G_n^m)_\ell, \tag{2.3}$$

where the coefficients $C(n,m)$ are to be determined from the boundary condition on the sphere. This will be satisfied if the coefficients $C(n,m)$ satisfy a doubly infinite system of the form

$$C(n,m) + \sum_{N=0}^{\infty} \sum_{M=0}^{N} \left(\frac{a}{\ell}\right)^{N+n+1} b(n,m:N,M)\, C(N,M) = U_n^m, \tag{2.4}$$

and in this system the coefficients $b(n,m;N,M)$ are known explicitly as double or single integrals. These coefficients depend on n, m, N and M, and also on the parameters Kf and f/ℓ, and it remains to compute them numerically. The doubly-infinite system (2.4) must then be solved for each set of values of the three parameters $Kf, f/\ell$ and a/ℓ. It should not be difficult to show that this system has a solution in principle, except possibly at a certain discrete set of frequencies corresponding to trapped modes.

3 Construction of the multipole potentials $(G_n^m)_\ell$

In the construction of the multipoles $(G_n^m)_\ell$ an important part is played by various forms of the Havelock wavemaker theory, see [Havelock, 1929]. Havelock expansions are expansions in which the variation in the y-direction is expressed in the form

$$f(y) = Ae^{-Ky} + \int_0^\infty B(k)(k\cos ky - K\sin ky)\, dk, \tag{3.1}$$

where

$$A = 2K \int_0^\infty f(y) e^{-Ky}\, dy, \tag{3.2}$$

and

$$B(k) = \frac{2}{\pi(K^2+k^2)} \int_0^\infty f(y)(k\cos ky - K\sin ky)\, dy. \tag{3.3}$$

This expansion is associated with the boundary condition (1.2) . Here we shall consider only the case $n = m = 0$ which is typical, and we shall write G_∞ and G_ℓ in place of $(G_0^0)_\infty$ and $(G_0^0)_\ell$. As has already been seen in (2.1), we find that

$$G_\infty = \frac{1}{r} + \int_0^\infty e^{-k(y+f)} \frac{k+K}{k-K} J_0(k\rho) dk, \tag{3.4}$$

where it can be shown that the radiation condition is satisfied if the path of integration passes below the pole $k = K$. We also need two Havelock expansions for G_∞ in rectangular coordinates. One of these

is valid for $x > 0$, the other is valid for $x < 0$. These can be found explicitly, either by deforming the contour of integration in (3.4) or by using Green's Theorem. It is found that

$$G_\infty(x,y,z) = 2Ke^{-K(y+f)} \int_{-\infty}^{\infty} \frac{d\nu}{(\nu^2-K^2)^{1/2}} \exp\{-|x|(\nu^2-K^2)^{1/2}\}e^{-i\nu z} \tag{3.5}$$

$$+ \frac{2}{\pi}\int_0^\infty \frac{dk}{K^2+k^2}(k\cos ky - K\sin ky)(k\cos kf - K\sin kf) \times$$

$$\times \int_{-\infty}^{\infty} \frac{d\nu}{(\nu^2+k^2)^{1/2}} \exp\{-|x|(\nu^2+k^2)^{1/2}\}e^{-i\nu z}, \tag{3.6}$$

where the contour of integration in (3.5) passes above $k = -K$ and below $k = K$. We next suppose that side walls are present. Then the image potential must have a Havelock expansion of the form

$$G_{image}(x,y,z) = e^{-Ky}\int_{-\infty}^{\infty} d\nu\, A(\nu)\, \cosh\{x(\nu^2-K^2)^{1/2}\}e^{-i\nu z} \tag{3.7}$$

$$+ \frac{2}{\pi}\int_0^\infty dk(k\cos ky - K\sin ky)\int_{-\infty}^{\infty} d\nu\, B(k,\nu)\, \cosh\{x(\nu^2+k^2)^{1/2}\}e^{-i\nu z}, \tag{3.8}$$

because it is clearly an even function of x. From the boundary condition

$$\frac{\partial}{\partial x}(G_\infty(x) + G_{image}(x)) = 0 \text{ on } x = \ell$$

we can now find $A(\nu)$ and $B(k,\nu)$, using the Havelock expansions (3.5) and (3.6) for G_∞. We find that

$$(\nu^2-K^2)^{1/2}A(\nu)\{\sinh \ell(\nu^2-K^2)^{1/2}\} - 2Ke^{-Kf}\exp\{-\ell(\nu^2-K^2)^{1/2}\} = 0, \tag{3.9}$$

and

$$B(k,\nu)(\nu^2+k^2)^{1/2}\sinh\{\ell(\nu^2+k^2)^{1/2}\} - \frac{k\cos kf - K\sin kf}{K^2+k^2}\exp\{-\ell(\nu^2+k^2)^{1/2}\} = 0. \tag{3.10}$$

This completes the construction of the potential G_ℓ.

4 Expansion near the centre of the sphere

The integrals (3.7) and (3.8) are typically of the form

$$I(x,y,z) = \int A(v)\exp\{\xi(v)x + \eta(v)y + \zeta(v)z\}\, dv, \tag{4.1}$$

where the integrals may be single or double integrals, and where

$$\xi^2 + \eta^2 + \zeta^2 = 0,$$

since the integral satisfies Laplace's equation. In the integral (4.1) we write

$$\xi = i\eta(v)\cos\beta(v),\ \zeta = i\eta(v)\sin\beta(v) \text{ and } x = r\sin\theta\sin\alpha, y = f + r\cos\theta, z = r\sin\theta\cos\alpha. \tag{4.2}$$

Then

$$I(x,y,z) = \int A(v)\exp(\eta(v)f)\exp\left(\eta r\{\cos\theta + i\sin\theta\sin(\alpha+\beta(v))\}\right)\, dv. \tag{4.3}$$

In this integral we write

$$\exp\left(\eta r\{\cos\theta + i\sin\theta\sin(\alpha+\beta(v))\}\right) = \sum_{N=0}^{\infty}\frac{(\eta r)^N}{N!}\{\cos\theta + i\sin\theta\sin(\alpha+\beta(v))\}^N, \tag{4.4}$$

and in the series we use the known identity

$$\begin{aligned}(\cos\theta + i\sin\theta\cos(\alpha+\beta))^N \\ = \ & \mathrm{P}_N(\cos\theta) \\ + \ & 2\sum_{M=1}^{N}(-i)^M\frac{N!}{(N+M)!}\mathrm{P}_N^M(\cos\theta)(\cos M\alpha\cos M\beta - \sin M\alpha\sin M\beta). \end{aligned} \tag{4.5}$$

This argument shows that the coefficient of $r^N\mathrm{P}_N^M(\cos\theta)\cos M\alpha$ in (2.2) involves the integral

$$\int A(v)\exp\{\eta(v)f\}\{\eta(v)\}^N\cos M\beta(v)\,dv.$$

In this way all the coefficients can be determined, and the boundary condition on the sphere can then be applied.

5 Discussion

There are still many aspects which we have not discussed. We mention only a few.

(1) The precise form of the coefficients $b(n,m:N,M)$ in equation (2.4) must be studied; these involve six parameters . Calculations show that these coefficients actually depend on fewer parameters. Similarly in two dimensions the parameters depend on three parameters, not on four.

(2) For $|z| > a$ there must be a modal expansion in each direction, of the form

$$(G_n^m)_\ell = \frac{1}{2}\Phi_n^m(y,z;0;\ell) + \sum_{s=1}^{\infty}\cos\frac{s\pi x}{\ell}\Phi_n^m(y,z;s;\ell), \tag{5.1}$$

where the functions $\Phi_n^m(y,z;s;\ell)$ must be found. It has been shown that these functions have Havelock expansions in the y-direction and can be found either by deformation of contours or by Green's Theorem.

(3) The method can readily be extended to the general case where the centre of the sphere is not necessarily midway between the vertical walls.

(4) We have not discussed the expansion of G_∞ near the sphere. This presents little difficulty. We have already noted that the calculation of the expansion for the general multipole potential $(G_n^m)_\ell$ is similar to the calculation for the source potential, given above.

References

[Bateman, I, 1953] *Bateman Project, Higher Transcendental Functions,* Vol.1. New York, McGraw-Hill

[Bateman, II, 1953] *Bateman Project, Higher Transcendental Functions,* Vol.2. New York, McGraw-Hill

[Havelock, 1929] Forced surface-waves on water. Phil.Mag. (7), 8, 1929, 569-576

On modeling nonlinear water waves

by Theodore Yaotsu Wu
California Institute of Technology, Pasadena, CA 91125, U.S.A.

1 Introduction

My interest in studying nonlinear dispersive long waves has an origin in the stimuli I received from Professor Georg Weinblum during my sabbatical visit in 1964-65 at the Schiffbau Instituet. Apparently, there had been in existence among a handful of the master experimentalists a puzzle that in conducting towing tank tests with ship models towed at transcritical velocities in shallow water, perplexing difficulties were invariably encountered in attempt to attain data with the ususal repeatability commonly known to their previous experience with noncritical cases. Subsequent studies later led to the interesting discoveries reported by Huang et al. (1982) and Wu & Wu (1982).

In modeling weakly nonlinear and weakly dispersive long waves, it has been a common practice to taking two key parameters, namely

$$\epsilon = h/\lambda\ , \qquad \alpha = a/h, \tag{1}$$

for characterising waves of typical length λ, amplitude a in water of undisturbed depth h. In this respect, it is so well said by Julian Cole (1968) that theories can be sought to show how different expansions based on different parametric regimes lead to different approximate equations.

In making attempts to explore and determine the basic mechanism underlying the remarkable phenomenon of periodic generation of upstream-radiating solitons by disturbances moving steadily at transcritical velocity, efforts have been devoted to examine the effects of theoreticl models of accuracy higher than that of Boussinesq's equations, as demonstrated by a previous study by Wu & Zhang (1996). To facilitate further studies, this work is an attempt to establish an exact model for describing propagation and generaton of nonlinear dispersive gravity-capillary waves of arbitrary amplitude on water of uniform depth. With this study, I wish to join my colleagues to commemorate the Centennial Celebration of Georg Weinblum.

2 The basic equations

Here we consider the class of three-dimensional long waves on a layer of water of uniform depth h, when undisturbed. The fluid moving with velocity $(\boldsymbol{u}, w) = (u, v, w)$ occupies the flow field in $-h \le z \le \zeta(\boldsymbol{r}, t)$, where $z = -h$ is a rigid horizontal bottom, $\zeta(\boldsymbol{r}, t)$ is the water surface elevation from the undisturbed plane at $z = 0$, measured at the horizontal position vector $\boldsymbol{r} = (x, y, 0)$ at time t, and $\boldsymbol{r}$ is unbounded, $|\boldsymbol{r}| < \infty$. Assuming the fluid incompressible, the velocity field irrotational, so the motion satisfies the Euler equations of continuity, horizontal and vertical momentum:

$$\nabla \cdot \boldsymbol{u} + w_z = 0, \tag{2}$$

$$\frac{d\boldsymbol{u}}{dt} = \boldsymbol{u}_t + \boldsymbol{u} \cdot \nabla \boldsymbol{u} + w\boldsymbol{u}_z = -\frac{1}{\rho}\nabla p, \tag{3}$$

$$\frac{dw}{dt} = w_t + \boldsymbol{u} \cdot \nabla w + ww_z = -\frac{1}{\rho}p_z - g, \tag{4}$$

where $\nabla = (\partial_x, \partial_y, 0)$, ($\partial_x = \partial/\partial x$, etc.) is the horizontal projection of the vector gradient operator, p is the pressure, ρ the density and g the gravitational acceleration. Here, the subscripts t and z

denote differentiation. The boundary conditions are

$$w = D\zeta \qquad (D = \partial_t + \hat{\boldsymbol{u}} \cdot \nabla, \quad \text{on } z = \zeta(\boldsymbol{r}, t)), \tag{5}$$

$$p = p_a(\boldsymbol{r}, t) - \rho\gamma\nabla \cdot \boldsymbol{n} \qquad (z = \zeta(\boldsymbol{r}, t)), \tag{6}$$

$$w = 0 \qquad (z = -h), \tag{7}$$

where $p_a(\boldsymbol{r}, t)$ is a given external pressure disturbance gaged over the constant basic pressure (which is zero), $\rho\gamma$ is the uniform surface tension and $\boldsymbol{n}$ is the outward unit vector normal to the water surface.

The continuity equation (1) can be averaged over the water column $-h < z < \zeta$ under the kinematic boundary conditions (5) and (7), yielding the depth-mean continuity equation (Wu 1979, 1981),

$$\eta_t + \nabla \cdot (\eta\overline{\boldsymbol{u}}) \;=\; 0 \quad (\eta = h + \zeta), \tag{8}$$

where the quantities with an overhead bar denote their depth-mean,

$$\overline{f}(\boldsymbol{r}, t) = \frac{1}{\eta}\int_{-h}^{\zeta} f(\boldsymbol{r}, z, t)dz \quad (\eta = h + \zeta), \tag{9}$$

On the other hand, the horizontal momentum equation can be converted into an equation for $(\hat{\boldsymbol{u}}, \zeta)$ where $\hat{\boldsymbol{u}}$ is the horizontal velocity at the water surface. For an arbitrary flow variable $f(\boldsymbol{r}, z, t)$, it assumes its free surface value

$$f(\boldsymbol{r},\ \zeta(\boldsymbol{r}, t), t) = \hat{f}(\boldsymbol{r}, t), \tag{10}$$

say. Clearly, the rates of variation of these functions with respect to $\boldsymbol{r}$ and t satisfy the following relations

$$\partial_t\hat{f} = \partial_t f \;+\; \frac{\partial f}{\partial z}\Big|_\zeta \partial_t\zeta \qquad (z = \zeta), \tag{11}$$

$$\nabla\hat{f} = \nabla f \;+\; \frac{\partial f}{\partial z}\Big|_\zeta \nabla\zeta \qquad (z = \zeta). \tag{12}$$

¿From these fundamental relations it immediately follows that we have the theorem (see e.g. Choi 1995)

$$\frac{df}{dt}\Big|_{z=\zeta} = D\hat{f} \qquad (D = \partial_t + \hat{\boldsymbol{u}} \cdot \nabla) \tag{13}$$

Making use of these formulas, we readily deduce from (2)-(4) the result

$$D\hat{\boldsymbol{u}} + [g(t) + D^2\zeta]\nabla\zeta = -\frac{1}{\rho}\nabla p_a + \gamma\nabla \cdot \boldsymbol{n} \tag{14}$$

Here, we have extended our consideration to include the more general case of Faraday's waves produced in a horizontal water tank under resonant vibration, a case which is equivalent to having a time-dependent gravity acceleration with refenence to the tank frame. This resulting equation, though superficially involving only $(\hat{\boldsymbol{u}}, \zeta)$, actually has incorporated the vertical momentum equation as well as the kinematic and dynamic conditions at the free surface to yield this equation of overall equilibrium. Furthermore, it is exact.

Thus, we have obtained two exact equations, one being the depth-mean continuity quation (8) for $(\overline{\boldsymbol{u}}, \zeta)$, and the other the momentum equation (14) for $(\hat{\boldsymbol{u}}, \zeta)$. This system of equations, however, is not closed because there are more unknown variables than the number of equations. Closure of the system can be achieved by further seeking the general solution to the field equation satisfied by the velocity potentail so as to provide an exact relation between the two sets of dependent variables, as will be shown below.

3 Nonlinear dispersive water wave models

Since the two new equations for the continuity and momentum are exact, we may ignore the nonlinearity parameter α by regarding it as arbitrary and consider first the special case of long waves by assuming the dispersion parameter $\epsilon = h/\lambda$ to be small. (It turns out that this assumption can also be eventually relaxed.)

Thus, with the vertical length scaled by h, horizontal length by λ, the three-dimensional Laplace equation satisfied by the velocity potential ϕ involves the parameter ϵ

$$\phi_{zz} + \epsilon^2 \nabla^2 \phi = 0 \qquad (-1 \le z \le \zeta). \tag{15}$$

Further, with ϕ scaled by $c\lambda$, where $c = \sqrt{gh}$ is the linear wave speed, ϕ satisfying (12) may assume an expansion of the form

$$\phi(\boldsymbol{r}, z, t; \alpha, \epsilon) = \alpha \sum_{n=0}^{\infty} \epsilon^{2n} \Phi_n(\boldsymbol{r}, z, t) = \alpha \sum_{n=0}^{\infty} \frac{(-1)^n}{(2n)!} [\epsilon(1+z)]^{2n} \nabla^{2n} \phi_0(\boldsymbol{r}, t; \epsilon). \tag{16}$$

Here, ϕ, jointly with the horizontal velocity $\boldsymbol{u}$ (scaled by c) and the elevation ζ (scaled by h) are assumed to be of order α, which is arbitrary. The function $\phi_0(\boldsymbol{r}, z, t; \epsilon)$, which is the only unknown involved in ϕ, may depend on the parameter ϵ resulting from appropriate regroupings of the complimentary solutions of the higher-order equations such that $\phi_0(\boldsymbol{r}, z, t; \epsilon) = O(1)$ as $\epsilon \to 0$. This regrouping is admissible provided the medium is uniform (h =const.) and unbounded, in the absence of any boundary effects of specific order in magnitude. From this expansion of ϕ, we deduce the horizontal and vertical velocity components, $\boldsymbol{u}$ and w, both scaled by c, from $\boldsymbol{u} = \nabla\phi$, $w = \epsilon^{-1} \partial\phi/\partial z$, giving

$$\boldsymbol{u} = \alpha \sum_{n=0}^{\infty} \epsilon^{2n} \boldsymbol{u}_n = \alpha \sum_{n=0}^{\infty} \frac{(-1)^n}{(2n)!} [\epsilon(1+z)]^{2n} \nabla^{2n+1} \phi_0(\boldsymbol{r}, t; \epsilon), \tag{17}$$

$$w = \alpha \sum_{n=1}^{\infty} \epsilon^{2n-1} w_n = \alpha \sum_{n=1}^{\infty} \frac{(-1)^n}{(2n-1)!} [\epsilon(1+z)]^{2n-1} \nabla^{2n} \phi_0(\boldsymbol{r}, t; \epsilon), \tag{18}$$

where $\boldsymbol{u}_0(\boldsymbol{r}, t) = \nabla\phi_0$. Now, the horizontal velocity at the bottom plane ($z = -1$) is simply

$$\alpha \boldsymbol{u}_0 = \alpha \nabla \phi_0. \tag{19}$$

We further have the depth-mean velocity $\overline{\boldsymbol{u}}$ and the on-surface velocity $\hat{\boldsymbol{u}}$ as

$$\overline{\boldsymbol{u}} = \alpha \sum_{n=0}^{\infty} \frac{(-1)^n}{(2n+1)!} [\epsilon(1+\zeta)]^{2n} \nabla^{2n} \boldsymbol{u}_0, \tag{20}$$

$$\hat{\boldsymbol{u}} = \alpha \sum_{n=0}^{\infty} \frac{(-1)^n}{(2n)!} [\epsilon(1+\zeta)]^{2n} \nabla^{2n} \boldsymbol{u}_0. \tag{21}$$

The present solution is of significance in drawing the conclusion that if $\boldsymbol{u}_o$ is analytic everywhere in the flow domain, the above series are all convergent within their radius of convergence, which is infinite. In such circumstances, the last two equations then define the functions

$$\overline{\boldsymbol{u}} = \overline{\boldsymbol{u}}(\boldsymbol{u}_o, \zeta) \qquad \text{and} \qquad \hat{\boldsymbol{u}} = \hat{\boldsymbol{u}}(\boldsymbol{u}_o, \zeta) \tag{22}$$

as analytic within the flow domain. Finally, from this result we may derive any one of the three basic sets of velocities, explicitly as a function of another by means of series inversion, the resulting series being noted to possess a finite radius of convergence.

In summary, we have now obtained three sets of models for describing nonlinear dispersive gravity-capillary waves on water of uniform depth in terms of the three sets of basic variables. In principle, these three models are equivalent in being exact for predicting this class of waves without limitation to the order of nonlinearity and dispersion, except that the fluid is taken to be incompressible and the flow, irrotational. For numerical computation based on these models, effective algorithms are being investigated. For the special case of nonlinear waves under small dispersive effects represented with the series truncated to some high orders, reference is made to Wu and Zhang (1996).

References

[1] Choi, W. 1995 Nonlinear evolution equations for two-dimensional surface waves in a fluid of finite depth. *J. Fluid Mech.* **295**, 381-394.

[2] Cole, J. D. 1968 *Perturbation methods in applied mathematics*, Blaisdell Pub. Co..

[3] Huang, D.B., Sibul. O.J, Webster,W.C., Wehausen, J.V., Wu. D.M. & Wu. T.Y., 1982 Proc. Conf. Behavior of ship in restricted waters, Varna: Bulgarian Ship Hydrodynamics Center, 1982

[4] Wu, T. Y. 1979 *Tsunamis – Proc. National Science Foundation Workshop*, May 7-9, 1979, pp. 110-149, Pasadena: Tetra Tech. Inc.

[5] Wu, T. Y. 1981 Long waves in ocean and coastal waters. *J. Engng Mech. Div. ASCE* **107**, 501-522.

[6] Wu, D.M. & Wu, T.Y., 1982 Three-dimensional nonlinear long waves due to moving surface pressure, Proc. 14th Symp. on Naval Hydrodynamics, Ann Arbor, Mich., USA, 102-125.

[7] Wu, T.Y. & Zhang, J.E. 1996 On modeling nonlinear long waves. In "Mathematics is for solving problems: A Volume in honor of Julian Cole on his 70th brithday, 233-249, SIAM

Georg Weinblum Memorial Lectures

1978/79	JOHN V. WEHAUSEN Ship Theory, Ship Design and Georg Weinblum. Transient Phenomena Observed in Passage over Obstructions
1979/80	OTTO GRIM Propeller and Vane Wheel as Possible Propulsion Device for Ships
1980/81	TAKAO INUI From Bulbous Bow to Free Surface Shock Wave – Twenty Years' Trend of Researches on Ship Waves at the Tokyo University Tank
1981/82	LOUIS LANDWEBER Interactions between Viscosity and Ship Waves
1982/83	GEORGE E. GADD Some Effects of Scale in Ship Model Testing
1983/84	THEODORE Y. WU The Shallow Water Effects – Do Steady Disturbances Always Result in Steady Responses?
1984/85	MARSHALL P. TULIN Surface Waves from the Ray Point of View
1985/86	FRITZ J. URSELL Mathematical Observations on the Method of Multipoles
1986/87	SOM DEO SHARMA On the So-Called Memory Effect in Ship Hydrodynamics
1987/88	HAJIME MARUO Evolution of the Theory of Slender Ships
1988/89	JOHN NICHOLAS NEWMAN The Numerical Towing Tank – Fact or Fiction?
1989/90	KARL WIEGHARDT A Characteristic of Three-Dimensional Free Turbulence
1990/91	ERNEST OLIVER TUCK Ship-Hydrodynamic Free-Surface Problems without Waves
1991/92	JOHN PERSHING BRESLIN Induced Effects on Propeller Inflows
1992/93	ODD MAGNUS FALTINSEN On Seakeeping of Conventional and High-Speed Vessels
1993/94	MASATOSHI BESSHO A Consistent Linearized Theory of Wave-making Resistance of Ships
1994/95	TOUVIA MILOH Ship Motion in Non-Homogeneous Media
1995/96	LARS LARSSON CFD in Ship Design – Prospects and Limitations
1996/97	JUSTIN E. KERWIN Experience in Modeling and Computing Flows with Lift

List of participants

Twelfth International Workshop on Water Waves and Floating Bodies

B. ALESSANDRINI
Ecole Centrale de Nantes
LMF, DHN
1, Rue de la Noë
44071 NANTES Cedex 03, FRANCE
Fax: 33 2 40 37 25 23
bertrand.alessandrini@ec-nantes.fr

M. BA
CEAT
43, Avenue de l'Aérodrome
86036 Poitiers Cedex, FRANCE
Fax: 33 5 49 49 80 89
ba@algor.univ-poitiers.fr

P.J.F. BERKVENS
MARIN
POB 28
NL 6700 AA Wageningen, THE NETHERLANDS
Fax: 31 317 493 245
p.berkvens@marin.nl

H.B. BINGHAM
ICCH
Danish Hydraulic Institute
Agern Alle 5
DK-2970 Hoesholm, DENMARK
Fax: 45 45 76 25 67
hrb@dhi.dk

Ms A.K. BRATLAND
MARINTEK
Klaebuveien 192
N 7031 Trondheim, NORWAY
Fax: 47 55 99 69 28
anne.katrine.bratland@nho.hydro.com

B. BUCHMANN
ISVA - DTU
Building 115
DK 2800 Lyngby, DENMARK
Fax: 45 45 93 28 60
buchmann@isva.dtu.dk

J.A.P. ARANHA
Dept. of Naval and Ocean Engineering
EPUSP
Cidade Universitaria
CEP 05508-900 Sao Paolo, SP, BRAZIL
Fax: 55 11 818 5717
japaran@usp.br

R.F. BECK
University of Michigan
Dept. of Naval Architecture & Marine Eng.
2600 Draper Rd
48109 Ann Arbor, Michigan, USA
Fax: 1 313 936 88 20
rbeck@engin.umich.edu

V. BERTRAM
IFS
Univ. Hamburg
Lämmersieth 90
D-22305 HAMBURG, GERMANY
Fax: 49 40 29 84 31 99
bertram@schiffbau.uni-hamburg.d400.de

A. BORTHWICK
Oxford University
Dept. of Engineering Science
Parks Road
OX1 3PJ Oxford, UK
Fax: 44 1865 27 30 10
alistair.borthwick@eng.ox.ac.uk

J.P. BRESLIN
Calle Dinamarca 7
San Miguel de Salinas
03193 Alicante, SPAIN
Fax: 34 6 572 04 35

T.H.J. BUNNIK
Delft Univ. of Techn.
Dept. Applied Math.
Mekelweg 4
NL 2628 CD Delft, THE NETHERLANDS
Fax: 31 15 2787209
bunnik@twi.tudelft.nl

X-B. CHEN
BUREAU VERITAS (CRD)
10, Rue Jacques Daguerre
92565 Rueil-Malmaison Cedex, FRANCE
Fax: 33 1 47 14 43 99
xchen@bureauveritas.com

P.J. CLARK
Heriot-Watt University
Dept of Civil and Offshore Engineering EH14
4AS Edinburg, UK
Fax: 44 131 451 50 78
p.j.clark@hw.ac.uk

D. DANMEIER
M.I.T.
77, Massachusetts Ave.
Room 5-324
MA 02139 Cambridge, USA
Fax: 1 617 253 8125
danmeier@mit.edu

F. DESIT
DSA/SPN/ST/PFN/BS
8, Boulevard Victor
PARIS 00303 ARMEES, FRANCE
Fax: 33 1 40 59 23 91

Y. DOUTRELEAU
Bassin d'Essais des Carènes
Chaussée du Vexin
27100 VAL DE REUIL, FRANCE
Fax: 33 2 32 59 77 79
doutrele@becvdr.dga.fr

S. ETIENNE
ESIM
Dept. Génie Mer
Technopôle de Château-Gombert
13451 Marseille Cedex 20, FRANCE
Fax: 33 4 91 05 46 15
etienne@esim.imt-mrs.fr

O. FALTINSEN
Norwegian Inst. of Technology
N-7034 Trondheim, NORWAY
Fax: 47 73 59 55 28
oddfal@marin.ntnu.no

P. FERRANT
SIREHNA
Immeuble Atlanpole
1, Rue de la Noë
44071 Nantes Cedex 03, FRANCE
Fax: 33 2 40 74 17 36
pierre.ferrant@sirehna.ec-nantes.fr

J.M. CLARISSE
CEA/LV
94195 Villeneuve St Georges, FRANCE
Fax: 33 1 43 86 74 29
clarisse@limeil.cea.fr

A. CLEMENT
ECN - LMF
1, Rue de la Noë
44071 NANTES Cedex 03, FRANCE
Fax: 33 2 40 37 25 23
alain.clement@ec-nantes.fr

l'ICA J-C. DERN
DSA/SPN/ST/RIES
8, Bd Victor
00303 Armées, Paris, FRANCE
Fax: 33 1 40 59 16 64

F. DIAS
INLN
1361, Route des Lucioles
06560 VALBONNE, FRANCE
Fax: 33 4 93 65 25 17
fdias@bolero.unice.fr

R. EATOCK TAYLOR
Univ. of Oxford
Dept. of Eng. Science
Parks Road
OX1 3PJ UK Oxford, UK
Fax: 44 1865 27 30 10
r.eatocktaylor@eng.ox.ac.uk

D.V. EVANS
University of Bristol
School of Mathematics
University Walk
BS8 1TW Bristol, UK
Fax: 44 117 928 7999
d.v.evans@bristol.ac.uk

T.H. FARSTAD
AKER NC
Box 1358 VIKA
0113 Oslo, NORWAY
Fax: 47 22 94 59 00

Ms. S. FINNE
Matematisk Institutt
Box 1053 Blindern
N-0316 Oslo, NORWAY
Fax: 47 22 85 43 49
styrk@math.uio.no

E. FONTAINE
ECN - LMF
1, Rue de la Noë
44071 NANTES Cedex 03, FRANCE
Fax: 33 2 40 37 25 23
emmanuel.fontaine@ec-nantes.fr

A. GARAPON
ICCH
Danish Hydraulic Institute
Agern Allé 5
DK-2970 Horsholm, DENMARK
Fax: 45 45 76 25 67
ang@dhi.dk

G. GRAZIANI
Univ. Di Roma "La Sapienza"
Via Eudoss/Ana, 18
00184 Rome, ITALY
Fax: 39 6 484 854
giorgio@graziani.ing.uniroma1.it

S. GRILLI
University of Rhode Island
Dept. Ocean Eng.
211 sheets building
RI 02882 Narragansett, USA
Fax: 1 401 874 68 37
grilli@mistral.oce.uri.edu

A.J. HERMANS
Delft Univ. of Techn.
Dept. Applied Math.
Mekelweg 4
NL 2628 CD Delft, THE NETHERLANDS
Fax: 31 15 27 87 209
a.j.hermans@math.tudelft.nl

Y. HUANG
M.I.T.
Room 5-329
77, Massachusetts Avenue
MA 02139 Cambridge, USA
Fax: 1 617 253 81 25
yifeng@eolos.mit.edu

Y. HUGOT
ESIM
Dept. Génie Mer
Technopôle de Château-Gombert
13451 Marseille Cedex 20, FRANCE
Fax: 33 4 91 05 46 15

H. IWASHITA
IFS
Univ. Hamburg
Lämmersieth 90
D-22305 HAMBURG, GERMANY
Fax: 49 40 29 84 31 99
bertram@schiffbau.uni-hamburg.d400.de

A.M. FRANK
Computing Centre
Akademgorodok
660036 Krasnoyarsk, RUSSIA
Fax: 7 39 12 439 830
frank@sf.krasnoyarsk.su

L. GENTAZ
Ecole Centrale de Nantes
LMF, DHN
1, Rue de la Noë
44072 NANTES Cedex 03, FRANCE
Fax: 33 2 40 37 25 23
lionel.gentaz@ec-nantes.fr

D.M. GREAVES
Dept. of Mech Eng.
UCL
Torrington Place
WC1E 7JE London, UK
Fax: + 44 0171 388 01 80
d_greaves@meng.ucl.ac.uk

J. GRUE
Univ. of Oslo
Dept. of Mathematics
POB 1053 Blindern
N-0316 Oslo, NORWAY
Fax: 47 22 85 43 49
johng@math.uio.no

J. HUANG
Univ. of Oxford
Dept. of Eng. Science
Parks Road
OX1 3PJ UK Oxford, UK
Fax: 44 1865 27 30 10
jianbo.huang@eng.ox.ac.uk

Z.J. HUANG
Centre for Marine Vessel
Design and Research
POB 1000 Halifax
B3J 2X4 Nova Scotia, CANADA
Fax: 1 902 423 9734
huangz@newton.ccs.tuns.ca

R. HUIJSMANS
MARIN
P.O. Box 28
6700 AA Wageningen, THE
NETHERLANDS
Fax: 33 317 49 32 45
r.h.m.huijsmans@marin.nl

C.E. JANSON
Chalmers Univ. of Technology
NAOE
S-41296 Gothenburg, SWEDEN
Fax: 46 31 772 3699
cej@na.chalmers.se

S. KATO
Ship Research Institute
6-38-1 Shinkawa
Mitaka 181 Tokyo, JAPAN
Fax: 81 422 41 31 43
kato@srimot.go.jp

Ch. KHARIF
IRPHE
163, Avenue de Luminy
Case 903
13288 Marseille, Cedex 13, FRANCE
Fax: 33 4 91 41 96 20

Y. KIM
M.I.T.
Room 5-329
77, Massachusetts Avenue
MA 02139 Cambridge, USA
Fax: 1 617 253 81 25
yonghwan@argo.mit.edu

O. LAGET
PRINCIPIA
Zone Portuaire de Brégaillon
83507 La Seyne-sur-Mer, FRANCE
Fax: 33 4 94 06 58 83
princip@world-net.sct.fr

L. LARSSON
Chalmers Univ. of Technology
NAOE
S- 41296 Gothenburg, SWEDEN
Fax: 46 31 772 36 99
larsl@na.chalmers.se

Q.W. MA
Univ. College London
Dept. of Mech. Eng.
Torrington Place
WC1E 7JE London, UK
Fax:
ma-q@meng.ucl.ac.uh

S. MALENICA
BUREAU VERITAS (CRD)
10, Rue Jacques Daguerre
92565 Rueil-Malmaison Cedex, FRANCE
Fax: 33 1 47 14 43 99

S. MAYER
ICCH
Danish Hydraulic Institute
Agern Allé 5
DK-2970 Horsholm, DENMARK
Fax: 45 45 76 25 67
stm@dhi.dk

T. KHABAKHPASHEVA
zhemchuzhnaya 14-4
630090 Novosibirsk, RUSSIA
Fax: 7 383 2 35 40 50
tana@hydro.nsc.ru

M-H. KIM
Departement of Civil Engineering
Texas A&M University
College Station
TX 77843-3136, Texas, USA
Fax: 1 409 862 81 62
m-kim3@tamu.edu

N. KUZNETSOV
University of Bristol
School of Mathematics
University Walk
BS8 1TW UK Bristol, UK
Fax: 44 117 928 7999
n.kuznetsov@bristol.ac.uk

M. LANDRINI
INSEAN
Italian Ship Model Basin
Via di Vallerano 139
00128 ROMA, ITALY
Fax: 39 6 50 70 619
landrini@piva.ing.uniroma1.it

C.M. LINTON
Dept. of Mathematical Sciences
Loughborough University of Technology
Loughborough
LE11 3TU Leicestershire, UK
Fax: 44 15 09 223 969
c.m.linton@lboro.ac.uk

A. MAGEE
Bassin d'Essais des Carènes
Chaussée du Vexin
27100 Val de Reuil, FRANCE
Fax: 33 2 32 59 77 77
magee@becvdr.dga.fr

H. MARUO
Yokohama National University
98-34 Honmoku Manzaka
Naka-ku
231 Yokohama, JAPAN
Fax:

M. McIVER
Dept. of Mathematical Sciences
Loughborough University of Technology
Loughborough
LE11 3TU Leicestershire, UK
Fax: 44 1509 223 969
m.mciver@lboro.ac.uk

P. McIVER
Dept. of Mathematical Sciences
Loughborough University of Technology
Loughborough
LE11 3TU Leicestershire, UK
Fax: 44 1509 223 969
p.mciver@lboro.ac.uk

B. MOLIN
ESIM
Dept. Génie Mer
Technopôle de Château-Gombert
13451 Marseille Cedex 20, FRANCE
Fax: 33 4 91 05 46 15
molin@esim.imt-mrs.fr

J.C. MOULIJN
Delft Ship Hydro. Lab.
Mekelweg 2
2628 CD Delft, THE NETHERLANDS
Fax: 31 15 278 1836
j.moulijn@wbmt.tudelft.nl

M. NACIRI
S.B.M.
P.O. Box 199
MC 98007 Monaco Cedex, MONACO
Fax: 377 92 05 32 22

T. NGUYEN
Dept. Naval Architecture &
Offshore Engineering
University of California
CA 94720-1780 Berkeley, USA
Fax: 1 510 692 61 28
nguyen@eddy.berkeley.edu

J.O. NYGAARD
Univ. of Oslo
Dept. of Mathematics
POB 1053 Blindern
N-0316 Oslo, NORWAY
Fax: 47 22 85 43 49
jnygaard@math.uio.no

E. PALM
Institute of Mathematics
PO Box 1053 Blindern
N-0316 Oslo, NORWAY
Fax: 47 22 85 43 49
enokp@math.uio.no

M. PERLIN
University of Michigan
Dept of Naval Architecture
208 Name Building
MI 48109-2121 Ann Arbor, USA
Fax: 1 972 3 640 7334
mperlin@eng.tau.ac.il

T. MILOH
Univ. of Tel-Aviv
School of Eng.
Ramat-Aviv
69978 Tel-Aviv, ISRAEL
Fax: 972 3 640 7334
miloh@eng.tau.ac.il

O. MOTYGIN
Inst. of Problems of Mech. Eng.
V.O. Bolshoy
Pr. 61
199178 St Petersburg, RUSSIA
Fax: 7 812 2 178 614
mov@snark.ipme.ru

S. MURASHIGE
Ship Research Institute
Ministry of Transport
6-38-1, Shinkawa, Mitaka
181 Tokyo, JAPAN
Fax: 81 422 41 3056
sunao@srimot.go.jp

J.N. NEWMAN
MIT
Room 5-324
77, Massachusetts Ave.
MA 02139 Cambridge, USA
Fax: 1 617 253 8125
jnn@rainbow.mit.edu

F. NOBLESSE
CDNSWC
Code 542
MD 20084 Bethesda, USA
Fax: 1 301 227 3883
noblesse@dt.navy.mil

M. OHKUSU
RIAM
Kyushu University
6-1 Kasuga-kohen
816 Kasuga-city, JAPAN
Fax: 81 92 592 48 32
ohkusu@riam.kyushu-u.ac.jp

D.H. PEREGRINE
School of Mathematics
University Walk
BS8 1TW Bristol, UK
Fax: 44 117 928 7999
d.h.peregrine@bristol.ac.uk

D. PIZER
Japon Marine Science and
Technology Center
2-15 Natsushima-cho
237 Yokosuka, JAPAN
Fax: + 81 468 66 57 46
pizer@jamstec.go.jp

R. PORTER
School of Mathematics
University of Bristol
University Walk
BS8 1TW UK Bristol, UK
Fax: 44 117 928 7999
richard.porter@bris.ac.uk

R.C.T. RAINEY
W S Atkins
Berkshire House
171 High Holborn
WC1V 7AA London, UK
Fax: 44 171 379 8563

S.A. RIGAUD
PRINCIPIA
Zone Portuaire de Brégaillon
83507 La Seyne-sur-Mer, FRANCE
Fax: 33 4 94 06 58 83
princip@world-net.sct.fr

P.D. SCLAVOUNOS
M.I.T.
Room 5-326c
MA 02139 Cambridge, USA
Fax: 1 617 253 8125
pds@argo.mit.edu

S.M. SCORPIO
University of Michigan
Dept. of Naval Architecture & Marine Eng.
2600 Draper Rd
48109 Ann Arbor, Michigan, USA
Fax: 1 313 936 88 20
sscorpio@engin.umich.edu

O.D. SHISHKINA
Inst. of Applied Physics RAS
46, Ul'janov st.
603600 Nizhny Novgorod, RUSSIA
Fax: 7 831 2 365 976
ols@appl.sci-nnov.ru

J. SKOURUP
ICCH - DHI
Danish Hydraulic Institute
Agern Alle 5
DK-2970 Hoesholm, DENMARK
Fax: 45 45 76 25 67
jes@dhi.dk

K. TANIZAWA
Ship Research Institute
6-38-1, Shinkawa
181 Mitaka, Tokyo, JAPAN
Fax: 81 422 41 3056
tanizawa@srimot.go.jp

H. PUJOL
ESIM
Dept. Génie Mer
Technopôle de Château-Gombert
13451 Marseille Cedex 20, FRANCE
Fax: 33 4 91 05 46 15
pujol@esim.imt-mrs.fr

V. REY
I S I T V
B.P. 132
83957 LA GARDE Cedex, FRANCE
Fax: 33 4 94 14 324 48

W.W. SCHULTZ
University of Michigan
ME+AM
313 Auto Lab.
MI 48109-2121 Ann Arbor, USA
Fax: 1 313 764 42 56
schultz@engin.umich.edu

Y-M. SCOLAN
ESIM
Dept. Génie Mer
Technopôle de Château-Gombert
13451 Marseille Cedex 20, FRANCE
Fax: 33 4 91 05 46 15
scolan@esim.imt-mrs.fr

S.D. SHARMA
Mercator University
Institute of Ship Technology
Building BK
D-47048 Duisburg, GERMANY
Fax: 49 203 379 2779
sharma@nav.uni-duisburg.de

Ms L.M. SIEREVOGEL
Delft Univ. of Techn.
Dept. Techn. Math.
Mekelweg 4
NL 2628 CD Delft, THE NETHERLANDS
Fax: 31 15 278 7209
l.m.sierevogel@math.tudelft.nl

K. TAKAGI
Osaka Univ.
NA+OE
2-1 Yamadaoka Suita,
565 Osaka, JAPAN
Fax: 81 6 878 53 64
takagi@naoe.eng.osaka-u.ac.jp

G. TCHEOU
M.I.T.
Room 5-329
77, Massachusetts Avenue
MA 02139 Cambridge, USA
Fax: 1 617 253 81 25
gtcheou@mit.edu

E.O. TUCK
University of Adelaïde
Applied Math. Dept.
GPO Box 498
SA 500 Adelaïde, AUSTRALIA
Fax: 61 8 8303 3696
etuck@maths.adelaide.edu.au

F. URSELL
Dept. of Mathematics
Manchester University
M13 9PL Manchester, UK
Fax: 44 161 275 5819
fritz@ma.man.ac.uk

M. VOGT
Chalmers Univ. of Technology
NAOE
S-41296 Gothenburg, SWEDEN
Fax: 46 31 772 36 99
vogt@na.chalmers.se

J.V. WEHAUSEN
University of California
Nav. Arch. & Offshore Eng.
CA 94720 Berkeley, USA
Fax: 1 510 642 61 28
wehausen@garnet.berkeley.edu

T.Y. WU
California Institute of Technology
Room 104-44
CA 91125 Pasadena, USA
Fax: 1 818 795 9839
tywu@cco.caltech.edu

L. ZHANG
University of Oxford
Dept. of Eng. Science
Parks Road
OX1 3PJ Oxford, UK
Fax: 44 1865 27 30 10
liang.zhang@eng.ox.ac.uk

M.P. TULIN
University of California
Ocean Engineering Laboratory
CA 93106-1080 Santa-Barbara, USA
Fax: 1 805 893 49 27
mpt@vortex.ucsb.edu

R. VAN'T VEER
Delft Ship Hydro. Lab.
Mekelweg 2
2628 CD Delft, THE NETHERLANDS
Fax: 31 15 278 1836
r.vantveer@wbmt.tudelft.nl

W.C. WEBSTER
Students Affairs Office
College of Eng. 308
Mc Laughlin Hall 1702
CA 94720-1702 Berkeley, USA
Fax: 1 510 643 86 53
wwebster@coe.berkeley.edu

D.J. WOOD
School of Maths.
Univ. of Bristol
BS8 1TW Bristol, UK
Fax: 44 117 928 7999
deb.wood@bristol.ac.uk

R.W. YEUNG
Dept. Naval Architecture &
Offshore Engineering
University of California
CA 94720-1780 Berkeley, USA
Fax: 1 510 642 61 28
rwyeung@garnet.berkeley.edu

Q. ZHU
M.I.T.
Dept. of Ocean Eng.
Room 5-321
MA 02139 Cambridge, USA
Fax: 1 617 253 81 25
zhuqiang@mit.edu